Open Research Online

The Open University's repository of research publications
and other research outputs

Gravity studies of the Guayabo Caldera and the Miravalles geothermal field, Costa Rica

Thesis

How to cite:

Hallinan, Stephen Eric (1992). Gravity studies of the Guayabo Caldera and the Miravalles geothermal field, Costa Rica. PhD thesis The Open University.

For guidance on citations see FAQs.

© 1991 The Author

https://creativecommons.org/licenses/by-nc-nd/4.0/

Version: Version of Record

Link(s) to article on publisher's website:
http://dx.doi.org/doi:10.21954/ou.ro.0000d395

Copyright and Moral Rights for the articles on this site are retained by the individual authors and/or other copyright owners. For more information on Open Research Online's data policy on reuse of materials please consult the policies page.

oro.open.ac.uk

Gravity Studies of the Guayabo Caldera and the Miravalles Geothermal Field, Costa Rica.

A thesis presented for the degree of

Doctor of Philosophy

STEPHEN ERIC HALLINAN

B.A. (Hons) Trinity College, Dublin

Department of Earth Sciences

The Open University

Milton Keynes

October, 1991

31 0124848 8

DX177030
UNRESTRICTED

Gravity Studies of the Guayabo Caldera and the Miravalles Geothermal Field, Costa Rica.

A thesis presented for the degree of

Doctor of Philosophy

STEPHEN ERIC HALLINAN

B.A. (Hons) Trinity College, Dublin

Department of Earth Sciences

The Open University

Milton Keynes

October, 1991

Thesis number: M7025.9
Date of submission: 18th October 91
Date of award: 22nd January 1992

Paginated blank pages are scanned as found in original thesis

No information is missing

Abstract

Gravity techniques have been used firstly to determine the sub-surface structure of the Guayabo caldera together with the related part of the Guanacaste Arc, and secondly to study the temporal evolution of the Miravalles Geothermal Field. Detailed density and stratigraphy studies of both the drilled and exposed geology have both complemented and constrained the caldera gravity models. A new caldera volume - erupted mass balance model is proposed that computes the buried, intra-caldera mass and volume parameters in terms of the mass deficiency commonly associated with silicic calderas.

The 10 km diameter topographic expression of the Guayabo caldera comprises nested collapse structures, the boundaries of which are defined within the caldera by distinct gravity discontinuities. The modelled structure shows that the Guayabo caldera formed by multistage collapse across discrete sub-parallel sets of ring faults, rather than by chaotic collapse. The resultant overall structure resembles a funnel caldera, and it is possible that similar structures may be present but remain undetected in comparable calderas. The 200-400 m collapse across the faulted topographic margins is far less than the previous estimate of 2400 m, where the entire drilled stratigraphy was thought to comprise the fill to the caldera. Most of the stratigraphy drilled on the eastern margin of the caldera pre-dates the formation of the caldera, contrary to the previous theories. Furthermore, the caldera volume far exceeds the volume of the Guayabo tuffs and post-tuff subsidence, possibly related to the build-up of the recent Miravalles stratocones on the caldera margin, is required to explain the imbalance. An important result of the revised caldera model is that the geothermal reservoir host rocks continue beneath the caldera margin, and therefore the volume of the reservoir may be greater than previous estimates.

The 35 mGal gravity couple over the inner margin of the Nicaraguan depression is modelled as the near-surface outcrop of the Cretaceous ophiolitic basement, previously thought to be present at several km depth beneath the Guanacaste arc. Gravity data show that the extensive Plio-Pleistocene silicic pyroclastics of Guanacaste do not have detectable deep-seated low-density plutonic equivalents.

Repeat gravity studies at Miravalles identified 40 μGal fluctuations on a monthly time-scale, due to groundwater movement in the Guayabo caldera rather than geothermal-related sources. Experimental data have shown that LaCoste and Romberg gravimeters record repeatable gravity decreases of up to 700 μGal when subjected to vibration at specific harmonic frequencies. This accounts for the gravity decreases observed during well testing in 1988, that could not be explained by reasonable mass changes. Taking these points into consideration, a repeat gravity monitoring program was designed to both test and complement the future reservoir simulation models.

Acknowledgements

This project was funded by the Overseas Development Administration. Geoff Brown is thanked for his support, advice, editorial skills and encouragement throughout. Thanks to Hazel Rymer for support and morale boosters but maybe not for introducing me to gravimeters. Many of the ideas presented here have benefitted from discussions with other O.U. staff, in particular Richard Thorpe and Steve Blake. The constructive criticism offered by both Peter Francis and John Milsom is much appreciated.

The fieldwork in Costa Rica would not have been possible without the support of many ICE personnel. Alfredo Mainieri is thanked for the generous hospitality at the Hotel Guayabo. Freddie is solely responsible for keeping the vehicle in the land of the living. Mayra Corella and Oscar Mora are thanked for endless discussion and debate in the field. Diego Meña, Carlos Arlee, Lionel Vaca, Mayra and others provided much valuable encouragement during extra-curricular activities.

Back in sunny MK there are various admirable people who have flagrantly broken all the rules to ensure that life must be taken beyond the MK background levels. Tim - jjjjjust a column to turn on - lets get plastered - Elliott still owes me some Bollinger. Jon - Ma - Davis for keeping the dreadful score cards out of the appendices. Ta Fiona for typing the references, Mincho for convincing me that it is possible to enjoy life in any country, regardless of the pace. Jugs - sort of...well...that's not on...- Stevenson gets first prize for cynicism in science, and Dentinho - no...you're wrong...- Vasconcellos comes a close second. Thanks to Kathia for nearly fresh bread, Min for leaving tasty meals unattended, Maria for keeping me awake in these last few days. There are countless other offendees but this thing is already monstrous. By the by, the boys of the Thames Valley force are thanked for taking care of all my motoring requirements.

Finally, the last word must go to my patient and very supportive family, I'll write soon.....

Table of contents

1 Introduction and a Review of the Geology of Costa Rica..... 1

1.1 General Introduction: Aims and Objectives..... 1

1.2 Geological History of Northern Costa Rica..... 6
1.2.1 Present tectonic setting of northern Costa Rica..... 6
1.2.2 The geological history..... 10
1.2.3 Implications for the nature of the Guanacaste crust..... 17

2 Stratigraphy of the Guayabo Caldera..... 19
Introduction..... 19

2.1 The Miravalles Geothermal Project (MGP)..... 20

2.2 Previous Ideas on the Guayabo Caldera..... 26
2.2.1 The Guayabo caldera..... 27
2.2.2 The extra-caldera tuffs (part of the Santa Rosa Ignimbrite Plateau)..... 32
2.2.3 The radiometric ages..... 37
2.2.4 The ELC (1986 a) intra-caldera stratigraphy..... 38
2.2.5 The ELC (1986 a) structural evolution model..... 43

2.3 The Revised Stratigraphy of This Study..... 47
2.3.1 The Ignimbrite Unit (IG)..... 50
2.3.2 The Volcano-Sedimentary Unit (VS) (including the Lava-Tuff Unit (LT) of ELC, 1986 a)..... 51
2.3.3 The Acidic Andesite Unit (AA)..... 52
2.3.4 The Cabro Muco Andesite Unit (CMA)..... 54
2.3.5 The Pumice Unit (PUM) (revised to include only the lowermost part of the Pumice Unit of ELC,1986 a)..... 54
2.3.6 The Late Cabro Muco Volcanic Unit (LCMV). A re-definition of the ELC (1986 a) Post C. Muco Volc. U..... 55
2.3.7 Geochemical constraints on the stratigraphic position of the caldera margin lavas..... 57
2.3.8 The southern caldera border..... 62
2.3.9 The western caldera border and the extra-caldera lavas..... 67
2.3.10 Intra-caldera tuffs and possible extra-caldera equivalents..... 70

2.4 Implications for the Caldera Evolution..... 77

3 Gravity Models of the Guayabo Caldera..... 81
Introduction..... 81

3.1 The Importance of Full Terrain Corrections and the Correct Choice of Reduction Density..... 82
3.1.1 Terrain Corrections..... 84
3.1.2 Choice of Datum Plane and Reduction Density..... 86

3.2 The Gravity Data Set Used in This Study..... 93
3.2.1 ICE Miravalles Geothermal Project Data..... 93
3.2.2 ICE Tenorio Geothermal Project data..... 94
3.2.3 Gravity data measured during this study..... 95
3.2.4 Compilation of the three data sets..... 95
3.2.5 The regional gravity field and the main features of the BCG map..... 97

3.3 Surface Density Measurements..... 105
3.3.1 Pre-caldera lava densities..... 107
3.3.2 Tuff densities (and country rock density constraints from lithic densities)..... 107

3.3.3 Lavas of the Miravalles volcanic edifice....110
3.3.4 The density of the caldera walls from Nettleton Profiles....110

3.4 Borehole Densities and Hydrothermal Alteration....115
3.4.1 Correcting the cuttings densities (rr) for porosity....126
3.4.2 Alteration mineral assemblages....130
3.4.3 The borefield density structure....135

3.5 Previous Resistivity and Gravity Models....141
3.5.1 Relationship between electrical conductivity, density and alteration mineralogy....143
3.5.2 Mapping the southern stratigraphy using geoelectric sections....151
3.5.3 Previous gravity models....153
3.5.4 Summary of the results of previous geophysical studies....156

3.6 The Gravity Models of this Study....157
3.6.1 The modelling technique....159
3.6.2 The models of the Guayabo caldera structure....178
3.6.3 The deep structure of Volcán Miravalles and Bajo Los Chiqueros....189
3.6.4 The southern margin of the Nicaraguan Depression....202

3.7 Geothermally Induced Gravity Anomalies....204
3.7.1 The contribution of deep propylitization to the gradient over the northern borefield....205
3.7.2 The PGM-4 High....206
3.7.3 Summary of geothermal-related mass distribution and evolution....211

3.8 Summary of the Gravity Modelling Results....212

3.9 The Incremental Collapse Model of the Guayabo Caldera....216

4 Constraining the Mechanisms of Caldera Collapse Using Gravity Data....221
Introduction....221

4.1 A Review of Proposed Caldera Morphologies....222
4.1.1 Piston collapse....223
4.1.2 Funnel collapse....225
4.1.3 Overview of other mechanisms of caldera formation....228
4.1.4 Summary....229

4.2 Gravity Anomalies Over Calderas....230
4.2.1 The gravity signatures of piston and funnel calderas....230
4.2.2 Basement structure and sub-caldera intrusions:....233
4.2.3 Summary of caldera-related gravity interpretation....235

4.3 A New Caldera Mass Balance Model....236
4.3.1 The derivation of the model....237
4.3.2 The sensitivity of the model....241

4.4 Application of the Model at Guayabo....244
4.4.1 Computing the mass deficiency, M*....244
4.4.2 The pre-caldera volume, V_c....247
4.4.3 The densities ρ_r, ρ_{ip} and ρ_m and the lithic fraction f_o....248
4.4.4 The extra-caldera tuff mass, M_x, derived from exposure....249
4.4.5 Comparison of M_x with the predicted M_o....251
4.4.6 The mass deficiency at the Aira caldera, Japan....255
4.4.7 Summary of the caldera mass balance model....256

4.5 Features of Guayabo that are Diagnostic of Funnel Calderas....257

5 Dynamic Gravity Models of the Miravalles Geothermal Field 259
Introduction 259

5.1 Microgravity Monitoring of Geothermal Fields 259
5.1.1 Wairakei 260
5.1.2 The Broadlands and Bulalo fields 263

5.2 The Miravalles Geothermal Reservoir 265
5.2.1 The Miravalles outflow plume 268
5.2.2 The boiling and vapour zones 274
5.2.3 Recharge and the PGM-2 acidity question 278

5.3 Pre-Production Gravity Changes at Miravalles 282
5.3.1 Technique and errors 283
5.3.2 The 1987 and 1988 microgravity data 287
5.3.3 The 1989 microgravity data 292

5.4 Production Test Related Gravity Changes 299
5.4.1 The 1988 interference test 299
5.4.2 The 1989 reinjection test 307
5.4.3 The effects of induced vibration on gravimeter G-105 309

5.5 Monitoring Future Production 313
5.5.1 The simulated reservoir models of ELC (1988) 313
5.5.2 The predicted gravity changes 318

5.6 Recommendations For Future Microgravity 323

6 Conclusions and Implications 327
6.1 The interpretation of gravity anomalies in volcanic terrain 328
6.2 The multi-stage evolutionary history of the Guayabo caldera 328
6.3 The implications for the Miravalles Geothermal Field 331
6.4 The structure of the Guanacaste Arc 331
6.5 The implications for caldera studies 333
6.6 Repeat gravity monitoring at Miravalles 334

References 337

Appendix 2 Major Element Geochemistry 353

Appendix 3A Gravity Data 355

Appendix 3B The Elevation Data 371

Appendix 3C Densities 377

List of Tables

Table 2.1 Selected K-Ar ages from the Guanacaste Arc..... 31
Table 2.2 The Santa Rosa Ignimbrite Plateau nomenclature. 33
Table 3.1 Summary of the surface densities (Mg m-3) and porosities (%)..... 106
Table 3.2 Comparison between the crushed and whole rock grain densities..... 106
Table 3.3 Core densities measured by ICE geophysicists. 126
Table 3.4 Average stratigraphic group wet densities..... 127
Table 4.1 The parameters used in the M_o sensitivity test..... 241
Table 4.2 The Guayabo caldera mass deficiency data..... 245
Table 4.3 Estimated volumes the Guayabo tuffs. 251
Table 5.1 The 1987-1988 elevation data for the PGM-11 stations..... 285
Table 5.2 Tide corrected repeat gravity changes from 1987 to 1989 at Miravalles..... 288
Table 5.3 Repeat gravity (μGal) for the general caldera stations. 290
Table 5.4 The 1989 gravity variations in the PGM-2 and 11 area..... 294
Table 5.5 The 1988 PGM-1, 10, 11 and 12 well tests..... 300
Table 5.6 Elevation data from the 1989 well test..... 309
Table 5.7 The gravity changes predicted during production 320

List of Figures BC denotes inside back cover.

Figure 1.1 Structural map of southern Nicaragua, Costa Rica and northern Panama.... 3
Figure 1.2 Tectonic setting of Central America..... 7
Figure 1.3 Stratigraphy of the sedimentary basins of northern Costa Rica..... 11
Figure 2.1 Map of spring locations and geothermal sites in Guanacaste. 20
Figure 2.2 a Hydrothermal manifestations at Miravalles 22
Figure 2.2 b The Miravalles geothermal reservoir..... 23
Figure 2.3 Geological sketch of northern Costa Rica..... 28
Figure 2.4 Topographic map of the Guayabo caldera. 29
Figure 2.5 Geology of the Guayabo caldera ..... BC
Figure 2.6 The main features of the ELC (1986 a) borehole stratigraphy..... 40
Figure 2.7 a-b The ELC (1983 and 1986 a) evolution of the Guayabo caldera..... 44
Figure 2.7 c-d (continued) 45
Figure 2.8 Summary of the ELC (1986 a) Guayabo caldera stratigraphy..... 46
Figure 2.9 a Detailed east-west borehole stratigraphy ..... BC
Figure 2.9 b Detailed north-south borehole stratigraphy ..... BC
Figure 2.10 a Shallow stratigraphy from Temperature Gradient (PH-) Boreholes..... BC, 48
Figure 2.10 b Structural contour map of the Late Cabro Muco Volcanic Unit 49
Figure 2.11 Structural evolution sketch at PGM-1..... 53
Figure 2.12 a K_2O against SiO_2 discrimination diagram. 59
Figure 2.12 b MgO against SiO_2 discrimination diagram.. 60
Figure 2.13 Summary of the Guayabo caldera stratigraphy..... 67
Figure 2.14 Proposed intra- to extra-caldera tuff correlations. 72

Figure 3.1 The distribution of the gravity surveys.....83
Figure 3.2 a Terrain-correction section.....84
Figure 3.2 b Lost terrain correction *vs* elevation graphs.....85
Figure 3.3 The effect of using the wrong reduction density.....86
Figure 3.4 Bouguer corrected gravity vs station elevation for all ICE MGP data.....88
Figures 3.5 a-d Bouguer corrected gravity relative to topography. 90
Figure 3.6 a 3-D perspective map of Bouguer gravity draped on topography.....98
Figure 3.6 b 3-D Guayabo caldera BCG *vs* topography.....99
Figure 3.7 1 mGal computer contoured BCG map.....100
Figure 3.8 0.5 mGal BCG map of the southern Guayabo caldera.....101
Figure 3.9 Regional Bouguer gravity map of Costa Rica.....102
Figure 3.10 Nettleton profiles over Cerro Mogote.....112
Figure 3.11 Nettleton profiles across Cerros la Montañosa. 113
Figure 3.12 The correlation of the PGM-5 and PGM-5R densities.....116
Figure 3.13 General Key of grain density (ρ_r) and % alteration of whole rock.....117
Figure 3.13 a PGM-1. 118
Figure 3.13 b PGM-2.....119
Figure 3.13 c PGM-3. 120
Figure 3.13 d PGM-5.....121
Figure 3.13 e PGM-10.....122
Figure 3.13 f PGM-11.....123
Figure 3.13 g PGM-12.....124
Figure 3.13 h PGM-15. 125
Figure 3.14 Average stratigraphic unit saturated densities.....128
Figure 3.15 Range of rock and mineral densities. 133
Figure 3.16 Change of rock density due to alteration. 134
Figure 3.17 Resistivity profile location map.....142
Figure 3.18 Selected resistivity profiles of Duprat and Leandro (1986). 144
Figure 3.18 (continued).....145
Figure 3.19 Gravity and resistivity profile models of Geosystems (1988). 146
Figure 3.19 (continued).....147
Figure 3.20 Guayabo Unit model of Lezema et al. (1988). 156
Figure 3.21 Gravity profile location map in the southeastern caldera. 158
Figure 3.22 Gravity Profile AA.....163
Figure 3.23 Gravity Profile BB.....165
Figure 3.24 Gravity Profile CC.....167
Figure 3.25 a Gravity Profile WSE (full length) 169
Figure 3.25 b Gravity Profile WSE (detail over the Guayabo caldera).....171
Figure 3.24 c Gravity Profile CM1.....173
Figure 3.27 Gravity Profile NS.....175
Figure 3.28 Gravity Profile VV.....177

Figure 3.29 a Hand contoured BCG data over Volcán Miravalles. 192
Figure 3.29 b Computer contoured BCG data over Volcán Miravalles. 193
Figure 3.30 a Uppermost Santa Rosa Profile 1 (SR1)..... 197
Figure 3.30 b Santa Rosa Profile 2 (SR2)..... 199
Figure 3.30 c Santa Rosa Profile 3 (SR3)..... 201
Figure 3.31 Part 1 The multi-stage evolution of the Guayabo caldera. 217
Figure 3.31 Part 2..... 219
Figure 4.1 Schematic cross-sections of various caldera collapse models..... 223
Figure 4.2 Models of the U- and V-shaped gravity profiles 231
Figure 4.3 Caldera collapse *vs* evacuated magma balance model..... 237
Figure 4.4 The lithic sensitive caldera balance model..... 239
Figure 4.5 a Theoretical M_o sensitivity to V_c, M* and f_o..... 242
Figure 4.5 b Theoretical M_o sensitivity to V_c, M* and f_o. 242
Figure 4.6 The limits of the area integrated to derive M*..... 246
Figure 4.7 The tuff distribution model used to approximate V_o..... 250
Figure 4.8 M_o sensitivity graphs for the Guayabo caldera..... 252
Figure 5.1 Gravity changes at the Wairakei geothermal field, New Zealand..... 261
Figure 5.2 Hydrology of a water-dominated geothermal reservoir..... 263
Figure 5 3 Location of the repeat gravity stations used in 1988-1989 266
Figure 5.4 Map of the hydrothermal manifestations at Miravalles. 267
Figure 5.5 The Miravalles outflow plume..... 269
Figure 5.6 The Miravalles geothermal reservoir. 270
Figure 5.7 Thermal, hydrological and geochemical data pertinent to the location of the upwelling convective plume feeding the Miravalles system. 271
Figure 5.8 Shallow reservoirs at the adjacent wells PGM-5 and 5R..... 275
Figure 5.9 The departures of the reservoir temperatures from the boiling curve..... 279
Figure 5.10 Apparent gravity changes observed by ICE at Las Hornillas..... 283
Figure 5.11 a Repeat gravity data for the 1987-1988 PGM-11 stations..... 289
Figure 5.11 b Gravity changes in the Las Hornillas fumarole area. 291
Figure 5.12 Map of the 1989 reinjection test gravity stations..... 293
Figure 5.13 a 1989 temporal gravity variation graphs..... 295
Figure 5.13 b Gravity variations at individual station to the north of PGM-11..... 296
Figure 5.14 Groundwater fluctuations for a given gravity change 297
Figure 5.15 Tide corrected gravity data from the 1988 well closures..... 302
Figure 5.16 The proposed cone model of an expanding steam zone..... 305
Figure 5.17 Expansion cone dimensions for a given gravity change 306
Figure 5.18 The 1989 well test gravity data from the N+10 to N+50 stations..... 308
Figure 5.19 Vibration induced gravity changes for meter G-105..... 311
Figure 5.20 Steam zone expansion and temperature decline (30 years production)..... 315
Figure 5.21 a Predicted evolution of the reservoir pressure drawdown. 316
Figure 5.21 b, c and d The predicted reservoir temperature decline..... 317

Figure 5.21 e The evolution of the steam saturation at 200 m b.s.l.....317
Figure 5.22 The saturation levels predicted after 30 years production 317
Figure 5.23 Predicted temporal gravity decrease due to expansion of a steam zone.....322
Figure 3.24 Proposed layout for the future repeat gravity program at Miravalles.....324
Figure 5.25 Cross-section of a suitable design for a repeat gravity station. 325

CHAPTER 1

INTRODUCTION AND A REVIEW OF THE GEOLOGY OF NORTHERN COSTA RICA

1.1 General Introduction: Aims and Objectives

This thesis concerns the characteristics of a geothermal field associated with the Guayabo caldera in northern Costa Rica. The factors that determine the economic viability of generating electricity from a particular geothermal field are various, and have as much to do with socio-economic arguments (e.g. supply and demand, price of competing energy sources; see recent review by Ungemach and Economides, 1987) as the physical characteristics of the geothermal reservoir, discussed during this thesis. A review of exploited geothermal fields by DiPippo (1986) shows that the majority are associated with the Circum-Pacific destructive plate margins. Subduction-related magmatism gives rise to shallow intrusions that drive the convective hydrothermal systems (Donaldson, 1982; Henley and Ellis, 1983), and these in turn control the loci of the geothermal fields. The upper crustal groundwater can either remain in a convective, liquid state, resulting in a liquid-dominated reservoir or, more rarely, temperatures above the boiling curve exist in the geothermal reservoir, resulting in a vapour-dominated field (White *et al.*, 1971; Donaldson, 1982). In either case, energy is 'mined' by drilling to intersect the hot fluids (generally in excess of 200°C) and either flashing the hot water as pressure is reduced, or using the dry steam directly, if available, to drive electricity generating turbines.

Sustainable volumes of fluid can only be guaranteed where there is sufficient permeability to prevent rapid pressure decline during production. Often the permeability is of a secondary nature, governed by open fractures produced during Holocene tectonic activity (Reeder, 1987). It is therefore necessary to explore those factors that control the volume and permeability of the aquifer, together with the temperature of the resource, before assessing its economic value. A full understanding is never possible without executing an extensive and expensive drilling program, but a very useful, and cheaper, model of the reservoir

dimensions can be built up by running geophysical surveys and integrating the results to find the most acceptable geological solution.

The focus of this study was the Miravalles Geothermal Field, located in the Pleistocene Guanacaste Arc, Costa Rica (Figure 1.1). It is a liquid-dominated geothermal field where temperatures in excess of 245°C have been drilled at depths of 1 km (Mainieri *et al.*, 1985; a more detailed introduction to this Geothermal Project is given in Chapter 2). The reservoir rocks have previously been described as the volcano-sedimentary fill to the Guayabo Caldera (G in Figure 1.1) and the heat source has been postulated as the cooling intrusive stock of the later Volcán Miravalles (Mainieri *et al.*, 1985, ELC, 1986 a). The field is expected to be able to support at least two 55 MW power plants (ELC, 1988) but the true extensions of the field remain to be determined. Several geophysical techniques have been applied to determine the dimensions of the reservoir; including heat flow, resistivity, gravity and magnetics studies (Blackwell *et al.*, 1977; Corrales *et al.*, 1977; Furgerson and Afonso, 1977; Duprat and Leandro, 1986 and Leandro *et al.*, 1988 and 1989), but the existing interpretations of the data have yet to be reconciled with a detailed self-consistent geological evolutionary model. In short, the geophysical data do not easily support the existing geological models, particularly those that limit the reservoir host rocks to within the Guayabo caldera.

A first objective of the present study, therefore, was to re-build the geological evolutionary model by integrating: i) the available lithological and stratigraphic information, ii) field geological observations made during this study, iii) data from existing geophysical studies and iv) the results of extensive gravity surveying during this work. To this end, the stratigraphical information is reviewed and revised in Chapter 2 and is then combined with the gravity models of this study and previous geophysical models in Chapter 3. The resultant evolutionary model differs considerably from those previously proposed, but because the model has been derived from an integrated approach, it is generally believed to be more satisfactory, and it has been reviewed by and revised in detail following discussions with local geologists.

Figure 1.1 Structural map of southern Nicaragua, Costa Rica and northern Panama, showing the position of Volcán Miravalles, M and the Guayabo caldera, G. Basement rocks (Nicoya Complex) are exposed along the outer arc (adapted from Seyfried *et al.*, 1991; Weyl, 1980 and deBoer *et al.*, 1988). Cross-section AB shows the arc related structure. The Central American volcanic arc is shown below and the tectonic setting of Central America is shown in Figure 1.2.

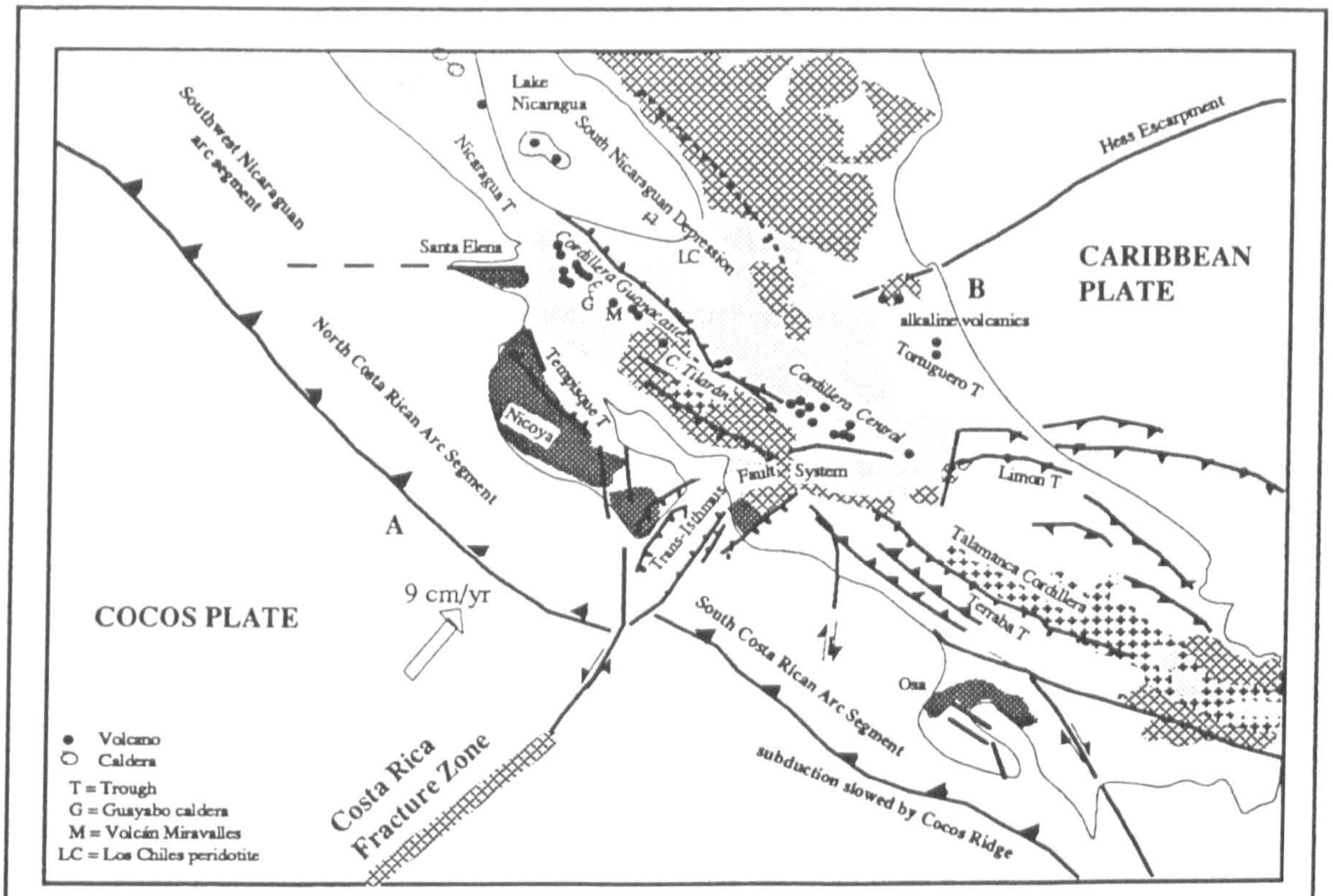

Previous gravity studies (Duprat and Leandro, 1986) showed a steep gravity gradient over the Miravalles Field with gravity decreasing towards the centre of the caldera and an isolated gravity high outside the borefield at a proposed site for future drilling. Initially, the gradient was considered to be regional and the more local gravity highs reflected the presence of the less permeable, andesitic bodies found in the drilled parts of the borefield, but later it was postulated that deep propylitization could at least contribute to the gravity highs. To examine the relative importance of lithological and hydrothermal control a detailed density

study was made of the borehole cuttings (Chapter 3). Although the deep, high-T_2 alteration products increase the density, neither the steep gradient nor the local gravity highs can be explained in terms of alteration alone. Lithology largely controls the gravity field.

The uses of gravity data in the studies of silicic calderas, commonly characterised by low density fill, are reviewed in Chapter 4. The first objective was to outline how the nature of the gravity field can discriminate between the end-member caldera structure models that have been proposed to date; chiefly 'piston' from 'funnel' types. The many studies of the structure of calderas, of silicic calderas especially, have suggested that the caldera floor subsides in response to the evacuation of the sub-caldera magma chamber during the eruption of the associated ashflow tuffs. This implies a balance between the total volume of erupted products and the volume of the caldera, but often it is difficult to assess the intra-caldera components of the equation. The second objective of Chapter 4 was, therefore, to set up a volume and mass balance model to test this relationship, using the negative gravity anomaly to constrain the mass of erupted material within the caldera. Finally, in Chapter 4, the proposed model for the evolution of the Guayabo caldera is compared to the current models of caldera evolution. Here the objective was to examine the caldera in its own right, rather than force a conclusion that the Guayabo caldera is one of the existing end member types. It is shown that the characteristics of the Guayabo caldera most resemble those of the Japanese funnel-shaped calderas; but it is emphasised that the recent proposals that many calderas form by chaotic collapse are not consistent with the evidence in this case. Instead, the caldera formed as the result of i) a series of temporally distinct eruptions that resulted in small collapse events centred over a long lived magma chamber and ii) further post-tuff eruption subsidence, possibly related to the caldera margin stratocone activity. It is possible that other similar calderas could have evolved in a similar fashion.

Volcán Miravalles formed as a stratocone in the eastern part of the caldera. The evolution of the associated hydrothermal system, the latest stage in the geological evolution, is considered in terms of the effect of geothermal exploitation in Chapter 5. As a geothermal field is exploited, one of the commonly observed effects is a reduced pressure zone in the reservoir; reflecting the inability of the natural fluid recharge to cope with the rates of mass

withdrawal. At present, the Miravalles Field is in the pre-production stage of development, and a further objective of this research was to monitor possible mass changes related to long term production tests using microgravity techniques. This technique is well established and has been used to examine the effects of 10 or more years of liquid drawdown (mass loss) at other producing fields (e.g. in New Zealand; Allis and Hunt, 1986). The period of maximum rate of pressure drawdown tends to occur directly after production begins, and the consequent rate of natural recharge increases as a pressure gradient is developed in the aquifer until, eventually, it may equal the production rate. Unfortunately, as a result of unavoidable delays in the testing program it was not possible to monitor a significant production period. Much has been learned, however, from a limited monitoring program which was undertaken; for example, it has been possible to examine the amplitude and temporal nature of significant non-production related gravity changes, interpreted as seasonal changes in the groundwater table. A microgravity program has been designed to monitor the field during its productive life and, in due course, it will be possible to test mass changes predicted by existing reservoir simulation models which are developed and discussed in Chapter 5.

A further objective of this study was to model the regional gravity field across a part of the Quaternary volcanic arc, the Cordillera de Guanacaste, Costa Rica (Chapter 3). Before this is possible it is important to understand the likely basement composition and structure with an emphasis on possible lateral density changes that will affect the gravity field. Unfortunately, exposure of the pre-Quaternary stratigraphy is limited to the Pacific coastal area, some 30 km to the southwest of Guayabo, and the Cordillera de Tilaran 30 km to the southeast (Figure 1.1). The purpose of the remainder of this Chapter is to review the tectonic setting of northern Costa Rica and its tectonomagmatic history to try to constrain the possible nature of the crust that underlies the Quaternary arc.

To summarise, the principal objectives of this research are:

1) To evaluate the crustal structure of northern Costa Rica; the available evidence is reviewed in Chapters 1 and 2 and the regional gravity field is modelled in Chapter 3.

2) To construct a geological evolutionary model for the Guayabo caldera (Chapters 2 and 3) and to compare/contrast the results with published ideas on caldera formation (Chapter 4).

3) To outline the use of caldera gravity data to a) discriminate caldera structure and b) constrain the intra-caldera parameters necessary to test for the caldera mass and volume balance predicted by current models of caldera formation (Chapter 4).

4) To examine the hydrothermal control on density and determine the extent of the geothermal reservoir host rocks (Chapter 3 and Chapter 5).

5) To evaluate the pressure-induced changes in mass flow within the geothermal aquifer during well production tests and make recommendations for long-term monitoring of the field in relation to reservoir simulation models (Chapter 5).

1.2 Geological History of Northern Costa Rica

Costa Rica lies between Panama to the south and Nicaragua to the north, which collectively form Southern Central America (Figure 1.1). This part of the isthmus is the legacy of the gradual continentalisation of oceanic crust by a process of post-Cretaceous arc volcanism, tectonics and sedimentation (Seyfried *et al.*, 1991), processes that are common to many accretionary destructive plate margins. The Guayabo caldera is located in the Guanacaste Arc (Figure 1.1), and the following sections concentrate on the evolution of this area, with reference to adjacent regions where appropriate. The present tectonic framework of Costa Rica is summarised first, followed by the geological history, and finally the implications for the crustal composition in Guanacaste are considered.

1.2.1 Present tectonic setting of northern Costa Rica

The present morphology of Central America is a direct consequence of its tectonomagmatic history. The Quaternary volcanic chain (Figure 1.2) has previously been thought to extend from the Guatemala-Mexico border to central Costa Rica only (e.g. Carr *et al.*, 1982), but deBoer *et al.* (1988) showed that the most recent volcanics of the Panamanian arc are also of Quaternary age. The volcanic chain is clearly the result of the northeast subduction of the Cocos plate beneath the Caribbean plate (Molnar & Sykes, 1969). The current relative rate of plate motion is 9 cm yr^{-1} (Minster and Jordan, 1978). The other adjacent plates: the

North American, South American and the Nazca Plates and the nature of their boundaries are shown in Figure 1.2.

Figure 1.2 Tectonic setting of Central America showing the distribution of the tectonic blocks in relation to the major plates (from Bourgeois *et al.*, 1984 and Berrangé and Thorpe, 1987). G.f.z = Gatun fracture zone; P.f.z = Parrita fracture zone.

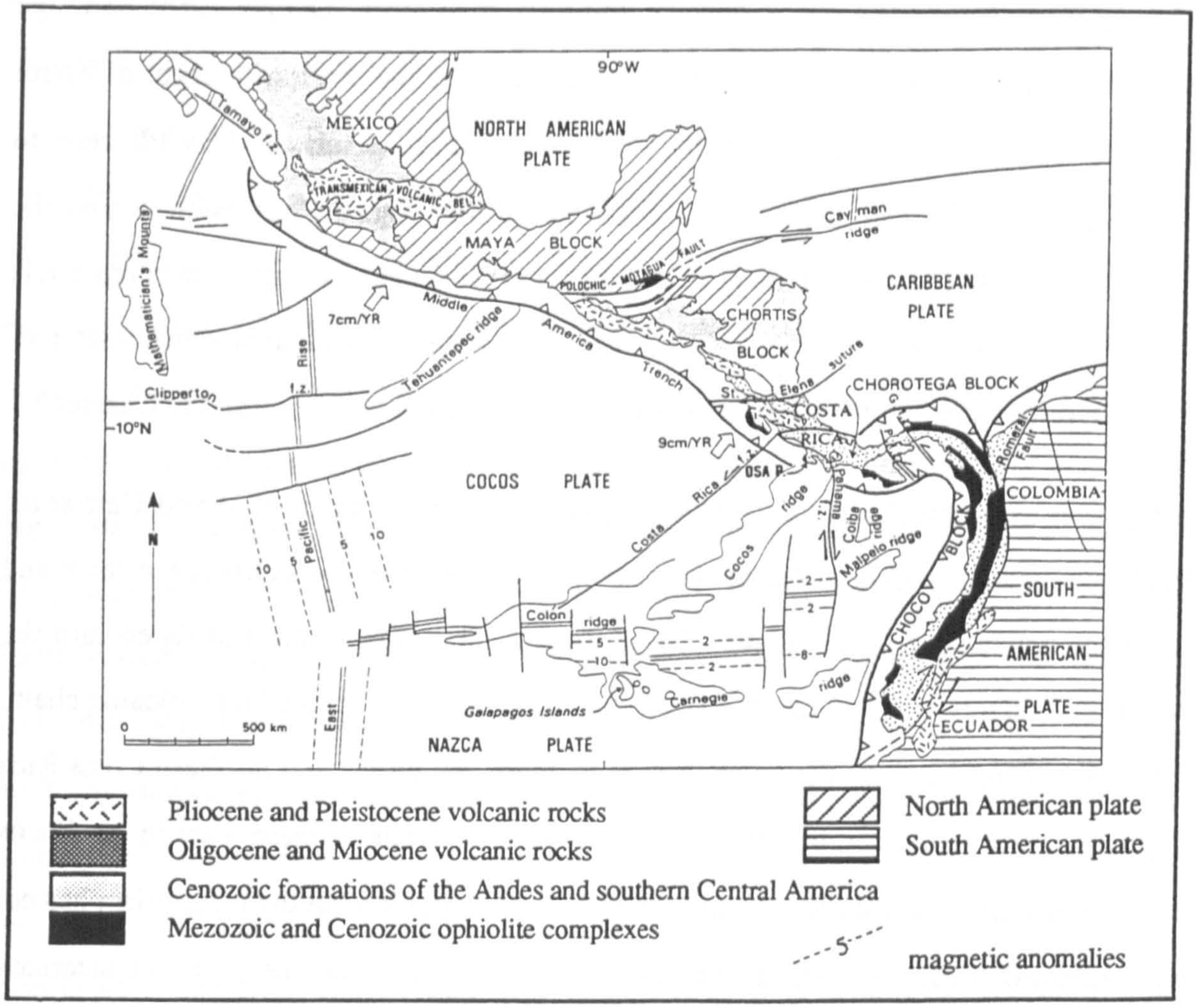

Weyl (1980) subdivided Central America into three provinces on the basis of crustal type and contrasting tectonic provinces as follows. Southern Central America, including Costa Rica and Panama, is characterised by a basement of Mesozoic oceanic crust; it lacks the Palaeozoic crystalline basement and the Upper Palaeozoic and Mesozoic continental and epi-continental deposits of northern Central America (Figure 1.2). Northern Central America is separated into two blocks by the left-lateral east-west transcurrent Polochic-Motagua fault in northern Guatemala to produce the northern Maya block and the southern Chortis block (Figure 1.2). Originally both were parts of the North American Plate, but the Chortis block has now become detached from the North American Plate and is coupled to the Caribbean Plate (Weyl, 1980).

Southern Central America is separated from northern Central America by the Santa Elena suture (deBoer, 1979, Figure 1.2), and is further subdivided by the Gatun Fracture Zone into the Chorotega block (virtually identical to the Noba block of deBoer, 1979) which makes up Costa Rica and western Panama, and the Choco block (Dengo, 1985; Berrangé and Thorpe, 1987) which comprises eastern Panama and the western margin of South America. The eastern extension of the Santa Elena suture is obscured by Pliocene to Pleistocene volcanics and is cut by the more recent Nicaraguan Depression behind the Guanacaste Arc, but Seyfried *et al.* (1991) suggested that the Hess escarpment (Figure 1.1) could be a continuation. The relationship between the Santa Elena suture and the outcrop of oceanic-type basement in Northern Costa Rica is further discussed below and in Chapter 3.

Rather than using breaks in the overriding plate, Stoiber & Carr (1973) and Carr *et al.* (1982) subdivided the Central American arc on the basis of offsets and changes in strike and dip of the subducting Cocos Plate. These breaks, they argued, are translated into the pronounced offsets and changes in strike separating eight segments of the volcanic chain. The 40 km offset between the volcanoes of southern Nicaragua and northern Costa Rica (Figure 1.1) was explained by Stoiber and Carr (1973) as one of these tears in the Cocos Plate. They proposed that the tears promoted caldera formation but the mechanism has not been explained or substantiated and few examples were given. The one obvious Quaternary caldera structure in northern Costa Rica, the Guayabo caldera, does not lie on one of their segment boundaries - though there are probably many other calderas that are obscured by more recent volcanics.

VanNess Burbach *et al.* (1984) argued that teleseismic data show evidence for only three major segments in the subducting slab for the whole Middle American Region and while the geometry of the slab varies within segments, it does so continuously. They proposed that there is a major tear southeast of Nicoya which separates southern Costa Rica on the basis that there are no seismic events recorded from depths below 70 km in this southern segment. VanNess Burbach *et al.* (1984) postulated that this tear is caused by slow subduction of the Cocos Ridge (Figure 1.2), an anomalously thick part of the Cocos Plate that formed prior to spreading on the Colón Ridge (Figure 1.2). They argued (following

Nixon, 1982) that the segmented nature of the volcanic front is due to discontinuities in the overriding plate rather than in the subducted plate.

More recently the Cocos plate has been subdivided by Lew *et al.* (in press, reported by Berrangé and Thorpe, 1987) into two geophysically and morphologically distinct parts (Figure 1.2). They proposed that the Costa Rica fracture zone separates rough crust to the southeast with an east-west alignment of magnetic stripes generated at the Colón ridge, from smoother crust with north-south stripes generated at the East Pacific rise or its ancestor. The southeastern Cocos Plate is today dominated by north-south compression, following the locking of the subducted Cocos ridge beneath southern Costa Rica and northern Panama. Subduction of the northwestern Cocos plate continues under northern Costa Rica by way of transcurrent motion on the Costa Rica fracture zone. The boundary between the segments of VanNess Burbach *et al.* (1984) coincides with the subducted part of the Costa Rica Fracture Zone. The Costa Rica Fracture Zone is also aligned with the Trans-Isthmus Fault System separating northern and southern Costa Rica, (Figure 1.1, Seyfried *et al.*, 1991, discussed below, Section 1.2.2) although the structural mechanism whereby motion on the lineament is transferred from the subducting plate to the overriding plate is not clear. As a result of the subduction of the Cocos Ridge, the southern Costa Rican arc is dominated by compressional stress (see predominant thrust structures in Figure 1.1), but transcurrent motion across the Trans Isthmus Fault System means that this regime does not continue into the northern Costa Rican arc, where compressional structures are generally less pronounced.

Turning to the structure across the arc, normal to the Middle America Trench, Costa Rica was sudivided by Dengo (1962) into the Outer Arc (the high relief headlands along the Pacific coast, including the ophiolitic Santa Elena, Nicoya and Osa Peninsulas), the Inner Arc (the Cordilleras de Guanacaste, Tilaran, Central and Talamanca, Figure 1.1) and the Caribbean Lowlands behind the arc. More recent studies have adopted a similar system, (as shown in Figure 1.1 adapted from Seyfried *et al.*, 1991) where the Caribbean Lowlands of Dengo represent a back-arc environment. The topographic depression behind the Guanacaste arc, however, continues into the Nicaraguan Depression, the site of the present

volcanic arc in southern Nicaragua. Earliest subsidence in the Nicaraguan Depression dates from the Miocene (Seyfried *et al.*, 1991), but this structure is distinct from older Nicaraguan *Trough* which accumulated ~8000 m of largely marine sediments (Section 1.2.2) from the Late Cretaceous until the Miocene. The southern margin of the Nicaraguan Depression is further discussed below (Section 1.2.3) and also in Chapter 3. On the other side of the volcanic arc, the outer-arc is uplifted into a series of arc-tilted blocks (Nicoya; Fischer, 1980 and Osa; Berrangé and Thorpe, 1987). Seyfried *et al.* (1991) considered that the outer-arc is structurally decoupled from the arc (Figure 1.1).

To summarise, southern Central America is a part of the Caribbean Plate and present volcanism in north-central Costa Rica is the result of subduction of the Cocos Plate beneath the Caribbean Plate. Southern Central America is made up of discrete blocks mainly separated by transcurrent faults; the Guanacaste arc lies within the Chorotega Block, south of the Santa Elena suture. Northern Costa Rica is bounded to the north by the southern margin of the Nicaraguan Depression, and to the south by the Trans Isthmus Fault System, an extension of the Costa Rica Fracture Zone. The evolution of these features is now considered in terms of the general geological history of northern Costa Rica.

1.2.2 The geological history

Seyfried *et al.* (1991) provided a comprehensive history of the south Central American arc, drawing on the results of several structural, sedimentological and magmatic studies. The objective of this section (and the next on the magmatic history) is to consider the likely nature of the crust beneath the Guanacaste Arc, where pre-Pliocene strata are not exposed. The pre-Pliocene magmatic history of the Guanacaste arc has been reconstructed by examining the trench-slope, outer-arc and fore-arc sedimentary stratigraphy (Figures 1.1 and 1.3).

The Basement: The earliest history of the arc is recorded in the rocks of the Nicoya Complex, which form the Mesozoic basement to the upfaulted outer-arc (Figures 1.1, 1.2 and 1.3). The Santa Elena and Nicoya Peninsulas were first mapped in detail as an ophiolitic suite, the Nicoya Complex, by Dengo (1962).

Figure 1.3 The stratigraphy of the sedimentary basins of northern Costa Rica (from Seyfried *et al.*, 1991) and southern Nicaragua (Seyfried *et al.*, 1991 and Weyl, 1980), location of troughs shown in Figure 1.2. The vertical scale shows the cumulative thicknesses. The timescale and regional unconformities, shown by dashed lines, have been added to show how the sequences compare temporally. Calc-alkaline volcanic sediments in the fore-arc date back to the Maastrichtian, suggesting that the Arc has been active from this time.

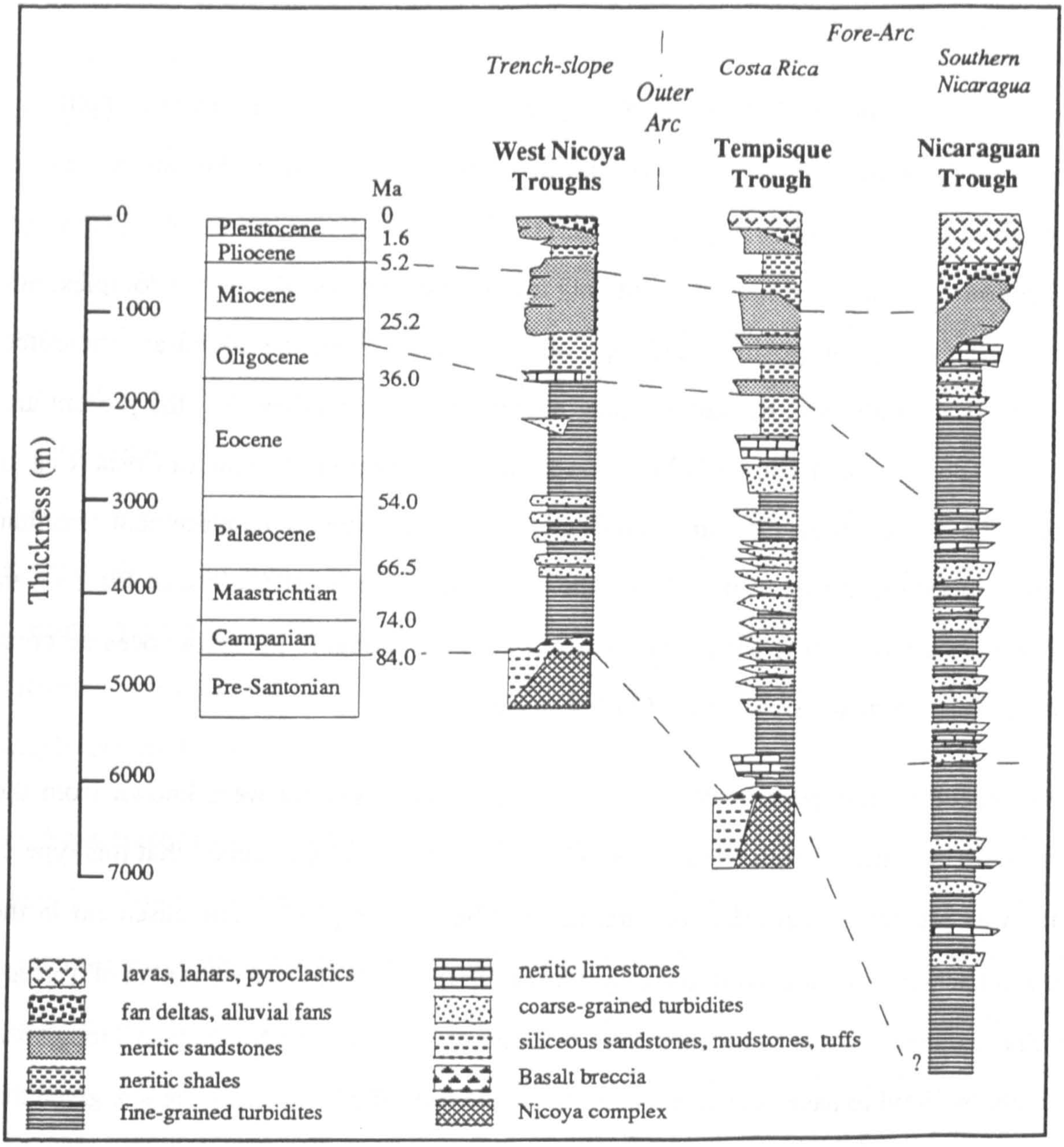

The sequences comprise hartzburgites, lherzolites, dunites, gabbros, plagiogranites, ocean ridge basalts (N-MORB and T-MORB), within-plate alkali basalts and tholeiites, and island-arc tholeiites; radiolarites from between the basalts have yielded Liassic to Santonian ages (literature reviewed by Seyfried *et al.*, 1991). H-J Gursky (1988 and 1989, reported by Seyfried *et al.*, 1991) further subdivided the Nicoya complex into a Lower Nicoya Complex, comprising the oceanic suite and the Upper Nicoya Complex, comprising the island-arc tholeiites and their associated sediments. Similar rocks are exposed along the

outer arc at the Herradura and Quepos headlands and south at the Osa and Burrica Peninsulas (all on the Pacific coast); these are believed to represent the basement throughout Costa Rica (Galli-Oliver, 1979; deBoer, 1979; Kuijpers, 1980; Bourgeois *et al.*, 1984; Berrangé and Thorpe, 1987).

The oceanic suite in the Nicoya Complex appears to have been emplaced by intracrustal overthrusting of oceanic layers during north-south compression in the late Mesozoic (Bourgeois *et al.*, 1984). Seyfried *et al.* (1991) believed that an early Campanian subduction reversal was responsible not only for the obduction of the Nicoya complex, but also for the change in position and type of magmatism: from the island-arc tholeiites exposed in the outer-arc, to calc-alkaline magmatism located at roughly the present arc position. Berrangé and Thorpe (1987) suggested a similar event in southern Costa Rica to explain the outcrop of the Osa suite in the outer arc. The question of emplacement direction is only important to the origin of the outer-arc crust (overthrust Caribbean Plate or an obducted 'slice' of Pacific Plate), but in either case the probable Mesozoic oceanic crust beneath the present arc is part of the Caribbean Plate.

Until recently, no exposures of Nicoya Complex-type basement were known from the Caribbean margin, but following Dengo (1962) it was generally assumed that this type of crust was present beneath the fore-arc, arc and back-arc regions. The basement in the present back-arc area was considered by Weyl (1980) to lie below the ~8,000 m of Tertiary marine sediments that accumulated in the Nicaraguan Trough. The Nicaraguan Trough was thought by Weyl to have been a precursor to the present Middle America Trench, given that it extended from the present limit of the Nicaraguan Depression in the north-east out to the present Pacific shelf in the southwest. However, Weyl suggested that the Trough also continued to the east, beneath and *behind* the present arc, to the Limon Trough in southeastern Costa Rica (Figure 1.1). The supposed 8000 m thickness of fill is largely based on exposures in southern Nicaragua and Limon, but *not* from northern Costa Rica. Ironically, we are fortunate that a petroleum exploration well drilled in the Nicaraguan Depression, near Los Chiles, Costa Rica on the southern edge of Lake Nicaragua (Figure 1.2) encountered ultramafics at a depth of only 400 m (Seyfried, *pers comm.*). Drilling was

naturally abandoned, so it is not clear exactly what was present. Nearby, in the banks of the Rio San Juan, peridotite exposures have also been reported (Seyfried, *pers comm.*). If oceanic in origin, these rocks offer tantalising evidence that not only is there oceanic basement close to the surface on *both* sides of the Guanacaste arc, but that the back-arc depression in northern Costa Rica is not nearly as deep as the ~8000 m proposed for the Nicaraguan Trough by previous workers (e.g. Seyfried *et al.* 1991, Figure 1.3).

In summary, the Nicaraguan Trough does *not* extend into the present region behind the Guanacaste Arc, and furthermore, cannot continue into the Limon Trough. It is suggested here that the Santa Elena suture does continue eastwards from the Outer Arc beneath the present arc. The basement to the south of the suture is uplifted relative to the north. This explains both i) the restriction of outer arc ophiolite exposures to the south of the suture (Figure 1.2) and ii) the contrast between the 8000 m Tertiary fill in southern Nicaragua and the exposed basement behind the arc in northern Costa Rica. It is reasonable to assume therefore that the basement beneath the Guanacaste Arc should not be as deep as that in southern Nicaragua, but the story is complicated by the development of the Tempisque Trough fore-arc basin during the Tertiary.

The Post-Basement Sedimentary Cover: Three generalised stratigraphic columns in Figure 1.3 (from Seyfried *et al.*, 1991) indicate that a similar sedimentary history is shared by the fore-arc sequence in both southern Nicaragua (the Nicaraguan Trough) and northern Costa Rica (the Tempisque Trough). There is a major early Campanian unconformity, marked by a basalt breccia (Figure 1.3), separating the Nicoya Complex basement from the subsequent sedimentary sequences in northern Costa Rica, but the basement is not exposed in southern Nicaragua. This episode of uplift has been related by Seyfried *et al.* (1991) to the subduction reversal obduction event that constructed the outer-arc; the unconformity can be traced throughout the sedimentary basins of Costa Rica. The breccias of the outer and fore-arc areas are followed by an early Maastrichtian carbonate sequence that records a gradual subsidence (relaxation) of these formerly uplifted areas (Figure 1.3), with greatest subsidence in the fore-arc.

The southern Nicaraguan sequence does not record the Campanian uplift event but shows a gradual shallowing upwards sequence from Late Cretaceous fine grained turbidites through coarser turbidites to carbonates and finally terrestrial deposits by the mid-Miocene. This implies that this fore-arc area enjoyed a different early tectonic history to that in northern Costa Rica.

During the Maastrichtian, the fore-arc sedimentation style in northern Costa Rica changed to turbidite deposition, with andesitic detrital input derived from the evolving arc (Figure 1.3), similar to the situation in southern Nicaragua. The turbidite phase continued until the late Palaeocene in Costa Rica, while becoming coarser, but there is a more marked discontinuity at the end of the Maastrichtian in Nicaragua. Here sedimentation recommenced in the Palaeocene with a coarse conglomerate (Weyl, 1980), not noted in Costa Rica. The Eocene saw an increase in volcanic input (interpreted as an increase in arc activity in the Mid-Eocene), and by the end of the Eocene both the Tempisque and Nicaraguan Troughs were almost entirely filled.

Gradual shallowing up in the fore-arc continued into the early Oligocene but was accompanied by compression, related to uplift of the outer arc. The Late Oligocene sedimentation commenced on an angular unconformity on the outer edge of the outer arc, as large parts of the northern Costa Rica fore-arc and outer arc became emergent (Seyfried *et al.*, 1991). A contemporaneous unconformity is also present in southern Nicaragua (Weyl, 1980 and Figure 1.3) but although the Oligocene to Lower Miocene sedimentation had effectively ceased in the Costa Rican fore-arc, the sequence in Nicaragua is ~1500 m thick. Volcanic intercalations here are less common than in the Eocene (Weyl, 1980).

From the Miocene onwards, marine sediments are rare in the Tempisque Trough, dominated instead by estuarine and alluvial sediments (Figure 1.3) that can be shown to be the infill of fault angle depressions. The recent Gulf of Nicoya is the remnant of the previous Tempisque Trough fore-arc basin, possibly kept open by the Trans-Isthmus Fault System (Seyfried *et al.*, 1991). In the Nicaraguan Trough, a thick sequence of volcanogenic sediments (Weyl, 1980) interlock with the central Nicaraguan Miocene volcanics. Towards

the top of this sequence, deltaic deposits with a high volcanoclastic and pyroclastic content take over and these are followed by the thick pyroclastics of the Pliocene to Pleistocene Las Sierras Group (up to 680 m, discussed below).

The Magmatic Suite: The oceanic rocks of the Nicoya Complex basement have been described earlier. The first record of the subsequent calc-alkaline arc is recognised in Maastrichtian fore-arc sediments. The identification of rhyolitic boulders in the fore-arc detritus has hinted that the first climax in the differentiation was reached in the Eocene. Products of the early Tertiary arc in southern Costa Rica (mainly Eocene andesites) are exposed in the Cordillera de Talamanca (location in Figure 1.2) but there are no contemporaneous rhyolites (Pilcher and Weyl, 1975). Although the measured transport directions in the fore-arc sediments (Astorga, 1987, reported by Seyfried *et al.*, 1991) suggest that the northern Costa Rica arc had developed to the north-east of the fore-arc, the exact location of the early Tertiary arc here is poorly known.

There appears to have been a hiatus in activity during the Oligocene in Costa Rica generally, as no magmatic rocks are known from this time. Seyfried *et al.* (1991) reported that compressional deformation started at the end of the Eocene in the fore-arc, and there is little evidence for Early Oligocene sedimentation. Sedimentation during the Late Oligocene began on an angular unconformity (Figure 1.3) and they interpreted this as uplift of the area due to increased plate coupling during the Early Oligocene. This implies that subduction was reduced or halted and explains the apparent lack of Oligocene magmatism. A similar lack of magmatism today in southern Costa Rica is due to the arrival of the Cocos Ridge (Figure 1.2).

The easternmost Tertiary volcanics are dominated by pyroclastics. These are exposed in northern Costa Rica and the Miocene to Pliocene volcanics in Nicaragua some 50-100 km north-east of the Quaternary arc (Figure 1.1), suggesting that the subduction zone may have been shallower in the Late Tertiary, but steepened by the Pliocene. To the south, in the Cordillera de Talamanca, Miocene calc-alkaline plutonic and volcanic rocks are exposed. Contemporaneous andesitic volcanics are also exposed in parts of the Cordillera Central and the Cordillera de Talamanca (Weyl, 1980, Figure 1.1). The plutonics are dominantly quartz

monzonites but range from gabbros through granites to alkaline rocks (aplite granites) (Weyl, 1980). The Middle to Upper Miocene plutonism of Talamanca (11.4 to 8.5 Ma, Weyl, 1980) predates the Upper Miocene to Pliocene plutonism in Tilarán to the north. Miocene to early Pliocene alkali volcanics, undersaturated in SiO_2, and volcanoclastic deposits of the Cordillera de Tilaran have not been been mapped as distinct units, but placed together in the Aguacate Group. Plutonic rocks of any age are not exposed in the Cordillera de Guanacaste. The Miocene to Pliocene plutonism is generally interpreted as an increase in the rate of subduction (e.g. Weyl, 1980). This would also explain the shallower angle of subduction proposed for the Tertiary pyroclastics exposed in the Nicaraguan Depression. The topography of Costa Rica shows that the Cordillera de Talamanca and the Cordillera Central are at a greater elevation than the northern Cordillera and the Bouguer gravity map (from Weyl, 1980) shows 20 to 50 mGal negative anomalies over the former Cordillera. Greater uplift and negative Bouguer anomalies would be expected where there has been abundant intracrustal silicic plutonism. (The regional Bouguer gravity map is further discussed in Chapter 3).

The oldest *in situ* volcanic rocks of the Guanacaste arc belong to the lowermost ignimbrites of the important Santa Rosa Ignimbrite Plateau (Chiesa *et al.*, 1987) and date from the Upper Miocene (7.85±0.16 Ma, Gillot *et al.*, 1990). At least 300 m of these pyroclastics, identified from boreholes (Seyfried *et al.*, 1991), overlie the Tertiary sediments of the inner Tempisque Trough (located in Figure 1.1) and are also present within the back-arc depression. The number of distinct ignimbrites and their possible source areas are both poorly understood (Chiesa *et al.*, 1987), but the distribution of the ignimbrites (further discussed in Chapter 2) implies that the source calderas are buried beneath the more recent stratovolcano chain in Guanacaste. Much radiometric dating of the ignimbrite plateau remains to be done before the age relations are fully understood, but the available ages suggest that the pyroclastic activity was concentrated even later during the Late Pliocene and the Quaternary (Bellon and Tournon, 1978, Tournon, 1984, ICE, *comm. lit.*, Gillot *et al.*, 1990). The Santa Rosa Ignimbrites are broadly contemporaneous and in line with the Las Sierras pyroclastics exposed in southern Nicaragua, suggesting that the processes responsible for this explosive hiatus in volcanic activity were operating independently of any

divide between Nicaragua and Costa Rica. To explain the westward shift of the volcanic arc between the Miocene and Pliocene the subduction site is thought to have retreated oceanward. Furthermore, from the Pliocene to the Pleistocene an increase in the rate of subduction is inferred to produce the widespread pyroclastics.

The more recent Quaternary stratovolcano formation in Costa Rica has been concentrated in the Cordillera de Guanacaste and the Cordillera Central, where it continues today (Figures 1.1 and 1.2). Quaternary volcanism has not been reported from the Cordillera de Talamanca (Weyl, 1980), which is consistent with the slowing/cessation of subduction beneath southern Costa Rica discussed in Section 1.2.1. (The Quaternary volcanism of Guanacaste is described in more detail in Chapter 2). The present volcanic chain in Nicaragua, as discussed earlier, is offset some 40 km to the east of the Guanacaste arc (Figure 1.1), again suggesting either a tear in the subducting plate (Stoiber and Carr, 1973) or a discontinuity in the overriding plate, coincident with the Santa Elena suture.

In summary, the magmatic history of Costa Rica shows a gradual increase in silica content (Weyl, 1980), reflecting the gradual transition from oceanic crust into continental crust during island arc magmatism. This process is more advanced in the south Costa Rican arc, where greater uplift has taken place and where the negative Bouguer anomalies (not present in the Guanacaste arc) are believed to be due to extensive Miocene plutonic bodies beneath those exposed today in the Talamanca Cordillera. Generally, both the Tertiary and the Quaternary volcanic arcs of Nicaragua are offset from those in Costa Rica, supporting the proposed long-lived discontinuity between the two areas. The exact position of the arc during the Tertiary in northern Costa Rica may have been further east than the present position, but without detailed ages for the Tertiary volcanics it is not possible to be certain of the timing of the arc migration.

1.2.3 Implications for the nature of the Guanacaste crust

Considering the sedimentary and magmatic evidence summarised above, the Quaternary Cordillera de Guanacaste, and possibly parts of the back-arc depression, must be underlain

by products of an evolving island arc. The crust is neither truly oceanic nor continental but transitional; how far this transition has progressed is uncertain, as discussed below.

The basement is thought to comprise Nicoya Complex-type rocks, part of the Caribbean Plate, but there is little evidence from topographic or gravity data for major silicic plutonism in Guanacaste. Nevertheless, silicic pyroclastics of the Santa Rosa Ignimbrite Plateau are widespread and do suggest that large scale differentiation of magma *has* occurred here, so at least some related plutonics should be expected at shallow crustal levels. Seyfried *et al.* (1991) argued that the post-basement fore-arc sequence is developed to a greatest thickness in the inner fore-arc (Section AB, Figure 1.1), a result of arcward tilting of this area during the cycles of uplift and relaxation of the outer arc, proposed to be related to the amount of plate coupling.

The evidence for the continuation of the Santa Elena suture beneath the northern part of the Guanacaste Cordillera is i) the recently reported exposures of basement behind the arc show that the Nicaraguan Trough does not continue into eastern Costa Rica , ii) there are contrasts between the Tertiary histories of the Nicaraguan and Tempisque Trough fore-arc regions, iii) there is a 40 km offset between the Quaternary arcs on either side of the suture. The greater thickness of the Nicaraguan Trough fill compared to the Tempisque Trough fill and the restriction of exposed basement (on both sides of the arc) to the south of the suture, implies differential subsidence across the suture during the development of the arc. The basement in the depressed area behind the Guanacaste Arc is much shallower than previously believed, and it is reasonable to suggest, therefore, that the basement should be shallower beneath the Guanacaste arc than beneath either the Costa Rican fore-arc or the southern Nicaraguan arc.

This working model of the structure of the Guanacaste arc will be examined during the analysis of the regional gravity anomalies in Chapter 3.

CHAPTER 2

STRATIGRAPHY OF THE GUAYABO CALDERA

Introduction

The reservoir rocks of the Miravalles geothermal field have previously been described as tuffs and lavas that make up part of the fill of the Guayabo caldera (ELC, 1986 a). The limits of the caldera were therefore considered natural boundaries to the reservoir and one of the objectives of the previous and present geological and geophysical studies was to delineate the southern boundary of the caldera, close to the main geothermal production area.

During this study the geological and geophysical models evolved in parallel, with an emphasis on understanding all the available stratigraphic data to constrain the interpretation of the geophysics. The purpose of this chapter is to provide a stratigraphic model of the geological evolution of the Guayabo caldera, based on detailed *stratigraphic* criteria from surface outcrop and borehole logs. This "working" evolutionary model is of a three dimensional nature only within the borefield area, but it is used to constrain the more laterally extensive structural models derived from geophysics that are presented in the following chapter. The stratigraphic model is the result of an objective review and reinterpretation of data presented in previous, largely unpublished, technical reports written during the exploration and development of the Miravalles Geothermal Project (MGP). A dominant theme throughout this chapter is an emphasis on the contrasts between the stratigraphic models proposed by previous workers and the new stratigraphic model presented here. For the first time, correlations between intra- and extra-caldera stratigraphy are proposed and the most important proposed divergence from previous stratigraphic and structural models is that the *present* topographic expression of the Guayabo caldera is the result of the collapse of only the most recent intra-caldera stratigraphy. Most of the geothermal reservoir rocks predate the collapse of the Guayabo caldera and may therefore extend well beyond the caldera margins, with important implications for the geothermal reservoir limits. This hypothesis is tested and supported by the geophysical models presented in the following chapter.

2.1 The Miravalles Geothermal Project (MGP)

The history of the exploration and development objectives of the MGP is outlined here to provide a background to the present study.

Exploration for geothermal resources in Costa Rica began as a response to the 1973-1974 energy crisis (ELC, 1988). At the time of the crisis 30% of the national electricity generating capacity was thermoelectric (oil) and 70% hydroelectric. The difference between the precipitation rates during the wet and dry seasons, however, prohibits the sole reliance on the cheaper hydroelectric energy. Costa Rica has no major proven resources of hydrocarbons, so, short of importing electricity from neighbouring Central American States, alternative indigenous energy sources have had to be investigated.

Since 1968, various United Nations missions have identified localities for possible geothermal exploration. Hot water springs with a geochemistry suggesting a high-temperature source (i.e. temperatures in excess of 200°C calculated from geothermometer systems using the Na-K-Ca concentrations of chloride springs) are found only on the Pacific margin of the recent volcanoes of the Guanacaste Cordillera (see temperatures in parentheses in Figure 2.1). Exploration began at the most favourable localities on the southern flanks of Volcán Rincon de la Vieja and Volcán Miravalles (Corrales *et al.*, 1977). The subsequent development can be divided into four phases:

i) In 1975 ICE initiated prefeasibility studies on an area of 500 km^2 including shallow temperature gradient well drilling, fluid geochemistry and geophysical studies (Blackwell *et al.*, 1977; Gardner and Corrales, 1977 and Furgerson and Afonso, 1977). These showed that there were strong indications of the presence of hot geothermal brine, suitable for power generation, in the triangular area between Las Hornillas, La Union and La Fortuna (ICE, 1976) southwest of Volcán Miravalles (Figure 2.2 a).

Figure 2.1 (opposite) Map of spring locations and geothermal sites south of Rincon de la Vieja and Miravalles in Guanacaste, Costa Rica. No data are shown from the Tenorio Geothermal Project (not available). The measured fluid temperatures and the Na-Ca-K calculated temperatures (in parentheses) are shown at each site. Note the chloride springs related to the Miravalles outflow plume at La Fortuna, Salitral and Bagaces and those at Borinquen related to the Rincon system. Details of the Miravalles site in Figures 2.2 a and b.

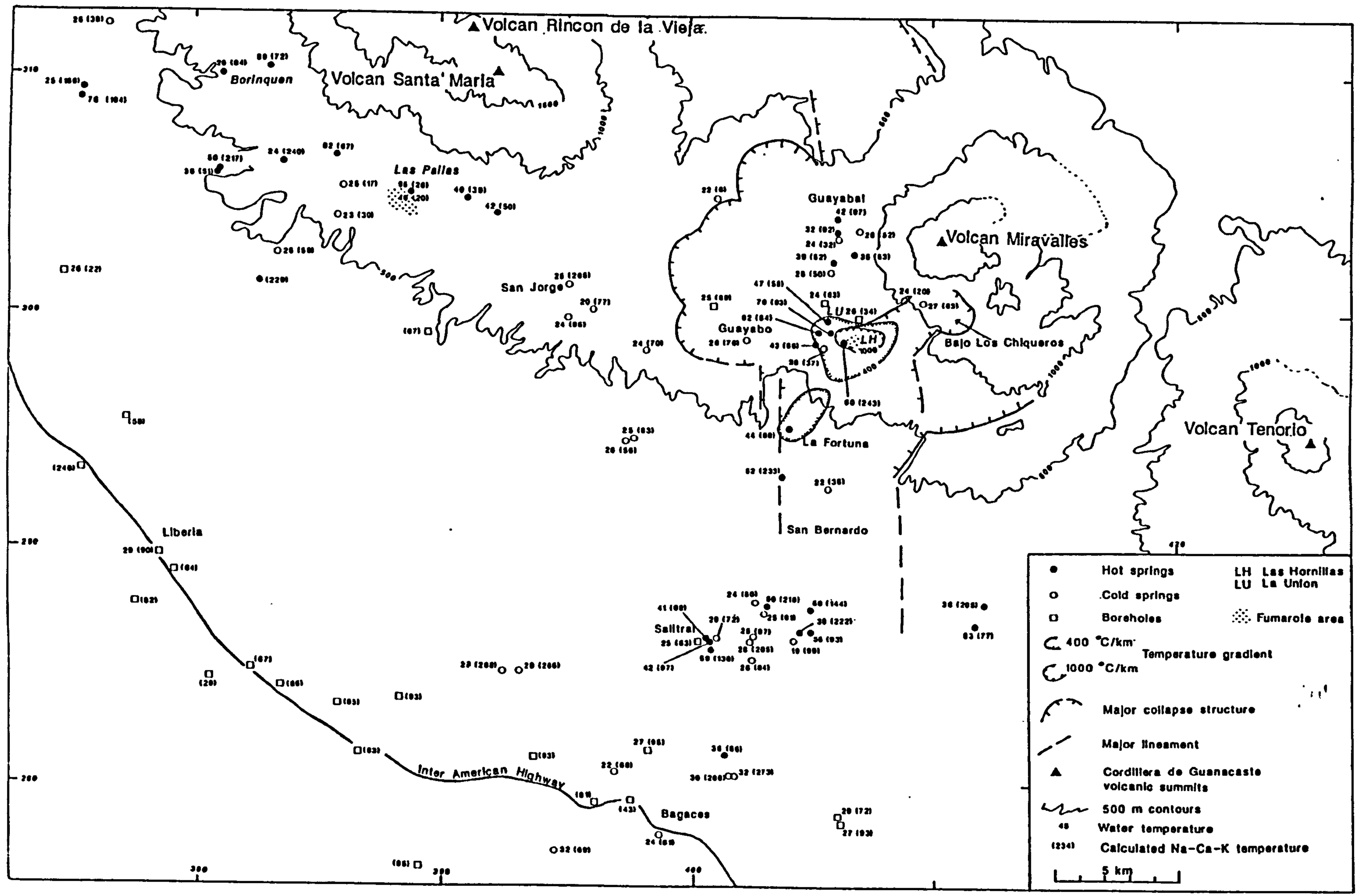
Volcan Rincon de la Vieja
Volcan Santa Maria
Borinquen
Las Pailas
Guayabal
Volcan Miravalles
San Jorge
Guayabo
LH
Bajo Los Chiqueros
La Fortuna
Volcan Tenorio
San Bernardo
Liberia
Salitral
Inter American Highway
Bagaces
Hot springs
Cold springs
Boreholes
LH Las Hornillas
LU La Union
Fumarole area
400 °C/km
1000 °C/km
Temperature gradient
Major collapse structure
Major lineament
Cordillera de Guanacaste volcanic summits
500 m contours
Water temperature
Calculated Na-Ca-K temperature
5 km

Figure 2.2 a The hydrothermal manifestations in Miravalles geothermal field showing association with recent faults (loc. Fig 2.1). Temperature gradients and alteration map from ELC (1986 a), ICE (unpubl. data) and this study. Spring and fumarole locations from ELC (1984) and ICE (unpubl. map). Locations of the deep reservoir temperature profiles, WE and NS (Figure 2.2 b) are also shown.

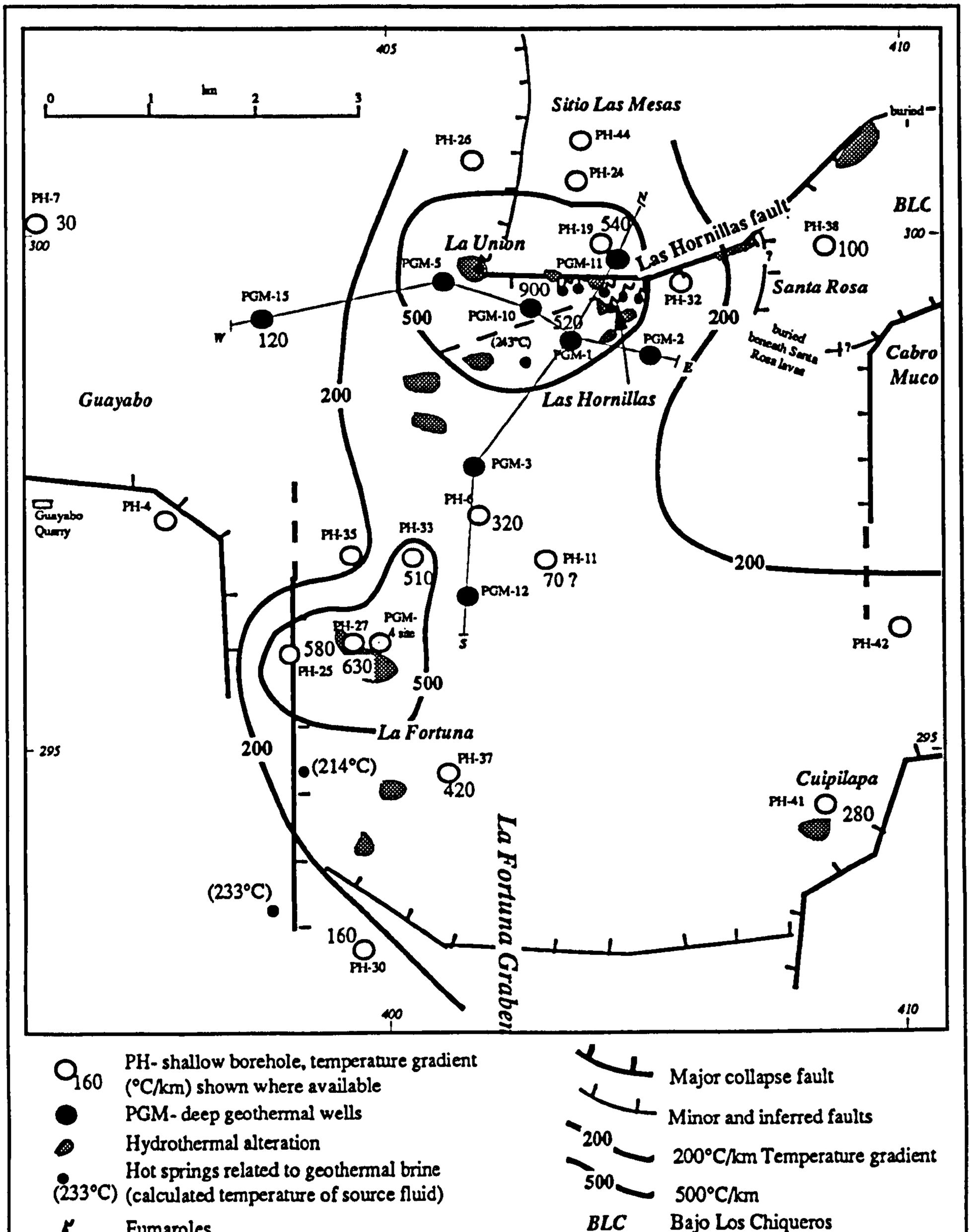

ii) During the second phase (1979-1981), ICE, together with their consultants Rogers Engineering and Geothermex, drilled three production test wells (PGM-1, 2 and 3) within the high temperature area west and southwest of Las Hornillas (Figure 2.2 a and area LH on

Figure 2.1) to a depth of approximately 1100 m into neutral chloride fluids containing 8000 ppm of dissolved solids at a maximum temperature of 240°C (Koenig, 1980).

Figure 2.2 b Cross sections of the Miravalles geothermal reservoir (loc. in Figure 2.2 a). The geological structure is adapted from, but differs from the ELC (1986 a) versions (Figure 2.6). The top of the liquid-dominated reservoir (the static water level), below the vapour zone, is distinct from and 150-200 m below, the perched near-surface water table (not shown). The upflow region is controlled by the Las Hornillas fault and the outflow plume is to the south. Temperatures from ELC (1988).

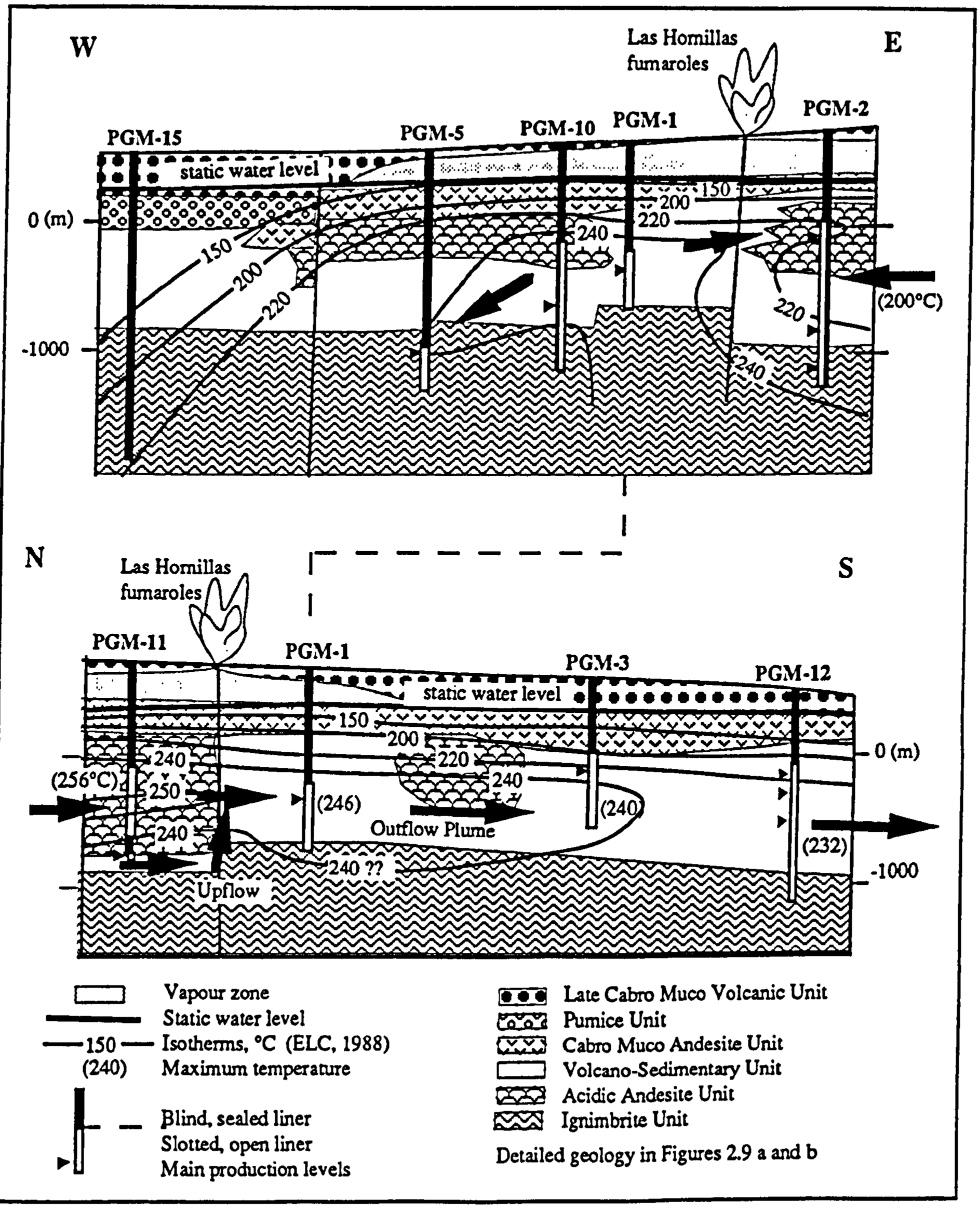

iii) The third phase (1983-1986), during which ICE employed Electroconsult (ELC) as their consultants, included drilling temperature gradient wells, complementary geoscientific

studies and drilling of additional production wells. The five extra deep geothermal wells enabled the upflow region of the geothermal reservoir to be defined close to the Las Hornillas Fault, in the north-central borefield, with a maximum temperature of 256°C at 1100 m depth in PGM-11 (Figures 2.2 a and b). The promising findings proved the feasibility of an initial 55 MW geothermoelectric power unit (ELC, 1986 a). Funding was secured by ICE, to be supervised jointly by the Government of Japan and the International Development Bank.

iv) The fourth and current phase (1987-1994 ?) includes installation of the first 55 MW unit and examining the feasibility of three more 55 MW units at Miravalles (ELC, 1988).

Reservoir hydrology: The hydrology of the geothermal reservoir is discussed in detail in Chapter 5, but is summarised here (Figure 2.2 b) to illustrate the relationship between the geology, discussed in this Chapter, and the reservoir. The west-east and north-south cross-sections are located in Figure 2.2 a, and are comparable to the detailed geology cross-sections described later. The borehole temperature logs define the flow regime; the high temperatures in the north (near PGM-11) are close to the Las Hornillas fault upflow region; the gentle temperature gradients to the south (towards PGM-12), compared with the steeper gradients to the west (PGM-15) and the east (PGM-2) define the outflow plume (i.e. the direction of maximum natural fluid flow). This southwards directed outflow plume supports the suggested Miravalles source for the geothermal springs observed from La Fortuna to Bagaces (Figure 2.1). The pressure and temperature logs together define the fluid state in the reservoir. The top of the liquid-dominated reservoir, as defined by the static water level in the wells under non-producing conditions, is at a depth of 200 to 400 m (data from ELC, 1988). A shallower, meteoric water table is required, however, to explain the surface distribution of cold springs, rivers and streams, but the low pressures at the top of the deep reservoir suggest that the shallow water table cannot extend to this depth and must therefore be perched. It is considered likely that the shallow groundwater zone is supported by an impermeable layer (argillic clays and lavas) associated with the vapour zone, rather than directly supported by the vapour zone.

Exploration outside the MGP area: The other geothermally attractive site recognised in the prefeasibility phase, at Las Pailas, Rincon de la Vieja (Figure 2.1), is located inside one of Costa Rica's National Parks; this presently prohibits any investigatory drilling or development. The extensive thermal manifestations of a near surface vapour zone at Las Pailas suggest the presence of a deeper geothermal reservoir. The fluid geothermometry results, however, failed to show evidence for a deep high temperature reservoir at the actual Las Pailas site, whereas the hot springs to the southwest of Las Pailas (and west of Borinquen) give Na-K-Ca source temperatures of up to 240°C (Figure 2.1). This fluid pattern is common at other geothermal sites where an outflow plume is present (reviewed by Henley and Ellis, 1983) and this study therefore considers that the hot pools and springs at Las Pailas represent steam-heated surficial groundwater; the steam relates to boiling of a deeper geothermal brine during which the soluble salts are retained in the brine. The geochemical signature of the deep reservoir is therefore lost, preventing any Na-K-Ca geothermometer calculations from fluids derived from fumaroles. It is possible then that the boiling reservoir beneath Las Pailas shares at least a common magmatic heat source, beneath the Volcán Rincon de la Vieja complex, with the deep geothermal fluids that have been sampled at Borinquen (which is 7 km to the west of but at a similar elevation to the fumaroles at Las Pailas). Given this evidence for a deep, extensive hot reservoir beneath the southwestern flanks of Rincon de la Vieja, this should be an exciting prospect area, providing the environmental restrictions can be balanced during any future proposed exploration and exploitation.

In an effort to locate further exploitable geothermal reserves, preliminary investigations which include drilling several temperature gradient wells are underway at a third site, on the southwestern flanks of Volcán Tenorio (Figure 2.1). This is a relatively recent project and no scientific reports were available to be incorporated in this study; hence no data from the Tenorio Geothermal Project are shown in Figure 2.1.

During the development of the MGP it became apparent that the dominant control on the distribution of the fumaroles and hot springs, upflow zones and the permeability of the geothermal reservoir at Miravalles is *structural* and therefore secondary (ELC; 1983, 1984 c,

1986 a and 1988). One of the aims of this study, therefore, is to examine the geophysical expression of the structure at the drilled and proven resource in the Miravalles area and thereby provide a working model for exploration at future sites in Guanacaste.

One of the most intriguing features of the known geothermal manifestations in Guanacaste is that they are all located on the southwestern Pacific flank, no reported hot springs or brines are on the northeastern Atlantic flank (Figure 2.1). It is considered unlikely by this author that this is due to an offset of the heat source as there is no evidence for a similar offset in the pattern of volcanic vents. The fumarole locations at Las Pailas and Miravalles are controlled by increased vertical permeability along the Coyol Grande and Las Hornillas faults respectively. This allows upwelling of the deep fluids to boiling and steam saturation conditions (as will be shown in a detailed discussion of the Miravalles reservoir in Chapter 5). A steam zone develops, capped by an impermeable argillic layer, but steam escapes to the surface along the faults, where it either mixes with groundwater (mudpots and springs) or vents directly to the atmosphere (fumaroles). Without the presence of these faults it is unlikely that the deep reservoir would have comparable surface manifestations. If deep hot brines are present but similar structures are lacking below the northern slopes, it is possible that they would therefore remain permanently below the groundwater and never reach the surface. The outflow plume at Miravalles is further examined in terms of the reservoir evolution model in Chapter 5.

2.2 Previous Ideas on the Guayabo Caldera

The culmination of geoscientific studies conducted during development phases (i) to (iii) is presented in the Final Geological Report (ELC, 1986 a). There are two distinct sources of geological information available; (i) surface exposure and (ii) drill cuttings and cores from the MGP shallow temperature gradient (PH-) wells, and cuttings and cores from the deep production (PGM-) wells. The ICE and ELC geologists concentrated on the deep borehole stratigraphy to define the geothermal reservoir lithologies and paid less attention to the outcrop geology; this was considered to be largely unrelated to the deep drilled stratigraphy. As a result, in the ELC (1986 a) geological evolution model there was no attempt to correlate

any of the individual drilled tuffs with the abundantly exposed extra-caldera tuffs, some of which are clearly related to sources within the caldera.

The objective of this review of the ELC (1986 a) model is to demonstrate the problems it poses, especially regarding the relative ages of the intra-calderic succession and the lavas exposed in the caldera walls. In addition, the picture derived by combining the geophysical evidence from previous work with new gravity data and modelling in this study is at variance with the ELC (1986 a) model and a revised stratigraphic model integrating the geophysical data will be described in Chapter 3.

2.2.1 The Guayabo caldera; a topographic definition

The Guayabo caldera is located in the Guanacaste Cordillera of northern Costa Rica, between the more recent stratovolcanic complexes of Volcán Rincon de la Vieja-Santa Maria and Volcán Miravalles (Figures 2.1 and 2.3). The caldera is defined *topographically* by ELC (1986 a) as an 11 km diameter depression, with a present day floor at 550 m average above sea level (Figure 2.4); the caldera is bounded on its northern, western and southwestern margins by steep, predominantly andesitic lava scarps of up to 200 m vertical expression (Figures 2.4 and 2.5). The caldera geology in Figure 2.5, and other figures that are referred to frequently, are included as 'pull-outs' inside the back cover. The southern and northeastern caldera margins have been obscured by downfaulting within the north-south trending La Fortuna graben and Aguas Claras depression respectively (Figure 2.5) causing the displacement of the 500 m elevation contour in these areas (Figure 2.4). The eastern margin is completely buried by the post-calderic edifices of Volcán Miravalles and the ancestral Palaeo-Miravalles, but the buried caldera margin in this area has previously been related (ELC 1983 and 1986 a) to an exposed morphotectonic scarp separating Miravalles from Palaeo-Miravalles (Figure 2.5). The Cerro Espiritu Santo fault scarp (Figures 2.4 and 2.5) marks the continuation of the caldera margin east of the La Fortuna graben, but it is not clear how this scarp relates to the supposed caldera border of ELC (1983 and 1986 a) buried beneath the Miravalles edifice to the north, as it clearly continues to the southeast of La Giganta (Figure 2.5).

Figure 2.3 Geological sketch of northern Costa Rica emphasising the distribution of the volcanic units. Adapted from Chiesa (1991) and Alvarado *et al.* (1990 a). (Guayabo Caldera = GC, 405:305).

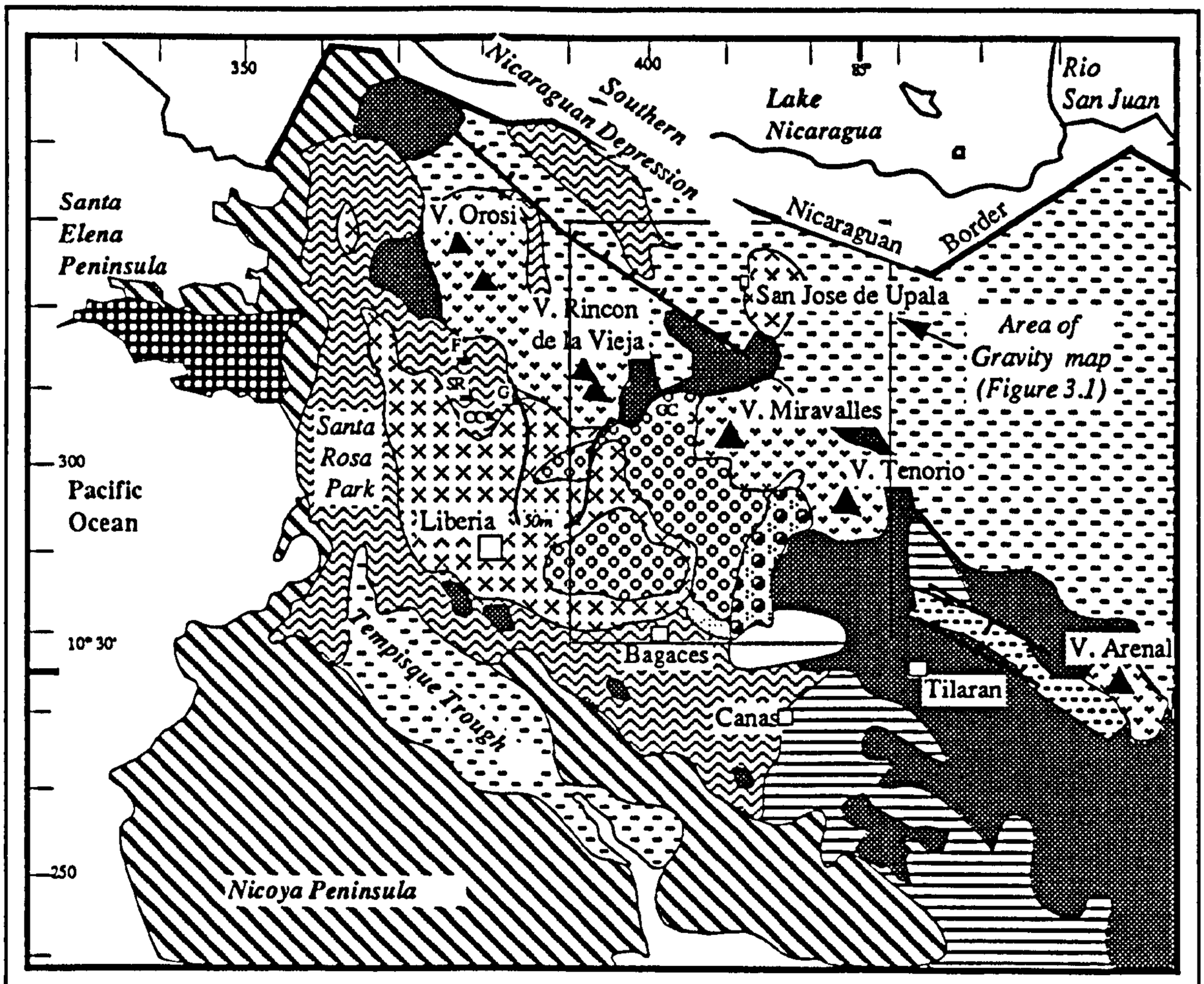

All the lavas exposed in the caldera walls and below the tuffs immediately *outside* the caldera walls have been grouped into the Pre-Caldera Lava Unit by ELC (1986 a), although it was shown that they could be spatially divided into distinct series based on their major element geochemistry (ELC, 1983). For the geological map in this study (Figure 2.5) the lavas have been divided into stratigraphic units, but where stratigraphic correlation has not been

considered possible or probable in the view of this author (as described in the forthcoming discussion) the divisions are geographic.

Figure 2.4 Topographic map of the Guayabo caldera area from 1:50,000 maps of the National Geographic Institute, Costa Rica. The walls of the flat caldera are well defined to the north (C. La Montañosa), west (C. Mogote) and southwest, but are obscured to the east by the later Volcán Miravalles edifice and to the southeast by the La Fortuna graben (the indentation of the 500 m contour here). Geology and structure shown in Figure 2.5.

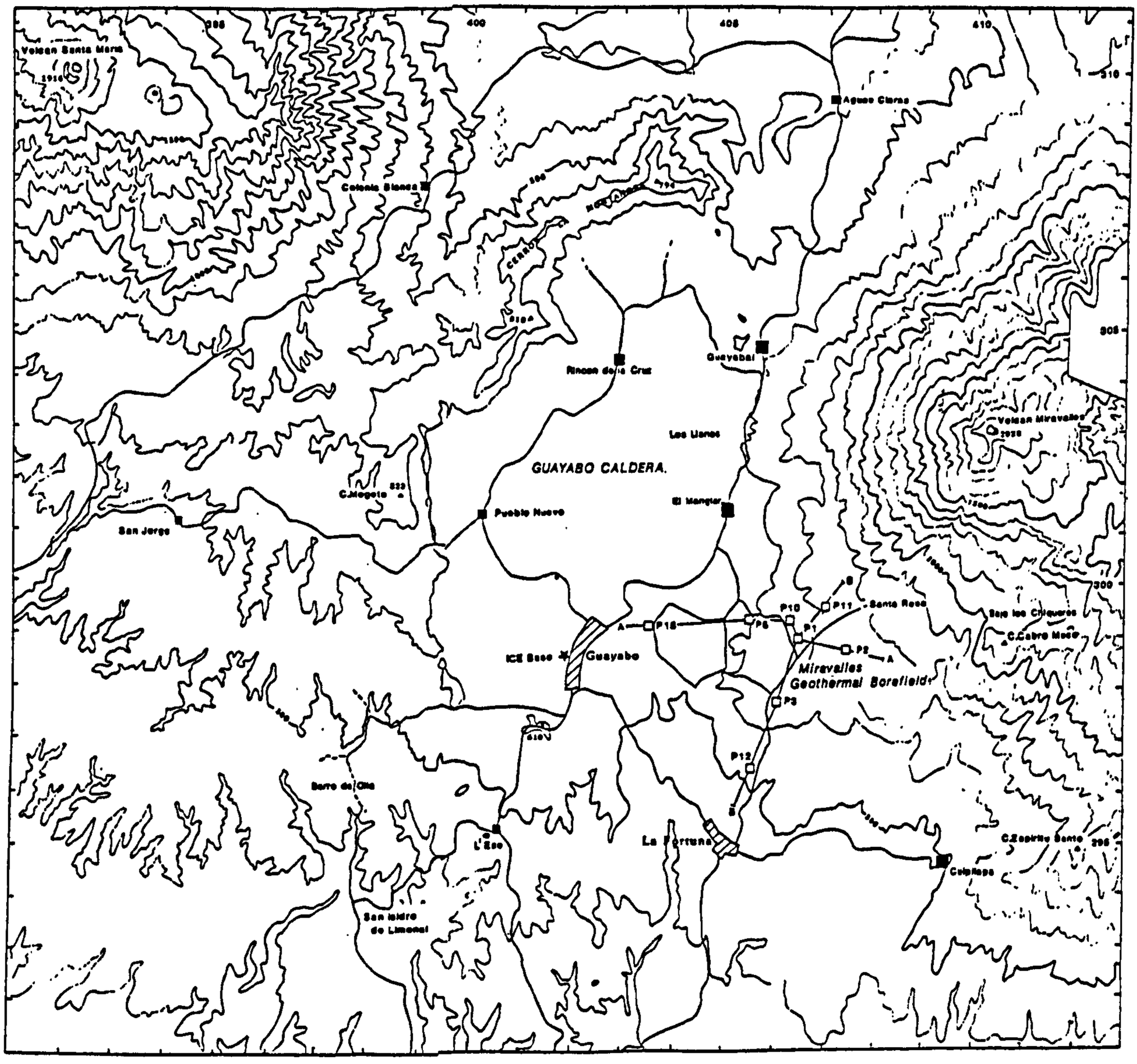

Gillot *et al.* (1990) and Alvarado *et al.* (1990) have assigned the caldera wall lavas to the same stratigraphic level as the upper Monteverde Formation andesites (Late Pliocene to Early Pleistocene) exposed northeast of Cañas (Figure 2.3); part of an early Pleistocene Volcán Guayabo-Volcán Espiritu Santo stratovolcano complex, which according to them collapsed about 1.0 Ma ago forming the Guayabo caldera. The age of the collapse of the Guayabo caldera, however, is *not* well constrained due to the scarcity of dates of the outlying tuffs related to the caldera collapse (section 2.2.2) and the low K content (hence the unreliable K-Ar dates) of the caldera wall lavas and tuffs in general (section 2.2.3). It became clear during this study that the distinctive basalt lava cone of Cerro Mogote (Figure 2.5), built along the western caldera ring fault during or following caldera collapse according to ELC (1983), is cut by the caldera subsidence event and is therefore *pre*-calderic. A sample from Cerro Mogote (sample 5v; Table 2.1) yielded a K-Ar date of 0.622 ± 0.205 Ma (ELC, 1983). An older western caldera wall lava, sample 187a from the quarry north of Cerro Mogote (location as for sample 23, Figure 2.4), yielded a date of 2.1 ± 0.5 Ma (ICE, unpubl. report, 1989). The 0.6 Ma Cerro Mogote age does not therefore give the the approximate age of ring fault formation and caldera collapse (as suggested by ELC, 1983 and 1986 a), but provides the most recent maximum limit for the age of collapse.

The stratigraphic position of the caldera wall lavas is further discussed in Section 2.3 following new geochemical analyses and the re-examination of the stratigraphy undertaken during this study.

Previous concepts of the evolution of the Guayabo caldera have been prejudiced by the assumption that the lavas exposed in the western caldera walls, that define the topographic depression of the Guayabo caldera, underlie the *entire* drilled intra-caldera succession (over 2,200 m thick at PGM-15, located in Figure 2.5) (ELC, 1986 a). The tuffs that are abundantly exposed south of the caldera have been described as products of the Guayabo caldera (ELC; 1983 and 1986 a) but have yet to be correlated with specific horizons of the drilled intra-caldera facies. Mora (1988) suggested that these are the products of several temporally and spatially distinct stages of caldera collapse of which the Guayabo caldera area is the probable source for only the most recent tuffs (details in section 2.2.3). In Section

2.3 it is shown that at least the southern caldera walls are partly made up of recent tuffs (the Guayabo Proximal Breccia, Figure 2.5) which can be correlated with drilled tuffs, and therefore the present Guayabo caldera depression post-dates some of the caldera fill.

Table 2.1 Selected K-Ar ages from the Guanacaste Arc. The dates are listed in order of, and sometimes contradict, the ELC (1986 a) stratigraphy (Figure 2.8). Sources are ELC =ELC (1983); G= Gillot *et al.* (1990); ICE (unpubl. data); BT = Bellon and Tournon (1978) and Be = Bergoeing (1982). K and ^{40}Ar data not available from all sources.

Sample	Stratigraphic Unit		Grid Reference		K %	^{40}Ar	^{40}Ar rad	Age (Ma)	Ref
10 v	Volcán Miravalles		408.0	306.5			~0	(< 0.05)	ELC
1 v	Volcán Palaeo-Miravalles		408.0	304.7			~0	(< 0.05)	ELC
7 v	Late Cabro Muco And. U.		403.0	298.0	1.23	1.09	4.97	0.228 ±0.109	ELC
"	"			"		1.58	7.52	0.331 ±0.074	ELC
2 v	C. Espiritu Santo scarp		410.6	295.5	1.00	0.85	8.56	0.219 ± 0.063	ELC
"	"			"		0.86	9.16	0.222 ± 0.134	ELC
3 v	C. Cabro Muco-La Giganta		411.6	296.4	1.14	1.84	13.50	0.414 ± 0.147	ELC
"	"			"		1.71	13.59	0.386 ± 0.063	ELC
12 v	Cabro Muco And. U., PH-35		404.7	296.8	1.25	2.20	6.61	0.452 ± 0.123	ELC
"	"			"		2.50	7.93	0.515 ± 0.089	ELC
πG49P	La Ese Pumice	glass	400.5	295.0	2.80	6.81	16.84	0.58 ± 0.01	G
"		plagioclase		"	0.39	7.43	2.60	0.62 ± 0.01	G
23a	? probably La Ese Pumice		400.7	295.6				1.01 ± 0.58	ELC
5 v	C. Mogote		398.8	301.6	0.57	1.38	2.51	0.622 ± 0.205	ELC
TM-14a	Upper Grey Ignimbrite ?		288.6	401.3				0.5 ± 0.15	ICE
ICE xx	Biotite Tuff ? Hbl. Tuff ?		407.2	288.8				0.5 (± ?)	ICE
H63	Hornblende Tuff		405.9	283.6	0.34	2.53	5.20	1.456 ± 0.036	G
πG 49A	Upper Grey Ig.	glass	400.0	286.3				1.57 ± 0.05	G
"		plagioclase		"				1.29 ± 0.03	G
CR-15b	Biotite Tuff		(399	282.3)				1.44 ± 0.0	ICE
πG 490	Biotite Tuff	glass	390.5	278.4	3.52	40.14	51.22	1.393 ± 0.03	G
"		glass		"		39.68	52.20	1.420 ± 0.03	G
"		plagioclase		"	0.59	33.66	11.25	1.83 ± 0.03	G
"		biotite		"	4.93	4.37	82.92	1.61 ± 0.06	G
MU-10	Bagaces Group		not available					0.6 ± 0.2	BT
132a	Bagaces Group		373.4	295.7				0.64 ± 0.04	ICE
21a	Pre-Caldera Lava Unit		(412	295)				0.27 ±0.1	ICE
22a	Pre-Caldera Lava Unit		(412	295)				1.07 ± 0.09	ICE
187a	Pre-Caldera Lava Unit		399.0	302.9				2.3 ± 1.0	ICE
13a	C. Cañas Dulces dacite dome		(378	303)				1.55 ± 0.5	ICE
CU-38	C. San Roque dacite dome		(376	306)				1.6 ± 0.5	BT
226a	Bagaces Group		(381	305)				4.3 ± 1.0	ICE
B-2	Bagaces Group		(390	276)				1.2 ± 0.07	Be
B-3	Bagaces Group		(382	275)				3.06 ± 0.2	Be
132b	Bagaces Group		(373	296)				3.8 ± 0.5	ICE
226b	Bagaces Group		380.8	305.3				7.5 ± 2.0	ICE
CR-18	Bagaces Gp. Flujo Carbonal		357.3	296.2				6.5 ± ?	ICE
πG 49S	Flujo Carbonal	glass	356.9	295.8	3.01	47.69	246.0	7.810 ± 0.160	G
"		glass		"		43.34	250.9	7.990 ± 0.160	G
"		plagioclase		"	0.69	31.50	21.52	7.850 ± 0.160	G
CR-12	Aguacate Group andesite		407.6	259.9				5.45 ± 0.23	ICE

2.2.2 The extra-caldera tuffs (part of the Santa Rosa Ignimbrite Plateau)

Since geothermal investigations began at Miravalles, the level of interest in the important Santa Rosa Ignimbrite Plateau escalated. These tuffs underlie parts of the most recent stratovolcanoes of the northern Guanacaste Cordillera and are abundantly exposed along the Inter-American highway from Cañas to the Nicaraguan frontier (Figure 2.3). Their collective name derives from the extensive exposures southwest of the highway in the Santa Rosa National Park. Little integration of the borehole studies of Guayabo caldera fill and these outlying tuffs has been realised, so the review of the previous studies of both is treated separately here. Much work remains to be done, including basic differentiation of the oldest units and large scale mapping, but useful studies have been started recently by ICE geologists M. Corella, O. Mora and G. Alvarado, in collaboration with Sergio Chiesa and others from Bergamo, Italy. Table 2.2 shows how the tuffs of the Plateau have been divided up as the work has progressed.

Early ideas of the stratigraphy of the Santa Rosa Ignimbrite Plateau were based on very little fieldwork. Dengo (1962) suggested that there were two units, the lowermost Bagaces Tuff and the overlying Liberia Tuff, broadly following Dondoli (1950, as reported by Mora, 1988) who differentiated between a Grey Tuff and an overlying White Tuff (Table 2.2). The pervasive Bagaces Tuffs exposed from Cañas to the Nicaraguan border, were described by Dengo (1962) as a heterogeneous mass of unstratified, unsorted pumice and lithic fragments held together by welded glass fragments; petrographically it is a welded dacite tuff. Its widespread distribution led Dengo to suggest that its source was a buried fracture along a line extending from Volcán Orosi to Volcán Tenorio (Figure 2.3). Dengo described the less voluminous Liberia Tuff as an incoherent rhyolitic tuff with evidence of welding towards the base and suggested from its distribution that it, "originated from the central vent of the Rincon de la Vieja volcano".

In a more comprehensive study of the plateau, Chiesa *et al.* (1987) and Chiesa (1991) have shown that both the Bagaces and the Liberia Tuffs are in fact composed of several distinct

tuffs, with different areal distributions, at least some of which are separated by well developed palaeosols. They suggest, therefore, that the old nomenclature should be abandoned and that the tuffs need to be described and mapped separately. The single most extensive tuff is in fact the major unit in what was previously the Liberia Formation and is referred to in this study as the Biotite Tuff (Table 2.2, after the Flujo Biotitico del Rio Liberia of Chiesa *et al.*, 1987 and Chiesa, 1991).

Table 2.2 Evolution of the nomenclature used for the tuffs of the Santa Rosa Ignimbrite Plateau, leading to the tuff names used during this study. The proposed source areas are also given. Stratigraphic order is implied. (For tuff distributions see Figures 2.3 and 2.5).

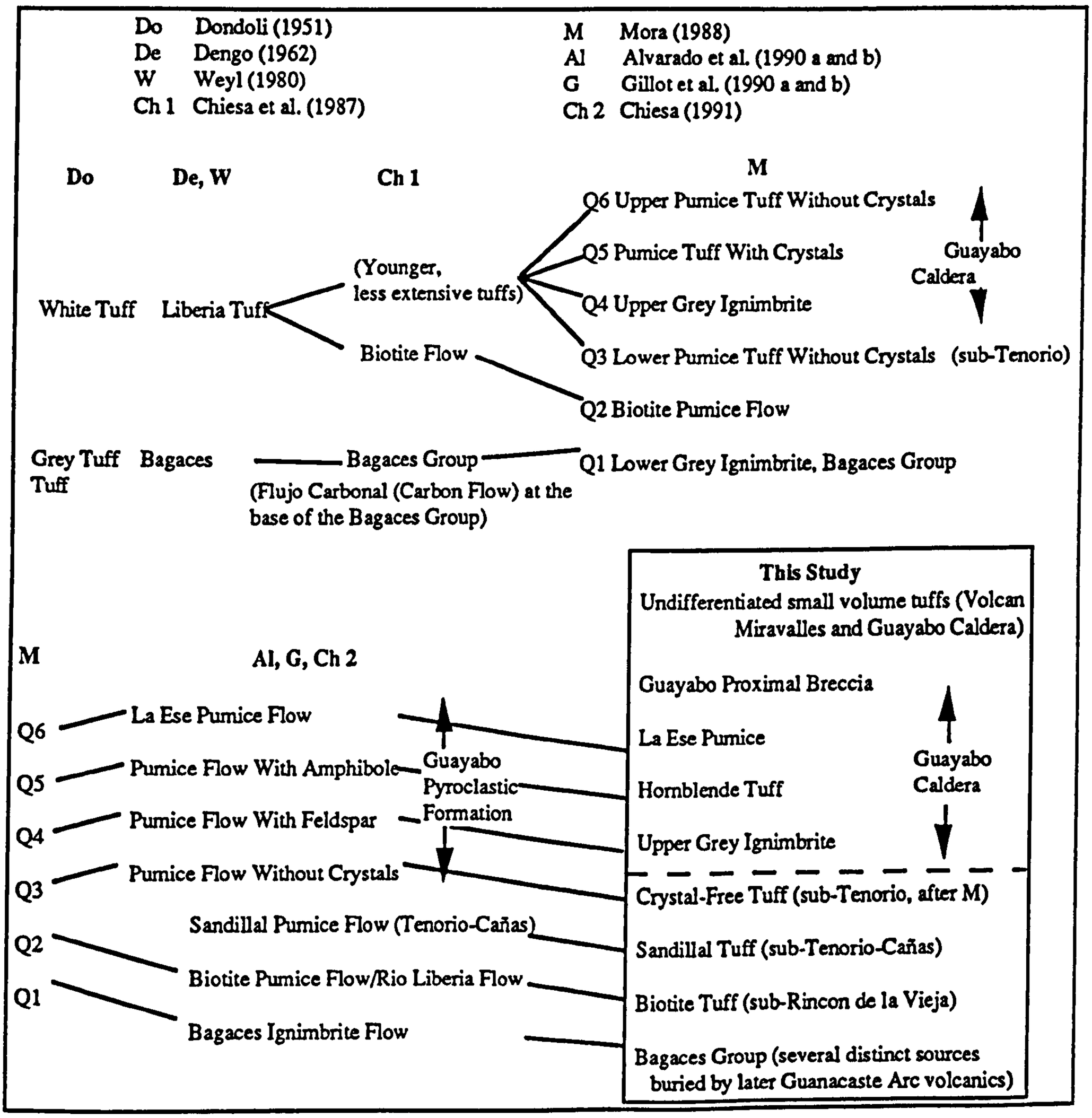

Bagaces Group: The oldest recognisable flow is the Carbon Flow (Flujo Carbonal of Chiesa *et al.*, 1987), a welded dacitic ignimbrite exposed in the Santa Rosa Park, with vertical (possibly cooling) fractures, dated at 6.5 Ma (sample CR-18; Table 2.1, from ICE

unpubl. data). Its name is derived from the very dark, glassy lava texture. This primitive flow overlies Tertiary sediments (the Brito Formation in the Tempisque Trough, Figure 2.3) but other basal flows associated with the Carbon Flow are intercalated with fine sediments of a possibly lacustrine origin suggesting a flat lying environment. The Late Miocene age for the Carbon Flow is quite distinctly older than the Late Pliocene to Pleistocene ages of other sampled flows of the Bagaces Group tuffs (except sample 226b, 7.5 Ma). The Bagaces Group tuffs are underlain in the east (sometimes separated by a palaeosol) by lavas correlated with the Tertiary Aguacate Group (Figure 2.3). The Aguacate Group comprises many distinct units covering a large area and though its age is broadly Tertiary, it is not a very useful stratigraphic marker.

Some dacitic domes in the Cañas Dulces area (north of Liberia) have been correlated by Dengo (1962) and Weyl (1980) with the Aguacate Group and form inliers to the surrounding tuffs (Figure 2.3). However, Cerro San Roque gives a date of 1.6 ± 0.5 Ma (ICE, 1976) and a sample from Cerro Cañas Dulces has been dated at 1.5 ± 0.5 Ma (Bellon & Tournon, 1978), much younger than the 5.45 ± 0.23 Ma date for an Aguacate Group lava (Table 2.1). Chiesa *et al.* (1987) considered the domes to be generally contemporaneous with the pyroclastic activity of the Bagaces Group. More recently, Gillot *et al.* (1990) dated tuffs from the Santa Rosa Ignimbrite Plateau and lavas of the Aguacate Group from the area between Volcán Arenal and Volcán Rincon de la Vieja (Figure 2.3). Their preliminary results suggest that the Guanacaste Arc evolved during four pulses of volcanic activity. The location of the stratigraphic units is shown in Figure 2.3 and selected ages are given in Table 2.1.

Phase 1 (8.0 to 1.4 Ma) Santa Rosa Ignimbrites (Bagaces Group and Biotite Tuff); vents aligned parallel to but trenchward of the present day arc. Events separated by repose times.

Phase 2 (contemporaneous with parts of Phase 1) The Aguacate Group lavas including the Cañas Dulces domes.

Phase 3 (~1.2 Ma) Build-up of the 700 km^3 lava plateau of the Monteverde formation.

Phase 4 (0.1 Ma to Present) present cycle of activity dominated by stratovolcano formation, the Guanacaste Volcanic Arc from Volcán Orosi to Volcán Arenal.

If the consistent ages of both the Cañas Dulces domes and the uppermost Bagaces Group tuffs (Table 2.1) are significantly older than the 0.6 Ma date quoted by ELC (1983) for the Cerro Mogote lavas of the western caldera wall, then the Guayabo caldera is an unlikely source for these tuffs. Furthermore, the stratigraphically youngest Guayabo caldera-related tuff, the La Ese Pumice (Figure 2.5), has an age of 0.6 Ma (Gillot *et al.*, 1990, Table 2.1), placing the age of caldera collapse between Phases 3 and 4 of Gillot *et al.* (1990), not within Phases 1 or 2. For the purposes of this study, the various poorly studied, but generally dark and coherent tuffs that underlie the Biotite Tuff are treated together (including the Carbon Flow) and will be referred to as the Bagaces Group. This simplification is not to underestimate the individual nature of these flows, that probably also have distinct source areas, but it is necessary as no detailed divisions have yet been attempted. Furthermore, it is considered that only the younger flows are important to the evolution of the Guayabo caldera itself.

Biotite Tuff: This is a poorly consolidated pumice rich rhyolitic tuff with slightly increased welding towards the base (Chiesa *et al.*, 1987; Mora, 1988 and Chiesa, 1991). It marks a significant change to more acidic and poorly welded pale coloured tuffs from the generally dacitic and more consolidated grey tuffs below. The matrix and coeval pumice contain crystals of quartz, acidic plagioclase, hornblende, characteristic biotite and oxides (in order of decreasing proportion). A sample of this flow from an exposure 4 km north of Bagaces has been dated at 1.44 Ma (ICE, unpubl. data). An exposure from near San Bernardo, of what has been mapped as the same tuff has also given a date that is nearly 1 Ma younger (0.66-0.44 Ma). The latter locality has been visited during this study and the exposure is of a flow that contains small quantities of biotite but is quite different in textural character from the Biotite Tuff. This is probably a different and indeed younger flow, unfortunately originally mapped together with the Biotite Tuff as part of the Liberia Formation. Isopach mapping by Chiesa (1991) shows that the thickness of the Biotite Tuff increases to greater than 50 m towards the northeast, in the area of Hacienda Guachepelin,

10 km south of Volcán Rincon de la Vieja, and the presumably buried source is postulated to lie somewhere *beneath* the modern Rincon de la Vieja complex (Figure 2.3), *not* within the Volcán Rincon de la Vieja summit area as proposed by Dengo (1962).

On the Atlantic side of the cordillera close to San Jose de Upala in the low lying extensional area related to the Nicaraguan Depression (Figure 2.3), there are also significant outcrops of a tuff that closely resemble the Biotite Tuff (Chiesa *et al.*, 1987 and Chiesa, 1991). This has recently been dated at 1.6 Ma (Gillot, *pers. comm.*), further suggesting that the Biotite Tuff outcrops on both sides of the arc. More recent tuffs have not been reported from this area.

Tenorio area tuffs: The Sandillal Tuff (Table 2.2 and Figure 2.3) is not recognised close to the Guayabo caldera and is considered to be related to a source in the Tenorio area (older than the present Volcán Tenorio) following Alvarado *et al.* (1990 a and b). The distribution of the younger Crystal-Free Tuff suggested to Mora (1989) that its source was also in the Tenorio area and this hypothesis is preferred here to the Guayabo caldera source proposed by Alvarado *et al.* (1990 a and b) and Gillot *et al.* (1990 a and b). These tuffs are not considered further.

Guayabo caldera related tuffs: Mora (1988) conducted a detailed study of tuffs between Guayabo and Bagaces recognising no fewer than four individual, dominantly rhyolitic tuffs above the Biotite Tuff (Table 2.2), some of which are separated by well developed palaeosols, suggesting that they did *not* form during one continuous eruptive cycle. These four tuffs are also recognised west of Rio Tenorio (the Guayabo-related tuffs shown 5-10 km northeast of Bagaces in Figure 2.3) but were given different names (Alvarado *et al.*, 1990 a and b). Table 2.2 shows how the names used in this study combine aspects of previous nomenclature systems but avoid some of the cumbersome terminology. The distributions of the three uppermost tuffs of Mora (1988) (the Upper Grey Ignimbrite, the Hornblende Tuff and the La Ese Pumice) and the overlying Guayabo Proximal Breccia, recognised during this study, suggest that the adjacent Guayabo caldera is the source area (Figures 2.3 and 2.5). This raises the question of correlation of these upper units with at least *some* of the intra-calderic tuffs identified in the borehole sections and, as attempted in the light of geological investigations carried out during this study.

2.2.3 The radiometric ages; a question of interpretation

While developing previous evolution models of the Guayabo caldera, much use has been made of largely unpublished radiometric ages of exposed lavas and tuffs (summarised in Table 2.1). Often no mention is made of the technique employed, let alone a breakdown of the isotope concentrations given, so that an independent analysis of the meaning of many ages is not possible. Where mentioned, the tuff and lava ages are K-Ar ages and it is assumed that this is true of the remainder, but it is not clear whether these are whole rock or mineral separate analyses. Some of the ages contradict the stratigraphy. For instance the 0.2 Ma age of a Cerro Espiritu Santo lava (sample 2v; Table 2.1 and Figure 2.5) is "younger" than the stratigraphically younger Cabro Muco-La Giganta lava (sample 3v) date of 0.4 ± 0.1 Ma It is possible that this is a stratigraphic error as Sample 2v is a lava block that may actually be an explosive product of Cerro Cabro Muco, and not derived from the scree of Cerro Espiritu Santo. The 1.44 Ma date for the Biotite Tuff is older than two of the ages of the supposedly stratigraphically older Bagaces Group tuffs sampled to the west (Table 2.1). This may be stratigraphic problem, however, rather than a radiometric one and some of the younger Bagaces Group tuffs that are not in the vicinity of exposures of the Biotite Tuff may indeed be younger.

The standard deviation on a given age is, in part, inversely proportional to the fraction of total ^{40}Ar that is radiogenic (Dalrymple and Lanphere, 1969). This is because the error in the atmospheric argon correction is much more serious when it represents the major fraction of total argon. The ELC (1983) samples have low radiogenic ^{40}Ar fractions of between 2.5 and 14 %, and those much below 10% (i.e. all samples except 3v and perhaps 2v) are possibly too low to use the K-Ar dating technique (Simon Kelly, *pers. comm.*).

Systematic, rather than analytical, errors can be incurred by argon loss, atmospheric contamination or, worse still, leaching and/or exchange with circulating fluid, especially one that is of hydrothermal origin in the geothermal field area, probably carrying argon from previous water-rock interaction. A repeatable result, therefore, only implies analytical precision but not necessarily an accurate age for a rock that may have been altered, albeit

uniformly. Many of the lava outcrops typically are badly weathered as a result of the humid tropical conditions and it is often difficult to find suitable exposure. The exposed tuffs are very porous and have certainly been open to circulation of meteoric waters.

The main implications for this study are that K-Ar ages quoted in the literature without a breakdown of the data or technique cannot be accepted without caution. The more recent K-Ar ages of the low-K rocks from Gillot *et al.* (1990) (Table 2.1), are of both glasses and mineral separates, and as these are in good agreement they are considered the most reliable. For the purposes of this study the emphasis will be placed on the actual field relations between the stratigraphic units, using radiometric ages only to provide a broad framework rather than an absolute stratigraphy.

2.2.4 The ELC (1986 a) intra-caldera stratigraphy

The intra-caldera stratigraphy according to ELC (1986 a) and other published and unpublished ICE and ELC reports up to 1986 is summarised as a prelude to developing a revised, integrated stratigraphy in Section 2.3.

Most of the intra-caldera stratigraphy is not exposed and the deeper levels have only been identified from drill cuttings and several cored sections of eight deep geothermal production boreholes drilled in the southeastern part of the caldera (Figures 2.2 a and 2.5). These were drilled specifically to delineate the permeable horizons within the high temperature geothermal reservoir and therefore, in many sections, the primary lithology has been at least partially overprinted by alteration products. Total loss of the drill chippings with the drilling fluid within or below the permeable horizons often resulted in downhole stratigraphic gaps between cored sections; in these cases the changes in drilling speed, related to the hardness of the rock, gave some very basic lithological information. As a result of the overall loss of primary geological information, the individual stratigraphic units, such as distinct lava flows and tuffs, are sometimes difficult correlate between wells. As a necessary simplification ELC (1986 a) defined larger stratigraphic units discriminated by distinctive general characteristics (see the borefield cross sections; Figure 2.6) as follows:

The Ignimbrite Unit: This was the deepest unit recognised in the intra-caldera succession (Figure 2.6), present below 800 m b.s.l. in five wells and it was believed to be the densest and basal fraction of the caldera collapse products. Five cores from three wells showed that it was a coherent tuff composed of unsorted polygenetic lava clasts set in a glassy matrix. Fiamme can be recognised, showing evidence of partial resorbtion and welding. The base of this unit was not drilled and the 800 m thickness at PGM-15 implied a caldera floor subsidence of at least 2400 m as this unit was considered by ELC (1986 a) to be younger than the Pre-Caldera Lavas exposed in the caldera walls.

The Lava-Tuff Unit: A thickness of 200-300 m was recognised by ELC (1986 a) above the Ignimbrite Unit at the western three wells (PGM-5, 10 and 15). Recognised only from cuttings, the unit consisted of an alternating sequence of lavas and tuffs in an approximate ratio of 2:1. Lavas of this unit may also have been drilled at the base of PGM-1 where the drilling speed slowed rapidly. This unit was presumed to represent the products of a now collapsed and buried polygenetic volcano, located in the northwestern borefield area.

The Volcano-Sedimentary Unit: A variable thickness of 100-1000 m was recognised from drill cuttings in all wells and seventeen cores from PGM-1, 2, 3 and 12. It consisted of tuffs, lacustrine sediments (not found in the Lava-Tuff Unit) and occasional lavas. The principal lacustrine mud intercalation (up to 50 m thick) provided a useful horizontal stratigraphic marker. The Volcano-Sedimentary Unit was thought to reflect an environment undergoing rapid morphological changes between the contemporaneous lava domes of the Acidic-Andesite Unit.

The Acidic-Andesite Unit: ELC (1986 a) reported this unit as the **Dacite-Latite Unit**, but subsequently (as reported by ELC, 1988) it was learned that the composition of this lava sequence was in fact acidic andesite. There are some horizons of andesite, but the lavas of this unit can generally be distinguished by the presence of abundant K-feldspar in the matrix. A thickness of up to 900 m was recognised in four northeastern wells (PGM-2, 5, 10 and 11), but as this unit corresponds to the geoelectric resistive basement, resistivity profiles allowed its lateral extent to be mapped between wells (Figure 2.6 and for further

details see Chapter 3). The limited lateral extent of this thick sequence of andesites had suggested that the lavas may have formed as domes, but it was also argued by ELC (1986 a) that there may be some lateral faults separating the sequence from the contemporaneous Volcano-Sedimentary Unit.

Figure 2.6 The main features of the ELC (1986 a) borehole stratigraphy. All the units shown were believed to be the infill of the Guayabo caldera. The details of the stratigraphy are shown in Figures 2.9 and 2.10.

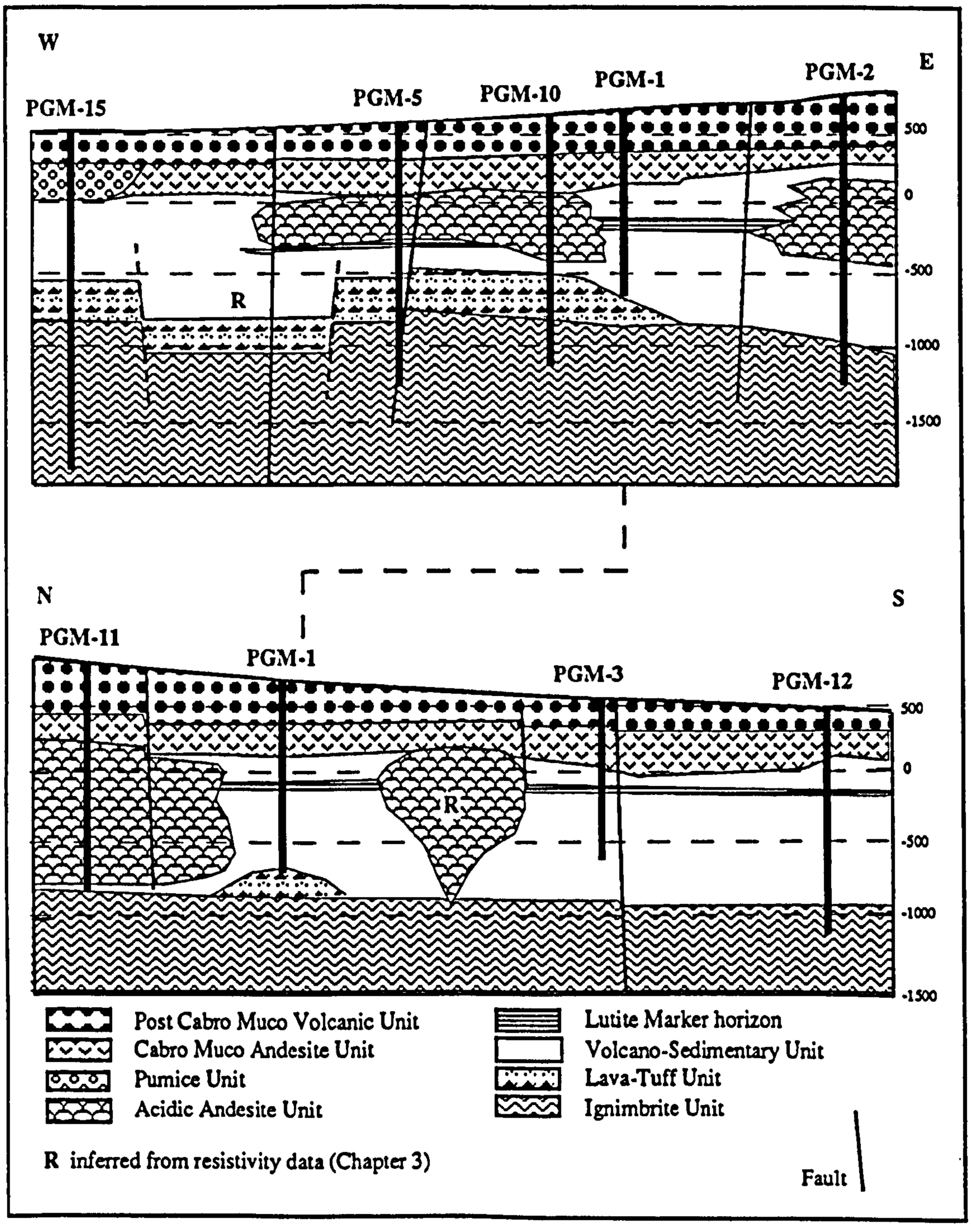

The Cabro Muco Andesite Unit: 100-400 m of these lavas were identified in every well, except PGM-15, and the unit was cored in PGM-1. It consisted of a series of compositionally uniform porphyritic andesites, with an intercalation of tuff only at PGM-12.

Its thickness, distribution and stratigraphic position (Figure 2.6) suggested that it could be correlated with the Cerro Cabro Muco-La Giganta complex to the east (Figure 2.5). ELC (1983) gave an age of 0.48 Ma for a Cabro Muco Andesite Unit lava from PH-35 (sample 12v, Table 2.1) and an age of 0.4 Ma for a lava from the Cerro Cabro Muco edifice. These ages are considerably older than the Volcán Miravalles edifice samples (< 50,000 years old, ELC, 1983), but only 0.2 Ma younger than the Cerro Mogote lavas (0.6 Ma).

Pumice Unit: 300 m of this unit was drilled *only* at PGM-15. It comprised a basal pumice-rich pyroclastic deposit and an upper portion that was largely made up of reworked basal material. A proposed source area was not clearly defined by ELC (1986 a) but the great thickness at PGM-15 was attributed to a possible palaeo-valley there. This unit was thought to be laterally contemporaneous with the Cabro Muco Andesite Unit, as it occurred at the same stratigraphic level (Figure 2.6).

The Post-Cabro Muco Volcanic Unit: This was identified in the upper 250-300 m of all wells. It included all the recent volcanic products (lavas and tuffs) and intercalated lahars and sediments that make up the present day caldera floor (Figure 2.5). There were rapid lateral changes in lithology and thickness of the individual units. The eastward increase in surface elevation and thickness of this unit suggested that it was related to the collapse of various edifices in the east, including parts of the Cerro Cabro Muco-La Giganta complex into what is now the fault-bounded Bajo los Chiqueros depression (Figure 2.5). A lava block from the lahar (sample 7v, Table 2.1 and Figure 2.5) has a K-Ar age of 0.28 Ma (ELC, 1983), younger than the Cabro Muco Andesite Unit and Cerro Cabro Muco edifice lavas, but similar to the 0.22 Ma age of the supposed Cabro Muco block (sample 2v) on the Cerro Espiritu Santo scarp (Figure 2.5).

The younger stratigraphy was not described in detail by ELC (1986 a) but a resumé of other reports is presented:

The Volcán Miravalles Edifice: This was distinguished by ELC (1983) from the Post Cabro Muco Volcanic Unit. The Miravalles edifice comprises many vegetated and scarred coalescing centres, the summits of which form a northeast to southwest chain that is

presently inactive (Figure 2.5). Volcán Miravalles itself is the product of the most recent activity along this line, with previous centres to the north-east making up what has been referred to as Palaeo-Miravalles (ELC, 1983, and 1984 c). The boundary is a well defined (but vegetated) morphotectonic scarp on the southern flank of the present edifice (Figure 2.5) but is less clear on the northern side. Some of the Post Cabro Muco Volcanic Unit had been attributed to the collapse of Palaeo-Miravalles, as well as Cabro Muco itself (ELC, 1983). The K-Ar ages for the two samples from the north flank (1v and 10 v, Table 2.1, Figure 2.5) have such small quantities of radiogenic Ar, indicating to ELC (1983) that both were less than 50,000 years old. This suggests that there may have been a significant repose time (0.2-0.4 Ma) between the build-up of the Cabro Muco-La Giganta edifice and the formation of the Miravalles edifice.

The Santa Rosa Lavas: These porphyritic, scoriaceous and massive andesitic lavas are the most recent lavas dated from the Miravalles volcanic complex. Melson *et al.* (1986) gave a tentative age of 8,000 yr BP for the blocky lavas (technique not known as the reference is unavailable, but reported by Newhall and Dzurisin, 1988 and a similar age was quoted by Mainieri *et al.*, 1985). Recent mapping by ICE geologists (Alvarado *et al.*; unpubl. map) suggested a source region close to the northwestern margin of the Bajo Los Chiqueros collapse sector (Figure 2.5). There is also a small volume pumice-rich tuff, of similar age to the lavas (7,000 yr BP, Melson *et al.*, 1986; as reported by Newhall and Dzurisin, 1988). The scattered exposures of this pumice over the Santa Rosa area and Sitio las Mesas are not shown in Figure 2.5, but the exposure thicknesses and the pumice and lithic size distribution, observed during this study between the borefield and Bajo los Chiqueros, suggests that the vent is towards the northwest of Bajo los Chiqueros, possibly Volcán Miravalles itself, in a similar area to the supposed Santa Rosa Lava source.

Historical Activity: Hantke (1951, as reported by Newhall and Dzurisin, 1988) reported a steam eruption from high on slopes of Volcán Miravalles in 1946, which formed a crater 20 m in diameter but Miravalles has not shown any effusive volcanic activity in historical times. It is not known if this eruption was from the Las Hornillas area (at 700 m, Figure 2.3), or indeed higher up the flanks. The steep-sided, vegetated crater of Volcán Miravalles

was visited during this study and no evidence of thermal activity was found. The only present surface manifestations of volcanic activity are the boiling mud pools and fumaroles of Las Hornillas and La Union (Figure 2.2 a) and the more widespread associated hot springs to the south (Figure 2.1). The magmatic heat source for the Miravalles geothermal system is considered to be located northeast of the borefield, beneath the southern flanks of Miravalles (ELC, 1986) and it is probable that the magmatic source is related to the most recent volcanic activity of the Santa Rosa lavas and the small pumice eruption. A full discussion, related to the evolution of the geothermal field, follows the interpretation of the available geophysics in Chapter 3.

2.2.5 The ELC (1986 a) structural evolution model

This section summarises the ELC (1986 a) structural interpretation of the Guayabo caldera, developed using the stratigraphy described above, but without the aid of geophysical survey results, which were largely carried out and presented later. Figure 2.5 shows the location of the exposed faults and morphotectonic screes that are pertinent to the structural setting. The evolution was divided into four phases (Figure 2.7) by ELC (1983 and 1986 a) with the emphasis of the model on the deep borehole stratigraphy; i.e. the *intra*-caldera geology. A summary of the stratigraphic relationships between the units of the drilled and exposed geology, derived from ELC (1983 and 1986 a) is given in Figure 2.8. This illustrates the most important corollary of the model; the entire drilled stratigraphy to a depth of over 2,400 m *postdates* all the caldera wall lavas.

Phase 1 Major Caldera Collapse (~ 0.6 Ma): Eruption of the extra-caldera pyroclastic flows and penecontemporaneous collapse of the Guayabo caldera, that may have been influenced by east-west extension resulting in the activation of the N-S trending graben fault system (Figure 2.7 a). No detailed mapping of the extra-caldera tuffs had been undertaken at the time this model was proposed (1983-1986) and therefore no specific tuffs were assigned to the collapse event; both the Bagaces Formation and Liberia Formation ignimbrites were correlated with the collapse of the Guayabo caldera, mainly with the intra-caldera Ignimbrite Unit. Lava domes (e.g. Cerro Mogote) developed along the caldera ring fractures about 0.6 Ma, which thereby provided ELC (1983) with an inferred date for the

caldera collapse. It is not clear from the ELC model, however, whether the Cerro Mogote dome had been interpreted as just pre-, syn- or post-major caldera collapse. During and following collapse, the caldera filled with pyroclastics of the Ignimbrite Unit, followed by lavas, tuffs and sediments of the Lava-Tuff Unit (a central vent source), the Acidic-Andesite Unit (an eastern source) and the Volcano-Sedimentary Unit (no source area specified).

Figure 2.7 a-b The ELC (1983 and 1986 a) evolution of the Guayabo caldera, Phases 1 and 2.

a) Phase 1 (0.6 Ma): Caldera collapse in arcuate sectors, formation of Outflow tuffs, Ignimbrite Unit (IG), peri-caldera domes, Lava-Tuff Unit (LT).

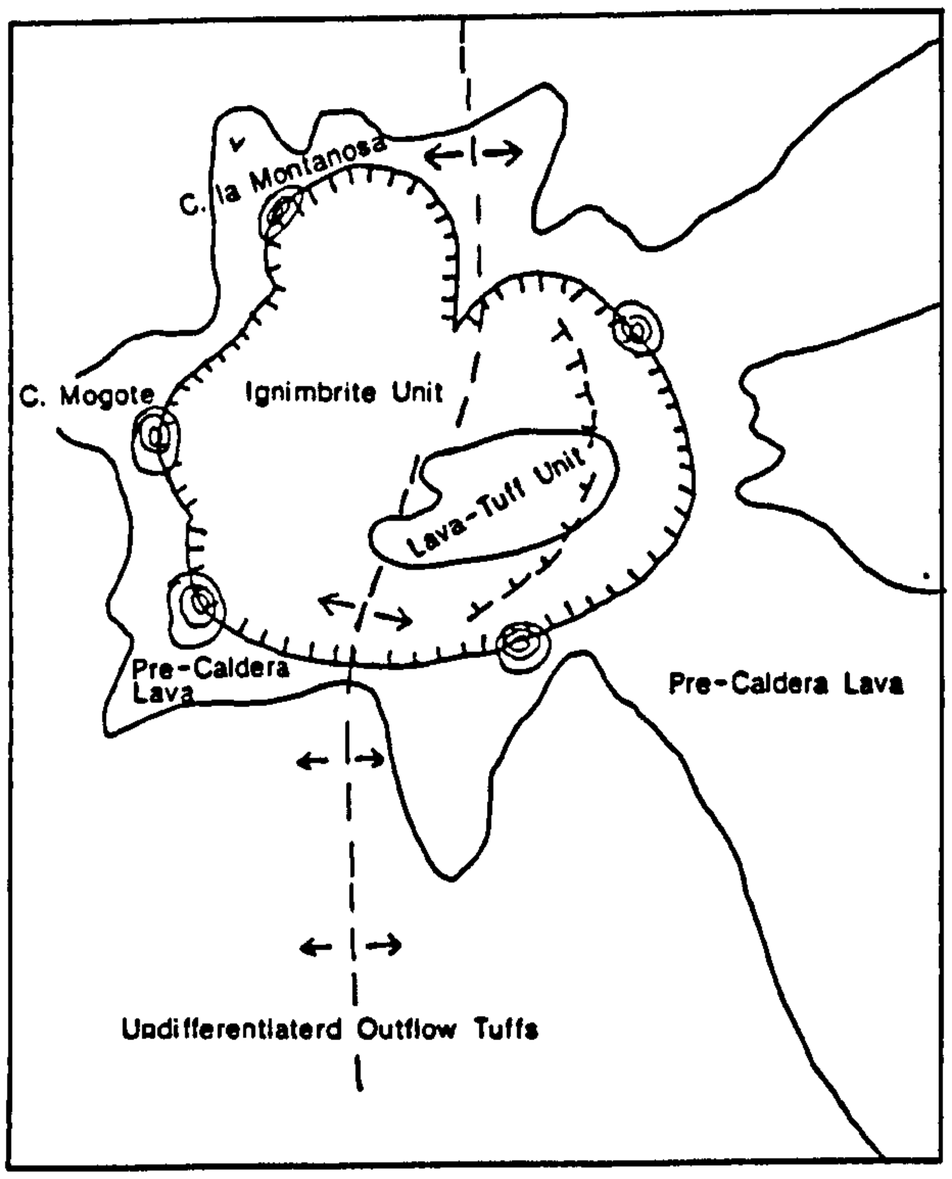

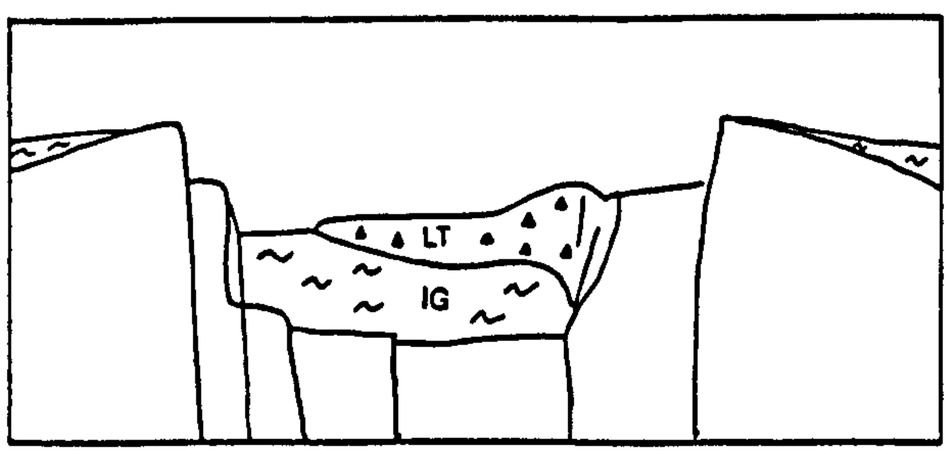

b) Phase 2 (0.4 Ma): East-west extension, caldera fills with Volcano-Sedimentary Unit (VS) and Acidic Andesite Unit (AA). Growth of Cabro Muco-La Giganta complex in southeast (CMA).

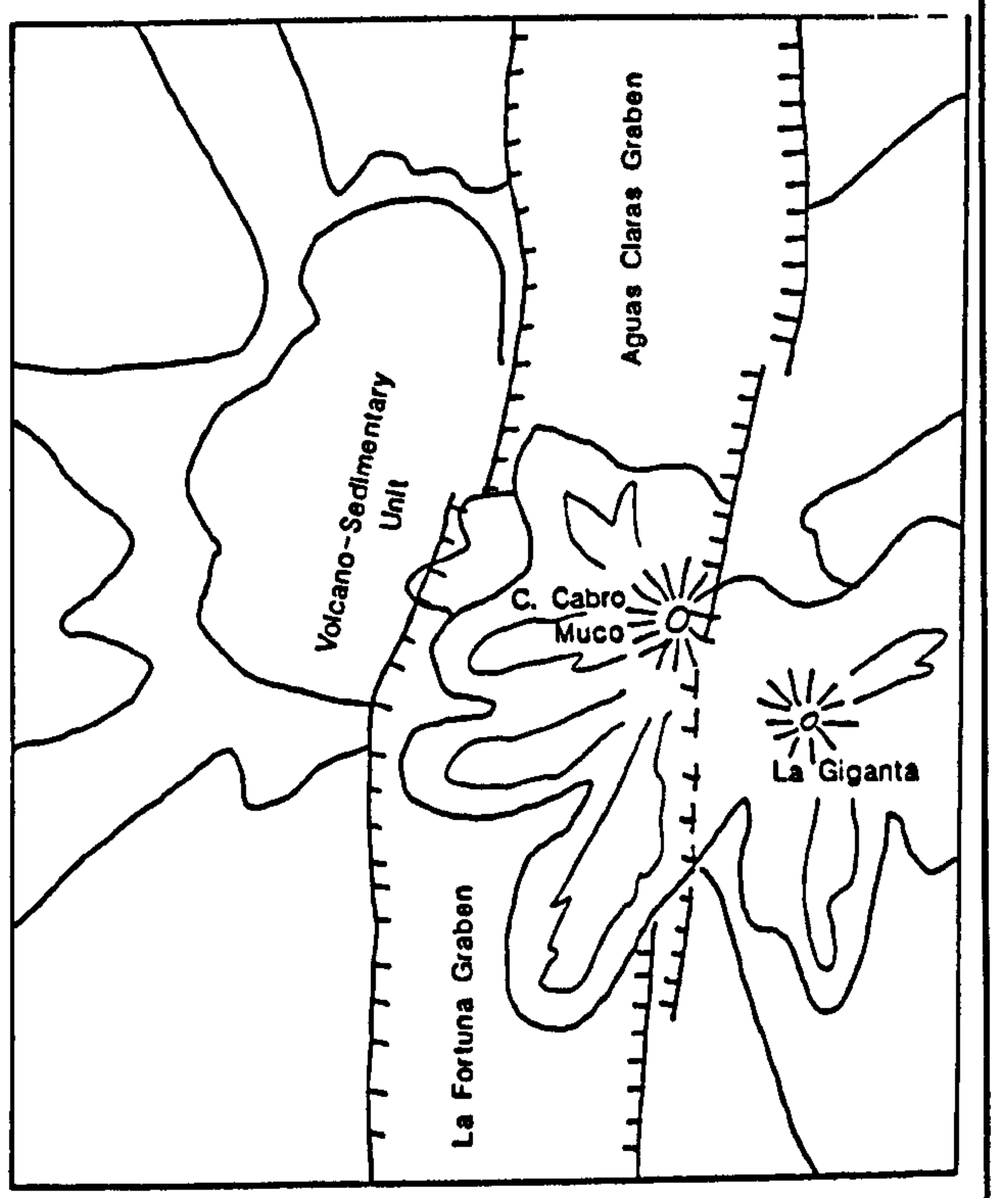

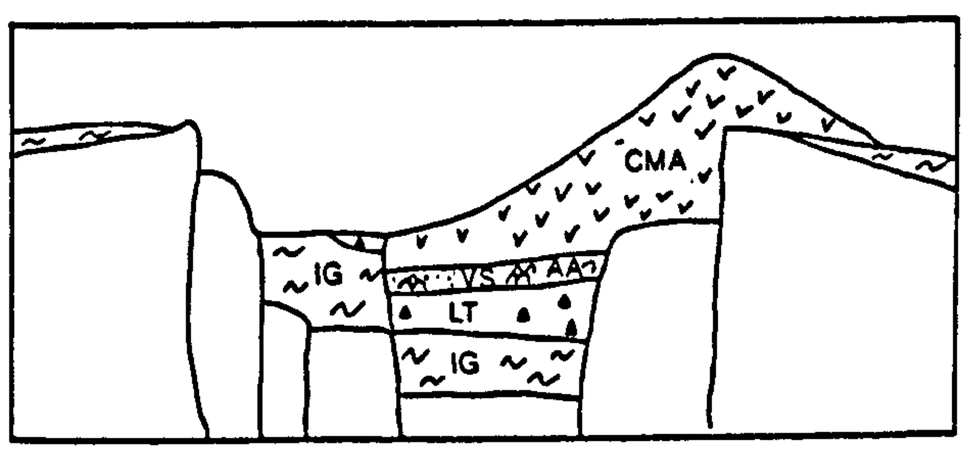

Phase 2 Volcán Cabro Muco Developed (~ 0.4 Ma): Infilling of the Aguas Claras and La Fortuna grabens by debris flows from the graben flanks and pyroclastic flows from the new eastern volcanic complex of Cabro Muco-La Giganta, dated at about 0.4 Ma (sample 2v, Table 2.1) (Figure 2.7 b). The N-S system of faults must also have had an important lateral component to explain the southwards displacement of the southern caldera margin by more than 1 km in the La Fortuna area.

Phase 3 Volcán Palaeo-Miravalles Developed (< 0.2 Ma): Volcanism continued on the eastern caldera margin with the inception of the stratovolcano complex of Palaeo-Miravalles along a NE-SW fault line. This was followed in the east and southeast of the caldera by the collapse of Palaeo-Miravalles on its western flank and Volcán Cabro Muco in arcuate sectors into the Bajo Los Chiqueros area (Figures 2.5 and 2.7 c). Concomitant explosive activity was responsible for the Post Cabro Muco Volcanic Unit lahars, breccias and minor tuffs.

Figure 2.7 c-d (continued)

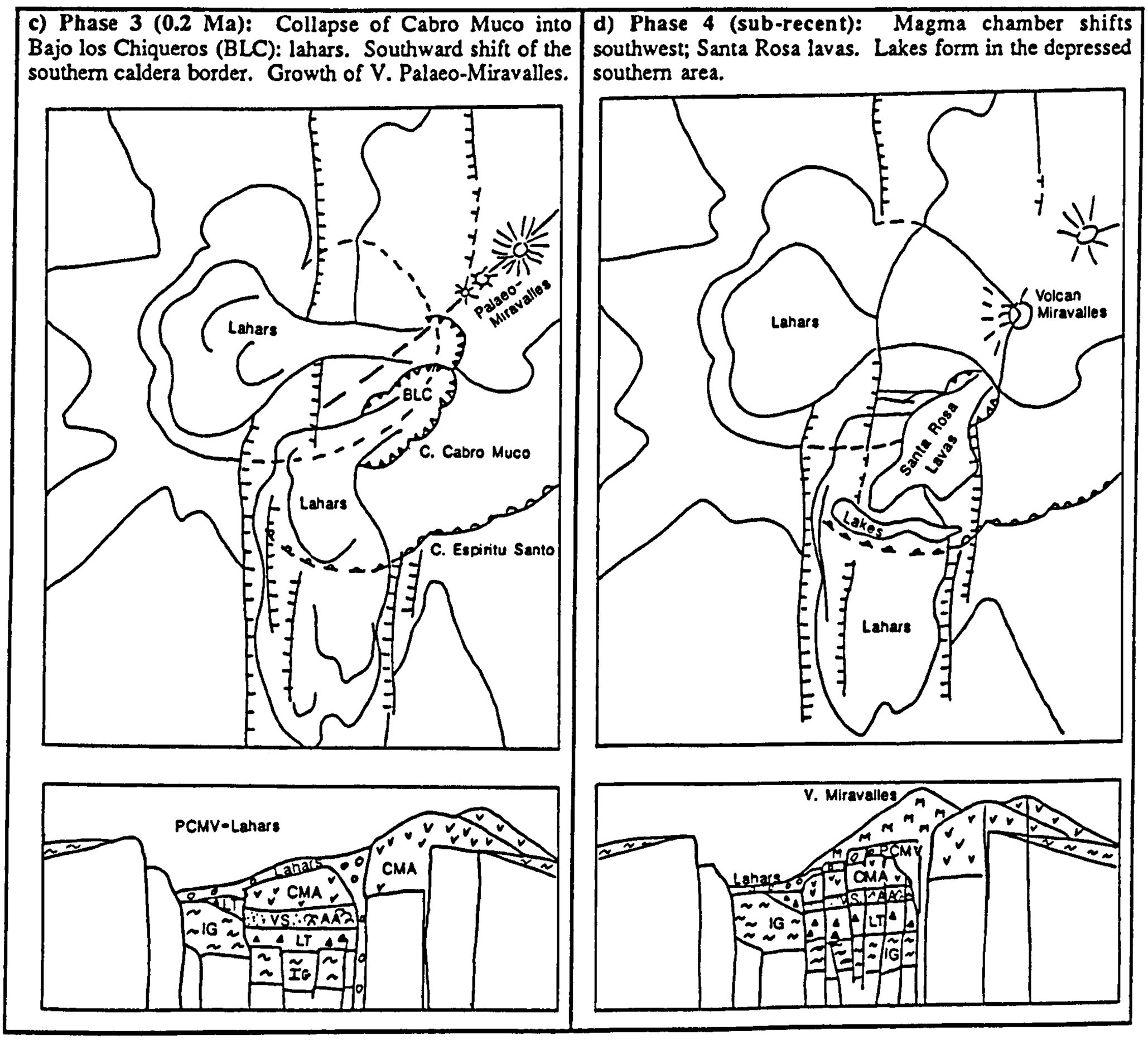

Phase 4 Volcán Miravalles Developed (< 0.05 Ma) Following the collapse of Palaeo-Miravalles the focus of volcanism shifted southwest along the NE-SW lineament to beneath Volcán Miravalles (Figure 2.7 d). The magmatic focus was subsequently displaced

further to the southwest resulting in the fissure eruptions of the Santa Rosa lavas and the associated local scoriaceous pumice deposit from the southwest flanks of Volcán Miravalles (Figure 2.5). (It is considered by this study that the Santa Rosa lavas are not derived from fissures, which have not been located, but from the Miravalles summit area itself). Reactivation of the N-S graben system, resulting in formation of the lacustrine depressions overlying the lahars at La Fortuna, La Union and the PGM-15 area.

Figure 2.8 Summary of the ELC (1986 a) Guayabo caldera stratigraphy. PGM-borehole intra-caldera stratigraphy is in bold type. All the caldera margin lavas are older than the drilled stratigraphy.

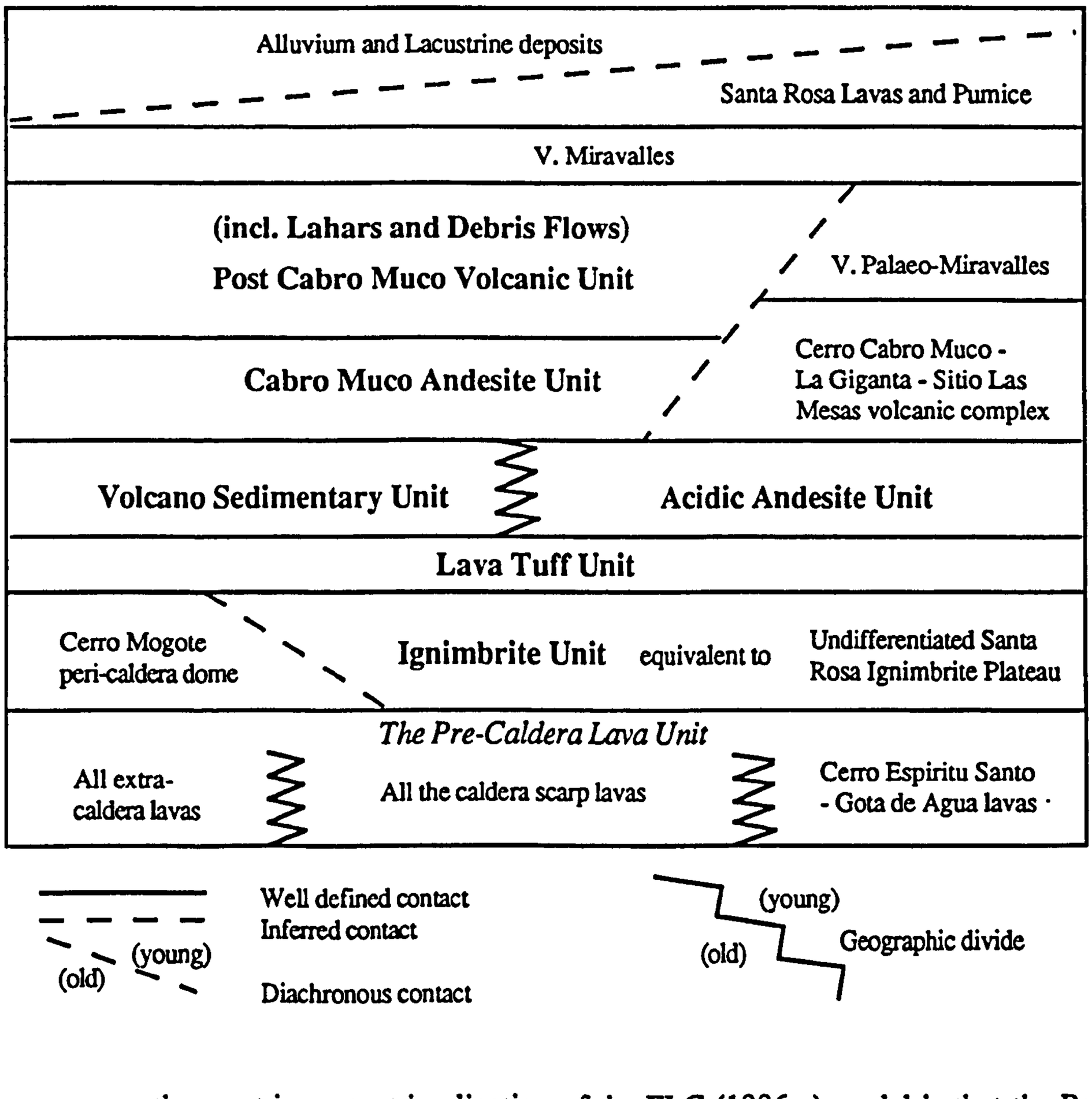

In summary, the most important implication of the ELC (1986 a) model is that the Pre-Caldera Lavas, exposed in the caldera walls from Cerros la Montañosa through Cerro Mogote to Espiritu Santo, are downfaulted within the caldera more than 2400 m, *below* the unseen base of the Ignimbrite Unit (as indicated in Figure 2.8). As the Ignimbrite Unit has been drilled at PGM-12, this implies a southern shift of the caldera border, after collapse,

within the La Fortuna graben (Figure 2.5). Aspects of all the Phases 1 to 4 of the ELC (1986 a) model are challenged by the findings of this study, but the timing of the caldera formation in relation to the drilled stratigraphy is the most fundamental issue, as it determines the boundaries of the geothermal reservoir rocks.

2.3 The Revised Stratigraphy of This Study

A detailed re-examination of the original descriptions of the borehole lithological logs (described by Koenig, 1980; ELC, 1984 a; 1984 c; 1985 a; 1985 b; 1985 c and 1986 b) has been undertaken to improve inter-borehole stratigraphic correlations and as a result some of the stratigraphic units used by ELC (1986 a) have been revised. A further review of the available literature on the exposed geology and work undertaken during this study on the relationships at the caldera margin has resulted in the first attempt at correlating specific intra-caldera units with their proposed extra-caldera equivalents. The basic borehole lithological information from the literature, the stratigraphic units used in this study, the suggested inter-well correlations and the inferred faults are shown in two cross-sections through the deep boreholes, one east-west and one north-south (Figures 2.9 a and b, available as 'pull-outs' inside the back cover), comparable to the WE and NS cross-sections of ELC (1986 a, Figure 2.6, located in Figure 2.2 a). The remainder of this chapter provides the justification for the correlations shown.

Temperature gradient (PH-) wells continuously cored to depths of up to 350 m provide useful constraints on the near surface geology especially near the southern caldera margin. A summary of log descriptions from an unpublished ICE report is shown in Figures 2.10 a and b (Figure 2.10 a is also available as a pull-out). Original data were taken from this report, rather than the graphic logs shown in ELC (1983) which sometimes contradict the original information. The uppermost 300 m of the deep (PGM-) wells are also shown in Figure 2.10 a to provide continuity.

ELC (1983 to 1988 inclusive) distinguished between basaltic, normal and acidic andesites on the basis of mineralogical (largely the Fe-Mg minerals), not geochemical differences. The minerals are given in order of abundance.

Figure 2.10 a (Also available as a pull-out inside the back cover). Shallow stratigraphy from Temperature Gradient (PH-) Boreholes, Deep (PGM-) Boreholes and surface samples. Faults are shown in Figures 2.5 and 2.10 b. Some of the thin LCMV andesites drilled may be large blocks in debris flows rather than in situ lavas. Discussion of correlations in text.

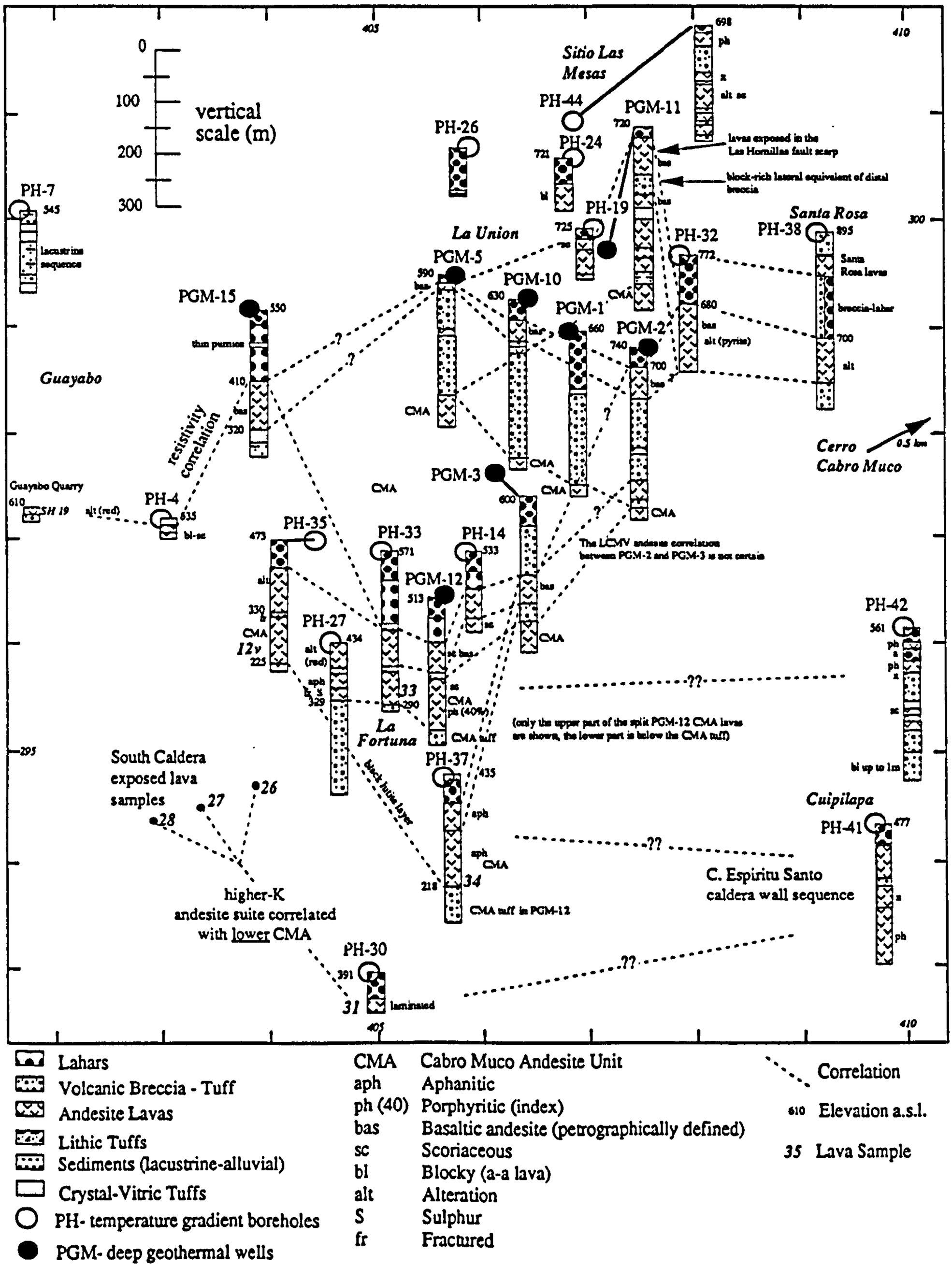

Lahars	CMA	Cabro Muco Andesite Unit	Correlation
Volcanic Breccia - Tuff	aph	Aphanitic	610 Elevation a.s.l.
Andesite Lavas	ph (40)	Porphyritic (index)	35 Lava Sample
Lithic Tuffs	bas	Basaltic andesite (petrographically defined)	
Sediments (lacustrine-alluvial)	sc	Scoriaceous	
Crystal-Vitric Tuffs	bl	Blocky (a-a lava)	
PH- temperature gradient boreholes	alt	Alteration	
PGM- deep geothermal wells	S	Sulphur	
	fr	Fractured	

Figure 2.10 b Structural contour map of the top of the most recent Late Cabro Muco Volcanic Unit lavas. Exposed pre-Santa Rosa lavas are stippled (for surface geology see Figure 2.5). The higher-K southern caldera lavas are older than LCMV, but Cerro Cabro Muco and the youngest Cerro Espiritu Santo lavas are believed to be equivalent to the LCMV.

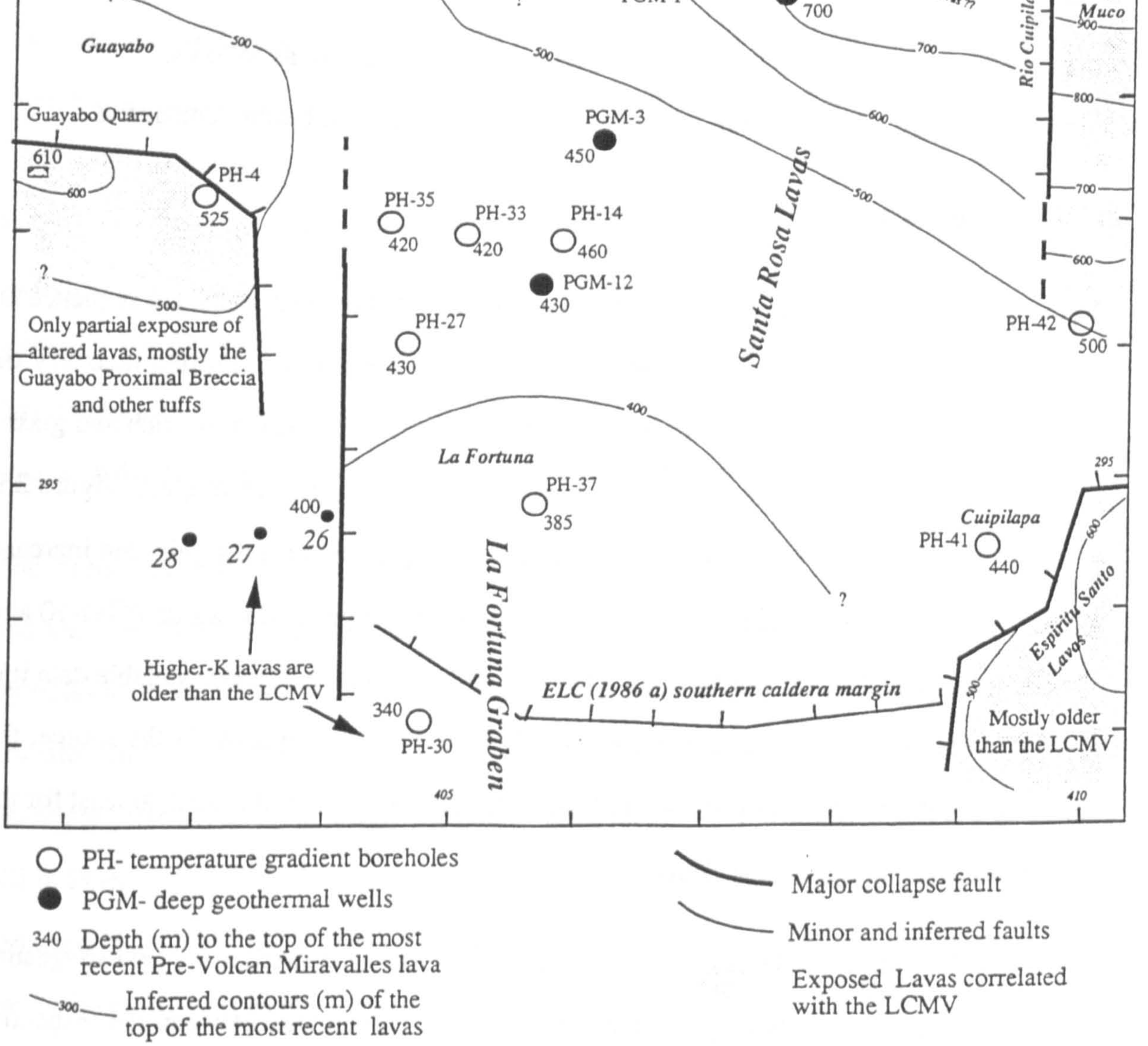

Basalts	Olivine, orthopyroxene, clinopyroxene
Basaltic Andesite	Orthopyroxene, olivine, clinopyroxene
Andesite	Clinopyroxene, orthopyroxene, hornblende (and andesine plagioclases)
Acidic Andesite	Clinopyroxene, hornblende (and oligoclase plagioclases). (Prior to ELC (1988) these were erroneously called **Dacite-Latite**)

Acidic andesites are further distinguished by generally lower porphyritic indicies than the normal andesites. These distinctions and the broad stratigraphic units adapted by ELC (1986 a) (Figure 2.6) are retained during this study but there are several important differences described below.

Mineral abbreviations used below and in the appropriate Figures are as follows:
Pl plagioclase, Cpx clinopyroxene, Hbl hornblende, Ol olivine, Bi biotite, Qtz quartz.

2.3.1 The Ignimbrite Unit (IG)

Although the Ignimbrite Unit has been drilled at the base of five deep wells, the sequence at PGM-15 (ELC, 1986 b) is the only one not to have suffered from a limited recovery of cuttings. At PGM-15 below 1200 m b.s.l. the cuttings are dominantly lithic-rich and glass-poor in sharp contrast to the uppermost IG which is lithic-poor but rich in glass (Figure 2.9 a). Data from ELC (1984 a, b and 1985 c), however, suggest there is a significant increase in lithic content and lithic size in the available cores of the upper unit towards PGM-10 and PGM-12. No core data are available for PGM-2, but based on the limited available data it is postulated that as lithic size and content should generally increase towards the source, the vent(s) may have been towards the east of the borefield, rather than the west, at least for the upper section of the Ignimbrite Unit.

The top of the Ignimbrite Unit is a more or less horizontal plane across the area suggesting that there have been no *major* post-ignimbrite vertical movements between the respective wells, though smaller movements of the order of 100 m are suggested by the correlations of the overlying units as shown in Figure 2.9 and explained below. At the very base of PGM-1, however, in the permeable zone of total recovery loss there was a marked decrease in the

drilling speed (Koenig , 1980). The increased hardness is postulated to be due to either a coherent lava or possibly the top of the Ignimbrite Unit. This possibility has very significant implications for the structure in the PGM-1 area, since the presence of IG requires PGM-1 to be located on a block uplifted by some 250 m (this is further developed below during the discussion of the reasons for the absence of the Acidic Andesite Unit at PGM-1).

2.3.2 The Volcano-Sedimentary Unit (VS) (including the Lava-Tuff Unit (LT) of ELC, 1986 a)

This unit incorporates up to almost 1000 m of intercalated lavas and tuffs and is identified in all wells, except possibly PGM-11 (ELC, 1985 a). The lava-rich basal part at wells PGM-5, 10 and 15 has previously been separately defined as the Lava-Tuff Unit (ELC, 1986 a). It is not clear to this author, however, that this is reason enough to divide the sequence, as there is a similarly lava rich part in the stratigraphically higher Volcano-Sedimentary Unit of ELC (1986 a) at PGM-15 (ELC, 1986 b and Figure 2.9 a). The lavas appear to come from at least two sources. There are acidic andesites at PGM-5 and 10 (below the main Acidic Andesite Unit) with minor regular andesites, which contrast with rock type and therefore probably source with the normal andesite lavas of PGM-15. These acidic andesites are postulated precursors to the overlying thick Acidic Andesite Unit which probably have a source to the northeast of PGM-2 and 11, the thickest drilled acidic andesite sequence.

The interstitial tuffs at PGM-10 contain clasts of andesite and acidic andesite (ELC, 1984 b) and are therefore believed to share a common source with the vent occasionally producing pyroclastics rather than lava. The PGM-15 sequence of normal andesite lavas and tuffs (that contain similar normal andesite clasts) is probably related to a separate source, that is postulated to have been a stratovolcano close to, but to the north-west of PGM-15. In the VS in PGM-1, PGM-3 and PGM-12, only minor amounts of normal andesite cuttings were returned from PGM-12 at ~250 m b.s.l., in between the cored sections, but no other lavas are believed to be present. Due to the more concise style, however, of the Koenig (1980) drilling report compared to the detailed drilling reports of ELC, there is little information on the stratigraphy of PGM-1, 2 and 3 and it is not possible to correlate lavas or tuffs within the VS to these wells. The 150-200 m lithic tuff identified at PGM-5 and 15 contains Pl, Hbl

and Bi in both sequences and is correlated with the similar lithic tuff in PGM-10. This suggests, therefore, that although a separate eastern source is proposed for the acidic andesites and some of the tuffs at the base of the VS in PGM-5 and 10, it is possible that tuffs from the western, PGM-15, source may interleave with these at PGM-5 and 10.

Welding and resorbtion are not features of the generally porous tuffs in the VS, so that major hot avalanches resulting in thick intra-caldera cooling units are not likely to explain their formation. It is more probable that the tuffs formed from relatively minor explosive events, interspersed between lava flows; a common sequence observed for stratovolcano facies. The rounded lithics in some sections suggest that at least some VS tuffs are reworked products, rather than true thicknesses of fallout deposits.

The only horizontal horizon that may be correlated with some confidence between wells is the distinctive layer of lacustrine silts and muds at PGM-1, 5 and 10. This has been used as a reliable indicator of vertical movement between PGM-1 and 10 of 200-250 m and between PGM-5 and 10 of 60-100 m with downthrow towards PGM-10 in both cases. A similar displacement of the older units again supports the interpretation that the low drilling velocities at the base of PGM-1 indicate upfaulted Ignimbrite Unit (Figure 2.9 a).

2.3.3 The Acidic Andesite Unit (AA)

Thick sequences developed at PGM-2, 5, 10 and 11 but are notably absent at PGM-1 and the more distant wells PGM-3, 12 and 15. Since, as mentioned in Section 2.2.4, the AA is impervious and of high resistivity, it can be very effectively mapped by vertical electric soundings (Duprat and Leandro, 1986, and details in Chapter 3) and an apparently similar body has been identified between PGM-1 and 3. The origin of these thick but laterally restricted lavas is not certain, but it is unlikely that they are intrusive given the fine grained nature of the matrix. Furthermore, had they formed a densely spaced dyke system then there should be evidence of some interstitial material. The explanation preferred in this study is that they are viscous extrusive domes that built up contemporaneously with the VS. While their higher viscosity limited the extent of lateral flow, a further reason is required for the lack of AA at PGM-1, less than 0.5 km from the 500 m thick sequence developed at

PGM-10. One possibility is that the proposed post-Ignimbrite Unit uplift of the PGM-1 area occurred before and/or during the eruption of the AA, forming a highland barrier to at least the lowermost AA lavas. A possible additional solution is to allow subsequent sinistral movement on the buried branch of the Las Hornillas fault already proposed between PGM-1 and PGM-10 (Figure 2.11).

Figure 2.11 Proposed structural evolution sketch to explain the absence of the Acidic Andesite Unit at PGM-1. Sinistral movement on the buried southern branch of the Las Hornillas Fault predates the Cabro Muco Andesite Unit. PGM-1, 2 and 3 moved east relative to PGM-5, 10, 11 and 15.

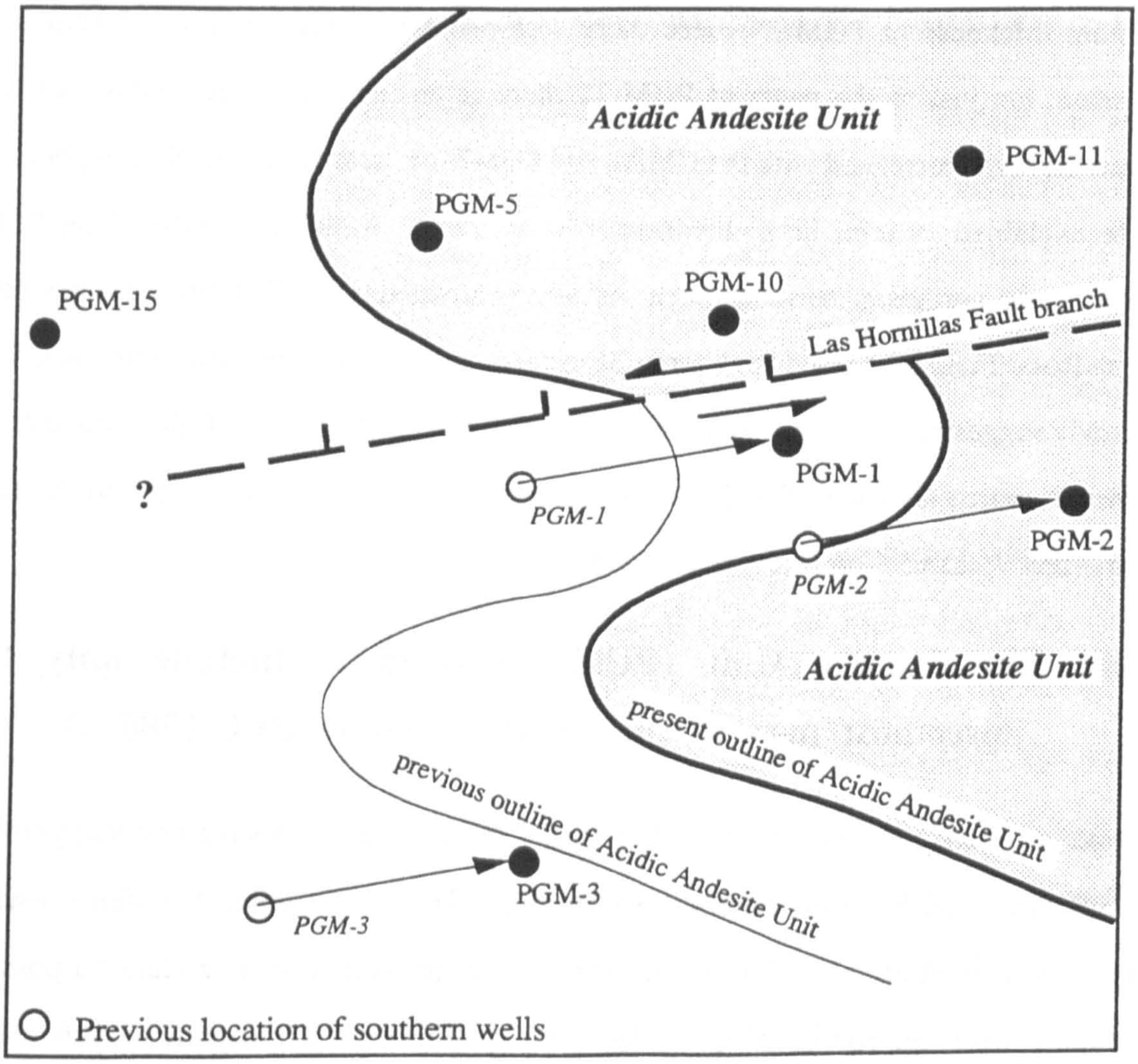

If correct, then most of the lateral and vertical movement on the fault must have occurred after the AA development but before the Cabro Muco Andesite Unit activity commenced, as both this Unit and the Late Cabro Muco Volcanic Unit do not appear to have undergone major vertical or lateral tectonic disruption in this area (Figure 2.9). The reconstructed scenario would also explain why the distinctive lacustrine mud horizon within the Volcano-

Sedimentary Unit is 50 m thick at PGM-1 and 5, but only 5 m thick at PGM-10 (ELC, 1984 a; 1984 c and 1986 a).

2.3.4 The Cabro Muco Andesite Unit (CMA)

This has been confidently identified across the borefield, except at PGM-15 (Figures 2.9 and 2.10 a). The lavas are porphyritic (index of 10-40 %), with andesine plagioclase, and are therefore mineralogically defined as andesite by ELC (1986 a). The CMA attains a maximum thickness at PGM-3 where there was possibly some ponding of lava in a depression, but just to the south at PGM-12 there is an important intercalation of tuff between the lavas correlated with the CMA. At PGM-2 the lavas are relatively thin, but this may be explained by their high elevation (Figure 2.9 a). As the elevation of the CMA increases to the northeast, the source area has been postulated by ELC (1986 a) to have been at Santa Rosa (Figure 2.5), and the Cerro Cabro Muco edifice was correlated with the CMA. This study suggests, however, that although the surficial lavas on Cerro Cabro Muco share a common source area with the CMA, the former are proposed to be related to the Late Cabro Muco Volcanic Unit lavas, described below.

2.3.5 The Pumice Unit (PUM) (revised to include only the lowermost part of the Pumice Unit of ELC,1986 a)

This has only been identified at PGM-15 (ELC, 1986 b); it represents the first true pumice-rich tuff described from the borehole succession. The 170 m thick, low density white pumice contains Pl and rare Hbl, but *no* lithics were recovered; this precludes a possible correlation with the compositionally similar but lithic-rich white pumice tuffs of the Hornblende Tuff (Table 2.2) exposed south of, and related to, the Guayabo caldera (Figure 2.5). A correlation with the La Ese Pumice is proposed instead (described below, Section 2.3.10). The reworked pumice and lacustrine sediments overlying this tuff had been included in the PUM by ELC (1986 a and b) but it is suggested here that they correlate with the reworked tuffs overlying the CMA in the nearest well, PGM-5 and the rest of the borefield (Figure 2.9 a).

The very low density of the PUM unit is a very important factor in the gravity modelling; its distribution and thickness can be correlated with the distinctive gravity low centred 2 km north of PGM-15 (fully discussed in the following chapter). The centre of the gravity low is interpreted as the greatest thickness of the PUM and may therefore be close to its source area.

2.3.6 The Late Cabro Muco Volcanic Unit (LCMV). A re-definition of the ELC (1986 a) Post C. Muco Volc. U.

This unit includes all the post-CMA and post-PUM stratigraphy, except the Volcán Miravalles products. The near total replacement of the original lithologies in areas of this uppermost unit by hydrothermal alteration minerals (mostly clays) means that some of the distinctive lavas will have been "lost". This may explain the lack of lavas within this unit in PGM-1. Alteration rank and intensity is discussed in the context of its effect on density in Chapter 3.

Overlying the CMA in all wells and the PUM in PGM-15 are breccias and lithic tuffs up to 200 m thick (PGM-10), parts of which are thought to represent more or less contemporaneous collapse events in the vicinity. Above the Pumice Unit at PGM-15 is a unit of reworked pumice in a fine tuffaceous matrix containing crystals of Pl, Cpx and Hbl which is very similar to the pumice of the underlying Pumice Unit. The identification of a freshwater gastropod and other fossil impressions in the upper part (ELC, 1986 b) suggests a lacustrine environment of deposition. The 80 m of largely reworked PUM at PGM-15 is important, suggesting that the PUM may have been present at the other nearby wells but has then been eroded and removed to the low lying area at PGM-15. These tuffs and sediments are followed by interbedded lavas, breccias, lahars and minor tuffs that can be traced through most of the wells in the centre and south of the borefield (Figure 2.10 a), suggesting intermittent lava eruption and pyroclastic activity.

The Post Cabro Muco Volcanic Unit of ELC (1986 a) has been redefined in this study to the Late Cabro Muco Volcanic Unit as the sequence is a broad continuation of the CMA activity, from the same source area, and a distinct temporal break is not evident from the available

data. The Sitio Las Mesas lavas, exposed in the Las Hornillas fault scarp 0.5 km to the east of PGM-11 (Figure 2.10 b), correlate with the uppermost basaltic andesite of the adjacent Post Cabro Muco Volcanic Unit in PGM-11 (Figure 2.10 a). The Sitio Las Mesas lavas dip to the northwest (distinct from the younger southwest sloping lavas of Volcán Miravalles) and were thought by ELC (1983, 1984 c and 1986 a) to be part of the collapsed northern flank of the opposing south-dipping Cerro Cabro Muco edifice (Figure 2.5). The lavas of the *older* CMA, however, had been attributed by ELC (1986 a) to the activity at Cerro Cabro Muco. As it has now been shown that the Post Cabro Muco Volcanic Unit lavas (of ELC, 1986 a) (and, by association, the Sitio Las Mesas lavas) correlate with Cerro Cabro Muco, they are redefined as part of the Late Cabro Muco Volcanic Unit (LCMV) in this study.

Basaltic andesites have been identified in the uppermost sections of the LCMV in most wells (except PGM-1) (Figure 2.10 a). The lava unit is thicker and at a lower elevation in PGM-15 than the lavas in PGM-5 but is at a similar elevation to that in southern wells near PGM-12 (Figure 2.10 b). The distribution of the LVMV basaltic andesites, the CMA and the Cerro Cabro Muco edifice (Figures 2.10 a and b) indicate that they share a common source area in the Santa Rosa-Bajo Los Chiqueros area. Geochemical constraints have been used in this study to correlate the LCMV with lavas drilled in the La Fortuna area, and this is developed further in the following Section.

The basaltic andesites are immediately overlain by lahars/debris flows that cover the geothermal area and much of the caldera (Figure 2.5). It is clear from the lahar distribution that the La Fortuna Graben acted as a broad channel out of the southern caldera area, whereas the western caldera walls were not "breached". The breccias and lahars at the foot of the northern slopes of Volcán Miravalles and in the Aguas Claras Graben are distinguished from the lahars to the south (Figure 2.5) because they were derived from a different source; the flanks of Palaeo-Miravalles and possibly Miravalles itself, rather than the collapse of Cerro Cabro Muco.

By describing the intra-caldera stratigraphy in detail it is now possible to attempt to correlate some of the units with the stratigraphy exposed in the walls of the caldera, as they are described below, and to determine the true throw across the exposed caldera margin.

Firstly, geochemistry is used to discriminate caldera wall lava suites and identify the possible intra-caldera lava equivalents of the lavas exposed outside the caldera margin, in the southern caldera area. Secondly, correlations are proposed between the extra-caldera tuffs and the tuffs identified in the boreholes, based on lithological and petrographical criteria.

2.3.7 Geochemical constraints on the stratigraphic position of the caldera margin lavas

Due to discontinuous nature of the surface exposures of lavas around the caldera rim and their broad visual similarity (mostly laminated, porphyritic andesites) it is difficult to discriminate between them using primary characteristics alone. Geochemical analyses were introduced into this project for two reasons: firstly, to correlate geographically separated, but possibly cogenetic lavas in the southern and eastern caldera area, including lavas of the shallow boreholes within the La Fortuna Graben, and secondly, to determine whether any of the western caldera lahars were derived from the western caldera walls and not *exclusively* from the east as proposed by previous workers (ELC, 1983 and 1986 a). ELC (1983) presented major element analyses (technique not specified) of lavas from both surface exposures and some temperature gradient wells (sample locations; Figure 2.5) and further samples were analysed using the Energy Dispersive XRF at the Open University (technique given in Potts *et al.*, 1984, both data sets in Appendix 2).

It is useful at this stage to take stock of the stratigraphic constraints that must be satisfied by any proposed geochemical correlations, thereby highlighting the areas where geochemistry may be useful to discriminate between alternative, but less secure stratigraphic correlations. Most importantly, the lavas of the southern caldera margin, to the west of the La Fortuna Graben, are *overlain* by the youngest Guayabo caldera related tuffs (the Hornblende Tuff, the La Ese Pumice and the Guayabo Proximal Breccia, Figure 2.5). The La Ese Pumice is correlated with the PUM in PGM-15 (details in Section 2.3.10), and therefore the LCMV lavas that overlie the PUM at PGM-15, but are also present in the La Fortuna Graben (in the PH-wells), cannot correlate with the southern caldera lavas. It is also important that the CMA lavas identified in all the northern wells are split in PGM-12 (Figure 2.9 b) by the CMA tuff (also shown in Figure 2.10 a). The *lowermost* CMA lavas in PGM-12 are <u>not</u>

drilled in any of the southern PH- wells, only the *uppermost* CMA lavas and part of the CMA tuff. (The CMA tuff was sometimes identified as a breccia in the PH- wells, not strictly a tuff). The LCMV lavas correlate with the Sitio Las Mesas lavas and so it is reasonable to assume that although the drilled LCMV lavas were not sampled, the sampled Sitio Las Mesas lavas are comparable. A more tenuous correlation is proposed between the LCMV and the Cerro Cabro Muco lavas.

The relationship between the Cerro Espiritu Santo edifice and the stratigraphy to the north is even less clear, but as the morphological form suggests a source to the north in the Cerro Cabro Muco-La Giganta area, some relationship may be possible if not all the Cerro Cabro Muco sequence is younger than the Cerro Espiritu Santo edifice. Cerro Espiritu Santo appears to be older than the Guayabo caldera related tuffs exposed to the south (as proposed by Alvarado *et al.*, 1990 a and b), although there is no direct contact known to this author (Figure 2.5). The relationship between the lavas on either side of the La Fortuna graben, the southern caldera lavas and the Cerro Espiritu Santo lavas, is also not clear. The western caldera wall lavas are geographically distinct from the rest of the caldera stratigraphy, including the southern caldera wall material, and it is difficult to attempt any possible correlations without some extra information. With these points in mind the geochemical arguments can be used in a stratigraphic context.

All the lava samples strictly belong to the medium-K fractionation suite (Figure 3.12) of Le Maitre (1989) but they have been discriminated here into lower, medium and higher-K magmatic fractionation suites; broadly following ELC (1983), but with some alternative interpretations. Mg has also been used as a discriminant, particularly in the southern caldera area (Figure 2.12 b). The broad groups are described and the important exceptions and possible explanations for these are then discussed:

Lower-K, Higher-Mg Lavas: These include the western caldera wall lavas (with the possible exception of the Hill 777 dacite, sample EC49, located in Figure 2.5), the Cerro Mogote basalts (defined petrographically as basalts due the content of Ol (> 5%)), the Cerro Espiritu Santo lavas and the uppermost CMA lavas. It is difficult to conceive of a single stratovolcano source, however, for the Cerro Espiritu Santo lavas and the distant western

caldera wall lavas, though they may have had a common fractionating magmatic source. Moreover, the Cerro Mogote basalts are more basic than the underlying western caldera wall lavas and are unlikely to represent a fractionated equivalent. Indeed, there is a distinct SiO_2 break between the western caldera wall andesites and the Cerro Mogote basalts.

Figure 2.12 a K_2O against SiO_2 discrimination diagram to show the distinction between the higher-K southern caldera wall lavas and the uppermost intra-caldera stratigraphy (for sample locations see Figure 2.5). The Cerro Cabro Muco lavas are distinct from the Sitio Las Mesas-Miravalles and the caldera wall suites. The chemistry of the intra-caldera laharic blocks suggests a Sitio Las Mesas, Cerro Cabro Muco or Palaeo-Miravalles source. Data from ELC (1983) and this study (see Table 2.3).

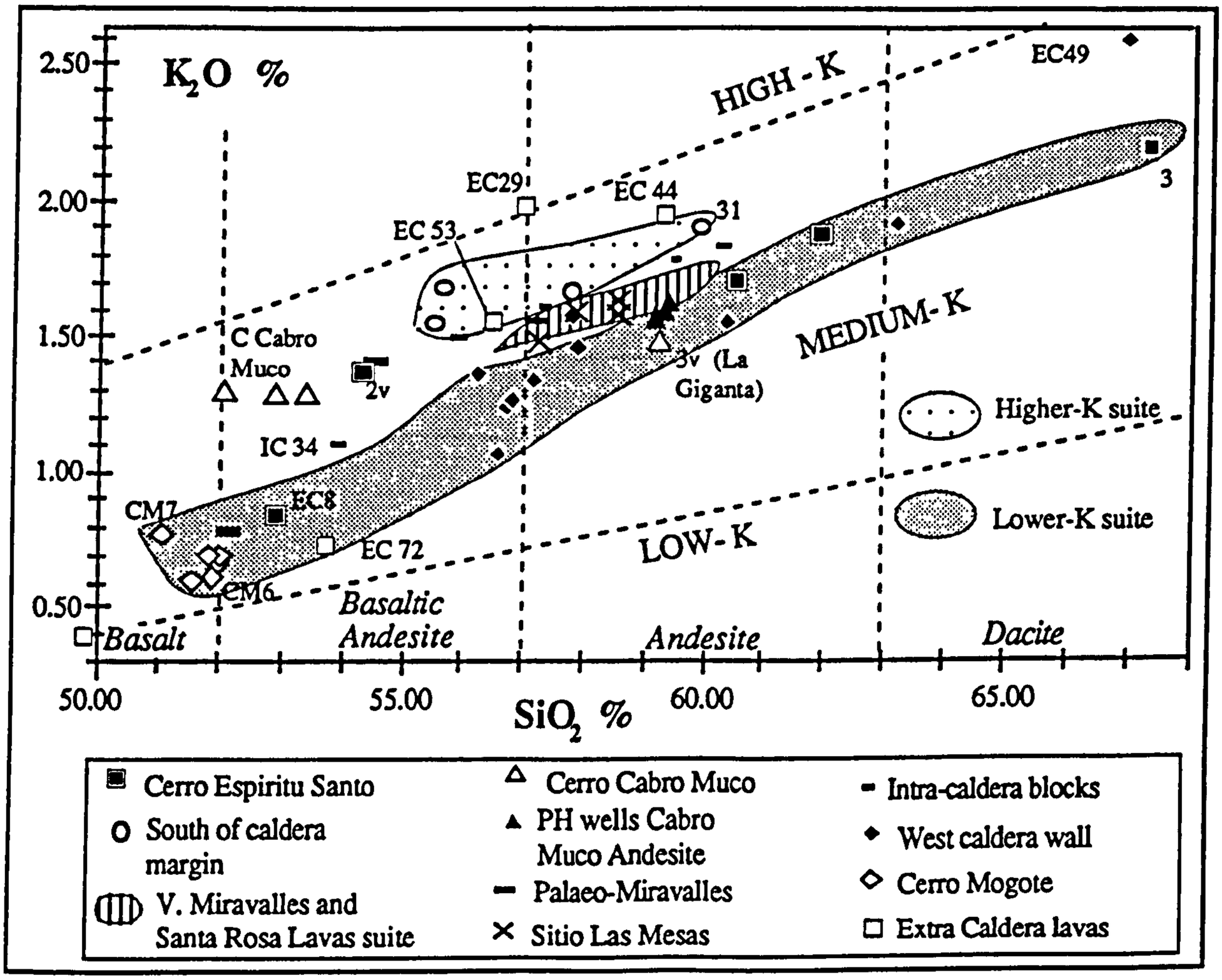

This geochemical classification of andesites is distinct from the petrographical one adopted by ELC (1986 a) and this study (Section 2.2). Some of the petrographically described basaltic andesites (e.g. the Sitio Las Mesas lavas drilled at PGM-11) are normal andesites on geochemical grounds. K-classification from Le Maitre (1989); after Peccerillo and Taylor (1976).

Medium-K Lavas: This suite is distinguished simply to show the similarity of the most recent eastern andesites; the Sitio Las Mesas lavas, Palaeo-Miravalles, Volcán Miravalles and the Santa Rosa lavas (Figure 2.12 a and Appendix 2). The Late Cabro Muco Andesite Unit (LCMV) lavas of Sitio las Mesas are shown as part of the medium-K andesite suite (except sample 32; well PH-32) but may not be geochemically distinct from the underlying,

(but uppermost) Cabro Muco Andesite Unit (uppermost CMA) sampled in the southern shallow boreholes (Figure 2.12 a).

Figure 2.12 b The Cerro Espiritu Santo and CMA lavas have generally higher MgO % than either the Cerro Cabro Muco edifice or the southern caldera lavas.

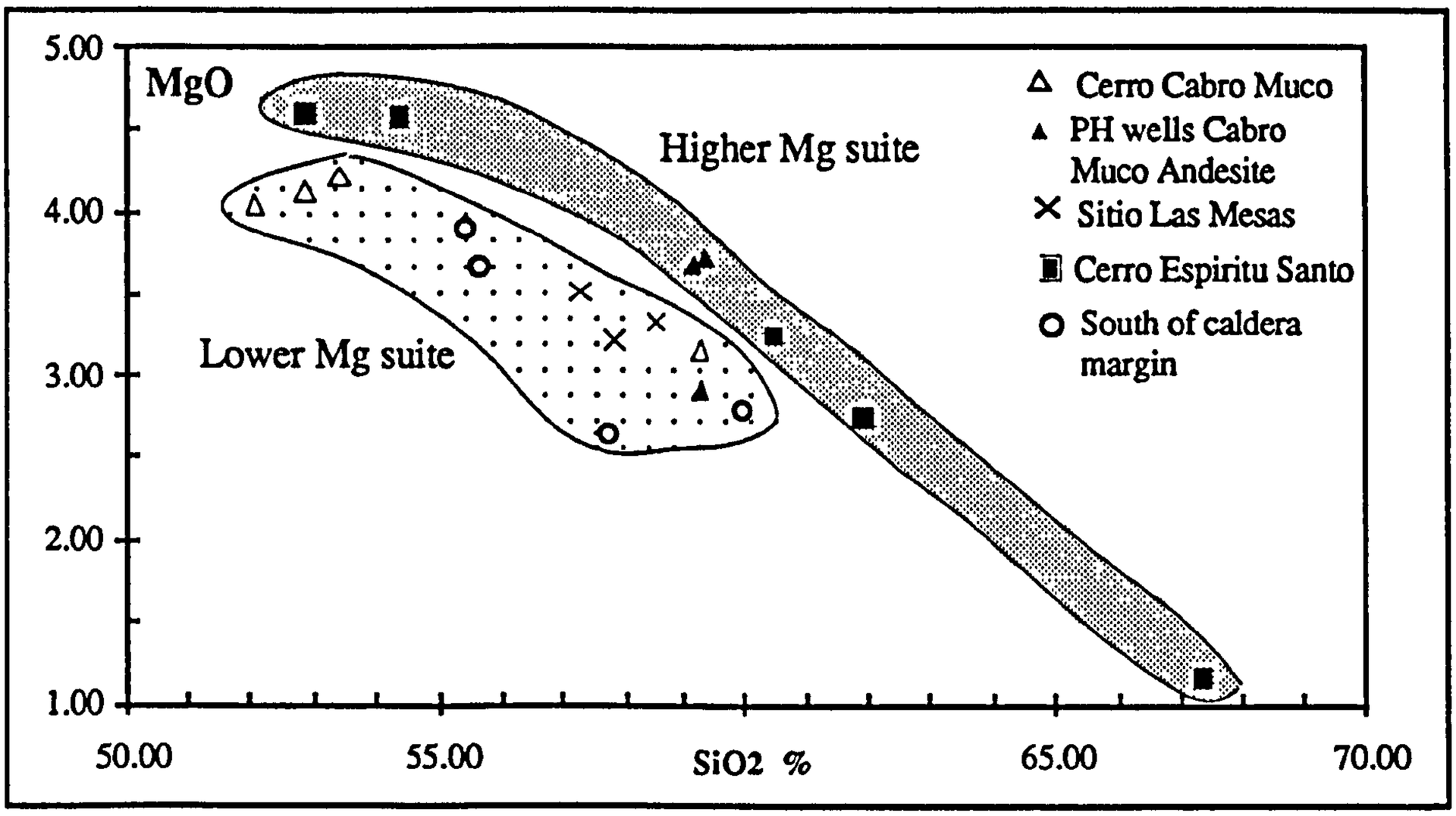

Higher-K, Lower-Mg Lavas The southern caldera andesite samples 26, 27 and 28 belong to a higher-K, lower-Mg suite distinct from the lower-K, higher-Mg western caldera wall andesites, the uppermost CMA lavas and are possibly also geochemically distinct from the medium-K Sitio Las Mesas (LCMV Unit) and the Miravalles lavas. It is important to note that the southern caldera wall samples do not come directly from the caldera wall scarp but from exposures below the Hornblende Tuff *outside* the ELC (1986 a) Guayabo caldera border (Figure 2.5 and 2.10 b). Sample 31 from borehole PH-30 has similar characteristics to this group, and this has important implications for the position of the buried caldera border of ELC (1986 a), placing it north of PH-30 as the higher-K lavas are indeed truly pre-Guayabo caldera as suggested by ELC (1983 and 1986 a, Figures 2.10 a and b).

The LCMV samples from the Sitio Las Mesas area are geochemically similar to the more recent Volcán Miravalles and Santa Rosa lava samples. The uppermost CMA lavas from the southern intra-caldera PH- wells form a tight cluster close to the more recent lava samples, and it is therefore reasonable to infer that a similar magmatic source was active during the ~0.4 My of their collective evolution. Most of the andesites of the actual Cerro Cabro Muco

edifice however (except the La Giganta sample, 3v), are significantly more basic than (though possibly from the same suite as) the LCMV Sitio las Mesas andesites, so it is difficult to support the proposed stratigraphic correlation of the LCMV lavas (or the uppermost CMA) with the Cerro Cabro Muco lavas, on the basis of geochemical arguments.

There is a tendency for the lower-K and the higher-K suites to lose their distinction at progressively higher SiO_2 values. It is therefore difficult to decide whether the CMA lavas belong to a trend from the Cerro Cabro Muco edifice lavas, through the LCMV lavas, to the uppermost CMA lavas, or the separate lower-K suite (Figure 2.12 a and b). It is postulated that in general the geochemistry may reflect differences between separately evolving magmatic sources, a higher-K source beneath the Late Cabro Muco-Volcán Miravalles complex and a lower-K source responsible for the western caldera wall lavas and Cerro Espiritu Santo lavas in the southeast of the caldera. The Cerro Espiritu Santo lavas and the lowermost CMA (and very probably all the western caldera lavas) pre-date the LCMV-Volcán Miravalles suite, suggesting that the age of the separate suites is possibly more important than the geographic position.

Most of the intra-caldera laharic block samples may be included in either the medium-K or higher-K suites (Figure 2.12 a), in general agreement with the proposed LCMV to Cerro Cabro Muco source area. IC34 is a possible significant exception and its proximity to the similar, lower-K, western caldera wall andesites (Figure 2.5) suggests that some of the debris flows/lahars, distributed over the present-day floor of the caldera, may be derived from the caldera walls.

One of the more important results of the geochemistry study is that the southern caldera lavas and the PH-30 sample are distinct from not only the western caldera lavas but do not correlate either with the uppermost CMA or more recent stratigraphy. With this in mind, how do the southern caldera lavas relate to the rest of the southern caldera stratigraphy, in particular with the lavas of Espiritu Santo across the La Fortuna Graben? These issues are now treated in more detail below.

2.3.8 The southern caldera border

The samples from the southeastern caldera area do not divide into simple groups, but it is possible to suggest some reasons for the observed divisions nonetheless (Figure 2.12 a). The tightly grouped uppermost CMA samples; 12v, 33 and 34 from wells PH-33, 35 and 37 respectively (Figure 2.12 a), are included in the lower-K group and are similar to the Cerro Espiritu Santo suite. If the Cerro Espiritu Santo edifice can be correlated with the uppermost CMA, this means that proposed caldera collapse that resulted in the formation of the Cerro Espiritu Santo scarp post-dates the CMA. How can this be resolved in terms of the other constraints in this area, and how does the CMA relate to the higher-K southern caldera lavas?

The lithologically and geochemically similar lavas sampled from PH-33, 35 and 37 are from an unspecified borehole depth, but as the alteration is reported to be most severe in the uppermost sections, it is likely that the samples are from the cleaner deeper sections (the uppermost CMA). The PH-33 succession is very similar to that of the PGM-12 succession less than 1 km to the southeast (Figure 2.10 a) and the same distinctive porphyritic lavas at 200 m depth in PGM-12 (porphyritic index of 40%) belong to the *uppermost* CMA (ELC, 1986 a and 1985 c, Figure 2.9 b). The uppermost drilled intra-caldera succession, at least, can thus be traced across the geothermal area from PGM-11 through PGM-12 to PH-37, albeit by means of the proposed southern continuation of the uppermost CMA, with no apparent vertical discontinuity. The continuation of this stratigraphy to the east towards Cerro Espiritu Santo, and to the west towards the southern caldera higher-K lavas, is less certain.

The PH-30 lavas are geochemically very similar to the southern caldera higher-K lavas and as these underlie the Hornblende Tuff and are part of the ELC (1986 a) Pre-Caldera Lava Unit (see Section 2.3.7), the ELC (1986 a) model requires ~2000 m throw between PGM-12 and PH-30, at or close to their proposed southern caldera scarp, (Figures 2.5 and 2.10 b) to place the Pre-Caldera Lava Unit below the Ignimbrite Unit in PGM-12. The least requirement would be an offset between PH-30 and PH-27 assuming that the PH-30 lavas

pre-date the 300 m PH-27 succession. The CMA tuff is at least 200 m thick at PH-27 where a thick volcanic agglomerate and fault breccia have been drilled below an aphanitic lava similar to the correlative of the uppermost CMA lavas drilled at PH-37. What has happened to the CMA tuff and the younger succession in the PH-30 area, if the PH-30 lavas are older than the CMA tuff but are directly overlain by the lahar?

One of the several implications of the correlations proposed in this study is that there is an important distinction between the CMA tuff and the younger LCMV breccia. These are separated by the uppermost CMA lavas in PGM-12 and the southern area where the CMA tuff predominates, whereas the LCMV breccia is thickest in the northern borefield and absent in PH-37 in the south. This becomes important when the breccias and tuffs are correlated with parts of the extra-caldera tuff succession in the discussion below.

At the Guayabo quarry on the southwestern caldera border (Figure 2.10 a) there is an exposure of hydrothermally altered, lithic dominated tuffs/breccias, sloping away from the caldera (Plate 2.1), that are *overlain* by a similarly hydrothermally altered two pyroxene andesite that is part of the caldera wall sequence (sample SH19, for location see Figure 2.5). Examination of this exposed lava/breccia sequence during this study shows that the breccia *overlies* the La Ese Pumice (and therefore the PUM; details in Section 2.3.10); it is called the Guayabo Proximal Breccia. The quarry exposure shows a very similar lithological succession and degree of alteration to that at PH-27 (Figure 2.10 a), but it not clear whether it is possible to correlate the breccia with the LCMV breccia or the CMA tuff. PH-27 is somewhat anomalous compared to the nearby wells, in that the combined CMA and LCMV lava thickness at PH-27 is much reduced, but the CMA tuff thickness is much greater. The lava-tuff contact at PH-27 is some 270 m below that at the quarry, but also some 100 m above that at PH-35 (Figure 2.10 a). PH-27 is close to the western boundary fault of the La Fortuna graben (Figure 2.10 b) and it is proposed that the apparent vertical displacements are structural, rather than a consequence of a dipping contact. Furthermore, the increased tuff thickness at PH-27 may be a result of a misinterpretation of fragmented and subsequently altered lava/breccia close to the La Fortuna fault, rather than original tuff thickness.

Whatever the case, the thick breccias overlain by andesites of the "caldera wall" facies at the quarry are not believed to be fundamentally different (older and ~2000 m structurally displaced in the ELC model) from the LCMV/CMA lava-tuff/breccia sequence at the top of the intra-caldera succession in the nearby shallow boreholes. As the Guayabo Proximal Breccia postdates the Guayabo related tuffs and therefore the higher-K southern caldera lavas, this implies that the higher-K lavas must *pre-date* the Proximal Breccia equivalents (the LCMV or the CMA breccias/tuffs) in the southern borefield sections. It will be shown in the following chapter that the extent of the LCMV basaltic andesite in PGM-15 that overlies the Pumice Unit can be mapped using resistivity and that although a sharp lateral break exists between PGM-15 and PGM-5, the andesite shallows gradually to PH-4 and the Guayabo quarry. This implies that the Guayabo quarry andesite (sample SH19) may be equivalent to the LCMV lavas at the top of the PGM-15 sequence. If the correlation is valid then it follows that the underlying Pumice Unit at PGM-15 is older than, and may therefore extend beneath, the Guayabo quarry sequence. This point is further discussed in Section 2.3.10, where it is proposed that the Pumice Unit correlates with the La Ese Pumice.

The higher-K, southern caldera wall lava suite cannot be equivalent to either the LCMV lavas, for stratigraphic reasons, or the geochemically distinct uppermost CMA, but they could possibly correlate with the unsampled lowermost CMA (below the CMA tuff in PGM-12). If the lowermost CMA is pre-Guayabo caldera, this avoids the necessity of 2000 m throw on the buried southern caldera margin between PH-30 and PH-37, as proposed by ELC (1983 and 1986 a), but would still imply at least 200-300 m throw. Furthermore, the collapse of the La Fortuna graben and the southern part of the Guayabo caldera would *postdate* the lowermost CMA, but *predate* the CMA tuff, the uppermost CMA lavas, the LCMV breccia, the basaltic andesite and the lahars that subsequently filled the caldera and the La Fortuna graben. An implicit feature of this model is that the CMA tuff may be related to the extra-caldera tuffs (including the Pumice Unit); products of the collapse of the Guayabo caldera that overlie the higher-K lavas to the west of La Fortuna.

The proposed model presents no contradictions to either the exposed or drilled stratigraphic relationships to the west of the La Fortuna Graben, but poses a question over the idea that

the sampled, pre-Guayabo caldera Espiritu Santo lavas could be related to the uppermost CMA by their similar geochemistry. The problem is that if the CMA tuff is related to the caldera collapse products, and if the Espiritu Santo edifice is older than these tuffs as suggested by Alvarado *et al.* (1990 a and b), then Espiritu Santo cannot correlate with the younger, uppermost CMA lavas.

To the east of the La Fortuna graben the caldera boundary of the ELC (1986 a) model runs just to the north of the Cerro Espiritu Santo scarp (Figure 2.10 b). The 300 m thick tuff/breccia dominated volcanic sequence of PH-42 (Figure 2.10 a) is proposed in this study to be a part of the Cerro Cabro Muco edifice succession. Examination of the ~100 m Rio Cuipilapa fault scarp bounding Bajo Los Chiqueros (location in Figure 2.10 b), indicates that Cerro Cabro Muco appears to be similarly bereft of major lavas. A correlation is tentatively proposed between the thin porphyritic lavas at PH-42 and the uppermost lavas at PGM-12 nearly 4 km to the east, but again this may be supported by the results of the resistivity profiles in this area, presented in Chapter 3.

Conversely, the lava dominated sequence of PH-41 (Figure 2.10 a) is correlated with the adjacent Cerro Espiritu Santo remnants of an ancient collapsed stratovolcano that now makes up part of the pre-caldera stratigraphy in the ELC (1986 a) model. This implies that the main caldera fault is between PH-42 and PH-41. The majority of the Cerro Espiritu Santo samples are from the very western uppermost exposures, closest to the southern borefield (Figure 2.5). The uppermost CMA lavas are geochemically similar and it is proposed here that they may be equivalent. Sample 2v is from the uppermost Cerro Espiritu Santo succession and is important because it is similar to the higher-K Cerro Cabro Muco edifice samples. Conversely, the La Giganta sample (3v, inside the collapse scarp, Figure 2.5) is similar to the uppermost CMA samples and the older Espiritu Santo samples (Figure 2.12.b). These correlations suggest that the older parts of Cerros Cabro Muco, in the La Giganta area, Cerro Espiritu Santo and the uppermost CMA are parts of the same edifice, but are now separated by a post-Cabro Muco collapse event. The more recent basaltic andesites of Cerro Cabro Muco, conversely, are related to the LCMV basaltic andesites and andesites of the LCMV at Sitio Las Mesas.

It is proposed here that the sampled parts of Cerro Espiritu Santo could be younger than the majority of the Guayabo related tuffs and therefore younger than the CMA tuffs and the higher-K lavas on the western side of the La Fortuna graben. This contradicts the proposal of Alvarado *et al.*, (1990 a and b), but as the exposed geology does not show the tuffs directly overlying the Cerro Espiritu Santo lavas, the tuffs may indeed be older.

A summary of the relationships between the drilled and the exposed Guayabo caldera succession proposed in this study is shown in Figure 2.13; a diagramatic west-east sketch of the correlations in stratigraphic order. Some of the points shown in Figure 2.13 are relevant to later discussions in the following two sections, but it is useful to introduce the summary of the southern caldera area at this stage. The southern caldera model implies that the higher-K lavas are the oldest rocks exposed in the southern caldera area, but these are proposed to correspond to the lowermost CMA lavas, suggesting that the Volcano-Sedimentary Unit (VS) probably continues beneath the caldera wall lavas.

The higher-K lavas do not correlate with either the uppermost CMA or any of the younger stratigraphy, but on the other hand these lavas have not been proved to be equivalent to the lower CMA. However, a model that implies correlation of the southern caldera wall material with the shallow, rather than deep (VS or deeper), drilled stratigraphy is supported by the geophysics data presented in the following Chapter. Gravity models show a continuation of the density structure across this caldera margin and the resistivity profiles show that the deep conductor corresponding to the VS in the geothermal field also continues across the southern caldera margin. The overall impression is that the southern caldera area is composed of a number of volcanic successions that are distinct in certain areas (such as the PGM-12 CMA-LCMV succession) but parts of these interdigitate with adjacent successions. As a result, it is difficult to correlate complete successions laterally, but this is believed to be a common feature of stratovolcanic successions. The major element geochemistry suggests that although equivalent lavas may be identified, it is difficult to recognise a consistent pattern of geochemical evolution, either temporally or spatially.

Figure 2.13 Summary of the Guayabo Caldera stratigraphy and correlations proposed by this study, details in text, bold type for stratigraphic units in the PGM- wells. Structural details in Chapter 3. There is an approximate west-east orientation to the section for the post-Bagaces Group units only. LCMV = Late Cabro Muco Volcanic Unit; PUM = Pumice Unit; CMA = Cabro Muco Andesite Unit.

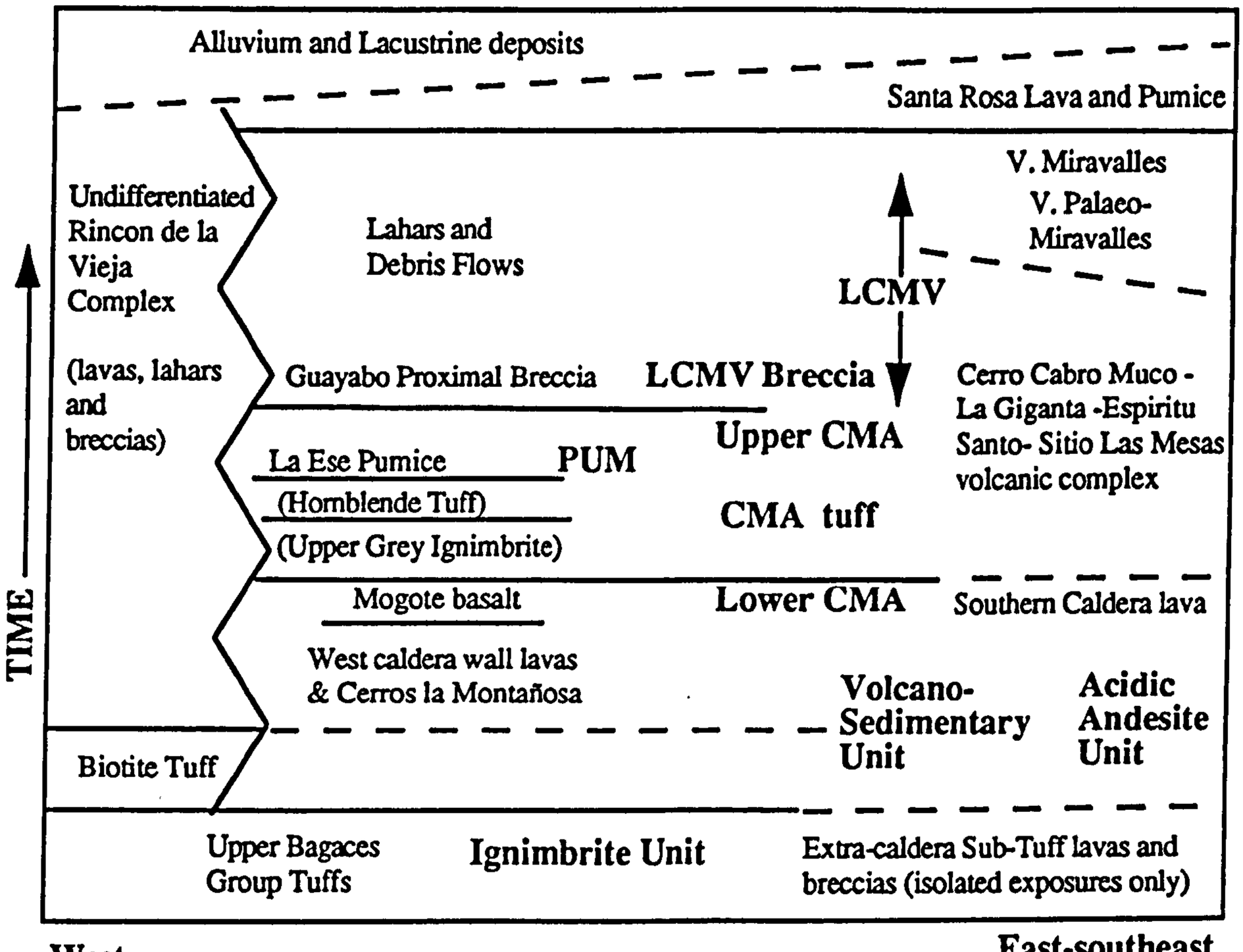

Attention is now switched to the stratigraphy of the western caldera margin and the small outcrops of lava that are exposed beneath the Guayabo caldera-related tuffs outside the caldera.

2.3.9 The western caldera border and the extra-caldera lavas

The objective here is to examine to what extent the western caldera scarp lavas and those exposed outside the caldera really are of pre-caldera age and underlie all of the outflow tuffs of the Guayabo caldera as proposed by ELC (1986 a).

The lavas abundantly exposed in the western walls of the Guayabo caldera, including those of Cerro Mogote, were examined during this study and generally dip away from the caldera at shallow angles (up to 15°). This suggests that their source, postulated to be a stratovolcano complex (in agreement with Alvarado *et al.*, 1990 b), was located within the

Guayabo caldera and was active prior to caldera collapse. As there are no wells in the western intra-caldera area it is not possible to determine the displacement across the caldera margin; this has been estimated from i) gravity profiles across the caldera margin (discussed in Chapter 3) and ii) tentative correlations of the caldera scarp lavas with lavas in PGM-15.

The tuffs exposed outside, but within a few kilometres of the caldera have, almost exclusively, lowermost contacts with older tuffs or palaeosols, but seldom with lavas (Mora, 1988). All the extra-caldera lava outcrops sampled during this study (sample locations in Figure 2.5) are treated as Pre-Caldera Lavas in the ELC (1986 a) model, and were therefore considered older than the Biotite Tuff and the tuffs associated with the Guayabo caldera. It is suggested here , however, that some of these may be inter-tuff lavas, of the type found by Chiesa *et al.* (1987) between the tuffs of the older Bagaces Group.

An andesite from Finca Estrella, 2 km northeast of San Jorge (Figure 2.5), contains xenoliths (up to 1 cm diameter) of microdiorite, very similar to lavas exposed on the Rincon road along the western ridge of the Rio Salto Gorge (SH 21, Figure 2.5) that certainly overlie the 50-100 m thick Biotite Tuff exposed below. The lavas are of an unknown affinity but given their location they are more likely to be related to the Rincon de la Vieja complex (Figure 2.5), rather than the source for the western Guayabo caldera wall lavas. If the Biotite Tuff is *younger* than the western caldera wall lavas, as proposed by ELC (1986 a), then it is unusual that no exposures of the Biotite Tuff have been found overlying the caldera scarp lavas, considering the proximity of the thick Biotite Tuff sequence west of San Jorge. It is proposed here that the Biotite Tuff may, in fact, be *older* than both the exposed lavas to the northwest of San Jorge and some, if not all, the caldera wall lavas and that therefore it *predates* the collapse of the Guayabo caldera.

Only the most recent tuffs associated with the Guayabo caldera, are definitely underlain by the western caldera wall lavas. Mapping reported by ELC (1984 a) and sampling during this study show that the southwestern flanks of Cerro Mogote are covered by a badly degraded lithic tuff at least 5 m thick (Figure 2.5). Clean basaltic andesite lithics from this tuff (samples CM6 and CM7) are low-K basalts similar to the underlying collapsed Cerro Mogote lavas (Figure 2.12). This lithic tuff is thought by this study to be temporally

equivalent to the uppermost tuffs and breccias that overlie the La Ese Pumice mapped south of the caldera by Mora (1988) (Figure 2.5) and have thus been included in the Guayabo Proximal Breccia of this study (described in section 2.3.10).

The lava blocks scattered to the west of the caldera near San Jorge (samples EC53 and EC55; Figure 2.5) are porphyritic two pyroxene andesites with no olivine and the one sample analysed (EC53) is clearly of a medium-K suite that may be distinct from the lower-K suite olivine andesites of the western caldera walls (Figure 2.12 a) and is certainly unrelated to the Mogote basalts. These blocks are typical of the exposures of supposed lavas in this area and my simply represent large blocks in a debris flow or lithic-rich tuff, rather than preserved parts of an otherwise weathered lava. The exact stratigraphic relationship between these blocky deposits and the Biotite Tuff, exposed at lower elevations than the lavas in the San Jorge area (Figure 2.5), is not certain; no exposed contact is known to this author, but it seems reasonable to suggest that they are younger than the Biotite Tuff, and have been tentatively placed within the late Guayabo caldera-related tuff stratigraphic level, similar to the Guayabo Proximal Breccia. This does not mean therefore that the original lavas are younger than the Biotite Tuff but may be older.

5 km south of Cerro Espiritu Santo, Leandro *et al.* (1988) recognised lavas underlain by thick (50 m) volcanic breccias and lithic tuffs. Isolated lavas are also exposed nearby at Quebrada Santa Fe (410.5 287.0, just off the southern edge of the area in Figure 2.5) below all the tuffs in the area including isolated exposures of the Biotite Tuff. 5 km to the southwest of the caldera in the Quebrada Gloria river bed (sample EC44, Figure 2.5) there is an exposure of lava underlying the Biotite Tuff. Its chemistry is similar to the higher-K suite of the southern caldera lavas, 8 km to the east (Figure 2.12), but *not* to the lower-K suite of the closer western caldera wall olivine andesites. Weathered sub-tuff lavas are also exposed in Rio Cerro Gordo (location of density sample EC56, Figure 2.5), closer to the caldera than EC 44 but petrographically similar to EC44 andesite (no olivine).

The overall conclusion is that the older lavas that can be proved to underlie the Biotite Tuff and the younger tuffs related to the Guayabo caldera, belong to a distinct higher-K suite than the lavas in the western caldera walls. It is not unreasonable to suggest on geochemical

grounds that they could therefore be related to the higher-K lavas of the southern caldera margin, which are proposed to be the oldest rocks exposed in this area. This possibility is shown in the summary in Figure 2.12, but the alternative is also shown, that the extra-caldera, sub-tuff lavas could be older than the VS.

Leandro *et al.* (1988) have grouped all the caldera wall lavas (from Cerro Espiritu Santo to Cerros La Montañosa), the extra-caldera lavas described above and their underlying breccias/lithic tuffs into the **Guayabo Group**. They proposed that this sequence is the legacy of the stratovolcano Volcán Guayabo, which subsequently collapsed in arcuate segments to produce the outlying tuffs and the Guayabo caldera. The scale of the area covered by the component parts of the Guayabo Unit requires a single gargantuan stratovolcano of some 25 km diameter, unlikely in the opinion of this author in an arc environment. The outlying tuffs are usually underlain by older tuffs, excepting the lava examples above, separated by a palaeosol in many cases (Mora, 1988). This author believes that the few outcrops of extra-caldera lavas cannot unequivocally be correlated with the caldera wall lavas. An alternative explanation and evolutionary model is proposed in Chapter 3 based on the contrasting geophysical expression of the caldera wall and the extra-caldera lavas.

2.3.10 Intra-caldera tuffs and possible extra-caldera equivalents

In a review of caldera-related facies, Lipman (1984) noted that in general, intra-caldera facies are thicker, show greater welding and density, and lithic size and content, than their outflow counterparts. Intercalations of lavas are also common in the intra-caldera sequences, close to the ring-fracture controlled volcanic vents, but some of these may flow out of the caldera, depending on the topography. The Guayabo succession has yet to be presented in such terms.

Mora (1988) divided the extra-caldera tuffs into six units (Flows Q1 to Q6; Table 2.2). Similar divisions, but with a different nomenclature, have been used during subsequent mapping of the area to the south and southeast of the Guayabo caldera (Alvarado *et al.*, 1990 a and b). The nomenclature used during this study (Table 2.2) contains aspects of the most

recent previous systems, but avoids some of the cumbersome terminology. The regional distribution of the Bagaces Group tuffs, the Biotite Tuff, the Sandillal Tuff, the Crystal-Free Tuff and the tuffs related to the Guayabo caldera are shown in Figure 2.3. The geological map of Mora (1988) showing the distribution of the tuffs related to the Guayabo caldera abundantly exposed south and southeast of the caldera, was unfortunately not available to this study. However, the distributions of the tuffs in the area to the east of the 400.0 line (Figure 2.5) are from Alvarado *et al.* (1990 a) who integrated the maps of Mora (1988) and Civelli *et al.* (1990, unpubl. map). The tuff distribution to the west of the 400.0 line is from Chiesa (1991). The areal limits of the Upper Grey Ignimbrite, the Hornblende Tuff, the La Ese Pumice, the Guayabo Proximal Breccia and the later small volume tuffs suggested to Mora (1988) and Alvarado *et al.* (1990 a) that the Guayabo caldera is the probable source area. Alvarado *et al.* (1990 a) further suggested that the Crystal-Free Tuff is also from the Guayabo caldera area, but Mora (1988) believed that as its outcrop is limited to the southeast (Figure 2.3) and thickens towards the east, its source may be in the Volcán Tenorio area.

The extra-caldera tuffs are compared to the detailed intra-caldera PGM-15 sequence of ELC (1986 b) (Figure 2.14). PGM-15 is the most complete (i.e. no loss of drill cuttings) and the least hydrothermally altered borehole stratigraphy; it is also one of the boreholes closest to the extra-caldera tuffs (Figure 2.5). Some of the correlations shown in Figure 2.14 partially result from the elimination of improbable and stratigraphically impossible alternatives, rather than strict positive and direct identifications.

The Bagaces Group Tuffs ~ The Ignimbrite Unit: The >800 m of Ignimbrite Unit is the only major drilled welded tuff; it is unlikely to have formed in anything but an intra-caldera environment. The lithics are andesite lavas and the matrix contains broken plagioclase crystals and some quartz (ELC, 1986 b). It may correlate with one or more of the compositionally similar and widespread Bagaces Group tuffs (Figure 2.3).

Figure 2.14 Proposed intra- to extra-caldera correlations between PGM-15 and the extra-caldera tuffs (note different vertical scales). See Table 2.2 for tuff nomenclature, Figure 2.5 for localities, Figure 2.9 a for PGM-15 key. Only correlations for the Ignimbrite Unit and units younger than and including the Pumice Unit are considered confident. The other tuffs may be present in the central and western parts of the caldera.

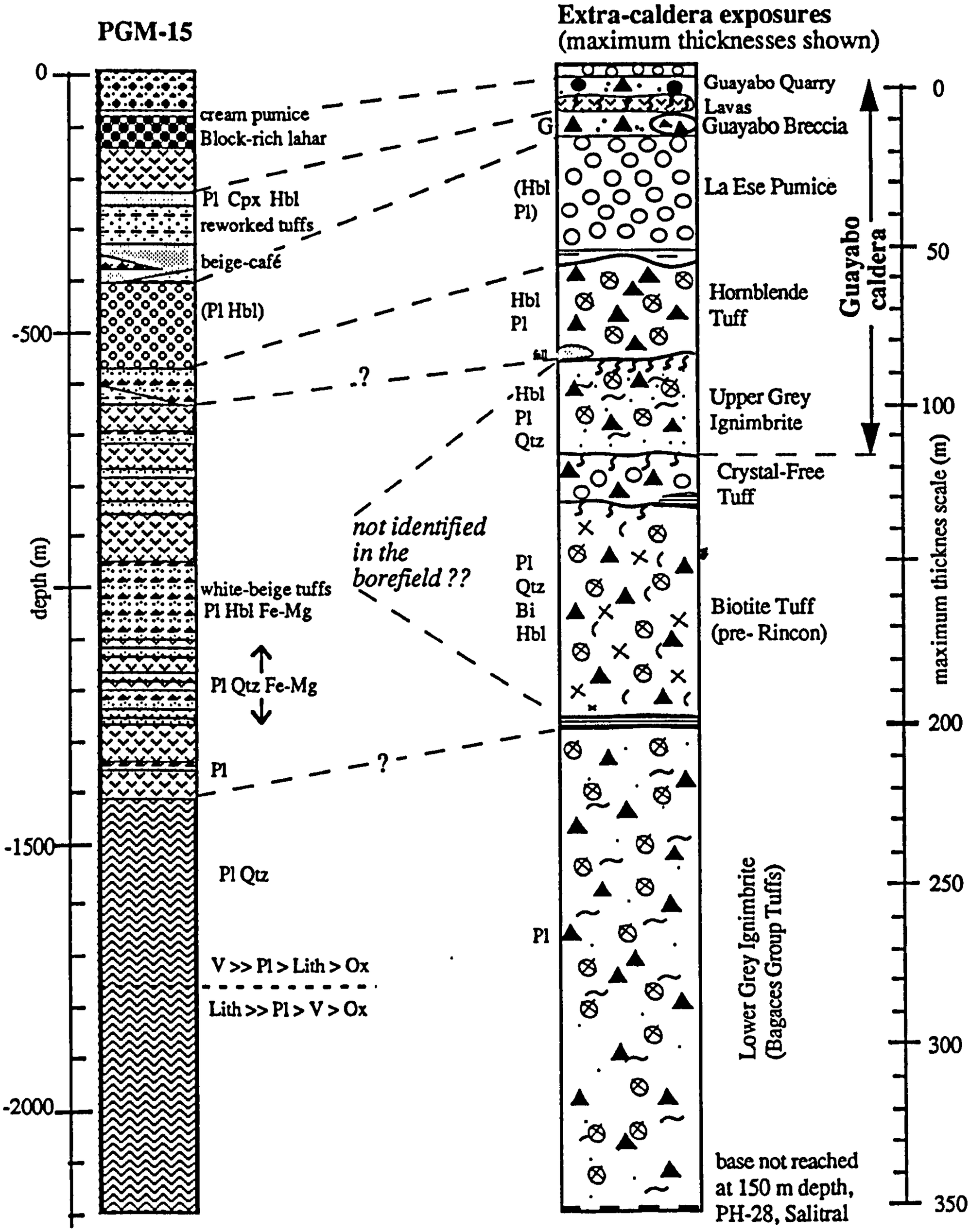

The Bagaces Group has been shown to comprise several temporally distinct but generally grey welded tuffs (K-Ar ages in Table 2.1) but there are no exposures of these tuffs close to the lavas of the caldera wall or the Cerro Espiritu Santo lavas, so they are not necessarily younger than the Guayabo caldera. 150 m of the lower grey ignimbrite of the Bagaces Group was drilled by ICE (unpubl. data), without encountering the base, at Salitral (PH-28), some 15 km south of the borefield (location; Figure 2.1). The thickness and areal extent of the Bagaces Group tuffs suggest that at least one large caldera should be expected in the source area, and this is likely to be significantly pre-Guayabo. Indeed, considering all the more recent geology and the associated evolution of the topography, if a part of one of the Bagaces calderas has been drilled in the Miravalles Borefield, it does not follow that this caldera is necessarily *the* Guayabo caldera. The Ignimbrite Unit/Bagaces Group caldera may well have been larger than the Guayabo caldera, which is proposed to have resulted from the collapse of a volcanic complex that built over the Ignimbrite Unit. Thus, the presently exposed Guayabo caldera is likely only to be related to the more recent tuffs that significantly post-date the Bagaces Group. No detailed study of the Bagaces Group tuffs has yet been undertaken (see section 2.2.3) and it is not possible to confirm the proposed source area without commonly used data such as the tuff thickness, the variation in the degree of welding and lithic size fraction distribution.

The Biotite Tuff; no major drilled equivalent: The very distinctive poorly welded, cream coloured Biotite Tuff, with Qtz, Pl, Hbl, Bi and oxide minerals (relative order from Chiesa, 1991), does not have a major drilled representation. This is not surprising, considering the proposed source area beneath Rincon de la Vieja (Chiesa, 1991; discussed in section 2.2.3). However, if as proposed by this study, the Bagaces Group is equivalent to the Ignimbrite Unit then the younger Biotite Tuff should be present in those parts of the wells above the Ignimbrite Unit, as it is found to the north and south of the caldera (Figure 2.3). The only intra-caldera tuffs with a possibly similar composition to the Biotite Tuff are documented at the base of the Volcano-Sedimentary Unit at PGM-15 and PGM-5. At 1150-1250 m b.s.l. in PGM-15, crystals of Pl, Qtz and unidentified mafic crystals (possibly Hbl, Bi, or oxides) lie in tuffs separated by thin lavas, but overlying this sequence is a 100 m thickness of a white-beige lithic tuff with Pl, Hbl and mafic minerals that could also be the

Biotite Tuff; however no Qtz was reported. This later tuff at PGM-15 is correlated with a tuff at a similar depth in PGM-5 and 10 (Figure 2.9 a), but it is possible that some or all of these tuffs may be reworked older material, rather than primary tuff deposits. As Qtz is the major mineral phase in the Biotite Tuff a correlation with the Qtz-bearing tuffs is preferred here. If the borefield area was the site of a stratovolcano complex and therefore elevated when the Biotite Tuff was erupted, then only a limited thickness would be expected.

It is concluded that none of tuffs in the borefield sequence are sufficiently similar to the distinctive Biotite Tuff, and therefore no direct correlation is shown in Figure 2.14.

The Crystal-Free Tuff (Figure 2.3) is thought to be derived from the Tenorio area, because of its greater thickness towards this area (Mora, 1988). It is indistinctive and therefore has not been positively identified within the borehole sequence.

The Upper Grey Ignimbrite; no major drilled equivalent: The Upper Grey Ignimbrite, (distinct from the older, but similar, grey ignimbrites of the Bagaces Group) is the first and most widespread of the extra-caldera tuffs, considered by their distribution, to be associated with the Guayabo caldera (Mora, 1988). It is partially welded, forming the distinctive "egg-box" topography between Guayabo and Bagaces. It contains andesite lava lithics and Pl, Qtz and Hbl in the pumices and the matrix. It is reasonable to assume therefore, that an intra-caldera equivalent should be a welded lithic-tuff, but apart from the Ignimbrite Unit, no other welded tuff has been documented in the wells. Only broken Pl (and some Qtz in PGM-15) has been recognised in the Ignimbrite Unit, and no Hbl is found in the PGM-15 sequence as seen in the exposed Upper Grey Ignimbrite. A suitable mineral assemblage is present in the lithic tuffs at the base of the Volcano-Sedimentary Unit in PGM-15, but these are thin tuffs, interbedded with lavas, and welding fiamme have not been documented from the cuttings. No suitable equivalent thickness of the Upper Grey Ignimbrite has been recognised in the drilled succession.

The Volcano-Sedimentary Unit has been well-cored in PGM-12 (Figure 2.9 b) where lithic tuffs and vitric tuffs but no lavas have been recovered; different from the lava-rich PGM-15 section. Only Pl crystals have been identified in most of the PGM-12 tuffs, but it is possible

that other primary minerals may have been replaced or removed during hydrothermal alteration. Chlorite, for example, is a common alteration mineral and may have replaced the original mafic minerals in the tuffs. A tentative correlation, therefore, is proposed between the lowermost Volcano-Sedimentary Unit tuffs and the Upper Grey Ignimbrite.

The Hornblende Tuff ~ Beige Tuff of the Volcano-Sedimentary Unit? The cream white Hornblende Tuff, with lithics and Hbl and Pl crystals is apparently similar to the 120 m thick, beige-white, lithic tuffs identified in PGM-5, 10, 15 and possibly 12. Although no details of the compositions of the tuffs in PGM-1, 2 and 3 are given by Koenig (1980), some of the thick tuffs must be equivalents of those recognised in the Volcano-Sedimentary Unit in the other wells (Figure 2.9 a and b). This implies that if there is a drilled equivalent of the older Upper Grey Ignimbrite, it underlies this tuff.

If the Hornblende Tuff is present as a part of the in VS at 1000 m depth in PGM-15, but is exposed *above* the higher-K andesites that may correlate with the lower CMA at PGM-12, there is a contradiction; both correlations are incompatible and one at least must be false. The Hornblende Tuff to beige tuff (VS) correlation implies a downthrow of ~1100 m between PGM-15 and the southern caldera higher-K lavas, whereas a higher-K lavas to lower CMA correlation implies only ~400 m. The gravity models (presented in the following chapter) suggest that 1100 m downthrow is unlikely and therefore the tuff correlation is also unlikely, whereas the lavas may be equivalent. It is possible that the Hornblende Tuff correlates with the lithic tuff directly beneath the Pumice Unit, as indicated in Figure 2.14.

It has not been possible to correlate, with any great confidence, either the Biotite Flow, the Upper Grey Ignimbrite or the Hornblende Tuff with any of the drilled intra-caldera deposits. If the Bagaces Group correlates with the Ignimbrite Unit, and the Upper Grey Ignimbrite and the Hornblende Tuff *are* associated with the Guayabo caldera, then any significant thicknesses of the intra-caldera equivalents, if present, must be in the central or western part of the caldera, outside the borefield.

The La Ese Pumice ~ The Pumice Unit: The most distinctive tuff in the boreholes is the Pumice Unit in PGM-15; a white, 150 m thick, lithic-free pumice tuff with traces of Pl and Hbl. This is correlated with the La Ese Pumice, exposed only 5 km to the southwest (40 m thick at La Ese, Figure 2.5), which comprises a white, practically lithic-free pumice tuff that contains minor (less than 2 %; Mora, 1988) Pl and Hbl. The older Hornblende Tuff contains a greater quantity of the same crystals but, most importantly however, has a much more significant lithic content, not seen in the Pumice Unit cuttings. The proposed correlation of the Pumice Unit with the La Ese Pumice is very important, as it constrains the stratigraphic level at which other intra- to extra-caldera correlations are made. The Pumice Unit is at a depth of 400-550 m depth in PGM-15 and the implied caldera margin downthrow of ~500 m (Figure 2.14) is compatible with the proposed correlation of the higher-K lavas with the lower CMA.

The Guayabo Proximal Breccia ~ LCMV breccia: The area between the La Ese quarries and the Guayabo caldera has not been accurately mapped, but it is crucial to understanding the timing of caldera formation. Mora (1988) has mapped this area as the Pre-Caldera Lavas of ELC (1986 a) but there is not one lava exposure here known to this author that underlies any of the extra-caldera tuffs described above. The only lavas exposed between La Ese and Guayabo are the proposed Late Cabro Muco Volcanic Unit lavas *above* the breccias and lithic-rich tuffs at the Guayabo quarry (Figure 2.14, discussed in Section 2.3.8). The breccias and minor crystal-free lithic tuffs form a continuous southward-dipping sequence amply exposed in road-cuts between Guayabo and La Ese; they also age southwards due to the steeper slope of the topography than the dip, and definitely post-date the La Ese Pumice (Figures 2.5 and 2.14). These breccias include andesite blocks up to 2 m in diameter (Plate 2.2) responsible for the blocky terrain that has previously been mapped as the Pre-Caldera Lavas, but are more similar to the lag breccias of Walker (1985). Considering their relative stratigraphic positions it is reasonable to correlate the Guayabo Proximal Breccia with the LCMV breccia as shown in Figure 2.14.

In summary, a positive correlation between the extra-caldera tuffs and the drilled tuffs has only been possible between the La Ese Pumice and the Pumice Unit and a less confident

correlation is proposed between the Bagaces Group and the Ignimbrite Unit. The distinctive Biotite Tuff is not recognised in the borefield. This is surprising, because even though the source is believed to be beneath Rincon de la Vieja, the Biotite Tuff is exposed to the north and south of the Guayabo caldera. Without further data, such as trace element geochemistry, it is not possible to discriminate the lithic tuffs of the VS, and match any of these to the extra-caldera tuffs. It is always possible that some of the intra-caldera equivalents of the Upper Grey Ignimbrite and the Hornblende Tuff, associated with a source within the Guayabo caldera, *are* younger than the VS and are present in the west and centre of the caldera but have not been encountered in the borefield. This implies that these tuffs may correlate with the CMA tuff, as suggested by the correlation of the higher-K southern caldera lavas with the lowermost CMA andesites. This possibility has been tested by using the gravity data to model a suitable downthrow across the caldera margin (discussed in Chapter 3), and it is proposed that the topographically defined Guayabo caldera is composed of smaller nested calderas.

2.4 Implications for the Caldera Evolution

It is now possible to outline some general criteria that will help to constrain the new structural model developed using the geophysical data in Chapter 3; a summary of the proposed stratigraphic relationships between the lithologies described in this Chapter is given in Figure 2.13.

(i) The main Pumice Unit in PGM-15 *does* have an exposed lateral equivalent outside the Guayabo Caldera; the La Ese Pumice, a tuff that underlies parts of the topographic caldera margin south of Guayabo. Parts of the intra-caldera sequence must, therefore, continue beneath the present southern topographic margin of the Guayabo caldera.

(ii) The caldera border immediately south of Guayabo is composed of a lithic dominated unconsolidated breccia, the Guayabo Proximal Breccia, that overlies the La Ese Pumice and correlates with the Late Cabro Muco Volcanic Unit breccia, the LCMV breccia. The Guayabo quarry lava (sample SH19) is correlated with the uppermost basaltic andesite in the

Late Cabro Muco Volcanic Unit (LCMV) cannot therefore be considered as a "Pre-Caldera Lava" that underpins the deep borehole stratigraphy, as defined by ELC (1986 a).

(iii) The higher-K southern caldera lavas pre-date the Guayabo caldera related tuffs (at least the Hornblende Tuff and younger tuffs) and are correlated with the PH-30 lavas and possibly the unsampled lowermost Cabro Muco Andesite (CMA) lavas in PGM-12. This implies that the CMA tuff may correlate with one or more of the extra-caldera tuffs related to the Guayabo caldera.

(iv) Some of the older Espiritu Santo lavas may correlate with the older Cerro Cabro Muco edifice lavas of La Giganta and the *uppermost* CMA andesites (post-dating the CMA tuff but not equivalent to the LCMV) in PGM-12 and the southern PH- wells. The uppermost lavas of Cerro Espiritu Santo, however, are more similar to the most recent Cerro Cabro Muco lavas, suggesting that the two stratovolcano remnants are related and not the products of temporally distinct events, as previously believed by ELC (1983 and 1986 a) and Alvarado *et al.* (1990 a and b). It is possible that some collapse along the Cerro Espiritu Santo fault may have occurred during the latter stages of activity of Cerro Cabro Muco, prior to the collapse of Cerro Cabro Muco in the Bajo Los Chiqueros area.

(v) The most recent movements on the Guayabo caldera ring faults, responsible for the present topographic expression of the caldera, post-date the uppermost LCMV basaltic andesite, and therefore by inference, also the Sitio Las Mesas-Cerro Cabro Muco-Espiritu Santo edifice. The Cerro Cabro Muco volcanism had previously been thought of as a post-caldera event.

(vi) The Ignimbrite Unit is proposed as an intra-caldera equivalent of one or more of the Bagaces Group tuffs. The ring fractures defining the Ignimbrite Unit caldera are buried between the borefield and the nearest exposure of the Bagaces Group (8 km south of San Bernardo), but are unlikely to be related in any way to the present topographic margin of the Guayabo caldera.

(vii) Multi-stage collapse is required to account for the extra-caldera tuffs and breccias (at least four distinct units from the Upper Grey Ignimbrite to the Guayabo Proximal Breccia

inclusive) that have common source areas in the general Guayabo caldera area, but are separated by the time intervals represented by the palaeosols that developed between the tuff eruptions. The source areas for the both the Upper Grey Ignimbrite and the Hornblende Tuff are tentatively proposed to be in the central and the western caldera, as no drilled equivalent has been identified.

The models of ELC (1986 a) and Leandro *et al.* (1988) have been shown to be too simplistic to account for the evolution of the Guayabo caldera. A refined model using geophysical constraints is presented in Chapter 3.

CHAPTER 3

GRAVITY MODELS OF THE GUAYABO CALDERA

Introduction

The objective of this chapter is to verify and amplify the revised model for the evolution of the Guayabo caldera proposed in Chapter 2, in the areas outside the borefield, using available geophysical data and gravity data introduced during this study. Gravity surveys have been widely used to study silicic calderas since Yokoyama (1962) recognised that some calderas of the Japanese island arc were characterised by negative gravity anomalies due to a low density fill, approximately coincident with the caldera outline. (A review of the uses of gravity data in the examination of the structure of calderas is given in Chapter 5). The Bouguer gravity map of Duprat and Leandro (1986) over the geothermal area suggested a negative gravity anomaly was associated with the Guayabo caldera and at the beginning of this study it was considered likely that the Guayabo caldera could be analogous to the Japanese examples. The previous ICE gravity surveys of the Miravalles and Tenorio Geothermal Projects have been combined with new data introduced in this study resulting in an extensive Bouguer Corrected Gravity (BCG) map covering an area of 1400 square kilometres over the Guayabo caldera and surrounding areas. The deep structure of the Guayabo caldera and Volcán Miravalles are examined. The gravity data from Bagaces to Victoria near the Nicaraguan border also provides the first traverse across the full width of the Guanacaste Volcanic Arc (Figure 3.1).

The results of over 600 new density measurements of surface exposure and borehole samples from up to 2200 m depth, combined with previous studies of the hydrothermal mineral assemblages and their zonation provided the basis for objective two-and-a-half dimensional (2.5-D) gravity modelling of the subsurface structure of the caldera. Some of the lateral and vertical density variation in the geothermal reservoir is shown to be caused by hydrothermal alteration: de-densification of lithologies in the shallow vapour-dominated zone and densification in the deeper liquid-dominated reservoir.

The revised stratigraphy developed in the previous Chapter and geophysical studies conducted by ICE scientists during the MGP development, have been integrated into the gravity models. The resistivity and gravity studies of Duprat and Leandro (1986) showed that there was no major geophysical discontinuity across the southern caldera margin; the gravity models of this study show that this can be explained by the lack of major displacement on the topographical caldera ring fault and a continuity of most of the drilled stratigraphy across this boundary, as proposed in Chapter 2. A new evolutionary model for the Guayabo caldera is presented as a concluding section.

3.1 The Importance of Full Terrain Corrections and the Correct Choice of Reduction Density

The standard techniques of gravity data reduction that were used during this study are given in Appendix 3A, but emphasis is given here to understanding terrain corrections, the choice of reduction density and base station and datum plane definition. The formula used to generate the Bouguer corrected gravity anomaly (BCG) at each station is given here for reference in the following sections:

$$BCG = g_O + C_L + C_E + C_T - C_B \quad ...(1)$$

where g_O is the observed gravity relative to a reference station, C_L is the latitude correction (the 1967 formula, Tsuboi, 1983, was used), C_E is the free air correction, C_T is the terrain correction and C_B is the Bouguer correction. Both C_T and C_B are linearly proportional to the choice of density that has to be assumed for the both the missing terrain and the Bouguer slab (formulae in Appendix 3A); this density is called the reduction density. The choice of reduction density is critical to understanding the relationship between the BCG anomalies and the topography.

The surface elevation of the 1400 km^2 covered by the combined gravity data set varies from near sea level on either side of the volcanic arc, to over 2200 m above sea level (a.s.l.) at the summit of Volcán Miravalles (Figure 3.1). The surface geology varies from low density

tuffs of the Santa Rosa Ignimbrite Plateau on the Pacific margin, to the high density basaltic andesites of the western caldera wall scarps (locations in Figure 2.5).

Figure 3.1 The distribution of the gravity surveys of previous ICE studies (enclosed areas) and the new stations of this study (points) in relation to the Guayabo caldera and Volcán Miravalles. The axes show the Costa Rica grid reference system (in kilometers), which is used throughout this study for direct comparison of maps drawn at different scales. The regional geology is shown in Figure 2.3, the geology of the Guayabo caldera in Figure 2.5 (inside the back cover). The Bouguer gravity contour maps of the same area as this Figure are shown in Figures 3.5 a-d. The dashed line indicates the northern limit of the Bouguer maps of Figures 3.6 a and 3.7.

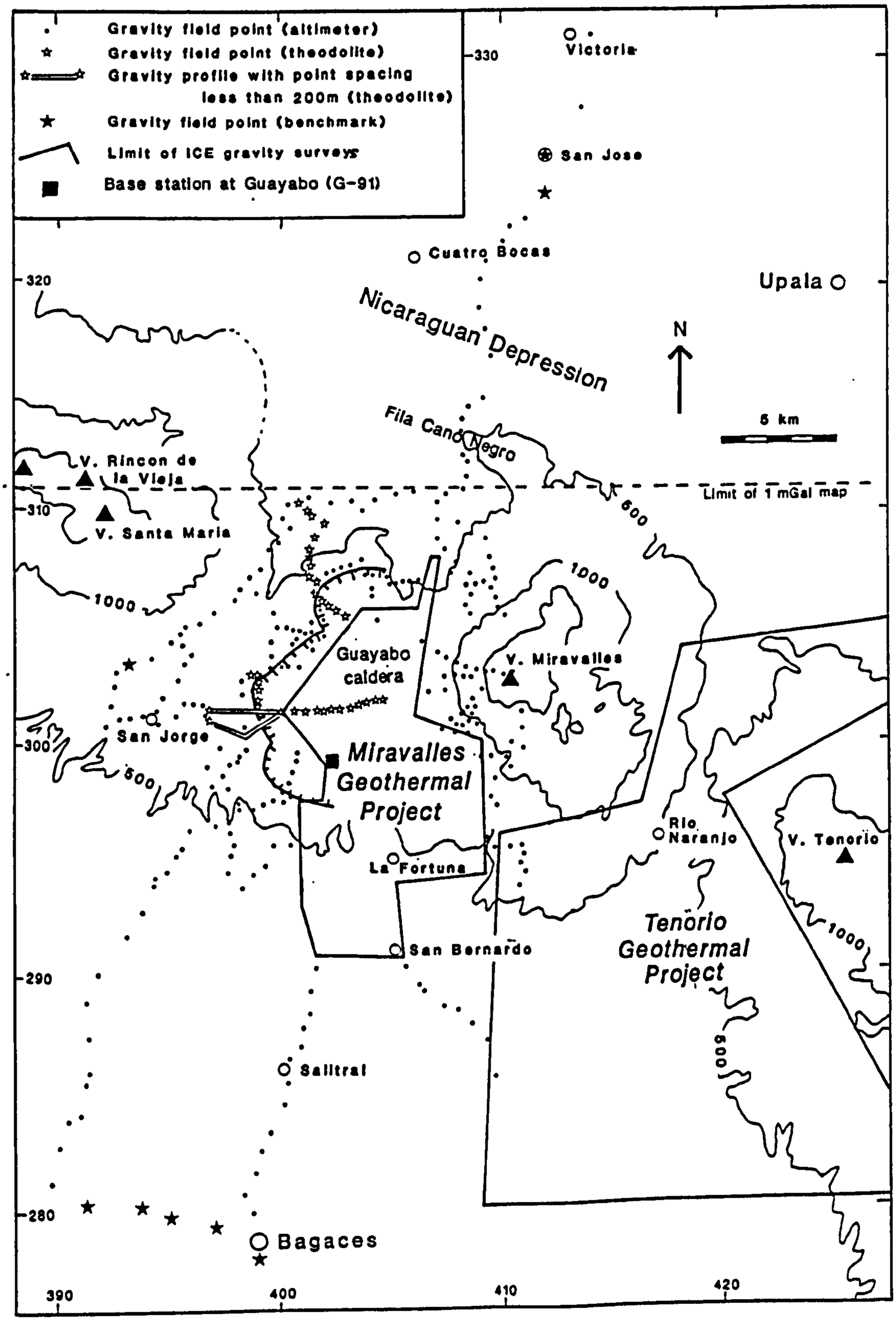

Presenting a BCG map using a unique reduction density over such a topographically and lithologically diverse area requires consideration of the terrain correction technique employed and a justification of the choice of reduction density.

3.1.1 Terrain Corrections

It is possible to significantly underestimate the total terrain correction by limiting the corrections to an area close to the survey area and not considering the full terrain out to infinity (Figure 3.2 a).

Figure 3.2 a Perspective Terrain Correction cross-section illustrating the volume of the outer uncorrected terrain compared to the volume of the corrected terrain and showing the parameters used in Figure 3.2 b.

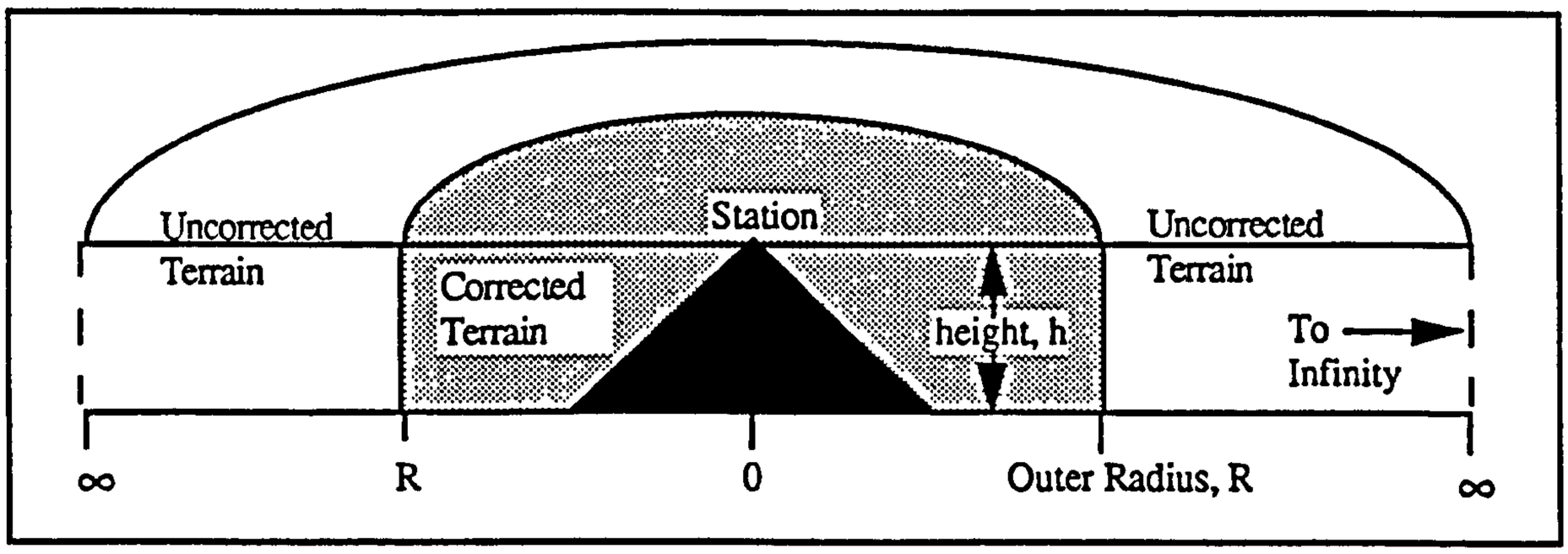

In areas of high relief the magnitude of the terrain correction depends largely upon the elevation of the gravity station above the mean topographical surface. The volume of 'missing terrain' beyond the chosen outer radius (Figure 3.2 a) becomes increasingly important for the elevated stations. The relationship between the error (the underestimate of the total terrain correction) and the outer radius is shown in Figure 3.2 b, for different station heights above the mean topography (not strictly equal to the elevation a.s.l.). For example, if terrain corrections have only been made out to 20 km (the outer radius of the M zone of Hammer, 1939 is 22 km) the lost terrain correction for the zone from 20 km out to infinity increases with station elevation (Figure 3.2 b) from less than 1 mGal for a station at 500 m elevation (the Guayabo caldera floor stations are at 550 m) to 11 mGal for a station at 2000 m (the Volcán Miravalles summit station is at 2208 m). This means that if the zone beyond 20 km is neglected, then a false Bouguer anomaly of -10 mGal is created at the Miravalles summit area relative to the caldera floor. Similarly, corrections for stations on

the flanks of Miravalles will be proportionally underestimated, resulting in a false negative anomaly over the whole volcano. The error, however, decreases as the outer limit of the corrected area, R, increases and a compromise must be sought between time expended extracting minimal corrections for distant zones and the danger of underestimating the total terrain correction by not "going out" far enough, especially when computing the terrain corrections for the highest stations. As all but the Miravalles summit stations in this survey area are below 2000 m, the lost terrain correction beyond ~ 200 km is less than 1 mGal (Figure 3.2 b); this has therefore been chosen as the outer terrain correction limit for this study.

Figure 3.2 b The relationship between the radius of the area for which terrain corrections have been made and the error incurred by not including the area beyond this outer radius; for different station heights, h above the mean topography.

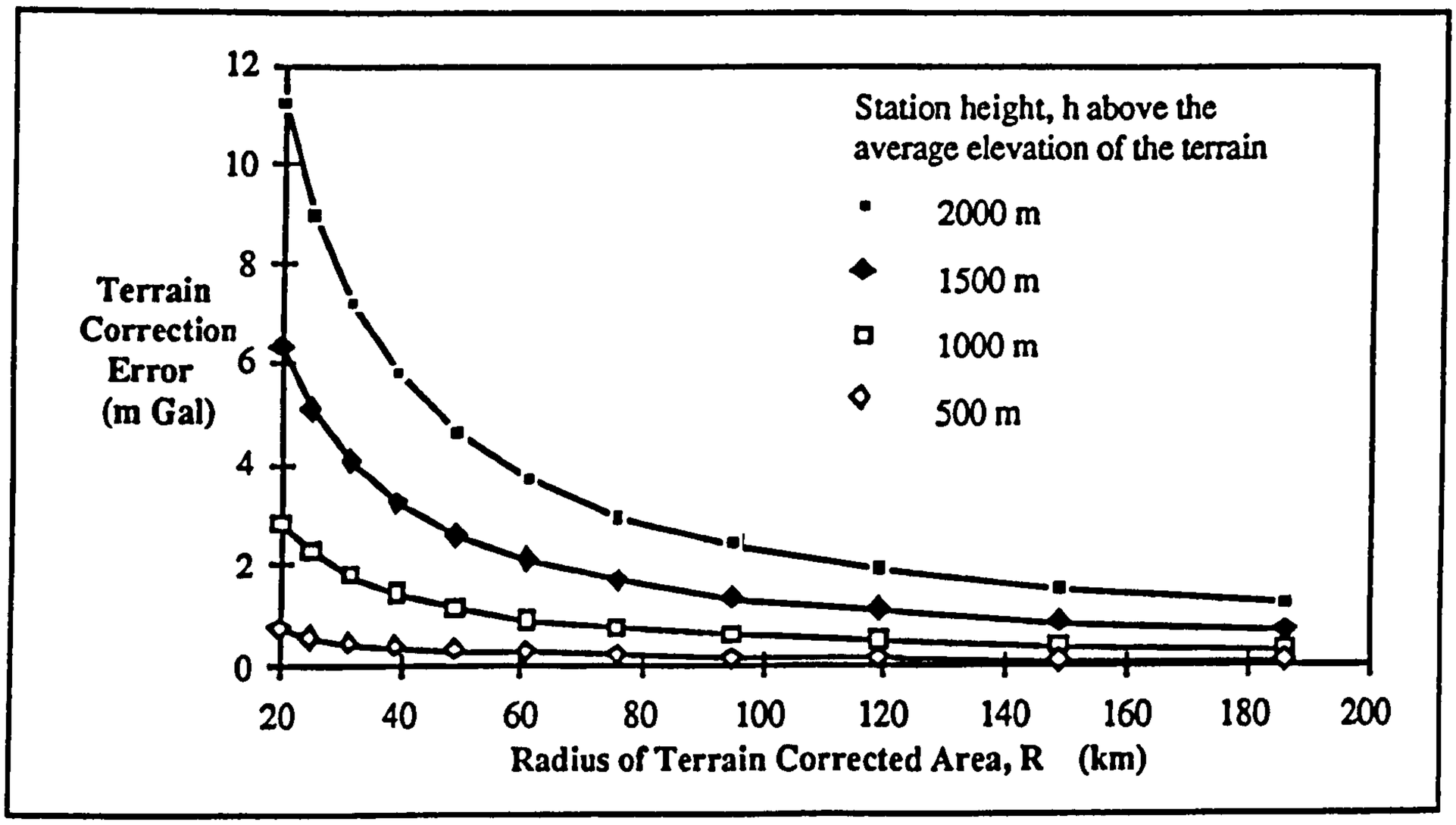

Terrain corrections for the data from previous studies had been made out to 22 km and have been extended to be incorporated into this study. For closely spaced stations, the terrain correction beyond this radius varies as a function of the elevation of the station above the terrain; this relationship comes out of the standard terrain correction formulae (Appendix 3A). To speed up calculations therefore, the survey area was divided into approximately 5 km diameter clusters of stations that shared a similar outer terrain. In practice, this time-saving exercise was made more efficient by defining fewer, ever larger clusters (of up to 20 km diameter) for the more distant terrain zones. In this fashion it was possible to extend the

outer radius of the terrain corrections for previous data without laboriously repeating similar calculations for each individual station.

3.1.2 Choice of Datum Plane and Reduction Density

For gravity surveys over limited areas, all the gravity values are internally related and the *relative* magnitudes of the BCG anomalies are constant for a given reduction density, irrespective of the choice of elevation of the reduction datum plane. The datum plane used in this study is at 548.50 m a.s.l., the elevation of the base station Gra-91, located in the town of Guayabo (Figure 3.1). The terrain correction at Gra-91 was included in the BCG calculations, which ensures for the sake of convenience that the base station BCG is always zero, regardless of the choice of reduction density.

Figure 3.3 The Bouguer corrected gravity when the mountain density exceeds the reduction density. The sketch shows 2-D slices through the cylinder-shaped slab and terrain zone and conical mountain.

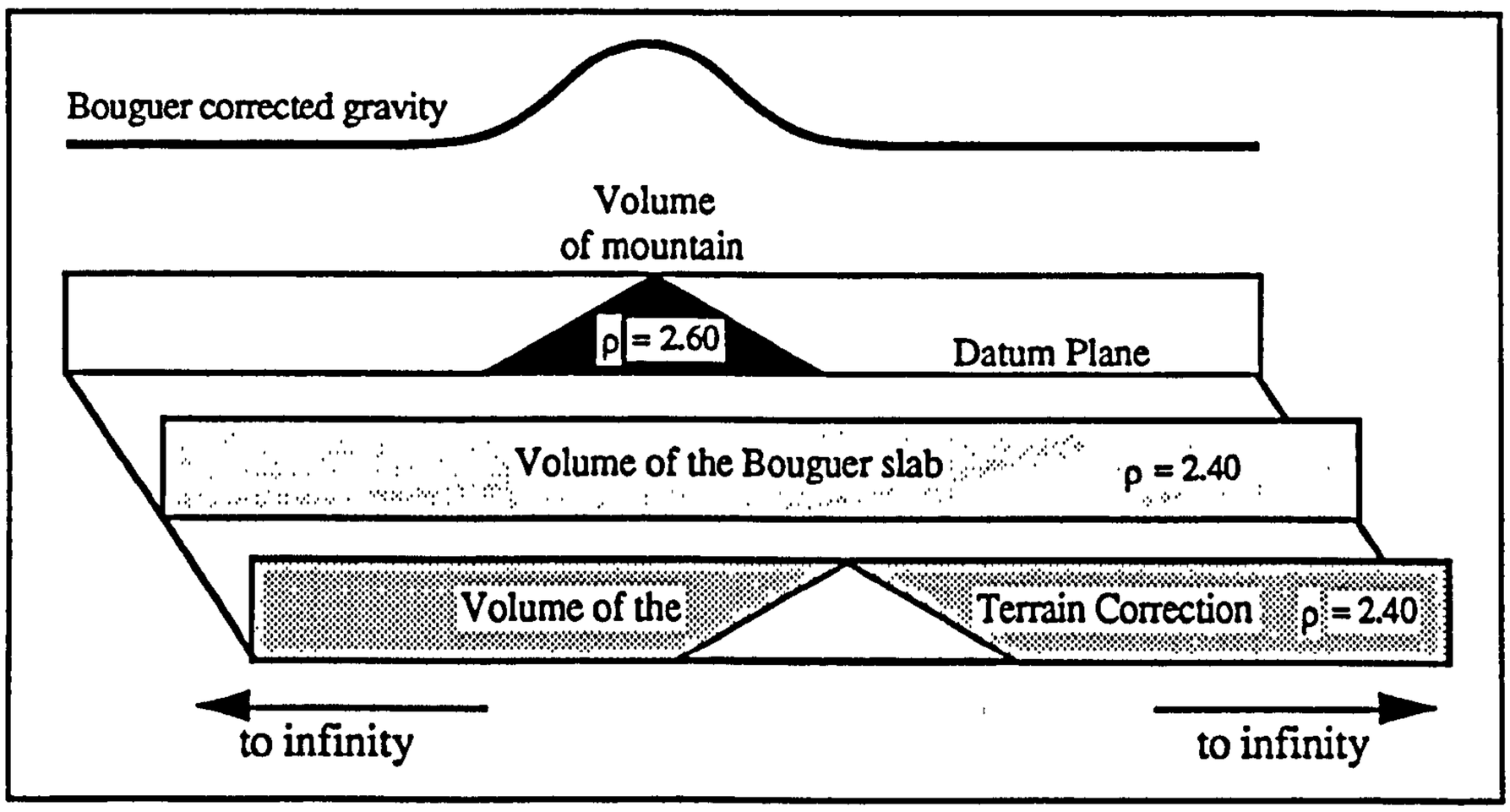

To demonstrate the relationship between the reduction density and the BCG anomaly it is useful to examine the simple case of a gravity reading on a mountain top, with the datum plane at the foot of the mountain (Figure 3.3). The terrain correction (added to the observed gravity) and the Bouguer correction (subtracted) cancel out except for the volume of the Bouguer slab that corresponds to the volume of the mountain (Figure 3.3). The chosen reduction density (2.40 Mg m^{-3}) is less than the true density of the mountain (2.60 Mg m^{-3} in this model) producing a positive BCG anomaly. Generally, therefore, a close correlation between the topography and the BCG suggests that the mass of the terrain has been over- or

under compensated by using the wrong reduction density. Recognising the density that produces the least correlation between topography and the gravity anomaly is the basis of the Nettleton method of reduction density derivation (Nettleton, 1939); it is frequently used by workers in volcanic areas of strong relief (e.g. in the Cascades; Williams and Finn, 1985). It is significant however, that a subsurface distribution of anomalous mass coincident with the overlying topography could produce a BCG anomaly *apparently* related to the topography (Williams and Finn, 1985). Due to the non-uniqueness of potential field interpretation, it is not always possible to discriminate between deep and shallow seated anomalies; and thus reduction densities that have been derived using the Nettleton method should be treated with caution, especially in areas where deep structure may be related to the terrain.

In order to examine the relationship between topography and BCG at Miravalles the Nettleton method has been used in three dimensions, rather than the commonly used 2-D profiles. BCG values of the ICE gravity data from the entire geothermal area (the ICE MGP data set, Section 3.2.1), rather than from a single profile, have been plotted against the station elevation for different reduction densities from 2.00 to 3.00 Mg m^{-3} (Figure 3.4). Generally, there is a positive correlation for low reduction densities and *vice versa* and a reduction density of around 2.67 Mg m^{-3} results in the least correlation. Applying the Nettleton method qualitatively would therefore argue in favour of a high reduction density of around 2.67 Mg m^{-3}, to remove the topography-related Bouguer anomalies. This is an unusually high edifice density for a composite volcano; gravity studies of other similar volcanoes in Costa Rica suggest that edifice densities of 2.3 - 2.6 Mg m^{-3} (Brown *et al.*, 1987) are more normal. At Miravalles, only the six stations above ~1500 m (Figure 3.4) show that low reduction densities (~2.20 Mg m^{-3}) produce the least correlation between Bouguer gravity and topography. Examination of the equivalent plots in map format however, (Figures 3.5 a-d) shows that the MGP data area is clearly located between a buried mass excess in the Volcán Miravalles area and a mass deficiency associated with the Guayabo caldera to the west. Even when the topography of Volcán Miravalles is overcompensated by using an unrealistically high reduction density of 3.00 Mg m^{-3}, there is still a residual positive BCG anomaly over the southern flank. At the reduction density of

3.00 Mg m^{-3} the positive anomaly is still located at an elevation of ~1000 m, well above the datum plane (548.5 m), which suggests that there is a genuine dense body beneath this area. If there was no genuine mass excess beneath the southern part of Volcán Miravalles then the change in the distribution of the Bouguer anomalies, resulting from the increase in the reduction density, should have been equal for all parts of the edifice that are at the same elevation. Instead, at a reduction density of 3.00 Mg m^{-3}, the residual positive anomaly is only present on the southern flank.

Figure 3.4 Bouguer corrected gravity vs station elevation for all ICE MGP data and V. Miravalles data of this study, reduced using a reduction density of 2.00 to 3.00 Mg m^{-3}. The plots show the least correlation for 2.67 Mg $^{-3}$; this suggests, according to the Nettleton method, that this density should be used to avoid terrain-related gravity anomalies. A sub-volcanic intrusion, rather than the terrain, however, could produce the apparent terrain related trends (see text and Figures 3.5 a-d).

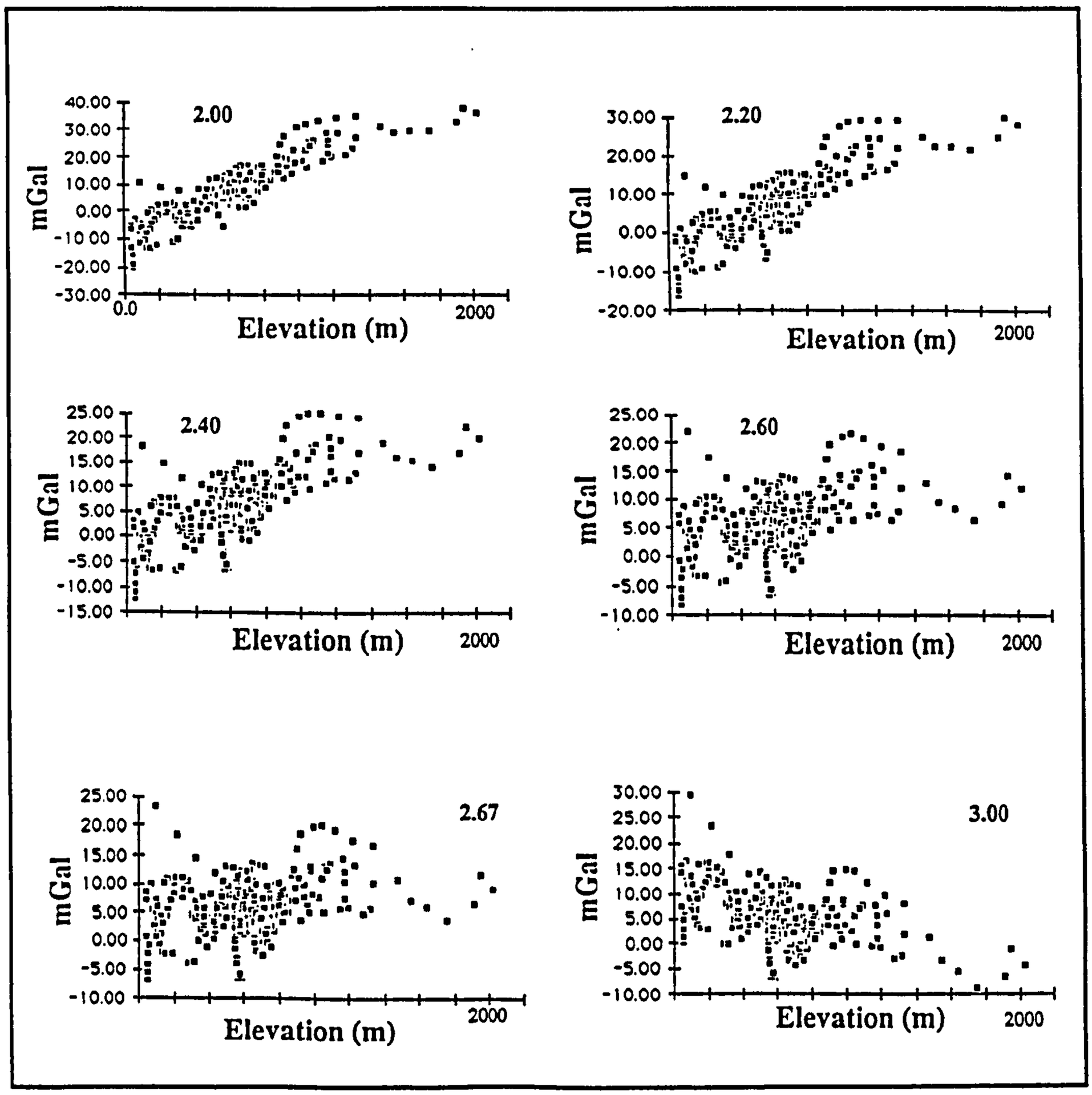

The apparent correlation of gravity with topography over Miravalles at the lower reduction densities reflects the fact that the topography and the deeper mass anomalies are both the

result of the volcano-tectonic evolution; mass excess beneath the elevated stratovolcano complex (Volcán Miravalles) and mass deficiency in the area of collapse (the Guayabo caldera). Again, it is important to point out the ambiguity inherent in any interpretation of the depth to the anomalous mass in potential field studies. Clearly, there are genuine mass anomalies that 'survive' the variation in reduction density, but in the Miravalles area it is difficult to ascertain precisely, for each reduction density, what fraction of the anomaly is related to the choice of reduction density. This problem however, is overcome in the modelling process described below.

Nettleton profiles have been used in this study to examine the composition of *individual* topographic features, rather than in the choice of the general reduction density and are further discussed below (Section 3.3) in the context of the surficial density determinations.

Before choosing the reduction density, it is important to consider that the primary objective of the gravity study is to define the subsurface density structure by 2.5-D gravity modelling. For example, the choice of reduction density is important because the reference (or background) density in the modelling process must be the same as the reduction density. The observed BCG anomaly in Figure 3.3 is due to a "wrong" choice of reduction density but it can be matched in the gravity model by giving the mountain a density contrast with the background density of + 0.2 Mg m^{-3} (2.60 - 2.40). In this case, the "wrong" choice of reduction density has been compensated for in the modelling process, but this is only possible because the background density in the model is equivalent to the reduction density. Any other choice of background density would necessarily result in a wrong estimation of the density and/or the subsurface dimensions of the anomalous mass during modelling.

Figures 3.5 a-d (overleaf) Contour maps of Bouguer corrected gravity (coloured contours) relative to topography (white contour lines). North is towards the top of each diagram and the axes show the Costa Rica grid reference system (in kilometers) for comparison with the location map, Figure 3.1. The positive anomaly apparently related to the Volcán Miravalles edifice (V. Mir) is centred to the south of the summit at Bajo Los Chiqueros (BLC High). The anomaly is present even when the terrain is over-corrected for at high reduction densities (3.00 Mg m^{-3}). See Section 3.1.2 for discussion of this feature and the gravity model VV (cf. Figure 3.28) for the interpretation.

Bouguer gravity relative to topography

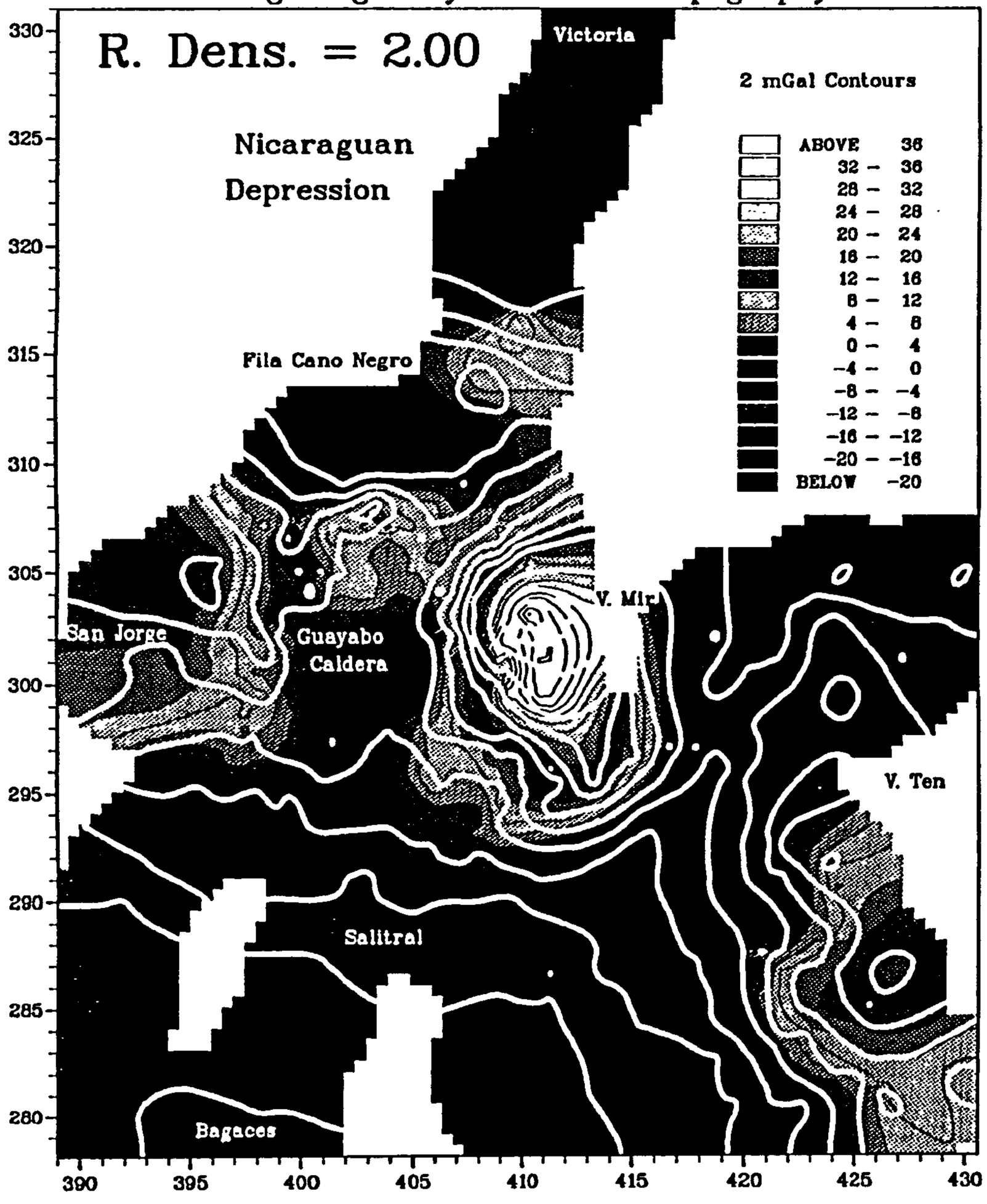

Bouguer gravity relative to topography

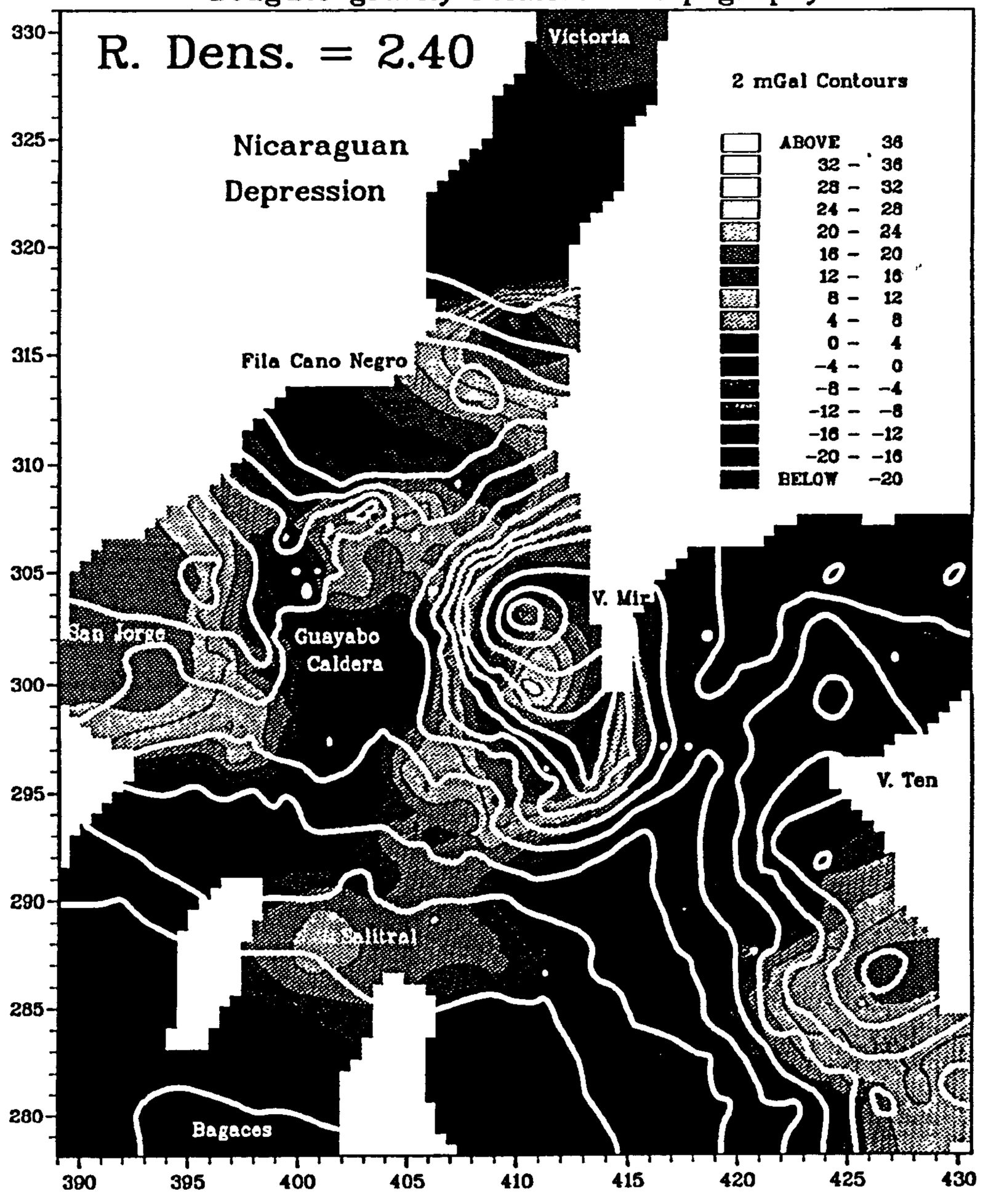

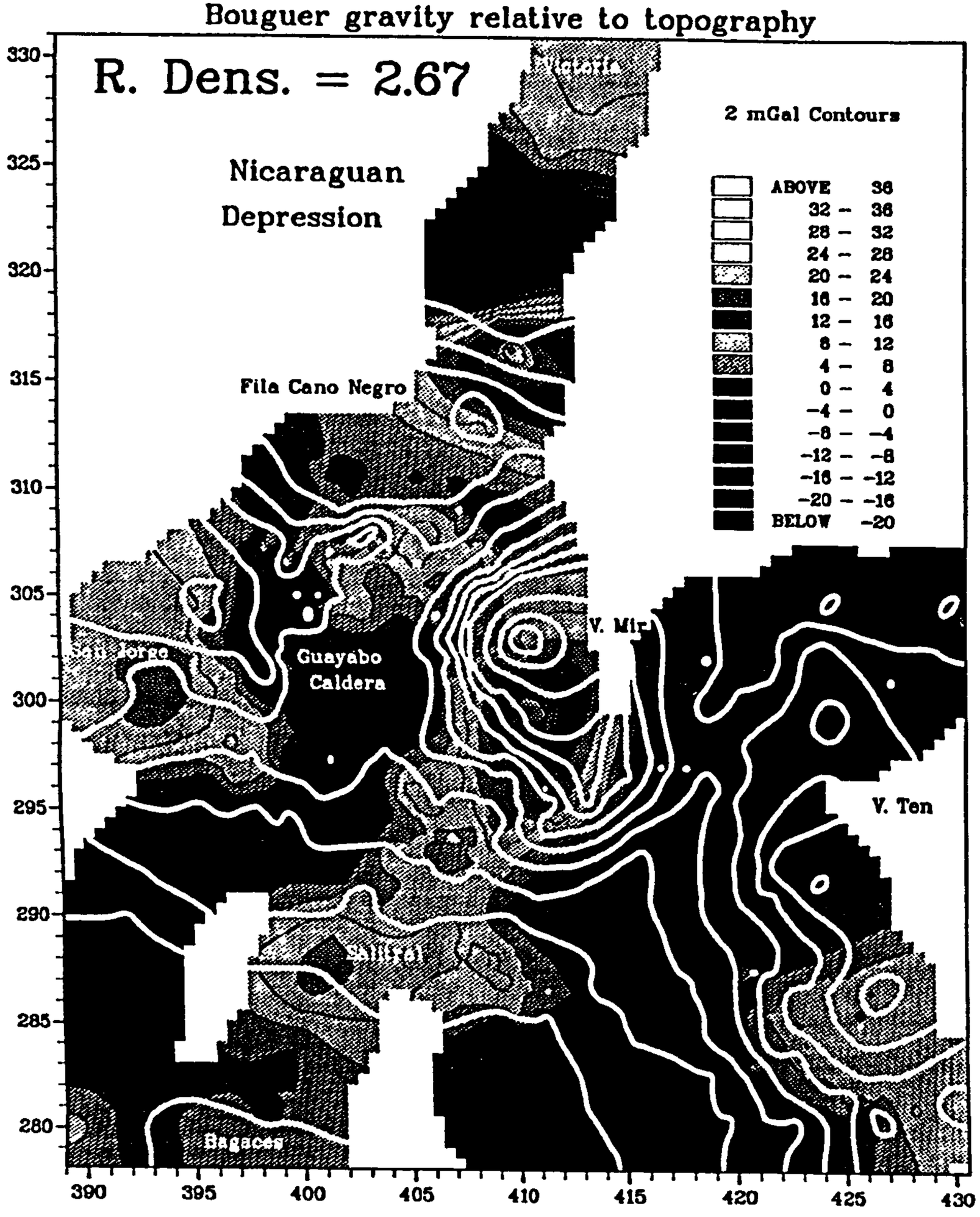
Bouguer gravity relative to topography
R. Dens. = 2.67
2 mGal Contours
ABOVE 36
32 – 36
28 – 32
24 – 28
20 – 24
16 – 20
12 – 16
8 – 12
4 – 8
0 – 4
–4 – 0
–8 – –4
–12 – –8
–16 – –12
–20 – –16
BELOW –20
Victoria
Nicaraguan
Depression
Fila Cano Negro
San Jorge
Guayabo
Caldera
V. Mir
V. Ten
Salitral
Bagaces
330
325
320
315
310
305
300
295
290
285
280
390
395
400
405
410
415
420
425
430

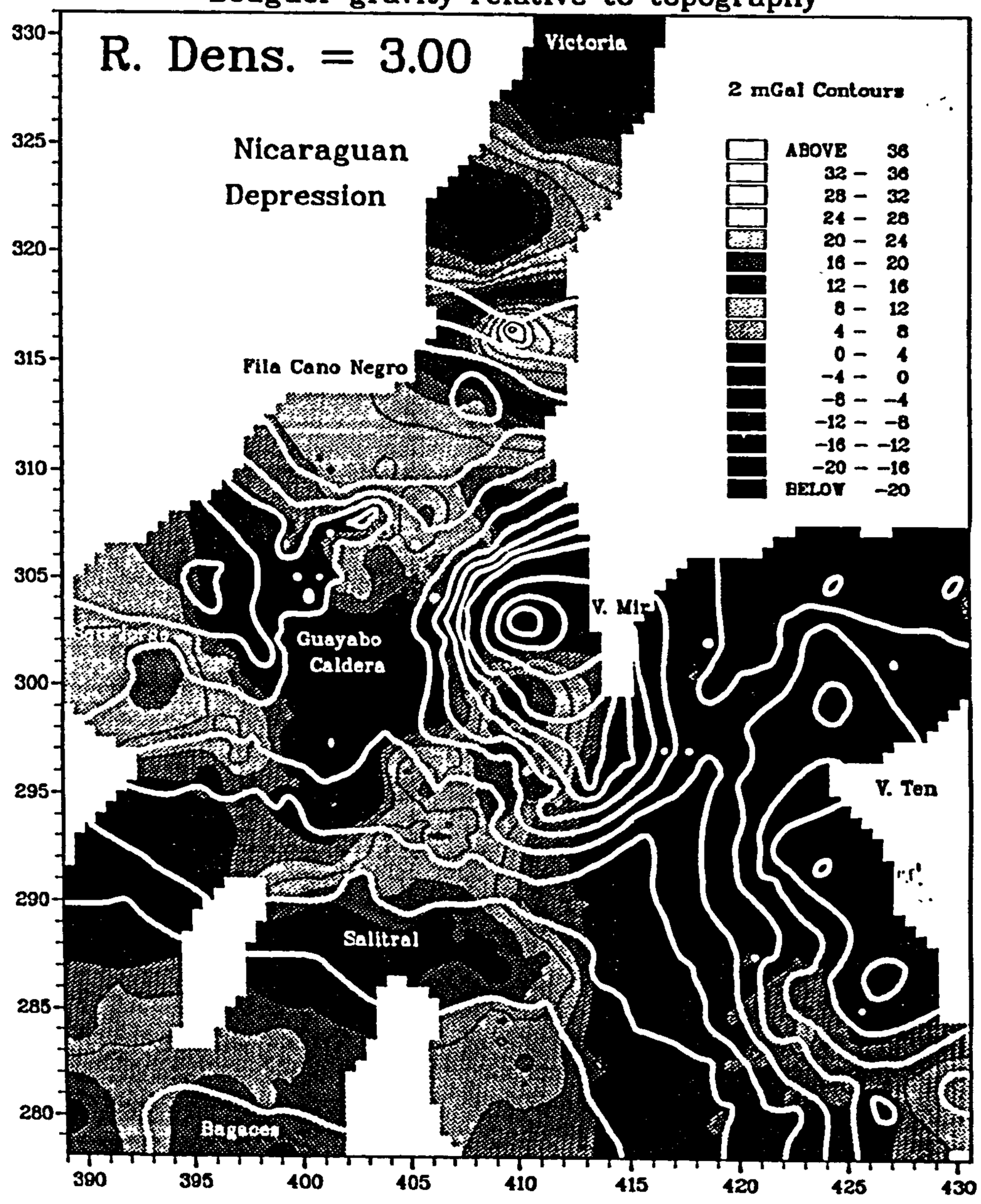
Bouguer gravity relative to topography
R. Dens. = 3.00
2 mGal Contours
ABOVE 36
32 – 36
28 – 32
24 – 28
20 – 24
16 – 20
12 – 16
8 – 12
4 – 8
0 – 4
–4 – 0
–8 – –4
–12 – –8
–16 – –12
–20 – –16
BELOW –20
Victoria
Nicaraguan
Depression
Fila Cano Negro
Guayabo
Caldera
V. Mir
V. Ten
Salitral
Bagaces
330
325
320
315
310
305
300
295
290
285
280
390
395
400
405
410
415
420
425
430

It is reasonable to suggest, therefore, that the choice of reduction density should not influence the results of the modelling process so long as the background density used during modelling is the same as the BCG reduction density. (It will be seen later, Section 3.6.1, that this is only strictly true, in the 2.5 D modelling case, for gravity profiles that are parallel to the maximum gradient of the gravity field). The concept is demonstrated below (Section 3.6) by modelling two coincident Bouguer gravity profiles over Volcán Miravalles (Profile VV, Figure 3.28), one reduced using a reduction density of 2.00 Mg m^{-3} and the other using the chosen 2.40 Mg m^{-3}. The structure interpreted from both models is the same when the background density in each model equals the Bouguer reduction density.

The reduction density question thus switches to a debate about the choice of background density instead. The density of the upper crust (deeper regions cannot be resolved considering the scale of this study) generally increases with depth, so it is unrealistic to consider the background density as a reference density for the entire crustal thickness. In a simple layered Earth model density only varies in the vertical dimension and no matter what the vertical density contrasts are, no gravity anomaly would exist. It is only lateral changes in density that are responsible for gravity anomalies. If, for example, lateral density contrasts are restricted to the upper 2 km, then the background density should be the average density of the upper 2 km in an area that is defined by the background BCG value (usually zero).

The density of the Guanacaste upper crust is not well understood because of the lack of exposure of pre-Pliocene stratigraphy, but it reasonable to postulate that the recent volcanic cover rocks are underlain by Tertiary volcanoclastic sediments and the Aguacate Group volcanics (see Figure 2.4 and discussion in Chapters 1 and 2). There is no evidence for the major Miocene plutonism typical of the Central and Talamanca Cordilleras, nor is there any outcrop of metamorphic basement (Weyl, 1980). Density analyses of both MGP borehole samples and surface exposure show that there is a wide range of densities from <1.00 Mg m^{-3} (the Pumice Unit) to 2.85 Mg m^{-3} (Cerro Mogote basalts) (for a full discussion see Sections 3.3 and 3.4 below). The density of the postulated deeper Tertiary sediments is unknown but they are not likely to have the relatively high density of a metamorphic or

crystalline basement. Therefore, the commonly quoted background density of 2.67 Mg m^{-3} used during the modelling of gravity of the large silicic calderas in the cratonic western U.S. (e.g. Long Valley; Carle, 1988) is considered too high for this region.

A density of 2.40 Mg m^{-3} has been estimated from density measurements as a reasonable average density for the uppermost 2 km (full discussion in Sections 3.4 and 3.5) of the Guayabo caldera area; this is similar to that used by workers studying some of the Japanese calderas (e.g. Yokoyama, 1963 and 1987) and geothermal areas (Baba, 1975). It is still possible to model lateral density variations below this depth providing that reasonable density contrasts with the background density are used (models discussed in Section 3.6.1).

3.2 The Gravity Data Set Used in This Study

Gravity data measured in this study (405 stations, located in Figure 3.1) have been integrated with the data from exploration surveys conducted by ICE over the Miravalles and Tenorio geothermal fields, comprising a total of 1400 gravity stations. A fourth data source, a Bouguer gravity map covering the Pacific flanks of the Guanacaste Cordillera (ICE, 1985, unpubl. map) has not been incorporated because the original unreduced data are not available and the low reduction density of 2.00 Mg m^{-3} that was used has resulted in a strong relationship with topography. A list of the stations surveyed during this study is given in Appendix 3A, and includes the grid references, elevation, observed gravity (relative to Gra-91), latitude correction, full terrain correction and finally the Bouguer corrected gravity (reduced at 2.40 Mg m^{-3}).

3.2.1 ICE Miravalles Geothermal Project Data

The MGP gravity data were originally presented as a BCG map reduced at a density of 2.20 Mg m^{-3} (e.g. Duprat and Leandro, 1986). Nearly 800 stations cover the Miravalles Geothermal Field and the area immediately around it (area outlined in Figure 3.1, station locations on the compiled BCG map; Figure 3.7). The terrain corrections were computed by ICE from a rectangular digitized grid, 44 km square, but the inner 2 km were worked out by hand from 1:50,000 topographic maps using the standard Hammer zones (Hammer, 1939). Stations were levelled by theodolite to a quoted accuracy of 5 cm (Leandro, *pers.*

comm.). All gravity readings were tied to a base station, Gra-91, near the ICE field headquarters at Guayabo (Figure 3.1) and were measured initially by a Worden gravimeter and subsequently re-measured using a LaCoste & Romberg gravimeter (Recope, unpubl. data, 1986). The original Miravalles and Tenorio gravity data have been made available on computer disc by Prof. German Leandro (ICE, San Jose). The terrain corrections made by ICE at 2.20 Mg m^{-3} were recomputed during this study at 2.40 Mg m^{-3} and extended to 186 km by clustering the stations and using the terrain correction-elevation relation as described in Section 3.1.1 and Appendix 3A.

3.2.2 ICE Tenorio Geothermal Project data

The gravity data over the Tenorio Geothermal Project (Figure 3.1) were originally reduced at 2.35 Mg m^{-3} (ICE, 1989, unpubl. map). They have been incorporated into this study only to get a fuller picture of the regional gravity field to the east of the Guayabo caldera. Elevation and gravity field data measurements are as described above for the ICE MGP data. Unfortunately, only the hand worked terrain correction data out to 2 km were specified and the terrain corrections out to 186 km have been computed during this study. The correction beyond 2 km could have been worked by hand, but as the data has only been incorporated for regional purposes these were estimated from the terrain correction-elevation relationship described in Section 3.1.1. The estimated corrections compare well with hand worked full terrain corrections made for stations of this study close to the Tenorio stations (see area of overlap near Cerro Espiritu Santo in Figure 3.1 and Appendix 3A). This naturally introduces larger BCG errors for the other stations in the Tenorio area, but these errors are not believed to exceed a few mGal for most of the stations as the elevations are generally below 1000 m a.s.l.. The overall BCG errors are acceptable for the purposes of this study; i.e. to examine the regional field gradients to the east of Miravalles and to get a broad view of the Tenorio gravity field, but would certainly not be acceptable for a detailed study of the Tenorio area. The Tenorio gravity data have been tied to the MGP data at coincident stations measured during this study (Appendix 3A).

3.2.3 Gravity data measured during this study

During this study the existing gravity network was extended to the west, north and south of the Guayabo caldera and over the more accessible western and northern parts of Volcán Miravalles (Figure 3.1). Most of the data were collected over rugged terrain with minimal manpower and station spacing up to 1 km and even 2 km, so that most of the station elevations were measured by altimeter (dots in Figure 3.1). These surveys were always closely tied to either: i) levelled benchmarks (large open stars), ii) closely spaced gravity profiles across the caldera margin measured by EDM theodolite during this study (small open stars), or iii) levelled ICE gravity stations of the Miravalles and Tenorio geothermal projects. A rigorous technique for correcting diurnal barometric variations (Appendix 3B) gives a maximum error for each station elevation of less than 5 m (often only about 2 m), resulting in a BCG error of less than 1 mGal.

3.2.4 Compilation of the three data sets

All the data were reduced relative to the ICE base gravity station Gra-91 at Guayabo (filled star in Figure 3.1), using the 1967 Gravity Formula, the Universal Gravitational Constant value of 6.67×10^{-11} N m^2 kg^{-2}, a Free Air Gradient (FAG) of 0.3086 mGal m^{-1}, the elevation of Gra-91 (548.50 m) as the datum plane, a reduction density of 2.40 Mg m^{-3} and terrain corrections out to a radius of 186 km (Appendix 3A). To produce a useful BCG map it is only rational to use a unique FAG value. Local variations in the FAG value have been measured in the MGP borefield but cannot be assumed to have a regional significance as they are located on a strong gravity gradient (Figure 3.6).

The irregularly spaced Bouguer corrected gravity data were computer interpolated onto a regular grid and contoured using UNIMAP (UNIRAS, 1990). The program is flexible and allows the user to specify the gridcell size (the node spacing), the interpolation method and parameters used during this interpolation process: For the bilinear interpolation method used (interpolation specifics given by UNIRAS, 1989), the value at each station is assigned to the nearest grid node, but if several values chose the same node, the node value is the average of these. Those nodes for which a value has been assigned are used in the

interpolation formula to generate the function value at the nodes where no value has been assigned. The user may specify the distance to which the valueless node may look for node(s) with an assigned value, this is called the search radius (SR in Figures 3.6 to 3.8). Within the search area the values at different nodes are distance weighted. The search radius effectively determines how much interpolation is allowed between widely scattered data (greater spacing than the gridcell size); small values result in a close fit to the observed data, but gaps in the contour map. The final option is smoothing of the interpolated grid by quadratic interpolation, resulting in a new weighted average of the values at the neighbouring nodes, the distance to these can again be specified. The smoothing option was not applied until each map had been checked for erroneous data. These data were easily picked and deleted/corrected from a preliminary map for which the sensitivity was maximised by specifying a fine grid spacing and small search radius.

Further to standard 2-D solid colour, or line contour maps, UNIMAP allows the Bouguer gravity to be presented in 3-D, "draped" over the topography (as interpolated from the station elevations). Thus the relationship of the BCG anomalies to the exposed volcanic features has been revealed (Figure 3.6).

Two conventional line contour BCG maps are also presented; the first (1 mGal contours and a 1 km interpolation grid, Figure 3.7) covers the same area as Figure 3.6 and the second (0.5 mGal contours and 0.5 km grid, Figure 3.8) shows details of the Miravalles geothermal field. The station locations (dots), the caldera margin of the geological map (Figure 2.5), the PGM boreholes and the modelling profile locations are also shown for reference. To highlight the Guayabo caldera area the single line of data across the southern margin of the Nicaraguan Depression, shown in Figures 3.1 and 3.5, has not been included in the solid and line contour maps of Figures 3.6 to 3.8. This station line is included in modelling Profile NS (Figure 3.27 and Section 3.6.4) to examine the southern margin of the Nicaraguan Depression.

Gra-91 was tied to the IGF (San Jose Airport) by ICE geophysicists using a model-G LaCoste & Romberg gravimeter (Leandro, *pers. comm.*) and the gravity at Gra-91 is 978099.55 mGal (as quoted by ICE, 1988 a, unpubl. data). The error on this value at Gra-

91 is unknown, but this is only important if the BCG map of this study is to be compared to the national or international BCG network and does not affect the relative values within this study. The Gra-91 absolute value reduces to a BCG value of -0.57 mGal, using a sea level datum and a reduction density of 2.67 Mg m^{-3} (or +5.64 mGal using 2.40 Mg m^{-3}). Unfortunately, this data did not come to light *before* the Bouguer maps of this study were compiled, and therefore the gravity values shown are not relative to the IGF.

3.2.5 The regional gravity field and the main features of the BCG map

The Bouguer gravity map of Costa Rica (Figure 3.9 from Weyl, 1980; after Monges Caldera, 1961 and deBoer, 1974) shows the sparse gravity coverage in the Cordillera de Guanacaste. Although not specified by Weyl (1980), it is assumed that the commonly quoted reduction density of 2.67 Mg m^{-3} was used. The steep gradients towards the positive anomaly associated with the ophiolitic Nicoya Complex of the Pacific coast contrast the negative anomaly associated with the Miocene granitic plutonics (Weyl, 1980) underlying the Cordilleras Central and Talamanca (discussion in Chapter 1, geology shown in Figure 1.1). The Cordillera de Guanacaste, however, is characterised by a low magnitude positive anomaly, suggesting that it may not be underlain by low density plutons; the suspected lack of thick granitic crustal basement also accounts for the generally lower elevation of the Guanacaste Cordillera. This raises the question of the depth to the Nicoya Complex-type basement beneath Guanacaste, if, as postulated by other workers (e.g. Weyl, 1980 and deBoer, 1979) and this study, it does underlie the area; this is more fully discussed in the modelling section below (Section 3.5).

Figure 3.6 a A 3-D perspective map of Miravalles (from SW) of Bouguer gravity (2 mGal contours) draped on a 1 km grid of topography. The area is equivalent to the lower half of Figure 3.1, and directly comparable to the line contour map in Figure 3.7. Notice the gravity lows over the Guayabo caldera (detail in Figure 3.6 b) and the Rio Tenorio depression. The gravity high to the south of the caldera is modelled as a buried (sub-tuff) extension of the Aguacate Gp. volcanics exposed in the southeast (cf. Figure 3.27).

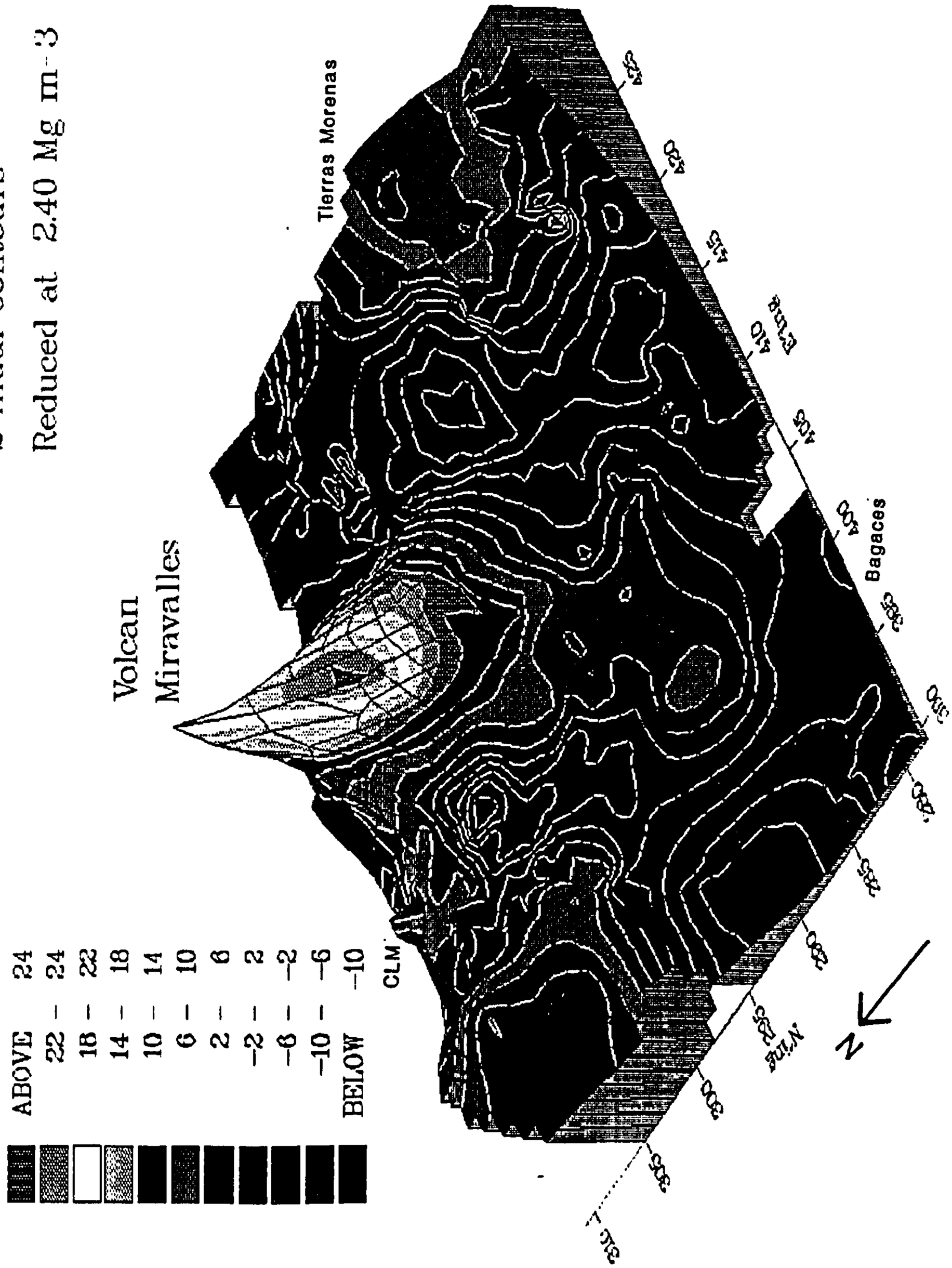

Figure 3.6 b 3-D perspective view of the Guayabo caldera BCG from the west (1 mGal contours) on a 0.25 km grid (compare axes with Figure 3.6 a for location). The Bajo Los Chiqueros (BLC) gravity high is clearly displaced from the Miravalles summit (see Section 3.1.2 for discussion). The western caldera walls are not clearly related to the positive gravity anomalies, e.g. there are negative anomalies between C. La Montañosa (CLM) and C. Mogote and over the southern caldera margin.

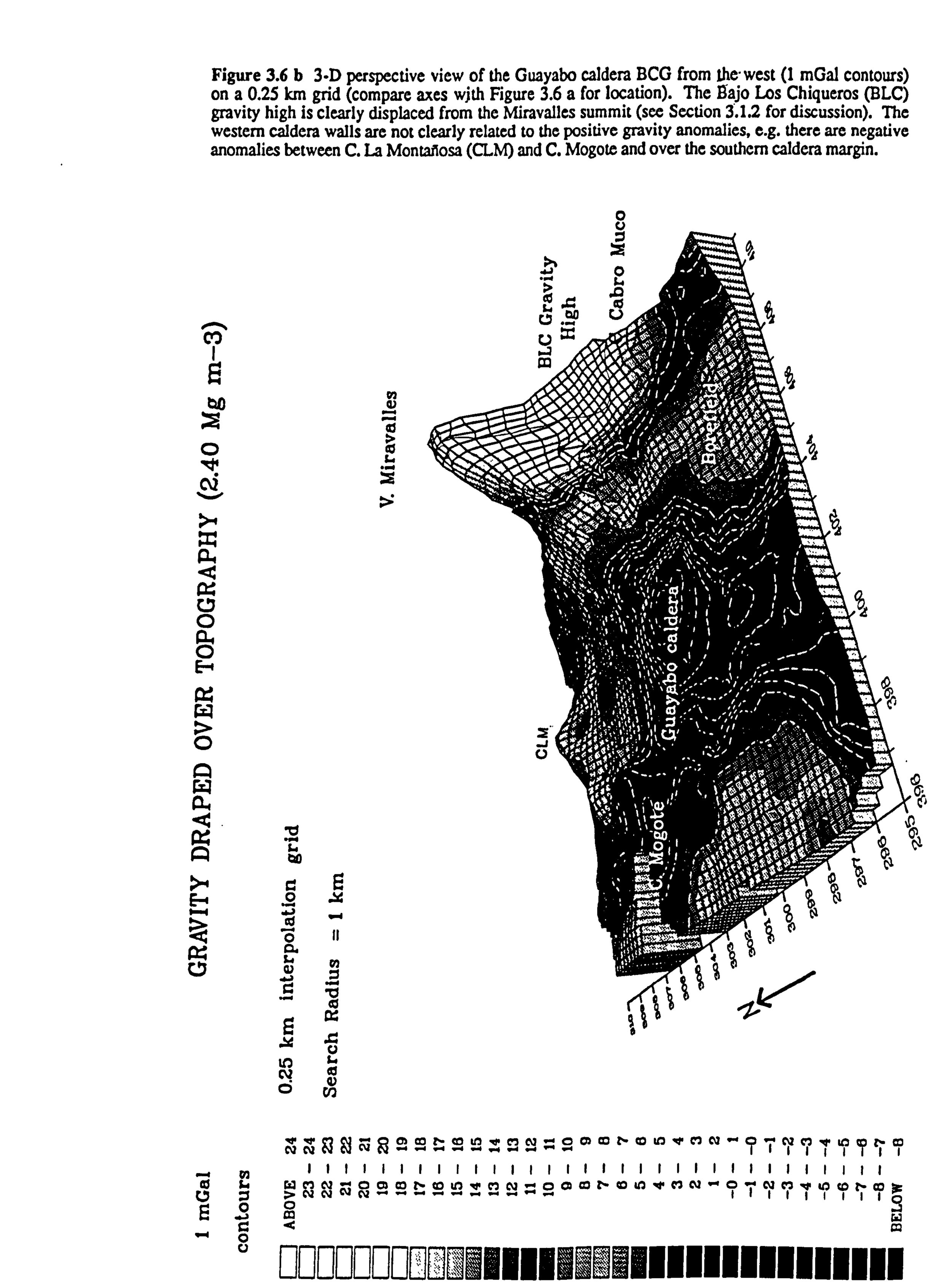

Figure 3.7 The 1 mGal computer contoured BCG map (2.40 Mg m^{-3}). Location in Figure 3.1 and directly comparable to Figure 3.6 a. Stations are marked by small dots and the limits of the Miravalles Borefield are indicated by wells PGM-11, 12 and 15 (marked *, see Figure 3.8 for borefield detail). Small, sub-tuff extra-caldera lava exposures (marked as solid Δ) are related to the gravity highs which are modelled as parts of the Aguacate Gp and Monteverde Fm. volcanics exposed at Tierras Morenas (in the southeast). The location of the gravity models NS, VV, WSE and CC are shown though the northern part of the NS Profile is not shown on this map (see Figures 3.1 and 3.5 b). The dashed box is the outline of the 0.5 mGal map (Figure 3.8).

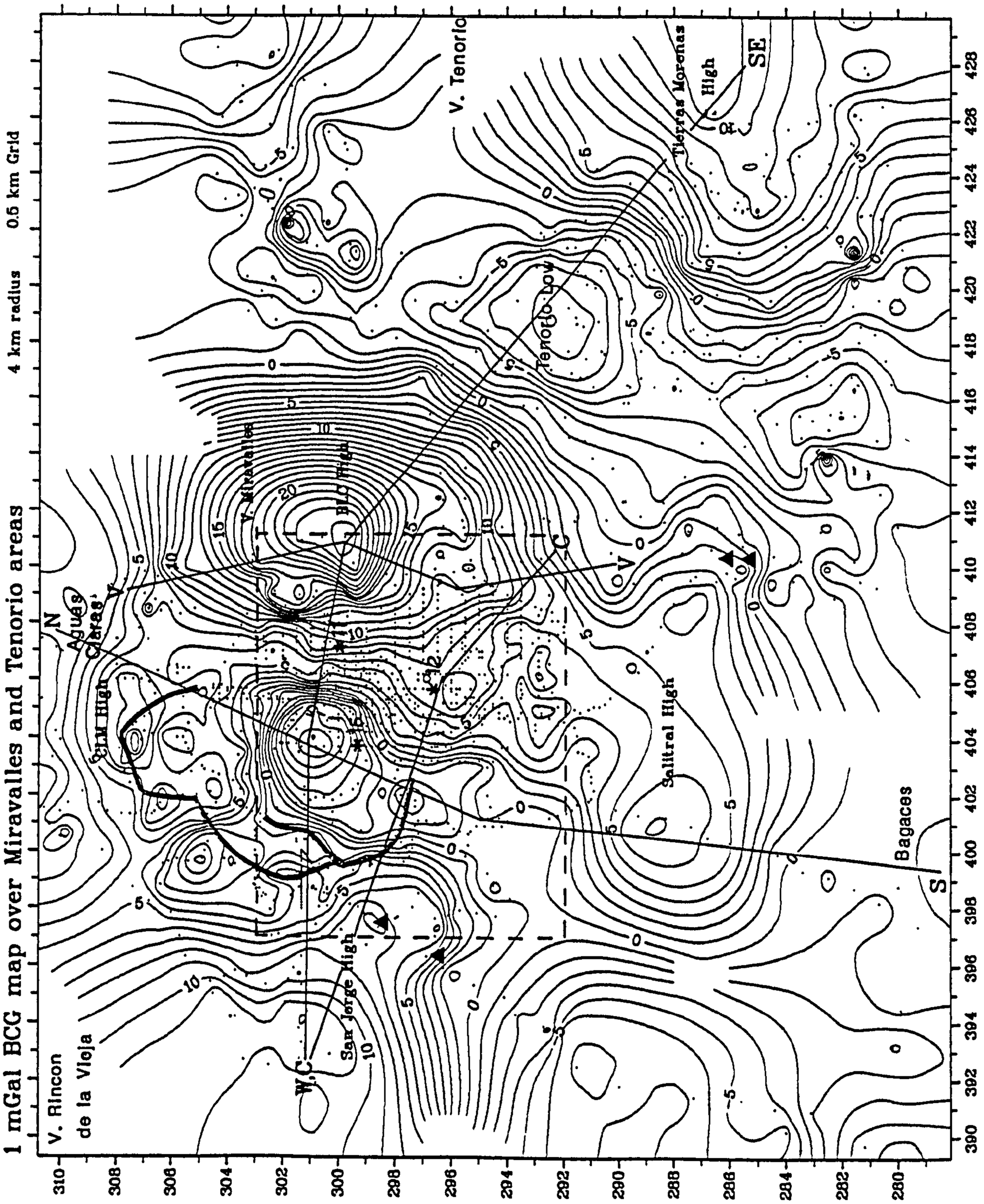

Figure 3.8 The 0.5 mGal BCG map of the southern Guayabo caldera and the Miravalles geothermal area (located in Figure 3.7). All the geothermal wells (*) and the locations of the gravity models AA, BB and parts of CC and WSE are shown. The Guayabo Low is partially open to the south, traversing the caldera margin (geology in Figure 2.5) but there are small positive anomalies inside the caldera margin here (at Gra-91) and at C. Mogote. The PGM-4 High is clearly distinct from the BLC High. PGM-15 is projected onto profile AA (Figure 3.22) along the -4 mGal contour.

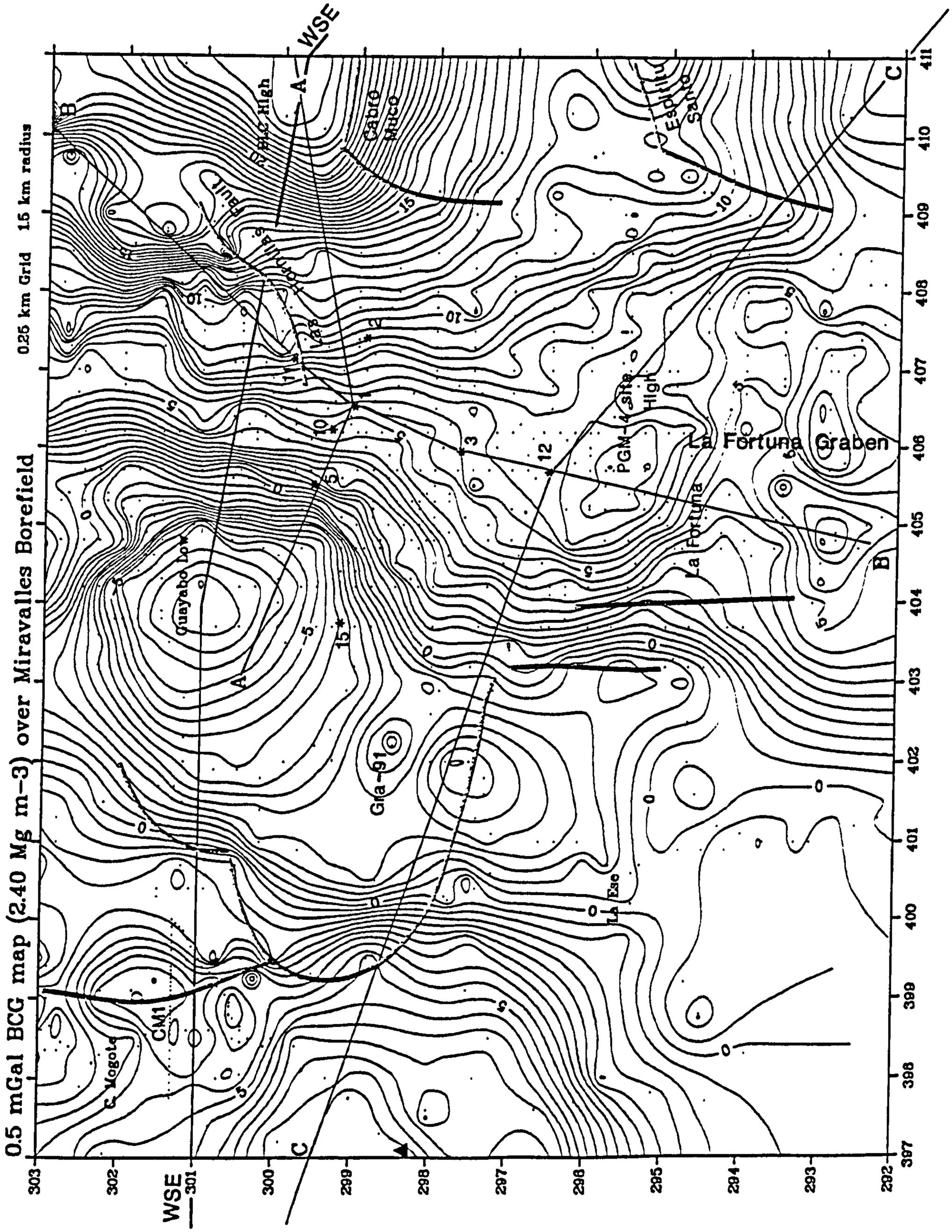

Figure 3.9 Regional Bouguer gravity map of Costa Rica from Weyl (1980, compiled from maps by Monges Caldera, 1961 and deBoer, 1974). The reduction density was not given by Weyl, but is assumed to be 2.67 Mg m^{-3}. There is a paucity of data over the Cordillera de Guanacaste but the strong gradient associated with the Nicoya Peninsula ophiolitic complex (geology described in Chapter 1, Figure 1.1) is not present over the Guayabo-Volcán Miravalles area (box = 1 mGal map area) and there is no evidence of a similar low anomaly to that associated with the southern Miocene plutonics.

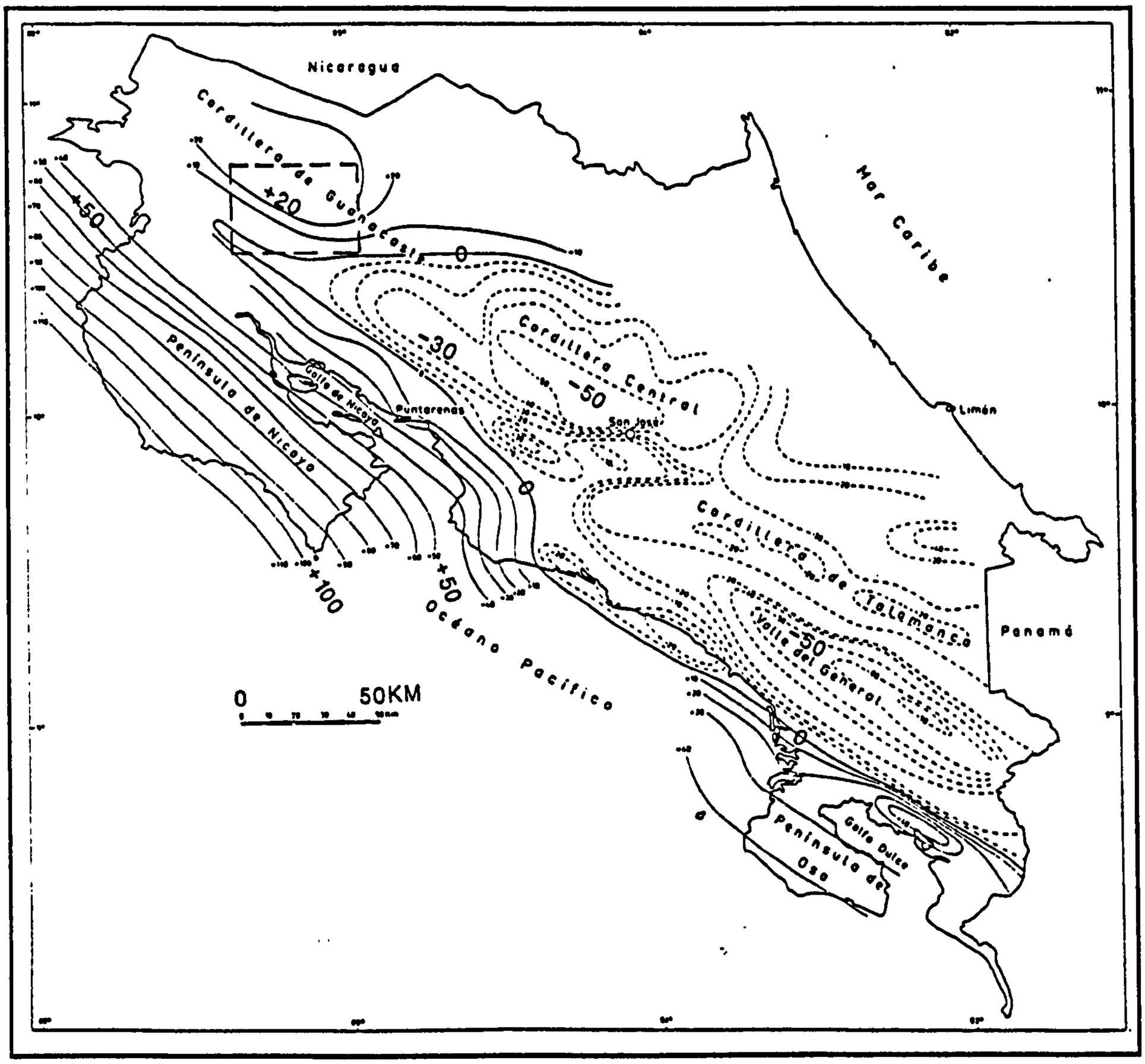

The regional gravity map given by Weyl (1980; reproduced here in Figure 3.9) shows that the steep increase in Bouguer gravity towards the Pacific across the Nicoya Peninsular does not continue across the Guanacaste Arc. The regional free-air gravity map of Bowin (1976) shows an isolated 100 mGal positive free-air anomaly over the Nicoya Peninsular, greater than would be expected for relatively low-lying crust, implying that the dense ophiolitc material exposed in the Nicoya Peninsular (Figure 1.1, Chapter 1) *does* contribute to the oceanward increase in the Bouguer gravity southwest of the Guanacaste Arc. No obvious southwestward increase can be identified within the area covered by this study (see Figures 3.5 a-d, inset area in Figure 3.9), and therefore no regional field has been removed.

The slightly positive Bouguer anomaly over the Guanacaste Arc is unusual, and the negative anomalies across the central and southern Costa Rican arc (Figure 3.9) are more typical of most destructive oceanic margins (e.g. Indonesia; Wollard and Strange, 1962). Negative Bouguer anomalies over arcs, coupled with positive oceanic anomalies, reflect both the oceanward decrease in the depth to the Moho and the contrast between the low density plutonics comprising the arc crust and the relatively high density oceanic crust. The positive Bouguer anomaly over the Guanacaste Arc suggests firstly that the arc is out of isostatic equilibrum and secondly that the arc is not underlain by the plutonics characteristic of southern and central Costa Rica (Chapter 1). Parts of the Pacific margin of northern Costa Rica are presently rising (Fischer, 1980) but this is thought to be related to the back-tilting of the outer arc blocks (Seyfried *et al.*, 1991, Berrangé and Thorpe, 1988, see discussion of regional geology in Chapter 1), rather than isostatic compensation of the entire Guanacaste arc. The Upper Miocene plutonics exposed in the Cordillera de Talamanca have enjoyed considerable uplift since their emplacement and this part of Costa Rica, at least, is still rising at a rate of 1-2 mm yr^{-1} (Miyamura, 1975).

The debate about the composition of the crust in northern Costa Rica (addressed in Chapter 1) concerns the extent to which the ophiolitic crust, exposed along the Pacific margin, continues beneath Costa Rica. The positive Bouguer anomaly over the Guanacaste Arc is interpreted as a continuation of this obducted ophiolitic material beneath the Guanacaste Arc, at a shallower depth than beneath the rest of the arc in Costa Rica. This discussion is expanded below (Section 3.6.4) following the interpretation of the north-south gravity profile, NS.

It is useful to identify the more important mass anomalies as an introduction to the detailed breakdown of the density structure. The Guayabo caldera is clearly related to a negative gravity anomaly, the Guayabo Low (Figures 3.6, 3.7 and 3.8), but this low is not confined within the southwestern and northwestern caldera margins. The gravity 'transgressions' are important because they demonstrate geophysical continuity across parts of the present topographic caldera margin (Section 3.6.2), in agreement with the stratigraphic continuity proposed in Chapter 2. Over the stratovolcanic complex on eastern caldera margin, the

prominent gravity high is offset from the most recent centre, Volcán Miravalles (though the exact position depends on the reduction density, discussed in Section 3.1.2), and is associated with the collapsed area of Bajo Los Chiqueros, the proposed site of the previous Cabro Muco volcanic centre (the BLC High in Figures 3.6 ff, Section 3.6.3). A ring of smaller amplitude gravity highs (the CLM High in Figures 3.6 and 3.7) distinguish the Cerros la Montañosa caldera sector from the rest of the caldera and suggests that the Guayabo caldera comprises several coalescing collapsed volcanic centres.

The gravity highs outside the caldera are commonly associated with small exposures of extra-caldera lavas (e.g those located in Figure 3.7) and it is proposed in Section 3.6.2 that they are related to a thinned cover of the low density tuffs over the largely buried equivalents of the Aguacate Group and Monteverde Formation volcanics (regional geology in Figure 2.3, from Alvarado *et al.*, 1990). These volcanics are exposed at Tierras Morenas and are believed to be responsible for the gravity high there (Figure 3.6 a and 3.7). The northernmost line of gravity stations (Figures 3.1 and 3.5 b) define a very steep gravity gradient over the topographic discontinuity of the southern margin of the Nicaraguan Depression from a +18 mGal high at the foot of the depression scarp towards a -13 mGal gravity low centred only 4 km from the margin (shown in the BCG map, Figure 3.5 b, but best shown in the north-south gravity model, NS, Figure 3.27, discussed in Section 3.6.4).

The Miravalles geothermal field is located on the flanks of the BLC High but the distinct, small amplitude gravity high south of PGM-12, at the site of a proposed geothermal well PGM-4 (Figure 3.8, the PGM-4 High), has been the cause of much debate. Initially, ICE (Leandro, *pers. comm.*) and the preliminary gravity models of this study (presented by Brown *et al.*, 1988) suggested that the PGM-4 High is located over a buried extension of the dense Acidic Andesite Unit. This has important geothermal implications for drilling at the PGM-4 site as the Acidic Andesite Unit is a low permeability lithology (ELC, 1986 a), but more recent modelling (Section 3.7) shows that the gravity high may, alternatively, relate to either an intrusive body below ~1 km depth, and/or hydrothermal propylitization. The strong gravity gradient over the MGP borefield (Figure 3.8) can be partially modelled in terms of density contrasts within the drilled stratigraphy but, as is explained in Section

3.6.2, it is also necessary to model a deep extension of the BLC intrusion. A detailed study of the densities of the drilled and exposed lithologies has been a vital pre-requisite to the gravity modelling of this project and the results are described below.

3.3 Surface Density Measurements

A representative suite of samples from surface exposure (105 samples) and geothermal boreholes (504 cuttings samples) have been measured for density; the methodology, results and significance of the results are given here. The 35 core densities measured by ICE (1988 b, unpubl. data) have also been incorporated. Nettleton Profiles have been used to test whether the measured densities are useful estimates of the overall (formation) density of certain parts of the topographic caldera margin (Section 3.3.4). Densities were determined using the simple Archimides principle of comparing weights in air to those in water; three distinct density types are considered:

ρ_r the grain density, the density of the solid material (porosity not accounted for).

ρ_w the wet bulk density (water saturated porosity accounted for).

ρ_d dry bulk density (air filled porosity accounted for).

If M_a is the dry mass in air (15-150 g sample size range), M_a' is the water saturated mass in air and M_w is the water saturated mass in water then:

$$\rho_r = \frac{M_a}{M_a - M_w} ; \qquad \rho_w = \frac{M_a'}{M_a' - M_w} ; \qquad \rho_d = \frac{M_a}{M_a' - M_w} ;$$

The porosity is given by: $\emptyset = \frac{M_a' - M_a}{M_a' - M_w} \times 100\%$, which is equivalent to $(\rho_w - \rho_d) \times 100\%$. (The latter difference is divided by the density of water, 1.00 Mg m^{-3}, and therefore the porosity is dimensionless). Table 3.1 gives a summary of the densities of the surface samples, grouped stratigraphically and discussed in the following section; a full list of the samples including lithology, grid coordinates, densities and porosities is given in Appendix 3C. The densities used in the gravity modelling (Sections 3.6 and 3.7) are wet density values, ρ_w, unless otherwise specified.

Samples were firstly weighed in air, giving M_a (range of ~20-100 g). They were then soaked overnight in water (to which a small amount of detergent had been added to reduce

the surface tension) to fill the pores with water. The mass of the soaked sample in water (i.e. submerged) gave M_w. The sample was then taken directly from the water and placed onto the *dry* weighing pan to get $M_{a'}$, the mass of the soaked sample in air. Uncertanties in this simple but rapid procedure were largely associated with i) the efficiency of the soaking process and ii) the loss of water from the sample immediately before the $M_{a'}$ measurements.

Table 3.1 Summary of the surface densities (Mg m^{-3}) and porosities (%), grouped according to the stratigraphic units. **n** is the number of samples, the standard deviations are given in italics. Full list in Appendix 3C. * The 2 LCMV samples are from lavas associated with the late stage of the Cerro Cabro Muco activity, but not the actual Cerro Cabro Muco edifice (locations in Appendix 3C).

Stratigraphic Unit	n	ρ_r		ρ_w		ρ_d		Ø	
Caldera wall lavas	24	2.72	*0.08*	2.70	*0.10*	2.68	*0.11*	1.9	*1.7*
Extra-caldera lavas	12	2.64	*0.11*	2.64	*0.10*	2.63	*0.11*	1.1	*1.1*
Extra-caldera tuffs	9	2.10	*0.22*	1.96	*0.13*	1.76	*0.25*	20.3	*12.4*
Tuff lithics (andesites)	10	2.55	*0.19*	2.46	*0.24*	2.42	*0.27*	3.7	*3.5*
" (welded tuffs)	11	2.48	*0.04*	2.37	*0.05*	2.30	*0.07*	7.1	*3.2*
" (granodiorite)	5	2.57	*0.09*	2.49	*0.09*	2.44	*0.09*	5.0	*0.9*
V. Miravalles lavas	13	2.59	*0.08*	2.49	*0.12*	2.42	*0.16*	6.8	*5.0*
Santa Rosa lavas	9	2.56	*0.13*	2.48	*0.15*	2.44	*0.17*	4.4	*2.6*
V. Palaeo-Miravalles	4	2.72	*0.1*	2.66	*0.09*	2.64	*0.09*	2.8	*1.0*
LCMV lavas*	2	2.71	-	2.67	-	2.65	-	2.0	-

To provide a measure of the analytical error, 12 samples were crushed (to less than ~2 mm) to remove the porosity and the grain density was re-measured. The results are presented in Table 3.2 along with some repeat measurements of whole rock density determinations.

Table 3.2 Comparison between the crushed rock and whole rock determinations of the grain density, ρ_r . The difference, $\Delta\rho_r$, is a maximum for the porous tuffs, suggesting that the pores were not completely filled during the soaking of the whole rock samples. The whole rock repeat measurements show the heterogeneity of the Biotite Tuff (part of the extra-caldera tuff average data in Table 3.1).

Sample	Stratigraphic Unit	ρ_r crushed	ρ_r whole	$\Delta\rho_r$ *diff.*	ρ_w	ρ_d	Ø
R3e1	V. Miravalles Andesite	2.64	2.61	*0.03*	2.57	2.55	12
EC1	Upper Grey Tuff	2.30	2.21	*0.09*	2.04	1.90	14
EC2	Biotite Tuff	2.39	2.33	*0.06*	1.95	1.67	28
EC3 (1a)	Biotite Tuff	2.29	2.19	*0.10*	1.79	1.46	33
EC3 (1b)	Biotite Tuff	2.31	2.17	*0.14*	1.77	1.43	34
EC3 (2a)	Biotite Tuff	1.87	1.74	*0.13*	1.55	1.29	26
EC3 (2b)	Biotite Tuff	1.96	1.81	*0.15*	-	-	-
EC15	Biotite Tuff	2.09	1.84	*0.25*	-	-	-
EC33	Biotite Tuff	1.80	1.58	*0.22*	-	-	-
EC25	Fila Caño Negro Andesite	2.50	2.47	*0.03*	2.45	2.44	1
EC25	Fila Caño Negro Andesite	2.53	2.55	*-0.02*	2.54	2.53	1
EC13c	Microgranite (Tuff Lithic)	2.26	2.13	*0.13*	2.06	2.00	6

The crushed rock measurements yield higher grain densities than the whole rock samples in all but one case (EC 25), suggesting that during soaking of the whole rock the air in the

pores was not entirely replaced by water. The small values of $\Delta\rho_r$ for the andesites and the microgranite in Table 3.2 suggest that the precision of the wet densities determined from the whole rock technique was perfectly adequate for the coherent samples of lava and welded tuff where the porosity was relatively low and the pores relatively small (less than ~2 mm). The high porosities of the tuffs, however, resulted in both incomplete saturation during soaking and water loss during measurement of M_w. The level of uncertainty is therefore greatest for the densities of the tuffs. Furthermore, the repeat density measurements of EC3, the Biotite Tuff sample, of both the whole and crushed rock, show strong variation, indicating the heterogeneity of the Biotite Tuff, even at the outcrop level. The question of the formation density for the tuffs is further considered below (Section 3.3.2).

3.3.1 Pre-caldera lava densities

The lavas exposed in the caldera walls are generally unporous, massive, porphyritic andesites, with minor basalts and dacites. The average density of 2.70 Mg m^{-3} is a formation maximum for the caldera walls because any interleaved tuffs will lower the overall density; this is much higher than the drilled intra-caldera fill of poorly consolidated breccias, tuffs and lavas (described below in Section 3.4). Therefore, if the caldera wall lavas have a significant subsurface expression, then a steep gravity gradient should be expected over any major caldera margin fault. The Nettleton profiles, however, show that this is generally not the case (Section 3.3.4).

Extra-caldera lavas are those exposed outside the topographic margin of the Guayabo caldera and are stratigraphically differentiated from the lavas exposed in the caldera walls (Figure 2.5, stratigraphy in Chapter 2). The former are all olivine-free andesites with an average density of 2.64 Mg m^{-3}, whereas the caldera wall andesites (average density of 2.70 Mg m^{-3}) are usually olivine-bearing.

3.3.2 Tuff densities (and country rock density constraints from lithic densities)

The stratigraphic sequence of the tuffs exposed close to the Guayabo caldera, both those older than and those associated with the caldera, have been described in Chapter 2 (Figures

2.5 and 2.16 and Table 2.1). The tuffs are poorly welded (Mora, 1988, Chiesa *et al.*, 1987) and generally friable and it has therefore been difficult to determine the densities accurately using the simple technique adopted for the cohesive lavas and welded tuffs. Samples sometimes disaggregated when immersed in water and in these cases it was impossible to measure the water-saturated mass in air, $M_{a'}$. Although the grain densities were not affected for these samples (M_a and M_w can always be measured), it was not possible to calculate the porosity or the dry and wet densities. Of nine tuff samples, $M_{a'}$ could be measured from four (Table 3.2) yielding an average porosity of 20.3% and a wet density of 1.96 Mg m^{-3} (Table 3.1). The values for the wet and dry densities are probably maxima, as it is likely that the measured porosities are underestimates of the formation porosities. During the measurement of the wet mass in air, and the mass of the sample immersed in water, it is inevitable that some of the pores of the sample are not completely saturated; this results in low estimate for both $M_{a'}$ and M_w and therefore the porosity would be underestimated. The true formation porosity is possibly as high as ~50%, resulting in a *minumum* wet density of ~1.5 Mg m^{-3}. Conversely, it is possible that buried equivalents of surface exposures of poorly welded tuffs could be compacted and the densities of the surface samples are therefore underestimates of the formation density.

The water-table on the drier Pacific flanks of the cordillera changes significantly between the wet and dry seasons. During the dry season many of the rivers and streams that cut through the poorly welded tuffs dry out so it assumed that at least the uppermost tuffs, above stream base level, are relatively dry. The general extra-caldera tuff density used in this study is 1.90 Mg m^{-3}, lower than the average wet density of 1.96 Mg m^{-3}, reflecting the foregoing arguments. This value is applied to the Bagaces Group tuffs, the Biotite Tuff, the Upper Grey Ignimbrite and the Hornblende Tuff. The La Ese Pumice has a higher pumice content than the older tuffs and has been assigned a density equal to the intra-caldera counterpart, the Pumice Unit, which has an average wet density of 1.58 Mg m^{-3} measured from PGM-15, discussed in Section 3.4.3). The general value may overestimate the density of the Biotite Tuff and the poorly-welded upper tuffs close to the Guayabo caldera, but is thought to be more representative of the most voluminous partially welded, grey ignimbrites of the Bagaces Group.

For comparison, Aramaki (1984) quoted outlying pumice tuff densities from the Aira caldera, Japan of between 0.7 and 1.1 Mg m^{-3}, much lower than the values here, but they are much richer in pumice and it is probable that the values are dry densities. For a gravity model of the Long Valley caldera, Carle (1988) used measured densities of 2.35 and 2.05 Mg m^{-3} for the welded and unwelded parts of the intra-caldera Bishop Tuff. The relatively high densities reflect the both a higher degree of welding and probably lower porosity of the Bishop Tuff, as compared with the Guayabo-related tuffs.

Tuff Lithics: The lithics within the exposed tuffs are dominantly andesitic lava fragments, with additional welded tuffs and granodiorite fragments in the Guayabo Proximal Breccia (Table 3.1, for location see Figure 2.5). The average wet density of the andesite lithics is 2.46 Mg m^{-3}, significantly lower than the caldera wall andesites (2.70 Mg m^{-3}). The andesite lithics from the Guayabo Proximal Breccia are also olivine poor in contrast to the generally olivine bearing andesites exposed in the caldera wall. This is important because it suggests that the andesite lithics in the Guayabo Proximal Breccia are *not* derived from the destruction of the proposed pre-caldera stratocone(s). A thorough comparison of the lithics from the Guayabo-related tuffs with the intra-caldera strata and the caldera wall lavas was beyond the scope of this study, but trace element geochemistry, for example, would certainly be a very useful constraint on the caldera evolution model.

Granodiorite clasts are exposed in a lithic-enriched degassed pocket of the Guayabo Proximal Breccia at the La Ese quarry and have an average grain density of 2.57 Mg m^{-3}. The granodiorite clasts are partially friable, and the average measured porosity of 5% is therefore thought to be secondary (Table 3.1); the grain density is considered a more reliable estimate of the primary 'tight' density. These clasts may represent either ripped up, frozen magma from the chamber or vent walls and therefore provide a possible constraint on the density of any high level more acidic plutons beneath the caldera.

The average grain density of the unaltered welded tuff lithics (2.48 Mg m^{-3}) is significantly lower than the average grain density of the Ignimbrite Unit measured from PGM-15 cuttings (2.57 Mg m^{-3}, Section 3.4.3 and Appendix 3C). Either the welded tuff lithics are unrelated

to the Ignimbrite Unit; or the difference in density reflects the proportion of relatively dense andesite lithics in the Ignimbrite Unit. Alternatively the alteration rank and intensity may be sufficient at this depth in PGM-15 to account for the density increase (cf Figure 3.12 h and Section 3.4). The welded tuff lithics, however, show a greater degree of banding (reflecting a higher temperature of deposition) than the few core samples of the Ignimbrite Unit, suggesting that indeed, the lithics are not derived from the Ignimbrite Unit. No other welded tuffs have been recognised in the boreholes, so it is possible that either the lithics are derived from pre-Ignimbrite Unit strata, or from shallower strata within the central, undrilled, part of the caldera.

3.3.3 Lavas of the Miravalles volcanic edifice

One of the objectives of the gravity study is to determine the likely composition and structure of Volcán Miravalles and compare the results with other documented gravity studies of andesite stratovolcanoes. To get a general estimate of at least the lava densities, samples were collected from the exposed, and therefore most recent, flows of the western and northern flanks of Volcán Miravalles and the most recent Santa Rosa lavas (Figure 2.5). The lavas are generally blocky, sometimes vesiculated, have a higher SiO_2 content (Figure 2.13) and, not surprisingly, are thus less dense (average of 2.49 Mg m^{-3}) than the caldera wall lavas (2.70 Mg m^{-3}, Table 3.1). The exposed lavas and debris flow blocks of the ancestral Palaeo-Miravalles are more basaltic and therefore denser (2.66 Mg m^{-3}). Overall, the densities of the lava samples may represent upper limits for the density of the edifice as there is probably a significant proportion of lower density lithic tuffs, lahars and breccias that commonly make up stratovolcanoes (Cas and Wright, 1988). Similar arguments apply to the few Late Cabro Muco Volcanic Unit (LCMV) lava samples (2.67 Mg m^{-3}) associated with the collapsed Cerro Cabro Muco edifice.

3.3.4 The density of the caldera walls from Nettleton Profiles

The use of so-called Nettleton profiles to determine the near surface density in an area of topographic relief (Nettleton, 1939) has been described in Section 3.1.2. Two detailed traverses across the topographic caldera margin are examined here. One profile traverses the

margin south of Cerro Mogote (CM1, Figure 3.10, located in Figures 3.1 and 3.8) and the second is across Cerros la Montañosa (CLM, Figure 3.11, located in Figure 3.1). All the Nettleton gravity stations were levelled by theodolite and at least one repeat gravity measurement was made at each station (a general discussion of the precision of the gravity data is given in Appendix 3A). Thus, the greatest source of uncertainty in the Nettleton data is from the terrain correction estimation. The most difficult estimates were for the near station Hammer zones A-D, for which the slope approximation tables of Sandberg (1958) were used. The maximum slope of the caldera margin walls at Cerro Mogote are ~30° and thus an overall slope estimation error of 5° would result in a terrain correction error of ~0.35 mGal (using a reduction density of 2.40 Mg m^{-3}). This means that the roughness in the gravity data hown in the CM1 profiles at the foot of the caldera margin scarp (Figure 3.10) is not significant.

The Cerro Mogote area has been studied in detail since it was recognised as part of a basaltic cone (Figure 2.5), overlying the generally andesitic caldera wall lavas, but cut by at least the most recent movement on the caldera ring fault. Because of the thick vegetation over Cerro Mogote, CM1 passes 300 m south of the summit (Figure 3.10), and so strictly the Nettleton profiles are over the flanks of Cerro Mogote. CM1 traverses the generally west to east sloping gradient of the Guayabo Low (see the detailed BCG map; Figure 3.8) but there is a major break at the foot of the scarp. The detailed BCG map (Figure 3.8) shows a small positive gravity anomaly (+2 mGal) at the foot of the scarp through which the CM1 profile (Figure 3.10) passes. If the andesites exposed in the scarp (average ρ_w = 2.70 Mg m^{-3}) made up the whole of the topographic caldera wall, up to the level of the Mogote basalts, then the high reduction density profiles should be relatively flat over the brow of the margin (Figure 3.10). However, it is the low density profiles that produce the least correlation with topography and the high density profiles show negative anomalies. This suggests that at least the uppermost part of the caldera wall (stippled in Figure 3.10) is made up of low density material, probably the lithic-rich tuff containing blocks of Mogote basalt (Chapter 2). The fact that the lavas exposed in the scarp dip away from the caldera and are not exposed on the outer flanks supports this conclusion.

Figure 3.10 Nettleton profile CM1 over the caldera margin at Cerro Mogote (located in Figures 3.1 and 3.8) in which Bouguer corrected gravity is calculated for different reduction densities at a series of stations (marked on the topographic profile). Note that the gravity high is over the foot of the caldera margin scarp, not over the brow of the margin. Over the brow (stipple), the data reduced using 2.00 to 2.10 Mg m^{-3} show the flattest profile, suggesting that the hill is not composed solely of the lavas exposed in the scarp but also includes tuffs and breccias. The gravity profile reduced at 2.40 Mg m^{-3} is modelled in Profile CM1 (Figure 3.22).

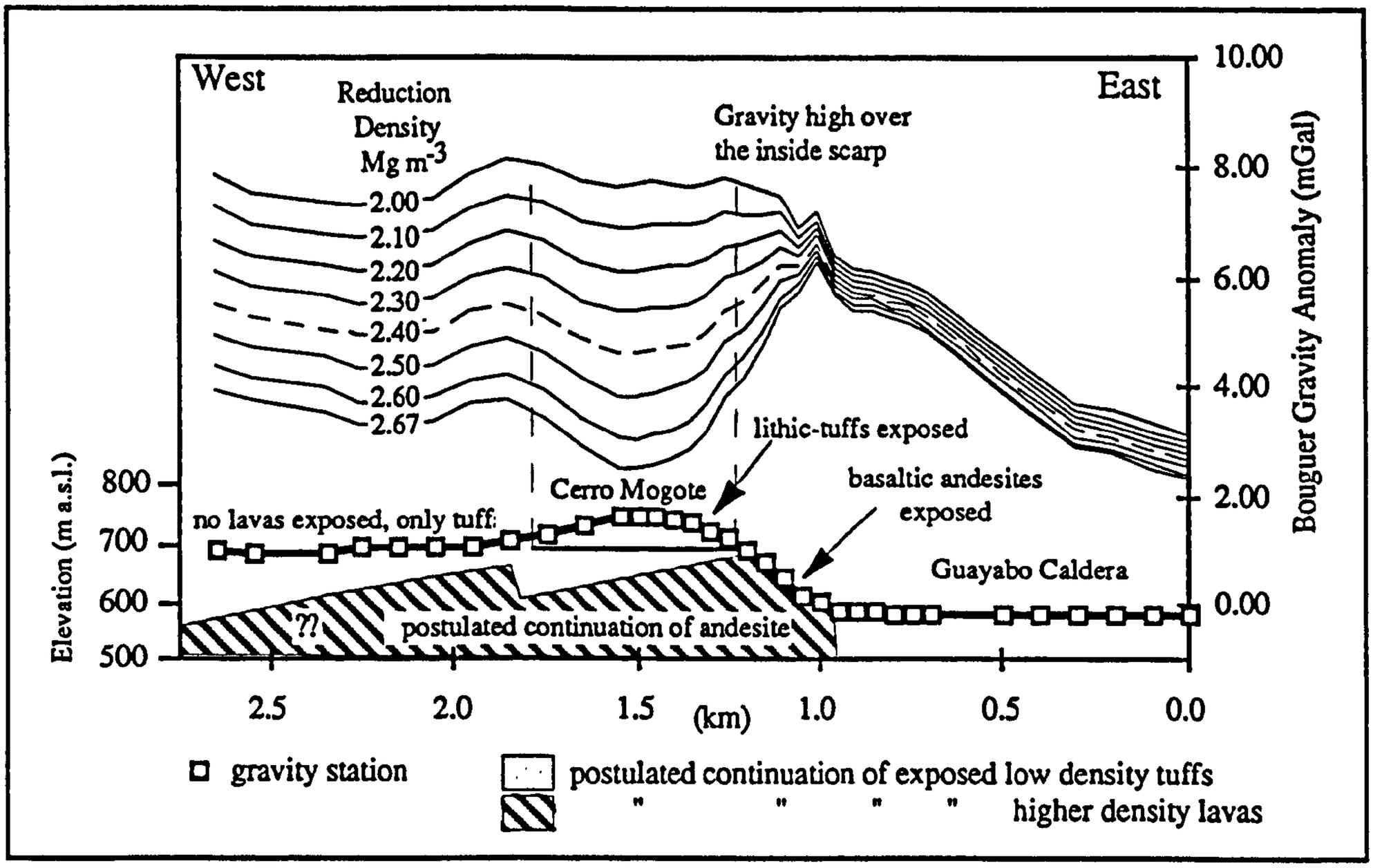

The Cerros la Montañosa collapse sector is characterised by a ring of small positive gravity anomalies around the base of the scarp (Figure 3.6 b) and it is postulated that the hills are the remnant of a pre-Guayabo caldera stratovolcano that was located over the centre of these gravity highs. The hills are vegetated and deeply weathered with a few exposures of andesite or basalt blocks, set in a reddish soil, and therefore Nettleton profiles are used to examine the density of the topography in this area of the caldera margin. The Nettleton profiles across the CLM (Figure 3.11) are complicated by a south to north gravity gradient, but this should not necessarily affect the interpretation of the results over the topographic expression of the margin. Bouguer gravity remains largely independent of the reduction density for points that are at the same elevation as the datum plane (there is no Bouguer slab correction, but the magnitude of the terrain correction will differ). Therefore, in the CLM Nettleton profiles there is a northern point outside the caldera at the datum elevation where the gravity profiles intersect and cross (the cross-over point in Figure 3.11). The caldera floor is also effectively at the datum elevation and thus by drawing a line on the Nettleton

profiles (Figure 3.11) between the gravity at the edge of the caldera floor and that at the outer cross-over point, it is possible to examine the relationship between Bouguer gravity and the topography. As for the Cerro Mogote profile, there is a gravity high over the inner scarp, but the brow and northern slopes of Cerros la Montañosa before the cross-over point are characterised by a gravity low for higher reduction densities. This suggests that a low reduction density should be used to remove the effect of the Cerros la Montañosa topography but the Nettleton profiles in Figure 3.11 show that the overall relationship between topography and gravity is complicated by the deeper structure. The broad similarities with the margin at Cerro Mogote suggest a similar geological explanation; buried lavas on the scarp side, dipping away from the caldera and tuffs/breccias forming the crest and outer slopes, as postulated in Figure 3.11.

Figure 3.11 Nettleton profiles across Cerros la Montañosa (located in Figure 3.1). Analysis of terrain related gravity anomalies should be restricted to the topography between the two points of equal elevation, as defined by the the Nettleton profile cross-over points shown. Clearly, the hill is located on a northward gradient that is unrelated to the topography. The thick dashed line joining the cross-over points is the gravity field that would be expected for the least correlation between reduced gravity and topography. Due to anomalies unrelated to the terrain however (such as the high over the inside scarp) none of the profiles are close to this line over its entire length and it is therefore difficult to see which reduction density is most appropriate to this particular terrain. See text for discussion.

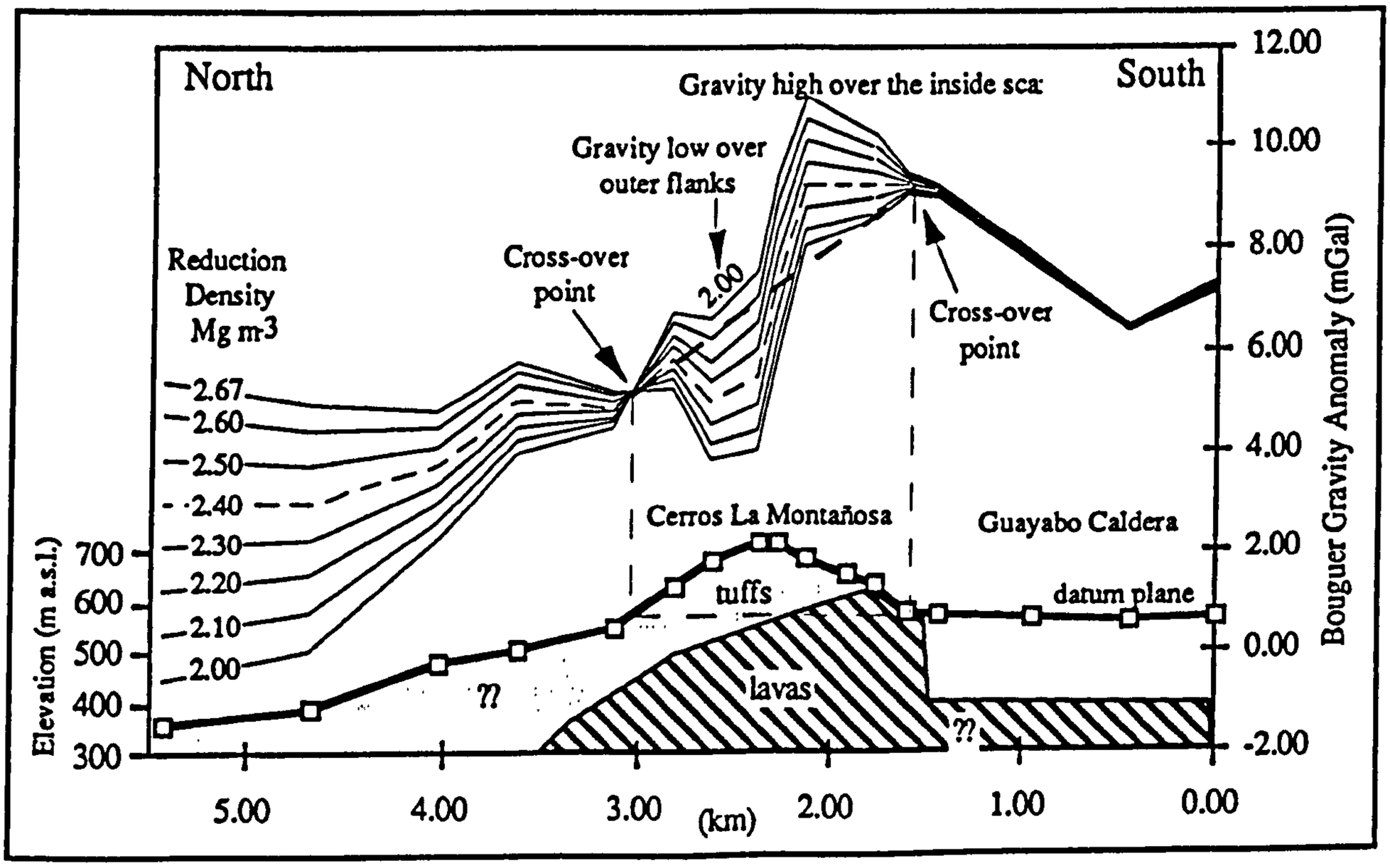

Summary of the implications of the surface densities

An important result of this Section is that the density structure responsible for the Nettleton profiles over the caldera walls cannot be reconciled with a lava-rich composition for the

caldera walls; the alternative model of a low density sequence resting on basalt/andesite lavas is further discussed during the data interpretation (Section 3.6.2). (On a stratigraphic note, the extra-caldera exposures of andesite are generally olivine-poor and less dense, 2.64 Mg m^{-3}, than the olivine-bearing caldera wall lavas, 2.70 Mg m^{-3}, and may therefore be distinct, as proposed in Chapter 2).

The average density of the surficial lavas of Volcán Miravalles, 2.49 Mg m^{-3}, is thought to represent an upper limit to the overall edifice density, due to the unknown quantity of unconsolidated breccias and tuffs that also make up the edifice.

The densities of the extra-caldera tuffs are variable but a general density of 1.90 Mg m^{-3} has been estimated for the pre-La Ese Pumice tuffs. In general therefore, the results of both the surface sample measurements and the Nettleton profiles imply that the caldera margins and the terrain outside the Guayabo caldera has a lower density than the chosen reduction density of 2.40 Mg m^{-3}. As explained earlier (Section 3.1.2), however, any terrain-related Bouguer anomaly can be accounted for in the modelling procedure by choosing the reduction density as the background density in the models, and therefore the structural interpretation of the gravity data should not be affected by the initial choice of reduction density. The Volcán Miravalles model discussed below (Section 3.6.3) demonstrates this approach.

The lithics of the outflow tuffs provide constraints on the possible density of pre-caldera strata: The olivine-poor andesite lithics (2.46 Mg m^{-3}) are less dense than the caldera wall lavas (2.70 Mg m^{-3}) and are thought to be derived from the destruction of separate, probably older, pre-caldera volcanics. The granodiorite clasts (2.56 Mg m^{-3}) provide a constraint on the density of any possible high level silicic plutonics beneath the caldera. The welded tuff lithics (2.46 Mg m^{-3}) are not related to the Ignimbrite Unit, drilled below ~1400 m in the borefield, but provide a further constraint on the composition and density of either the sub-borehole stratigraphy, or possibly parts of the undrilled central caldera strata.

3.4 Borehole Densities and Hydrothermal Alteration

The major aims of this section are twofold: i) Define the density structure of the drilled stratigraphy so that, during the data interpretation (Sections 3.6 and 3.7), the gravity anomalies calculated from the observed density variations may be confidently separated from any remaining anomalies due to the deeper, inaccessible density structure. ii) To understand the way in which density changes associated with hydrothermal processes have overprinted the primary (stratigraphic) density values. The alteration mineralogy at Miravalles has been studied by workers at ICE, ELC and the BGS, Keyworth and the results are discussed here in the context of the effect of alteration on density.

The geothermal drilling program was monitored by ICE geologists and 50-200 g of returned cuttings were packaged every 6' for PGM-1, every 10' for PGM-2, 3, 5, 10 and 11 and every 3 m for PGM-12 and 15. Cores were generally only drilled where there was total loss of drilling fluid in the deeper, permeable zones of the reservoir. As drilling proceeded, ICE geologists mounted representative samples of the drilling chips on thin sections and recorded the petrology, the alteration mineralogy, modal analyses and whatever textural information was observable (the chips are generally <3 mm in diameter) with a petrological microscope (Mayra Corella, *pers comm*). The alteration mineral assemblage data were used for the early identification of high temperature zones, giving useful quantitative information without needing to let the well recover before running temperature logs. The alteration data used in this study (Figures 3.13 a-h) are from the individual drilling reports (ELC, 1984-1986) for wells PGM-5 to 15, but the data from the earlier wells, PGM-1, 2 and 3, were only available in graphical format from the final geological report, ELC (1986 a).

During the 1989 field season, 504 cuttings samples were measured for density at 20 m intervals (where possible) and every 10 m in the uppermost sections, using 20-25 g samples (summarised in Table 3.4, full data list in Appendix 3C). As cuttings samples could only yield the grain density, porosities from the core samples have therefore been used to correct, approximately, the cuttings densities for porosity. ICE geophysicists had measured the densities and porosities of 35 core samples (Leandro, *comm. lit.*, 1988, results in Table

3.3). PGM-5R (300 m), drilled 20 m from PGM-5 to intersect the shallow steam dominated geothermal reservoir, provided an opportunity to verify the cuttings density.log of PGM-5. The two independently-measured logs compare very well (Figure 3.12) suggesting that density measurements of cuttings do indeed provide consistent rock material densities.

Figure 3.12 The cuttings grain densities (ρ_r) of the adjacent wells PGM-5 and PGM-5R (20 m apart). The covariability of the two logs indicates that the lithology grain density, as determined from cuttings, is consistent within one lithology.

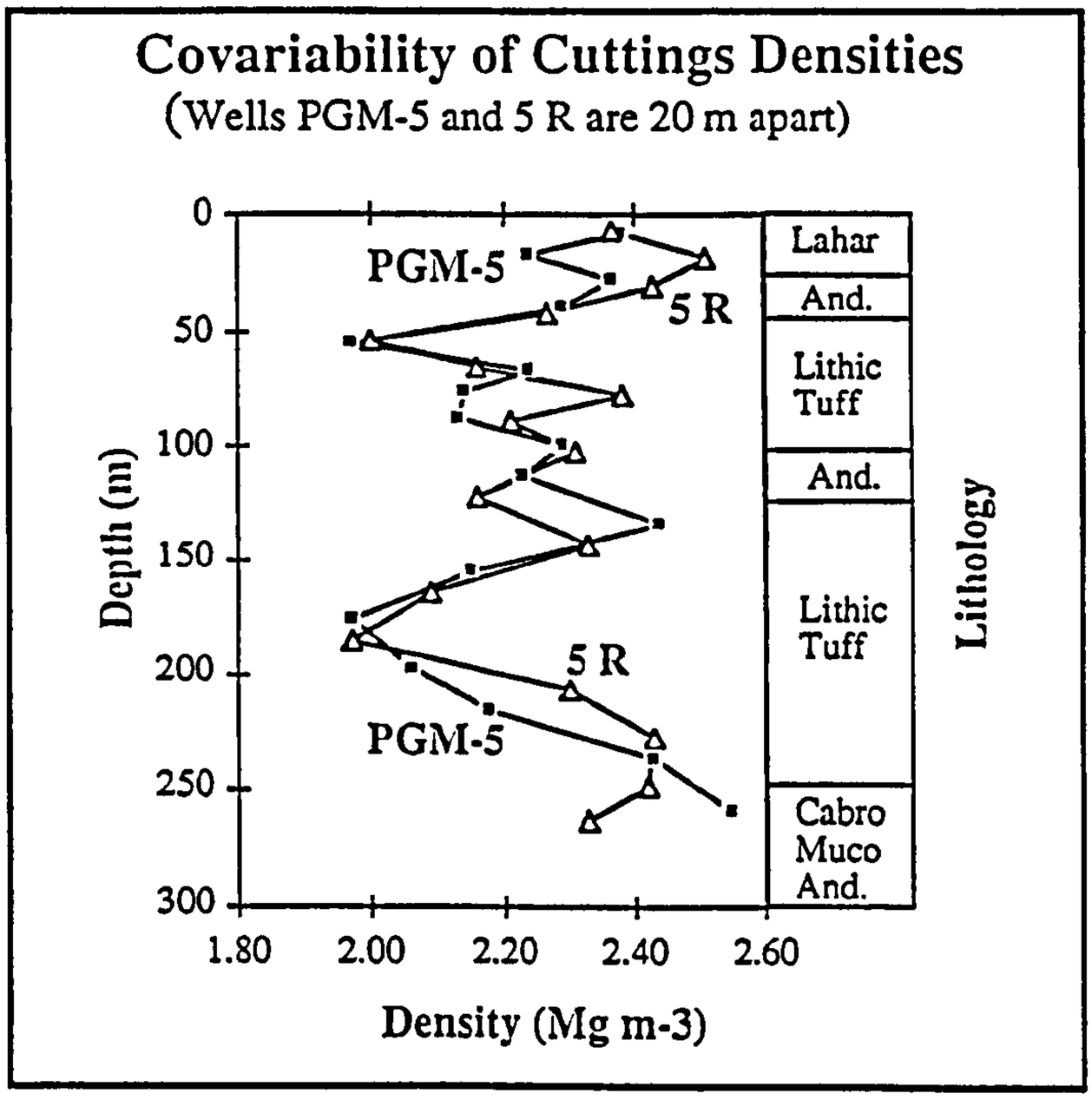

Figures 3.13 a to h show the grain density (ρ_r) logs measured from the cuttings of the eight deep geothermal wells PGM-1 to 15 respectively (location map; Figure 2.5) and the few core densities, measured by ICE (details in Table 3.4), are also shown. Note that the Volcano-Sedimentary Unit core samples are often smaller (up to 52 g) than the quoted lithic sizes in the tuffs (up to 4,500 g). (ELC, 1985 c quote a maximum lithic size of 15 cm diameter from core 4, PGM-12, Figure 3.13 g; which has a mass equivalent of over 4.5 kg assuming a density of 2.65 Mg m^{-3} and a spherical shape). This probably explains the range of densities for the same core that have been measured by ICE at different times (see cores marked by * in Table 3.3). Such small scale heterogeneities are averaged in cuttings samples and the overall grain density, ρ_r, from the cuttings is therefore a better estimate than

ρ_r from one small core sample, though this does introduce questions about formation porosity (see below, Section 3.4.1).

Figure 3.13 General Key PGM-1 to 15 logs of grain density (ρ_r) and % alteration of whole rock. Lithology and Stratigraphic Units are shown. Total - Clays % is the % of rock made up of alteration minerals that are not clay minerals. Resistivity values (Ωm) and Layers 1-4 are from Duprat and Leandro (1986) (discussed in Section 3.5.1); R is the resistive basement (Layer 4). Vapour zone (where it exists) and the depths to the liquid-dominated zone are shown for comparison with the resistivity and alteration zones.

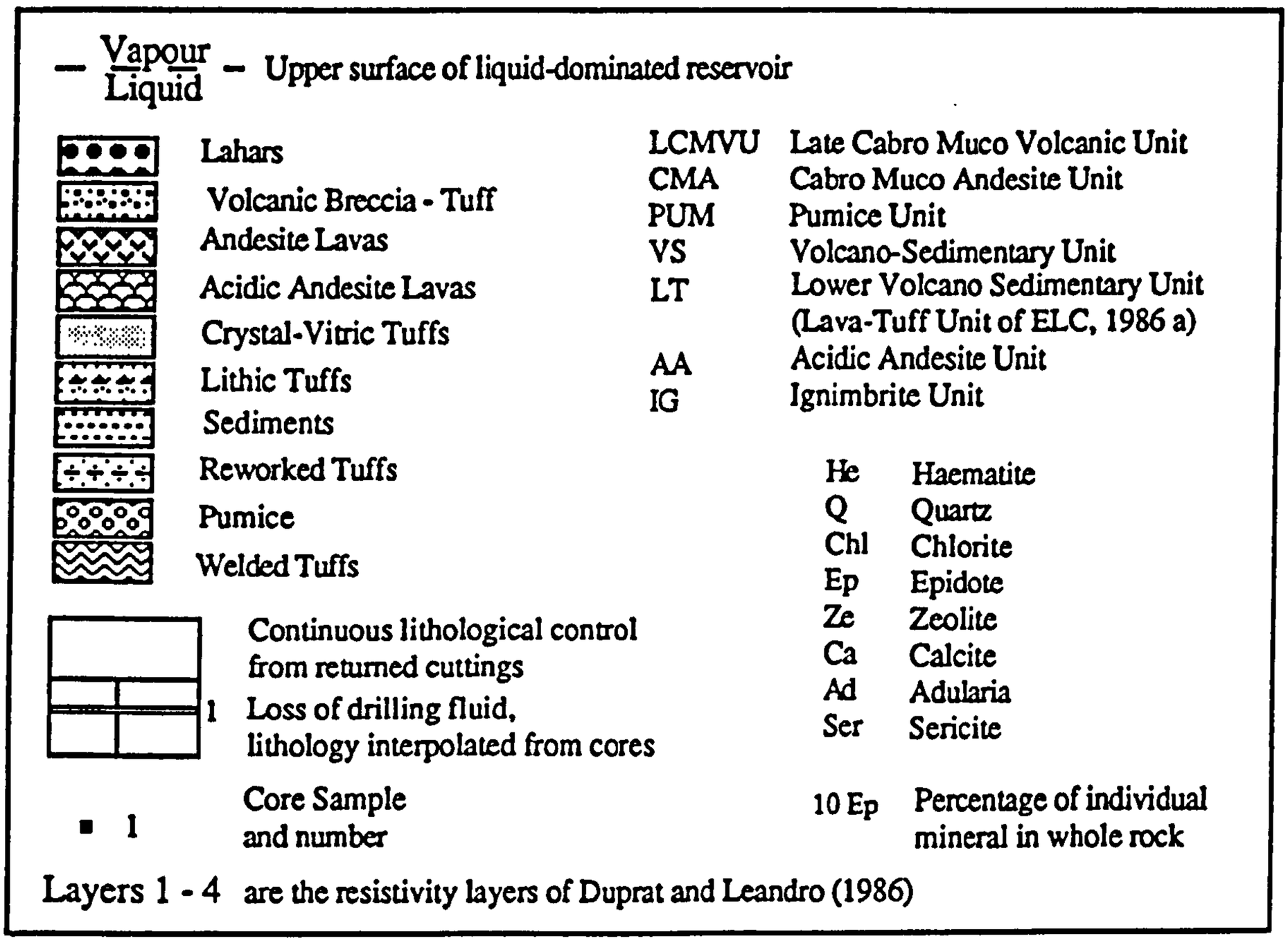

Figure 3.13 a PGM-1. Notice the low density of the upper CMA due to clay alteration. Also the inverse relationship between % alteration and density within the uppermost 450 m. Lithology and alteration logs from ELC (1986 a), resistivity layers from Duprat and Leandro (1986).

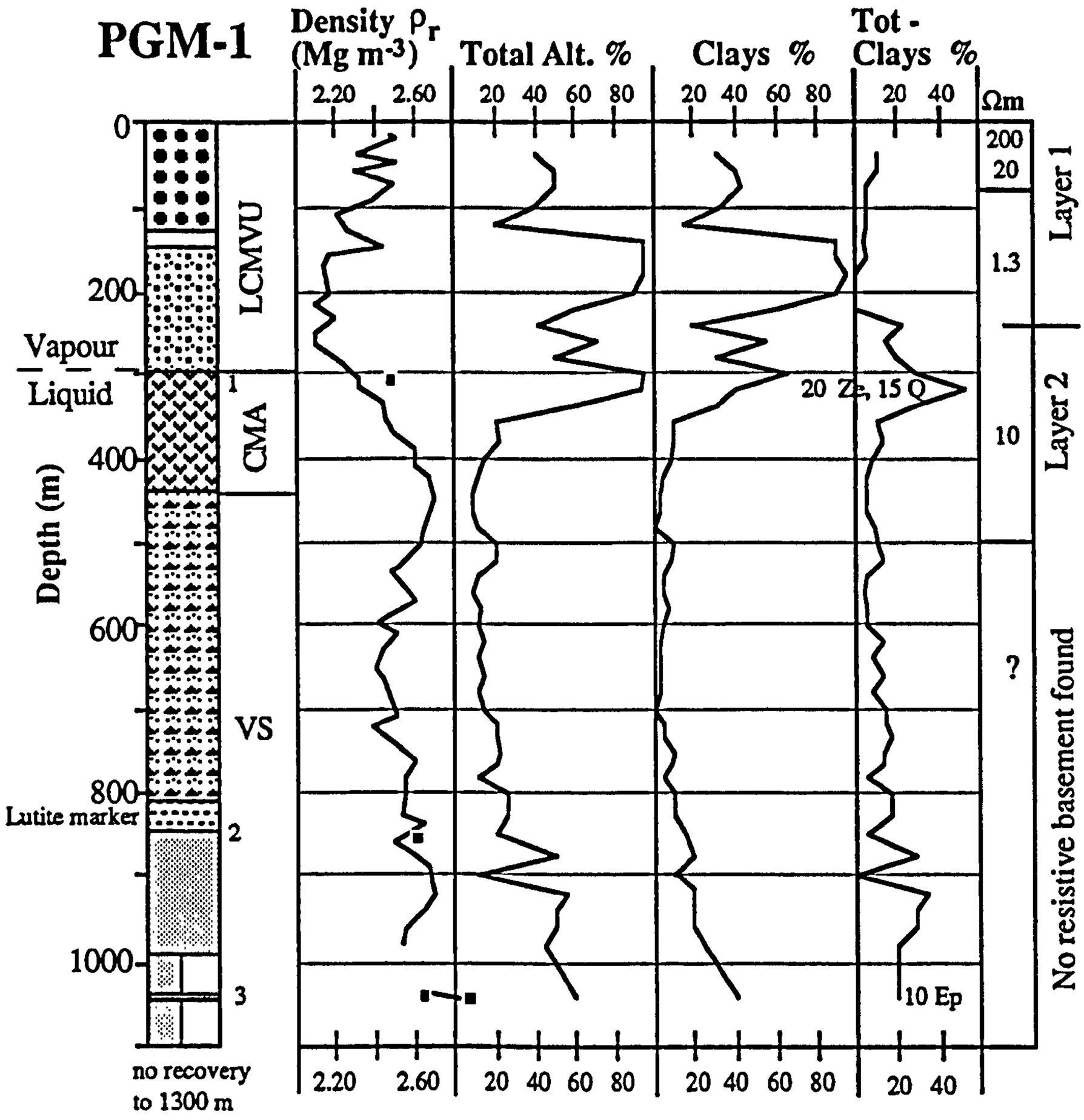

Figure 3.13 b PGM-2. Notice density reflects the lithological heterogeneity in the upper units, but homogeneity in the Acidic Andesite Unit. The density increases in the Epidote Zone. Lithology and alteration logs from ELC (1986 a), resistivity layers from Duprat and Leandro (1986).

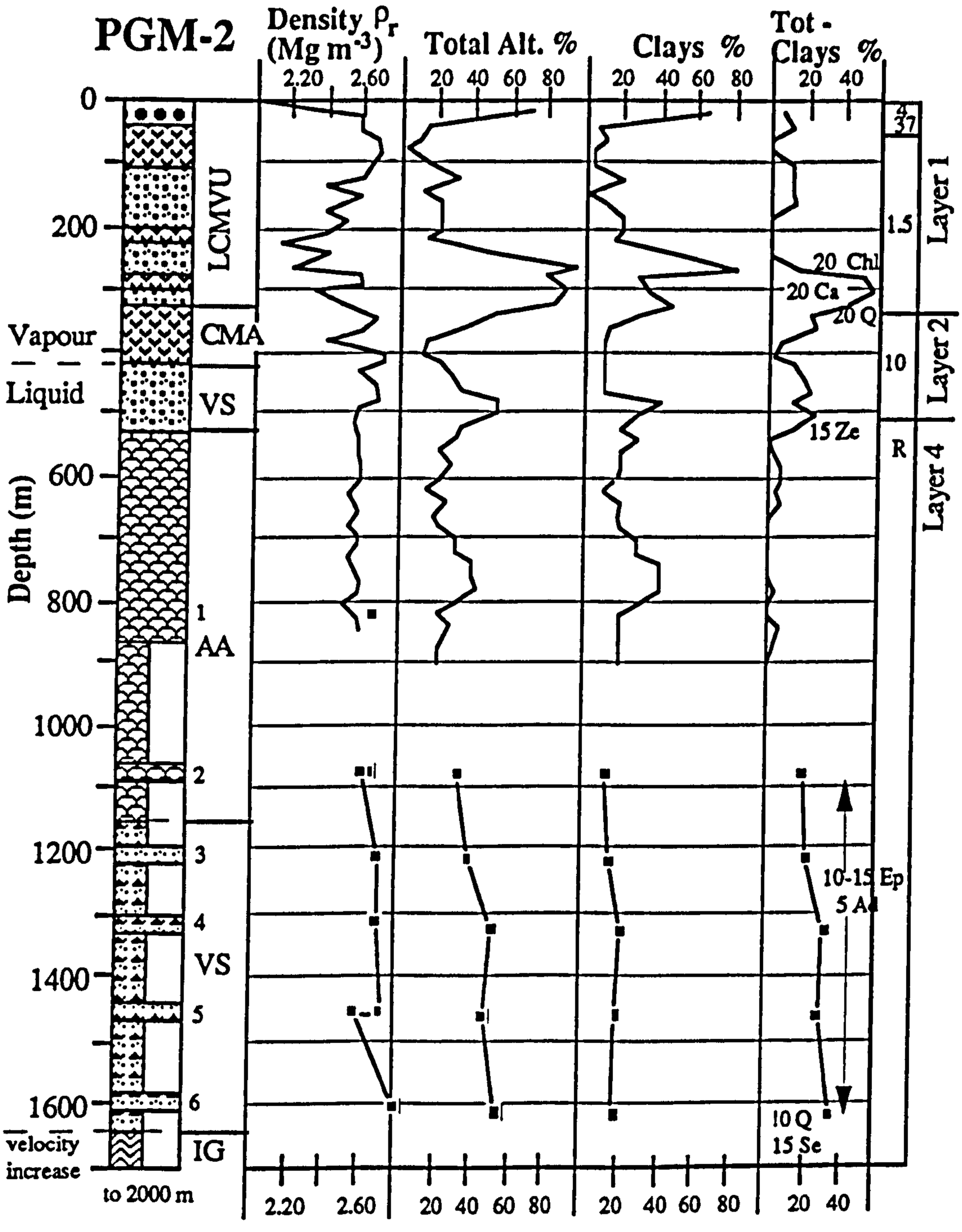

Figure 3.13 c PGM-3. Inverse relationship between density and % clay alteration for the whole depth. Density partially shadows the % non-clay alteration. Lithology and alteration logs from ELC (1986 a), resistivity layers from Duprat and Leandro (1986).

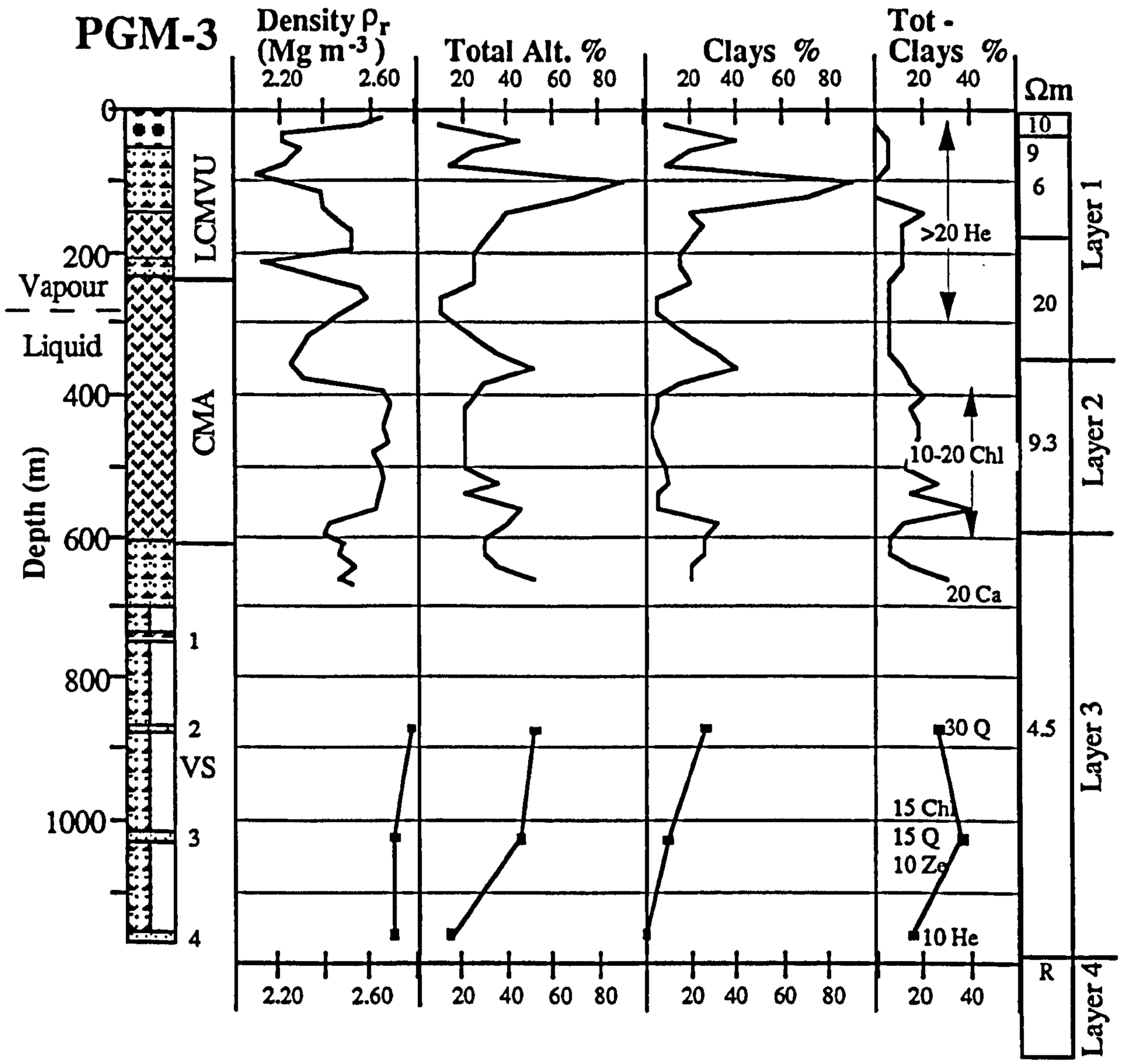

Figure 3.13 d PGM-5. Notice high % alteration and low density in the vapour zone, above the CMA. Lithology and alteration logs from ELC (1984 a), resistivity layers from Duprat and Leandro (1986).

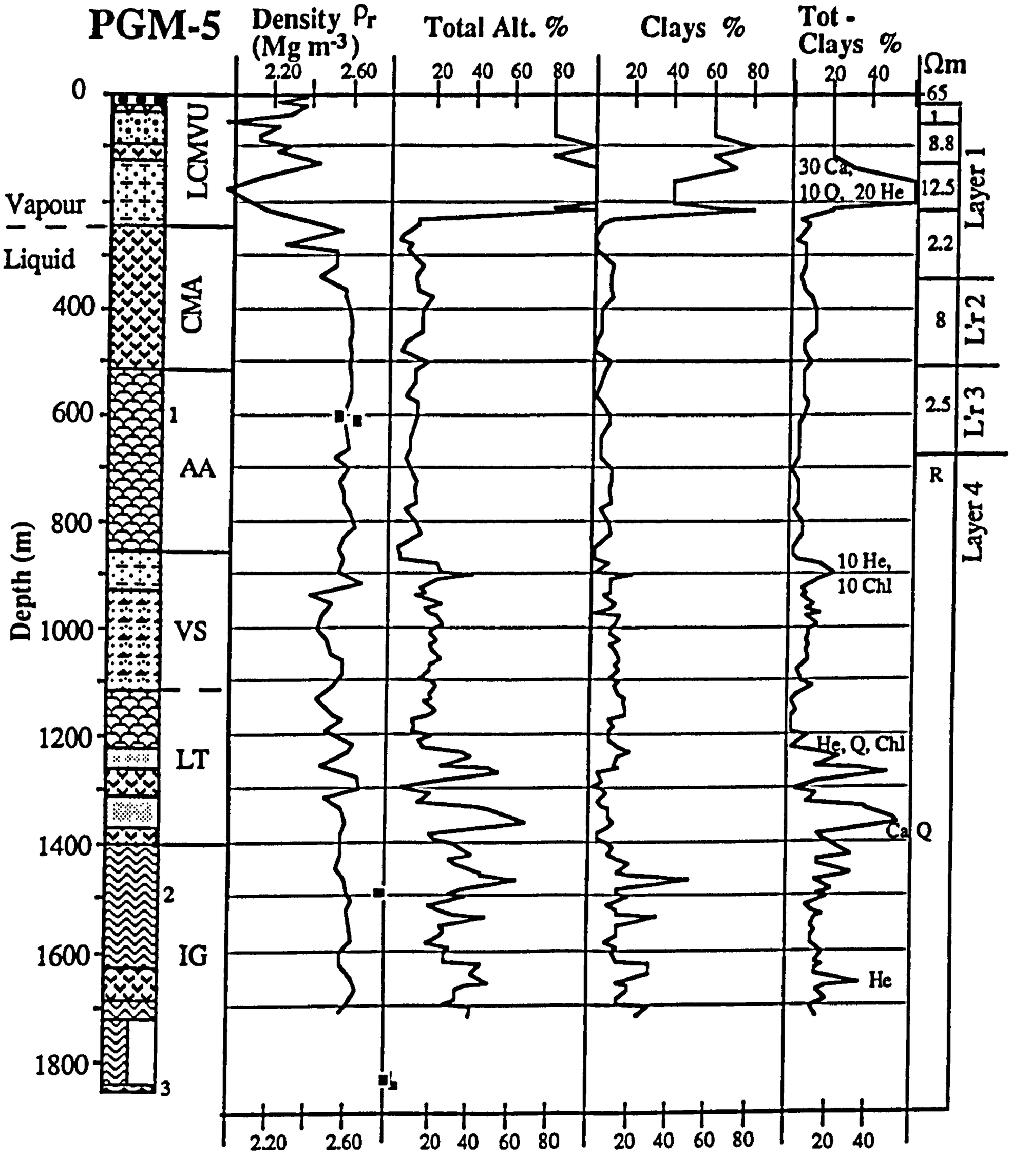

Figure 3.13 e PGM-10. The inverse relationship between density and % alteration in vapour zone, within LCMVU, changes to a generally positive relationship within the AA, where % chlorite increases. Lithology and alteration logs from ELC (1984 c), resistivity layers from Duprat and Leandro (1986).

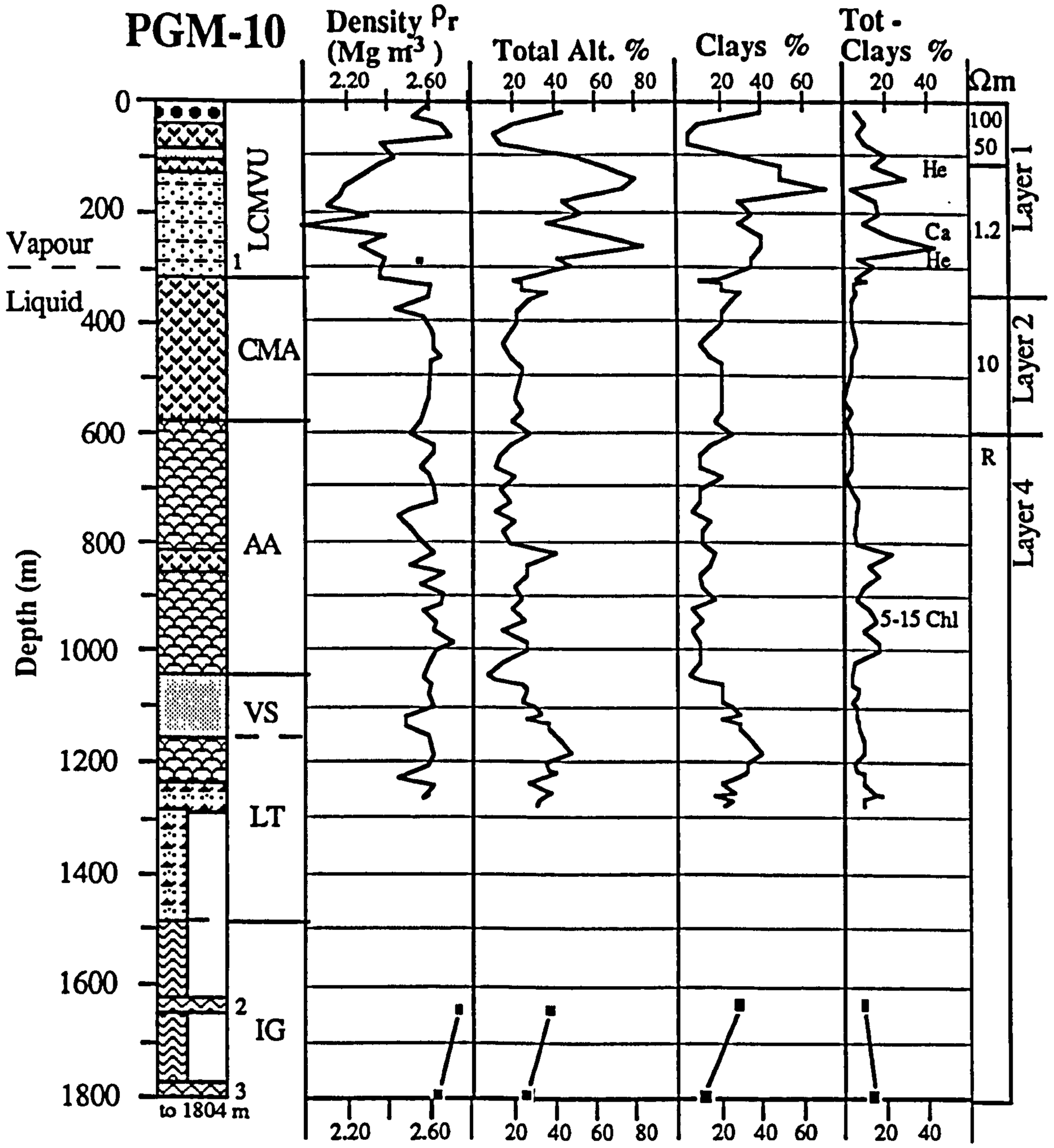

Figure 3.13 f PGM-11. Inverse relationship between % alteration and density is only clear in the vapour zone. High density at depth due to % epidote and chlorite. Lithology and alteration logs from ELC (1985 a), resistivity layers from Duprat and Leandro (1986).

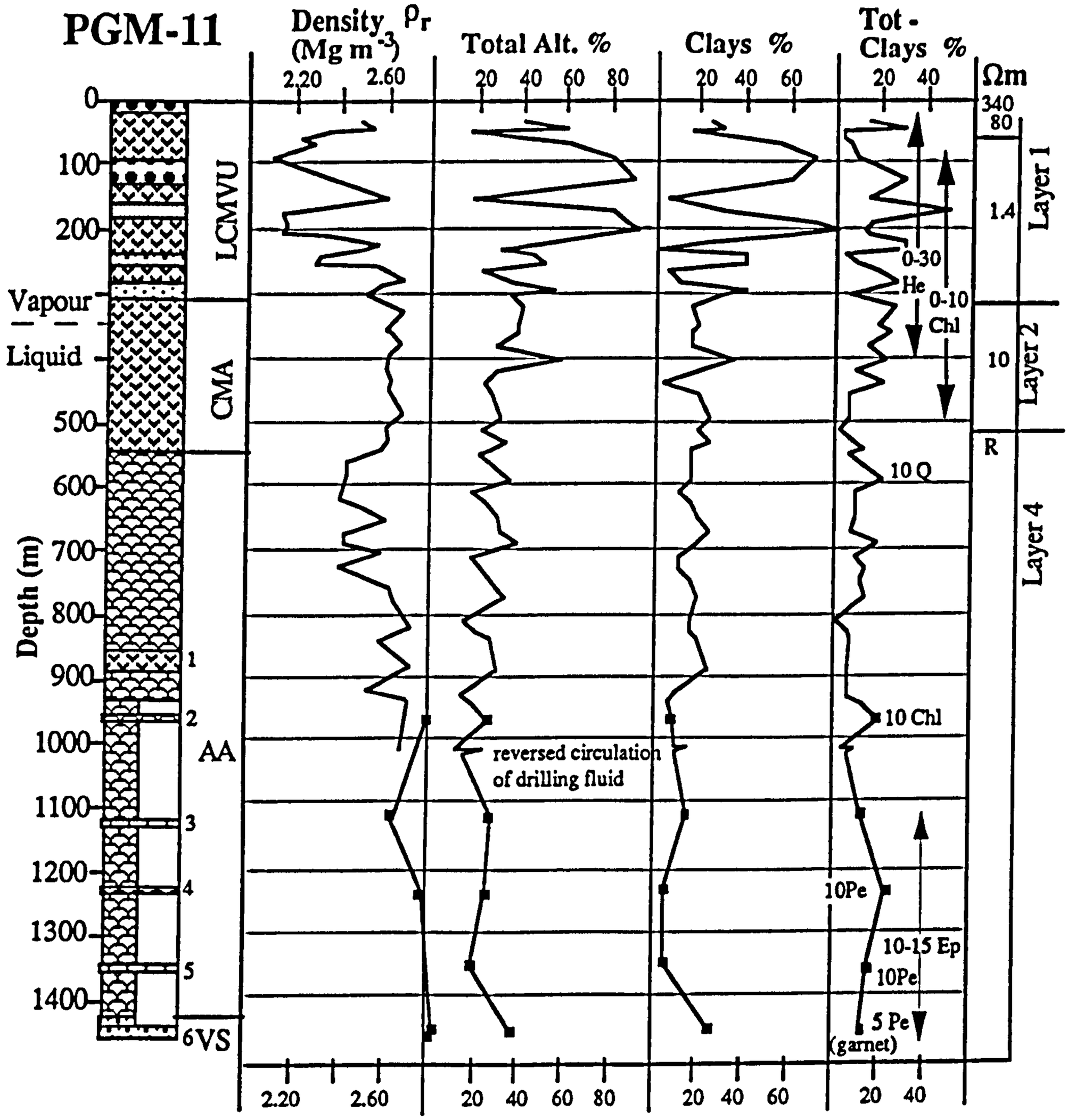

Pe Penninite is a form of Chlorite

Figure 3.13 g PGM-12. In the uppermost tuffs the % alteration is highest and density is lowest so that the inverse correlation is probably controlled by lithology, not % alteration alone. The VS core samples are often smaller than lithic size and densities may reflect the lithic density, rather than the whole rock density (see table 3.4 for core masses). Also shown are VS Unit relative proportions of glass (V), lithics (L), plagioclase crystals (Pl) and maximum lithic sizes. Lithology and alteration logs from ELC (1985 c), resistivity layers from Duprat and Leandro (1986).

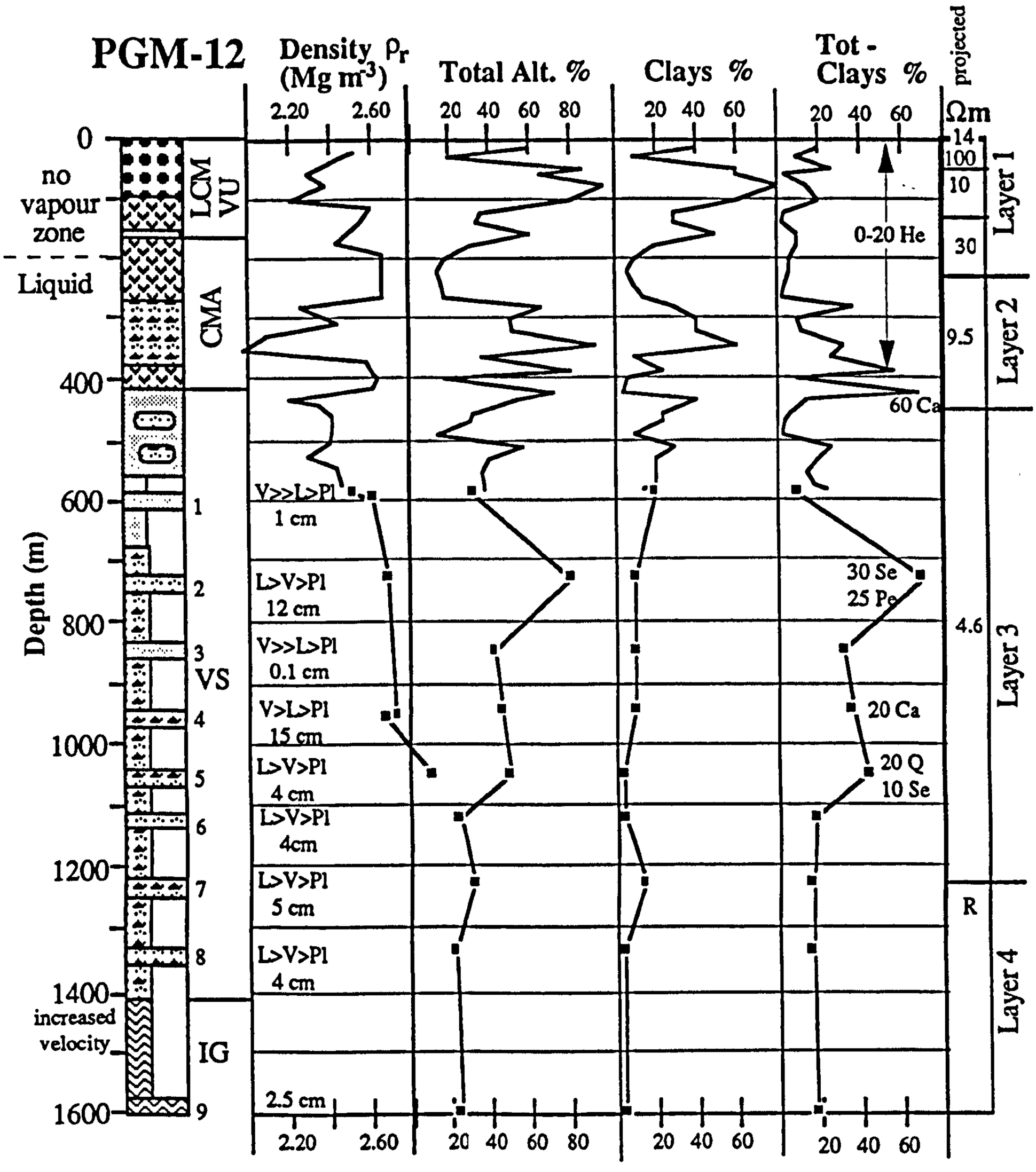

Figure 3.13 h PGM-15 Notice lower overall % alteration in this well (reflecting the lower temperatures) and the very low density of Pumice Unit. There is a strong lithological control on density in the VS alternating tuffs and lavas. Lithology and alteration logs from ELC (1986 b), resistivity layers from Duprat and Leandro (1986).

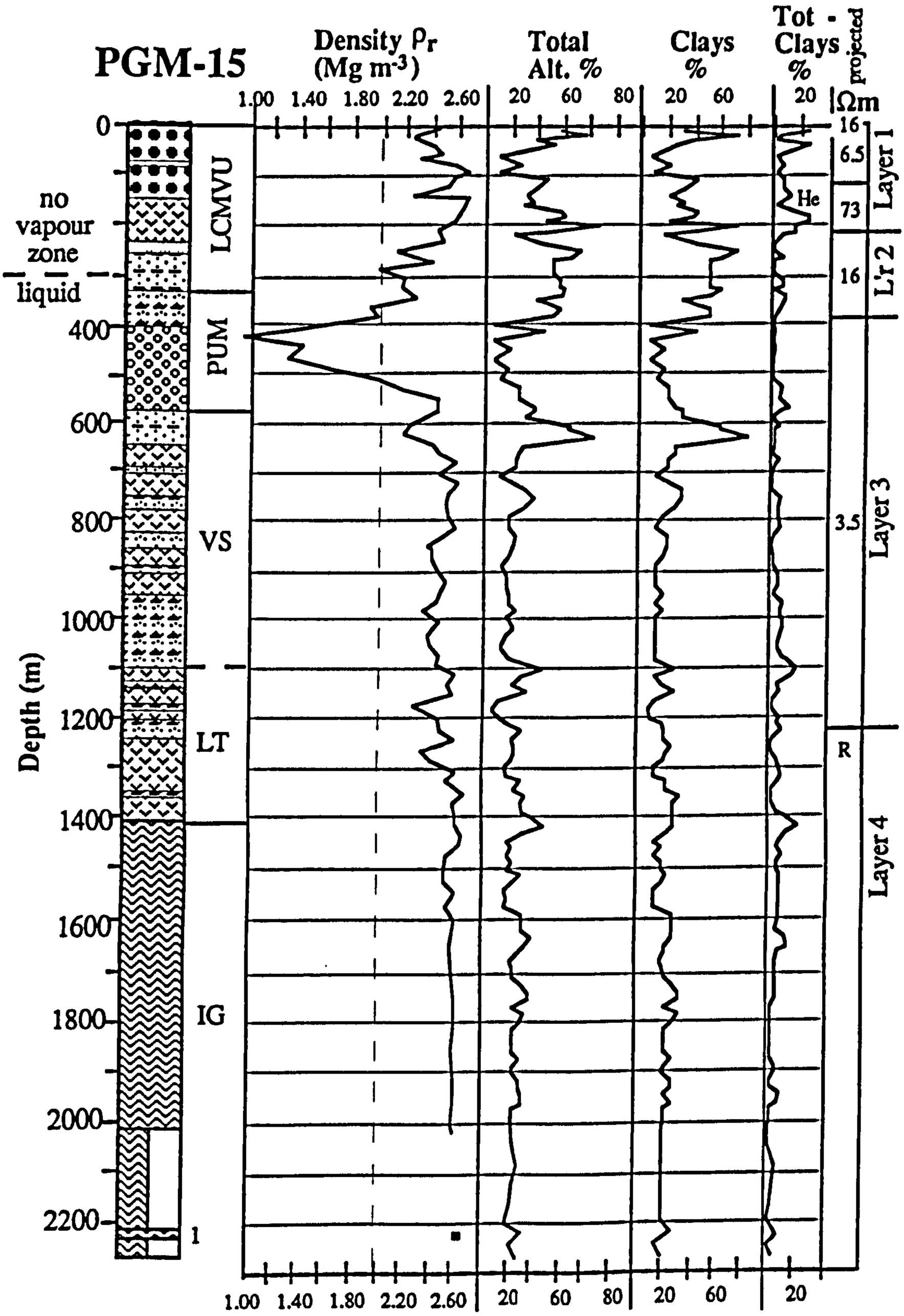

3.4.1 Correcting the cuttings densities (ρ_r) for porosity

Core samples are essential to provide estimates of porosity that can be applied to cuttings and the results have been extrapolated within stratigraphic units. It must be emphasised, however, that these critical corrections are based on comparatively few (35) porosity measurements (Table 3.3), made by ICE on small samples of core and therefore the error on the estimates of bulk wet density will have been affected proportionally.

Table 3.3 Core densities measured by ICE geophysicists (Leandro *comm. lit.*, 1988, * denotes data used by Duprat and Leandro, 1986, other samples measured in 1988). Masses in g, densities in Mg m^{-3}, porosity in %, core numbers correspond to those in Figures 3.13 a-h. LCMV = Late Cabro Muco Volcanic Unit, CMA = Cabro Muco Andesite Unit, AA = Acidic Andesite Unit, VS = Volcano-Sedimentary Unit, IG = Ignimbrite Unit. Summary in Table 3.4.

PGM	core	(m)	strat	M_a	M_a	M_a	ρ_r	ρ_w	ρ_d	Ø
1	1	310	CMA	-	-	-	2.48	2.18	1.98	20
1	2	866	VS	-	-	-	2.58	2.56	2.55	1
1	3	1030	VS	49.68	52.75	30.55	2.60	2.38	2.24	14
1	3	1040	VS	37.65	39.94	24.60	2.89	2.60	2.45	15
2	1	816	AA	63.00	64.80	39.23	2.65	2.53	2.46	7
2	2	1075	AA	43.41	45.19	27.00	2.65	2.48	2.39	10
2	*2	1075	AA	-	-	-	2.61	2.40	2.27	13
2	3	1208	VS	91.88	94.83	57.85	2.70	2.56	2.48	8
2	4	1318	VS	73.35	75.76	46.22	2.70	2.56	2.48	8
2	5	1454	VS	78.22	82.02	49.60	2.73	2.53	2.41	12
2	*5	1455	VS	-	-	-	2.58	2.41	2.30	11
2	6	1597	VS	72.29	73.51	46.60	2.81	2.73	2.69	5
3	2	871	VS	46.34	48.30	29.60	2.77	2.58	2.48	10
3	3	1023	VS	99.62	102.80	62.69	2.70	2.56	2.48	8
3	4	1156	VS	28.79	29.87	18.07	2.69	2.53	2.44	9
5	*1	600	AA	-	-	-	2.55	2.49	2.45	4
5	1	613	AA	54.47	55.78	33.87	2.64	2.55	2.49	6
5	2	1492	IG	86.69	89.56	55.58	2.79	2.64	2.55	8
5	*3	1850	IG	-	-	-	2.82	2.67	2.59	8
5	3	1854	IG	30.77	32.08	20.00	2.86	2.66	2.55	11
10	1	308	LCMV	49.22	54.75	30.00	2.56	2.21	1.99	22
10	2	1642	IG	105.85	109.95	67.06	2.73	2.56	2.47	10
10	3	1804	IG	89.54	90.57	55.60	2.64	2.59	2.56	3
11	2	968	AA	56.85	57.73	36.45	2.79	2.71	2.67	4
11	3	1117	AA	31.64	32.33	19.57	2.62	2.53	2.48	5
11	4	1232	AA	28.82	29.18	18.45	2.78	2.72	2.69	3
11	*6	1450	VS	-	-	-	2.82	2.67	2.59	8
11	6	1453	VS	69.10	72.75	44.53	2.81	2.58	2.45	13
12	*1	590	VS	-	-	-	2.53	2.32	2.18	14
12	1	592	VS	23.19	24.99	14.35	2.62	2.35	2.18	17
12	2	730	VS	-	-	-	2.67	2.32	2.11	21
12	*4	950	VS	-	-	-	2.73	2.37	2.16	21
12	4	953	VS	52.39	56.02	32.71	2.66	2.40	2.25	16
12	5	1053	VS	28.03	29.62	18.37	2.90	2.63	2.49	14
15	1	2208	IG	-	-	-	2.63	2.55	2.50	5

As coring was generally only necessary in the deeper stratigraphy where total fluid loss was more common, there is poor porosity control for the shallow stratigraphy (see number of

cores, *n*, in the last column of Table 3.4). Only one core has been measured, therefore, for each of the two uppermost Units, compared to nineteen cores in the Volcano-Sedimentary Unit, of which six are from the high permeability well, PGM-12 (Table 3.4).

Table 3.4 Average stratigraphic group wet densities (in bold) and standard deviations (s.d.) for each well, derived from porosity-corrected ρ_r data from cuttings (cf. Figure 3.14). Average core sample densities and porosities from ICE are shown (in italics) for comparison. Key as for Table 3.3; PUM = Pumice Unit, n is the number of core samples. The Volcano-Sedimentary Unit has been divided into the ELC (1986) divisions of an upper VS and lower LT to show that there is no significant cuttings density contrast between them.

Strat unit	well 1	2	3	5	10	11	12	15	Strat av.	std. dev.	Ø	std. dev.	n
LCMV	**2.02**	**2.16**	**2.07**	**2.00**	**2.09**	**2.12**	**2.12**	**2.16**	**2.09**	**0.06**			
s.d.	0.15	0.18	0.18	0.15	0.19	0.17	0.15	0.19					
cores	-	-	-	-	*2.22*	-	-	-	*2.22*	-	*22.0*	-	*1*
CMA	**2.40**	**2.43**	**2.37**	**2.39**	**2.43**	**2.45**	**2.35**	-	**2.40**	**0.04**			
s.d.	0.13	0.13	0.14	0.09	0.06	0.03	0.25	-					
cores	*2.18*	-	-		-	-	-	-	*2.18*	-	*20.0*	-	*1*
PUM	-	-	-	-	-	-	-	**1.58**	-	-			
s.d.								0.45					
cores	-	-	-	-	-	-	-	-	-	-	-	-	*0*
AA	-	**2.48**	-	**2.51**	**2.51**	**2.48**	-	-	**2.50**	**0.02**			
s.d.		0.03		0.03	0.06	0.11							
cores	-	*2.47*	-	*2.52*	-	*2.66*	-	-	*2.55*	*0.11*	*6.5*	*3.4*	*8*
VS	**2.39**	**2.45**	**2.34**	**2.37**	**2.40**	-	**2.15**	**2.29**	**2.34**	**0.10**			
s.d.	0.09	0.07	0.04	0.09	0.07		0.07	0.10					
cores	*2.52*	*2.56*	*2.56*	-	-	*2.62*	*2.39*	-	*2.51*	*0.12*	*11.8*	*5.1*	*19*
										*P-12**	*17.0*	*3.0*	*6*
LT	-	-	-	**2.40**	**2.42**	-	-	**2.35**	**2.39**	**0.04**			
s.d.				0.06	0.05			0.11					
cores	-	-	-	-	-	-	-	-	-	-	-	-	*0*
IG	-	-	-	**2.49**	-	-	-	**2.46**	**2.48**	**0.02**			
s.d.				0.03				0.04					
cores	-	-	-	*2.66*	*2.57*	-	-	*2.56*	*2.59*	*0.05*	*7.5*	*3.0*	*6*

* The porosities from the VS of PGM-12 are significantly higher than in the rest of the borefield.

The summary diagram of the estimated stratigraphic densities (Figure 3.14), shows a comparison with the stratigraphy, the present reservoir temperatures from ELC (1986 a) and the palaeo-temperatures, in parentheses, estimated by Rochelle (1991). The shallow vapour-dominated zone of the geothermal system is only present in the central-northern borefield according to ELC (1988). Thus, the extrapolated 20 % porosity for the Late Cabro Muco Volcanic Unit (LC, Tables 3.3 and 3.4) is an oversimplification of what is undoubtedly a complicated system of fractures and unconsolidated porespaces filled with a two-phase fluid. The depth to the top of the deep liquid-dominated geothermal reservoir (shown in Figures 3.13 a-h and 3.14) has been estimated from downhole pressure measurements of shut-in wells (ELC, 1988).

Figure 3.14 Average stratigraphic unit saturated densities for individual wells from cuttings data (core data for deep sections only, in parentheses). The Lava-Tuff Unit of ELC (1986 a) does not have a large density contrast with the Volcano-Sedimentary Unit but density increases within the VS in the higher temperature northeast area. Total Stratigraphic Unit averages (core averages in parentheses). See Table 3.4 for details.

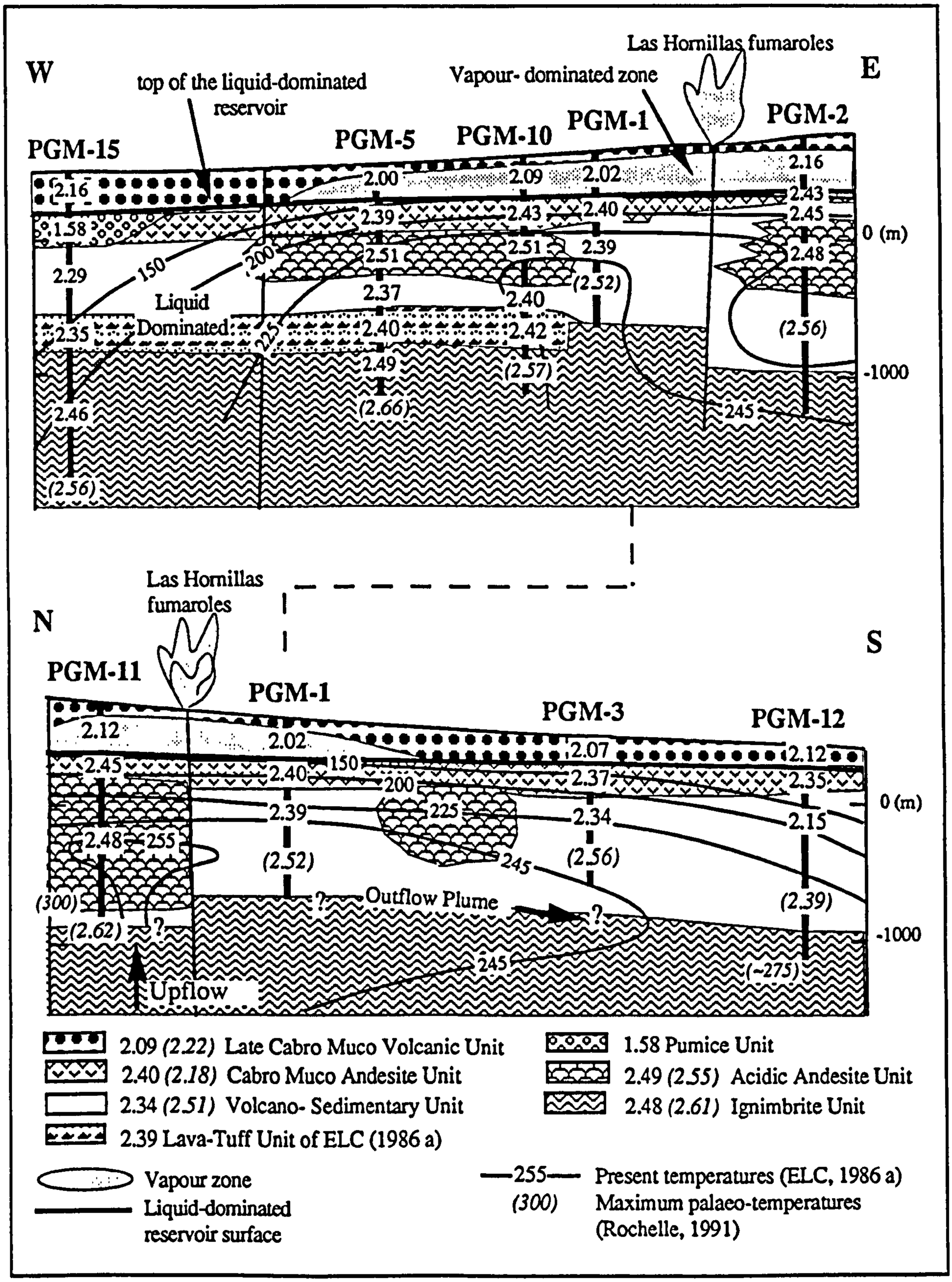

The Cabro Muco Andesite Unit (CMA) appears to act as a relatively impermeable cap to the deep liquid-dominated reservoir, but the top of the CMA has been severely altered by the shallow, corrosive vapour-dominated zone (e.g. PGM-1; Figure 3.13 a). Thus the 20% CMA porosity measured in PGM-1 (core 1) is probably more representative of the overlying Late Cabro Muco Volcanic Unit (LCMV) rather than the central or basal part of the CMA. The porosity of the CMA has therefore had to be estimated; the porosity of andesite lavas exposed at the surface (Table 3.1) is generally less than 5%, but may be higher in the CMA due to fracturing and brecciation, and thus a porosity of 10% has been assumed.

The relatively widely cored Volcano-Sedimentary Unit (upper part, VS and lower part, LT; Table 3.4) has an average porosity of ~10% in most of the borefield (8-15%, Table 3.3) but increases significantly at PGM-12 to an average of 17% (14-21 %, Table 3.3). The variation of porosity is an important cause of the lateral density variation in the VS (cf. Section 3.4.3). The VS has also been sub-divided to determine whether there is any significant density increase across the supposed stratigraphic boundary with the Lava-Tuff Unit (LT) of ELC (1986 a). The cuttings data suggest, however, that the units have a similar density (further discussion in Section 3.4.3).

There appears to be a porosity increase within the generally unporous (average 6.5%) Acidic Andesite Unit (AA) at PGM-2 (~10%, Table 3.3), but this trend is based on only three cores and the high porosity of the second PGM-2 core (10 and 13%, Table 3.3) may be anomalous. The electrical sounding data show that the AA is invariably a highly resistive unit (Section 3.5.1), implying very limited porosity, supporting the suggestion that the core 2 porosity in PGM-2 is not representative of the AA. A porosity of 5% has been applied to the whole AA unit for the purposes of correcting cuttings densities.

Porosity in the six cores of the Ignimbrite Unit (IG) varies from 3-11% with an average porosity of 7.5 %; the average has been applied to the whole unit.

The inter-well variation of the average wet density of each unit, summarised in Table 3.4 and Figure 3.14 is discussed in more detail following a description of the alteration mineral assemblages below.

3.4.2 Alteration mineral assemblages

Alteration (or secondary) mineralogy is interesting to this study because, generally, the density of alteration minerals increases with rank (the equilibrium temperature) and therefore the highest density assemblages should be expected in the high temperature areas (either those of the past or the present, depending on the equilibration conditions). The alteration logs for PGM-5, 10, 11, 12 and 15 (Figures 3.13 d-h) are compiled from tables given in the individual drilling and geological reports (ELC, 1984 a; 1984 c; 1985 a; 1985 c and 1986 b respectively). In the cases of PGM-1, 2 and 3 (Figures 3.13 a-c) no such data are available in the drilling report of Koenig (1980) and the data have been read off graphic logs presented by ELC (1986 a).

ELC (1984 a to 1986 b) distinguished alteration minerals by thin section examinations of cuttings. Quantitative data are available at approximately 10 m intervals on the percentage of hematite (mostly amorphous), chlorite, clay minerals (undifferentiated), calcite, secondary quartz (some of which may be the low temperature, low density form of hydrated amorphous silica), sericite, epidote and adularia. For the purposes of Figures 3.13 a-h the alteration minerals were grouped according to whether the mineralisation would generally result in an increase or decrease in density (discussed in this section). The total alteration is the percentage of the rock (not including porosity) made up of alteration products (i.e. the intensity of alteration). Total alteration was divided into clay minerals, that are most likely to reduce the density, and the remainder that are more likely to increase the density (total minus clay %; Figures 3.13 a-h).

Hydrothermal alteration at Miravalles can be divided into vein mineralisation and bulk rock replacement, of which the latter is dominant but produces a less diverse mineral assemblage (Rochelle, 1991). Milodowski *et al.* (in prep.) distinguished seven alteration mineral assemblage zones at Miravalles showing increasing rank with depth, from acid-silicic in the shallow vapour zone to a relict garnet-magnetite-epidote assemblage (T > 300°C) at the base of PGM-11.

1 **Acid-silicic** (0-200 m) Above the acidic, vapour-dominated reservoir and at the fumaroles. Sulphur, amorphous silica (± kaolinite, haematite, clays and quartz).

2 **Argillic Alteration** (0-400 m) Uppermost cooler, liquid-dominated reservoir. Haematite, kaolinite, mixed layer clays, smectite (± calcite, quartz,amorphous silica, pyrite, chalcopyrite, anatase and sulphur).

3 **Chlorite-Sericite-Calcite** (200-700 m) At the top of the reservoir, in the boiling zone. Appearance of chlorite (± quartz, calcite, anatase and sphene) and disappearance of haematite, smectite, amorphous silica and sulphur.

4 **Chlorite-Epidote-Sphene-Sericite-Albite-Laumonite** (300-1800) all wells. Appearance of epidote and laumonite and calcite (T_{max} 240-250°C) (± quartz, pyrite, K-feldspar, barite and anhydrite).

5 **Chlorite-Epidote-Sphene-Sericite-Albite-Wairakite** Appearance of wairakite (T_{min} 230°C), chlorite and epidote (± quartz, pyrite, K-feldspar, albite, sphalerite, sphene).

6 **Prehnite-Epidote** (PGM-2 and 11 only) Prehnite and epidote (± quartz, chlorite, K-feldspar, albite, pyrite, chalcopyrite, sphene and calcite).

7 **Garnet-Magnetite-Epidote** (very deepest sections of PGM-11 and 15 only). Epidote and magnetite (+ some garnet at PGM-11, T_{min} 300°C).

The reaction paths are sensitive to both temperature and pH, but the range of pressure changes in a typical geothermal reservoir are not thought to be important (Rochelle, 1991). The order of mineral replacement within the liquid-dominated geothermal reservoir at Miravalles has been described by Rochelle (1991) and is presented here in a general order of increasing resistance to alteration:

Primary lithology		to	Alteration products
Tuffs	Glass spherules	to	quartz, K-feldspar (± calcite)
	Pore spaces	to	chlorite, quartz, calcite
Lava matrix	Plagioclase laths	to	albite, K-feldspar
	Glass	to	chlorite, quartz
Lava phenocrysts	Pyroxenes	to	chlorite (via quartz)
	Plagioclase (Ca)	to	calcite (± quartz, epidote, chlorite)
	Magnetite, oxides	to	chlorite (± sphene)

This sequence was primarily a summary of the high-temperature alteration mineralogy (of the liquid-dominated reservoir) but the shallower vapour zone argillic alteration is at least as important for this study as it is a low density assemblage. Most of the replacements listed for the liquid-dominated zone will result in a density increase or no change at all depending on the mineralogy of the reactants and products (Figure 3.16, discussed below). At Miravalles the tuffs are generally more altered than the lavas at a given locality (Figures 3.13 a-h), reflecting their higher porosity and therefore greater susceptibility to fluid-rock interaction.

Milodowski *et al.* (in prep.) and Rochelle (1991) investigated fluid-mineral reactions in the Miravalles reservoir cores and cuttings and showed that there is a complicated history of mineral growth and overgrowth. Only the most recent mineral assemblages are in equilibrium with the present 245°C geothermal fluids, but there are relict assemblages of an earlier, more extensive, higher temperature phase of geothermal activity (see values in parentheses in Figure 3.14). For example, the hydrothermal garnet at the base of PGM-11 indicates equilibration temperatures of ~300 °C. This suggests that the present geothermal system may be in decline and there are therefore potentially significant relict zones of deep, high-temperature and therefore dense alteration assemblages.

The entire range of rock types at Miravalles has suffered density increases or decreases during alteration and the nature of this change depends on the density contrast between the primary and replacement minerals and the change in porosity. The range of densities of the primary rocks, minerals and secondary mineralogy are shown in Figure 3.15. Primary rocks within the geothermal reservoir are dominantly andesite lavas and poorly consolidated lithic tuffs giving way to welded tuffs in the deepest wells (Figures 2.9 and 3.13 a-h). The wet densities (ρ_w) can therefore be expected to lie between about 2.00, or less, to 2.70 Mg m^{-3} (tuffs to andesites, Figure 3.15). The densities of the constituent primary minerals (from Deer *et al.*, 1966) are mostly greater than the overall rock density because the interstitial glass density is lower (Figure 3.15).

The density change for a given rank and intensity of alteration can be predicted, given the densities of the primary rock and the secondary minerals, as shown in Figure 3.16. Two different initial wet densities are considered to demonstrate the contrasting effect of similar alteration of two different rocks (ρ_w = 2.20 and 2.60 Mg m^{-3}). In both cases only replacement by water-rich smectites (kaolinite is less common) and an increase in porosity can decrease the density. The effect for a given intensity (%) of alteration is greatest in the case of maximum density contrast (∂) between the initial and replacement materials (Figure 3.16). For example, a 50 % replacement of the 2.20 Mg m^{-3} rock by H_2O-rich smectite results in a density change of -0.1 Mg m^{-3}, but an equal replacement of the 2.60 Mg m^{-3} rock results in a density change of -0.3 Mg m^{-3}. Quartz and calcite alteration should have little effect on the density of andesites whereas they will increase the density of vitric tuffs. Chlorite and epidote deposition would increase the density of any volcanic rock, and finally, even fractional deposition of sulphide would have a major effect on density.

Figure 3.15 Range of rock densities, measured during this study, and primary and alteration (secondary) mineral densities from Deer *et al.* (1966).

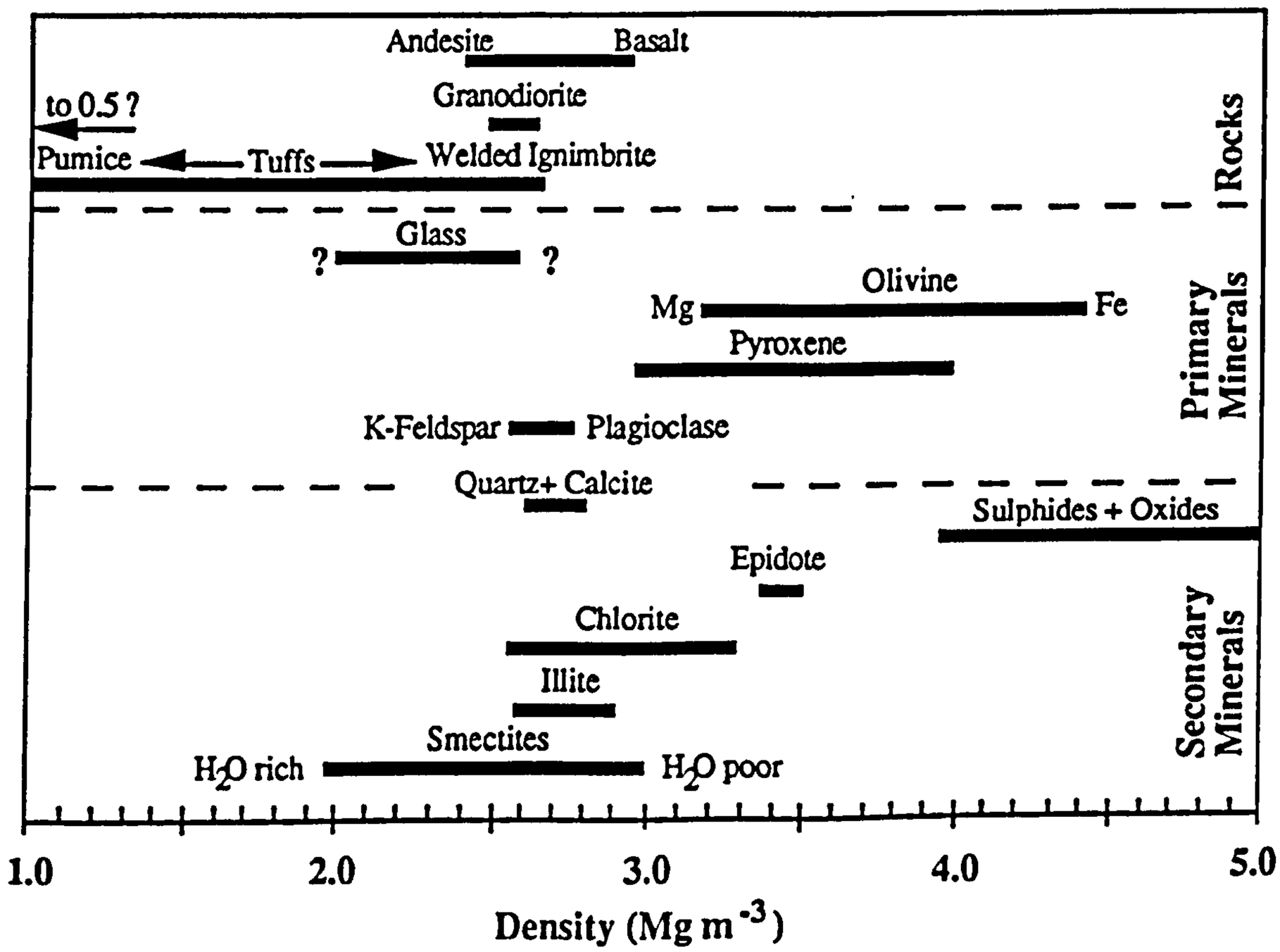

Not all the possible reactions are shown in Figure 3.16, but it is important to consider the type of alteration taking place and what constituent parts of the primary rock are being

replaced. For example, the replacement of glass in an andesite by chlorite will increase the density but an alternative equal replacement of olivine or ferrous pyroxene will result in a decrease in density (Figure 3.15). Mineral deposition involving vein mineralisation should be expected to decrease the overall porosity and therefore result in a density increase. The other extreme, however, is leaching by acidic fluids which removes material, thereby increasing porosity.

Figure 3.16 Change of Rock Density, from two initial conditions, ρ_r = 2.20 and 2.60 Mg m^{-3}, due to either an addition of secondary minerals or a change in porosity (density contrast, ∂). The change in density depends on not only the % and density of the alteration mineral, but also on the initial density of the rock. For example, for a 50% addition of low density smectite, the density decrease is greatest for the rock with the highest initial density.

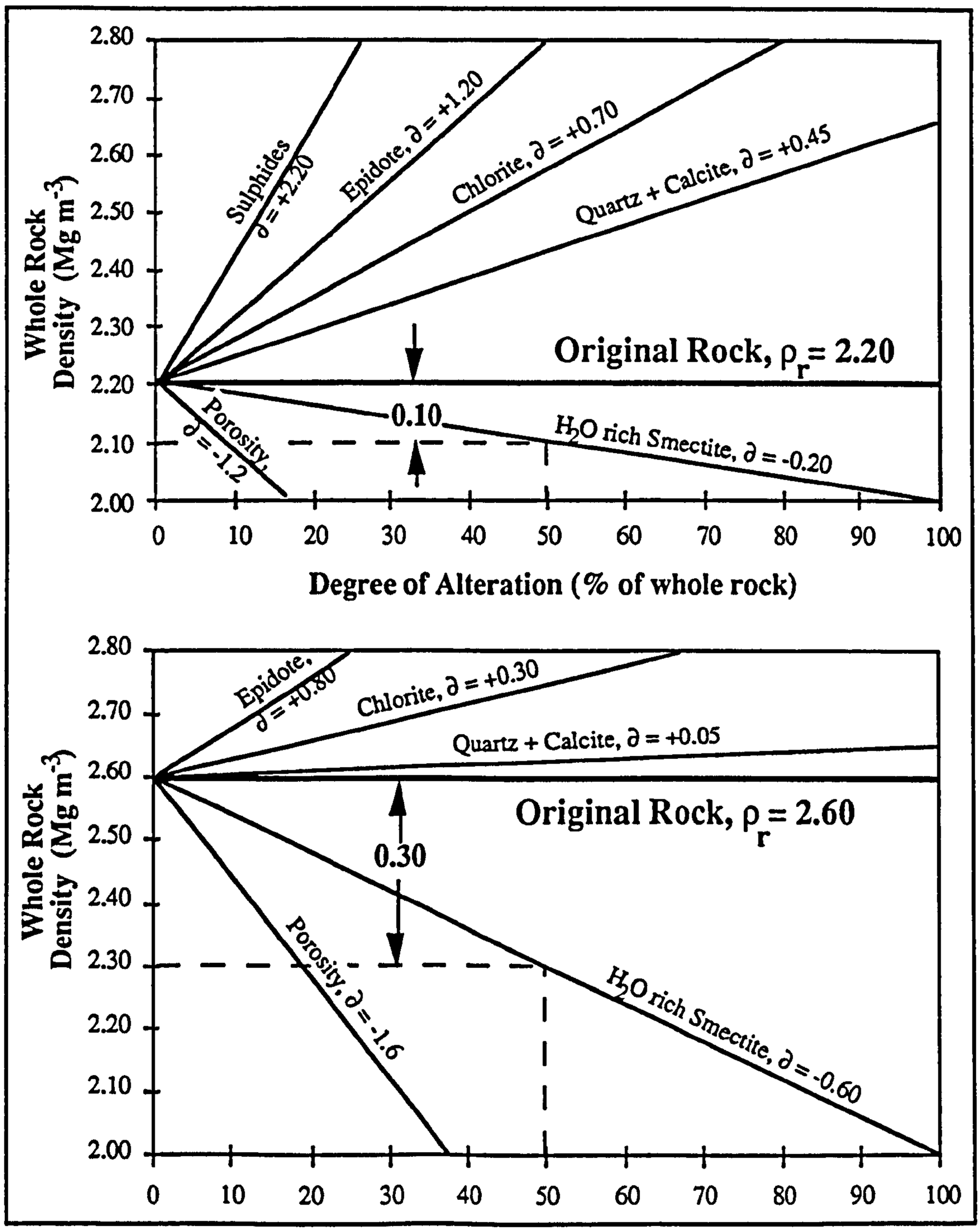

In summary, the alteration products recognised by previous workers in the borefield show increasing rank and therefore density with depth, as expected. The low-density clays common in the shallow, vapour-dominated zone (to 400 m depth) would be expected to reduce the density of at least the andesites of the Cabro Muco Andesite Unit (CMA) and the Late Cabro Muco Volcanic Unit (LCMV). Quartz, calcite and feldspar deposition would have little effect on the density of lavas but should increase the density the tuffs. The deeper, higher-temperature assemblages contain significant quantities of chlorite and epidote which would serve to increase the density of all the primary volcanic rocks in this area. In addition, the filling or creating of voids during the alteration process will naturally have an important effect on density.

3.4.3 The borefield density structure

To examine the effect of alteration alone, rather than porosity, the grain density, ρ_r was considered in the density and alteration logs shown in Figures 3.13 a-h. The objective was to compare the measured ρ_r with the alteration mineralogy already defined by previous workers. The density logs in Figures 3.13 a-h show a complicated variation of grain density with depth, especially in the more heterogeneous upper sections of the boreholes, and it is sometimes difficult to recognise well defined density contrasts between the stratigraphic units. Some of the grain density variation is caused by hydrothermal alteration, not solely by lithological changes, and as a consequence, some of the boundaries chosen to model the wet density structure effectively in the gravity data interpretation stage (Sections 3.6 and 3.7) cross-cut the stratigraphic boundaries. The degree of vertical variation can be gauged by the standard deviation on the average wet densities calculated for each unit within individual wells (Table 3.4 and Appendix 3C) and conversely, the lateral variation is defined by the difference in the averages calculated for each unit across the wells.

Given that the gravity data was modelled in 2.5 dimensional cross-sections it was preferable to address the lateral variations within the stratigraphic units rather than provide a monologue description of the vertical density and alteration distribution within each well. The wet densities shown in the summary table (Table 3.4) represent a best-fit compilation of

all the density observations that can be used in the gravity models (in this case grain densities converted for porosity to wet densities). The view that emerges, as the units are described in reverse stratigraphic order, is that the liquid and vapour dominated hydrothermal reservoirs define different components of the density structure. This is because they are associated with different types of alteration, and furthermore the density structure sometimes represents the legacy of ancestral and/or migrated reservoirs.

The Late Cabro Muco Volcanic Unit (LCMV): Above the upflow region this unit is host to the vapour dominated zone (Figure 3.14) and is therefore dominated by acidic conditions and clay alteration of zones 1 and 2 (Milodowski *et al.*, in prep.) (Figures 3.13 a-h). (The acidic conditions are related to increased levels of condensed volcanic gases that have partitioned to the vapour zone during boiling at the top of the liquid-dominated zone). The standard deviations for the average densities of the stratigraphic units within each well are highest for the LCMV (Table 3.4), notwithstanding the Pumice Unit. Conversely, the standard deviation of the inter-well average density of this unit is less (Table 3.4). This confirms the assumption, necessary in the later modelling stage, that the lateral variation in the overall density of this unit is less than the local vertical variation.

Much of the variation can be attributed to clay alteration, together with lithological differences between the andesites and the tuffs. Strongly altered sections show gradual density boundaries between tuffs and the underlying Cabro Muco Andesite Unit (e.g. PGM-1 and PGM-5 in Figures 3.13 a and d). The intensity of alteration is a maximum at PGM-1, where much of the upper 400 m is heavily replaced. In wells PGM-1, 2, 10 and to a lesser extent in PGM-5 the density decreases with depth in the LCMV, whereas the percentage of clay alteration increases. This confirms that the clay is a low density form, probably water-rich smectite, in agreement with the alteration zone stratigraphy described above (Milodowski *et al.*, 1988).

For the gravity models in Sections 3.6 and 3.7 the average density of 2.09 Mg m^{-3} has been used for the general LCMV, but for the detailed models over the borefield a lower density of 1.93 Mg m^{-3} was used for the central part of the argillic zone; this is the average wet density of the argillic, lower part of the LCMV in PGM-1 (see Figure 3.13 a and Appendix 3C).

The Cabro Muco Andesite Unit (CMA): Clay mineral alteration continues down into the CMA and the related inverse relationship between alteration intensity and grain density is particularly clear for the CMA in PGM-1 and 3 (Figures 3.13 a and c). As for the overlying LCMV this suggests that the replacement assemblage was deposited in, or above, the boiling zone (Figure 3.13). Generally, density is greatest in the least altered, central part of this lava sequence. The slight lateral variation in density (Table 3.4) can be explained either lithologically - lower density at PGM-12 where there is a 100 m intercalation of lithic tuff (Figure 3.13 g) - and/or by diverse alteration - the PGM-11 CMA has been partially altered to chlorite and therefore has the highest density (Figure 3.13 f), whereas clay alteration at PGM-3 has lowered the density. Higher temperature forms of alteration have permeated into the lowermost CMA above the main upflow zone (PGM-1, 2 and 11 are in this situation and have some of the highest CMA densities, Figures 3.13 a, b, f and 3.14 and Table 3.4).

For the gravity models, the average wet density of 2.40 Mg m^{-3} was used for most of the CMA, but 2.25 Mg m^{-3} was used for the low density uppermost CMA in the southern borefield (PGM-3 and PGM-12, Figures 3.13 c, g and 3.14 and Table 3.4).

The Pumice Unit (PUM): The identification of the extremely low average density of this unit ($\rho_w = 1.58$) was very important for the interpretation of the negative gravity anomaly in the centre of the caldera, close to PGM-15; the only well in which the Pumice Unit was drilled. The low density is solely due to the nature of the primary lithology, a pumice-rich tuff, and neither alteration intensity or rank are high (Figure 3.13 h). The unit is porous, even on the cuttings scale, and the cuttings from ~400 m depth in PGM-15 had a lower density than water (Figure 3.13 h, and Table 3.3). An additional porosity is assumed to have been lost during the drilling process and an estimated correction for 20% lost porosity has been made in Table 3.3. The stratigraphic boundary with the LCMV is redefined from the ELC (1986 a) position at 260 m depth in PGM-15 to 330 m, partially on the basis of the sharp change in density at this depth (Figure 3.13 h). This is because the lithic tuff immediately below 330 m depth has a high proportion of reworked pumice from the underlying pumice tuff (ELC, 1986 b).

The high standard deviation (0.45 Mg m^{-3}) of the average density of the Pumice Unit (1.58 Mg m^{-3}) is, not surprisingly, the maximum of all the stratigraphic units (Table 3.4). The Pumice Unit is only 250 m thick, as defined by this study (Chapter 2), with a depth to the top of 330 m. The density is a minimum in the central part of the drilled sequence (Figure 3.13 h). For the purposes of the gravity modelling the important density contrasts are lateral, not vertical and the unit has therefore been treated as one body with a density of 1.58 Mg m^{-3}, rather than several, thinner, overlapping bodies with different densities.

The Volcano-Sedimentary Unit (VS): During the re-examination of the borefield stratigraphy in Chapter 2, the Lava-Tuff Unit of ELC (1986 a) was considered as part of the overlying Volcano-Sedimentary Unit on the basis that both units comprised intercalated lavas and tuffs. To show any change in density across the supposed boundary, the density data were divided into a lower part (LT) and an upper part (VS) in Table 2.4 and Figures 3.13 a-h and 3.14, but certainly in PGM-5 and 10 there is no significant change. There is, however, a significantly higher average density in the LT at PGM-15 (+0.06 Mg m^{-3}, Figure 3.14 and Table 3.4), partly because of a higher proportion of lavas in the LT at PGM-15 (Figure 3.13 h), but there is also a slight positive correlation between total alteration (mostly clays) and density, suggesting that the clay fraction is denser here than in the overlying VS and certainly denser than in the shallower argillic zone.

The question of the difference between the cuttings and core densities: The density of most of the VS in PGM-2, 3 and 12 is only known from core measurements (Figure 3.14 and Tables 3.3 and 3.4). In most cases, the VS cores are from the deeper VS where the higher densities may genuinely be caused by dense alteration mineral assemblages; e.g. the 10-15% epidote (plus some chlorite content) at PGM-1, 2 and 11 correlates with high density (Figures 3.13 a, b and f). The densities of the core samples of all the other units, however, are mostly higher than cuttings densities from the same depth (e.g. in the upper VS in PGM-12, and also in the Ignimbrite Unit in PGM-5, Figures 3.13 g and d). Densities measured by ICE at different times from the same core also vary (e.g. core 5, PGM-2 and core 1, PGM-12, Table 3.3). The VS cores are made up of usually poorly consolidated lithic tuffs and therefore most of the low density material is not suitable

for core density measurements; thus the bias towards a higher core density may be the result of a selection bias. There is no such bias for the cuttings samples and thus the core densities should be higher. For example, the sample from core 5 in PGM-12, a lithic-rich tuff, (Figure 3.13 g) had a dry mass of 28 g (Table 3.3) and a grain density of 2.9 Mg m^{-3}; approximately equivalent to a 3 cm diameter spherical lithic which is less than the 4 cm maximum lithic size in the core (ELC, 1985 c). The grain density of 2.90 Mg m^{-3} measured by ICE is higher than the more common grain density of ~2.70 Mg m^{-3} for the unaltered exposures of andesite (Table 3.1), and cannot be explained by alteration as no significant quantities of dense alteration minerals (e.g. epidote or chlorite) have been noted (ELC, 1986 b). In summary, the question of the anomalously high density measurements by ICE of some of the cores remains at least partially unanswered. The density of the PGM-12 core 5 cannot be explained by secondary mineralogy and was therefore not included in the overall assessment of the density structure of the borefield.

The intra-well wet density variation of the VS is significant and therefore a number of densities have been defined for the VS for the purposes of the gravity models. The upper VS in PGM-12 is both lava-poor, porous and relatively unaltered, and therefore has the lowest density (2.15 Mg m^{-3}) as defined from the porosity corrected cuttings data; this should therefore be representative of the unaltered tuff-rich VS. The VS at PGM-15 is comparatively lava rich, but as a consequence of the lower alteration levels in PGM-15 the average VS density is lower here (2.29 Mg m^{-3}) than in the central borefield (where an average VS density of 2.40 Mg m^{-3} has been used). The PGM-15 VS density of 2.29 Mg m^{-3} is believed to be representative of the lava-bearing VS outside the geothermal area. The increased density of the lower (LT) part of the VS at PGM-15 (2.35 Mg m^{-3}) is similarly used for the deeper VS outside the borefield.

The Acidic Andesite Unit (AA): The density of this petrologically and lithologically homogeneous unit varies with both the porosity and alteration assemblages. The small % of clay alteration does not appear to have affected the AA cuttings density in PGM-2, 5 and 10, but may have lowered it in PGM-11 (Figures 3.13 b, d, e and f). The higher density of the deeper levels (cuttings and cores) of the AA in PGM-2, 10 and 11 again seems to be related

to increased levels of chlorite and epidote. The inter-well variation of the density of the AA is not significant (a standard deviation of 0.02 Mg m^{-3}, Table 3.4) and the average density of 2.50 Mg m^{-3}, as determined from the porosity corrected cuttings data, was used in the gravity models.

The generally higher density of the AA compared to the VS is an important lateral density contrast, significant in the gravity models.

The Ignimbrite Unit (IG): Cuttings samples from this thick, ubiquitous unit have only been recovered from PGM-5 and 15 but yield very homogeneous densities (standard deviations of only 0.03 and 0.04 Mg m^{-3}, Table 3.4). The core samples from PGM-5, 10 and 15, however, have significantly higher densities than the cuttings densities (e.g. cores 2 and 3 of PGM-5, Figure 3.13 d). The cores are from below the level of the cuttings data, however, (except core 2, PGM-5) and may therefore be related to either alteration or lithic bias, as explained above for the VS cores (the maximum lithic size and the alteration data are not given in the drilling reports for some IG cores, Table 3.3).

The unit average wet density of 2.46 Mg m^{-3} is based on the PGM-15 cuttings data (the most and the least altered data), and was chosen as the density of the Ignimbrite Unit away from the geothermal field for the gravity models. In the deeper parts of the north-eastern borefield, however, the gravity data suggested that the Ignimbrite Unit has a higher density (up to 2.65 Mg m^{-3}, Sections 3.6 and 3.7).

In summary, it has been shown that despite the high degree of alteration in parts of the field, the most important lateral change in density is lithological; between i) the low density Pumice Unit and both the Cabro Muco Andesite Unit and the Volcano-Sedimentary Unit, and ii) to a lesser extent between the Volcano-Sedimentary Unit and the Acidic Andesite Unit. It is shown below (Section 3.6) that the former density contrast is largely responsible for the inner negative gravity anomaly over the Guayabo caldera (Figure 3.8). In addition, the increase of density with depth in the high-T borefield can at least partially be attributed to the change from shallow low density argillic alteration to the high-T alteration mineral assemblages at depth. The high-T assemblages are also present at a shallower level in the

VS above the upflow region and this causes the lateral change in the tuff-rich parts of the Volcano-Sedimentary Unit. The local gravity high southeast of PGM-12, at the PGM-4 site, could therefore be modelled as a relict high-T area (cf. Section 3.7.2).

Before proceeding with the gravity models of this study, the resistivity models from previous studies of the MGP are presented, as these were integrated into the models of the previous and present gravity studies.

3.5 Previous Resistivity and Gravity Models

The objective of the initial ICE geophysical studies (synthesized by Duprat & Leandro, 1986) was to provide a structural sketch of the area of possible geothermal interest. High-T brines in porous reservoirs are commonly identified as a good conductors (e.g. the Broadlands field, New Zealand, Risk *et al.*, 1977) and therefore ICE geophysicists have concentrated on the interpretation of vertical electrical soundings to explore the Miravalles field. The vertical electrical soundings were modelled in turn by ICE and the resulting 1-D (vertical) apparent resistivity models were linked together to provide psuedo resistivity cross-sections of the survey area. The cross-sections are called geoelectric sections here, following the terminology of Kearey and Brooks (1984). Of particular interest to ICE was the extent of the rogue, low permeability, Acidic Andesite Unit (ELC, 1986 a) and any concealed structural lineaments (possible electrical discontinuities) that controlled the secondary (i.e. fracture-controlled) permeability (Chapter 2). The resistivity surveys did not therefore extend over the western and northern margins of the caldera, but were designed to investigate the eastern and southeastern high heat flow areas (the temperature gradients are shown in Figure 2.2 a and the geoelectric sections are located in Figure 3.17). In particular, the discovery of increased reservoir permeability in well PGM-12 (ELC, 1985 c, 1986 a and 1988) suggested that the geothermal field had significant potential to the south of the proven resource around the central and northern borefield. The high temperatures at PGM-11 (255°C, Figure 3.14, data from ELC, 1988) also suggested potential to the north of the borefield, provided that sufficiently permeable zones existed. Further geophysical studies were therefore carried out south of the La Fortuna-Cuipilapa area and in the Sitio Las Mesas

area (Leandro *et al.*, 1988; Geosystems, 1988 and Lezema *et al.*, 1988; located in Figure 3.17).

Figure 3.17 Geoelectric section location map. Sections selected for use in this study are; DL- sections from Duprat and Leandro (1986) and G- sections from Geosystems (1988) (see text). The outline of the shallow resistive basement, deduced from these and other geoelectric soundings not shown here, corresponds to the buried Acidic Andesite Unit. The main topographic features in the southern caldera margin area are shown, but for more geological detail see Figures 2.5, 2.7 and 2.9.

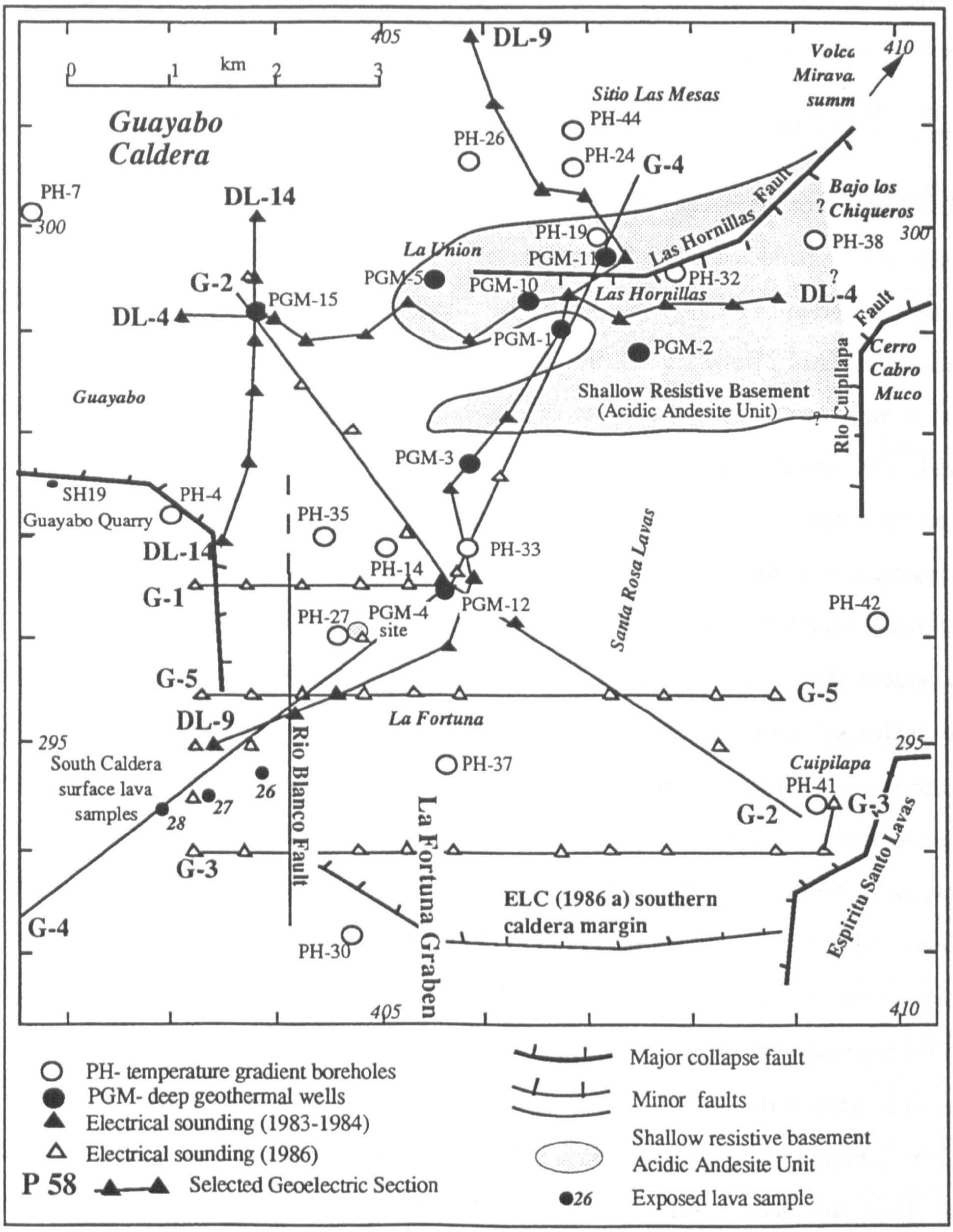

The labelling of the geoelectric sections in Figures 3.17, 3.18 and 3.19 is broadly consistent with the nomenclature used in the original ICE/ELC studies, but only a selection of the original range of sections were used in this study; hence the sections of Duprat and Leandro (1986) are DL-4, 9 and 14, and those of Geosystems are G-1, 2, 3, 4 and 5. The Geosystems sections also show gravity models, unlike those of Duprat and Leandro. The ordering of the G- sections in Figure 3.19 follows the geographical, north to south, order shown in the location map, Figure 3.17. Gravity profiles are shown in Figures 3.18 and 3.19 for comparison with the resistivity models; these and the gravity models of Geosystems (1988), shown on the G- sections (Figure 3.19), are discussed in Section 3.5.3.

3.5.1 Relationship between electrical conductivity, density and alteration mineralogy

During the drilling program at Miravalles, ICE conducted an electrical sounding survey at each borehole site; the 1-D resistivity inversion models were presented by Duprat and Leandro (1986). The resistivity models of Duprat and Leandro (1986) are shown in Figures 3.13 a-h in the right hand-columns, to enable a comparison with the borehole stratigraphy and alteration mineralogy described above and the density structure of this study. The objective of this section is to examine whether resistivity is related to the rock density; thereby justifying the use of the resistivity data to constrain the gravity models in Sections 3.6 and 3.7. In geothermal fields in general, however, the interpretation of resistivity data is not simple, and the bulk porosity, the conductivity of the pore fluid (air, vapour, fresh water or brine) and the proportion of conductive clay minerals are often the more important parameters that define the electrical conductivity (e.g. Duprat, 1987). A brief resumé of the hydrology of the Miravalles geothermal field was presented in Chapter 2 (Figure 2.2 b, for a full hydrology discussion see Chapter 5). During the discussion below, reference is made to the revised stratigraphy as discussed in Chapter 2. For details of the terminology of and relationships between the units, refer to the geological map in Figure 2.5 and the stratigraphic cross-sections of Figures 2.9 and 2.10.

Figure 3.18 Selected geoelectric sections of Duprat and Leandro (1986) with gravity added for comparison. In DL-4 gravity decreases with increasing depth to the resistive basement, not always the case in other sections. There is a partial relationship between lithology and conductivity (e.g. the CMA, AA and IG are resistors), but porosity, clay alteration and the presence of hot brine (Layer 3 conductor in the VS) are also important. See text for full discussion (Section 3.5).

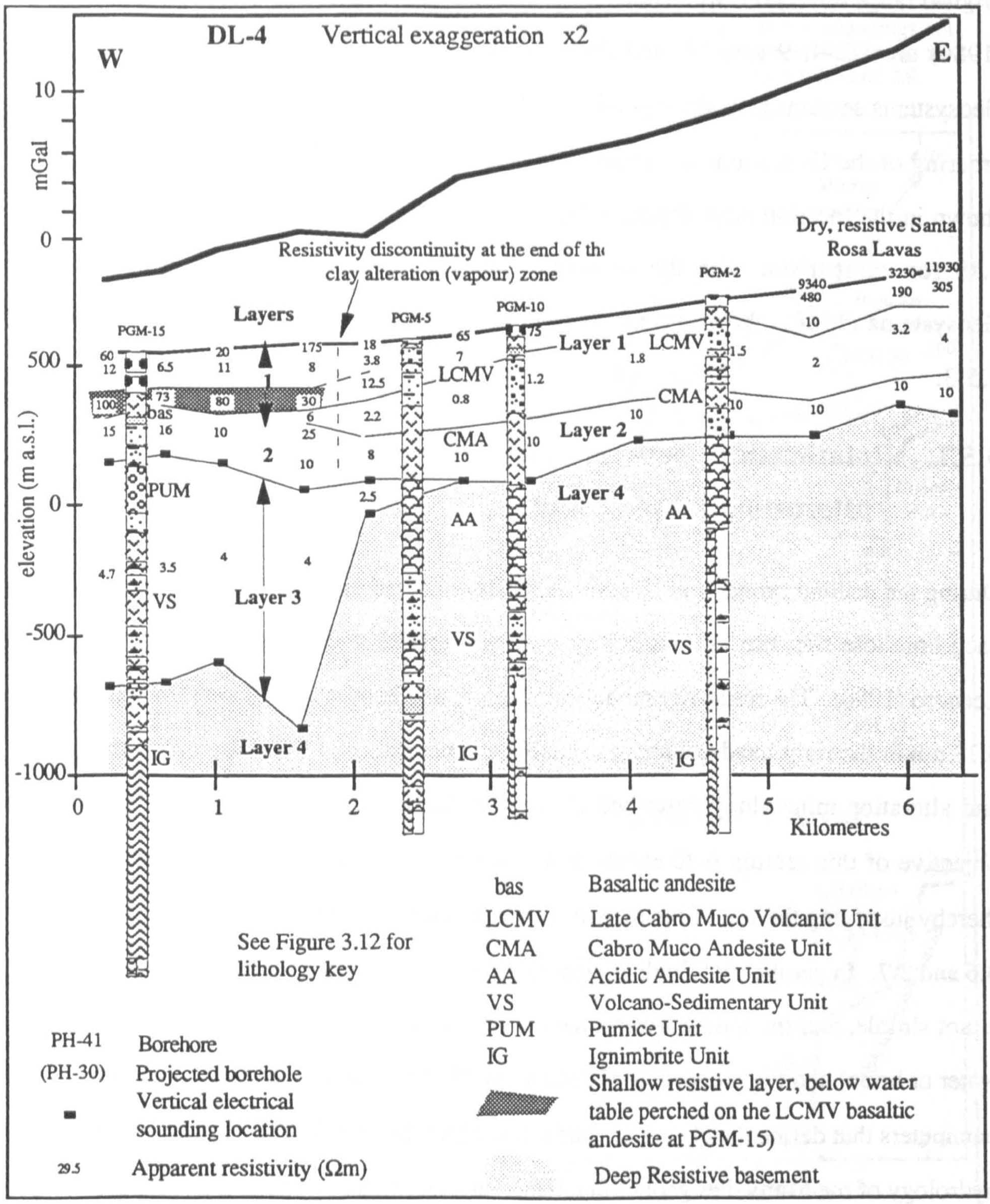

Duprat and Leandro (1986) suggested that the MGP area is characterised by four distinct resistivity layers within a (locally) more complex resistivity structure. These are shown in relation to the drilled stratigraphy and the wet rock density in section DL-4 (Figure 3.18, location in Figure 3.17 and the details for all wells are given in Figures 3.13 a-h).

Figure 3.18 (continued). In section DL-9 there is no correlation between the depth to the resistive basement and gravity, but there is in G-4 (Figure 3.19). DL-14 shows the shallowing of the resistor (basaltic andesite) towards the caldera margin.

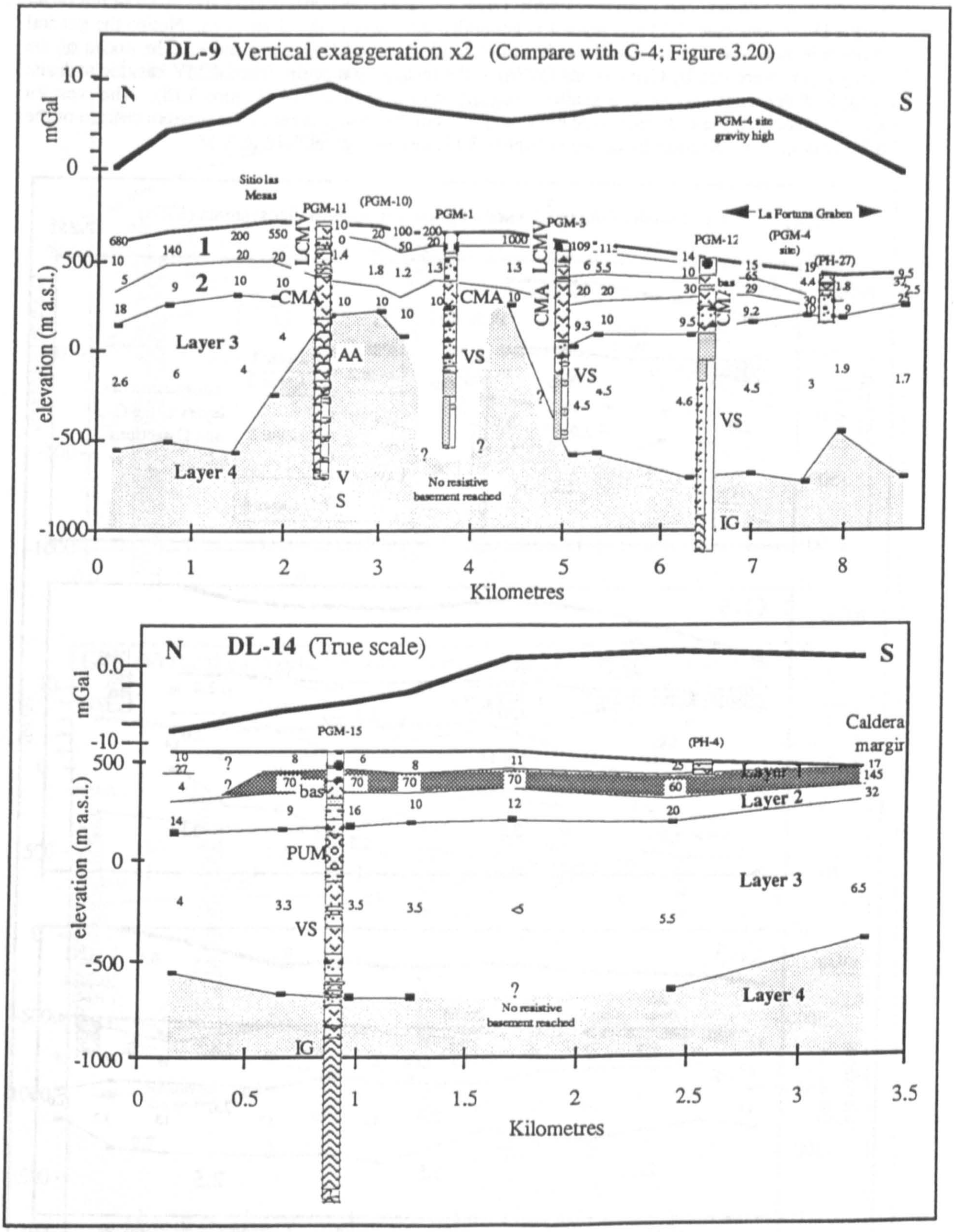

Figure 3.19 Gravity and geoelectric combination models, G-1 to G-5, of Geosystems (1988) and Leandro *et al.* (1988). Sections are arranged in geographical order (Figure 3.17). Resistivity and density values of the Geosystems (1988) models are shown. The G- section layers differ from the D-section layers of Duprat and Leandro (1986): Layer 2 of the G-sections incorporates much of the Layer 1 of the D-sections (see G-1) and layer 4 is generally shallower in the G-sections. Notice the general relationship between depth to resistive basement and observed Bouguer gravity. The nodes of the density layers were tied by Geosystems (1988) to the resistivity models. The LCMV basaltic andesite at PGM-15 does not appear as a shallow resistor in G-2 as in DL-14 (Figure 3.18). The western shallow resistors in the G-sections are either dry tuffs or the low-K lavas of the western margin of the La Fortuna graben. Section locations in Figure 3.17, key in Figures 3.13 & 3.18.

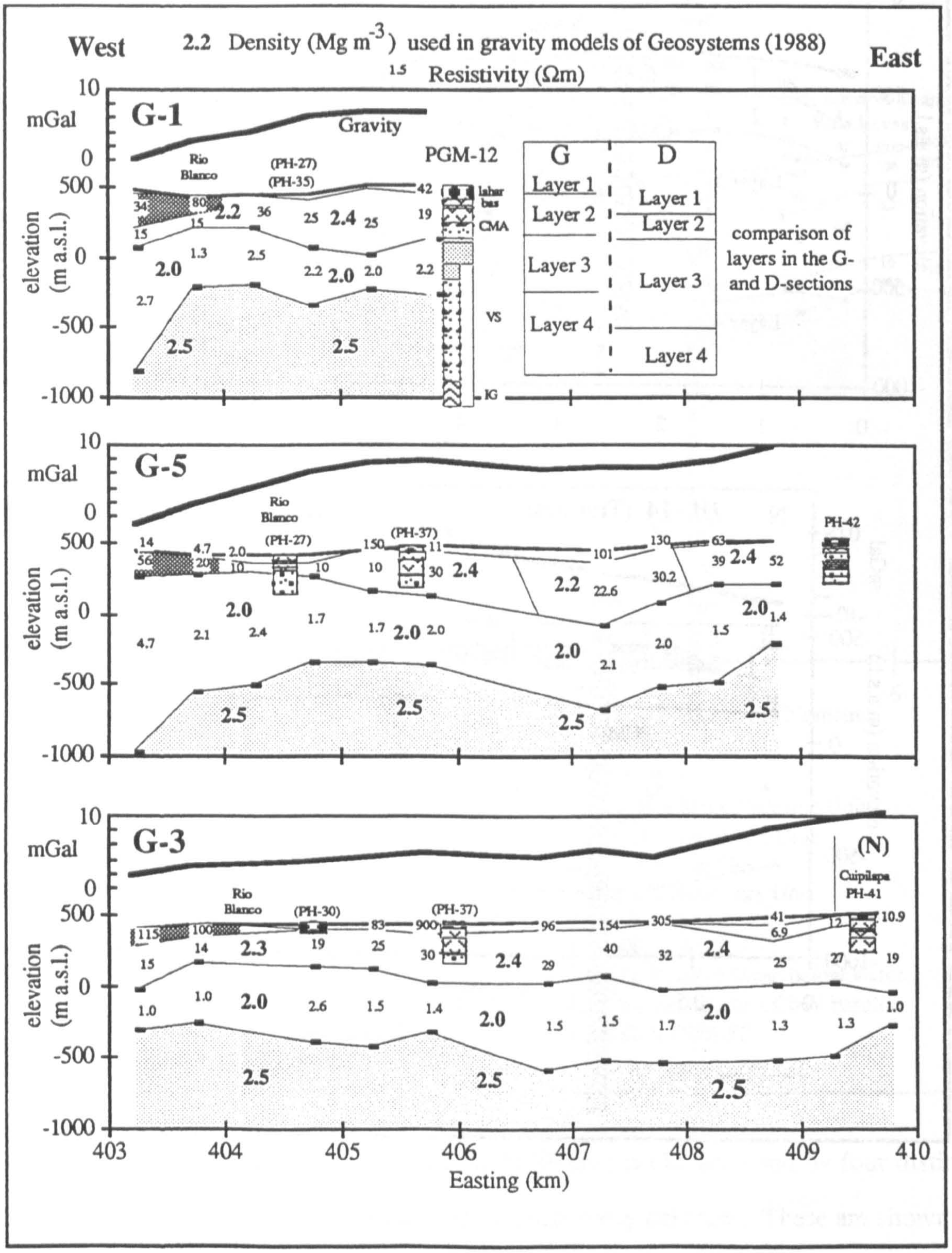

Figure 3.19 (continued) In section G-4 the deep conductor, Layer 3, shallows to the south of PGM-12, coincident with the PGM-4 site gravity high and a heat flow anomaly; this is believed to reflect rising geothermal brine over the basement high (cf. gravity model Profile BB, Figure 3.23).

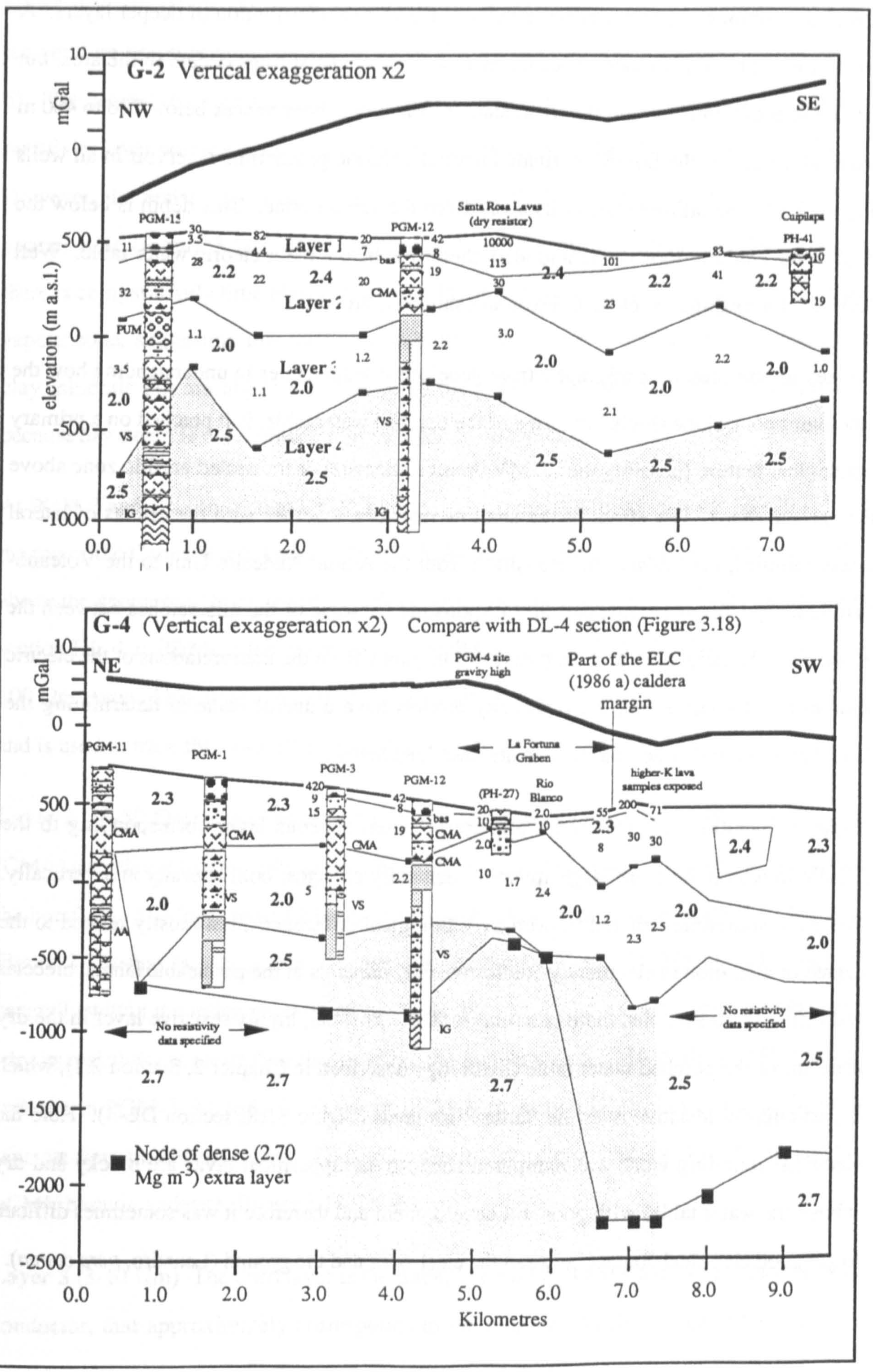

Shallow but extensive resistive layers, particularly the dry strata above the perched water table, have inhibited accurate interpretation of the vertical distribution of deeper layers. A perched water table is invoked because meteoric and acidic springs occurs in the area, but within the geothermal system the hydrostatic gradient only commences below 200 to 400 m depth, at the top of the liquid-dominated neutral-chloride geothermal reservoir in all wells (Figure 3.14), including those wells away from the vapour zone. This depth is below the level of the caldera floor rivers and also, therefore, below the meteoric water table. Well PGM-15, for example, is close to lakes and saturated ground.

The key to interpreting stratigraphy from geoelectric sections lies in understanding how the lithologies control the fluids. In terms of the perched water table, is it perched on a primary lithological feature (possibly the LCMV basaltic andesite) or the sealed argillic zone above the vapour zone? The effect of the shallow resistors, together with the effects of lateral discontinuities, particularly the transition from the Acidic Andesite Unit to the Volcano-Sedimentary Unit, is at least partially responsible for some of the mismatches between the actual drilled stratigraphy and the pseudo-stratigraphy from the interpretations of the electric soundings. Nevertheless, the resistivity models have a useful value in determining the lateral continuity between blocks and are described below:

Layer 1 (5-5000 Ωm) This is an uppermost heterogeneous layer corresponding to the LCMV in which there are large apparent resistivity changes, both laterally and vertically. These are sometimes related to primary lithological differences, but mostly related to the degree of alteration to electrically conductive clay minerals in the permeable lahars, breccias and tuffs. In all sections, there is a thin (< 50 m) surficial, highly resistive layer in the dry zone above the perched water table (hydrology described in Chapter 2, Section 2.1), which is particularily resistive over the Santa Rosa lavas (Figure 3.18, section DL-4). Here the electrical sounding work was hampered because the uppermost lavas are blocky and dry (above the water table) with poor soil development and therefore it was sometimes difficult to get good electrical contact between the electrodes and the ground (Leandro, *pers comm*).

Below the perched fresh water table the pore spaces and open fractures of the LCMV are either dry, or steam saturated in the vapour zone (vapour zones defined from the temperature-pressure borehole logs of ELC, 1988, a full discussion is presented in Chapter 5). The pervasive clay alteration in the vapour zone correlates very well with a thick low resistivity layer within Layer 1, except in PGM-2 (details of alteration in Figures 3.13 a-h). However, the resistivity of this zone rises towards PGM-3 and 5, the outer limits of the vapour zone (Figure 3.14), where there is still significant clay alteration. Furthermore, there is comparatively little clay alteration in PGM-2, but a thick low resistivity layer in the vapour zone; suggesting that the low resistivity values are not only due to the conductive clay minerals but are apparently related to the presence of vapour. This is surprising, because *dry* steam is not considered to be a good conductor.

At PGM-3 and 12, (on section DL-9; Figure 3.18), there is a resistive layer (20-30 Ωm) at the top of the Cabro Muco Andesite Unit (CMA) which corresponds to the part of the CMA above the geothermal brine together with the overlying basaltic andesite in the LCMV. On section DL-4 at PGM-15 the dense basaltic andesite ('bas' in Figure 3.18) corresponds to a 100 Ωm layer. This distinctive resistive layer can be identified in other vertical soundings and is used to trace this andesite in the southern caldera area (Section 3.4.2).

Layer 2 (10-50 Ωm) The more pristine lowermost lavas of the Cabro Muco Andesite Unit (CMA) are related to a more homogeneous and less resistive layer that can be traced across the borefield. The lowermost CMA has a relatively uniform density (average 2.40 Mg m^{-3}, Figure 3.14) that is higher than the average for the LCMV (2.09 Mg m^{-3}), but now is generally within the saline geothermal reservoir (Figures 3.13 c-g). This key factor explains why its resistivity is lower than that of either the non-saturated CMA or the LCMV basaltic andesite in PGM-3, 12 and 15. South of PGM-3, in section DL-9, Layer 2 is difficult to separate from the resistive parts of Layer 1 reflecting the closer spacing of the CMA and the LCMV basaltic andesite (Figure 3.18, DL-9).

Layer 3 (3-10 Ωm) The third layer is the thick, laterally pervasive and homogeneous main conductor, that approximately corresponds to the medium density Volcano-Sedimentary

Unit, (VS) and the low density Pumice Unit (PUM) but, more importantly, to the region of geothermal brines in the fractured porous reservoir. Porosity is a significant factor, because the thick, low porosity Acidic Andesite Unit (AA) reservoir rocks have a high resistivity (Layer 4) and it is this contrast between the VS and the AA that makes the resistivity technique ideal for mapping the boundary between them. Furthermore, the resistivity of Layer 3 does not increase with the temperature fall-off towards the cooler margins of the borefield (PGM-12 and 15) in the models of Duprat and Leandro (1986), but remains consistent within the VS; the technique is therefore a useful mapping tool for the VS.

Layer 4 The fourth layer is the resistive basement (> 50 Ωm; symbol 'R' in Figures 3.13 3.18 and 3.19), below which no further low resistivity layers could be identified. This correlates with the basal parts of the VS or the top of the Ignimbrite Unit (IG) (Figure 3.18), and probably reflects a drop in porosity due to the increased cohesivity of the matrix of the basal VS lavas and the IG unit as compared to the VS generally.

The geoelectric sections have been very effective in mapping the extension of the AA Unit in the north (Figure 3.17) where its presence is delineated by the steep shallowing of the resistive basement at the expense of Layer 3 in the north-eastern borefield (Figure 3.18). The outline of this shallow basement suggests that the AA Unit does not extend northwards beneath Sitio las Mesas (Figure 3.17 and Section DL-4, Figure 3.18). This has important implications for estimates of permeability to the north of the borefield, as the deep conductor identified within the permeable borefield (the VS) is also present in the Sitio las Mesas area.

In summary, the relationship between resistivity, density and alteration is complicated. In the argillic zone, alteration is responsible for both the low density and the generally coincident low resistivity which may be further related to the presence of the vapour zone above the deep geothermal brine. Within the liquid-dominated geothermal reservoir the porosity, and to a lesser extent the brine temperature, determine the resistivity. Lavas within the main geothermal reservoir are only responsible for high resistivity values where they are impervious (parts of the LCMV basaltic andesite, AA and the deep VS). The medium resistivity of the CMA lavas increases further above the brine level, again showing the relationship between resistivity and the fluid salinity.

As the AA Unit can be mapped as the resistive basement it is possible to justify fully the choice of a low porosity for the AA that was made to estimate the wet densities from the cuttings densities above (Section 3.5.1). It is important that although the resistivity models have shown the continuation of the drilled AA to the east, towards the Bajo Los Chiqueros area, the electrical soundings have not identified any bodies of the AA to the north of those drilled in the northern borefield.

3.5.2 Mapping the southern stratigraphy using geoelectric sections

The southern caldera margin as defined by ELC (1986 a) is located south of the town of La Fortuna but also includes part of the western margin of the La Fortuna Graben as shown in Figure 3.17. The DL-4 section described above and the more recent sections, G-1, 3, 4 and 5 (Figure 3.19) suggest a broad continuity of the PGM-12 stratigraphy across this part of the ELC margin, in agreement with the revised stratigraphy proposed in Chapter 2. The sections considered are located in Figure 3.17 relative to the main morphotectonic features and the boreholes to which the resistivity layers have been tied. The resistivity models of both the Duprat and Leandro (1986) and the Geosystems (1988) studies are similar, but the 1-D inversions were conducted separately and because the interpretation of resistivity data is non-unique, the two studies are not strictly compatible and have therefore been described separately. An example of the discrepancy can be seen near PGM-12 where the depth to the resistive basement is some 400 m deeper in DL-9 than G-4 (Figures 3.18 and 3.19). Furthermore, Layer 2 in the G-sections is much thicker than the same layer in the DL-sections (see G-1 at PGM-12, Figure 3.19) and incorporates the lower part of the DL- Layer 1. Layer 1 in the G- sections is therefore thinner and dominantly resistive. The shallow conductor identified within Layer 1 of the DL- sections (~ the argillic/vapour zone) is equivalent to the thin, 9 Ωm, conductor near PGM-3 in G-4 (Figure 3.19) but this conductor is not considered in the southern borefield G- sections selected for this study. Layer 3, corresponding to the deep conductor is broadly equivalent to the VS in both models, but Layer 4, the resistive basement, is generally shallower in the G- sections, as described below.

It is difficult to map the CMA and LCMV stratigraphy accurately using resistivity layer profiling because of the control of fluids, porosity and alteration products on the resistivity as described above; tentative correlations only are possible. In Layer 1, outside the argillic zone, the most important conductor is the perched water table. At PGM-15, PGM-12 and areas outside the argillic/vapour zone, the LCMV basaltic andesite appears to support the perched water table (G-2, Figure 3.19; DL-9 and DL-14, Figure 3.18).

The Geosystems (1988) sections G-1, 2 and 5 (Figure 3.19) show a 100-200 m thick near-surface resistive layer (~30-100 Ωm) west of the Rio Blanco fault (related to the western margin of the La Fortuna graben (Figure 3.17), interpreted as the expansion of the Layer 1 resistor at the expense of layer 2 (in G- 5 layer 2 is missing altogether). This is similar to the resistive character of the 100 m thick basaltic andesite at PGM-15, which shallows to the south along section DL-14 (Figure 3.18), close to the western end of G-1 (Figure 3.19). Section G-2 shows that layer 2 at PGM-15, which includes the LCMV basaltic andesite, can be traced to not only the LCMV basaltic andesite at PGM-12, but also to the CMA. Section G-4 suggests that the base of Layer 2 thins rapidly from PGM-12 towards PH-27, but then expands again at the western margin of the La Fortuna Graben. This suggests that the LCMV and the CMA can be traced from PGM-12 to the exposures of the higher-K lavas outside the western margin of the La Fortuna Graben. The stratigraphic study (discussion in Chapter 2) showed that the LCMV basaltic andesite was *younger* than the higher-K lavas, but the lower CMA was a possible equivalent, in agreement with the resistivity data.

To the southeast of PGM-12 there is a general continuity of the resistivity layers in sections G-2, 3 and 5 suggesting a broad similarity of reservoir properties, but to the southwest of PGM-12 (section G-4) there are discontinuities as described above and, furthermore, in sections G-1, 4 and 5 the depth to the deep conductor increases to the west and southwest. The shallowing of the deep conductor at PH-27 (the PGM-4 site) in section G-4, before the graben margin, is important because it coincides with an area of increased heat flow and chloride springs (Figure 2.2 a). This area is also characterised by a gravity high and it is suggested below (Section 3.7.2) that the brine upwelling is a response of the outflow plume to a shallowing of the basement in the PGM-4 area.

The depth to the resistive basement in sections DL-4, DL-9, G-1 and G-5 is approximately mirrored by the Bouguer gravity; suggesting that the high resistivity of the basement reflects an increase in density (i.e. increased cohesivity and reduced porosity). The relationship does not, however, hold true for all the other sections (e.g. DL-14) and the density-resistivity relationship is more fully examined below (Section 3.7).

3.5.3 Previous gravity models

In this section the most recent, previous, gravity studies of Duprat and Leandro (1986), Leandro *et al.* (1988) and Lezema *et al.* (1988) are discussed as an introduction to the gravity models of this study.

Duprat and Leandro (1986): Nettleton profiles in the borefield area were used by Duprat and Leandro (1986) to deduce a value of 2.2 Mg m^{-3} for the uppermost, topography-related densities; thereby defining the gravity data reduction density used. The Duprat and Leandro (1986) BCG map (area outlined as MGP survey in Figure 3.1) identified a strong east-west gravity gradient across the geothermal field. (The gradient was stronger than the gravity gradient in Figure 3.8 of this study because of the westwards decrease of elevation combined with the low reduction density used, 2.20 Mg m^{-3}). They believed the cause of the gravity gradient was the shallowing of dense basement to the east, in agreement with the eastward shallowing of the resistive basement (DL-4, Figure 3.18). On the basis of nine density determinations of cored samples from the wells (Table 3.3, 1986 values) and 2-D modelling, Duprat and Leandro (1986) suggested that the gravity data could be modelled in terms of the density contrast between the AA and the VS. They therefore suggested that the gravity high south of PGM-12, at the proposed site for PGM-4 and the shallower resistive basement here (DL-9, Figure 3.18) was due to a buried AA body. The detailed density analysis and gravity models of this study, however, dispute this conclusion (Section 3.6), and a shallower basement is proposed beneath the PGM-4 site area. The density and gravity analyses have further shown that the general borefield gradient is only partially related to the AA-VS density contrast and instead the most important features are: i) that the gravity gradient (Figure 3.8) over the eastern borefield is largely due to a dense intrusion in the Bajo

Los Chiqueros area and ii) the caldera-centred gravity low is related to the very low density Pumice Unit, identified in PGM-15 (Section 3.6). The gravity data across the caldera margin was not considered by the models of Duprat and Leandro (1986).

The more recent gravity models of Geosystems (1988) (reviewed by Leandro *et al.*, 1988), were included in this review in the geoelectric sections G-1 to 5 shown in Figure 3.19. The resistivity and gravity models of Geosystems (1988) are compatible because the depths to the nodes of the gravity model polygons were defined from the 1-D inversions of the vertical electric soundings. The only degree of freedom in the models therefore, was the density of the polygons; three basic density layers were used:

Upper Unit Medium density cap (2.2-2.4 Mg m^{-3}) corresponding to the resistivity Layers 1 and 2; stratigraphically equivalent to the CMA and LCMV.

Middle Unit Low density layer (2.0 Mg m^{-3}). The deep conductor (<5 Ωm, Layer 3), the porous VS.

Lower Unit Dense basement (2.5 Mg m^{-3}). The resistive basement; the IG, AA and lowermost VS.

In addition to these layers, a deeper high density layer (2.70 Mg m^{-3}) was added in section G-4 to account for the gravity high at the PGM-4 site (different to the AA body proposed by Duprat and Leandro, 1986) and the high to the north of PGM-11. The inversion technique has resulted in a density stratigraphy that is sometimes at variance with the densities measured in this study (for example, compare the densities in Figure 3.14 with those in section G-4; Figure 3.19). In particular, the density of VS had to be kept low by Geosystems (1988) to explain the gravity minima to the west and south of the borefield, and thus the thickness of the VS largely controlled the calculated gravity. The low density of the Pumice Unit of PGM-15 (Figure 3.14) was not modelled and, if included, would have obviated their need for the great thickness of VS west of the borefield. The main conclusion of the Geosystems models was that the basement defined by both the resistivity and the gravity models must become deeper from the borefield to the area outside the ELC (1986 a) southern caldera margin. Leandro *et al.* (1988) reviewed the Geosystems (1988) models and tentatively suggested i) that the Ignimbrite Unit may have a regional nature and ii) the

caldera wall unit volcanics were contemporaneous with the Plio-Pleistocene Monteverde Formation (and possibly the Aguacate Group volcanics) exposed 20-25 km to the southeast (Figure 2.3). This tentative revision required that the caldera wall lavas were related to post-IG stratigraphy, possibly the AA and VS.

Lezema *et al.* (1988) also produced two dimensional gravity models; using a similar technique to Geosystems (1988), but a different density stratigraphy. They recognised that the exposed caldera wall lavas were sometimes underlain by breccias (as discussed in Chapter 2) and therefore the caldera wall unit did not necessarily have a high density. They presented two alternative geological models to explain the gravity models of the southern caldera margin, shown here in Figure 3.20.

Model I (Figure 3.20) was an attempt to satisfy the traditional ELC (1986 a) caldera model and shows the caldera wall unit modelled with a density contrast of -0.2 Mg m^{-3} with the both the uppermost intra-caldera CMA and the LCMV. The VS and the IG had positive density contrasts of 0.25 Mg m^{-3} and 0.65 Mg m^{-3} respectively. To explain the apparent continuity of the deeper gravity bodies across the caldera margin, however, Model I required pre-caldera bodies of a similar density structure to the younger intra-caldera VS and IG bodies; a coincidence that was considered unlikely by Lezema *et al.* (1988).

In their alternative proposal, Model II (Figure 3.20), the lowermost drilled unit, IG, had a regional nature (as suggested by the Geosystems, 1988 models, Leandro *et al.*, 1988) and, in addition, the exposed pre-caldera lava-breccia stratigraphy, the Guayabo Unit (defined by Lezema *et al.*, 1988), was correlated with unspecified parts of the LT, VS and AA. The Guayabo Unit model still had an implicit requirement, however, of a downthrow within the caldera of some 500-1000 m; depending which of the intra-caldera lavas correlated with the caldera scarp lavas. Furthermore, Lezema *et al.* (1988) did not explain why the Guayabo Unit in the caldera walls had a negative density contrast of - 0.5 Mg m^{-3} with the supposed intra-caldera equivalents of the VS, LT or AA. Finally, neither Model I or II could explain the caldera-centred gravity low identified during this study (Figure 3.8).

Figure 3.20 A summary sketch of the two alternative gravity models proposed by Lezema *et al.* (1988). Model I is an attempt to satisfy the structural evolution hypothesis of ELC (1986 a), where the exposed caldera wall material pre-dates all the drilled stratigraphy. In the alternative scenario, model II, the IG and lower VS are part of the pre-Guayabo caldera stratigraphy; similar to the models proposed by this study. However, the density discontinuities at the caldera margin in both models I and II are difficult to explain geologically.

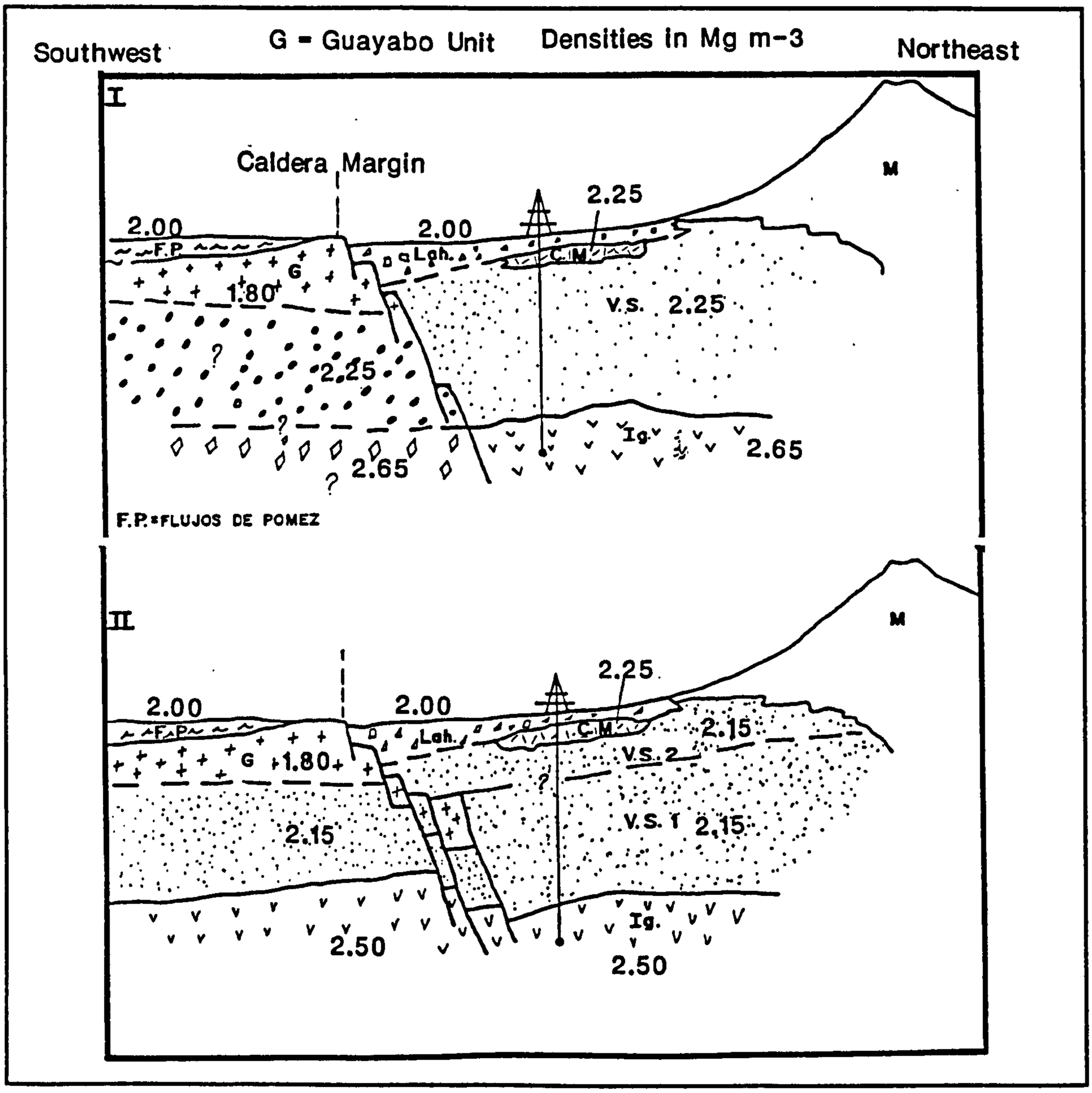

3.5.4 Summary of the results of previous geophysical studies

The traditional caldera evolution model of ELC (1986 a) as outlined in Chapter 2 (Figure 2.7) requires a downthrow of over 2200 m at the southern margin, between the base of the Ignimbrite Unit at PGM-12 and PGM-15 (the IG base must be below the 1650 m b.s.l. downhole limit of PGM-15) and the higher-K lavas to the west of the La Fortuna graben (exposed at 500 m a.s.l., shown as sample locations in Figures 2.5 and 3.17). This should be seen as a significant geophysical discontinuity given the contrast in physical properties

between the lavas of the pre-caldera stratigraphy (as mapped by ELC, 1986) and the largely poorly consolidated caldera fill of the VS in PGM-12 and PGM-15.

Geoelectric sections (Figures 3.18 and 3.19), however, showed a continuation of the main conductive layer, broadly equivalent to the VS, across the western margin of the La Fortuna graben (location in Figure 3.17) and show an *increase* in the depth to the resistive basement (identified within the lower VS, and the top of the AA). In the La Fortuna area, gravity decreases westwards over the pre-caldera strata rather than increasing as would be expected over a denser lava sequence (Figure 3.8). The gravity models of Geosystems (1988) and Lezema *et al.* (1988) suggested the continuity of the VS and the IG across the caldera margin, but correlations between the intra- and extra-caldera stratigraphy could not be derived from the simple models and still implied a 500-1000 m downthrow on the caldera margin, at variance with the geoelectric sections across the southern caldera margin. One of the objectives of the gravity models of this study is to provide sufficiently thorough geophysical models that are tied to the stratigraphy by the detailed density study.

3.6 The Gravity Models of this Study

The resistivity data, the alteration data, the new density data and the revised stratigraphy are all incorporated into the gravity models of this study. Six cross-sectional profiles have been chosen (located in Figures 3.7 and 3.8 and 3.21) to model the Miravalles geothermal field, the Guayabo caldera and Volcán Miravalles, and also to provide a general model of the Guanacaste Arc. All the profiles have been networked to tie into the constrained deep borehole density structure, either directly through a borehole, or by projecting the borehole data a short distance onto the profile along the gravity contour that passes through the borehole (Figures 3.7, 3.8 and 3.21). The interpretation of the structure of the Guayabo caldera is presented, following a description of the modelling technique. The modelling concentrated on the extrapolation of the well constrained borefield density structure to the central caldera, the caldera margins, and the extra-caldera areas, to test the revised caldera stratigraphy proposed in Chapter 2. A model is also proposed for the deep structure of the Volcán Miravalles/Bajo Los Chiqueros to explain the BLC High. Finally, in Section 3.7, the detailed structure of the geothermal field is examined in terms of the alteration-related

density changes that were important during the evolution of the field and what the implications are for the gravity high at the PGM-4 site.

Figure 3.21 Parts of the AA, BB, CC, WSE and VV gravity profiles of this study are shown relative to the PGM- and PH- boreholes, the DL- and G- geoelectric sections of Duprat and Leandro (1986) and Geosystems (1988) and the main structural features in the southeastern caldera area. (For geological detail see Figures 2.5, 2.9 and 2.10).

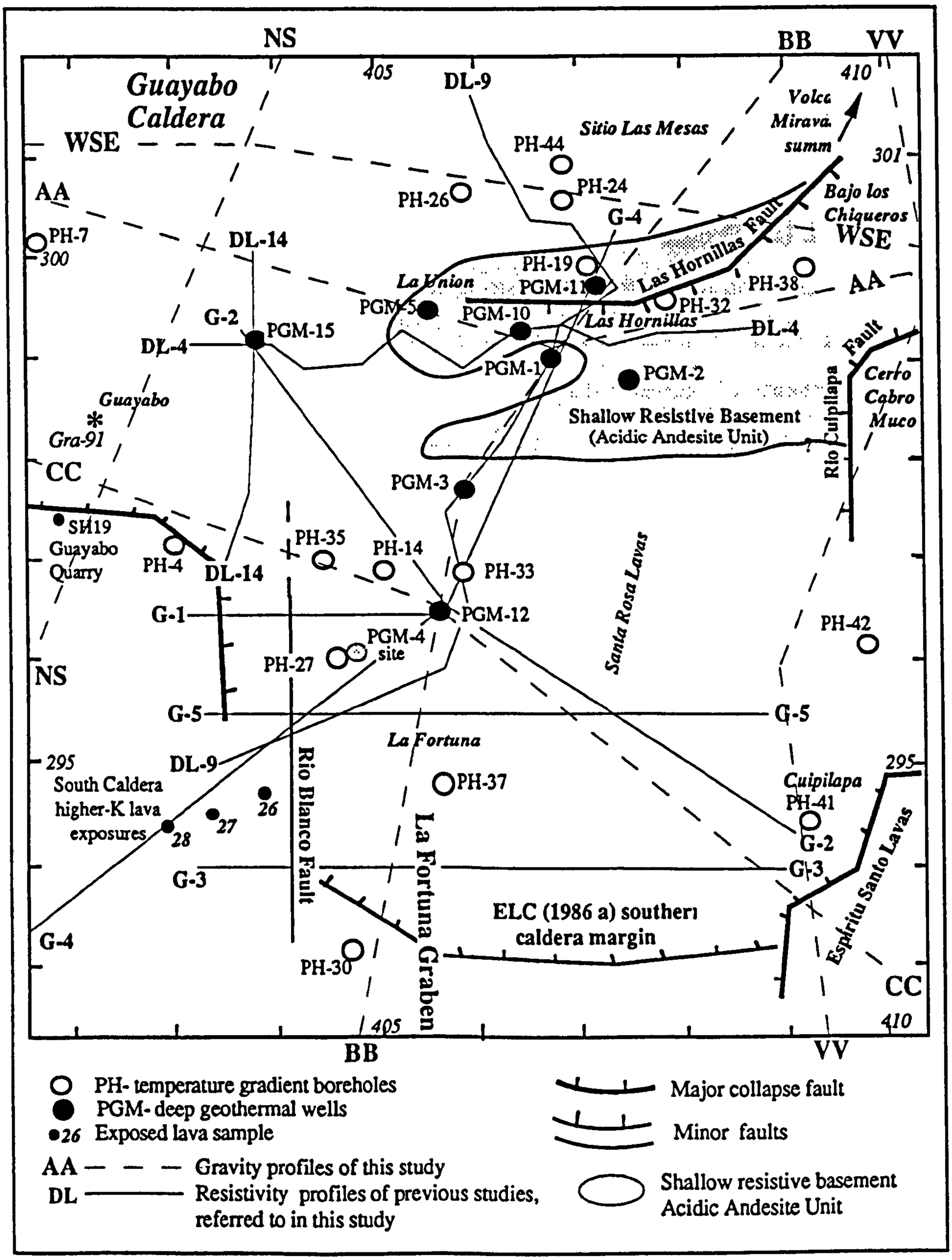

3.6.1 The modelling technique

The modelling program: An interactive two-and-a-half dimensional (2.5-D) gravity modelling program, GRAVMAG, designed by the British Geological Survey (Pedley, 1991) was used. 2.5-D programs differ from conventional 2-D programs in that they allow the operator to define the length of the model polygons in the unseen dimension (called the half-strike length). This is essential when building a picture of the three dimensional nature of bodies in volcanic environments (e.g. calderas, sub-volcanic intrusions and volcanic edifices). GRAVMAG permits a single value only for the half-strike length in *both* strike directions.

During modelling, the buried geology is constructed from of a series of user-defined interlocking polygons, each with a unique density and half-strike length. GRAVMAG models the polygons in terms of their density contrast with a chosen background density and allows the terrain to be defined. By choosing the reduction density as the background density, terrain-related anomalies that are the result of a wrong choice of reduction density (Section 3.1.2) are correctly modelled. Polygons can be defined within existing polygons; this is useful when modelling a body of limited half-strike length but which has a significant density contrast with the surrounding, more extensive medium that is itself anomalous compared to the background density. GRAVMAG is a highly interactive program, allowing the shape, density and half-strike-length of the individual polygons, and thus the calculated gravity, to be changed easily.

Referring to features of all the models: the background density of 2.40 Mg m^{-3} (the BCG reduction density) is less dense than the chosen basement density of 2.65 Mg m^{-3}; i.e. the basement has a positive density contrast in the model. All profiles have been modelled to the same depth (2.1 km below sea level) to prevent false shifts in the computed gravity between models due to inconsistent basement thickness (other than above this base level). Indeed, most of the observed gravity anomalies could be modelled in terms of density contrasts within this uppermost level of the crust. It is possible to model polygons below the baseline depth, providing that the density contrast with 2.40 Mg m^{-3} is the *effective*

contrast between the polygon and the basement density at this depth. For example, a sub-baseline intrusive body with an actual density of 2.80 Mg m^{-3} has a real density contrast of + 0.15 Mg m^{-3} with the basement density of 2.65 Mg m^{-3}, but in the model it must be given an effective density of 2.55 Mg m^{-3} in order to generate the correct effect on the calculated gravity.

The zero value in the gravity models has to be defined to ensure the compatibility of different profiles. The original BCG zero value was chosen arbitrarily as the value at the base station Gra-91 (Section 3.1.2) and therefore the observed gravity in all the profiles, although internally related to this defined zero, is floating in a regional context. In modelling it is therefore feasible, and quite acceptable, for the computed gravity profiles to be displaced from the observed data provided this is by a constant value *along the entire lengths* of the model profiles. Moreover, this displacement must be equal for all profiles and, for the purposes of this study, has been defined as the difference between the gravity calculated from the well constrained density structure at PGM-15 (modelled to a depth of 2.1 km b.s.l.) and the observed BCG value. The calculated difference was 4 mGal and this difference was then subtracted from all the gravity profiles. The gravity relative to the IGF network can be computed by re-calculating the gravity relative to the IGF value at Gra-91. (The gravity at Gra-91 has an absolute gravity value of 978099.55 mGal; tied to the IGF network by ICE, as discussed in Section 3.2.4, see also Appendix 3A).

The orientation, setting and objectives of the gravity models: A description of the objectives and location of each of the gravity profiles is given before the discussion of the results. The seven models AA, BB, CC, WSE, CM1, NS and VV (Figures 3.21 to 3.28) are located on the BCG maps (Figures 3.7 and 3.8) and the location of the intersections of the models AA, BB and CC with both the boreholes and the profiles of previous resistivity studies in the geothermal area are shown in Figure 3.21.

Gravity and topographic data were read off the BCG contour maps (Figures 3.7 and 3.8) and the 1:50,000 scale Costa Rica topographic maps at regular 0.25 km intervals for the shorter profiles AA and BB, 0.5 km intervals for profiles CC and VV, and at irregular intervals of approximately 1 km for the longer profiles WSE and NS. The spacing of data

for CM1, the detailed traverse across the Cerro Mogote margin of the caldera (coincident with part of Profile WSE), matches the actual gravity station spacing; between 50 and 200 m over the actual margin (stations located in Figure 3.8). The irregularity of the data spacing for the longer profiles is a result of the uneven gravity station coverage, particularly outside the caldera (Figure 3.1). The gravity data of the longer profiles are generally well-constrained within, and close to, the caldera, especially in the MGP area, but the station density falls off outside the caldera; the station locations are marked on the general location map (Figure 3.1) and the BCG maps (Figures 3.7 and 3.8). The station coverage is least dense in the areas to the north and to the south of the caldera, but although the gravity gradients at either end of the NS profile must be considered as estimates of the true gradient, they are perfectly adequate for the purposes of the general interpretation required of these areas. The implications of the uneven data coverage are discussed below, during the examination of the individual profiles.

The colour coding of the models is consistent (where possible) between models and refers to particular stratigraphic units, but the numbering identification system is unique for each model. The polygon densities (Mg m^{-3}), the stratigraphic nomenclature and the polygon half-strike lengths (km) are given in the polygon listings on the page opposite each model. During the discussion of the models, much reference is made to the geology and the inter-well stratigraphy of Chapter 2 and therefore the key diagrams, Figures 2.5, 2.9 and 2.10, have been included as 'pull-outs'.

The Profiles AA, BB and CC (Figures 3.22, 3.23 and 3.24) were designed i) to model the effects of geothermal alteration (cf. Section 3.7) using the very well controlled density structure of the borefield (density summary in Figure 3.14) and ii) to test the revised structural model for the evolution of this part of the caldera as proposed in Chapter 2. Profiles AA and BB are comparable to the east-west and north-south stratigraphic sections (Figures 2.9 a and b) through the borefield, and Profile CC traverses the southern borefield, intersecting PGM-12 only (locations in Figure 3.21).

The individual models are now presented in turn, followed by a discussion of the results.

Profile AA: Profile AA (Figure 3.22, true scale, location in Figures 3.8 and 3.21) is a detailed model of the eastern caldera margin, from the Guayabo Low near the centre of the caldera, through three boreholes, to the Bajo Los Chiqueros (BLC) High to the east. To intersect the BLC High, Profile AA changes direction at PGM-1 (Figure 3.8), but the angle of incidence to the gravity contours does not change significantly, except *at* the turning point, and therefore the dog-leg is not thought to affect the overall results of the model. In addition to the three boreholes intersected by Profile AA, PGM-2 and PGM-15 were projected onto Profile AA along the computed gravity contours (by distances of 0.3 and 1.5 km respectively, Figures 3.8 and 3.21). PGM-15 is therefore shown on Profile AA only 0.5 km from PGM-5 instead of the true 1.5 km, as shown in the stratigraphic cross-section (Figure 2.9 a).

Figure 3.22 (opposite) Detailed west-east Borefield Profile (AA) Guayabo Low to BLC, true scale (loc. Figure 3.8 and 3.21). Much of the gradient is due to the BLC intrusion, but the gradient steepens over the PUM boundary, which must be closer to PGM-5 than PGM-15. Densification increases within the VS towards the BLC intrusion, but the effects are difficult to separate east of PGM-2 (see density/temperature profiles in Fig. 3.14 and lithologies in Fig. 2.9 a).

No.	Stratigraphic Unit-Lithology	Density	HSL
1	LCMV (general)	2.09	3
2	PUM	1.58	2
3	CMA	2.40	3
4	AA (PGM-5 and 10)	2.51	1
5	AA (PGM-2)	2.48	2
6	Upper VS (PGM-15)	2.29	3
7	VS (PGM-1, 5 and 10)	2.40	3
8	IG	2.46	5
9	Lower VS (PGM-15)	2.35	5
10	Dense VS and IG (PGM-2)	2.56	3
11	BLC Intrusion/densification	2.65	3
12	Argillic/vapour zone (PGM-5, 10 and 1)	1.93	1
13	Basement	2.65	10
14	AA east of BLC intrusion	2.48	2
15	BLC intrusion core	2.75	1
16	Deep BLC intrusion	2.50	5
17	Santa Rosa/Volcán Miravalles lavas	2.50	1

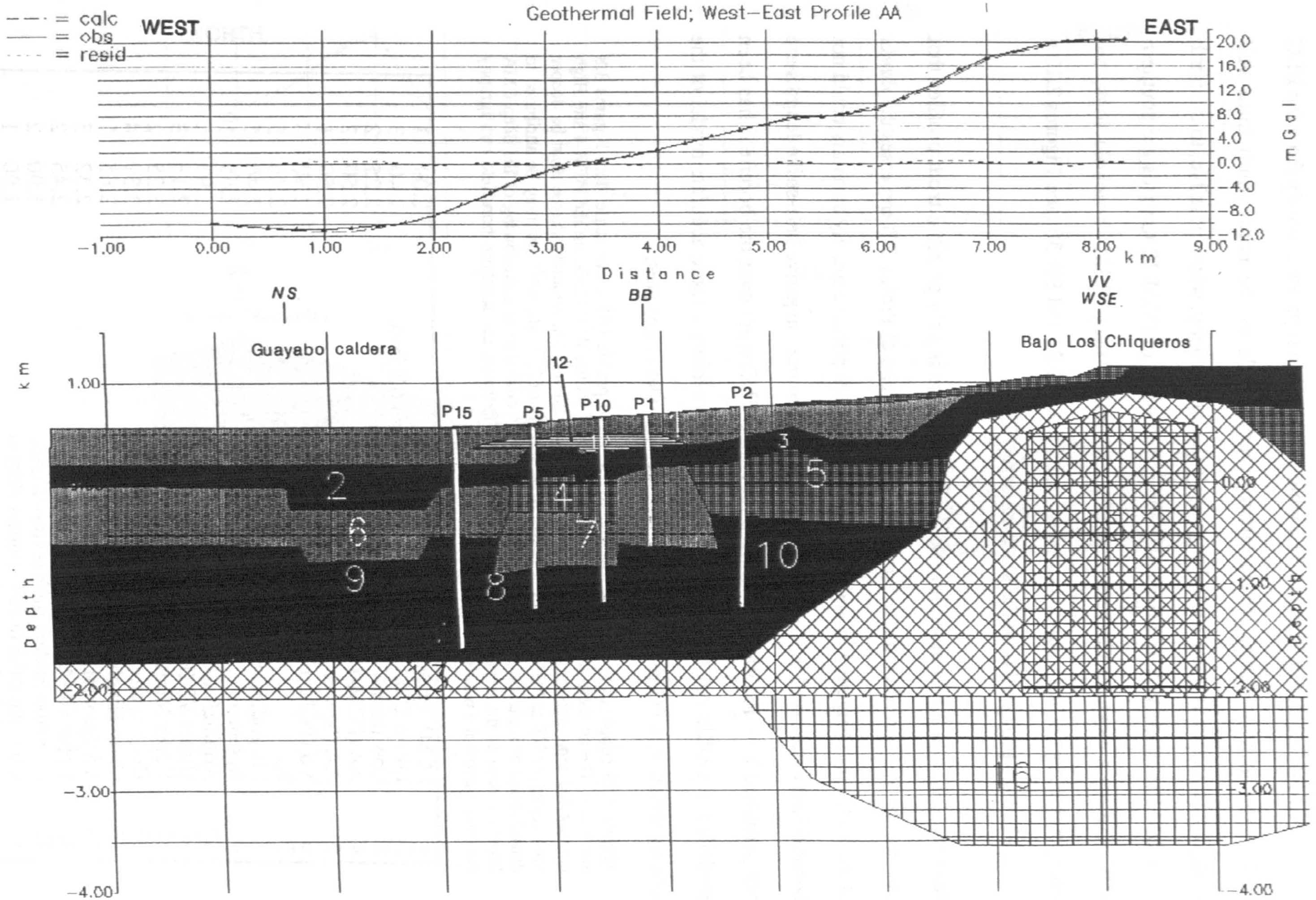
= calc
= obs
= resid
Geothermal Field; West–East Profile AA
WEST
EAST
20.0
16.0
12.0
8.0
4.0
0.0
−4.0
−8.0
−12.0
mGal
−1.00
0.00
1.00
2.00
3.00
4.00
5.00
6.00
7.00
8.00
9.00
km
Distance
NS
BB
VV
WSE
Guayabo caldera
Bajo Los Chiqueros
12
P15
P5
P10
P1
P2
1
2
3
4
5
6
7
8
9
10
13
1.00
−2.00
−3.00
−4.00
Depth
km

Profile BB: Profile BB (Figure 3.23, true scale, location in Figures 3.8 and 3.21) was designed to model the southern borefield, in particular the gravity high over the proposed site for PGM-4 (located in Figure 3.21), which clearly is a separate anomaly from the BLC High. The gravity model BB is directly comparable to the north-south intra-well stratigraphic section (Figure 2.9 b) but extends the stratigraphy, where possible, to the north of PGM-11 towards Volcán Miravalles and to the south of PGM-12 towards the southern part of the La Fortuna Graben. In addition to the deep PGM- borehole logs, the stratigraphic logs of the temperature gradient wells, PH-37 and PH-30 (see Figures 2.10 a and 3.21) were projected onto the southern part of BB.

Accurate 2-D and 2.5-D modelling of BCG anomalies is only possible from profiles that traverse the BCG maxima and minima. The northern end of Profile BB traverses the *flanks* of the BLC High (Figure 3.8) and therefore the northern positive gravity anomaly could not be modelled in terms of the 'off-profile' BLC dense source; negative half-strike lengths are not permitted by GRAVMAG. The effect of the BLC High over the borefield has been modelled in profile AA (Figure 3.22) and this is therefore a more accurate model of the density structure at PGM-1, 2 and 11 than the BB model in this area.

Figure 3.23 (opposite) Detailed north-south Borefield profile (BB), true scale (loc. Figures 3.8 and 3.21). The northern model is complicated by the off-profile BLC High, but the PGM-4 site High is modelled separately as a shallowing of the dense basement. The anomaly source must be deeper than the upper VS at PGM-12 (bright green, low density of 2.15 Mg m^{-3}) and may be attributed to densification or intrusion (see text). The PH-30 High is modelled as a shallowing of the deep CMA lavas (brown) at the expense of the CMA tuff, but otherwise the southern borefield stratigraphy continues across the margin.

1	LCMV (general)	2.09	3
2	Lower CMA and Southern caldera higher-K lavas	2.40	3
3	Low density CMA lavas and CMA tuff	2.25	2
4	AA (PGM-11)	2.50	2
5	AA (between PGM-3 and 12)	2.50	1
6	VS (PGM-11, 1 and 3)	2.40	4
7	IG	2.46	5
8	Miravalles lavas	2.40	5
9	Basement	2.65	10
10	Argillic/vapour zone	1.93	1
11	Upper VS (PGM-12)	2.15	3
12	Upper Miravalles lavas	2.25	2
13	Deep hydrothermal VS (PGM-12)	2.39	4
14	Cerro Hinchada ridge intrusion	2.65	1
15	VS (general)	2.32	3
16	Upper CMA and LCMV lavas	2.45	2
17	Guayabo caldera tuffs (extra-caldera)	1.90	2
18	Guayabo caldera tuffs (intra-caldera)	1.90	1
19	Ignimbrite Unit southern extension	2.46	5

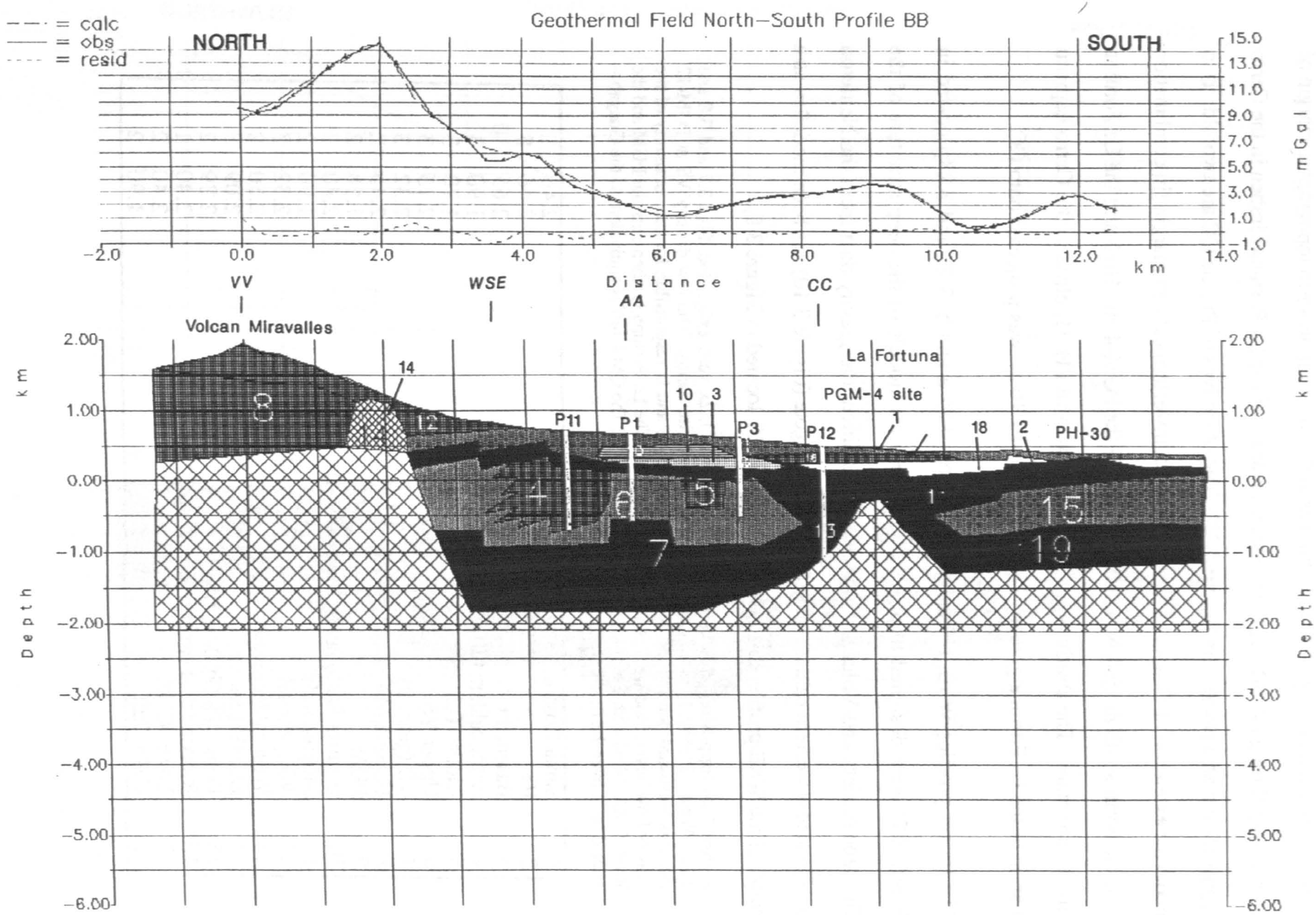
= calc
= obs
= resid
Geothermal Field North–South Profile BB
NORTH
SOUTH
15.0
13.0
11.0
9.0
7.0
5.0
3.0
1.0
-1.0
mGal
-2.0
0.0
2.0
4.0
6.0
8.0
10.0
12.0
14.0
km
VV
WSE
Distance
AA
CC
Volcan Miravalles
La Fortuna
PGM-4 site
14
10
3
P11
P1
P3
P12
1
18
2
PH-30
12
8
4
6
5
7
15
19
13
2.00
1.00
0.00
-1.00
-2.00
-3.00
-4.00
-5.00
-6.00
Depth
km

Profile CC: Profile CC (Figure 3.24, located in Figures 3.7, 3.8 and 3.21) is a west-northwest to east-southeast traverse from San Jorge, west of the caldera, across the southern caldera margin gravity low (but parallel to the southwestern topographic margin of the caldera), through PGM-12, to the eastern margin of the La Fortuna Graben in the Cerro Espiritu Santo area (located in Figure 3.21). The objectives of Profile CC are twofold: i) to model the extension of Guayabo Low over the southwestern caldera margin (in combination with the north-south model, NS) and ii) to model the PGM-4 site High and the La Fortuna Graben structure. The stratigraphy of the shallow well PH-41, close to the Cerro Espiritu margin of the La Fortuna graben (Figures 3.21 and 2.10 a), was projected onto CC.

The longer profiles WSE, NS and VV (Figures 3.25 a and b, 3.27 and 3.28; located in Figure 3.7) were designed to provide more general models of the deep structure of the Guayabo caldera and Volcán Miravalles. In addition, the gravity data from the Nettleton profile across western caldera margin at Cerro Mogote (Figure 3.10) has been modelled as a detail of the WSE profile; Profile CM1 (Figure 3.26, located in Figure 3.8).

Figure 3.24 (opposite) Southern caldera profile (CC), 2x vert. exag. (loc. Figs 3.7 and 3.8 and 3.21), West - PGM-12 - Southeast, San Jorge to Espiritu Santo. The low density VS at PGM-12 thickens westward beneath the southern caldera margin and is responsible for the continuity of the gravity Low beyond the western margin of the PUM. The La Fortuna Graben cuts the PUM and the lower CMA, filled with the upper CMA and the LCMV. The CMA tuff is equivalent to the Guayabo-related tuffs over the flanks of C. Espiritu Santo.

1	Santa Rosa Lavas	2.40	1
2	IG	2.46	5
3	Basement	2.65	10
4	Extra-caldera tuffs	1.90	3
5	Biotite Tuff (San Jorge)	1.70	3
6	Upper VS	2.15	3
7	VS (general)	2.32	3
8	Upper CMA and LCMV lavas	2.45	2
9	PUM	1.58	2
10	Espiritu Santo lavas (lower CMA)	2.40	2
11	Mogote tuffs	1.90	2
12	VS (general)	2.32	3
13	West caldera wall lavas	2.50	2
14	LCMV (general)	2.09	3
15	Dense VS (PGM-12)	2.39	2
16	Rincon lavas (west of San Jorge)	2.40	1
17	Lower CMA	2.40	2
18	CMA Tuff	1.90	2

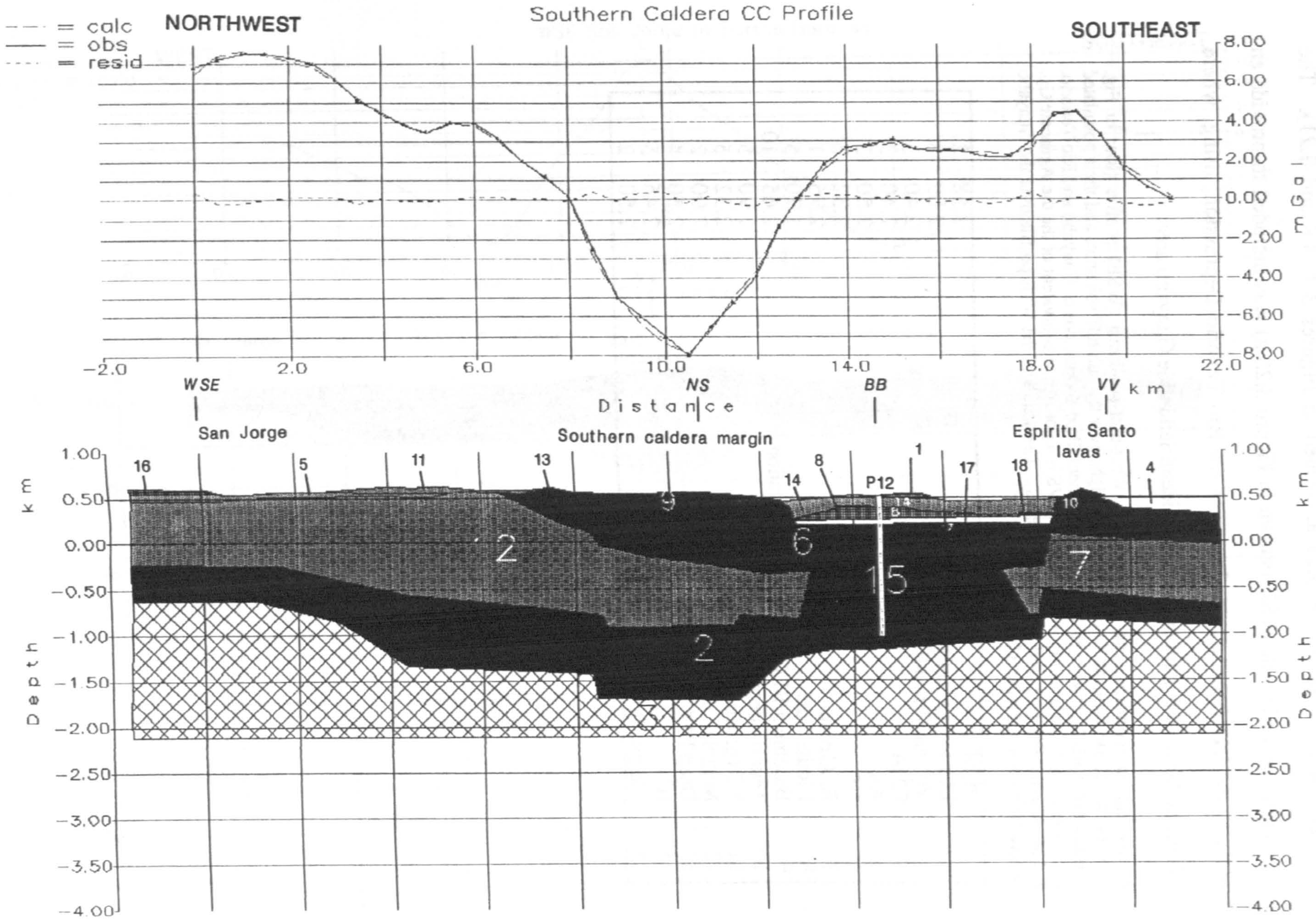
= calc
= obs
= resid
NORTHWEST
Southern Caldera CC Profile
SOUTHEAST
8.00
6.00
4.00
2.00
0.00
−2.00
−4.00
−6.00
−8.00
mGal
−2.0
2.0
6.0
10.0
14.0
18.0
22.0
WSE
NS
BB
VV
km
Distance
San Jorge
Southern caldera margin
Espiritu Santo lavas
16
5
11
13
14
8
P12
1
17
18
4
10
1.00
0.50
0.00
−0.50
−1.00
−1.50
−2.00
−2.50
−3.00
−3.50
−4.00
km
Depth
2
6
15
7
3

Profile WSE: The 43 km long WSE profile extends from San Jorge, through the Guayabo caldera, Bajo Los Chiqueros and the Rio Tenorio Depression to Tierras Morenas (shown at true scale in Figure 3.25 a, located in Figures 3.7, 3.8 and 3.21). The southeastern part of Profile WSE (shown in Figure 3.25 a) was included to provide an elementary model of the gravity low over the Rio Tenorio Depression, using, where possible, similar density structures to those identified in the Guayabo area.

Figure 3.25 a (opposite and b, overleaf) West-east-southeast (WSE) profile (loc. in Fig. 3.7), true scale, San Jorge to Tierras Morenas. Highs over the sub-tuff volcanics and their postulated intrusions (e.g. BLC), lows over the tuff and sediment filled depressions of Guayabo and Rio Tenorio. (Guayabo caldera details in Figure 3.24 b). The VS is a postulated equivalent of the the Aguacate Gp. and Monteverde Fm. (exposed at Tierras Morenas). The details of the WSE profile over the Guayabo caldera are shown in Figure 3.25 b.

1	PUM	1.58	2
2	LCMV (general)	2.09	3
3	Volcán Miravalles lavas	2.40	3
4	CMA	2.40	3
5	AA	2.50	3
6	VS	2.32	3
7	BLC core	2.75	1
8	Biotite Tuff	1.70	5
9	Basement/BLC intrusion/densification	2.65	10
10	Tenorio depression tuffs	1.90	5
11	VS (general) Tenorio	2.32	5
12	Mogote tuffs	2.00	2
13	Deep BLC intrusion	2.50	4
14	IG	2.46	5
15	Mogote lavas	2.50	2

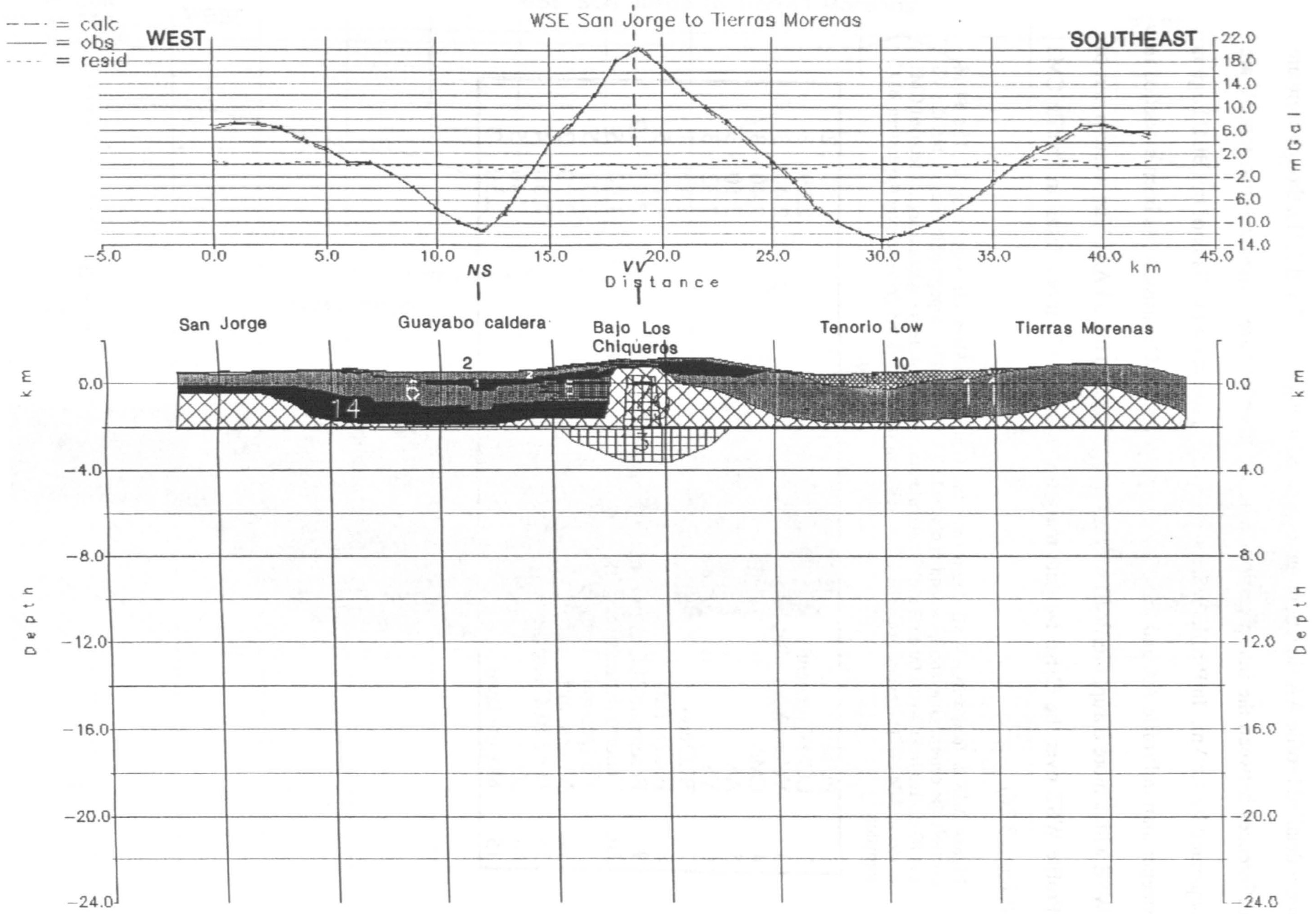
= calc
= obs
= resid
WEST
WSE San Jorge to Tierras Morenas
SOUTHEAST
22.0
18.0
14.0
10.0
6.0
2.0
−2.0
−6.0
−10.0
−14.0
mGal
−5.0
0.0
5.0
10.0
15.0
20.0
25.0
30.0
35.0
40.0
45.0
km
NS
VV
Distance
San Jorge
Guayabo caldera
Bajo Los Chiqueros
Tenorio Low
Tierras Morenas
2
10
14
km
0.0
−4.0
−8.0
−12.0
−16.0
−20.0
−24.0
Depth

The part of Profile WSE over the Guayabo caldera and the BLC High is shown in Figure 3.25 b (x2 vertical exaggeration). The eastern part of the caldera model is comparable to the more detailed Profile AA (locations are compared in Figures 3.8 and 3.21), though there are differences between the interpretations over the borefield area where the two models are separated by 1.5 km. In Profile WSE, the gravity gradient on the flank of the BLC High is steeper than in Profile AA and therefore the proposed BLC intrusion has been modelled in WSE with a more abrupt (vertical) western margin than in model AA. The western part of Profile WSE over the Cerro Mogote margin is modelled in more detail in Profile CM1 (Figure 3.26).

Figure 3.25 b (opposite) WSE detail over the Guayabo caldera (2x vert. exag.). The PUM controls the central Guayabo Low, and is confined 2 km within the topographic margin, but the VS and IG drilled in PGM-15 (at 13.3 km) is modelled *across* the western caldera margin (detailed CM1 model in 3.24 c). The extent of the IG is not well controlled, nor is the gradient over the eastern BLC intrusion.

1	PUM	1.58	2
2	LCMV (general)	2.09	3
3	Volcán Miravalles lavas	2.40	3
4	CMA	2.40	3
5	AA	2.50	3
6	VS	2.32	3
7	BLC core	2.75	1
8	Biotite Tuff	1.70	5
9	Basement/BLC intrusion/densification	2.65	10
10	Tenorio depression tuffs	1.90	5
11	VS (general), Tenorio	2.32	5
12	Mogote tuffs	2.00	2
13	Deep BLC intrusion	2.50	4
14	IG	2.46	5
15	Mogote lavas	2.50	2

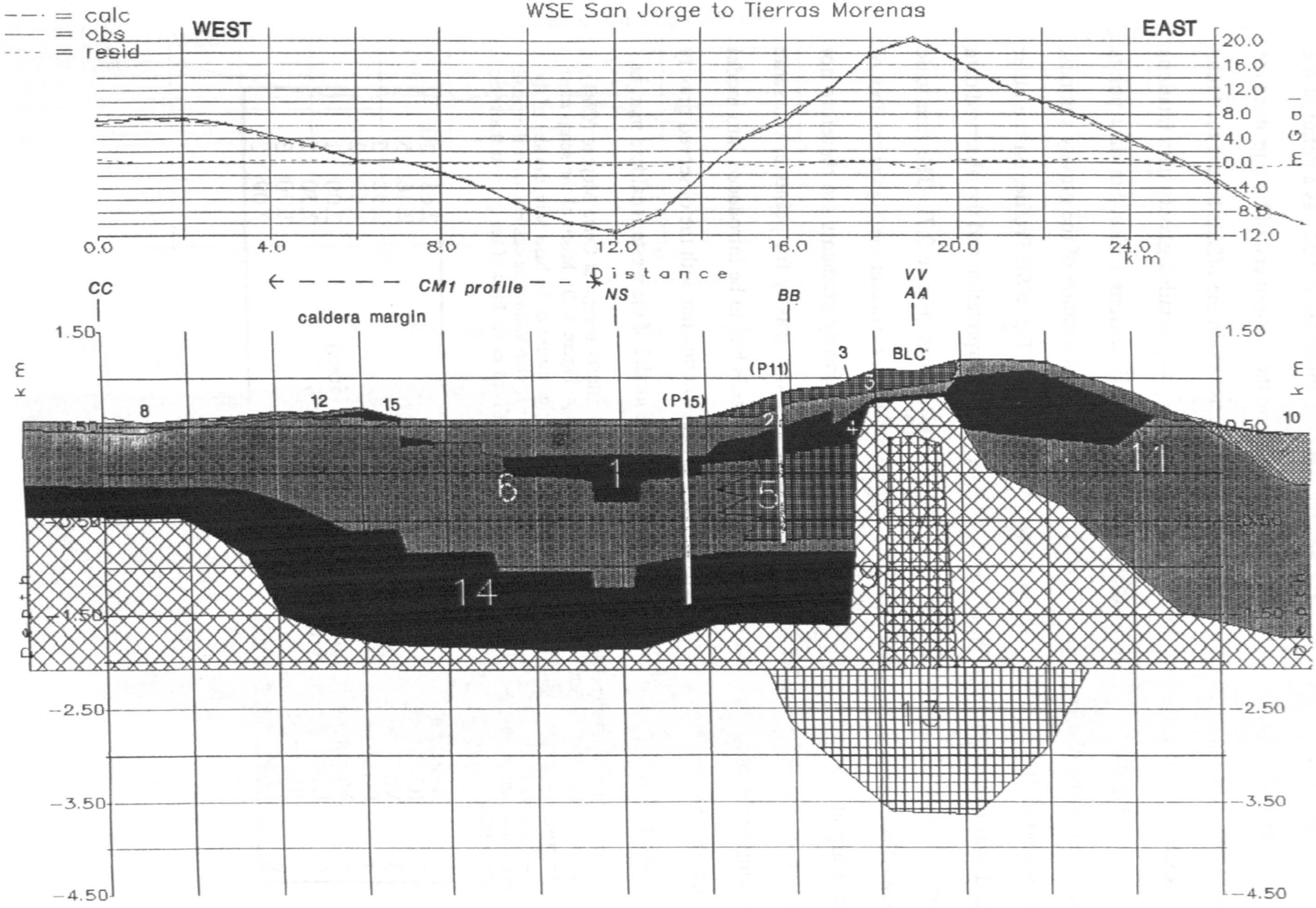
= calc
= obs
= resid
WSE San Jorge to Tierras Morenas
WEST
EAST
20.0
16.0
12.0
8.0
4.0
0.0
-4.0
-8.0
-12.0
mGal
0.0
4.0
8.0
12.0
16.0
20.0
24.0
km
Distance
CM1 profile
CC
NS
BB
VV
AA
caldera margin
1.50
km
(P11)
3
BLC
(P15)
8
12
15
2
4
5
10
0.50
6
1
11
14
9
13
Depth
-1.50
-2.50
-3.50
-4.50

Profile CM1: Profile CM1 (Figure 3.26, true scale, stations located in Figure 3.8) is directly comparable to the Nettleton profiles shown in Figure 3.10. The closely spaced data set over the caldera margin at Cerro Mogote has been modelled in CM1 as a detail of the coincident Profile WSE (the horizontal distances from the western end of both profiles are the same). The major objective of model CM1 is to constrain the offsets across the faults associated with the western caldera margin, using the very detailed gravity data (stations located in Figure 3.8). The spacing between the CM1 stations varies, but data points indicated on the observed profile coincide with the actual location of the gravity stations, spaced 50 to 100 m apart over the topographic margin. The WSE Profile, on the other hand, was modelled to provide a *general* trans-caldera interpretation and the observed data were taken at 1 km intervals from the 1 mGal contour map (Figure 3.7). The fine scale anomalies shown on the CM1 observed gravity profile (in particular the high at the foot of the scarp at 7.0 km) and the better resolution of the gravity gradients are therefore not shown on the WSE profile. As GRAVMAG calculates gravity for points at the same spacing as the observed data spacing, some extra details had to be introduced into model CM1, that are not shown in model WSE, to match the computed with the observed gravity anomalies. The CM1 model is naturally the preferred model of the western caldera margin.

Figure 3.24 c (opposite) WSE detail over the western caldera margin at Cerro Mogote (CM1), 4x vert. exag., station distribution and Nettleton profiles in Figure 3.10. Much of the scarp must comprise low density material, with lavas (2.60 Mg m^{-3}) dominant at the base only, the site of the small gravity high. The steepening of the gravity gradient 1.5 km within the caldera, over the small but significant scarp at Pueblo Nuevo (Figure 2.5), is modelled as the limit of the greatest thickness of the PUM .

1	Basement	2.65	10
2	IG	2.46	5
3	VS	2.32	5
4	PUM	1.58	2
5	Mogote tuffs (plus some lava-tuff intercalations)	2.00	1
6	Lower caldera wall lavas (exposed in scarp)	2.50	2
7	Biotite Tuff	1.70	3
8	LCMV (general)	2.09	3

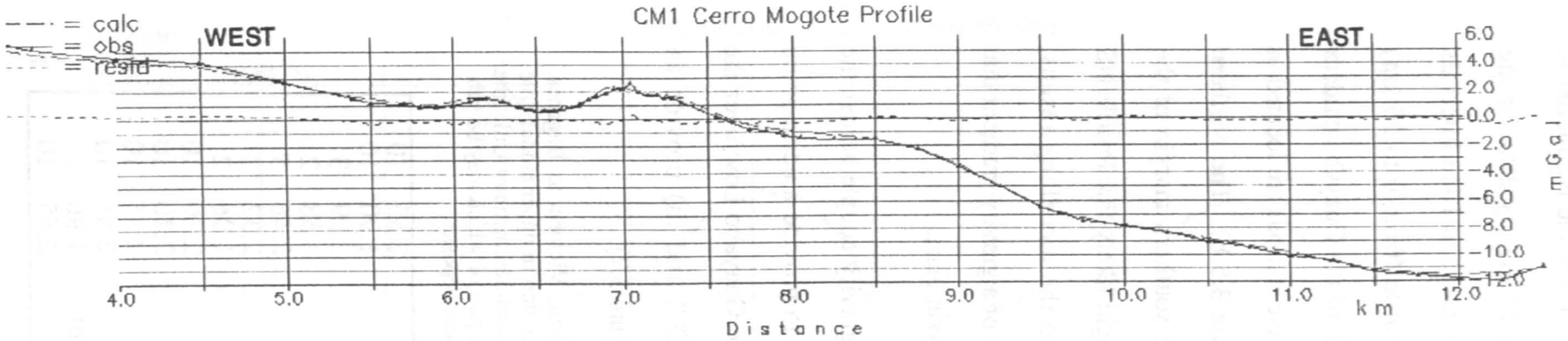
CM1 Cerro Mogote Profile
= calc
= obs
= resid
WEST
EAST
6.0
4.0
2.0
0.0
-2.0
-4.0
-6.0
-8.0
-10.0
-12.0
mGal
4.0
5.0
6.0
7.0
8.0
9.0
10.0
11.0
12.0
km
Distance

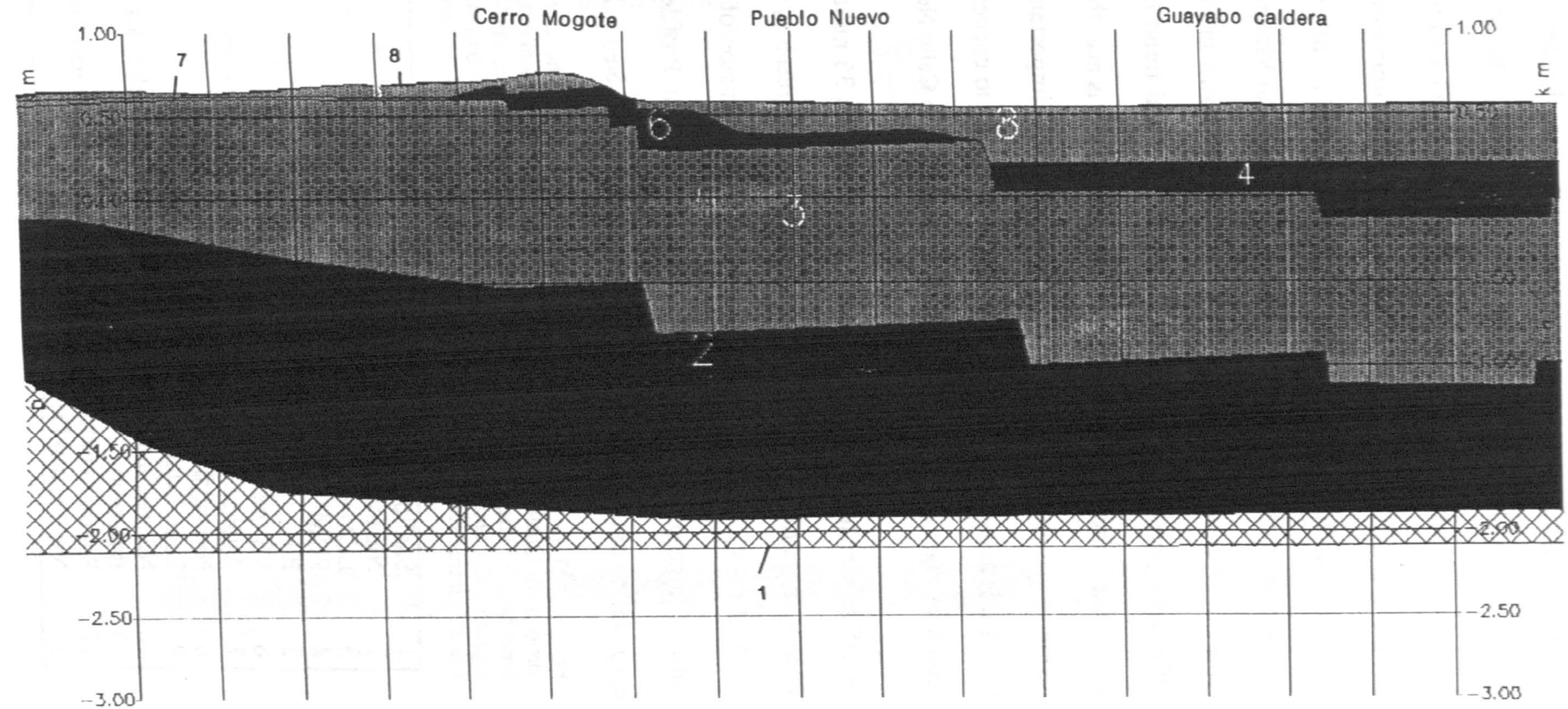
Cerro Mogote
Pueblo Nuevo
Guayabo caldera
1.00
m
7
8
6
3
4
3
2
1
-1.50
-2.00
-2.50
-3.00
km

Profile NS: Profile NS (Figure 3.27) is a 55 km north-south traverse across the Guanacaste volcanic arc, from Victoria in the Nicaraguan Depression, through the Guayabo caldera, to Bagaces on the Pacific flanks of the arc. Figure 3.27 shows the NS model at both the true scale and at x4 vertical exaggeration. The observed gravity data for the southern and central parts of the profile (from 20 to 54 km) were taken at 1 km intervals from the 1 mGal contour map (Figure 3.7), but the northern profile (from 0 to 20 km) shows the data from the single line of stations located to the north of the Guayabo caldera (from Aguas Claras northwards over Fila Caño Negro to Victoria, the stations are located in Figure 3.1, the interpolated gravity contours are shown in Figure 3.5 b). The northern profile runs perpendicular to the dominant structural trend (the southern margin of the Nicaraguan depression, Fila Cano Negro), and thus it is also thought likely that Profile NS is coincident with the maximum gravity gradient, important to the modelling results. Though this assumption could be wrong, it is difficult to conceive of a gravity gradient that is much stronger than that observed to the north of Fila Caño Negro at least.

The NS model has many objectives; i) to model the 35 mGal gravity couple across the southern topographic margin of the Nicaraguan Depression, ii) to provide a north-south model of the Guayabo caldera, in particular the extension of the Guayabo Low over the southern topographic margin (in conjunction with Profile CC) and iii) provide an interpretation of the broad gravity high over Salitral (located in Figure 3.7).

Figure 3.27 (opposite) North-south (NS) profile across the Cordillera, Victoria to Bagaces, through the Guayabo caldera (Figures 3.5 b and 3.7). 4x vertical exaggeration in upper model, true scale below. Highs are associated with shallow equivalents of the Volcano-Sedimentary Unit (the Aguacate Gp. and Monteverde Fm. volcanics) and the shallow basement, part of which may be sub-volcanic intrusives. Lows are modelled as thick low density tuff and sediment deposits.

1	Shallow Basement	2.65	10
2	Nicaraguan Depression tuffs	1.90	10
3	LCMV (general)	2.09	3
4	PUM	1.58	2
5	IG	2.46	5
6	VS (general)	2.32	3
7	Aguas Claras-San Isidro depression buried tuffs	1.96	2
8	Nicaraguan Depression Tertiary sediments	2.20	10
9	Tempisque Trough Tertiary sediments	2.20	10
10	Nicaraguan Depression Aguacate Group volcanics ?	2.35	10
11	Basement	2.65	10
12	Southern extra-caldera tuffs (including Bagaces Group)	1.96	3
13	Nicaraguan Depression basement	2.65	10

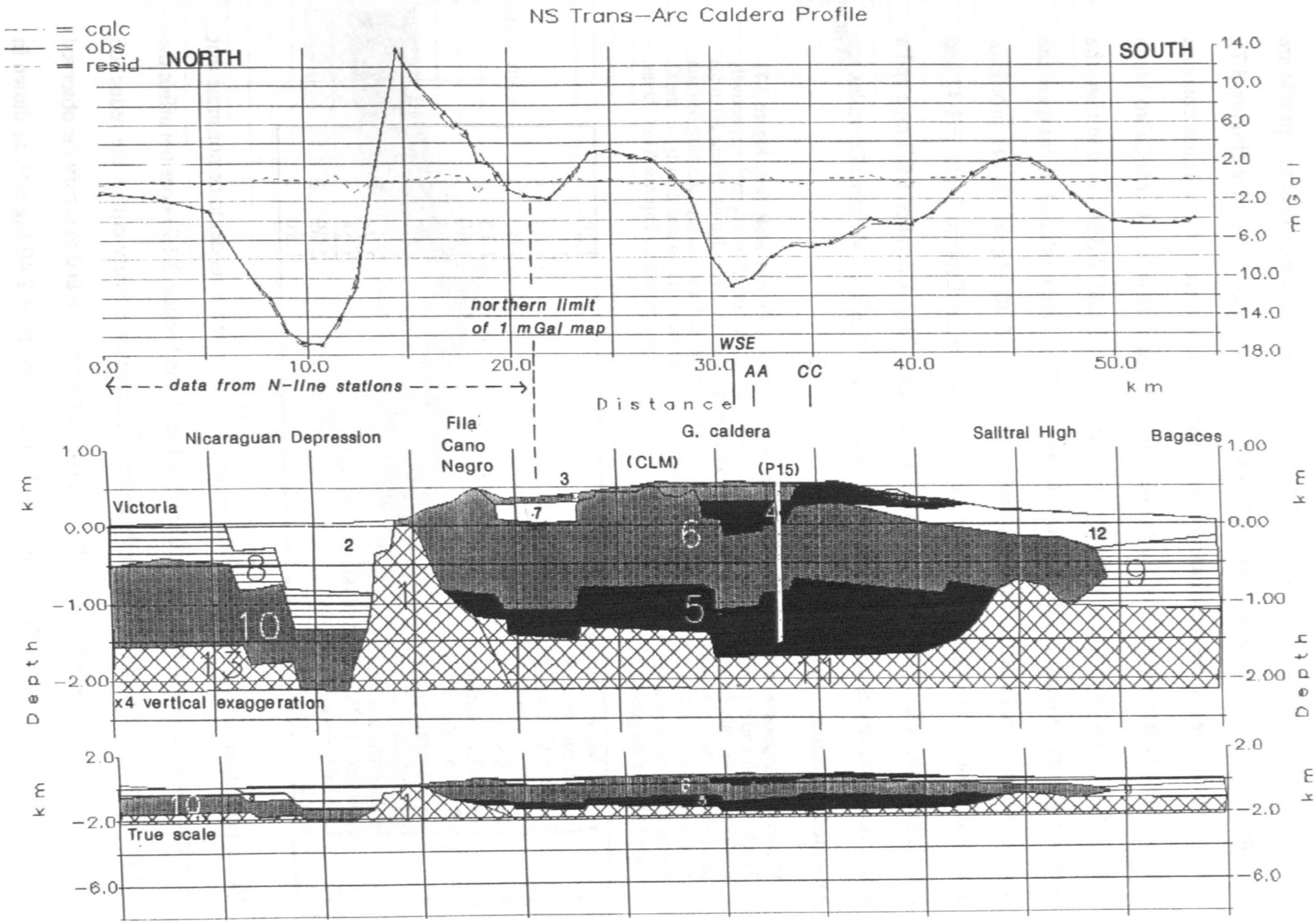
NS Trans—Arc Caldera Profile
= calc
= obs
= resid
NORTH
SOUTH
14.0
10.0
6.0
2.0
−2.0
−6.0
−10.0
−14.0
−18.0
mGal
0.0
10.0
20.0
30.0
40.0
50.0
km
northern limit
of 1 mGal map
WSE
AA
CC
Distance
← - - - data from N-line stations - - - - - →
Nicaraguan Depression
Fila
Cano
Negro
G. caldera
Salitral High
Bagaces
(CLM)
(P15)
Victoria
1.00
0.00
−1.00
−2.00
Depth
km
x4 vertical exaggeration
True scale
2.0
−2.0
−6.0

Profile VV: Profile VV (Figure 3.28 a, located in Figures 3.7 and 3.21) is a north-south traverse across Volcán Miravalles, the Bajo Los Chiqueros collapse sector, Cerro Cabro Muco and Cerro Espiritu Santo. The reasons for the changes in direction of this profile are to maintain, where possible, a profile across the maximum gravity gradient (Figure 3.7). The major objectives of this model are i) to model the deep structure of the volcanic complex on the eastern caldera margin, and ii) to model the collapse structure of Cerro Cabro Muco and Cerro Espiritu Santo (in conjunction with Profiles CC and WSE). In addition, the observed gravity reduced at 2.00 Mg m^{-3} (upper profiles) was modelled to compare the results with the model of the standard profile reduced at 2.40 Mg m^3 (lower profiles); discussed below. The shallow wells between Cabro Muco and Espiritu Santo, PH-42 and PH-41, were projected onto VV (wells located in Figure 3.21). A detailed BCG map and a model of the gravity ridge identified on the southwestern flanks of Volcán Miravalles are presented in Section 3.6.3.

Figure 3.28 (opposite) North-south Volcán Miravalles Profile (VV), true scale (loc. Figure 3.7). The lower and upper profiles are for observed data reduced at 2.00 and 2.40 Mg m^{-3} respectively together with the calculated gravity using equal background densities in the modelling (discussed in the text below). The depth to the sub-volcanic intrusion is reasonably constant, except the plug beneath the summit (see also Fig. 3.30 b). The BLC intrusion is concentrated (depth and density) in the C. Cabro Muco collapse area. The CMA lavas are modelled as the exposed C. Espiritu Santo lavas, responsible for the gravity high there.

1	Volcán Miravalles (general edifice)	2.40	3
2	BLC intrusion core	2.75	1
3	Basement/intrusion/densification	2.65	5
4	CMA & Cerro Espiritu Santo edifice	2.40	3
5	Upper VS	2.15	3
6	Deep BLC intrusion	2.50	3
7	VS (general, south)	2.32	3
8	VS (general, north)	2.32	3
9	Lahars/debris flows (from Palaeo Miravalles)	2.09	3
10	Volcán Miravalles feeder plug	2.75	1
11	Low density Volcán Miravalles north flank	2.25	3
12	LCMV (general)	2.09	3
13	Extra-caldera tuffs	1.90	2

Two sets of observed and calculated profiles are shown above the model to demonstrate that the initial choice of reduction density (discussed earlier in Section 3.1.2) does not affect the results of the models, providing the modelling background density equals the reduction density. The original dimensions of the VV polygons were modelled to satisfy the observed gravity reduced at 2.40 Mg m^{-3}, using a background density of 2.40 Mg m^{-3}, as shown in the lower pair of observed and calculated gravity profiles. The upper profiles show, for

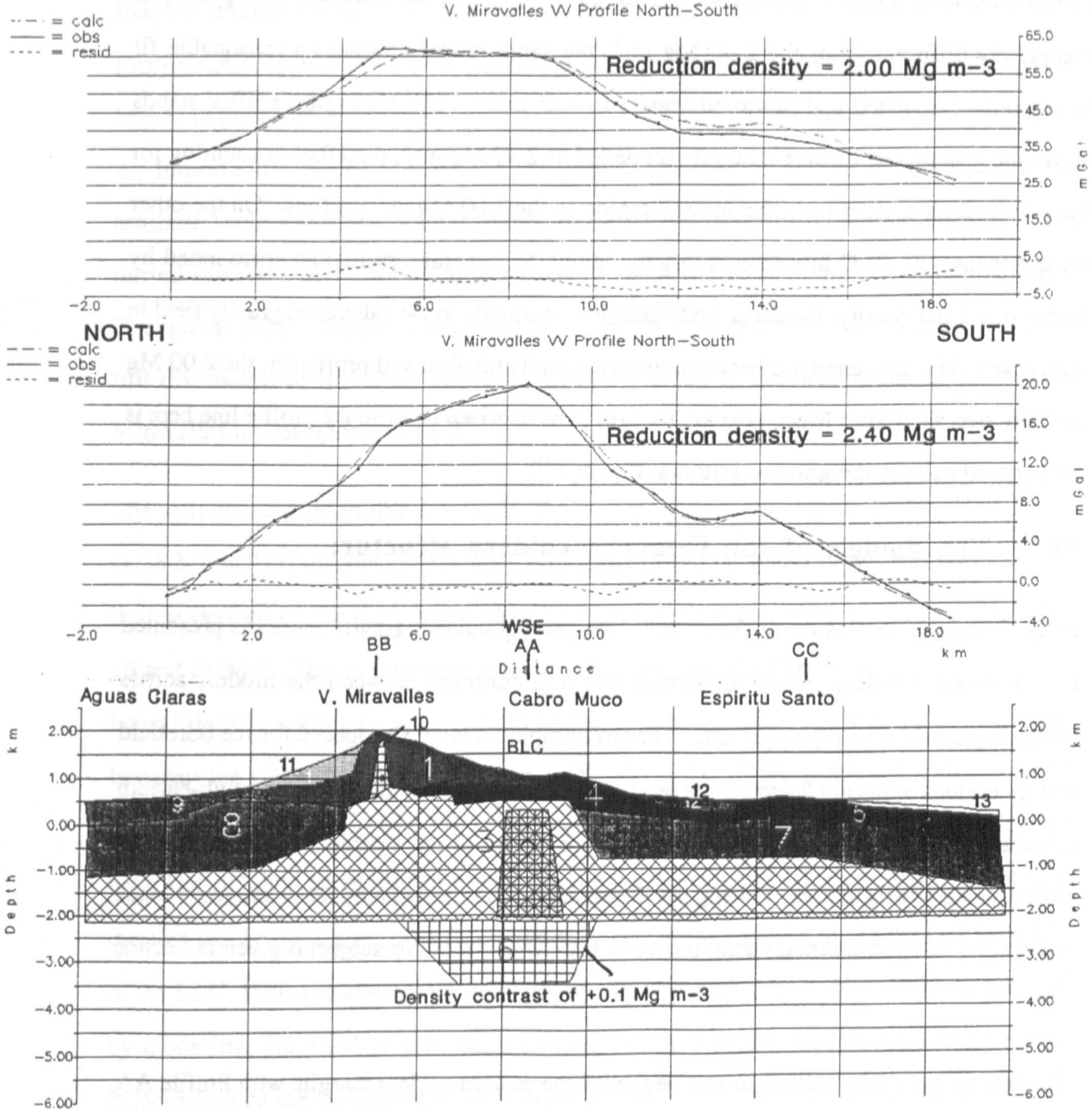
V. Miravalles W Profile North–South
– – · = calc
—— = obs
---- = resid
Reduction density = 2.00 Mg m–3
65.0
55.0
45.0
35.0
25.0
15.0
5.0
–5.0
mGal
–2.0
2.0
6.0
10.0
14.0
18.0
NORTH
SOUTH
V. Miravalles W Profile North–South
– – · = calc
—— = obs
---- = resid
Reduction density = 2.40 Mg m–3
20.0
16.0
12.0
8.0
4.0
0.0
–4.0
mGal
–2.0
2.0
6.0
10.0
14.0
18.0
km
WSE
BB
AA
CC
Distance
Aguas Claras
V. Miravalles
Cabro Muco
Espiritu Santo
BLC
10
11
1
2
8
4
12
13
5
7
3
6
Density contrast of +0.1 Mg m–3
2.00
1.00
0.00
–1.00
–2.00
–3.00
–4.00
–5.00
–6.00
Depth
km

comparison, the observed profile from data reduced at 2.00 Mg m^{-3} and the calculated profile obtained from the same model, but with a background density of 2.00 Mg m^{-3} instead of 2.40 Mg m^{-3}. Because of the higher density contrast between all the polygons and the background density of 2.00 Mg m^{-3} rather than 2.40 Mg m^{-3}, a constant value of 30 mGal was added to the entire length of the 2.00 Mg m^{-3} observed profile to allow direct comparison with the calculated field. Though the form of the 2.00 Mg m^{-3} profile is completely different from the 2.40 Mg m^{-3}, the same model produces a reasonable fit between the calculated and observed gravity in both cases. The Miravalles edifice stands above the general terrain and is largely modelled as 2.40 Mg m^{-3}, therefore accounting for the gravity high present over the summit region in the 2.00 Mg m^{-3} profiles. On the other hand, because the BLC intrusion is largely below the general terrain, and surrounded by bodies of a fixed density, the dense body contributes equally to the calculated gravity field in both cases. The discrepancies between the calculated and observed profiles in the 2.00 Mg m^{-3} case over the Cabro Muco area are thought to have arisen because the profile line here is not perpendicular to the gravity contours (Figure 3.7).

3.6.2 The models of the Guayabo caldera structure

In the following discussion of the models, the general caldera gravity model is presented first, followed by descriptions of similarities and contrasts between the models across different parts of the caldera margin. The stratigraphic relations proposed for the borefield and La Fortuna areas in Chapter 2 are tested by detailed gravity models of the south-eastern caldera. This is followed by the deep structure model of the Volcán Miravalles and the eastern caldera margin area. During the discussion of the caldera models, reference is made to the effect of hydrothermal alteration, and a full treatment of this subject is given in Section 3.7.

The description of the caldera model begins on the eastern caldera margin, with Profile AA, where maximum control of the density structure was possible. The general features of this model are then extrapolated to the other pertinent models to examine the other caldera margins in turn.

The eastern caldera margin: There is no topographic definition of the eastern caldera margin (Figure 2.5) but ELC (1986 a) postulated that the boundary runs beneath the post-caldera edifice of Volcán Miravalles. The revised stratigraphic model of Chapter 2 places the pre- and post-caldera stratigraphic boundary between the lowermost Cabro Muco Andesite and the Pumice Unit; i.e. the caldera margin should be between wells PGM-15 and PGM-5 (Figure 2.9 a). This boundary is modelled in Profile AA. The main features of Profile AA (Figure 3.22) are the general gravity gradient up to the east, and the two lateral breaks in the gradient, one between PGM-15 and PGM-5 and the other to the east of PGM-2. Importantly, the BLC High and the general gradient across the borefield cannot be attributed solely to any of the measured lateral density contrasts within the borefield and a buried intrusive body, the BLC intrusion, is proposed as the only reasonable solution. Though the BLC intrusion is important to the gravity models of the eastern caldera margin, a full discussion of its nature and significance is given in the description of the Volcán Miravalles models (Section 3.6.3).

The well constrained Profile AA model shows that the very low density Pumice Unit, PUM, (1.58 Mg m^{-3}) is responsible for the *central* part of the Guayabo Low. The eastern PUM limit is defined by the sharp, rather than gradual, change in gravity gradient between PGM-15 and PGM-5. This gravity discontinuity could only be modelled in terms of a maximum lateral density contrast; i.e. as a near-vertical boundary and very high density contrast between the CMA and the PUM ($\Delta\rho = -0.82$ Mg m^{-3}). There is a lesser lateral contrast between the Acidic Andesite Unit (AA) and the Volcano-Sedimentary Unit (VS) ($\Delta\rho = -0.22$ Mg m^{-3}) and an additional effect of some geothermal densification of the VS towards the east (cf. Section 3.7). (The VS in the gravity models includes the Lava-Tuff Unit, LT, of the ELC, 1986 a stratigraphy). Importantly, the observed gravity data cannot be matched by modelling the PUM as gradually thinning over a gradually thickening CMA towards PGM-5; hence the onlapping PUM shown in Figure 2.9 a is not entirely acceptable. A further thickening of the PUM towards the centre of the caldera is required to match the observed gravity data, and this has been modelled as a further step fault 150 m west of the projected position of PGM-15.

The near vertical PUM-CMA margin between PGM-5 and PGM-15 requires a (normal) fault with 300 m displacement west of PGM-5, the caldera margin fault as defined by this study. The implication of this scenario is that both the VS and the Ignimbrite Unit (IG) should be similarly displaced between PGM-5 and 15, but the IG-VS boundary is only 50 m lower in PGM-15 than in PGM-5 (Figure 2.9 a). The apparent contradiction can be explained by considering the pre-collapse IG-VS boundary as not horizontal, but sloping at an angle of ~6° towards PGM-5. The alternative explanation is that the fault is sub-vertical, displacing the VS in PGM-15, and therefore avoiding displacement of the IG between PGM-5 and PGM-15. However, the distance between the wells is nearly 2 km, requiring a fault plane slope of ~45°. This is not considered a feasible angle for a normal fault in these circumstances and besides, the gravity model requires a more vertical boundary.

If the caldera margin is marked by the near-vertical limits of the Pumice Unit, as defined by this study, then the ring faults are therefore well defined by the steep gradients of the *central* Guayabo Low in the BCG maps (Figures 3.7 and 3.8). In contrast, the boundaries of the topographic caldera margin are not well defined by gravity data and the gravity models of the western, southern and northern caldera margins are now described in turn. In general, only the central part of the Guayabo Low can be attributed to the density contrast between the syn- and post-collapse low-density products associated with the actual Guayabo caldera (i.e. PUM and LCMV) and the Pre-Guayabo stratigraphy as defined during this study (i.e. VS, AA and the lowermost CMA).

For the general profiles across the caldera, Profiles WSE, CM1 and NS (Figures 3.25, 3.26 and 3.27), the average density of the largely un-altered VS at PGM-15 (2.32 Mg m^{-3}) has been used for the VS density. The WSE model for the eastern margin of the caldera was modelled using Profile AA as a general guide, but according to the resistivity models, the Acidic Andesite Unit does not extend as far north as the WSE model (as shown in Figure 3.21). The BCG map of this area (Figure 3.8), however, does not show a direct correlation between the gravity data and the proposed outline of the Acidic Andesite Unit. The inference of this result is that there is little density contrast between the VS and the AA in this area, confirming the relatively small measured density contrast of ~0.10 Mg m^{-3}

(average AA-VS contrast for the northernmost wells PGM-2, 5, 10 and 11, results summarised in Table 3.4 and Figure 3.14).

The western caldera margin: The WSE caldera detail in Figure 3.25 b shows the western topographic margin and the position of the projections of PGM-11 and 15 (borehole locations in Figure 3.7) on the eastern caldera margin. The interpretation of the western caldera margin is based on the extrapolation of the PGM-15 stratigraphy across the caldera, given the east-west symmetrical shape of the Guayabo Low over the caldera (Profile WSE), but the western margin model is very different from the eastern margin. The detailed profile CM1 across the Cerro Mogote caldera margin (Figure 3.23) shows that the strong increase in the gravity gradient marking the inner Guayabo Low is not at the major (~200 m) topographic margin (at 7 km along the profile), but is more than 2 km inside, coincident with a significant 10 m morphotectonic scarp (at 9 km along the profile). The 10 m inner scarp is shown on the detailed BCG map and the geology map (Figures 3.8 and 2.5), and is aligned with the gravity gradient along the margin of the Guayabo Low. This was modelled as the western limit of the PUM (analogous to the eastern limit of the PUM between PGM-15 and 5), and shows that the present topographic margin is unrelated to the proposed ring faults bounding the PUM. The LCMV lahars that cover the present western caldera floor (geology in Figure 2.5) are younger than the PUM and the 10 m scarp implies post-PUM movement on the bounding fault.

The modelled displacement on the western PUM boundary fault is ~300 m, equal to that between PGM-15 and PGM-5 on the eastern margin. A second, but more subtle, intra-caldera gradient increase is present at 11 km along Profile CM1, modelled as a second vertical fault displacing the base of the PUM a further 170 m. The east-west distribution of the Pumice Unit in the caldera is therefore symmetrical, as modelled by the general WSE profile. What, then, is the significance of the 200 m western topographic caldera margin and the gravity high over the foot of at least the Cerro Mogote caldera margin scarp?

The Nettleton profiles across the caldera margin at Cerro Mogote (Figure 3.10, Section 3.4.4) showed that both the low density tuffs exposed above the Mogote basalts and tuffs inferred between the Mogote basalts and the older caldera wall andesites, probably make up

much of the margin crest (~2.00 Mg m^{-3}), rather than the caldera wall andesites exposed at the base of the scarp. The 2 mGal positive gravity anomaly at the base of the scarp was modelled as the outcrop of the exposed caldera wall lava unit. Although the average measured density of the exposed andesites is 2.70 Mg m^{-3} (Table 3.1), this value is too high to model the observed gravity data and a density of 2.50 Mg m^{-3} gives a better fit in the CM1 model. The use of a lower than measured density is justified by the proposed occurrence of low density material between the resistant exposed lavas, probably tuffs or weathered lavas; exposures of which have not been positively distinguished from the soils and talus of the scarp. Model CM1 shows that the greatest thickness of the lavas must be close to, but *inside* the base of the scarp. This implies that the topographic margin is indeed a ring fault with ~250 m downthrow of the caldera wall lava unit. The topographic margin cannot therefore be interpreted as the present erosional position of the PUM caldera boundary.

Profile WSE shows a reasonably smooth underlying gravity gradient across the western margin towards the San Jorge High (located on the BCG map, Figure 3.7) which is unlikely to be attributable to simple displacement across a major ring fault. The gradient was modelled instead as a shallowing of the dense basement towards the west, and as no deep discontinuity is required, the IG and the VS are modelled across the caldera margin. The 50-100 m thickness of the low density Biotite Tuff exposed in the area of the San Jorge High (geology in Figure 2.5) further suggests that the San Jorge gravity high must be attributed to source beneath the Biotite Tuff. Although the dense body was modelled as a shallow basement, this could be interpreted as a sub-volcanic intrusive body related to the volcanics of the VS that underlie the Biotite Tuff. Only the Pumice Unit (confined 2 km inside the margin) and the LCMV do not continue into the western caldera walls. Thus, the ~250 m displacement of the caldera wall lavas is the simplest model that fits the observed gravity in Profile CM1.

The models WSE and CM1 show the caldera wall lava unit thinning towards the caldera centre, but it would be possible to integrate the lava unit into the upper VS. Alternatively the caldera wall lavas could be stratigraphically equivalent to the CMA downfaulted on the

eastern margin, but this is considered unlikely, given that the source area for the CMA is postulated to be to the east of both the borefield and the caldera. The implication therefore is that the exposed caldera wall lavas are contemporaneous with the upper VS lavas drilled in PGM-15, part of the postulated pre-caldera Volcán Guayabo. This ancient stratovolcano would have been destroyed during the formation of the Guayabo caldera and intuitively it may have originally been sited at the centre of the later collapse. The collapse was accompanied by the formation of the Pumice Unit and therefore the centre of Volcán Guayabo would have been at the centre of the Guayabo Low. (A full discussion of the caldera evolution is given in Section 3.8, following consideration of all the gravity models).

The tuffs overlying the western flanks of Cerro Mogote, shown in WSE and CM1, have been correlated with the Guayabo Proximal Breccia (Figure 2.5) and, by association therefore, also with breccias of the LCMV (as discussed in Chapter 2). The present offset between these outlying tuffs and the LCMV in models WSE and CM1 does not, however, require post-depositional displacement, but could be an original collapse feature. There is no field evidence that the tuffs on the western caldera margin were cut by post-depositional fault movement, though there is evidence for this on the southwestern caldera margin.

The extra-caldera lava exposures: The distribution of the occasional exposures of the extra-caldera lavas beneath the Biotite Tuff and younger tuffs (discussed in Chapter 2) appears to be related to the edges of the positive gravity anomalies (the exposures known to this author are marked as filled triangles in Figures 3.7 and 3.8). These positive gravity anomalies are therefore modelled as concentrated thicknesses of this older volcanic group. The western limits of the San Jorge gravity high are not constrained but the high does extend to the southeast, ending abruptly outside the caldera margin. This part of the high was modelled in Profile CC (Figure 3.23) as the shallowing of the lavas exposed in this area (located in Figures 2.5 and 3.7) at the expense of the overlying low-density tuffs, including the Biotite Tuff. The stratigraphic relations in the area west of the caldera, as implied by the gravity models, suggest that the extra-caldera lava exposures are contemporaneous with the Volcano-Sedimentary Unit. The Ignimbrite Unit, therefore, must be older than at least the uppermost tuffs of the Bagaces Group that are exposed in parts of this area. This

contradicts the correlation postulated in Chapter 2 between IG and the Lower Grey Ignimbrite of the Bagaces Group (Figure 2.14), but it is possible that the IG is related to the older tuffs of the Bagaces Group (the oldest K-Ar date is from the late Miocene, Gillot *et al.*, 1990, see also Table 2.2). The positive anomalies are not always accompanied by lava exposures, however, and at the Salitral gravity high (located in Figure 3.7, south of the Guayabo caldera) 150 m of grey ignimbrites of the Bagaces Group were drilled in the temperature gradient borehole PH-28 (located in Figure 3.8) without encountering lavas.

The south-western caldera margin: This part of the southern margin has a unique gravity signature and is therefore described separately from the south-eastern (La Fortuna area) caldera margin. The detailed BCG map (Figure 3.8) shows steep gradients, parallel to the caldera margin, over the western, northern and eastern Pumice Unit boundaries but a less pronounced gradient towards the southern caldera margin where the Guayabo Low appears to continue southwards past La Ese, bounded by steep north-south trending gravity gradients that traverse the topographic caldera margin. These gradients are best shown on the Profiles CC and NS (Figures 3.23 and 3.26, located in Figure 3.7).

The distinctive western caldera wall lavas that are exposed almost continuously along the southwest margin of Laguna Mogote (Figure 2.5) are cut by the north-south depression south of Laguna Mogote within which the Guayabo Proximal Breccia is exposed (Figure 2.5). The gravity profiles NS and CC suggest that the gravity low over this breach in the caldera wall is related to a significant thickness (~200 m) of the Pumice Unit. This strongly supports the view that the La Ese Pumice and the Guayabo Breccia *are* equivalent to the Pumice Unit and the LCMV breccia, as suggested in Chapter 2. Profile NS (Figure 3.24) shows how the whole intra-caldera PGM-15 stratigraphy excepting the LCMV can thus be modelled across this south-western margin of the caldera. The small gravity high at the town of Guayabo (Figure 3.8) is believed to be genuine; although it is defined by only one station, this is the most frequently visited base station, Gra-91 (located in Figure 3.21). This high is located at 34 km on Profile NS and though it is modelled as a postulated buried continuation of the PUM boundary - marked elsewhere by the steep gravity gradient around the inner Guayabo Low - it would naturally be necessary to define the lateral form of the

anomaly with more stations before concluding that this explanation is the solution. The correlation between the buried Pumice Unit and the exposed La Ese Pumice requires some 200 to 250 m post-PUM displacement on the southwestern PUM boundary fault.

Profile CC (Figure 3.23) traverses the steep north-south gradients (Figure 3.8) and shows again how the PUM is confined to the east of the exposed western caldera wall lavas and to the west of the La Fortuna Graben. Profiles CC and NS show that the maximum thickness of the PUM in this area is directly beneath the southern caldera margin. The proposed elongate distribution of the Pumice Unit in the southwestern caldera area suggests that during deposition, the pumice tuff was bounded by a depression oriented in this direction. The implication is that the stress regime during this stage of formation of the caldera was not symmetrical, but extensional forces were parallel with the present orientation of the arc. The 1 mGal BLC map (Figure 3.7) shows a general elongation of the gravity anomalies in a similar fashion, perpendicular to the present and postulated past position (e.g. Weyl, 1980) of the volcanic arc. The focus of the extension in the southern caldera area shifted eastwards, however, to the more recent La Fortuna Graben area before the LCMV lahar formation.

The southeastern caldera margin and the La Fortuna Graben:

In Profile AA, between PGM-5 and 15, the CMA was modelled as the footwall to, and is therefore older than, the PUM. The LCMV breccia overlying the PUM and CMA is thought to be related to the Guayabo Proximal Breccia (Chapter 2, see the borehole sections in Figures 2.9 and 2.10 and the tuff correlations proposed in Figure 2.14). This breccia is thickest over the CMA in the northernmost borefield (>200 m in PGM-10) but thins to the south to less than 20 m in PGM-12, PH-33 and PH-35 and is possibly absent in other southern wells (Figures 2.9 b and 2.10 a).

West of the La Fortuna graben the exposed Guayabo-related tuffs overlie the higher-K lavas and likewise, to the east of the La Fortuna graben, the tuffs overlie the Cerro Espiritu Santo lavas (following the mapping of Mora, 1988 and Alvarado *et al.*, 1990, Figure 2.5). The higher-K lavas are tentatively correlated with the lowermost CMA lavas by this study

(Chapter 2). In model CC, therefore, a buried thickness of the low density Pumice Unit, the proposed intra-caldera equivalent to the La Ese Pumice, cannot account for the gravity low over the western margin of the La Fortuna Graben, as the older, higher-K lavas are exposed on this margin (located in Figure 3.21). Instead, it is necessary to increase the thickness of the low density upper VS of PGM-12 (2.15 Mg m^{-3}) to the west of La Fortuna (Profile CC, Figure 3.26). This implies that the density of the VS decreases from 2.32 Mg m^{-3} at PGM-15 to 2.15 Mg m^{-3} south of Guayabo and the Pumice Unit is therefore only *partially* responsible for the southern caldera gravity low. The caldera margin low north of Cerro Mogote (Figure 3.6 b), over the Hill 777 dacite (Figure 2.5), is explained in similar terms. The deep densification of the VS at PGM-12 is discussed below in the context of the geothermal field models, but otherwise the density of the VS should vary according to the ratio of lavas to tuffs, hence the lower density of the tuff sequence at PGM-12 than the lava-tuff sequence at PGM-15.

The density of the VS modelled beneath the southern caldera margin may be even less than the value of 2.15 Mg m^{-3} observed in the upper VS in PGM-12, in which case a lesser thickness of the PUM than the 200 m shown (CC) would be necessary to model the observed gravity.

The tuff that splits the CMA lavas in PGM-12 (the CMA tuff) must be older than the Guayabo Breccia and the PUM (Chapter 2, Figures 2.9 and 2.10). In the gravity models south of PGM-12 (Profile BB) the low density of the CMA tuff is incorporated into the underlying low density VS. The closely spaced upper CMA lavas and the LCMV basaltic andesite are treated as one density unit in the southeastern caldera models, but are distinct from the lowermost CMA lavas that make up the CMA in the rest of the borefield. The southern caldera higher-K lavas (including the PH-30 lavas) and the Espiritu Santo lavas may correlate with the lowermost CMA lavas; the CMA tuff (Figure 2.10 a) is therefore possibly equivalent to the Hornblende Tuff exposed over both the higher-K lavas and the Cerro Espiritu Santo lavas (Figure 2.5). The positive gravity anomalies over PH-30 and Cerro Espiritu Santo are therefore modelled in terms of a shallowing of these lavas (Profiles BB, CC and VV) at the expense of the overlying lower density CMA tuff and the younger LCMV breccias and lahars.

The gravity low between PGM-12 and PH-30 is modelled in Profile BB as an increased thickness of the low density VS and an added thickness of the younger tuffs equivalent to the extra-caldera tuffs (1.90 Mg m^{-3}). The gravity low between PH-30 and Cerro Espiritu Santo (Figure 3.8) is similarly explained as a sub-lahar depression, related to the La Fortuna graben, filled with low density tuffs equivalent to those exposed beneath the lahars to the south and east.

The thick volcanic breccias that are exposed below the extra-caldera tuffs south of Cerro Espiritu Santo (Lezema *et al.*, 1988, discussed in Chapter 2) are modelled as the low density upper VS (Profile CC and VV) and therefore underlie the proposed Espiritu Santo stratovolcano remnant. The gravity models CC and VV suggest that these low density breccias and/or the overlying tuffs become thicker to the southeast and are responsible for the broad gravity low over the Tenorio depression (modelled in profile WSE).

The northern caldera margin: The steep gravity gradient over the proposed PUM boundary is to the south of the Cerros la Montañosa (CLM) sector (Figure 3.8). This was interpreted to mean that there is no significant thickness of PUM within the CLM sector. In the north-south profile, NS (Figure 3.21), the CLM was modelled as an extrapolation of the VS with a density of 2.32 Mg m^{-3}. This choice of density is based on the lack of evidence of a dense, purely andesite lava make-up (2.60 to 2.70 Mg m^{-3}) for the CLM sector of the caldera wall from the Nettleton profiles (Figure 3.11, discussed in Section 3.4.4). Secondly, if, as suggested above (Section 3.4.4) the CLM is a stratovolcano remnant, then the overall density may be similar to that of the proposed stratovolcano sequence of the VS in PGM-15, average ρ_w = 2.32 Mg m^{-3}. The CLM gravity high has therefore only been modelled in terms of the density contrast between the CLM and both the younger PUM and the overlying LCMV lahars, similar to the model of the western caldera margin.

The main implications of the caldera models:

In summary, the gravity models of the Guayabo caldera show that the Pumice Unit is largely responsible for the Guayabo Low. The steep gravity gradients parallel to, but up to 2 km within the topographic margin of the Guayabo caldera, are interpreted as near vertical

ring fault boundaries of the Pumice Unit, with ~300 m displacement. The V-shaped centre to the Guayabo Low requires a further 170 m displacement of the central part of the Pumice Unit.

The VS and IG continue across the caldera margins and the caldera wall lavas are correlated with the upper drilled stratigraphy; the western lavas with the upper VS stratovolcano sequence at PGM-15, and the southern higher-K lavas and Espiritu Santo lavas with the lower CMA and possibly parts of the Cerro Cabro Muco edifice and the LCMV. This further implies that the distribution of the oldest recognised tuff, the Ignimbrite Unit, is not confined within the caldera but because of the relatively high density of the IG (2.46 Mg m^{-3} average in PGM-15), its limits are not well constrained by the gravity models.

The extension of the Guayabo Low over the southwestern margin has been modelled as the continuation of the Pumice Unit across the southwestern margin. This low must, however, be partially attributed to a low density equivalent of the Volcano-Sedimentary Unit, possible the upper VS drilled in PGM-12. To explain the displacement of the Pumice Unit and the LCMV breccia between PGM-15 and the southern margin exposures of the Guayabo Proximal Breccia, the displacement on the boundary fault, parallel to but 2 km inside the present topographic margin, must post-date the Pumice Unit and at least the latter part of the late fault movement must also post-date the LCMV breccia. A similar displacement of ~250 m is also required across the western and northern topographic margins.

The simplest unifying model to explain all the observed and modelled fault timings and displacements is as follows: The eruption of the Pumice Unit was accompanied by collapse along ring faults ~2 km *inside* the present topographic margins, except for the collapse confined by the proposed graben beneath the present southwestern caldera margin. At a later stage (during and following the LCMV breccia event) further collapse of a wider area, but centred on the Pumice Unit caldera, caused the displacement across the present topographic margins of the Guayabo caldera. Later still, the graben axis of the southwestern margin switched to the east, to the La Fortuna graben, before the deposition of the LCMV lahars. The caldera evolution model is fully explained at the end of Chapter 4,

following the discussion below of the Volcán Miravalles area and the eruption product mass balance analyses presented in Chapter 4.

3.6.3 The deep structure of Volcán Miravalles and Bajo Los Chiqueros

For gravity data reduced at 2.40 Mg m^{-3}, the ~15 mGal Bajo Los Chiqueros (BLC) High is not centred over the most recent stratovolcano, Volcán Miravalles, but over the collapsed remnant of Cerro Cabro Muco (Figure 3.6 shows the BCG draped over the topography). The significance of this displacement is discussed here in terms of the gravity models WSE and VV (Figures 3.25 b and 3.28), together with models of the finer details of the gravity anomalies in this area.

The station coverage of Volcán Miravalles is greatest over the partially accessible western and northern flanks, but it was not logistically possible to survey the densely vegetated and unmapped eastern Miravalles edifice (Figure 3.1). It must be stressed therefore, that the Bajo Los Chiqueros gravity high (the BLC High to the south of Volcán Miravalles, Figure 3.6 b and 3.7) is not constrained to the east and gravity may increase further over the poorly studied, eroded and vegetated eastern volcanic edifice. Gravity does decrease from the BLC High to the southeast towards the Tenorio area (Figure 3.6) but again the gradients are not well constrained due to the inaccessibility of the terrain and the consequent paucity of data between Miravalles and the Tenorio Geothermal Project survey area (station locations in Figures 3.1 and 3.8).

It follows that considerable difficulty was experienced in contouring the sparse Miravalles summit station data and there is a slight discrepancy between the BCG maps that have been computer contoured at different scales (a general introduction of the contouring technique is given in Section 3.2.4). The detailed maps - the 1 mGal contour 3-D map of the caldera, Figure 3.6 b, and the 0.5 mGal contour 2-D map over the geothermal area, Figure 3.8 - were designed to cover the more densely surveyed caldera area and were computer generated by interpolating data onto 0.25 km regular grid using a search radius of 1.0 and 1.5 km respectively. This process highlighted anomalies between the less reliable summit

data and left gaps in areas of poor coverage (Figure 3.6 b), whereas the general BCG maps (Figures 3.6 a and 3.7) used a 0.5 km grid and a search radius of 4 km to interpolate gravity over the areas with intermittent coverage, thereby showing effectively smoothed data over Volcán Miravalles.

To examine the Miravalles edifice gravity in terms of the geological and topographic setting the data have been manually contoured and the results show good agreement with the computed contours shown over a similar area (Figures 3.29 a and b respectively). Individual station BCG values are shown on the hand contoured map, rounded to the nearest mGal (full discussion of BCG errors and data list in Appendix 3A). The six summit stations are sited on the steep, vegetated ridge that borders the northern margin of the collapsed summit crater. Because of their elevation, the total terrain corrections are large, up to 50 mGals; but the largest single error is from the zone immediately around the station (Hammer zones A-D). The corrections for zones A-D have been estimated using the tables of Sandberg (1958) from the average slope of the topography away from the station, but because of intermittent cloud cover during the survey it was not always possible to determine this angle over its full effective distance.

An error of only 10° in the estimation of steep slope angles (30-60°) could result in a terrain correction error of up to 2 mGal. Another source of error is that the station elevations are poorly constrained by the altimeter data (Appendix 3B) and this may contribute to a further 1 mGal error (for a 5 m elevation error). Together, these factors probably explain the large variation of the closely spaced summit BCG data; a nominal BCG error of 3 mGal has been assigned to the summit values. Errors due to the incomplete terrain corrections beyond the outer limit of 224 km are related to the station elevation (Section 3.1.1, Figure 3.2) and would therefore only affect the inter station BCG anomalies if the stations are at significantly different elevations (i.e. separated by more than ~500 m).

Of the four 3-D Nettleton maps of the entire study area (Figures 3.5 a-d), gravity reduced at 2.67 Mg m^{-3} shows the least correlation with the general topographic edifice of Volcán Miravalles. This is not, however, a likely net edifice density as it is greater than the measured average density of the surficial Miravalles lavas (2.49 Mg m^{-3}, Table 3.1), which

is in turn an overestimate of the net density of the intercalated breccias, tuffs and blocky lavas that make up the volcano.

The gravity fields of other stratovolcanoes have similarly been modelled in terms of a low density edifice. For example, from a consideration of Nettleton profiles over the bimodal Medicine Lake Volcano in the Cascades, Finn and Williams (1982) suggested an edifice density of 2.20 Mg m^{-3} and attributed the residual summit centred positive anomaly to a sub-edifice mafic intrusion. Brown *et al.* (1987) modelled the complex gravity anomalies over edifices of other Costa Rican volcanoes; Poás, Irazu and Rincon de la Vieja - in terms of broad low density summit areas (1.8-2.2 Mg m^{-3}) made up of unconsolidated, largely pyroclastic material and denser within-edifice magma pipes responsible for the superimposed shorter wavelength positive anomalies. In fact, extended (~20 km long) north-south Nettleton profiles over Rincon de la Vieja presented by Rymer (1985) show the least correlation of gravity with topography for a reduction density of 2.60 Mg m^{-3}, similar to the Nettleton results of this study over Miravalles, but which similarly contradict the lower shallow edifice density suggested by the geology. It is suggested that the high Nettleton derived densities for both Rincon de la Vieja and Miravalles are at least partly due to sub-volcanic mafic intrusives that produce positive gravity anomaly wavelengths coincident with the topography of the associated volcanic edifice, possibly of a similar nature to the intrusions suggested by Finn and Williams (1982) beneath Medicine Lake Volcano.

A general edifice density of 2.40 Mg m^{-3} was therefore used in the gravity models WSE and VV (Figures 3.27 and 3.28), the same as the BCG reduction density. This means that the bulk of the edifice does not contribute to the gravity anomaly which was modelled instead in terms of the properties of the proposed deeper intrusion(s) together with some surficial lower density material, and a sub-crater dense feeder. The gravity high over the densely vegetated summit crater walls (Figure 3.29 a) cannot be explained by dense surficial material as the occasional landslides show the crater walls are made up of loosely consolidated, low density material, as observed at Volcán Rincon de la Vieja (Brown *et al.*, 1987).

Figure 3.29 a Hand contoured BCG data (2.40 Mg m^{-3}) over Volcán Miravalles. The Bajo Los Chiqueros (BLC) gravity high is not constrained to the east, but the Cerro Hinchada (CH at 409:302) gravity ridge is better constrained and is postulated to continue to the summit. The spine of the CH gravity ridge is located 0.5 km northwest of the Las Hornillas fault, (coincident with Quebrada Las Hornillas on the map). The topography contours show how the Santa Rosa lavas (e.g. 410.5:301.0) continue to the summit and do not have an obvious alternative source further downslope. The scarp at the Sulphur quarry is thought to predate the Santa Rosa lavas, and therefore continues to join the Las Hornillas Fault. Gravity profile SR (Figures 3.30 a-c) is located in the south-west of the area.

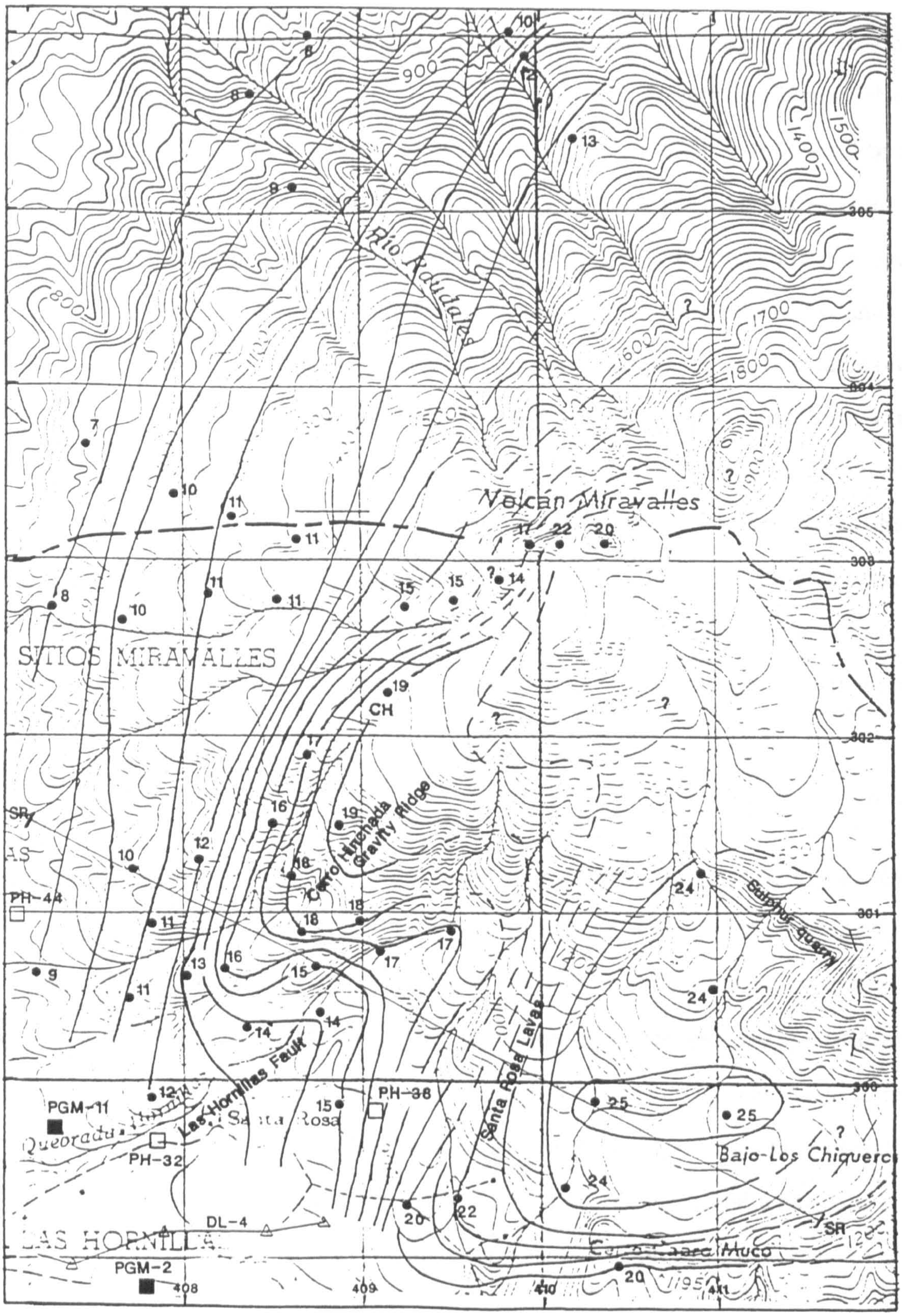

Figure 3.29 b Computer contoured BCG data over V. Miravalles (from 140 gravity stations). The area covered by hand contoured map opposite (Figure 3.29 a) is indicated for comparison. In this map, the 0.25 km interpolation grid and 1 km search radius resulted in a close fit of the contours to the original data and station distribution. The hand contoured map is similar but smoother.

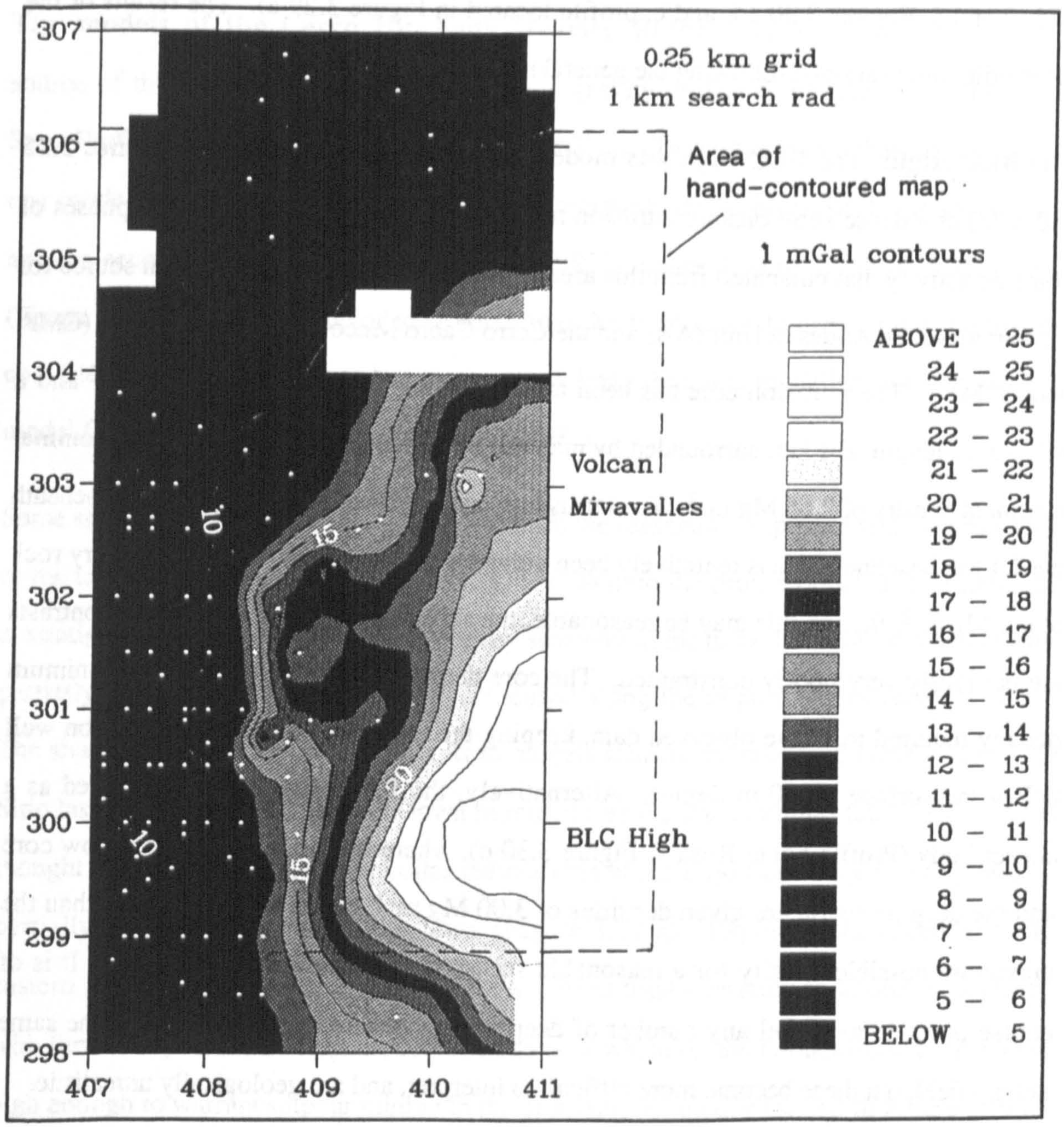

When examined in detail (Figure 3.29) the gravity high over the Volcán Miravalles area can be subdivided into the BLC High and a secondary gravity ridge on the southwest flanks, the northeast-southwest Cerro Hinchada ridge (located at CH, Figure 3.29 a). On the hand contoured map, the Cerro Hinchada ridge extends from the Volcán Miravalles summit area towards PGM-11, parallel to, but ~ 0.5 km north of the Las Hornillas Fault (the locus of the Quebrada Hornillas in Figure 3.29 a). There is a well defined gravity trough between this ridge and the BLC High. To the north of Bajo Los Chiqueros the few data points suggest that there is no clear distinction between the summit area gravity high and the BLC High. A

gravity profile from Sitio las Mesas to Bajo Los Chiqueros, the Santa Rosa profile, has been modelled to examine the Cerro Hinchada gravity ridge and the trough in detail (Profiles SR1, 2 and 3, Figures 3.30 a b and c, profile located in Figure 3.29 a). The results of the SR Profiles are examined following the general models for the BLC High:

The BLC High: The BLC High was modelled in Profiles VV and WSE (Figures 3.25 and 3.28) as a dense sub-volcanic intrusion related to one or more of the several phases of volcanic activity that emanated from this area. This area is the proposed eastern source for the buried Acidic Andesite Unit (AA) and the Cerro Cabro Muco-La Giganta activity (CMA and LCMV). The intrusion core has been modelled with a density of 2.75 Mg m^{-3} and a half-strike-length of 1 km, surrounded by material with a density equivalent to the nominal basement density of 2.65 Mg m^{-3}. The intrusion may continue as a density contrast beneath the 2.1 km baseline and has tentatively been given a density contrast with the country rock of 0.1 Mg m^{-3}; though this may be reasonable, the actual dimensions and density contrasts are obviously very poorly constrained. The core density of 2.75 Mg m^{-3} is the minimum density required to fit the observed data, keeping the top of the unexposed intrusion well below the surface (~200 m depth). Alternatively, the BLC High can be modelled as a denser body (Profile Santa Rosa 3, Figure 3.30 c), where both the intrusive shallow core and the deep intrusion are given densities of 3.00 Mg m^{-3}, believed to be greater than the maximum possible density for a reasonable sub-stratovolcano dioritic intrusion. It is of course possible to model any number of deeper, but denser, bodies to produce the same gravity field, but these become more difficult to interpret, and are geologically unrealistic.

The proposed geological significance of the BLC intrusive body is that it is a substantial replacement of the less dense country rock (equivalents of the IG and the AA or VS) by a sub-volcanic feeder-dyke complex, with the greatest degree of replacement beneath Bajo Los Chiqueros. The required density of 2.75 to less than 3.00 Mg m^{-3} suggests an intermediate to mafic (gabbroic or dioritic) intrusion, which might be expected beneath the dominantly andesitic volcanics, rather than more silicic intrusions (granite density is about 2.55-2.65 Mg m^{-3}). The comparable gravity high centred over exposed dykes of the partially eroded Goat Rocks Volcano in the Cascades has been modelled by Williams and

Finn (1987) as a 10-15 km diameter buried mafic or intermediate pluton with a density of 2.70 Mg m^{-3} to a depth of 8 km, using a country rock density of 2.55 to 2.59 Mg m^{-3}.

The models of the Cerro Hinchada Gravity Ridge: To examine the possible source of the Cerro Hinchada gravity ridge, a gravity profile across the ridge, the Santa Rosa Profile, was modelled (located in Figure 3.29 a). Two different models are presented; one modelling the ridge as a thick outcrop of relatively dense lava (SR 1, Figure 3.30 a), and the second models a dyke source (model SR 2, Figure 3.30 b). A third model, SR 3 (Figure 3.30 c), has been included to show that the Bajo Los Chiqueros (BLC) intrusion could be modelled as a denser but more narrow body than that modelled in either the VV model (Figure 3.28), or the models SR 1 and SR 3.

Some shallow geological control is possible from the reasonable exposure and the projection of the temperature gradient wells PH-44, 32 and 38 onto the profile (located in Figure 3.29 a; stratigraphy in Figure 2.10 a). The density structure in the drilled shallow strata is at least partially controlled by argillic alteration focused along the important Las Hornillas fault. The shallow stratigraphy in the Santa Rosa models reflects the proposed correlation of the Sitio las Mesas LCMV andesites (shown in red) across the Las Hornillas fault. This fault is thought to be related to the other collapsed margins of the Bajo Los Chiqueros depression, partially buried by late Miravalles lavas (Figure 3.29 a). Exposures of andesite in the eastern Bajo Los Chiqueros fault scarp show almost total alteration to kaolinite in places with further deposition of sulphur, concentrations of which on the northeastern margin were high enough to warrant sulphur mining in the past (sulphur quarry located in Figure 3.29 a). Although this area is now thermally inactive, the locus of hydrothermal activity is believed to have gradually migrated to the presently active Las Hornillas area, just southwest of PGM-11 (Figure 3.21), controlled by the Las Hornillas fault. Over the past 20 years the main focus of the fumarole activity has shifted westwards by over 100 m to the present location of the Las Hornillas mudpots (M. Corella, *pers. comm.*), which suggests that the initial migration is continuing.

Parts of the strata within PH-32, 38 and 44 show similarly intense alteration to the shallow low density argillic zone in nearby PGM-11 and have been given a density of 2.09 Mg m^{-3},

equal to the average LCMV density. A possible exception to this is the fresh basaltic andesite, exposed in the Hornillas fault wall, which thickens to the east (Figure 2.10 a); a fresh sample yielded a density of 2.67 Mg m^{-3} (Table 3.1). The youngest Volcán Miravalles lavas are the variably porous blocky Santa Rosa lavas (Figure 2.5).

The source area of the Santa Rosa lavas has previously been proposed in the north Bajo Los Chiqueros area, 2 km south of the actual Miravalles crater (e.g. Alvarado *et al*, 1988, unpubl. map). The topographic form of the lavas (Figure 3.29 a), however, suggests that they *can* be traced to the summit area, and their presence is responsible for the smooth slope west of the sulphur quarry area over the otherwise steep BLC marginal scarp.

The Santa Rosa lavas were sampled from Bajo Los Chiqueros to near PGM-2, and have an average density of 2.48 Mg m^{-3} (Table 3.1). As discussed above (in Section 3.3.3) lava sample densities are thought to be formation maxima and values of 2.60 Mg m^{-3} and 2.40 Mg m^{-3} were used for the LCMV andesite and the Santa Rosa lavas in the models (density choice discussed below). The basaltic andesite in PH-32 is located on the downfaulted side of the Las Hornillas fault and a correlation with the similar northwest-dipping lavas in the fault scarp suggests a downthrow of about 100-150 m. The scarp becomes more pronounced eastwards which may reflect an increase in the throw as shown in the Santa Rosa model (200 m in Figure 3.30 a).

Figure 3.30 a (opposite) The Santa Rosa model 1 (SR1), true scale (location Figure 3.29 a). All the SR models compute the BLC intrusion to its full depth as for Profile VV, but SR1 and 2 model the CH gravity ridge. The IG, VS and CMA units are not discriminated for the purposes of modelling the CH gravity ridge. In model SR1 an increased thickness of the LCMV lavas (red) in the Las Hornillas fault scarp does not model either the CH anomaly wavelength, or its amplitude.

		SR 1	SR 2	SR 3	HSL
1	Undifferentiated CMA, VS & IG	2.40			2
2	Basement	2.65			5
3	BLC intrusion core	2.75		3.00	1
4	Deep BLC intrusion (present in all, shown in SR 3)	2.50		2.75	3
5	LCMV (lahars, tuffs, argillic zone)	2.09			2
6	LCMV andesite (buried in Santa Rosa-BLC area)	2.40			2
7	Santa Rosa Lavas	2.40			1
8	LCMV (general, Sitio Las Mesas)	2.20			2
9	CMA (Cerro Cabro Muco)	2.40			2
10	AA	2.50			3
11	LCMV (Las Hornillas fault scarp exposure)	2.50			2
12	Undifferentiated CMA, VS & IG (in SR 2 and SR 3)		2.40	2.40	2
13	Cerro Hinchada (CH) intrusion (in SR 2 and SR 3)		2.75	2.75	2
14	LCMV (surficial Cerro Cabro Muco volcanics)	2.40			2

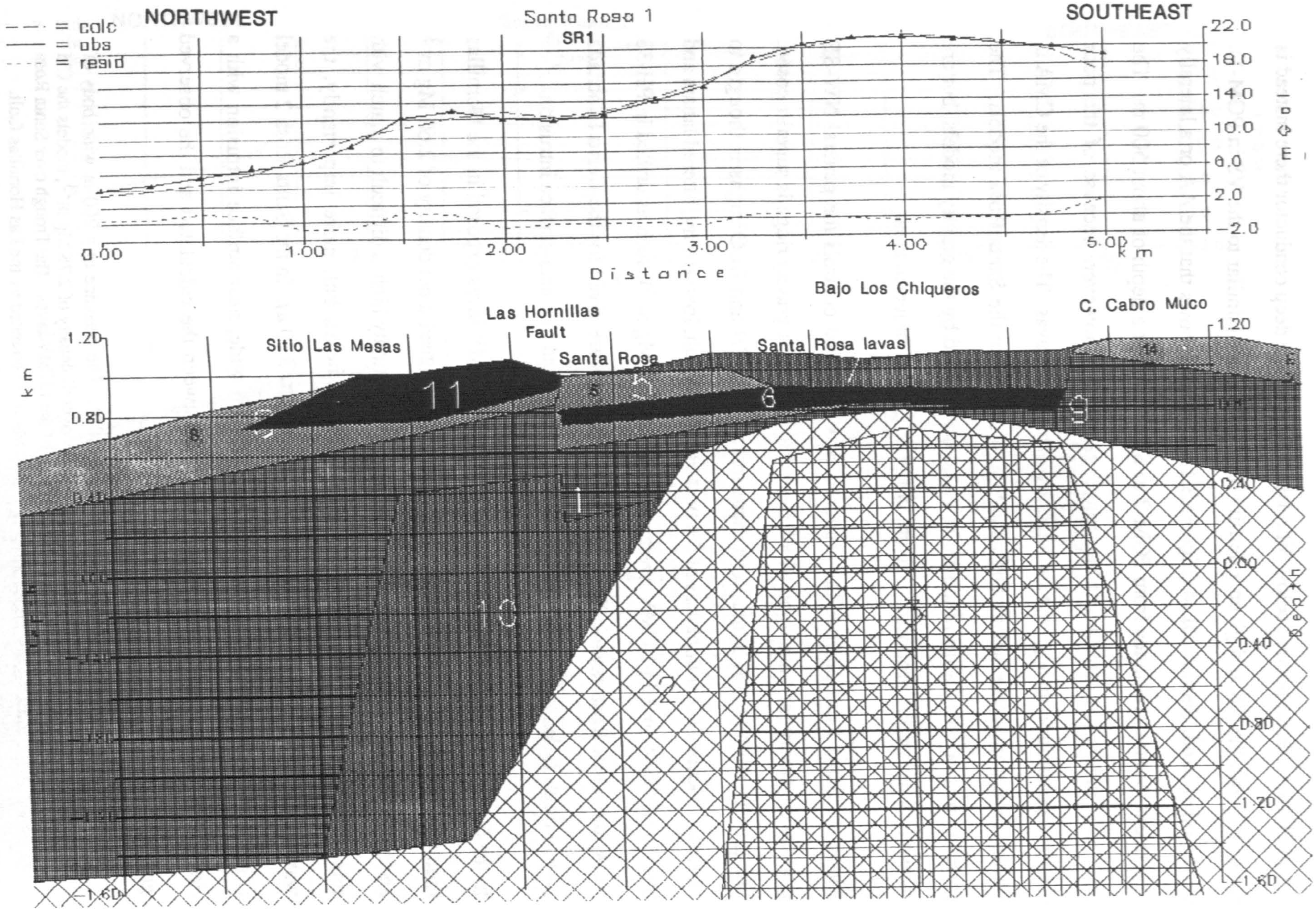
= calc
= obs
= resid
NORTHWEST
Santa Rosa 1
SR1
SOUTHEAST
22.0
18.0
14.0
10.0
6.0
2.0
-2.0
Depth
0.00
1.00
2.00
3.00
4.00
5.00
km
Distance
Bajo Los Chiqueros
C. Cabro Muco
Las Hornillas Fault
Sitio Las Mesas
Santa Rosa
Santa Rosa lavas
1.20
0.80
0.40
0.00
-0.40
-0.80
-1.20
-1.60
km
Depth
11
8
5
6
9
14
1
10
2

The pre-LCMV stratigraphy beneath Sitio las Mesas is extrapolated from the boreholes. The geoelectric section DL-9 (Figure 3.18) suggests that the resistive and slightly more dense AA in PGM-11 is not present below Sitio las Mesas and the deep conductor there instead is correlated with the VS and given a density of 2.40 Mg m^{-3} (similar to the VS in PGM-1). On the other hand, Section DL-4 (Figures 3.17 and 3.18) shows that the AA or a laterally equivalent resistor continues from PGM-2 to Santa Rosa at a depth of about 500 m. The resistivity inversions here must be treated cautiously, however, because of the poor electrical penetration through the surficial, dry Santa Rosa lavas. The density of the CMA is similar to and therefore not distinguished from the VS in the Santa Rosa models. The correlations to Cerro Cabro Muco are not well constrained by the gravity models, but are shown to illustrate the proposed structure of the Bajo Los Chiqueros area.

Along the Santa Rosa profiles the proposed BLC intrusion controls the general NW-SE gradient of gravity increase upon which the Cerro Hinchada gravity ridge is superimposed. The gravity minimum at Santa Rosa that separates the CH and BLC Highs is thought to partially reflect a 300 m thickness of the post-Hornillas fault, low density, altered lahars and breccias (PGM-2 and 11 LCMV average density is 2.14 Mg m^{-3}), such as drilled in PH-38 below the Santa Rosa lavas. Two alternative scenarios are given for the Cerro Hinchada gravity ridge: i) dense footwall lavas of Sitio las Mesas and ii) a near-surface intrusion.

In the first model (Santa Rosa 1, Figure 3.30 a) the LCMV lavas exposed in the Hornillas fault wall (associated with Cerro Cabro Muco) are assigned a net density of 2.60 Mg m^{-3} and a thickness of some 200 m. The amplitude of the gravity high is difficult to match with this thickness and is displaced 0.5 km to the northeast, but, more importantly, the wavelength of the calculated field is too broad (Figure 3.30 a). In the Santa Rosa 2 model (Figure 3.30 b), the ridge is modelled as a 0.4 km wide, near surface intrusion with a density of 2.75 Mg m^{-3}, providing a better fit between the calculated and the observed gravity.

Figure 3.30 b (opposite) Santa Rosa Profile 2 (SR2). The presence of a 200 m wide body of concentrated dyking (one intrusion unlikely), with an overall density of 2.75 Mg m^{-3}, models the CH Ridge well and permits a more reasonable thickness of the LCMV lavas. The Trough over Santa Rosa is modelled as a thick argillic zone (polygon 5; 2.09 Mg m^{-3}) bounded by the Las Hornillas fault.

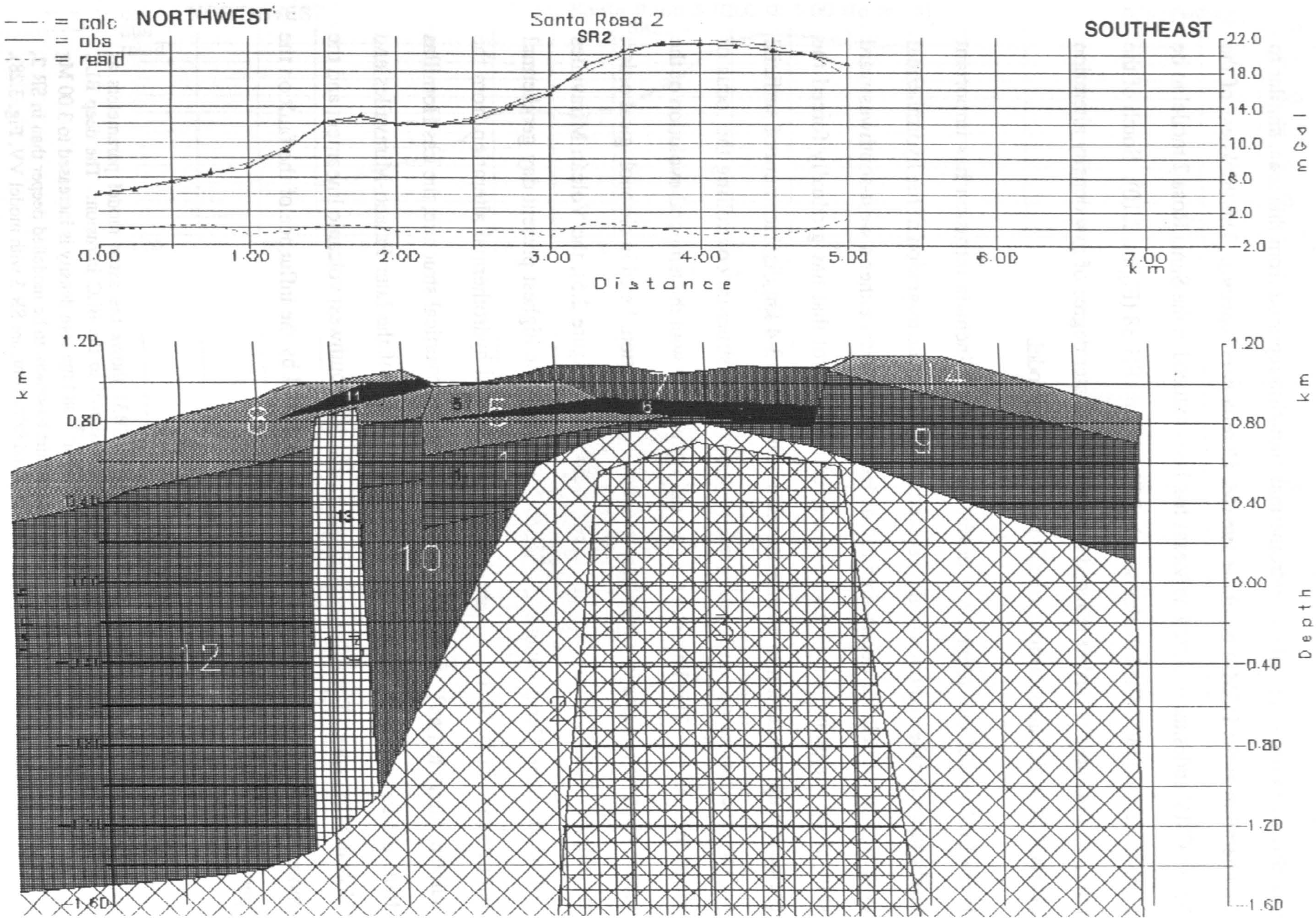
= calc
= obs
= resid
NORTHWEST
Santa Rosa 2
SR2
SOUTHEAST
22.0
18.0
14.0
10.0
6.0
2.0
-2.0
0.00
1.00
2.00
3.00
4.00
5.00
6.00
7.00
km
Distance
1.20
0.80
0.40
0.00
-0.40
-0.80
-1.20
-1.60
km
Depth
1
2
3
4
5
6
7
8
9
10
11
12
13

If the gravity ridge *does* continue to the Miravalles summit, as suggested by the available data (Figure 3.29 a) then the intrusion responsible may have fed the Cerro Hinchada cone (at CH, Figure 3.29 a), which is proposed to have produced the blocky andesite lavas here, and also given rise to the silicic hydrothermal alteration reported from this area, similar to the alteration at the PGM-4 borehole site (M. Corella *pers. comm.*). The thickness of the fresh LCMV andesites of Sitio Las Mesas has been reduced in the Santa Rosa 2 model to be compatible with the drilled thicknesses in PGM-11 and PH-38 (Figure 2.10). South of the fault, the thickness is further reduced to imply the greater degree of low density alteration observed here, this also improves the fit in the gravity model.

If the SR2 model interpretation is correct, the Cerro Hinchada intrusion has important implications for the evolution of the geothermal system. The migration of the hydrothermal system from the sulphur quarry area to Las Hornillas reflects either a west-southwestward shift of the magmatic heat source, or a structural control that has gradually forced the permeable upflow region to change location. Given the 3-4 km displacement of surficial activity, the former option is preferred, with basement structure controlling the locus of magmatic activity. This lineament is generally consistent with the temporal evolution of the recent volcanic features in a northeast to southwest direction, listed in chronological order: the ridge of Palaeo-Miravalles cones (as indicated in Figure 2.5), the Volcán Miravalles collapsed crater, Cerro Hinchada (Figure 3.29 a) and the highest present day geothermal temperatures in PGM-11 at 1 km depth. The surficial hydrothermal alteration from the sulphur quarry to Las Hornillas is located along a major vertical structure, the Las Hornillas fault and its continuation beneath the southern flanks of the later Palaeo-Miravalles and Volcán Miravalles. The offset between the northeast-southwest volcanic lineament and the more east-west geothermal trend is therefore explained by the influence of the fault on the geothermal manifestations.

Figure 3.30 c (opposite) Santa Rosa Profile 3 (SR3) shows the same model parameters as model SR2, except that here a greater density is assigned to the BLC intrusion. The deep BLC intrusion density contrast is increased to +0.35 Mg m^{-3}, and the core density is increased to 3.00 Mg m^{-3}. This allows the top of the BLC intrusion and the basement to be modelled deeper than in SR 2, but a relatively shallow intrusion core is still required (also compare SR 3 with model VV, Fig. 3.28).

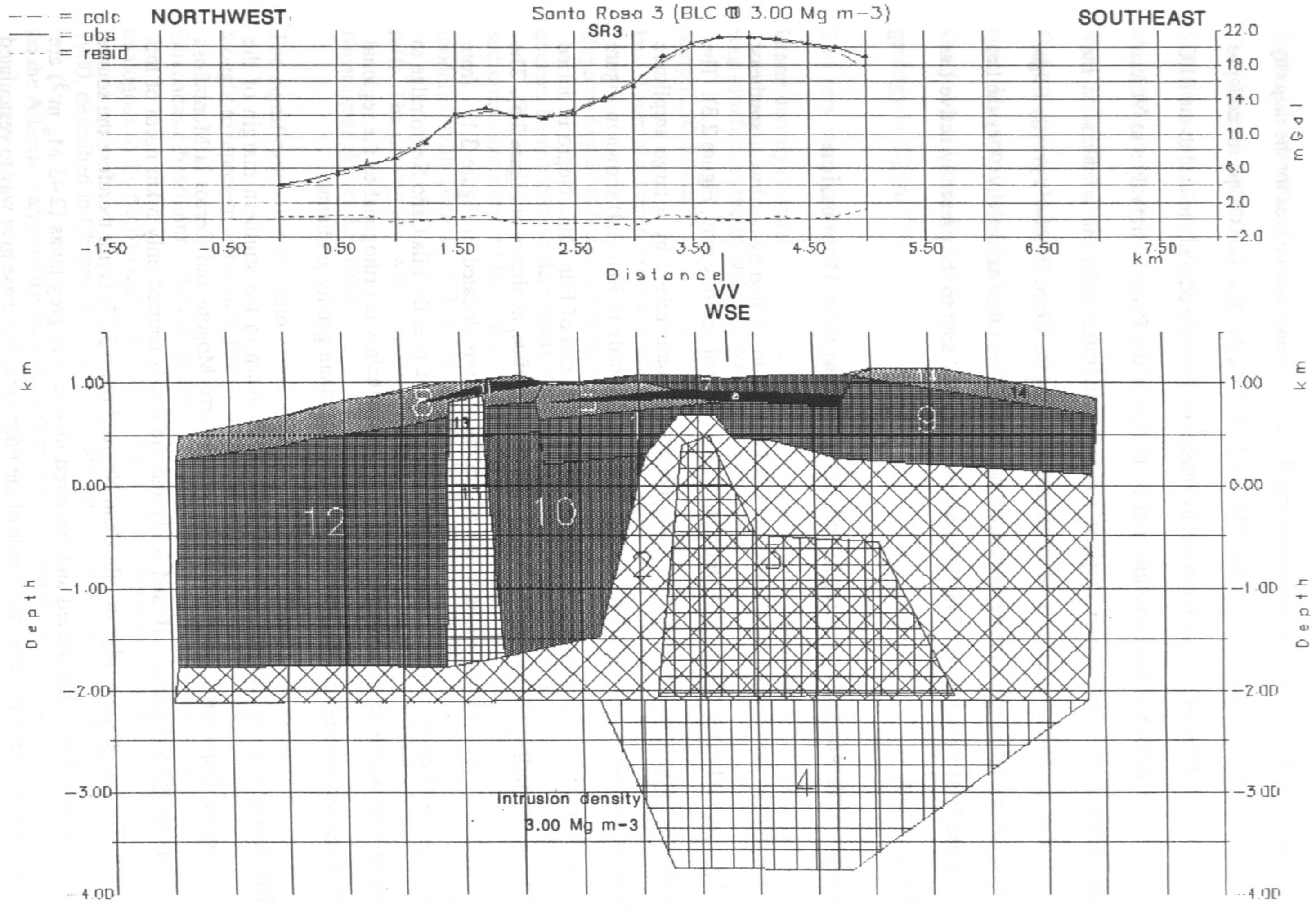
— — = calc
—— = obs
- - - - = resid
NORTHWEST
Santa Rosa 3 (BLC @ 3.00 Mg m-3)
SR3
SOUTHEAST
22.0
18.0
14.0
10.0
6.0
2.0
-2.0
mGal
-1.50
-0.50
0.50
1.50
2.50
3.50
4.50
5.50
6.50
7.50
km
Distance
VV
WSE
km
1.00
0.00
-1.00
-2.00
-3.00
-4.00
Depth
12
10
8
9
2
3
4
Intrusion density
3.00 Mg m-3

In summary, the gravity anomalies over the Volcán Miravalles area can largely be modelled in terms of the evolution of sub-volcanic intrusions. The BLC High indicates that intermediate to mafic intrusives are concentrated in the proposed source area for the majority of the drilled eastern lavas (the AA and CMA and LCMV), the Bajo Los Chiqueros collapse area. Volcán Miravalles is also underlain by intrusives, possibly partially related to the BLC intrusion but probably related to the later evolution of the Palaeo-Miravalles to Volcán Miravalles chain. This latest magmatic activity migrated from the northeast to the southwest, giving rise to the proposed intrusion causing the Cerro Hinchada gravity ridge. The migration also explains the evolution of the locus of hydrothermal activity along the Las Hornillas fault from the now inactive northeastern BLC area to the presently active Las Hornillas area.

3.6.4 The southern margin of the Nicaraguan Depression

The terrain to the north of the Guanacaste Cordillera is dominated by northwest-southeast ridges, parallel to the Nicaraguan Depression (see regional geology map, Figure 2.3). The southern topographic margin, Fila Caño Negro, is characterised by a large amplitude positive-negative gravity anomaly couple (the total anomaly is 30 mGal) shown in Figure 3.5 and Profile NS (Figure 3.27). (The south-eastern end of Fila Caño Negro is buried beneath the northern flanks of the Volcán Miravalles edifice, as shown in Figure 2.5). The NS profile is drawn from a single line of gravity stations (located in Figure 3.1) - from Victoria near lake Nicaragua, through San José de Upala, over the Fila Caño Negro ridge to Aguas Claras near the Guayabo caldera - that nevertheless is orthogonal to the regional structure, and is therefore thought to traverse the maximum gravity gradients.

The gravity high is located over the foot of the scarp to the southern margin of the Nicaraguan Depression, as for the case of the Cerro Mogote and Cerros la Montañosa caldera margins (Figures 3.10 and 3.11) and the low is centred only 5 km north of this point. The topographic ridge of Fila Caño Negro (Figure 3.27) is *not* therefore the source of the gravity high. Laminated and fractured low-density grey lavas (2.45 Mg m^{-3}) are exposed in a quarry on the northern side of the ridge crest, but these give way to vesiculated lavas and palaeosols exposed in a road-cutting just below, so again the formation density is

probably less than the measured lava density. The lamination dips shallowly to the south into the hillside, but it is not clear whether these lavas are *in situ* or are part of a large displaced structural block. Lava blocks on the southern slopes are more aphanitic and basic. The ridge is modelled as a part of the volcanics contemporaneous with the Volcano-Sedimentary Unit and therefore with a density of 2.32 Mg m^{-3}. It is difficult to match the observed gravity with a higher density for the ridge, justifying the lower formation density used in the models than the measured lava sample density. The gravity low between Fila Caño Negro and Cerros La Montañosa was modelled as low density tuffs (of unknown type, but some combination of the Bagaces group, Biotite Tuff or tuffs related to the Guayabo caldera) buried beneath the lahars, alluvium and lacustrine surface (surface geology in Figure 2.5).

The very steep gradient between the gravity couple (up to 6 mGal km^{-1}) requires a high lateral density contrast. The actual densities are poorly constrained but the observed gravity was satisfied in the model by a contrast between near surface basement at the foot of the scarp (2.65 Mg m^{-3}) and the depression fill (1.90 Mg m^{-3}), modelled to a depth of nearly 1 km. There are altered exposures of the Biotite Tuff in the gravity low region and tuffs of the Bagaces Group exposed along strike to the west (Figure 2.3). The depth of fill could, of course, be reduced by decreasing its density. North of the gravity low, tilted tuffaceous sediments are exposed in road-cuts, dipping to the south at an angle of 25°. These are modelled with a density of 2.20 Mg m^{-3} and are believed to pre-date the generally flat-lying tuffs. The gravity low was therefore modelled as low density infill within the south-tilted Nicaraguan depression block.

The significance of the shallow basement at the base of the scarp is not certain, but it is thought to represent a structural feature, rather than intrusive; a true shallowing of the actual Guanacaste basement. The composition of the pre-arc basement has been assumed to be analogous to the Nicoya Ophiolite and the Santa Elena ultramafics (e.g. Dengo, 1962; Weyl, 1980, described in Chapter 1, Figure 1.1), but equivalent rocks have not been documented on the Atlantic margin of the arc until very recently. A petroleum exploration well in the Los Chiles area near the Nicaraguan frontier (Figure 2.3) apparently drilled peridotite at a depth

of only 400 m and ultramafics have also been identified in the banks of the nearby Rio San Juan (Seyfried, *pers. comm.*). If these important preliminary observations are correct, then there is a possible continuity of the Santa Elena complex both beneath the Guanacaste Arc and across the Nicaraguan depression. No exposures of any similarly dense lithology have been recorded from the southern margin scarp but the shallow basement necessary to model the gravity might be explained in such terms. This positive anomaly need not reflect a purely ultramafic composition, which would have a density of over 3.00 Mg m^{-3}, but some admixture of dense lavas and indurated sediments of the Nicoya Complex, perhaps including some ultramafic rocks. The wider implications of the model are now developed.

The Santa Elena suture (Figure 1.1) is a major east-west lineament dividing northern Costa Rica and southern Nicaragua, that dates from the end of the Cretaceous, the time of obduction of the ophiolite sequence of the Outer Arc (e.g. deBoer, 1977 and Weyl, 1980, and see discussion in Chapter 1, final section). The extrapolated suture is buried beneath the volcanic arc products (including the Bagaces Group tuffs) of the northwest-southeast trending Guanacaste Arc, and cut by the arc-parallel Nicaraguan Depression, but the peridotite of the Los Chiles borehole is also close to the possible eastward continuation of the suture. The exposures of ophiolitic material along the Outer Arc from Costa Rica to Panama and northern South America (as reported by Berrangé and Thorpe, 1988) are not found to the north of the Santa Elena suture.

The upfaulting of the ophiolitic basement to the south of the suture is in agreement with the gravity model of the NS Profile, but the upfaulting may have been enhanced by the *later* movement on the southern margin of the Nicaraguan Depression. The model is tentatively proposed, based on a single - though impressive - line of gravity data, and a more complete gravity map of the region, together with a magnetic anomaly map, is required to examine the basement structure further.

3.7 Geothermally Induced Gravity Anomalies

The alteration-density relationships presented earlier (Section 3.4.3) are now examined in the context of the gravity field over the geothermal area (Figure 3.8) and the detailed models

AA and BB (Figures 3.24 and 3.25). These profiles are shown at true vertical scale and are directly comparable with the deep borefield stratigraphic cross-sections (Figure 2.9) and the measured density and temperature regime cross sections (Figure 3.14). A possible geothermal source for the PGM-4 site gravity high is discussed in terms of the alteration rank and intensity necessary to produce the anomaly.

3.7.1 The contribution of deep propylitization to the gradient over the northern borefield

On Profile AA (Figure 3.22), the steep gradient over the eastern boundary fault of the Pumice Unit can be matched entirely by using the measured borehole density stratigraphy and simply adjusting the lateral boundaries between the wells. However, the general east-west BCG increase between PGM-5 and PGM-2 cannot be reproduced using only the observed increase in density of the VS (Figure 3.14) within the borefield and the inferred density increase of the IG east of PGM-2 (in brown). By extending the Bajo Los Chiqueros (BLC) intrusion at depth towards the geothermal wells using similar east-west dimensions to those of Profile WSE and north-south dimensions of Profile VV the gradient can be matched. This introduces 2.65 Mg m^{-3} material at ~2 km depth in the zone between BLC and PGM-2. The other alternative explanation, possible deep hydrothermal densification of the IG and VS (and possibly the AA) to the east of PGM-2 cannot be discriminated separately from the intrusive body as shown in Figure 3.22. Similarly, the measured (more likely) broad increase in density of the deeper VS beneath PGM-2, due to increased hydrothermal epidote and chlorite mineralisation (Figure 3.14), suggests that an even greater density could occur locally, but again it is unlikely that the rank or intensity would be sufficient to account for the entire east-west gradient.

A shallow low density argillic zone (1.90 Mg m^{-3}) is modelled in both Profiles AA and BB (shown as the lined pattern within the LCMV) but does not significantly lower the computed gravity. In profile AA, an increased thickness of the low density LCMV is required for the short-wavelength inflexion in the gravity gradient 1 km east of PGM-2; part of this may be the relict low density alteration drilled in PH-38 (location in Figure 3.21), as modelled in the Santa Rosa profiles (Section 3.6.3).

3.7.2 The PGM-4 High; propylitization, structural high or intrusion?

Understanding the significance of the gravity high at the PGM-4 site on Profile BB (Figure 3.23) is important for aquifer permeability predictions south of the *high* permeability well, PGM-12. Initially there were fears that the High indicated the replacement of the VS (drilled in PGM-12) by the Acidic Andesite Unit in this area, but the geoelectric sections of Duprat and Leandro (1986) and Geosystems (1988) do not show a shallow resistive basement here as observed at the top of the AA in the northern borefield (Figure 3.17), so this suggestion is discounted. An alternative, deeper source model for the High is presented here.

Profile BB shows that gravity increases from PGM-3 to PGM-12, but importantly this gravity increase cannot be explained by the measured density trends. The density and thickness of the CMA and the density of the upper VS are lower in PGM-12 as compared with PGM-3. There is also a general continuity of the LCMV and upper CMA stratigraphy in the PH- boreholes to the south of PGM-12 (Figure 2.10 a), and therefore the source for the gravity increase towards the PGM-4 High has been modelled in Profile BB at the depths of the IG and lower VS. There are no densities measured from the deepest PGM-12 cores of the lower VS and IG (Figure 3.13 g), but the intensity of alteration is less in these cores than in the upper VS cores, suggesting that significant deep propylitization, at least in the VS and IG has not occurred at PGM-12 (details in Figure 3.13 g). A deep source for the increase in gravity from PGM-3 to 12 should therefore be below the deepest PGM-12 core in the Ignimbrite Unit (core 9 at 1080 m b.s.l.) and has been modelled in terms of a gradual shallowing of the 2.65 Mg m^{-3} basement. This is not, however, sufficient to explain the PGM-4 High, given the decrease in density of the CMA level strata, and an additional body with a density equivalent to the lower VS at PGM-12 (shown in red 2.39 Mg m^{-3}), is necessary at the level of the upper VS.

The southern and western gradients of the PGM-4 High are much steeper than the northern or eastern gradients (Figure 3.8). This was explained in Profiles BB and CC (discussed earlier in Section 3.6.2) as being due to an increased thickness of the low density VS

(measured for the upper VS in PGM-12, 2.15 Mg m^{-3}) to the south and west, combined with the effect of the low density (1.90 Mg m^{-3}) CMA tuff drilled in the southern wells.

The dome-like shape of the proposed shallowing dense body is possibly an unreasonably vertical geometry for a hydrothermally densified zone, but is required by the relatively low density measured in the VS in the nearby PGM-12. The PGM-4 High could equally be modelled by a body with a more vertical profile, suggestive of an intrusive body, and the arguments for and against a hydrothermal origin for the PGM-4 High are now discussed.

The core of the proposed dense body (2.65 Mg m^{-3}) shown in Profile BB below the PGM-4 site has a density contrast with the Ignimbrite Unit (IG) of + 0.19 Mg m^{-3}, and with the deep VS of + 0.25 Mg m^{-3}. The outer part of the body (in red) has a density contrast with the upper VS of + 0.24 Mg m^{-3}. It is possible to calculate the intensity of an alteration assemblage of the highest (and therefore densest) reasonable rank that would be required to produce these density contrasts, but it is important to understand whether the alteration assemblage is simply replacing the primary minerals or partially replacing the porosity also. The wet density of the altered product, $\rho_{w'}$, is given by:

$$\rho_{w'} = (1-\varnothing)(f_a\rho_a + (1-f_a)\rho_r) + \varnothing((1 - f_\varnothing) + f_\varnothing\rho_a)$$

where $\varnothing$ is the original porosity, f_a is the fraction of the original grain density (ρ_r) replaced by the alteration assemblage of density ρ_a, and $f_\varnothing$ is the fraction of porosity replaced by ρ_a.

$$\therefore \qquad f_a = \frac{\rho_{w'} - \varnothing((1 - f_\varnothing) + f_\varnothing\rho_a) - (1 - \varnothing)\rho_r}{(1 - \varnothing)(\rho_a - \rho_r)}$$

The maximum alteration assemblage density, ρ_a, shown in the following table, was derived by assuming that the high-T assemblages in the deeper PGM-2 and 11 cores were analogous (mineral fractions from ELC, 1986 a, mineral densities from Deer *et al.*, 1966):

Mineral	%	Density Mg m^{-3}
H_2O-poor clays	40	2.65
Epidote	20	2.90
Chlorite-penninite	20	2.90
Adularia	10	2.65
Quartz	8	2.65
Pyrite	2	4.50
	total = ρ_a	2.82

Using this alteration assemblage density, the case for no porosity loss is examined first. To produce the required density of 2.65 Mg m^{-3} from the IG (originally ρ_w = 2.46 Mg m^{-3} and $\varnothing$ = 5%) would require 71% replacement. It would be impossible to generate 2.65 Mg m^{-3} from the deep VS (ρ_w = 2.39 Mg m^{-3}) while retaining the 17% porosity, but a 67% replacement of the upper VS (ρ_w = 2.15 Mg m^{-3}) could generate the 2.39 Mg m^{-3} zone, while retaining the 17 % porosity.

An alternative explanation is to increase the density of the IG and the VS by removing some of the porosity during the propylitization. A depositional process implies that less actual replacement of primary material would be necessary to produce the density increase required by the gravity models. If the high porosity of the VS was reduced drastically by 50% beneath and to the south of PGM-12, an 87% replacement of the grain density would generate 2.65 Mg m^{-3}, whereas an 80% porosity reduction would only require 10 % replacement of the grain density. It is possible, of course, to generate an infinite number of replacement/porosity loss scenarios and the ones here only serve to constrain what are considered to be reasonable parameters. Whatever the parameters, however, the required density contrasts and form of the dense body imply a high temperature up-welling region, past or present, if a hydrothermal origin is proposed.

A contemporaneous hydrothermal origin? Firstly, what independent evidence is there for present hydrothermal activity in the south? The high contemporary temperature gradients and the surficial silicified zone at the PGM-4 site and the chloride springs 1 km to the south, suggest there is at least increased shallow heat flow (Figure 2.2 a). However, there are no fumaroles or any other surficial expression of a shallow vapour zone (as at Las Hornillas, above the upflow zone), and the reservoir cross-sections (Figure 3.14) show that present day liquid-dominated zone temperatures wane along the outflow zone to the south.

Moreover, temperatures in PGM-12 are entirely below the boiling curve for water (ELC, 1988 and discussed in Chapter 5; reservoir monitoring), indicating a relatively low-T regime compared with the northern borefield conditions. Unless the PGM-4 site is the upwelling part of an independent, deep geothermal system, and there is no srong geochemical evidence to suggest that the chloride spring fluids to the south are different to the borefield fluids (e.g. Rochelle, 1991, Grigsby *et al.*, 1990), it is not considered likely that a contemporary geothermal system could be responsible for the deep densification at the PGM-4 site. (An alternative reason for the increased heat flow and the silicic alteration at the PGM-4 site is presented in the following section).

A palaeo-hydrothermal origin? The higher temperature palaeo-system suggested by Bargar and Fournier (1988) and Rochelle (1991) has maximum temperatures of >300°C at the base of PGM-11 but only 275°C at the base of PGM-12 (values shown in italics in Figure 3.14), suggesting a similar temperature gradient regime to today's system (presently, T_{max} is 255°C at PGM-11, 235°C at PGM-12). It is possible to invoke a high-temperature palaeo-upwelling system at the PGM-4 site with an outflow plume to the south, separate to the regime responsible for the high palaeo-temperatures in the PGM-11 area. Though this is possible, the upwelling temperatures may have had to be cooler than those of the northern system, to explain the lower palaeo-temperatures observed in PGM-12. This suggests that the overall alteration rank may also have been lower than that of the northern borefield and implies higher degrees of alteration to attain the required density increase.

Although it is possible to propose a hydrothermal propylitization origin for a deep dense body beneath the PGM-4 site, the lack of supporting evidence for either an existing or past upwelling zone in this area, combined with the vertical profile of the required body, suggests that other alternatives must be considered:

Structural origin? The structural and geological outline of the southwestern caldera area is shown in Figure 2.5, and the main features are also shown on both the 0.5 mGal BCG map in Figure 3.8, and relative to the geoelectric sections and gravity profiles in Figure 3.20. The shallowing of the basement from PGM-3 to PGM-4 in Profile BB can be explained structurally by decreasing the thickness of the IG. The steep gravity gradient to

the south of the PGM-4 High, compared to the more gentle gradient to the north, is due to the thickening of the low density CMA tuff (contemporaneous with the Pumice Unit), as discussed earlier (Section 3.6.2). Similarly, the steep gradient to the west of PGM-12 locates the major PUM boundary and is also partially due to the proposed lateral density change within the deeper VS (Profile CC, Figure 3.24). There is still, however, a requirement for an *isolated* structural high in the PGM-4 area, below the level of the CMA tuff, of the dimensions shown in Profile BB. Although it would be possible to model a basement high, possibly with a more vertical outline than indicated in Profile BB, it is difficult to suggest an origin for an isolated structural block in this area. Whatever the supposed origin, the basement high would have to be related to an event before the CMA tuff and the La Fortuna graben.

Intrusive origin? An alternative suggestion is that the deep body may be intrusive in nature, with similar dimensions to those shown in Profile BB. The significance of the modelled density of 2.65 Mg m^{-3} for the intrusive zone is a gradual replacement of the country rock by a complex series of intermediate (possibly dioritic) dykes of a density up to 2.90 Mg m^{-3}, as proposed for the Bajo Los Chiqueros intrusion (Section 3.6.3). The relatively minor intrusion required to model the PGM-4 High could have set up a local hydrothermal system, and although this may have increased porosity during the initial vigorous activity, the porosity would have been reduced by mineral deposition in the fractures and pores during cooling.

In summary, *reasonable* hydrothermal and structural models, on their own, fail to account adequately for a deep source to the PGM-4 site gravity high. An intrusive body is considered to be the most likely alternative, possibly accompanied by some associated hydrothermal densification of the country rock.

The implications for the PGM-4 thermal anomaly: The increased heat flow in the PGM-4 area (Figure 2.2) is difficult to reconcile with the geometry of the present outflow plume (Figure 3.14) as the system cools from the upflow region close to PGM-11 towards the south. It is possible that the increased permeability along the western margin of the La Fortuna graben has allowed better communication between the deep reservoir and the

surface - analogous to the Las Hornillas fault. Furthermore, the proposed low permeability deep body at the PGM-4 site may cause the present outflow plume to be diverted towards the surface. This is supported by the shallowing of the top of the main conductor, likely to be the geothermal brine, at PGM-4 in profile G-4 (resistivity layer 3, Figure 3.19). Upwelling of the outflow plume over and above the deeper PGM-4 body would, at the same time, help to explain the thermal anomaly at this site and the location of the chloride springs 1 km south of this area (Figure 2.2).

The specific mineralogy of the deeper palaeo-system suggests deposition in a liquid-dominated reservoir, rather than a boiling or vapour zone (Rochelle, 1991), but this requires greater hydrostatic pressures than exist today at comparable depths, perhaps implying a shallower top to the deep reservoir. Therefore, the past liquid-dominated zone could have had a surficial expression at the PGM-4 site, explaining the silicic alteration exposed there, whereas the brines of the present outflow plume appear 1 km further south at La Fortuna (springs located in Figure 2.2).

3.7.3 Summary of geothermal-related mass distribution and evolution

Gravity anomalies at Miravalles may be related to hydrothermal activity, but it is difficult to distinguish competing causes, such as intrusive bodies *vs* deep propylitization or low density tuffs *vs* shallow argillic zones, without independent confirmation from boreholes or other geophysical techniques. Shallow de-densification due to low density, water-rich smectite replacement of lavas and tuffs of the LCMV is known to cause small, negative anomalies, most notably the alteration zone in the Santa Rosa area. Deep densification is directly observed from PGM borehole samples and increases with increasing rank (i.e. temperature of deposition). It is responsible for at least part of the northeastern borefield gravity gradient, but it is difficult to separate these effects from those of the BLC intrusive activity just east of the borefield.

The present geothermal system is not directly related to the Bajo Los Chiqueros intrusion which would have had its own system at the time of the associated Cabro Muco volcanism.

The more recent upflow region has apparently migrated westwards from the northern BLC area (sulphur mine, Figure 3.29 a) along the Las Hornillas fault to its present position beneath Las Hornillas. The Cerro Hinchada gravity ridge from Volcán Miravalles towards Las Hornillas is interpreted as a buried intrusion. The suggested E-W migration of the geothermal heat source is thought to be related to the NE-SW trend of the volcanic activity, from Palaeo-Miravalles to Volcán Miravalles to Cerro Hinchada. The apparent offset between the volcanic trend and the geothermal trend is thought to reflect the dominance of the structural control (the Las Hornillas fault) on the upflow zone, rather than solely the location of the heat source of the hydrothermal systems.

The PGM-4 High is best modelled in terms of an ancient, small intrusion with an associated local hydrothermal system. The waning stages of this activity are thought to have caused mineral deposition, reducing porosity and increasing the density of the country rock. A contemporaneous heat source beneath the present thermal anomaly in the PGM-4 area coincident with the deep source positive gravity anomaly is not necessary, as palaeo-geothermal systems are able to retain their densification signature after their demise. Rather, the denser basement is thought to deflect the present outflow plume (that has a distinct source to the north) upwards at PGM-4, giving rise to the higher heatflow and chloride springs just to the south at La Fortuna.

3.8 Summary of the Gravity Modelling Results

Over 400 new gravity data points were integrated with the previous gravity data from the Miravalles and Tenorio geothermal fields to produce a Bouguer gravity map covering the Guayabo caldera area. The new data provide, for the first time, a gravity traverse across the Guanacaste arc from the inner fore-arc margin, over the Guayabo caldera and Volcán Miravalles, to the Nicaraguan Depression behind the arc.

The 55 km trans-Guanacaste arc model shows that there is no regional gradient across the arc that would be expected if the dense ophiolitic basement exposed in the Outer Arc were dipping beneath the present volcanic arc. The implication is that the basement is at a reasonably constant depth beneath the arc, modelled in this study at about 2 km below sea

level. The inner, topographic margin of the Nicaraguan Depression is characterised by a 30 mGal gravity couple. The positive and negative anomalies are located over the base of the scarp and 5 km inside the depression respectively and can be modelled by bringing the basement close to the surface at the foot of the scarp in contrast to over 2 km low density (volcanic) fill within the depression. The model of the floor of the Nicaraguan Depression suggests that it is tilted towards the arc, and the similarly tilted exposed older parts of the fill and the discovery of peridotite at 400 m depth within the supposed centre of the depression, 20 km from the inner margin, support this model. The Outer Arc ophiolitic basement is not exposed to the north of the E-W Santa Elena suture, which pre-dates and is buried by both the Guanacaste arc volcanics and the Nicaraguan depression fill. The shallow basement defined by the gravity data over the inner depression margin, and the drilled peridotite are south of, and tentatively related to, the proposed extrapolation of the Santa Elena suture.

The results from over 600 new density measurements give a detailed knowledge of the density variation within both the exposed and the PGM borehole stratigraphy, which has resulted in well constrained gravity models of the Guayabo caldera. Primary lithological differences are the dominant controls on the gravity field, but hydrothermal alteration is at least partially responsible for some of the density variation within the drilled stratigraphic units. Water-rich smectites in the argillic zone, associated with the vapour-dominated phase above the geothermal upflow region, cause a decrease in density. The high-T alteration assemblages associated with both the past and present liquid-dominated reservoirs are responsible for the observed increase in density (propylitization) of the main reservoir host, the Volcano-Sedimentary Unit, towards the north-eastern borefield. The alteration rank and density increases with depth, and propylitization is therefore a more important control on the overall density structure than the more local low density argillic alteration.

Density increases due to reasonable propylitization, however, are insufficient to account for either the eastern increase in gravity over the borefield towards the Bajo Los Chiqueros gravity high or the more local high at the PGM-4 site. Buried intrusions are required at both sites to explain the gravity anomalies. The proposed BLC intrusion extends beneath the volcanics on the eastern caldera margin, including Volcán Miravalles, but is centred on the

ancient, collapsed, Cerro Cabro Muco volcanic centre. The entire BLC intrusion is thought represent a complex body, built up during the successive periods of pre- and post-caldera volcanism, including the Acidic Andesite, the Cerro Cabro Muco volcanics and the latest stratocones of the Miravalles edifice.

The distribution of the very low density Pumice Unit, drilled only in PGM-15, is shown to be the major control on the central negative gravity anomaly associated with the Guayabo caldera. The inner Guayabo Low is well defined by the consistent increase in the gravity gradient located ~2 km *inside* the topographic caldera margins and between PGM-5 and PGM-15 on the eastern margin. This gradient is modelled as the boundary fault of the Pumice Unit, with a displacement of 250 m. The boundary fault cuts both the Cabro Muco Andesite Unit and the Volcano-Sedimentary Unit, and shows that the central subsidence of the Guayabo caldera is associated with the Pumice Unit event. A further 170 m of Pumice Unit in the central caldera is required to match the observed gravity. Although the Pumice Unit drilled in PGM-15 has been correlated stratigraphically with the La Ese Pumice and possibly the Hornblende Tuff, the distribution of the Pumice Unit as defined by the gravity models, especially the deeper part, may be the intra-caldera equivalent of the Upper Grey Ignimbrite also.

The outer part of the Guayabo Low extends across the western and especially the southwestern topographic margins of the caldera. The topographic margins of the caldera are modelled as downfaulted ring fractures with ~300 m displacement. The timing of this displacement on the southern caldera margin post-dates the Pumice Unit which transgresses, and is also upfaulted on, the margin. The timing of the collapse of the western and northern caldera walls is not well constrained but, by association with the southern caldera walls, may also post-date, rather than pre-date, the Pumice Unit. The gravity models show, in agreement with the previous geoelectric sections, that the Volcano-Sedimentary Unit extends across the caldera margins. The distribution of the underlying Ignimbrite Unit is not well constrained by the gravity models, but by inference, also extends beyond the margins of the Guayabo caldera and is thought to be part of the ignimbrite shield basement to the Quaternary Guanacaste arc. The Cabro Muco Andesite Unit is correlated with the Cerro

Espiritu Santo scarp the Late Cabro Muco Volcanic Unit is correlated with the edifice of Cerro Cabro Muco.

The Nettleton Profiles across the western and northern topographic caldera margins show that the walls are low density features that must contain a proportion of tuffs and cannot be composed solely of the exposed lavas. The western margin lavas and tuffs are correlated with a similar sequence in the upper Volcano-Sedimentary Unit in PGM-15; both parts of the opposing flanks of the ancient Volcán Guayabo, thought to have been located in, and collapsed into, the centre of the present caldera. The Cerros La Montañosa sector of the caldera is associated with a ring of small amplitude positive anomalies and is modelled as a separate volcanic centre to Volcán Guayabo, but contemporaneous with the VS. The Acidic Andesite Unit is also contemporaneous with the VS, but is restricted to the eastern caldera margin, and is therefore thought to have a source to the east of the caldera. The pre-Guayabo caldera stratigraphy includes therefore, most of the PGM stratigraphy on the eastern caldera margin; the Ignimbrite Unit, the Acidic Andesite Unit, the Volcano-Sedimentary Unit and the lower Cabro Muco Andesite Unit.

The gravity highs over parts of the low density extra-caldera tuffs are sometimes associated with exposures of sub-tuff lavas. The San Jorge and Salitral Highs are therefore modelled as partially and sometimes completely buried outcrops of pre-tuff, lava-dominated volcanic centres that are thought to be broadly contemporaneous with the Volcano-Sedimentary Unit.

Both the results of the previous resistivity studies of the borefield area, and the well constrained gravity models presented in this Chapter have complemented and clarified the revised stratigraphic model of the Guayabo caldera presented earlier in Chapter 2. A mass and volume balance model for the products and collapse volume of the Guayabo caldera is presented in Chapter 4. The results show that the dense rock equivalent (DRE) volume of all the erupted products (intra- and extra-caldera) is significantly smaller than the volume of the Guayabo caldera. The imbalance supports the late stage subsidence (post-Guayabo tuffs) proposed earlier to explain the present topographic expression of the caldera. The evolutionary model of the caldera is now described.

3.9 The Incremental Collapse Model of the Guayabo Caldera

The Guayabo caldera formed by multi-stage, incremental collapse, both during and following the eruption of the several associated outflow tuffs. Importantly, the gravity models suggest that subsidence began in the central caldera at the time of the eruption of the majority of the caldera-related tuffs, including the Pumice Unit. This early subsidence was bounded by ring faults ~2 km inside the present topographic margin but was also partially controlled by graben-type tectonics across the southwestern margin. The present 11 km topographic margin is thought to be largely due to later subsidence across ring faults outside the Pumice Unit boundary faults, but some of the subsidence may have preceded the Pumice Unit event. A four stage evolution model is shown in Figures 3.31 a-d. The radiometric dates used for the ages of each stage are from previous studies reviewed by Gillot *et al.* (1990), and the geochemical analyses of the tuffs are from Mora (1988); the results of both studies are reviewed in Chapter 2.

Stage 1 The Santa Rosa Ignimbrite Shield (8-2.2 Ma?) The local stratigraphic sequence begins with the eruption of the grey, dacitic ignimbrites of the Bagaces Group. The time span of the Bagaces tuffs is bracketed between the 8 Ma Flujo Carbonal and the overlying, distinctive 1.6 Ma Biotite Tuff. It is proposed that the lithic-rich, partially welded Ignimbrite Unit (IG) is an intra-caldera fill equivalent of part of this sequence, but it is not clear if the >800 m of this unit is the result of either one or several collapse events. Though the Ignimbrite Unit extends across the buried margins of the Guayabo caldera, the absolute depth and dimensions of the presumed early Ignimbrite Unit caldera, shown in Figure 3.31 a, are not well constrained.

Stage 2 Pre-caldera stratocone volcanism (2.2-1.65 Ma) The style of volcanism seems to have changed from ignimbrite shield to stratocone formation. The Acidic Andesite Unit (AA) had a source to the east or north-east of the borefield, and the contemporaneous Volcano-Sedimentary Unit (VS) was probably related to several sources.

Figure 3.31 a-d, Part 1 The proposed multi-stage evolution of the Guayabo caldera (the dimensions of, and depth to, the associated magma chamber are poorly constrained and not shown). The schematic sections are aligned west to east-southeast and the vertical scale is exaggerated ~x2.

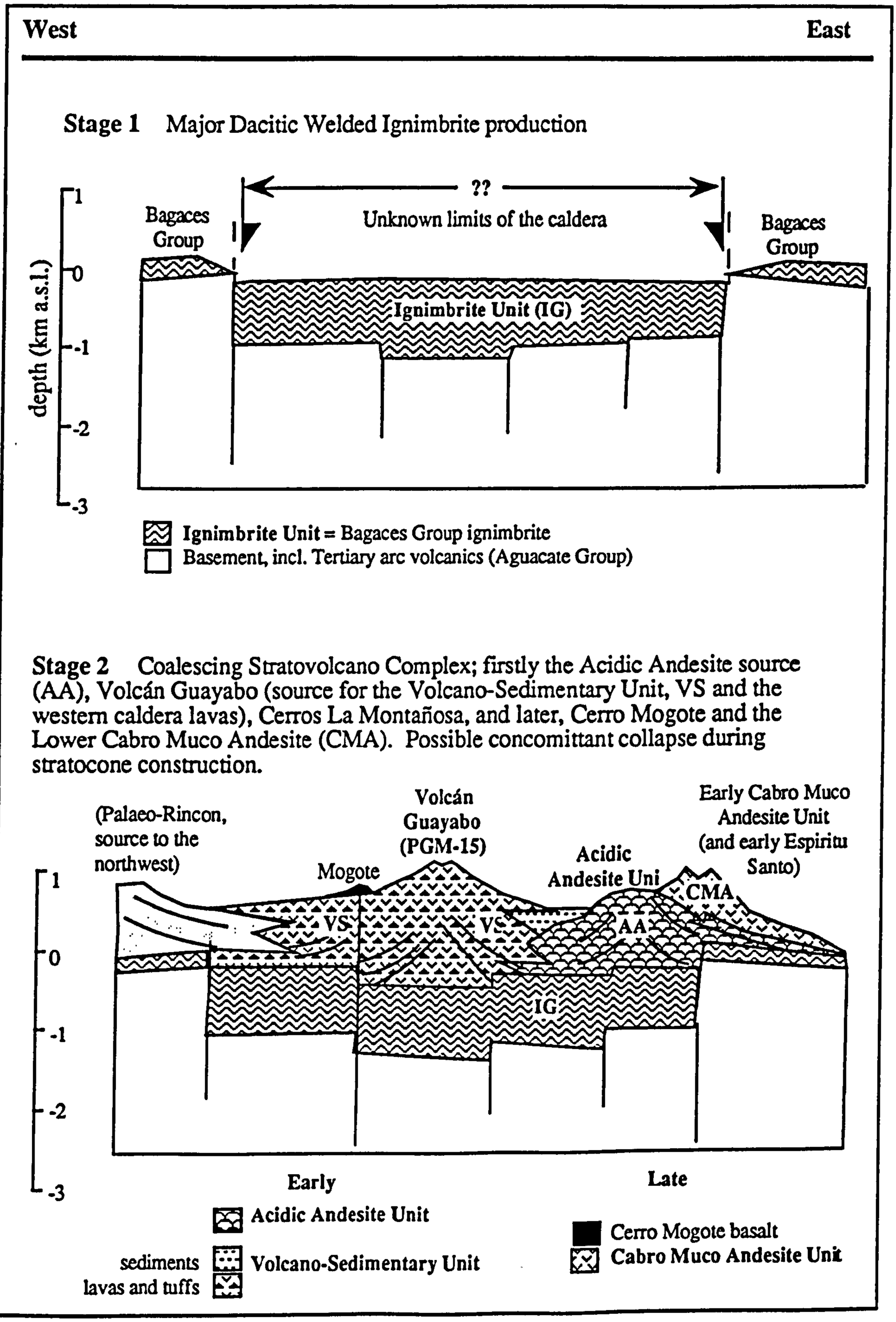

Volcán Guayabo, shown in Figure 3.31 b, is the proposed source for the PGM-15 lavas and tuffs, with a vent location in what is now the centre of the Guayabo caldera; the Cerros La Montañosa centre was a discrete edifice to the north. Volcán Guayabo is the proposed source for the outward-dipping lavas of the western caldera walls (one lava dated at 2.2 Ma) and therefore the upper VS pre-dates the formation of the Guayabo caldera. As is typical of basaltic andesite stratovolcanoes of Central America today, lava effusion was interrupted by several stages of tuff eruption, forming the lithic-rich tuffs that make up most of the southern borefield VS. Concomitant incremental, piecemeal subsidence of the central area is suggested to explain some of the subsidence of these early stratocones to their present sub-sea-level position both within and outside the caldera. The Biotite Tuff (1.65 Ma) erupted from a source beneath the present Rincon de la Vieja stratocone complex towards the end of the major stratocone building stage; some of the western caldera lavas may post-date the Biotite Tuff.

The VS and AA activity was superseded by activity along the margins of the incipient caldera margin. Thus, the early Cabro Muco/Espiritu Santo centre was the source of the Cabro Muco Andesite Unit, and the Cerro Mogote basalt may have been erupted at this time though Mogote volcanism could have post-dated the older (1.6 Ma) Guayabo tuffs but pre-dated the La Ese Pumice (0.6 Ma). (The 0.6 Ma K-Ar age from ELC, 1983 for Cerro Mogote may be unreliable due to the low $^{40}Ar_{rad}$ content).

Stage 3 Multi-stage caldera collapse (1.6-0.6 Ma): The outflow sequence from the Guayabo area begins with the dacitic Upper Grey Ignimbrite (65-68% SiO_2, dated at ~1.6 Ma). Though this is the most voluminous extra-caldera tuff it has not been positively identified in the borefield but may be the deeper part of what has been modelled as the Pumice Unit in the gravity models. The eruption was accompanied by coring of the central vent and collapse of the central part of the caldera, well within the present topographic margins of the caldera. There is a sharp compositional break before the eruption of the rhyolitic Hornblende Tuff (72-75% SiO_2, also ~1.6 Ma) and a further break to the younger La Ese Pumice (77.5% SiO_2, ~0.6 Ma).

Stage 3 Collapse of the Guayabo caldera in three stages producing three outflow tuffs ; I) Upper Grey Ignimbrite, II) Hornblende Tuff and III) La Ese Pumice. The Intra-caldera equivalents of II and III are the Pumice Unit(PUM). Continued magmatism on eastern caldera margin with growth of Late Cabro Muco and Espiritu Santo, Palaeo Miravalles and associated dense intrusives (responsibe for the Bajo Los Chiqueros gravity high, BLC).

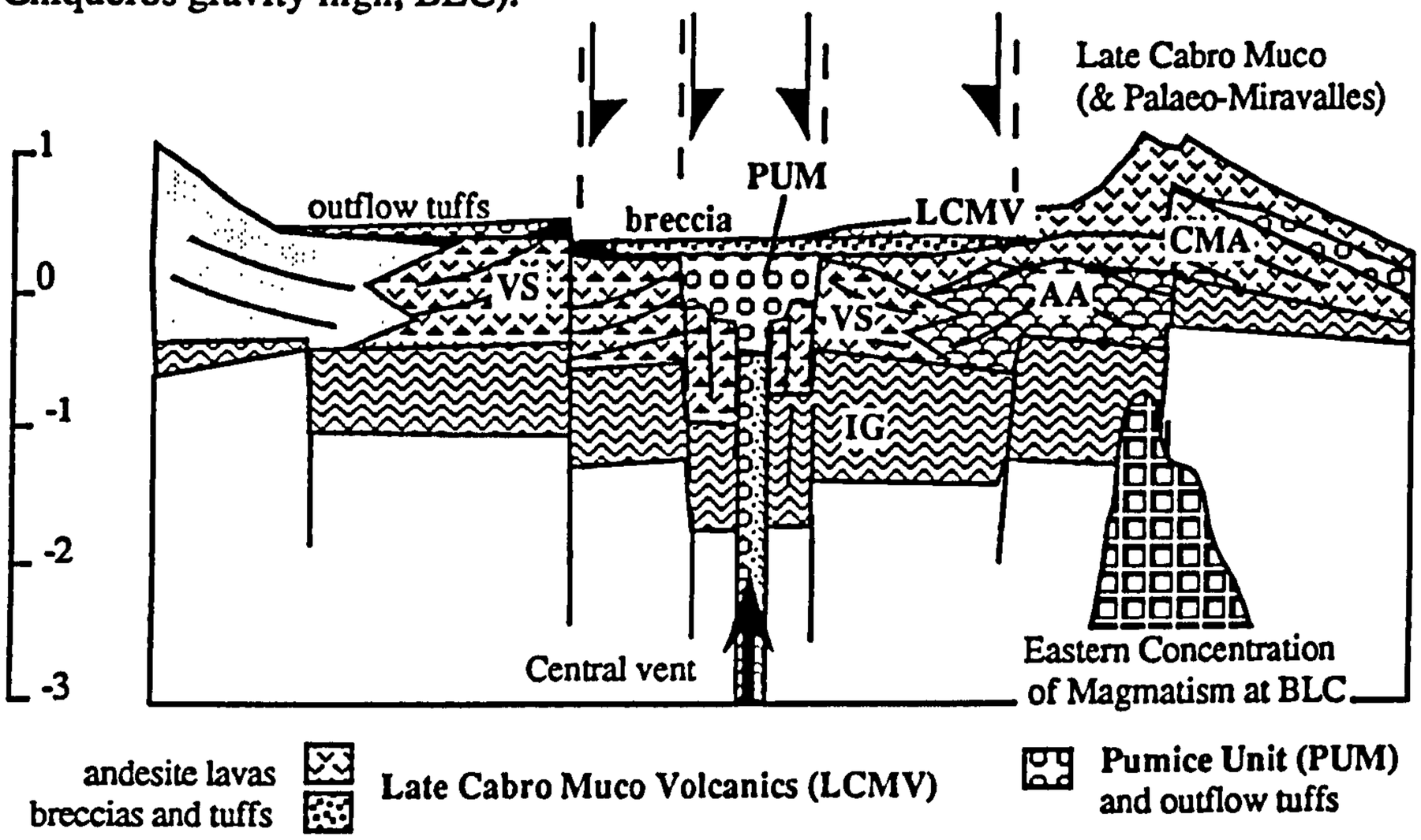

Stage 4 Further collapse of Cabro Muco and Palaeo-Miravalles at Bajo los Chiqueros and the activation of the NS grabens produces late CM breccia and lahars. Growth of V. Miravalles responsible for continued subsidence of caldera area as a result of magma withdrawl connected to a deeper, sub-caldera 5-10 km chamber. The cooling Bajo Los Chiqueros stock is the geothermal field heat source.

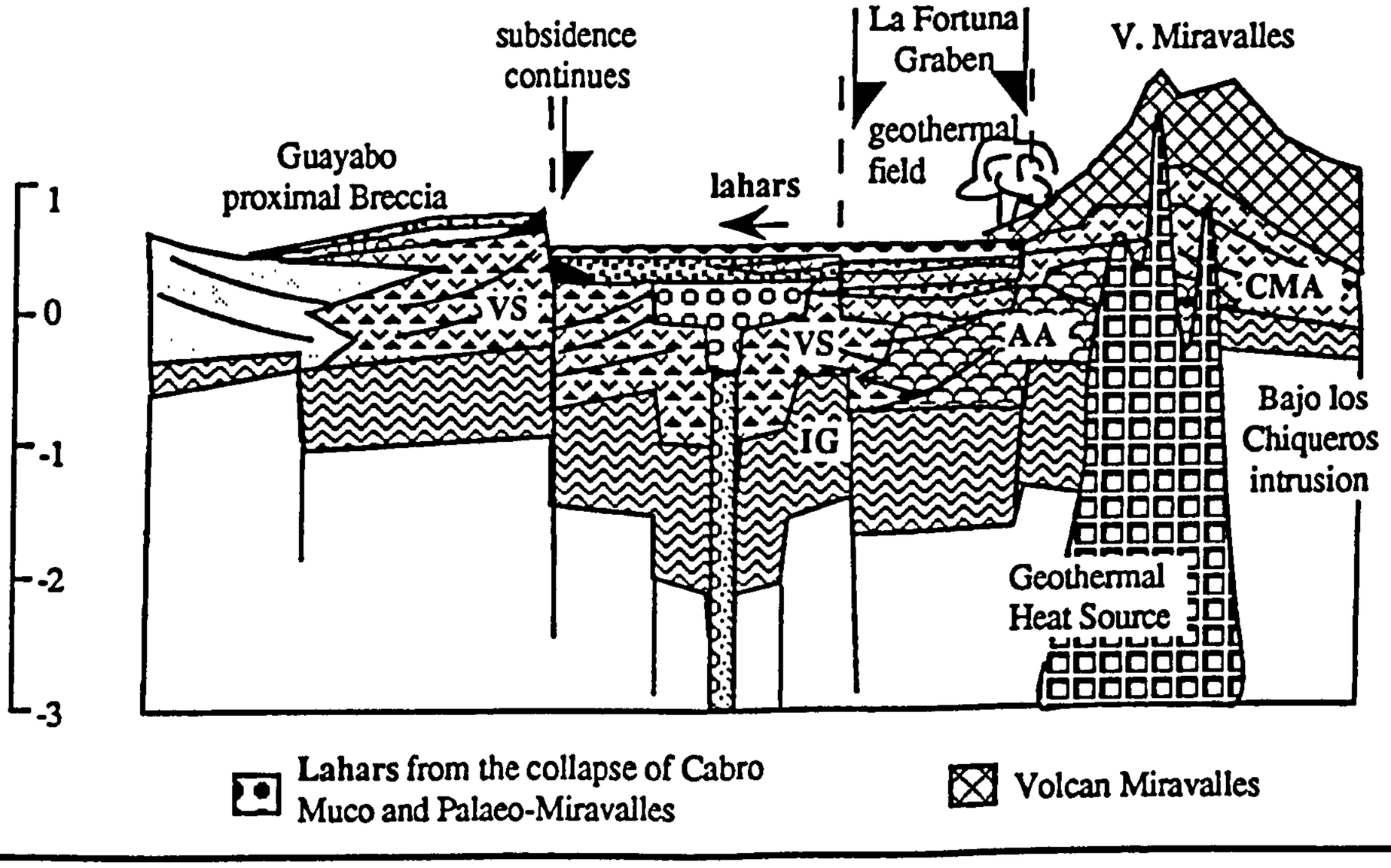

The extra-caldera La Ese Pumice and possibly the Hornblende Tuff are equivalent to the Pumice Unit, also concentrated in the centre of the caldera, and drilled only in PGM-15. The caldera-centred incremental collapse is responsible for the central, negative, V-shaped gravity anomaly. This major silicic pyroclastic activity was interrupted after 0.6 Ma and followed by a resumption of andesitic stratocone build-up and associated intrusive activity on the eastern caldera margin; the Cerro Cabro Muco/La Giganta area and later the Palaeo-Miravalles complex.

Stage 4 Post-caldera activity and continued subsidence (0.6 Ma to present): Post outflow tuff subsidence of the Guayabo caldera is required to explain the greater volume of the caldera compared with the total DRE volume of the Guayabo tuffs (details in Chapter 4). Growth and collapse of the eastern margin centres was now well advanced. The Bajo Los Chiqueros area collapsed to produce the Late Cabro Muco breccias (equivalent to the Guayabo Proximal Breccia) and much of the lahars that presently cover the caldera floor. The main phase of collapse on the Cerro Espiritu Santo fault and the formation of the La Fortuna and Aguas Claras grabens also occurred during this time interval (0.6 Ma to the present). Volcanism on the eastern margin was then confined to the build-up of Volcán Miravalles. The age of the Miravalles Geothermal Field is not precisely known, but several stages of mineral growth have been recognised (Rochelle, 1991) suggesting a link between the cooling stocks of at least the most recent eastern margin volcanic centres, and possibly the older ones aswell.

In summary, the Guayabo caldera evolved during cycles of stratovolcano construction with concomitant subsidence along a series of parallel arcuate faults. Increased subsidence along now-buried faults in the caldera centre occurred during the destructive periods that accompanied the evacuation of a temporally more advanced magma chamber, contemporaneously with the eruption of the Guayabo-related outflow tuffs. The most recent subsidence to produce the present day morphology was not accompanied by any major outflow tuff. This was focussed on the arcuate boundary faults in the west, and the graben in the east: it is proposed that this phase of subsidence may be related to the growth of the Volcán Miravalles edifice on the eastern caldera margin.

CHAPTER 4

CONSTRAINING THE MECHANISMS OF CALDERA COLLAPSE USING GRAVITY DATA

Introduction

Calderas are large collapse depressions, more or less circular in form, the diameters of which are many times the greater than the diameter of any included vents (Williams and McBirney, 1979). This definition infers a relationship between collapse and volcanic eruption but does not stipulate the type of volcanic eruption. The modern view that calderas form due to collapse (downward movement of material) following a pyroclastic eruption, rather than due to explosive coring, in which material moves upwards, is sometimes attributed to Williams (1941), but Fouqué (1879, as reported by McBirney, 1991) explained the origin of the Santorini caldera in terms of collapse. The devastating eruption of Krakatau in 1883 (Verbeek, 1885; reviewed by Simkin and Fiske, 1983) provided a focal point for many studies of the association between calderas and violent eruptions (e.g. Self and Rampino, 1981 and Yokoyama, 1981). Verbeek (1885) observed that the proportion of volcanic lithics from the original edifice in the erupted products was too small to account for the destruction of the whole edifice and that therefore the caldera formed by collapse rather than simply as a result of cataclysmic decapitation.

Since this time, many different calderas have since been described from the geological record; caldera structures range in size from those with kilometre scale diameters that erupted 1-10 km^3 or less of material to gigantic 60 km structures that erupted of the order of 1000 km^3 material. Most are of such diverse nature that it is considered unlikely that they could all have formed in the same manner and many different collapse models have been proposed. The shape of the caldera floor is predicted by the models and although the form is similar for some models it is very different for others. The distributions of the low density intra-caldera material are different in each case and therefore the form of the gravity field can be used as a discriminant. The advantages and limitations of this technique are described here, following a brief review of the proposed mechanisms of caldera collapse.

Whatever the nature of the collapsing floor, however, the recurrent theme in the majority of the models is that caldera collapse is directly related to the evacuation of the sub-caldera magma chamber. This implies that there should be a balance between the magmatic, or juvenile, volume of the erupted products and the volume of collapse. One of the major uncertainties in any balance model is the shape of the caldera floor and thus the intra-caldera volume; even with sophisticated geophysics techniques many questions remain. A related problem is separating the volume of the juvenile component of the intra-caldera deposits, important to the balance equation, from the often poorly constrained fraction of pre-caldera material, present as lithics. A new balance model is proposed that uses gravity data to constrain the actual mass of the juvenile intra-caldera deposit; thereby obviating the need for either the intra-caldera volume or the lithic fraction.

The balance model could be applied to any caldera but calculations show that the Guayabo caldera does not fit the 'simple evacuation during eruption' model; in effect the collapse volume far exceeds the volume of erupted material. Additional collapse during the post-caldera stratovolcano activity on the eastern margin is proposed to account for the deficit.

4.1 A Review of Proposed Caldera Morphologies

Studies of the mechanism of caldera collapse are concerned not only with the question of mass and volume balance during collapse, but also with how the subsiding floor of the caldera behaves. It is clear from the models presented in Chapter 3 that the collapse of the Guayabo caldera has occurred along well defined ring-fractures. The review presented here is therefore largely concerned with the distinguishing features of the two ring-fracture end-member models: the piston model and the funnel model (Figures 4.1 a and b). The major contrast between these two models is the behaviour of the magma chamber roof during collapse: Does the roof of the magma chamber collapse as a coherent piston-like block as the magma is erupted along the boundary faults, or does the roof collapse chaotically, with magma passing through, and engulfing, the disarticulated roof zone? From among the many reviews, the following are considered relevant to this debate: Lipman *et al.* (1984) introduced a thematic set of papers on calderas presented at the 1983 Krakatau Centennial,

San Francisco; Yokoyama (1987) reviewed the morphology of many of the calderas of Japan and Scandone (1990) examined the collapse *vs.* explosion debate for the formation of funnel-shaped calderas.

Figure 4.1 Schematic cross-sections of the different caldera collapse models, showing the morphologies, styles of collapse, eruption loci and type of deposit expected.

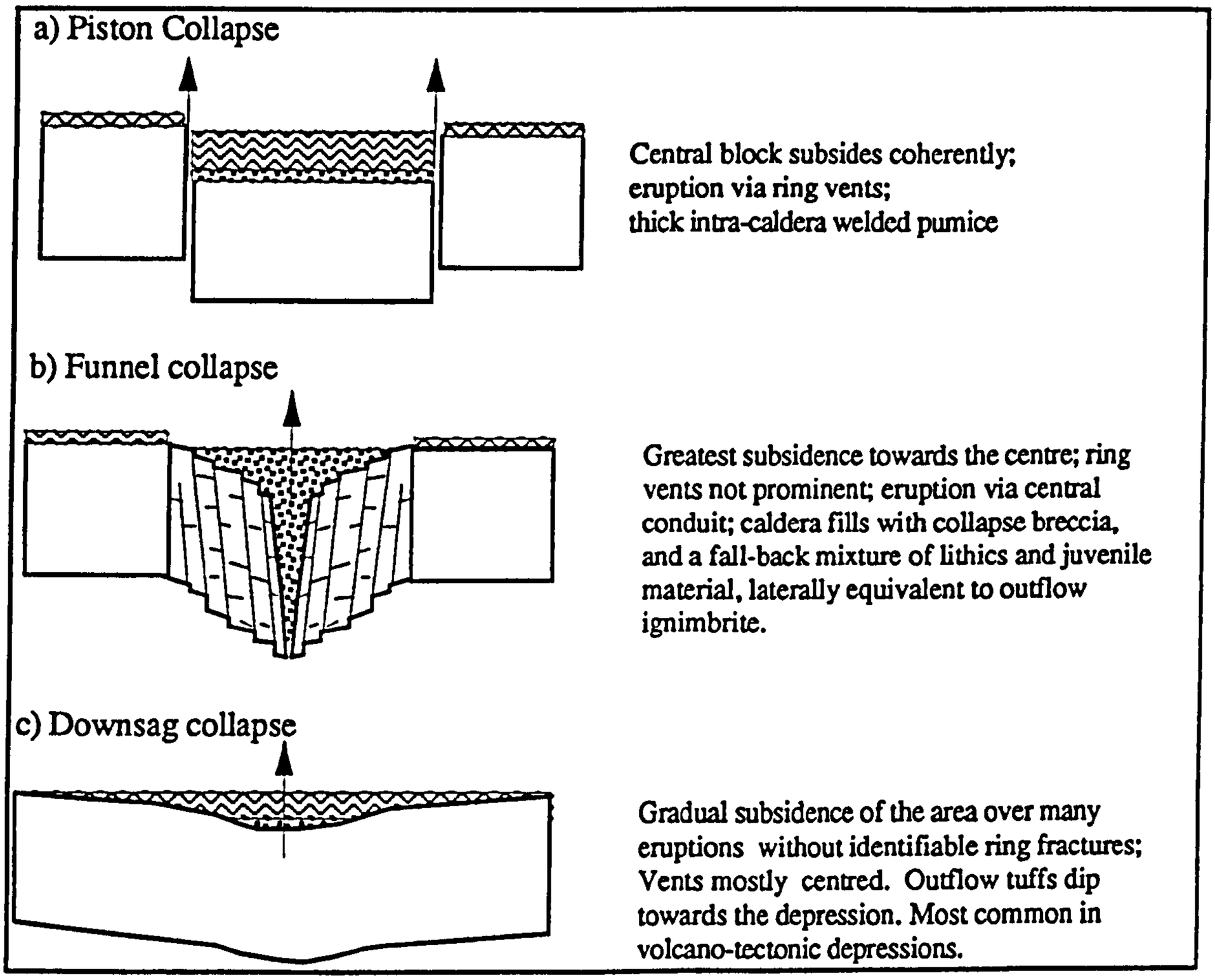

In the following discussion reference is made to the diameter of the calderas. This refers to the diameter of the *topographic* margin, unless otherwise stated. Due to erosion, this may be several kilometres larger than the original diameter of the caldera.

4.1.1 Piston collapse

The most significant feature of these calderas is that the caldera floor is believed to have collapsed as a single unit, like a piston (Figure 4.1 a), with displacement across a single set of ring fractures. This type of collapse has been invoked to model the formation of most large silicic calderas of the western U.S.A.. In a review of the roots of calderas with ash flow sheets, Lipman (1984) summed the evidence for piston collapse as follows: i) a few eroded calderas and ring complexes show structurally and stratigraphically coherent pre-

caldera floor sequences, ii) the thick ash flows that accumulated over the caldera floor have been little disrupted, iii) subsidence has been localised on steep ring faults and iv) post-subsidence volcanic vents are located along the ring faults. Only i) and iii) unequivocally demonstrate piston collapse, but documented evidence is scarce and often disrupted by post-subsidence remobilisation of the sequence.

Seismic refraction data from the 17 by 32 km diameter Long Valley caldera show that the basement is a relatively coherent block, bounded by steep sets of ring faults confined to zones around the caldera margin less than 1-2 km wide (structure reviewed by Rundle and Hill, 1988). The Long Valley basement and intra-caldera stratigraphy has been uplifted, however, by near-central, post-caldera resurgence, a process that has been recognised at many large calderas (Smith and Bailey, 1968). The large silicic calderas of the Western U.S.A. which are associated with major ash flows, are usually filled with a thickness of the erupted tuff that is many times greater than the thicknesses of the outflow tuff, proving that the floor subsided during the eruption. For example, nearly 2 km of Bandelier Tuff has been drilled at Valles, compared to the ~100 m thickness of the outflow sheet (Dondanville, 1978). The intra-caldera tuffs are generally more lithic-rich, show greater welding (thicker cooling units), greater devitrification, hydrothermal alteration and propylitization, and are therefore usually denser than their outflow equivalents (Lipman, 1984).

The location of post-caldera vents along the ring faults or similar arcuate lines is not recognised at all alleged piston collapse calderas, and is therefore a poor fingerprint. Indeed some vent distributions can be used to argue against piston collapse. For example, from 90 Quaternary calderas where vent location is clearly displayed, Walker (1984) found that only 8 calderas (with a *possible* 5 others) had vents that were aligned along arcuate lines parallel to the caldera margin. At 39 calderas the vents were distributed linearly, both within and beyond the caldera margins. This vent distribution is usually related to the regional tectonic stress pattern, indicating that regional lines of weakness are more important controls of magma paths than those induced by caldera formation. Centrally aligned vents (at 20 calderas) are common at medium to small calderas, which may indicate that magma feeders of collapsed volcanoes are not subdued by caldera forming events. Furthermore, it is

suggested here that a centrally aligned post-caldera cone would be expected if the caldera-forming eruption emanated from a central vent, this has been proposed for funnel-shaped calderas such as Aira (Aramakei, 1984; further details in Section 4.4.3).

Nearly all the large (>10 km) piston-type calderas and ring-complexes are recognised from Precambrian continental crust; rather than the epicontinental, young crustal setting of the majority of Quaternary calderas. Walker (1984) therefore proposed that rigid crystalline crust may be necessary to permit coherent block subsidence along clean ring faults.

4.1.2 Funnel collapse

Funnel (or V-shaped) morphologies have been invoked to characterise most of the Quaternary calderas of Japan (3-25 km diameter), and some other relatively small (<10 km in diameter) Quaternary calderas of the world (Figure 4.1 b). These calderas have been referred to as Krakatoan-type calderas, following Williams (1941); however as the buried morphology and mode of collapse of the 9 km diameter Krakatau caldera is not altogether clear (Yokoyama, 1981, Self and Rampino, 1983, Scandone, 1990) and could have involved piston collapse albeit on a small scale (Lipman, 1984), the term is not used here to describe funnel-shaped calderas. Funnel calderas differ from piston calderas in lacking a single large block of basement (Aramakei, 1984), and major ring faults do not accommodate the collapse. Rather, the calderas are thought to collapse chaotically, with increased subsidence towards the centre, accommodating the ash flow eruptions which issue from a central vent (e.g. Aramakei, 1984; Yokoyama and Ohkawa, 1986 and Scandone, 1990).

What is the evidence for the funnel-shaped basement? Yokoyama (1983) reviewed drilling results from four calderas in Japan, and suggested from a combination of both drilling and gravity data that all have a funnel shape. Later, by comparing the gravity fields of other calderas in Japan with those of the drilled calderas, Yokoyama (1987) concluded that all the calderas in Japan and many other similar sized calderas in the world may be of the funnel collapse type. (The use gravity data in caldera studies is reviewed below, Section 4.2). For example, at the 12 km diameter Shikotusu caldera lake, there is very good evidence from reflection seismics (reviewed by Yokoyama, 1987) for a gently dipping V-shaped caldera

margins, focused on a central 4-5 km diameter horizontal base at a depth of 2.5 km; the result is also consistent with the observed gravity data.

Of the drilling results reviewed by Yokoyama (1987), direct evidence from drilling for inward dipping caldera floors is only available from the Hakone and Nigorikawa calderas. Twenty geothermal exploration boreholes in the 8x12 km Hakone caldera, have shown that the top surface of the pre-caldera lavas becomes *gradually* deeper towards the centre of the caldera from about 600 m depth at 2 km from the caldera wall to over 1800 m depth at the centre (Kuno *et al.*, 1970). Subsidence is inferred to have occurred along a series of concentric faults with *inward* tilting of fault blocks. The story at Hakone is complicated, however, by evidence of multi-stage collapse; stratovolcano building punctuated by collapse events. Unfortunately, Kuno *et al.* (1970) did not find that any intra-caldera tuffs thicken towards the centre. Indeed, intra-caldera tuffs are not extensive and most of the stratigraphy consists of the products of subsequent stratocones. Hakone cannot, therefore, be considered as a useful benchmark example of funnel collapse.

In contrast, the drilling results from Nigorikawa are very convincing. The evidence comes from 26 geothermal wells drilled up to 2400 m depth and also from gravity, magnetic, seismic and other geophysical studies (Ando, 1981 and 1983; reported by Aramakei, 1984). Although it is a small caldera, only 3 km across, it is relatively young (~12,000 yr old, Aramakei, 1984) and the steep 60° to 70° walls are well preserved below 700 m, meeting with a horizontal floor.

Thick intra-caldera welded tuffs, that are typical of the calderas for which piston-type collapse has been proposed, are not recognised in any of the Japanese calderas (Aramakei, 1984). For example most of the sequence in the 1000 m well at the 20 km diameter Kuttayaro caldera (Yokoyama, 1983) comprises poorly consolidated lithic tuffs and minor agglomerates but subordinate andesite lavas were also identified. Similar deposits have been recognised at Nigorikawa (summarised by Yokoyama, 1983) and show, from the top; alluvium (~100 m), lake deposits (~350 m) landslide deposits (<150 m), post-caldera lava dome and lithic-rich unconsolidated tuffs and breccias (<1300 m).

The emplacement mechanism for these thick, lithic-rich, poorly consolidated intra-caldera deposits is not clear. Aramakei (1984) suggested that they are shattered wall rock fragments (collapse breccia) mixed with juvenile, vesiculated magmatic material, but how did they form? If they represent a product that filled the caldera contemporaneously with the caldera collapse and the eruption of the extra-caldera ignimbrites, why are no welded ignimbrites recognised? In part at least, the deposits may be analogous to the co-ignimbrite proximal lithic breccias (Walker, 1985) that have been recognised close to many calderas (e.g. Santorini, Druitt and Sparks, 1982; Crater Lake, Bacon, 1983; Aira, Aramakei, 1984; Aso, Suzuki-Kamata and Kamata, 1990) but on a much larger scale. Walker interpreted these deposits as products of the deflation zone around a collapsing eruption column, but the far greater volume of such deposits within the Japanese calderas requires either a much larger scale of fall-out during caldera collapse or an accumulation of several smaller fall-back depositional events.

Whatever their genesis, the unconsolidated brecciated intra-caldera fill of funnel-shaped calderas contrasts markedly with the dense welded units that are recognised within calderas for which piston collapse has been proposed. This suggests that not only is there a separate collapse mechanism, but the nature of the eruption must have also been different. Based on gravity observations and by relating the intra-caldera deposits to "fall back", rather than collapse breccia, Yokoyama (1966) challenged the traditional collapse model of Williams (1941) and proposed that funnel calderas form by explosion. The debate about the contrast between collapse and explosion origins for funnel calderas centres around the quantity of lithics in the erupted products. Most workers dispute that there are enough lithics in the ejecta to support an explosion hypothesis (e.g. at Krakatau; Self and Rampino, 1981 and 1982). Scandone (1991) suggested that the formation mechanism of funnel-shaped calderas involves a process of chaotic collapse, with greatest collapse towards the centre of the caldera, rather than explosive decapitation, as the energy required for decapitation is seldom available. The point is taken up again later following a discussion of the gravity evidence for caldera sub-structure.

The intra-caldera facies of the Japanese calderas is an essential element in the understanding of collapse mechanisms. These facies could be studied from the kilometres of existing geothermal drill core, but unfortunately many of the drilling reports are classified and therefore not available to the general scientific community (Aramakei, *pers. comm.*).

Evidently there can be common ground between piston and funnel collapse structures. For example, if the caldera floor collapsed chaotically rather than coherently but with the greatest displacement across ring fractures the result would be a similar general structure to that generated by piston collapse. In this case, many of the properties described above for piston collapse would be expected. Chaotic collapse, however, implies that caldera-forming eruptions could occur through numerous vents in the disaggregated caldera floor, rather than being restricted to vents along the ring faults (as in the piston model). The argument against chaotic collapse is that eroded calderas record evidence for chilled ring dykes, rather than scattered individual vents (review by Lipman, 1984).

4.1.3 Overview of other mechanisms of caldera formation

As well as the continuum of ring fracture calderas that may fall between the piston and funnel end-members, there are others that are unrelated, such as downsag calderas. In addition, there are calderas where there have been many stages of collapse and there are also mechanisms to explain collapse that do not require pyroclastic eruptions.

Downsag calderas: The criteria for recognising these calderas were summarised by Walker (1984) as follows; i) gradual inward slope of the ground towards the centre with a lack of tangential fault scarps, and ii) the presence of tilted features that can be shown to have been originally horizontal (Figure 4.1). The surface of the outflow material slopes consistently towards the caldera centre, as exemplified by the northeast end of the Lake Taupo depression where the ignimbrite valley ponds were originally horizontal (Walker, 1984). The volume of Lake Taupo more than accounts for the volume of the Taupo eruption, and the downwarping seems to be aligned with the tectonic depression of the Taupo Volcanic Zone where subsidence has occurred independently of volcanic activity (Grindley, 1965).

Multistage collapse and nested calderas: Incremental caldera collapse is intuitive where several, temporally distinct outflow tuffs can be shown to have a common source caldera. In addition, some apparently large calderas are composed of smaller discrete but nested calderas or volcano-tectonic depressions. Examples include Taupo (Self, 1983), Amatitlan (Wunderman and Rose, 1984), Aira (Aramakei, 1984), Toba (vanBemmelen, 1934), Valles and Toledo calderas (Smith and Bailey, 1966 and 1968), Yellowstone (Smith and Christiansen, 1980), Pantelleria (Mahood and Hildreth, 1983) and Guayabo, (this study). The 1916 eruption of the stratovolcano Sakurajima caused some further subsidence of the Aira caldera (Mayabe, 1934, as reported by Aramakei, 1984) providing direct evidence of incremental caldera growth.

Trapdoor collapse: Mahood and Hildreth (1983) suggested that the multistage collapse of the Pantelleria caldera floor occurred assymetrically, with greatest subsidence along one margin. Trapdoor subsidence has also been suggested by Fridrich *et al.* (1990) for the partially eroded Grizzly Peak caldera (Colorado), and for the Bonanza caldera (Colorado) by Varga and Smith (1984). Elston (1984) reported that some of the mid-Tertiary ash flow cauldrons of New Mexico have collapsed in a trapdoor fashion, formed by repeated eruptions separated by quiescent periods.

Collapse due to non-pyroclastic magma withdrawl: Gudmundsson (1987) reviewed the eruption mechanism of some basaltic calderas of Hawaii and Iceland and where caldera collapse can often be related to lateral magma withdrawl along dykes that connected extra-caldera fissure eruptions to a disc-like sub-caldera chamber. Hildreth (1990) suggested that the 1912 eruption of Novarupta, Alaska resulted in the concomitant collapse of Katmai caldera some 10 km away, suggesting a hydraulic link between the local magma reservoirs.

4.1.4 Summary

The diverse nature of the calderas outlined above shows that collapse cannot be attributed to a single mechanism. The central argument focuses on the question of the coherence of the caldera floor during subsidence. Two end-member models have been proposed. The piston

model is most applicable to large silicic calderas that have developed in a cratonic setting, within rigid crystalline crust capable of supporting a coherent block during subsidence. The funnel collapse model is more applicable to the majority of Quaternary calderas that have developed in a younger epicontinental setting, within weaker crust. Eruption in the piston model occurs along ring faults and involves little dismemberment of the wall rock, resulting in thick welded intra-caldera deposits. In contrast, the funnel model involves a central, flaring-upwards vent, resulting in an increased lithic content of the intra-caldera deposits, derived from the decapitated pre-caldera volcanics. The lack of welding of the intra-caldera lithic tuffs of funnel-shaped calderas, compared with the at least partially welded extra-caldera ignimbrites, is not well understood, but may be explained if the facies result from cool fall-back deposits rather than the deposits of hot ignimbrite flows.

4.2 Gravity Anomalies Over Calderas

Yokoyama (1961) divided calderas on the basis of their gravity anomalies: those with a positive anomaly and those with a negative anomaly, and found many more with the latter signature. More recently Rymer and Brown (1986) reviewed the gravity fields over volcanic structures. Positive anomalies generally characterised basaltic volcanoes (e.g. Medicine Lake, Finn and Williams, 1982; Kilauea, Furumoto *et al.*, 1976 and O-Sima, Yokoyama, 1969), and were modelled as a positive density contrast between the sub-volcanic intrusion (mafic to ultramafic) and the edifice (lavas intercalated with poorly consolidated material). On the other hand, negative anomalies characterised the majority of the Quaternary calderas (e.g. Yellowstone, Eaton *et al.*, 1975; Long Valley, Kane *et al.*, 1976; Krakatau, Yokoyama, 1981 and many Japanese calderas, Yokoyama, 1987) and were modelled as either, i) low density caldera fill and/or, ii) low density (silicic) intrusions. As the Guayabo caldera and most silicic calderas are of the type characterised by negative anomalies, these are now discussed in more detail.

4.2.1 The gravity signatures of piston and funnel calderas

The piston and funnel caldera shapes have been modelled, using the 2.5-D program, GRAVMAG (described in Section 3.6), to examine the general form of the predicted gravity

anomaly (Figure 4.2). The caldera areas are assumed to be circular and symmetrical about their centres. The 3-D form of the funnel calderas has been approximated by five stacked, tapered cylinders, each with a half-strike-length equal to the mean radius of each element. The surface areas of each caldera are equal, but the depth to the base of each caldera has been adjusted to produce an equal maximum gravity anomaly value. The *absolute* values of both the caldera dimensions (apart from the radius to depth ratio of the caldera) and the magnitudes of the anomalies are not important for the purposes of this discussion.

The standard contrast between the V- and U-shaped anomalies predicted for straight-sided funnels and right-angled pistons is shown in Figure 4.2. The maximum rate of change of the gravity gradient, the second vertical derivative, coincides with the caldera margin in both cases, but the gravity gradient over the caldera margins is steeper in the case of the piston caldera, where there is a maximum lateral density contrast.

Figure 4.2 Models of the U- and V-shaped gravity profiles predicted for piston and funnel-type caldera collapse. The circular shape of the calderas is approximated by using half-strike lengths adjusted to produce symmetrical square bodies; five blocks are used to approximate the funnel caldera. The maximum rate of change of gravity gradient, g" is coincident with the caldera margin.

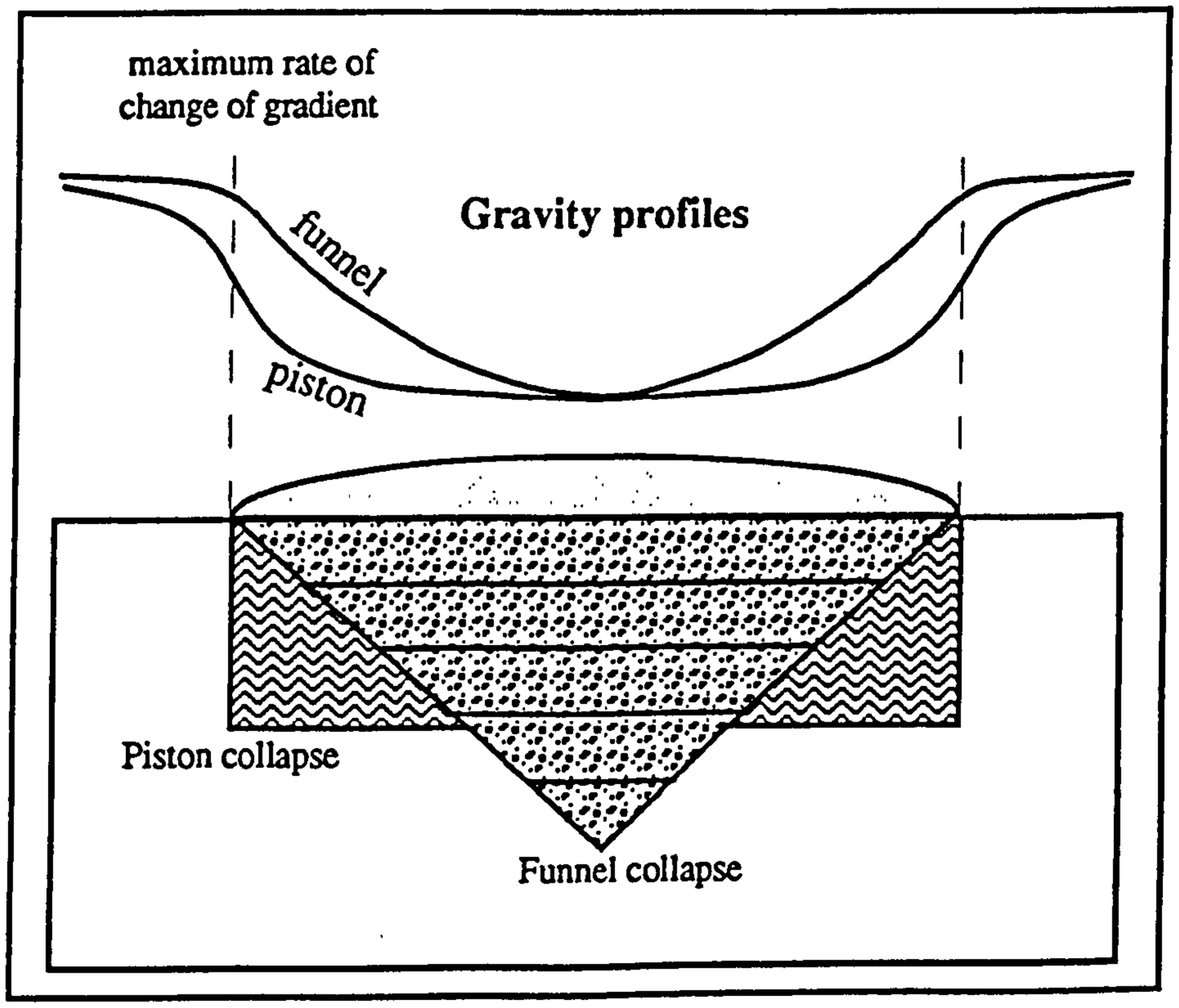

The observation of V-anomalies at most Quaternary calderas that are not of the large intra-cratonic type of the western U.S.A., has been a powerful argument for those in favour of funnel rather than piston structures (among others; Yokoyama, papers from 1961-1987,

Aramakei, 1984 and Scandone, 1990). Yokoyama has consistently modelled the V-shaped anomalies in terms of an inverted cone with a density contrast of -0.3 Mg m^{-3}, on the basis of drilling results from Kuttayaro (Yokoyama, 1983), where the core densities of the intra-caldera "fall-back" deposits increase with depth (approximately linearly) from 1.7 to 2.2 Mg m^{-3}, in contrast with the country rock, 2.0 to 2.5 Mg m^{-3}. He has assumed that the density contrast is constant for the entire model. Although this results in a good approximate fit of the calculated to the observed anomalies, the distribution of lateral density contrasts is almost certainly more complicated, at least within the caldera, as has been shown during this study at Guayabo (Chapter 3). The divergence of the observed anomalies from that predicted by simple density contrast models is as important as an aid to interpreting the caldera structure as the overall form of the anomalies.

The so-called V-anomaly generated by a straight-sided funnel is not strictly V-shaped (Figure 4.2), but slightly concave-upwards, due to the depth^{-2} proportionality law obeyed by potential fields. Even if the apex of the funnel is sharpened up, mimicking a caldera where the walls become increasingly steeper towards a central vent, it is never possible to generate a true V-anomaly with a homogeneous low density fill, let alone an anomaly where the gradient increases over some part of the anomaly inside the caldera margin. A straight-sided or a convex-upwards anomaly can only be generated by modelling a caldera-centred body that has a negative density contrast with the caldera fill. This can take the form of a shallow relatively flat body, or a deeper pipe-like body, or of course any intermediate variation. Observed so-called V-anomalies are often poorly defined near their centres, because some gravity surveys have had to be restricted to the margins of the caldera due to the presence of a caldera lake or invasion of the sea (e.g. Krakatau, Yokoyama, 1981 and Shikotsu, Yokoyama, 1987). It is difficult therefore, to make a general statement about the true shape of all alleged V-anomalies.

Scandone (1990) modelled a variety of caldera structures and sub-caldera intrusions, using simple geometric shapes and concluded that a good fit with observed data was possible with a collapsed chimney, flaring towards the top (from Santorini in this case, original data from Budetta *et al.*, 1984, as reported by Scandone, 1990). Although his calculated anomaly

matches the amplitude and overall form of that observed, there are differences in the gradients that cannot merely be attributed to the errors incurred by using simple geometric shapes. Scandone's calculated anomaly has a generally concave-upward form (as for the funnel in Figure 4.4), but the Santorini profile has a central, *convex*-upward part, that has to be attributed to a shallower low density body within the caldera fill, as described above.

The changes in the gravity gradient over the Guayabo caldera have distinguished the topographic ring fault from the ring-faulted boundary of the intra-caldera Pumice Unit (e.g. Profile CM1, Figure 3.26, Chapter 3). The identification of discreet ring-faults suggests that the multi-stage piston-type collapse occurred, rather than chaotic funnel-type collapse. The significant observed variation of the intra-caldera density at Guayabo (e.g. Profile WSE, Figure 3.25) models the negative anomaly sufficiently and there is no requirement to model a low density chimney, as proposed for similar calderas by Scandone (1990). It is suggested that a similar model, with less dense caldera fill concentrated towards the surface and the caldera centre, could certainly explain the V-shaped gravity anomalies of other multi-stage calderas.

4.2.2 Basement structure and sub-caldera intrusions:

Commonly, the gravity anomalies associated with calderas extend well beyond the margins, even taking into account the extra-caldera extension of the caldera fill related anomaly (Figure 4.2). In some cases the anomaly over the caldera is aligned with regional structure, reflecting one or more of following processes, i) there is a basement component to the total anomaly, ii) the morphology reflects collapse that was a function of regional stresses and is thus aligned with the basement structure, or iii) the associated pluton morphology is a function of the regional stress. If the basement structure did not contribute to the gravity field, then the anomaly should appear as a caldera related anomaly. Caldera-centred, pluton-related anomalies should be relatively easy to identify in the absence of anisotropic basement, but it is more difficult to separate basement induced anomalies from those due to plutons aligned with the basement.

The anomaly at Valles (Segar, 1974) could have a partial component from the negative gravity anomaly associated with the low density fill of the Rio Grande Rift (Cordell *et al.*, 1984 and Olsen *et al.*, 1986). The major extensional volcanic depressions of the Taupo Volcanic Zone (Cole, 1990) and Kagoshima Bay (Yokoyama, 1987) are the sites of caldera formation and have negative gravity anomalies aligned with the depressions (Yokoyama, 1987). The Basin and Range structures have a dominant component over the gravity field of the partially eroded Tertiary calderas of the Marysfield Volcanic Field (Steven *et al.*, 1984). Although the foci of these gravity anomalies are often coincident with the calderas, intuitively there must be at least a component of the basement signature included; this should be estimated and subtracted from the caldera-related anomaly before modelling the caldera structure.

Caldera-related plutons are commonly associated with the partially eroded Tertiary calderas of the western U.S.A. (reviewed by Lipman, 1984). In the San Juan Volcanic Field 17 calderas and associated ash flow sheets have been recognised (Steven and Lipman, 1976), but the broad 50 mGal Bouguer anomaly is largely the signature of a giant composite batholith, possibly 75x150 km at a depth of about 5 km beneath the area (Plouff and Pakiser, 1972; as reported by Lipman, 1984).

More isolated plutons have been inferred for some of the large Quaternary calderas of the western U.S.A. from the results of gravity data and seismics. The Yellowstone caldera is one of the worlds most hydrothermally active volcanic centres. Lehman *et al.* (1982) showed that the broad 60 mGal gravity anomaly, which extends beyond the caldera boundaries, could be modelled in terms of densities derived from seismic velocities. An upper low density layer corresponding to sediments and rhyolites, a low velocity upper crustal layer (5.7 km s^{-1}, compared with 6.05 km s^{-1} of the crystalline basement), and a deeper low-velocity layer (4.0 km s^{-1}). The coincidence of the 4.0 km s^{-1} zone with a gravity low, in the absence of any evidence for a different cause, was considered by Lehman *et al.* (1982) to be a zone of partial melt. At Long Valley, Carle (1988) modelled the gravity field in three dimensions and constrained the model with density measurements of drillcore. He found that the anomaly computed for the low-density caldera fill was

insufficient to match the observed anomaly. A low density sub-caldera region was therefore inferred, either a pluton or partially molten zone. Carle also suggested that the morphology Long Valley caldera was strongly influenced by pre-caldera structure.

4.2.3 Summary of caldera-related gravity interpretation

Silicic calderas are generally characterised by negative gravity anomalies due to low density caldera fill, whereas the mafic to ultramafic intrusions associated with basaltic calderas have positive anomalies. The Bouguer gravity anomalies observed over calderas are complex, often comprising the sum of signatures related to several geological sources. Models derived from the inversion of gravity data are not unique, which means that it is difficult to model caldera structure without independent control, such as borehole logs or seismic data. The mass deficiency integrated from the gravity field can be used, however, to examine whether there is an equivalence of collapse volume and erupted product as predicted by the simple collapse hypothesis, without necessarily knowing the volume of the intra-caldera volume. Ideally, gravity gradients and profiles may be used to separate i) buried, but true, caldera margins from topographic margins and ii) piston-type structures from funnel-shaped structures.

True V-shaped gravity profiles across calderas can only arise from a structure where the density decreases towards the centre of the caldera, preferably close to the surface. Anomalies due to basement structure may be recognised if the caldera centred anomaly 'overruns' the caldera margin by more than any anomaly that could be related to caldera structure. Plutons beneath silicic calderas may also give rise to broad anomalies, obscuring the caldera-fill anomaly. This is especially true of the caldera clusters of the Tertiary Volcanic Field in the western U.S.A. where a long period of magmatism has resulted in the formation of large composite batholiths and broad, deep-seated gravity anomalies from which it is difficult to identify individual caldera-related anomalies.

While it may be possible to infer generally funnel-shaped calderas from the nature of the gravity gradients, the gradients do not discriminate between a chaotic collapse and an explosion-related mechanism for these calderas. The lithic deficiency of caldera related

products in comparison with the missing caldera volume is the strongest argument against the explosion hypothesis; and explosive mechanisms are therefore not favoured by this study.

4.3 A New Caldera Mass Balance Model

If caldera collapse is due to evacuation of the sub-caldera magma chamber, then the collapse volume should equal the volume of magma extracted, regardless of the mechanism of collapse. This has previously been tested by comparing the caldera volume with the dense rock equivalent (DRE) volume of the volcanic products associated with the caldera formation. The uncertainties are i) the volume of the missing erupted products due to erosion and/or eolian fractionation (Sparks and Walker, 1977), ii) the volume of the buried caldera fill, iii) the pre-collapse topography, iv) the volume of pre-caldera strata removed by decapitation/vent coring and redistributed as lithics, v) whether the magma chamber is closed during caldera formation to recharge/lateral discharge and vi) post-caldera resurgence. In order to minimise some of these uncertainties it is useful to examine relatively modern (i.e. Quaternary) calderas, rather than eroded examples, but in these cases the largely buried intra-caldera volume is difficult to assess without borehole and/or geophysics control.

Of the geophysical methods, seismic interpretation (e.g. at Long Valley; reviewed by Rundle and Hill, 1988 and Laguna de Ayaraza, Guatemala; Poppe *et al.*, 1984) and gravity models that are constrained by deep borehole density measurements (e.g. at Long Valley; Carle, 1988 and Guayabo; this study) have yielded the most useful constraints on the sub-caldera structure. Where borehole and seismic information is not available it is not possible to ascertain the intra-caldera volume and therefore it is not possible to attempt a balance model. A new balance model is proposed that uses the mass deficiency commonly associated with silicic calderas to constrain the mass of the juvenile component of the intra-caldera volume. The sensitivity of the model to errors in each parameter is examined, firstly on a theoretical basis, and then in practical terms in the following section by applying the model to the Guayabo caldera.

4.3.1 The derivation of the model

The simplest case of caldera collapse is shown in Figure 4.3, where the collapse volume (V_c, the unfilled caldera volume, plus V_i, the filled caldera volume) is equal to the volume of erupted magma (V_m). A piston-type caldera is shown, but the model presented here is applicable to all types of caldera morphology. This preliminary model does not take into account the redistribution of lithics derived from either the magma roof or the pre-caldera rocks; this is considered later. The mass of erupted magma (M_m) is distributed both within (M_i) and outside (M_o) the caldera. For the purposes of this model, it is assumed that the gravity anomaly is entirely due to the density contrast between the intra-caldera fill (ρ_i) and the country rock (ρ_r). In the case of silicic calderas considered here, the pyroclastic and clastic caldera fill is normally less dense than the country rock, resulting in the negative gravity anomaly commonly observed (Rymer and Brown, 1986; Yokoyama, 1987), and there is therefore a mass deficiency (M*) associated with the caldera. As discussed earlier, basement structure or sub-caldera plutons may give rise to caldera-centred anomalies and though the wavelengths of these should be broader than any caldera fill anomaly, it is difficult to separate the amplitudes.

Figure 4.3 The caldera collapse model assuming that the evacuated magma volume equals the volume of collapse. A piston-type structure is indicated, but the model applies equally to any caldera structure. The parameters relate to the redistribution of mass, explained in the text.

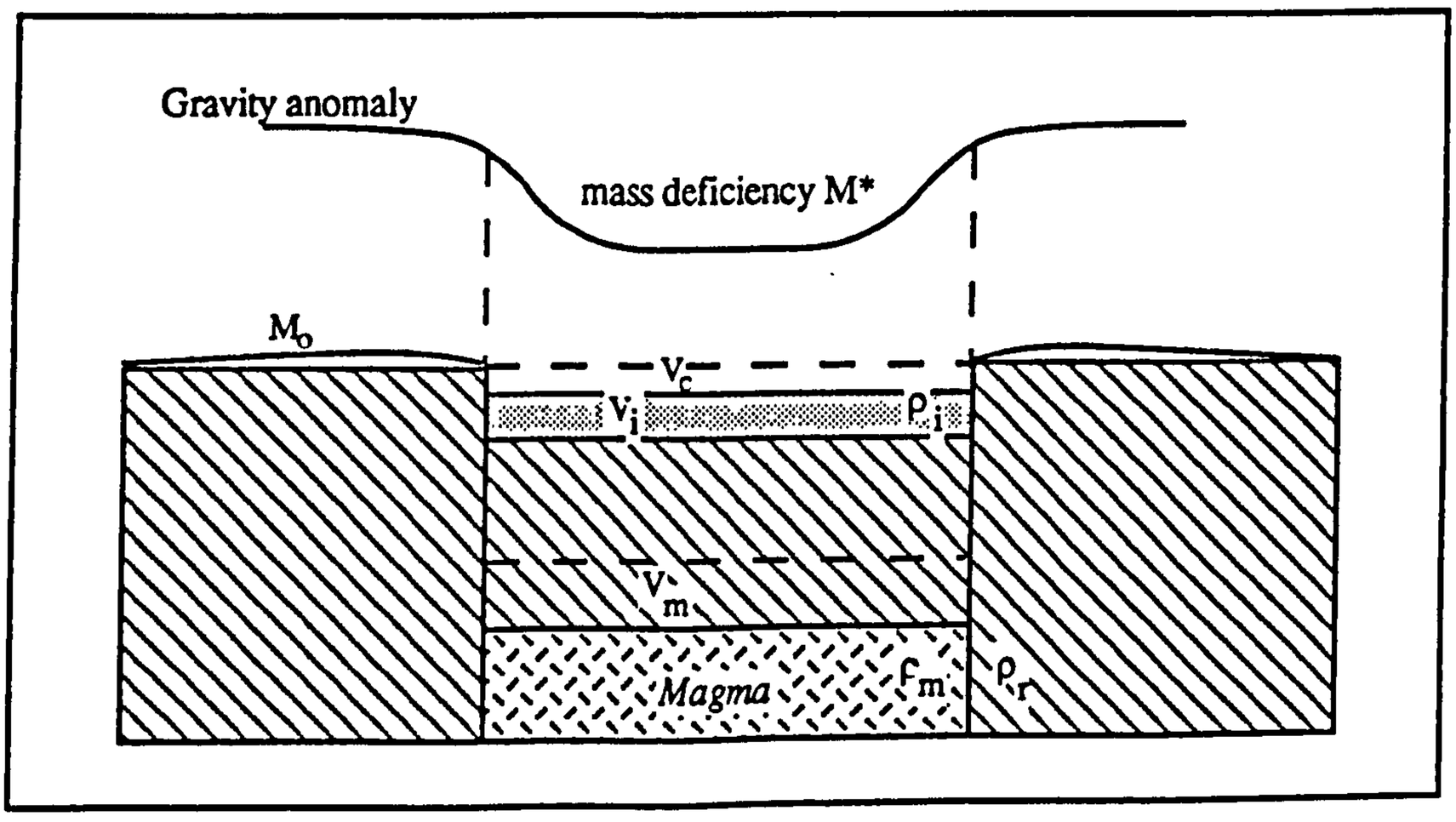

The model as represented in Figure 4.3 suggests that there would be a contribution to M* from the magma chamber if there was a density contrast between the magma and the country

rock (ρ_m - ρ_r). This is likely where a part of the magma chamber is still molten, as proposed by Eaton *et al.* (1975) at Yellowstone, but for the purposes of this model it is assumed that either this gravity anomaly has been separated from the caldera fill anomaly or the gravity field shown in Figure 4.3 is measured after the magma has frozen, thereby reducing (ρ_m - ρ_r) to a negligible difference. Similarly, country rock or basement structure anomalies are not considered in the model.

Yokoyama (1961) calculated M* over Aira caldera by using the Gauss theorem for the total gravity field over the area of the anomaly:

$$M^* = \frac{1}{2\pi G} \int_{-\infty}^{\infty} \int_{-\infty}^{\infty} \Delta g(x,y)\,dx\,dy \quad ...(1)$$

He found that for Aira, M* was broadly equivalent to the estimated mass of the erupted tuff beyond the caldera. However, this comparison is misleading as M* is not the mass missing from the caldera, but the mass deficiency due to the density contrast between the caldera fill and the country rock: $M^* = V_i(\rho_i - \rho_r)$ ...(2)

In a later review of 19 Quaternary calderas in Japan, Yokoyama (1987) showed that M* was always considerably less than the ejected mass, including the case at Aira where the ejected mass had been recalculated. Clearly, the theoretical inadequacies of Yokoyama's approach mean that the relationships between all the parameters related to the simple collapse model (Figure 4.3) need to be defined before it is possible to determine whether the volume balance and mass balance, predicted by the simple model, can be estimated to test the validity of the model: $V_m = V_i + V_c$ ...(3) and $M_m = M_i + M_o$ ...(4)

$$(3), (4) \Rightarrow \quad \rho_i V_i = \rho_m(V_i + V_c) - M_o \quad \Rightarrow \quad V_i = \frac{M_o - \rho_m V_c}{\rho_m - \rho_i} \quad ...(5)$$

$$(2), (5) \Rightarrow \quad M^* = \frac{\rho_r - \rho_i}{\rho_m - \rho_i}(\rho_m V_c - M_o) \quad ...(6)$$

This result means that $|M^*| = M_o$ (the Yokoyama assumption) only if both $\rho_m = \rho_r$ and the volume of the unfilled caldera, V_c is zero. As ρ_i in this model is expanded magma, the density contrast ratio in (6) is positive, and therefore if $V_c > 0$, then $M_o > |M^*|$ as observed

by Yokoyama (1987). In general terms, the mass deficiency calculated from the gravity anomaly over the caldera is always less than the mass of the erupted extra-caldera material if there is a topographic wall to the caldera.

Calculating for lithics Lithics derived from either i) a flaring of the vent(s) during eruption, effectively eroding the caldera floor, or ii) ripping of the magma roof are common in both intra- and extra-caldera deposits, especially in the former (Lipman, 1984). If present in a measurable quantity, the lithic content will render the above equations invalid. The adjustments are not too painful, however, but more parameters need to be introduced (Figure 4.4), thus increasing the number of unknowns for poorly understood calderas.

$$(3) \Rightarrow \qquad V_m = V_c + V_i(1-f_i) - V_o f_o \quad ...(7)$$

where f_i and f_o are the intra- and extra-caldera volumetric lithic fractions respectively (Figure 4.3). This is because the volumes $V_i f_i$ and $V_o f_o$ are parts of the missing caldera floor block, whether they were derived from the caldera floor or the walls of the magma chamber.

Figure 4.4 The case where the lithic fractions f_i and f_o in the intra- and extra-caldera volumes are taken into account. The lithic volumes are schematically shown as separate bodies, but in fact they are integrated with the tuffs. Other parameters as for Figure 4.3.

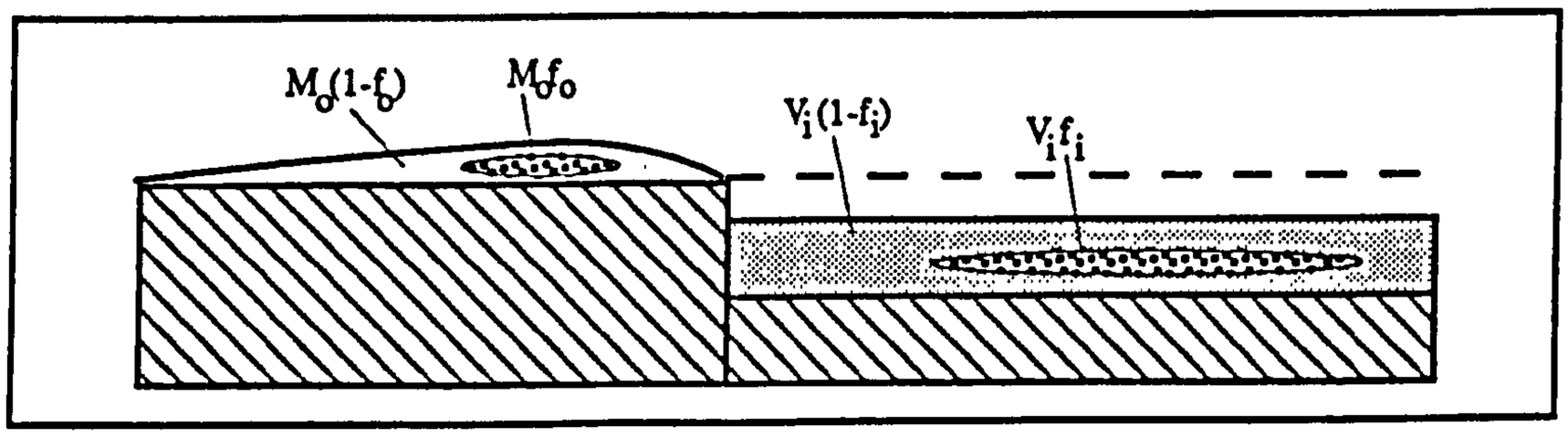

$$(4) \Rightarrow \qquad M_m = M_{im} + M_{om} \quad ...(8)$$

where M_{im} and M_{om} are the masses of the juvenile fraction of the intra- and extra-caldera masses. The lithic masses, M_{ir} and M_{or} are used later.

$$M_{im} = M_i\left(1 - f_i\frac{\rho_r}{\rho_i}\right) \quad ...(9) \qquad \text{and} \qquad M_{om} = M_o\left(1 - f_o\frac{\rho_r}{\rho_o}\right) \quad ...(10)$$

The net porosities of the intra- and extra caldera deposits are included within ρ_i and ρ_o; this accounts for the volume expansion of the lithics from their original state in the country rock. The total intra-caldera mass, M_i, is given by:

$$(8), (9), (10) \Rightarrow \qquad M_i = \frac{M_m - M_o\left(1 - f_o\frac{\rho_r}{\rho_o}\right)}{1 - f_r\frac{\rho_r}{\rho_i}} \quad \ldots (11)$$

$$(7), (11) \Rightarrow \quad M_i = \frac{\rho_m\left[V_c + V_i(1-f_i) - V_o f_o\right] - M_o\left(1 - f_o\frac{\rho_r}{\rho_o}\right)}{1 - f_r\frac{\rho_r}{\rho_i}} \quad \ldots(12)$$

As $M_i = V_i\rho_i$, $V_i = \frac{M^*}{\rho_i - \rho_r}$, from (2) and $V_o = \frac{M_o}{\rho_o}$ then;

$$(12) \Rightarrow \qquad \rho_i\frac{M^*}{\rho_i - \rho_r} = \frac{\rho_m\left[V_c + \frac{M^*}{\rho_i - \rho_r}(1-f_i) - \frac{M_o}{\rho_o}f_o\right] - M_o\left(1 - f_o\frac{\rho_r}{\rho_o}\right)}{1 - f_r\frac{\rho_r}{\rho_i}}$$

$$\therefore \qquad M^*\left\{\frac{\rho_i\left(1 - f_r\frac{\rho_r}{\rho_i}\right)}{\rho_i - \rho_r} - \frac{\rho_m}{\rho_i - \rho_r}(1-f_i)\right\} = -M_o\left\{1 + f_o\frac{\rho_m}{\rho_o} - f_o\frac{\rho_r}{\rho_o}\right\}$$

$$\therefore \qquad M^* = (\rho_r - \rho_i)\left\{\frac{\rho_m V_c - M_o\left[1 - \frac{f_o}{\rho_o}(\rho_r - \rho_m)\right]}{\rho_m(1 - f_i) - \rho_i\left(1 - f_i\frac{\rho_r}{\rho_i}\right)}\right\} \quad \ldots(13)$$

The lithic-sensitive expression (13) is complicated but M* is still proportional to the difference between V_c and M_o ; (13) reduces to the non-lithic case (6) when f_i and f_o are set to zero. As both M_o and $\rho_m V_c$ can both be larger than the magnitude of |M*| (as shown in the examples later) it is more useful to predict either M_o or V_c and compare these with the observed M_o or V_c, rather than predicting M*. The case for M_o is examined:

$$(13) \Rightarrow \qquad M_o = \frac{\rho_m V_c - \frac{M^*}{\rho_r - \rho_i}\left\{\rho_m(1 - f_i) - \rho_i\left(1 - f_i\frac{\rho_r}{\rho_i}\right)\right\}}{1 - \frac{f_o}{\rho_o}(\rho_r - \rho_m)} \quad \ldots(14)$$

The density of both the intra- and extra-caldera fill is at least partly proportional to the lithic fraction, if, as is normal, the lithics density (ρ_i) is greater than both the intra- and extra-caldera pumiceous matrix densities (ρ_{ip} and ρ_{op}). For linear proportionality;

$$\rho_i = f_i\rho_r + (1-f_i)\rho_{ip} \quad \text{and} \quad \rho_o = f_o\rho_r + (1-f_o)\rho_{op}$$

$$\Rightarrow \quad \rho_i = f_i(\rho_r - \rho_{ip}) + \rho_{ip} \quad ...(15) \qquad \text{and} \quad \rho_o = f_o(\rho_r - \rho_{op}) + \rho_{op} \quad ...(16)$$

$$(14), (15), (16) \Rightarrow \quad M_o = \frac{\rho_m V_c - \frac{\rho_m - \rho_{ip}}{\rho_r - \rho_{ip}} M^*}{\frac{f_o(\rho_m - \rho_{op}) + \rho_{op}}{f_o(\rho_r - \rho_{op}) + \rho_{op}}} \quad ...(17)$$

The parameter f_i has dropped out of the equation because effectively the model includes the intra-caldera lithics as part of the pre-caldera material (both have the same density).

4.3.2 The sensitivity of the model

The sensitivity of the model to the parameters in equation (17) is treated here in theoretical terms; the practical errors incurred during the actual estimation of the parameters are examined in the following section. To examine the sensitivity of M_o to the parameters in equation (17), each parameter was varied in turn, while keeping the others fixed (Figure 4.5). The fixed values, the upper and lower limits and the units used are given in Table 4.1, and are also indicated by the enlarged symbols in Figure 4.5.

Table 4.1 The parameter values used in the M_o sensitivity test of equation (17), as shown in Figure 4.5. The fixed parameter values, the units and the upper and lower values are given.

Parameter	Unit	Fixed value	Limits
V_c	km^3	10	0 to 40
M^*	Gt ($=10^{12}$ kg)	-20	0 to -40
f_o	fraction	0.2	0.0 to 0.4
ρ_r	Mg m^{-3}	2.50	2.10 to 2.60
ρ_{ip}	Mg m^{-3}	1.90	1.00 to 2.40
ρ_{op}	Mg m^{-3}	1.50	1.00 to 2.20
ρ_m	Mg m^{-3}	2.30	2.10 to 2.50

The units Gt, km^3 and Mg m^{-3} used in Table 4.1 and Figure 4.5 are consistent for use in equation (17), where M_o is given in Gt (1 Gt km^{-3} = 1 Mg m^{-3}). However, f_o is a fraction in (17) and is shown in Figure 4.5 a in units of % for comparison with the other parameters. The sensitivity test results have been divided into two diagrams to enable a comparison between the non-density parameters, V_c, M* and f_o (Figure 4.5 a) and a direct comparison between the four density parameters (Figure 4.4 b). A value of 10 km^3 was assigned to V_c

and to ensure the maximum sensitivity of equation (17) a value of -20 Gt was given to M* (the product $\rho_m V_c$ and M* were thus of similar magnitudes). The densities were kept within what are considered reasonable limits for caldera related facies (justifications are given below during the application test on the Guayabo caldera).

Figure 4.5 a M_o is more than three times as sensitive to changes in V_c than M*, and practically insensitive to F_o. (M* is shown as positive for comparison with the other parameters). The fixed parameter values are indicated by enlarged symbols.

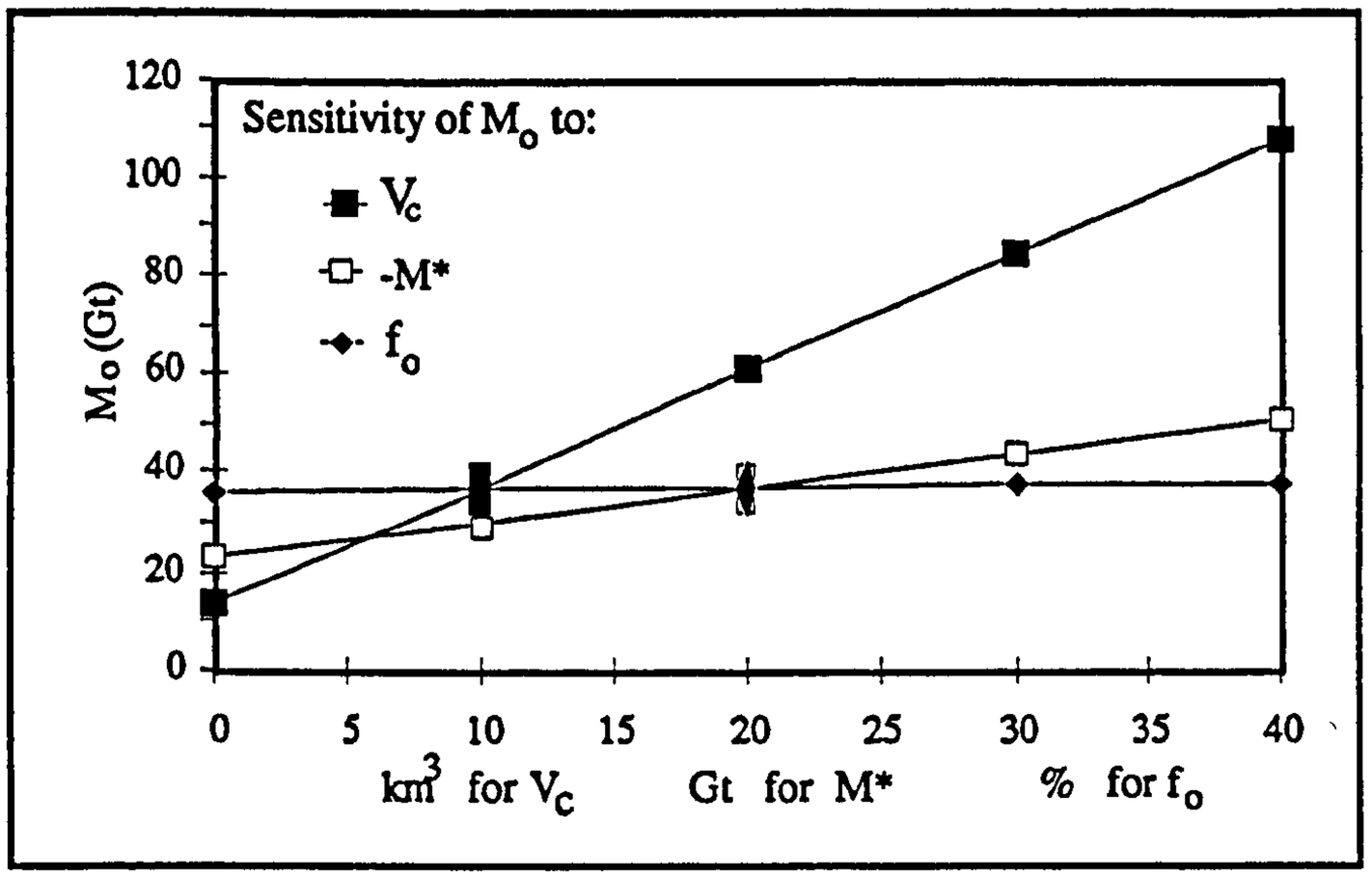

Figure 4.5 b Note the vertical, M_o, scale is half that in Figure 4.5 a. Of the density parameters, M_o is linearly sensitive to ρ_m but most sensitive to both ρ_r and ρ_{ip} when the densities are within 0.20 Mg m^{-3} of the fixed values of ρ_{ip} and ρ_r respectively. M_o is insensitive to ρ_{op}.

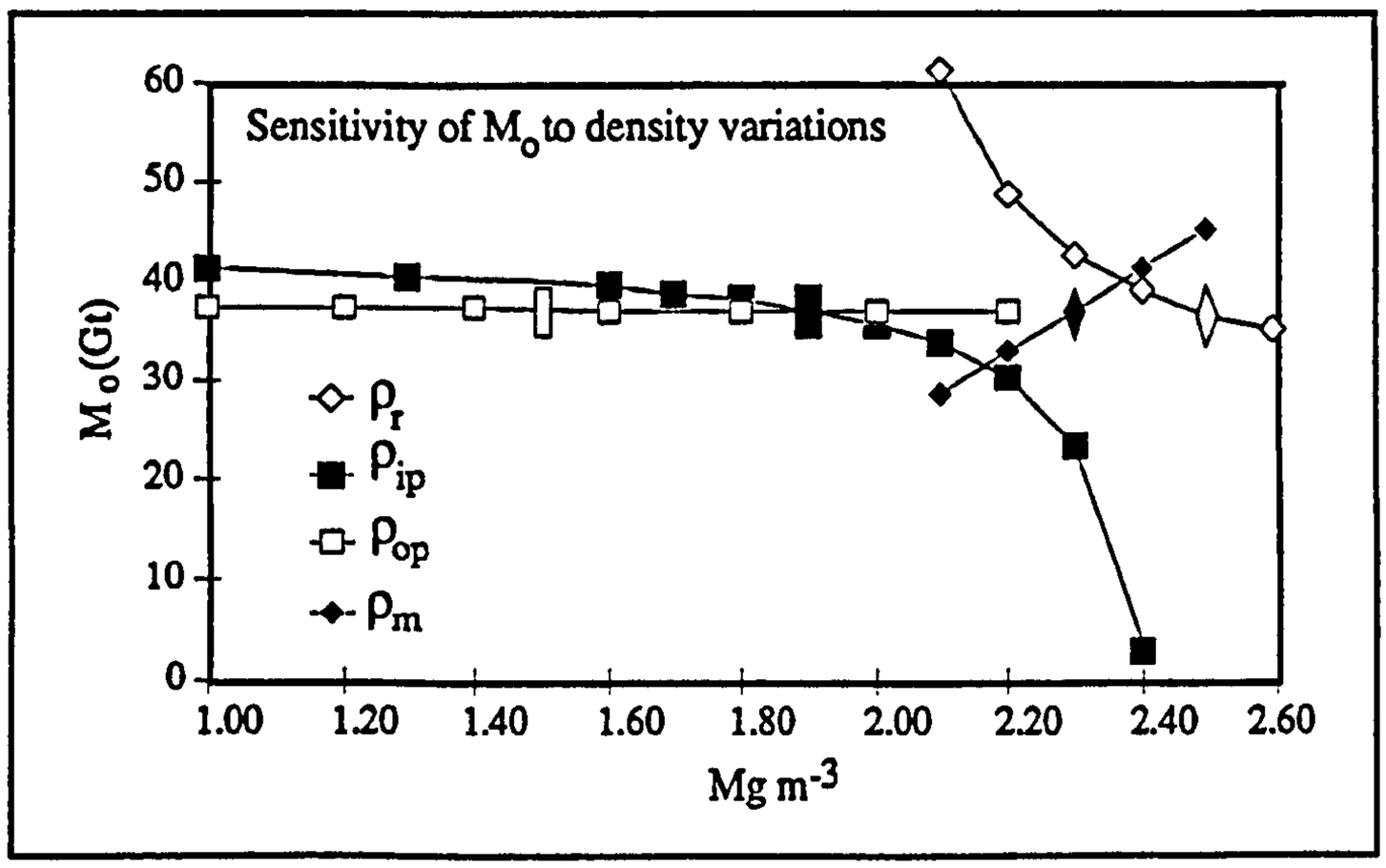

Varying V_c and M*, but keeping the other parameters fixed, equation (17) is reduced to

$$M_o = \frac{2.3V_c - \frac{2}{3}M^*}{K}, \text{ where K is the constant denominator from (17).}$$

As M* is negative, the model is linearly proportional to both V_c and M* but because of the different scalars (17) is more sensitive to changes in V_c than M*, as shown in Figure 4.5 a. The model is almost linearly proportional to ρ_m as it is scaled to V_c in (17). The slightly non-linear behaviour is due to the other, lesser, effects of ρ_m in (17).

The difference between the 'upper' and 'lower' parts of the denominator in (17) is minimal because i) both $(\rho_m - \rho_{op})$ and $(\rho_r - \rho_{op})$ are similar, 0.80 and 1.00 Mg m^{-3} respectively for the fixed density values chosen, and ii) the magnitude of ρ_{op} is larger than both the products $f_o(\rho_m - \rho_{op})$ and $f_o(\rho_r - \rho_{op})$, and therefore dominates both the 'upper' and 'lower' parts. The model is thus practically insensitive to variations in both f_o, as shown in Figure 4.5 a, and ρ_{op} as shown in Figure 4.5 b.

The difference $(\rho_r - \rho_{ip})$ in the denominator of the factor for M* in (17) is crucial to the predicted value of M_o (Figure 4.5 b). Examine the case where ρ_{ip} increases towards 2.50 Mg m^{-3}, the fixed value for ρ_r. As the fixed value for ρ_m (2.30 Mg m^{-3}) is lower than ρ_r; the numerator $(\rho_m - \rho_{ip})$ decreases more rapidly than the denominator $(\rho_r - \rho_{ip})$ and therefore the overall value of M_o decreases, as shown in Figure 4.5. When ρ_{ip} goes through $\rho_{ip} = \rho_m$, the numerator becomes zero, and then negative. This, coupled with the fact that the denominator is also approaching zero, means that the predicted value for M_o goes through zero and rapidly reaches negative infinity at $\rho_{ip} = \rho_r$; i.e. the model breaks down. The effect on M_o is similar when ρ_r is the variable and decreases towards a fixed ρ_{ip} (2.30 Mg m^{-3}), but this time M_o increases towards positive infinity (Figure 4.5 b). Generally the importance of $(\rho_r - \rho_{ip})$ diminishes for smaller values of M*, but will nevertheless dominate (17) if close to zero. So long as $(\rho_r - \rho_{ip})$ is greater than 0.2 Mg m^{-3}, the product $\rho_m V_c$ is the most important parameter in the model, and the predicted M_o is then most sensitive to errors in either ρ_m or V_c. The error in ρ_m should be no more than 0.10 Mg m^{-3}; the molar volumes for the component oxides of common silicate melts derived by Bottinga & Weill (1970) allow the melt density to be calculated from the weight % of these oxides in the outflow tuffs.

To examine the practicalities of applying the proposed balance model; the balance equation parameters were estimated firstly at the Guayabo caldera and secondly at the Aira caldera.

4.4 Application of the Model at Guayabo

A collapse history for the Guayabo caldera was given earlier in Chapter 3, based on an interpretation of the sub-caldera structure from 2.5-D gravity models tied to boreholes in the eastern caldera (summary in Section 3.9). It was suggested that a substantial volume of the present caldera depression is the legacy of subsidence that post-dates the eruption of the Guayabo outflow tuffs. The mass balance model presented above has therefore been tested at the Guayabo caldera where it was possible to estimate both the mass of the erupted outflow tuffs, M_x, and the parameters needed to predict M_o from equation (17). The predicted M_o at Guayabo turns out to be most sensitive to uncertainties in V_c, as M* is relatively small in magnitude and also the necessary densities can be constrained from borehole data. The estimation of each model parameter and the associated errors are described in turn.

4.4.1 Computing the mass deficiency, M*

The Bouguer maps and the gravity models presented in Chapter 3 show that the gravity field over the caldera is complicated (an amended version of Figure 3.7 is reproduced here in Figure 4.6). The computation has been complicated by contributions to the caldera-related anomaly from i) the Bajo Los Chiqueros intrusion (BLC High), ii) the presence of the Acidic Andesite Unit and deep hydrothermal propylitization in the east, iii) the sub-surface continuity of the Pumice Unit south of the caldera, iv) the gravity low over the proposed tuff-rich caldera wall to the north-northeast of Cerro Mogote and finally v) the gravity high associated with the proposed collapsed Cerros La Montañosa (CLM) volcanic edifice.

The central part of the Guayabo Low has been shown in Chapter 3 (Section 3.6.2) to be largely related to the distribution of the low density (1.58 Mg m^{-3}) Pumice Unit and to a lesser extent the Late Cabro Muco Volcanic Unit (LCMV) breccias and lahars. The mass deficiency, M*, has therefore been integrated over the area of their proposed intra-caldera

distribution. The intra-caldera LCMV distribution is defined to the north, west and south by the topographic caldera walls, but the eastern margin is obscured by post-caldera volcanics. The subsided PGM-4 site - La Fortuna graben area is not related to the major Guayabo caldera collapse event and was therefore not included in the area integrated for the mass deficiency over the caldera.

For the purposes of this exercise the integration area was divided into three sub-regions that are characterised by different gravity reference values (Figure 4.6). The region areas, total gravity anomaly and mass deficiencies are given in Table 4.2. Gravity over the CLM is higher than over the rest of the caldera and Figure 4.6 shows that over the CLM topographic margin the reference gravity value is 8 mGal. The region between the CLM region and the main caldera region is approximately a 1 km east-west strip, and gravity anomalies were given a reference value of 6 mGal. The average gravity over the western caldera wall is ~4 mGal and thus a reference value of 4 mGal has been used over the main region of the central and western parts of the caldera. The eastern limit of the main area has been drawn along the 4 mGal contour line (Figure 4.6). The gravity difference from the reference value has been estimated manually over a km^2 grid and M* was calculated from equation (1) (results in Table 4.2).

Table 4.2 The mass deficiency data broken down into the data from each sub-region as defined in Figure 4.6, underestimates due to the BLC High and the missing LCMV volume are explained in the text. The error is largely due to the choice of reference gravity.

Region	Area (km^2)	mGal km^2	M* (Gt)
CLM	10	-15	-0.35
303-304 strip	7	-17	-0.41
Main caldera	41	-200	-4.78
Sub-total	58	-232	-5.5
Underestimates	(15)	-30	-0.75
Reference error	(58)	±58	±1.4
Total		-262 ± 58	-6.2 ±1.4

The errors in the estimation of M* over the Guayabo caldera, which turn out to be less significant than the uncertainties in both M_o and V_c, have three sources; i) the definition of the integrated area, ii) the choice of reference gravity and iii) non-caldera related anomalies within the integrated area. The integrated area covers the central Guayabo Low which is the main contributor to M* (Table 4.2), and the areal error is thus only concerned with the possible missing contribution over the LCMV in the eastern borefield area. The mass

deficiency over this area is difficult to quantify, however, due to the BLC and PGM-4 site gravity highs. The average thickness of the LCMV is 200 m in the northern borefield, the density contrast with the reduction density is -0.31 Mg m^{-3}. As the LCMV is close to the surface, the gravity anomaly calculation approximates that for an infinite slab; ~2.5 mGal. Integrated over a ~5x2 km^2 strip over the northern borefield, east of the main caldera region, gives a mass deficiency of -0.6 Gt.

Figure 4.6 The Bouguer gravity map over the Guayabo caldera (from Figure 3.7) showing the areal limits of the gravity field integrated to derive M*. The area is divided into three subareas; the Cerros La Montañosa (CLM), the main caldera and a 1 km strip between these. See text for discussion.

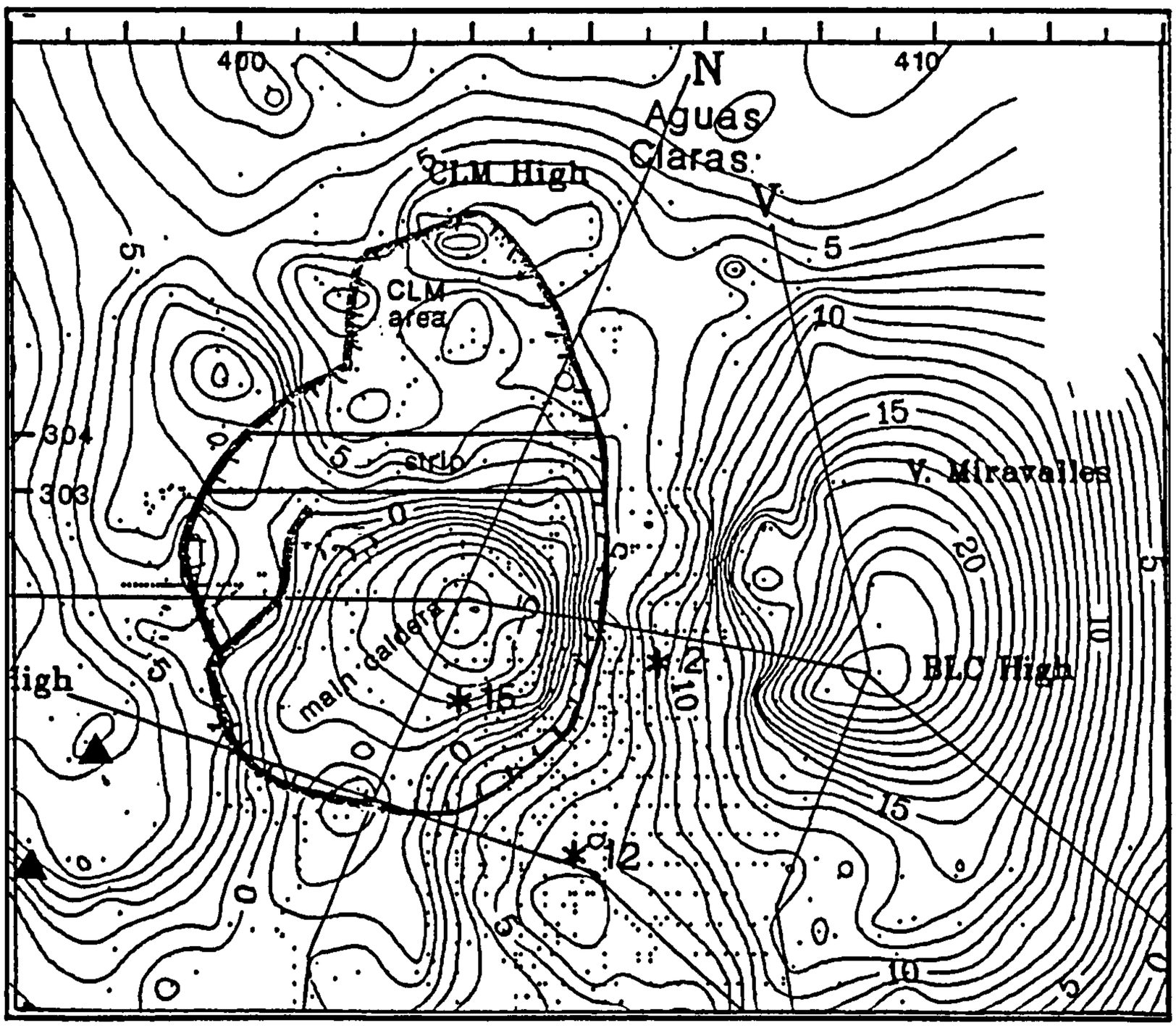

The chosen reference gravity value is not thought to be in error by more than 1 mGal, resulting in a total uncertainty of 58 mGal (= 1 mGal km^{-2} x 58 km^2). This produces an error of ± 1.4 Gt.

The dominant Guayabo Low is clearly defined but there is some interference from the eastern positive gravity anomalies. The contribution has been estimated by using the west-east gravity model, Profile WSE (Figure 3.26). The general west-east gravity gradient over the eastern caldera area (to the east of the Pumice Unit boundary) was modelled principally by a dense (2.65 Mg m^{-3}) intrusion in the Bajo Los Chiqueros area and the additional effect

of the Acidic Andesite Unit. By switching the density of both bodies to the 2.40 Mg m^{-3} background density and comparing the intrusion-free computed gravity to the observed gravity, the contribution of the dense bodies to gravity over the eastern caldera region was derived. At the PGM-15 intersection with the WSE profile (marked in Figure 4.6) the contribution is negligible, but at the intersection with the 4 mGal contour, the eastern integration limit, the difference is 2 mGal. The affected region within the integrated main caldera area is restricted to ~5 km^2, the average interference is ~1 mGal, and therefore the 'lost' mass deficiency is less than -0.15 Gt.

Other uncertainties in the mass deficiency are believed to be insignificant in comparison, and thus $M^* = -6.2 \pm 1.4$ Gt.

4.4.2 The pre-caldera volume, V_c

To estimate the volume of the unfilled caldera, V_c, it is necessary to know the pre-collapse morphology. In the simple model considered here (Figure 4.3) the topography was assumed to be flat, but at Guayabo it is likely that the caldera floor, the VS, comprised several coalescing stratocones. The exact number, shape or location of the stratovolcanoes is not known precisely; the Acidic Andesite Unit (AA) had a source to the east of the caldera, an area not included in the calculations. The form and gravity signature of the CLM suggests that it is restricted to the northern margin of the caldera. The intercalated lavas and tuffs of the VS at PGM-15 are believed to be a section through a collapsed stratocone flank, the source could not have been to the east (the location of the AA), but is proposed to have been at the present centre of the Guayabo, just to the north of PGM-15 (Figure 4.6). The lavas in the western caldera walls dip away from the caldera centre at an angle of around 15°, and as there is no evidence of resurgence within the caldera, this angle can be considered as a minimum edifice slope on the flanks of this pre-caldera stratovolcano. The present-day caldera wall lavas are continuous around the western and southwestern scarps, suggesting that a ring of individual cones located close to the margin (rather than a central larger cone) could not account for the pattern of lavas.

The missing volume, above the caldera fill, can therefore be approximated by a cylinder with a height equal to the average relief of the caldera margin (~700-550 = 150 m) plus an overlying cone with a slope angle of 15°, both with a radius of 4 km. This gives a volume of 24 km^3 and a summit elevation of 1770 m a.s.l. (reasonable considering the present height of Volcán Miravalles is 2208 m). The dimensions of the CLM cone have been calculated in a similar fashion (cone angle of 15°, wall height of 200 m, radius of 2 km) to predict an original volume of 8 km^3 and a summit elevation of 1300 m. This gives the total missing volume above the present caldera floor of $V_c = 32\ km^3$. Alternatively, assuming a flat pre-caldera surface, rather than a stratocone topography, V_c would be much smaller; 10 km^3; these values represent reasonable upper and lower bands on the quantity V_c.

4.4.3 The densities ρ_r, ρ_{ip} and ρ_m and the lithic fraction f_0

Both the parameters ρ_r and ρ_{ip} were estimated at Guayabo from the deep borehole density measurements (Chapter 3, Section 3.5). In calderas where there is no borehole information, these densities would have to be estimated within a certain tolerance range and then the model would need to be tested for sensitivity to the variation (as in Figure 4.5).

ρ_r The background rock density has been chosen at 2.36 Mg m^{-3}, the average density of the pre-caldera Volcano-Sedimentary Unit (VS = 2.32 Mg m^3) and the higher density Cabro Muco Andesite Unit (CMA = 2.40 Mg m^{-3}); thus there is a possible uncertainty in ρ_r of ± 0.04 Mg m^{-3}.

ρ_{ip} The lithic-free density of the caldera fill, ρ_{ip}, is the volume weighted average of the densities of the Pumice Unit and the LCMV. The porosity corrected wet densities of these are 1.58 and 2.09 Mg m^{-3} respectively, and the lithic fraction of the density must be removed. The lithic content of the Pumice Unit is negligible (ELC, 1986 b). The LCMV breccias and tuffs have a significant lithic fraction, but this was not quantified in the drilling reports (ELC, 1984 to 1986) and a value of 0.3 has been nominally assigned. Assuming a lithic density equal to the country-rock density, as specified in Section 4.3.2, this gives a ρ_{ip} density of 1.97 Mg m^{-3} for the LCMV. The Pumice Unit to LCMV volume ratio used here is a simple 1:1 ratio; this gives an average ρ_{ip} of 1.77 Mg m^{-3}. The possible total error

in ρ_{ip} is not thought to be worse than 0.10 Mg m^{-3} and thus the density contrast $\rho_r - \rho_i$ = 0.59 ± 0.14 Mg m^{-3} is significantly greater than 0.30 Mg m^{-3}, value below which the model becomes very sensitive to variations in this parameter (Figure 4.5 b).

ρ_m The value of magma density chosen, 2.30 Mg m^{-3}, lies between the densities measured by Murase and McBirney (1973) for the Newbury Rhyolite Obsidian (73.4% SiO_2, 2.20 Mg m^{-3}) and the Mt. Hood Andesite (61.7% SiO_2, 2.45 Mg m^{-3}). The whole rock geochemistry data of Mora (1988) give SiO_2 contents for the Guayabo-related tuffs between 65 and 77%; thus the density used in the calculations here (2.30 ± 0.05 Mg m^{-3}) should be considered as a reasonable average.

ρ_{op} and f_o The average measured wet density of the extra-caldera tuffs, 1.90 Mg m^{-3} (Chapter 3), gives a dry density of ρ_{op} = 1.60 Mg m^{-3} when corrected for 30 % porosity. The average lithic content (from Mora, 1988) used in the models is f_o = 0.1. The model prediction of M_o is not sensitive to variations in either of these parameters (Figure 4.5 a and b) but more accurate values are necessary for the estimation of the mass of the extra-caldera tuffs from exposures, M_x (discussed below).

The derivation of M_o from (17) is presented after the description of the estimation of M_o from the exposed extra-caldera tuff volume, so that a direct comparison can be made.

4.4.4 The extra-caldera tuff mass, M_x, derived from exposure

Very approximate estimates of the volume of the outflow tuffs have been made from the distributions and thicknesses reported by Mora (1988) and Alvarado *et al.* (1990 a). The distribution area of the tuffs on the Pacific slopes generally approximates a fan centred on the southern margin of the caldera (discussed in Chapter 2, see Figures 2.3 and 2.5). No Guayabo-related tuffs have been reported from the northern margin of the caldera or the Atlantic approaches to the arc, though the pre-Guayabo caldera Biotite Tuff is exposed in the Nicaraguan depression (Chiesa, 1991 and Figure 2.3). Though Mora (1988) and Alvarado *et al.* (1990 a) provided some details of these thicknesses, it is not yet possible to construct isopach maps for each tuff. What is generally clear is that the deposits have maximum thicknesses close to the caldera, but become gradually thinner downslope. The total extent

of the tuffs were not clearly defined by Alvarado *et al.* (1990 a) and the limits shown in their map (reproduced in Figure 2.3) are possibly controlled by erosion rather than by their original distribution. For example, the furthermost limit of the the Upper Grey Ignimbrite, the most extensive ashflow tuff associated with the Guayabo caldera, is shown by Alvarado *et al.* (1990 a) at 20 km from the caldera margin (Figure 2.3), close to the Central American Highway, but only 1-5 km 'inside' this limit they also observed regular thicknesses of 5-10 m of the tuff. Close to the southwestern caldera margin, Mora (1988) measured the maximum thickness of this tuff as 30 m.

For the purposes of this study an accurate picture of the tuff distribution around the Guayabo caldera is not feasible and therefore it has been necessary to adopt some suitable *approximate* model of distribution, using the scarce available data. The model adopted here (Figure 4.7) assumes the tuffs are restricted to an arc segment, α, of 80° with an apex 2 km inside the southern Guayabo caldera margin.

Figure 4.7 The tuff distribution model used to approximate V_o. The cross-sectional area is greater than for an exponential thickness decrease, sometimes used to model the distal part of V_o.

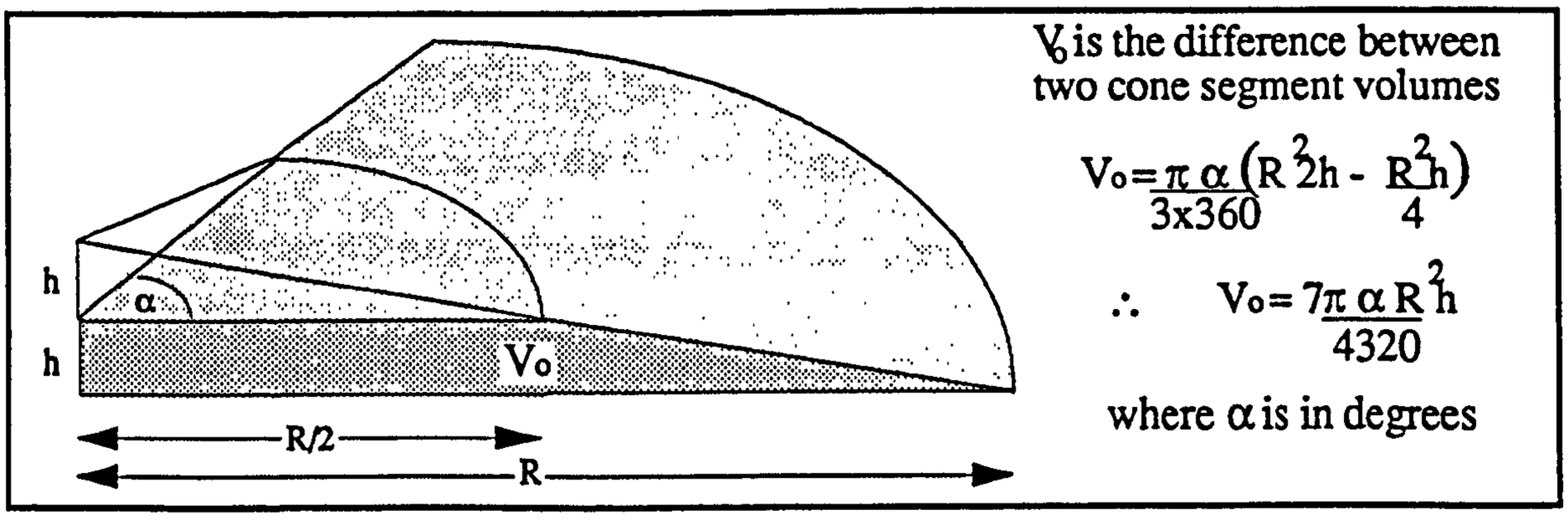

A non-linear falloff of thickness with distance is approximated by a flat cylinder/cone model (Figure 4.7). The volume is given by, $V = \frac{7\alpha}{12x360} \pi R^2 h$, where R is the radius and h the maximum thickness of the tuff distribution cone. The maximum radii of distribution (Table 4.3) are taken at 1.5 times that observed (rounded up to the nearest 5 km). This model of distribution obviously produces a much greater volume than that observed today but attempts to compensate for erosion and possible loss of co-ignimbrite air fall; the eolian fractionation (up to 35 wt.% loss) described by Sparks and Walker (1977). The uncertainty in the total volume is difficult to estimate but a 50% error gives a volume of 26 ± 13 km^3.

Table 4.3 Approximate volumes of tuffs associated with the Guayabo caldera. Maximum thicknesses and lithic fractions from Mora (1988). Areal distribution estimated from maps of Mora (1988) and Alvarado *et al.* (1990 a).

Tuff Unit	Max thickn's (m)	Max radius (km)	Areal angle°	Vol. (km^3)	Lithic fraction	Lithic vol. (km^3)	Juv. vol. (km^3)	DRE (km^3)
Proximal Breccia	30	5	160	0.6	0.5	0.3	0.3	0.2
La Ese Pumice	40	10	80	1.6	0	0	1.6	1.1
Hornblende Tuff	35	25	80	9.0	0.1	0.9	8.1	5.6
U. Gy. Ignimbrite	30	35	80	15.1	0.15	2.3	12.8	8.9
Total (rounded)	-	-	-	26	-	3.5	23	16

The average lithic contents of the tuffs were estimated from field observations by Mora (1988); 15, 10 and 50% for the Upper Grey Ignimbrite, the Hornblende Tuff and the Guayabo Proximal Breccia respectively (the quantity of lithics in the La Ese Pumice is insignificant). This gives a total estimated lithic volume of 3.5 km^3 of andesitic lithics which is assumed to have been derived either from the pre-caldera stratocones that were partially destroyed during the eruption, from coring of the vent and/or from collapsed fragments of the magma chamber. 3.5 ± 1.7 km^3 is more than an order of magnitude less than the missing caldera volume, V_c (10-32 km^3), and therefore the caldera could not simply have formed by explosion - the caldera formation mechanism favoured by Yokoyama (1987) for funnel-shaped calderas - but must have involved collapse.

The total juvenile volume of the extra-caldera tuffs is 23 ± 11 km^3 which gives a DRE volume of 16 ± 8 km^3 (using a conversion ratio of 1.6 : 2.3, the ratio of the lithic-free dry tuff density to the magma density). Finally, the total mass of erupted magma, M_x, is estimated to be 37 ± 18 Gt.

4.4.5 Comparison of M_x with the predicted M_o

It is now possible to compare the value of M_o as predicted from the mass balance model with the estimated mass of exposed tuffs related to the Guayabo caldera, M_x. The values of M_o calculated from (17) and the sensitivity of M_o to uncertainties in the model parameters are shown in Figure 4.8. The sensitivity test for Guayabo is similar to that described for the theoretical case (Section 4.3.2, Figure 4.5), but here only the parameters to which the model is most sensitive are shown. Not surprisingly, the model is most sensitive to the uncertainty in V_c. The value of V_c corresponding to a single pre-caldera stratocone, 32 km^3, was used

during the sensitivity tests for the other parameters, but the sensitivity was similar for lower values of V_c that correspond to a flatter pre-caldera topography. The sensitivity to the variation in $(\rho_r - \rho_{ip})$, shown in terms of the maximum variation of ρ_{ip} is least important.

The most important result is that the simple collapse model predicts a greater mass of erupted magma, M_o, than the mass of the Guayabo-related tuffs, M_x (shown in Figure 4.8 for comparison). The simple collapse model only fits the observed volume of caldera collapse if either V_c is in error or M_x has been underestimated by at least a factor of 2.

Figure 4.8 M_o predicted by the simple collapse model (17) is most sensitive to variations of V_c. The mass estimated from tuff exposures, M_x, is shown for comparison (black bar). A large V_c (corresponding to a single pre-caldera stratocone) predicts a greater M_o than M_x.

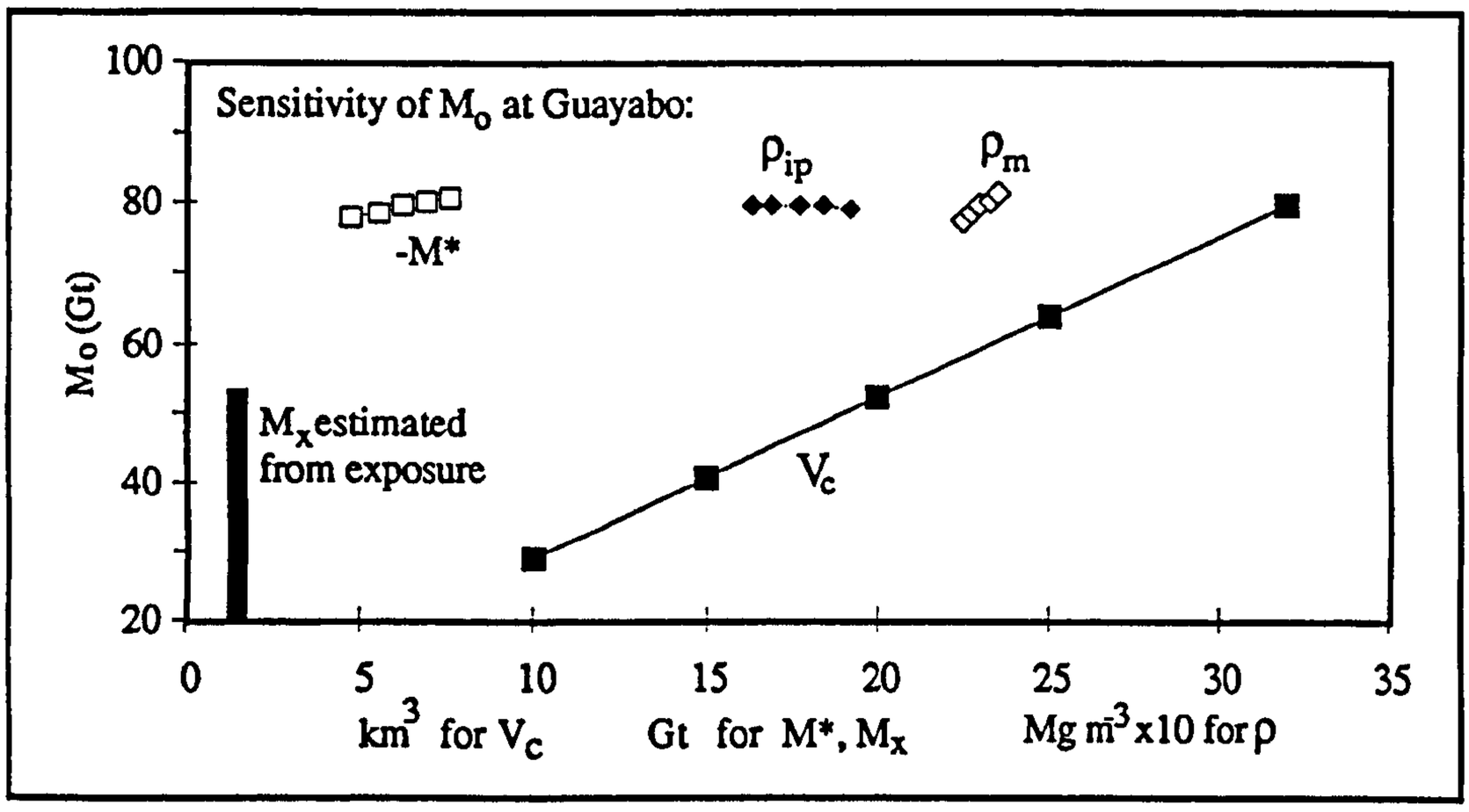

Errors in M_x: Although there are no reported occurrences of the Guayabo-related ignimbrites from the Atlantic approaches, it is always possible that significant volumes were initially laid down and then, because of the higher rainfall as compared with the Pacific approaches, were eroded away and/or rapidly degraded into soils. More detailed mapping of this area and close inspection of the soils would be necessary to test this possibility, but until otherwise proven, the initial assumption that the ignimbrites were originally absent from the Atlantic approaches is preferred. Erosion of the well exposed Pacific flank ignimbrites could be a problem, as mentioned above, but the thicknesses used here are the maximum exposed thicknesses, based on sections where the ignimbrite is preserved by an overlying palaeosol or subsequent non-erosive pyroclastic deposits.

A more difficult problem is to consider the loss of the fine grained material entrained in widely dispersed ashes. In general, the deposits of ignimbrite sequences would be expected to include a plinian air fall deposit preceding the main ignimbrite and co-ignimbrite air fall deposits sometimes interdigitating with the ignimbrite but more likely overlying it. The crystal enrichment found in crystal-bearing ignimbrites suggests that volumetrically, the co-ignimbrite ashes can be very significant, up to 40 wt % of the associated ignimbrite (Sparks and Walker, 1977). These ashes must therefore be accounted for in any volume estimates, but are usually extremely widely dispersed and the original volumes do not survive, unless rapidly buried by *non-erosive* sedimentary or volcanic deposits. The co-ignimbrite ashes of the 1815 Tombora eruption are dispersed over an area of 500,000 km^2 within the 1.0 μ isopach, largely in the Java Sea, (Self *et al.*, 1984) and represent about 2/3 of the ignimbrite mass (Sigurdsson and Carey, 1989). Walker (1980) showed from crystal concentration studies of the Taupo Pumice (*pre-ignimbrite ash fall*) that only 20 % of the original deposit fell on land and 80 % of the volume was 'lost at sea'. Wilson and Walker (1985) suggested that 7 km^3 (DRE) of the rarely preserved Taupo *co-ignimbrite ash* may have been lost due to erosion, equivalent to 2/3 of the ignimbrite DRE volume.

The implication for the M_X estimates at Guayabo is that although Mora (1988) suggested that the occasional air fall deposits between the ignimbrites are rare and volumetrically insignificant, pre-ignimbrite and co-ignimbrite ashes may have originally been very important, but have been lost either by wide areal dispersal and/or erosion. The occasional palaeosols up to ~2 m thick that separate the ignimbrites may well be candidates for possible air fall deposits. Given all these uncertainties, it is therefore difficult to be certain that the volume of the Guayabo caldera was not *initially* matched by an equivalent erupted volume. Furthermore, at other locations, unless detailed mapping and crystal concentration studies are conducted, it will be similarly impossible to obtain *precise* caldera to erupted product volume balances. It is proposed, however, that balances should still be attempted in order to highlight any discrepancies that arise. Insufficient erupted mass may be explained by loss of fine material, though this can be constrained, at least partially, by crystal enrichment

studies. More importantly, however, excess erupted mass requires an independent explanation, as at the Aira caldera (discussed below).

Errors in V_c: There are three ways that errors in the estimation of V_c could explain the misfit between M_x and M_o; i) the pre-caldera volcanic topography comprised a number of smaller stratocones with a volume of 10 to 15 km^3, ii) a caldera existed before the Guayabo products were erupted, or iii) caldera subsidence occurred after the Guayabo tuff eruptions due to post-caldera volcanism drawing on the sub-caldera magma chamber.

The outcrop pattern of the pre-caldera lavas exposed in the western caldera wall do suggest a common stratovolcano source, as suggested earlier, but, without detailed mapping, the possibility that a number of smaller cones are responsible cannot be ruled out entirely. However, even a smaller number of cones are unlikely to have had a net zero volume over and above the present caldera rim, and therefore subsidence unrelated to the tuff emplacement has to be invoked.

If the western caldera walls *do* correlate with the Volcano-Sedimentary Unit drilled in PGM-15, as proposed, then most of the observed subsidence must post-date this unit, but could possibly precede the eruption of the first Guayabo tuffs. On the other hand, post-caldera subsidence is needed to explain why the youngest caldera-related tuffs, the Pumice Unit and the Guayabo Proximal Breccia, are cut by the most recent subsidence on the southern caldera margin. This may indicate the need for several subsidence events: indeed incremental subsidence was demonstrated at the Aira caldera following the eruption of Sakurajima in 1916 (Omori, 1916 as reported by Aramakei, 1984) and more recent activity continues to affect the caldera (Ishihara, 1990). (The mass balance at Aira is described below). Post-Guayabo tuff caldera collapse may therefore be related to the withdrawl of magma during the build-up of the post-caldera Miravalles stratocone complex on the eastern caldera margin; the missing V_c volume is more than compensated by the estimated volume of Volcán Miravalles alone (~40 km^3, estimated from the 1:50,000 topographic map).

The alternative mechanisms of collapse mentioned earlier (Section 4.1.3) involve lateral flow of magma from the sub-caldera chamber along fissures (Gudmundsson, 1987 and

1988), or hydraulic connection along a volcanic chain (e.g. Hildreth, 1990), but there is no evidence that either system operated in the Guanacaste Arc. Another possibility is that cooling of the latest sub-caldera pluton (the La Ese Pumice is dated at ~0.6 Ma.) caused the post-caldera subsidence.

Whatever the cause for the post-La Ese Pumice subsidence, the implications of the mass balance test on the Guayabo caldera concur with the caldera evolutionary model presented in Chapter 3; the combined results of the revised caldera stratigraphy presented in Chapter 2 and the caldera structure derived from the gravity models presented in Chapter 3. The mass balance test could equally be applied to the many calderas that have a gravity low associated with the caldera fill, and the case of the Aira caldera is considered for comparison.

4.4.6 The mass deficiency at the Aira caldera, Japan

Yokoyama (1961) estimated a mass deficiency, M*, of 161 Gt over the Aira caldera and Aramakei (1984) reported that the total mass, M_x, of outflow tuffs from the multi-stage caldera was 414 Gt, assuming an outflow tuff density, ρ_{op}, of 1.1 Mg m^{-3}. Aramakei believed that the pre-caldera topography was a depression, much like the present topography, which means that V_c is effectively zero. Assuming similar densities to those used in the Guayabo model, the mass balance model predicts an outflow mass, M_o, of only 145 Gt. This cannot be explained by errors in the assumption of any of the parameters required in (17), except V_c. The implication is that the volume of erupted material was not compensated by a collapse of the magma chamber roof, but that syn-eruption recharge of the magma chamber was taking place (assuming voids did not form instead). The Aira caldera fits the collapse model, however, if V_c at Aira is *not* zero, as suggested by Aramakei (1984), but equal to 115 km^3. Given the 20 km diameter of the caldera, this volume implies a cylinder of almost 400 m depth, equivalent to the present topographic relief on the eastern caldera wall.

In summary, either the volume balance collapse model does not apply at Aira because replenishment accompanied multi-stage eruption, or syn-caldera subsidence is greater than that proposed by Aramakei (1984), and the pre-caldera depression was not as severe as that

observed today. The underestimate of the predicted erupted mass, M_o, at Aira is in contrast to the overestimate predicted at the Guayabo caldera, but the solution in both cases seems to be that the unfilled caldera volume, V_c, has been misinterpreted.

4.4.7 Summary of the caldera mass balance model

A new quantitative balance model is proposed that can be used to test whether the total volume of a silicic caldera matches the magma equivalent volume of the associated pyroclastics. The model uses the mass deficiency over the caldera, calculated from gravity data, to estimate the mass of juvenile material within the caldera, overcoming the usual problem of estimating the intra-caldera volume without either borehole or unique geophysical interpretation of the sub-caldera structure. This mass is integrated with the topographic caldera depression volume and an expression accounting for the proportion of caldera missing as lithics in the extra-caldera deposits, yielding a prediction of the mass of magma represented by the outflow tuffs. Tests for sensitivity to uncertainties in the parameters indicate that the model becomes too sensitive to uncertainties in the density contrast, $\rho_r - \rho_{ip}$, for contrasts smaller than ~0.2 Mg m^{-3}. The reason is that the mass deficiency becomes an ineffective way of constraining the unknown intra-caldera volume.

Neither the Aira caldera or the Guayabo caldera conform to a simple collapse model. At Guayabo the total volume of the caldera is far greater than the volume of magma represented by the caldera-related tuffs. The geophysical and stratigraphic evidence at Guayabo suggests that the excess caldera volume is the consequence of post-tuff, rather than pre-tuff subsidence. The preferred solution is that this is because of sub-caldera magma withdrawl during the post-caldera build-up of Volcán Miravalles at Guayabo. At Aira, in contrast, the caldera volume is too small to account for the volume of the outflow tuffs, but the volumes do balance if the existing depression at Aira is attributed to caldera collapse and not the pre-caldera depression proposed by Aramakei (1984).

4.5 Features of Guayabo that are Diagnostic of Funnel Calderas

During this chapter the uses of gravity data to study the structure and the mechanics of silicic caldera collapse have been examined. These are briefly reviewed here, followed by a summary of the geological features that are diagnostic of funnel-type calderas such as Guayabo.

Gravity studies are useful because commonly there is a significant density contrast between the caldera fill and the pre-caldera country rock and the nature of the gravity field can discriminate between different sub-caldera structures. In ideal circumstances, the gravity anomaly reflects the thickness of the caldera fill and thus the field mimicks the topography of the caldera floor. The gravity gradient over the caldera margins is greatest for a maximum density contrast. Therefore a U-shaped anomaly profile is predicted across piston-type calderas in contrast to a V-shaped anomaly across funnel-type calderas. In addition, buried ring fractures with associated lateral density contrasts can be identified by changes in the gravity gradient, as at Guayabo within the topographic caldera margin. The form of the caldera floor can be modelled from gravity data providing the density of both the caldera fill and the country rock can be constrained.

The Guayabo caldera does not conform to the piston collapse model; there is no geophysical (gravity and resistivity data) or stratigraphic evidence that the centre subsided as a coherent block, indeed many stages of collapse on different scales are inferred.

At least two (possibly three) distinct sets of concentric arcuate ring faults (but with individual displacements of generally <400 m) can be identified from the gravity and stratigraphic data both at and within the present topographic caldera margin, but subsidence is greatest towards the centre of the caldera. The resultant form of the caldera floor is typical of funnel collapse calderas. It is proposed, therefore, that some other so-called funnel calderas may have formed by similar multiple subsidence across concentric sets of ring faults, rather than by true chaotic collapse.

The outflow tuffs close to the caldera margin dip at shallow margins away from, rather than towards, the caldera and so downsag mechanisms (Walker, 1984) are unlikely to be important.

Multiple pyroclastic flows resulted in the incremental multistage collapse of the caldera. Collapse may have been restricted to different parts of the caldera during successive eruptions, reflecting changing vent locations between eruptions and resulting in the present segmented, arcuate nature of the caldera wall. These discreet flows are separated by repose times represented by intra-flow palaeosols and become progressively more silicic and less voluminous upsection, suggesting an evolving fractionating magmatic source beneath the caldera. This contrasts with the geochemically reverse zoned ashflows that represent the continuous evacuation of a zoned magma chamber (e.g. Blake, 1981).

There is no intra-caldera deposit of a major welded tuff that is typical of calderas for which piston-type collapse has been proposed. The parts of intra-caldera strata that are dominated by poorly-consolidated tuffs, breccias and reworked material are similar to the deposits observed in the bulk of the intra-caldera drillcore of the Aira, Kuttyaro and Nigorikawa calderas, Japan (Aramakei, 1984 and Yokoyama, 1987). The lack of welding implies that these deposits did not form from hot pyroclastic flows, but may be better described as fall-back deposits. A high quantity of lithics in the late caldera LCMV breccias (though not the Pumice Unit) derived from the pre-caldera volcanics and the basement strata suggests coring of the vent areas during eruption and partial destruction of the pre-caldera stratovolcanoes.

Post-caldera volcanism is restricted to stratocone activity on the eastern caldera margin only, rather than to multi-vent activity distributed along ring faults and there is no evidence of the type of caldera centred resurgence that is typical of many piston-type calderas.

The young transitional (towards mature continental type) nature of the crust is also typical of the setting of other calderas, for example in Japan, for which the funnel model has been proposed.

CHAPTER 5

DYNAMIC GRAVITY MODELS OF THE MIRAVALLES GEOTHERMAL FIELD

Introduction

Pressure drawdown during the productive life of a liquid-dominated geothermal reservoir may lead to the expansion (or creation and expansion) of the vapour zone at the expense of the liquid-dominated zone resulting in an overall mass decrease. Precision gravity studies (microgravity) can therefore be used to monitor the efficiency of the recharge that competes with the drawdown (e.g. Wairakei, New Zealand; Allis and Hunt, 1986). Establishment of the exploitation-induced vapour zone may immediately follow full production and therefore one of the monitoring requisites is a good pre-production gravity and elevation data set. This is rarely available for the older, well established fields.

The Miravalles Geothermal Project (MGP, introduced in Chapter 2) is in its pre-production development phase. It therefore offers the chance to examine any possible mass changes within the geothermal reservoir that are not production-related. Such changes would clearly need to be removed from a 'during production' data set. Flow tests and an injection test have also been monitored to examine any possible short-term effects on the shallow and deep reservoirs. Finally, a comprehensive gravity monitoring program has been designed to test the production-related mass changes that are predicted by the current reservoir model; a model based on a review of previous studies and observations of this study.

5.1 Microgravity Monitoring of Geothermal Fields

Liquid-dominated (hot-water) geothermal fields, such as Miravalles, are far more common than the vapour-dominated (dry-steam) type, such as the Lardarello and The Geysers fields (White *et al.*, 1971) that were initially considered essential for economic geothermal power production. It was first demonstrated at Wairakei, New Zealand that dry steam was not essential. Hot water (up to 260°C) partially flashes to steam within the wells as the fluid pressure decreases towards the wellhead. The steam is separated and is used to drive the

turbines. Over one hundred hot-water sites have since been developed in various volcanic settings in many countries, mostly in the circum-Pacific area (review in DiPippo, 1986). Of all the fields, very few have reported microgravity monitoring programs, the few that are known to this author are reviewed here: Wairakei and Broadlands, New Zealand and Bulalo in the Philippines. By way of the review, the general hydrology of hot-water system at Wairakei is introduced; providing a comparison for the Miravalles Field.

5.1.1 Wairakei

Production-induced mass changes measured by gravity at Wairakei from 1961 to 1968 were the first to be reported (Hunt, 1970) and ongoing studies have continued both there and at Broadlands (Hunt, 1977, 1984, 1987 and 1988, Allis and Hunt, 1984 and 1986). The original technique of studying mass loss and recharge using microgravity at Wairakei is described in Hunt (1970) and a modified technique, employed at Broadlands, is illustrated by Hunt (1987).

Gravity changes of up to -1000 μGals (corrected for up to 450 mm yr^{-1} subsidence) in the central 1 km^2 Wairakei borefield, and lesser decreases over a 50 km^2 area have occurred, largely during the first few years of production (1961 to 1967, map of changes shown in Figure 5.1). Uncertainty in the pre-production data set, however, has resulted in error estimates of 300 μGal for the initial gravity decrease. Since the late 1960s there has been a zero net gravity change over the whole field, indicating present mass flow equilibrium (Hunt, 1977 and Allis and Hunt, 1986). The principal cause of the initial gravity change has been liquid pressure drawdown of some 2.5 MPa (25 bar) allowing the development of a steam zone.

The present vertical distribution of fluids in the Wairakei borefield area, shown in Figure 5.2, is typical of the regime in many liquid-dominated fields, including Miravalles. The changes in pressure gradient (reservoir pressures are measured in non-flowing wells) delineate the transitions from the vapour dominated to the water-dominated regimes, but reservoir temperature profiles are required to detect the boiling zone where the fluid is usually close to the boiling curve (bold line in Figure 5.2).

Figure 5.1 The gravity changes (μGal) at the Wairakei geothermal field, New Zealand from 1961-1967. Also shown are the resistivity boundary of the reservoir and the area of maximum subsidence close to the main 1 km^2 borefield. (Adapted from Allis and Hunt, 1986).

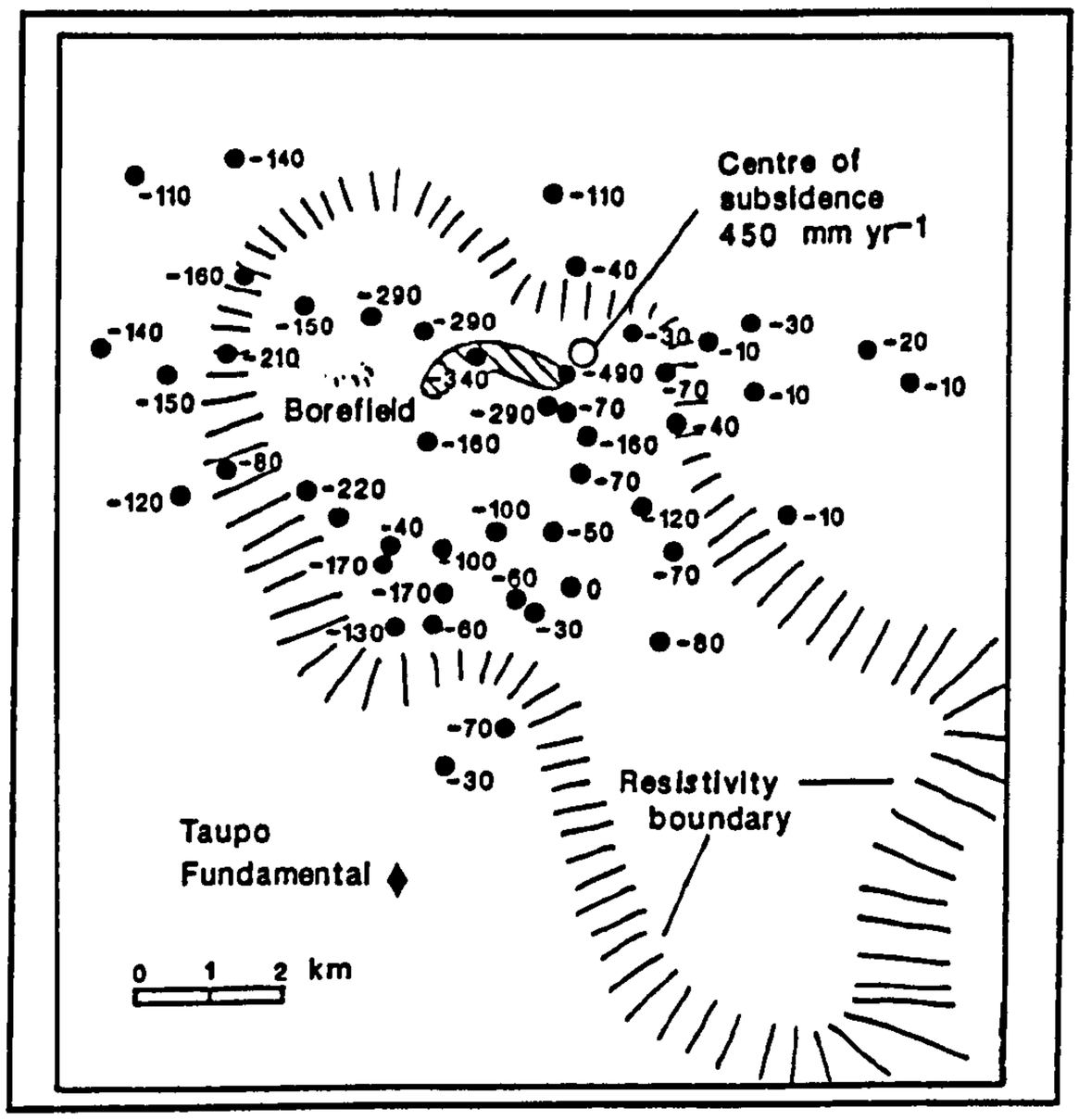

Pressure drawdown in the deep reservoir results from an imbalance between production and natural recharge of the reservoir. It causes the conditions at the top of the liquid zone to evolve towards saturation conditions (Figure 5.2) where boiling can commence, eventually changing to a slightly super-saturated state, forming the steam zone. It is a well documented fact, however, that downhole temperature measurements under static conditions are complicated by within-well flow and do not always reflect reservoir conditions; usually down-flowing water results in apparently isothermal deep reservoir profiles (e.g. Stefánson and Steingrínsson, 1980). If deep reservoir temperatures are actually higher and closer to the boiling curve, less pressure drawdown is required to expand the steam zone, an important consideration in behaviour prediction models.

The groundwater zone is perched above the steam zone, separated by an impermeable argillic alteration cap, and temperatures are below the boiling curve. Some natural steam transfer to the surface from the steam zone (or the boiling zone prior to the development of the steam zone) occurs along fractures through the perched water table, giving rise to fumaroles, or to boiling mud-pots where the steam condenses or mixes with groundwater. Exploitation can cause the style, mass flow and locus of these surface manifestations to

change, and any associated mass/density changes must therefore be included in the overall mass balance equation of the system.

Figure 5.2 Schematic distribution of fluids, pressure and temperature in a water-dominated geothermal reservoir, adapted from the Wairakei system (Allis and Hunt, 1986). The changes in pressure gradient locate the phase changes between different zones. The boiling curve for the observed pressure is shown for comparison with the observed temperatures. The steam zone is almost isobaric and the observed temperatures are above the boiling point; the boiling zone temperatures are close to the boiling curve (liquid-dominated) and finally, in the deep liquid zone the temperatures are below the boiling curve.

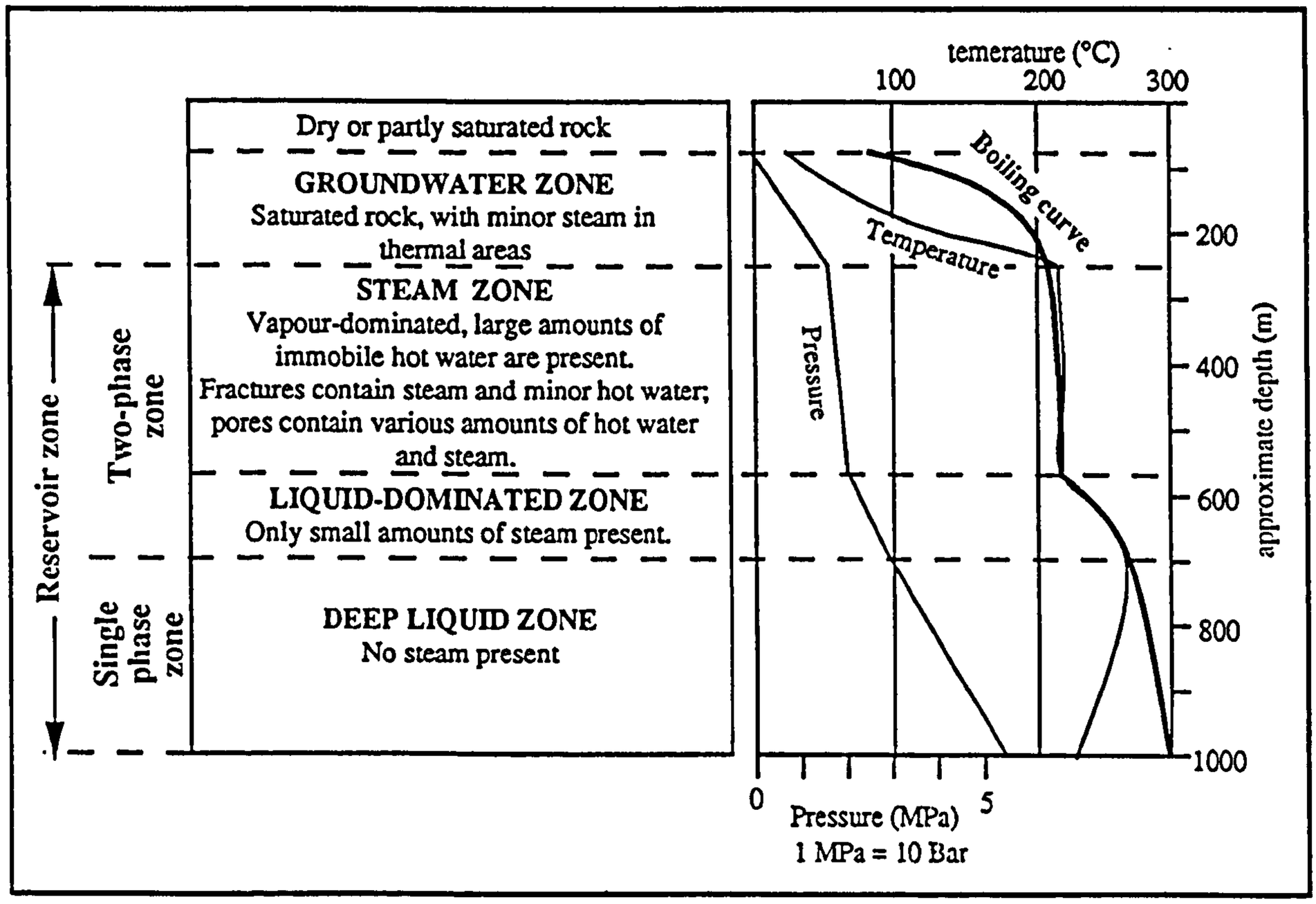

Allis and Hunt (1986) have shown that although steam zone expansion was the dominant mass change during the initial production at Wairakei, there are many other competing causes for gravity changes, the effects of some of which may be estimated independently only where good borehole data exist. There are density changes within established zones: the degree of saturation of the steam zone and the boiling zone can be calculated from the pressure gradients in the borefield. Similarly, the thermally controlled changes in fluid density can be monitored. A decrease in temperature of the deep zone increases the saturation and should result in a gravity increase in contrast to steam zone dry-out which causes a gravity decrease. The drawdown in the groundwater level, if more than a few metres, must be taken into account. Pore compaction and silica/calcite precipitation on the

other hand are not thought to contribute significantly to the mass equation at Wairakei (Allis and Hunt, 1986).

The individual contributions to mass change were calculated by Allis and Hunt (1986) to derive a best-fit to the observed gravity data for different parts of the field. The factors least well constrained by borehole logs are the definitions of the top and bottom of the steam zone and the saturation level of the zones. In this respect, modelling the gravity changes at Wairakei has provided new information on the nature of the steam zone and the causes of the temperature and pressure decreases. Ambiguities remain about saturation levels within the different stacked zones, but modelling has shown that as the reservoir has been in an approximate state of mass equilibrium since the steam zone dryout ceased by the early 1970s. The continued temperature and pressure decrease of the steam zone since then must be interpreted in terms of invasion of cold groundwater that condensed the steam.

One of the lessons learned from the study at Wairakei is that it is essential to have at least one set of precise gravity and levelling data prior to development of the field (Allis and Hunt, 1986). Gravity surveys beyond the borefield provide advantages over standard monitoring as information about the effects of liquid drawdown can be learned (Hunt, 1988). Non-uniform gravity changes in this area would indicate heterogeneity in the permeability and could indicate the areas of recharge. In this respect it is important to monitor the drawdown of the shallow groundwater outside the borefield, as well as inside.

5.1.2 The Broadlands and Bulalo fields

Broadlands Extensive drawdown testing at Broadlands from 1967-1971 produced a total of 35 Mt (liquid and steam). Gravity measurements in 1967 and 1974 showed decreases of the order of 80 to 120 μGal both inside *and outside* the borefield and simple modelling suggested that this was the result of a mass loss of 24-35 Mt and that there was therefore very little recharge (Hunt, 1984 and 1987). The reduced amount of withdrawl since 1972 (14 Mt total) was accompanied by a gravity *increase* of the order of 40 μGal over most of the field between 1974 and 1984, modelled as a net excess recharge for this period of 11 Mt

(Hunt, 1984 and 1987). These later gravity differences are small and are equal to the value of absolute significance of 40 μGal given by Hunt (1987).

The initial mass losses at Broadlands were modelled by a vertical cylinder below the production depth of 500 m, 200 m thick, 1.5 km radius (most of the field) and with density contrasts of between -0.016 to -0.025 Mg m^{-3} (Hunt, 1984 and 1987). Although this models the observed gravity changes, the density contrasts were the minimum required to produce an appreciable gravity difference and the cylinder radius was constrained by the limit of gravity changes, it is not clear what the physical significance of the cylinder is. Hunt (1987) estimated that up to one third of the gravity changes could be accounted for by observed or inferred groundwater level changes; these were difficult to correct for as few observations were available. The most significant result of the gravity changes at Broadlands is that mass changes were not restricted to the borefield area alone. This suggests that withdrawl occurred over a larger area than just the borefield, but the gravity differences were too small to define confidently the exact total area (Hunt, 1987). If the gravity decreases at Broadlands are comparable in nature, though much smaller in magnitude, to those observed during the initial production at the Wairakei field, as suggested by Hunt (1987), then it is possible to think of the cylinder model as an expanding steam zone (as in Figure 5.2). Without the pressure-temperature logs or knowledge of the degree of pressure drawdown, however, it is not possible to examine this further.

Bulalo At the Bulalo field in the Phillipines, Atkinson and Pederson (1988) used gravity measurements to test reservoir simulation models. The average least-squares error on a subsidence corrected gravity difference at a benchmark is given as 7 μGal (using a LaCoste and Romberg D-meter) and non-reservoir related gravity changes are quoted at ± 10 μGal. Mass production and injection were measured and natural discharge was estimated, but the subsurface inflows and outflows were calculated from the results of five gravity surveys from 1980-1987 covering the period *following* 1979, the first year of production. A maximum gravity change of 160 μGal corresponded to a net production of 115 Mt from 1980 to 1987 (estimated from the hourly production rates given in Atkinson and Pederson, 1988). The observed reservoir performance was reasonably approximated in the three-

dimensional simulation model by allowing only negligible deep recharge into the reservoir. The net gravity-measured influx matched the computed influx until 1985, but since then, at least until late 1986, the gravity-measured influx was apparently far greater (up to six times) than the simulated influx. Atkinson and Pederson (1988) suggested that near-surface or data processing effects were responsible, rather than a real increase in influx rate. Without the data processing technique, however, especially the subsidence and the free air gradient (elevation corrections in 'static' gravity data reduction are explained in Appendix 3A) used for the subsidence corrections, it is not possible to assess this proposition.

In summary, previous microgravity studies have shown that with significance levels of 10 μGal or a few 10s of μGal, production/recharge-related mass changes in liquid-dominated reservoirs can be monitored using repeat gravity studies. The observed changes are of significance to the reservoir mass balance characteristics, however, *only* if the non-reservoir effects can be eliminated or corrected for. The corrections for ground subsidence require knowledge of the local free air gradient, and the value chosen should always be specified so that the results can be independently assessed. Shallow borehole monitoring is essential to remove the near-surface gravity effects of the seasonal and longer-term fluctuations of the meteoric water table. The most significant gravity changes occur as the steam zone is established during the maximum pressure drawdown at the initiation of production. Following the development of the expanded steam zone, the total natural recharge may increase to eventually approach the fluid withdrawl rate. The natural recharge rate can be augmented by reinjection of the spent geothermal fluid, but the effectiveness of this relatively recent attempt to delay reservoir pressure drawdown has yet to be proven. At least some reservoir mass changes related to production occur outside the field, but as this is the area where gravity changes are at the limits of significance, the total extent of pressure drawdown or recharge outside the borefield is difficult to define.

5.2 The Miravalles Geothermal Reservoir

The geology and temperature regime of the Miravalles geothermal field (located in Figures 5.3 and 5.4) were introduced in Chapter 2 and the geophysical aspects were discussed in Chapter 3.

Figure 5.3 Location of the repeat gravity stations used in the 1988-1989 field seasons. There are more stations, not located in this Figure, in the PGM-11 area (Figures 5.10 and 11). ICE Base is the reference station at the ICE Headquarters at Guayabo. A second reference station to the south of Guayabo, Base 1, was used in 1988. The borefield details are shown in Figure 5.4. A section through the hydrothermal system, from Volcán Miravalles through La Fortuna, is shown in Figure 5.5.

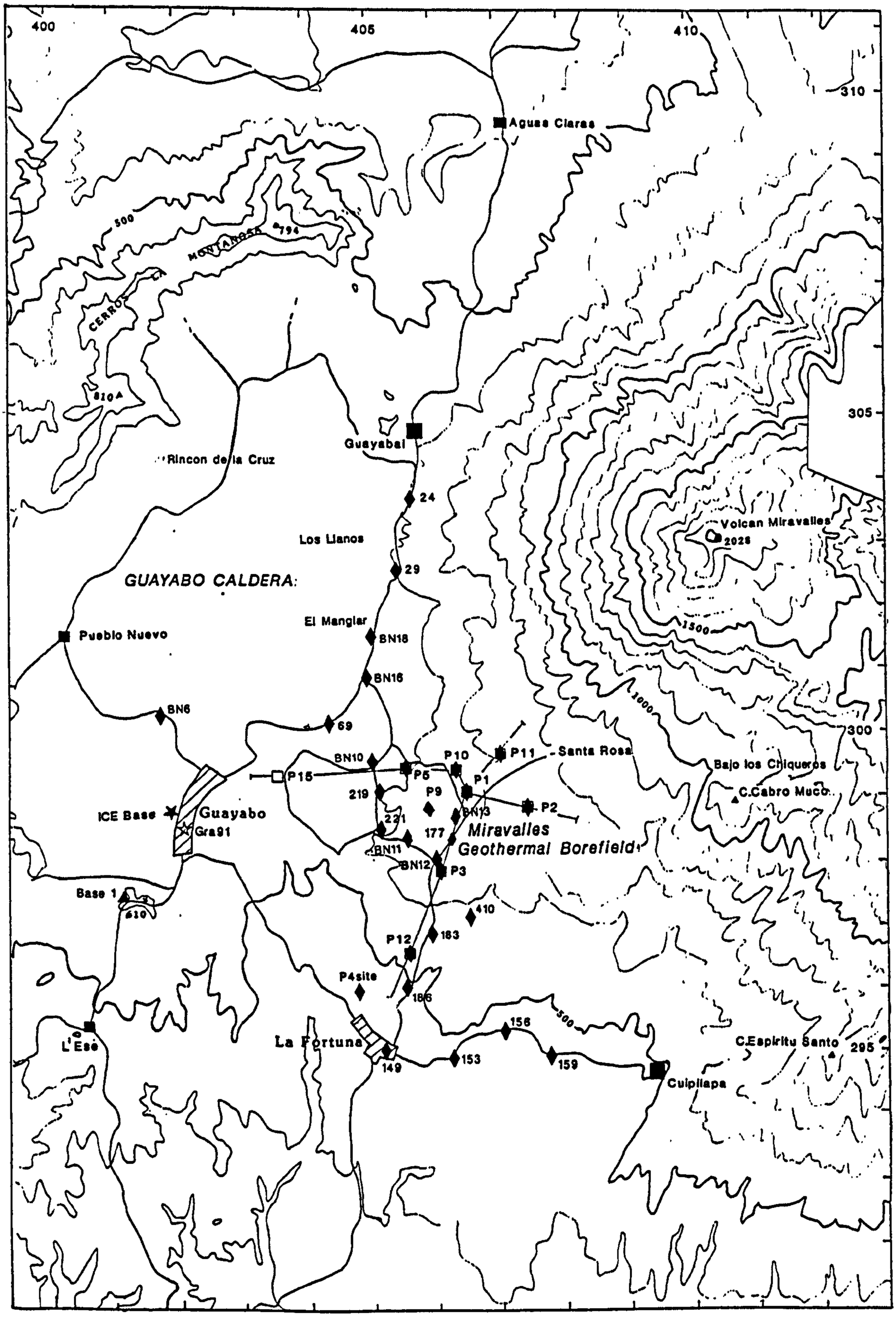

Figure 5.4 Map of the hydrothermal manifestations showing association with recent faults; the Las Hornillas fault in the north and the La Fortuna graben margin to the south. Temperature isograds and alteration map from ELC (1986 a), ICE (unpubl. data) and this study. Spring and fumarole locations from ELC (1984) and ICE (unpubl. map). Locations of the deep reservoir temperature profiles (WE and NS, Figure 5.6) are also shown.

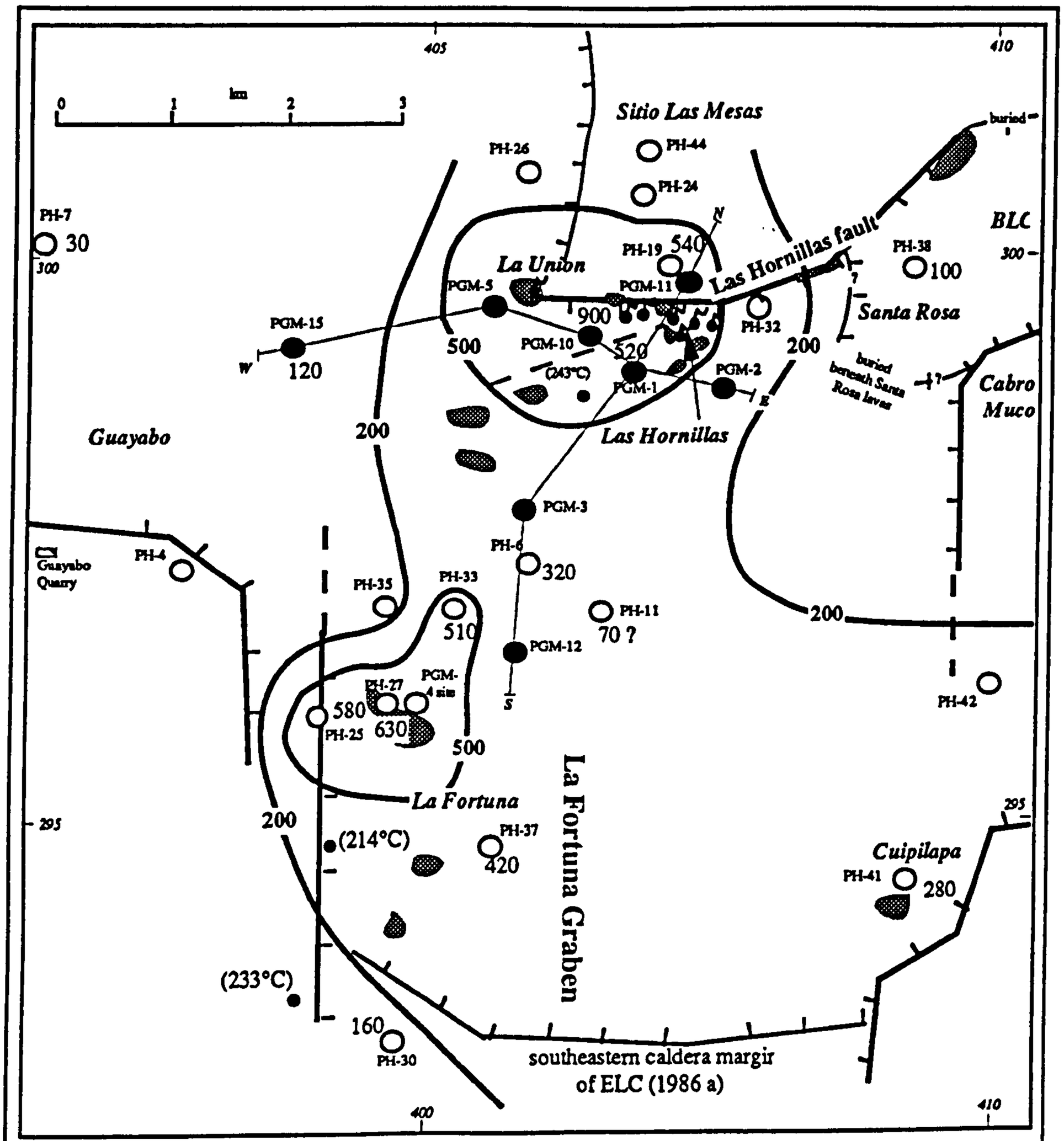

PH- shallow borehole, temperature gradient (°C/km) shown where available

PGM- deep geothermal wells

Hydrothermal alteration

Hot springs related to geothermal brine (calculated temperature of source fluid)

Fumaroles

Major collapse fault

Minor and inferred faults

200°C/km Temperature gradient

500°C/km

BLC Bajo Los Chiqueros

The hydrology of the system is now examined as a necessary prerequisite to the discussion of the applicability of a repeat gravity study. The hydrology is defined in terms of the pressure-temperature relationships of different parts of the reservoir to the boiling curve, in order to identify the areas that are likely to suffer maximum steam zone expansion during and following pressure drawdown once full production begins.

5.2.1 The Miravalles outflow plume

The Miravalles reservoir is best considered as the near-upflow part of an ouflow plume stretching from the lowermost flanks of Volcán Miravalles, southwards to Salitral (Figure 5.5, adapted from Grigsby *et al.*, 1988 and ELC, 1988). The system is analogous to the Valles and other outflow plumes described by Goff *et al.* (1988). The west-east and north-south details of the drilled reservoir are shown in Figure 5.6 (located in Figure 5.4, details of the geology are shown in Figures 2.9 a and b). The Miravalles plume is postulated to rise in the area to the north of the maximum temperature of 255°C in PGM-11, the fluid is then driven south, presumably by the pressure gradient forced by a Volcán Miravalles edifice waterhead, but confined within the north-south La Fortuna graben fracture system (located in Figure 5.4). The temperature reversals in PGM-2, 10 and 11 (Figure 5.6, PGM-2 also has cold water recharge from the east) are difficult to explain in terms of anything but an outflow plume. The elongation of the reservoir temperature profiles in the north-south direction define the proposed outflow plume vector, compared with the steep temperature fall-off towards PGM-15 to the west (Figure 5.6). The near-neutral reservoir fluid only appears at the surface in the diluted chloride springs from La Fortuna to Salitral and Bagaces (located in Figures 2.1 and 5.3) where it is partially mixed with meteoric water and sometimes with steam condensates (Grigsby *et al.*, 1988).

ELC (1986 a and 1988) defined the limits of the exploitable geothermal reservoir from temperature measurements of the deep wells drilled to date ($T > 200°C$, Figure 5.6) and the probable extension of these based on the outflow model. At other fields it has been possible to define the limits of a hot brine reservoir from resistivity data; where profiles show a steep lateral increase in apparent resistivity (e.g. from 2-5 Ωm inside to 10-50 Ωm outside the

reservoir at Broadlands, Risk *et al.*, 1977). However, the shallow resistors and the presence of resistive bodies within the reservoir (the Acidic Andesite Unit, areal limits in Figure 3.18) have rendered this technique inappropriate at Miravalles. The 1-D resistivity inversions of Duprat and Leandro (1986) and Geosystems (1988) (Figures 3.18 and 3.19) suggest that the conductor at reservoir depths (2-5 Ωm) is present to the north, west and south of the field, beyond the limits of the measured profiles and therefore outside the southern caldera margin. It is proposed therefore (Chapter 3) that the caldera margin is *not* the important reservoir barrier that ELC (1986 a) proposed. The La Fortuna graben on the other hand does appear to provide structural control on the outflow plume (Figure 5.4).

Figure 5.5 The Miravalles outflow plume, adapted from Grigsby *et al.* (1988) and Henley and Ellis (1983), showing the upflow region north of PGM-11, the shallow boiling level in PGM-10, the outflow to the south and the possible recharge system. A deep, two-phase region in the source area is not thought to exist at Miravalles. Note the inclusion of PGM-10, not PGM-1 in this section.

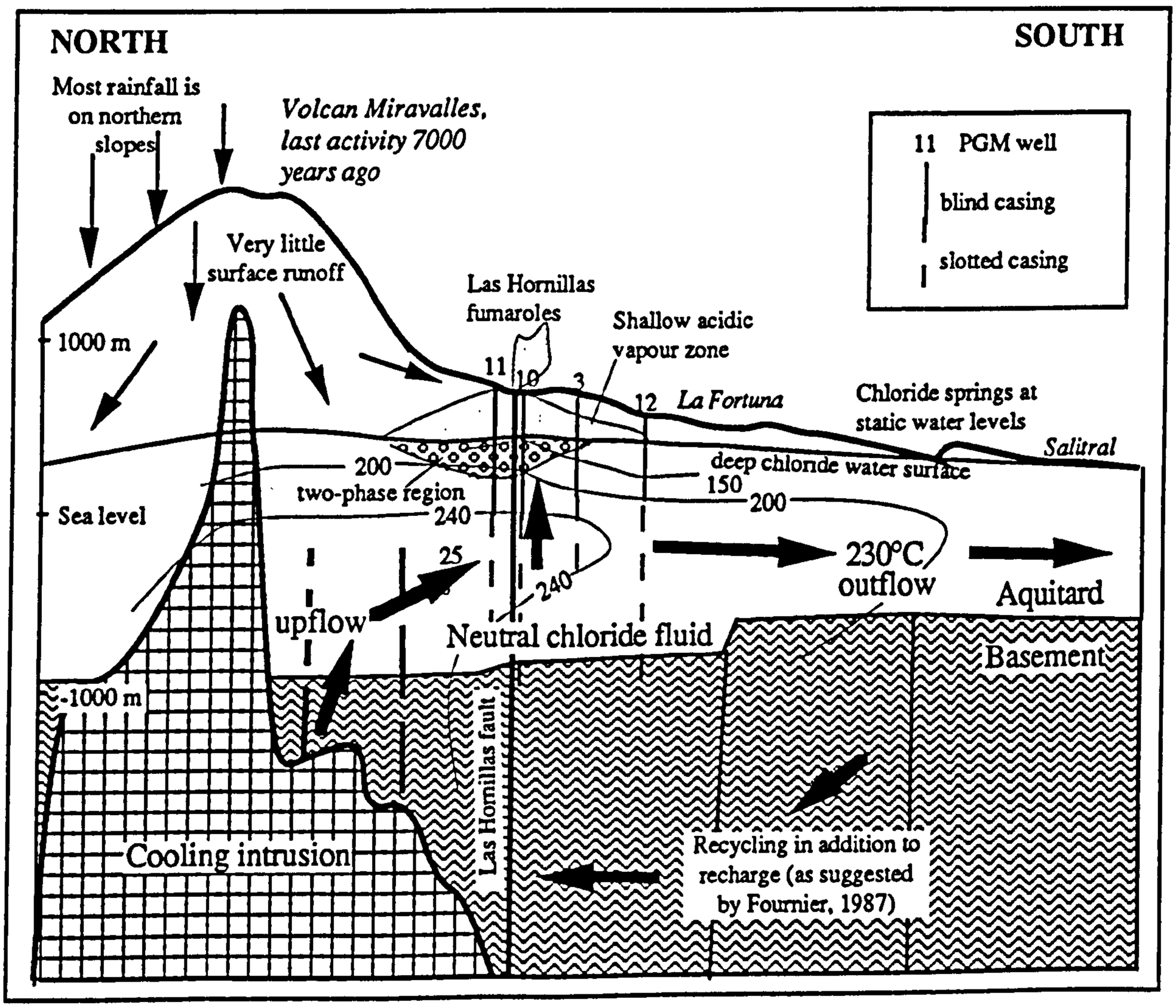

The position of the upflow region is undoubtedly in the northern part of the field but it is possible that it is in the PGM-1 to PGM-10 area as shown in Figure 5.6, not north of PGM-

11, as shown in Figure 5.5. The closed high temperature zone at 250-400 m b.s.l. in PGM-11 (the 255 °C contour in Figures 5.5 and 5.6) has previously been used to locate the inflow to the borefield (ELC, 1986 a and 1988 and Grigsby *et al.*, 1988).

Figure 5.6 The Miravalles geothermal reservoir, relative to the stratigraphy. The top of the liquid-dominated reservoir (the static water level) is distinct from, and 150-200 m below, the perched near-surface water table (not shown). The temperature reversals show the asymmetry of the outflow plume, partially caused by cold water inflow from the east (PGM-2). The proposed Las Hornillas fault control on the upflow region is additional to the ELC (1988) position north of PGM-11. Downhole temperatures from ELC (1988).

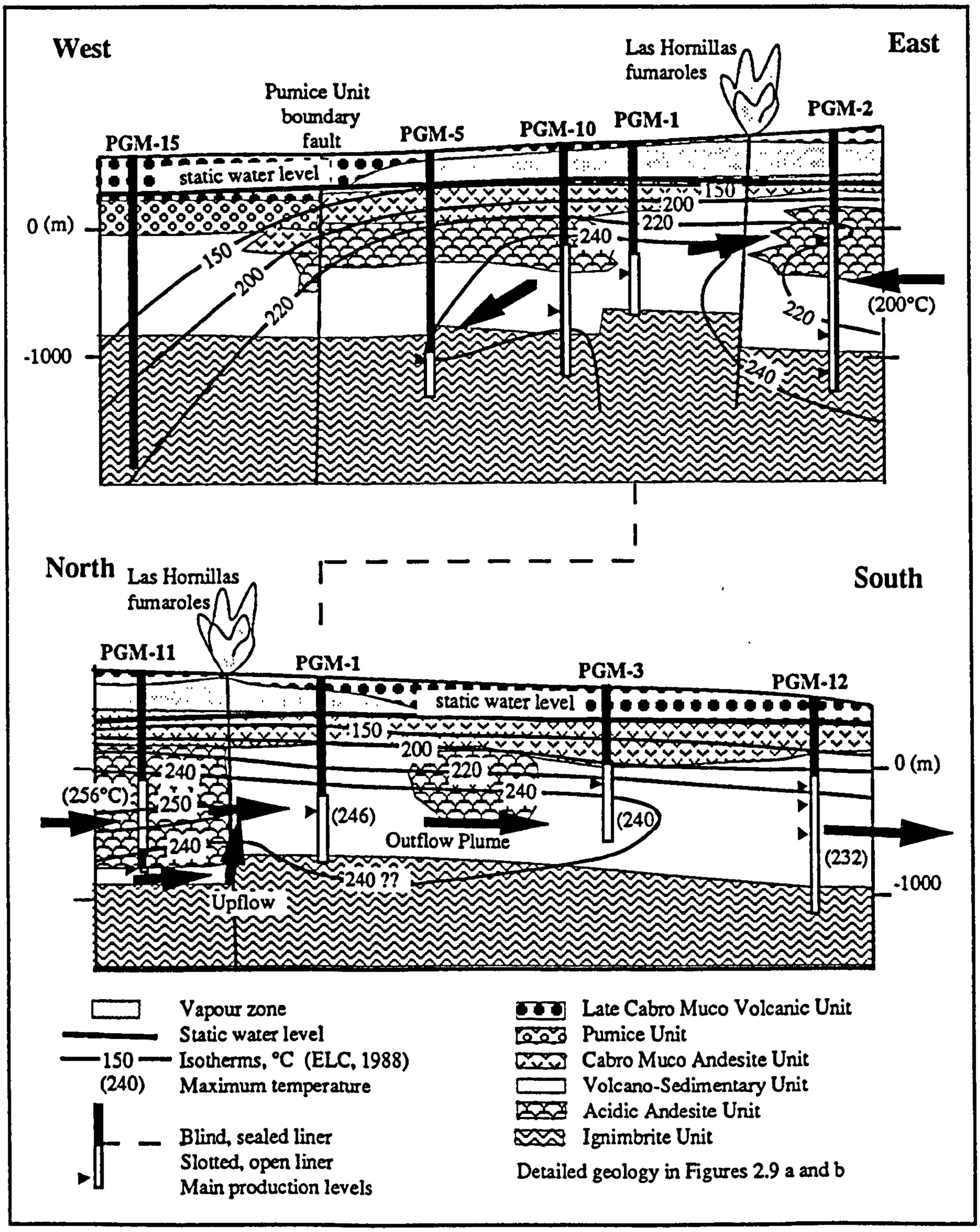

This places the upflow region to the north of PGM-11, with temperatures cooling to the south towards PGM-1. Pressure is very slightly higher at 200 m b.s.l. in PGM-1 and 11 than in PGM-10 and significantly higher than in all other wells (Figure 5.7, from ELC, 1988). The Las Hornillas fault (located in Figure 5.4) is the major structural control on the location of the northern shallow vapour zone and the surface manifestations (the La Fortuna graben controls the southern thermal anomalies), but is south of the supposed PGM-11 inflow. It is reasonable to assume that the Las Hornillas fault acts to increase the vertical permeability both within and below the drilled aquifer, and therefore controls the upflow region.

Figure 5.7 Thermal, hydrological and geochemical data pertinent to the location of the upwelling convective plume feeding the Miravalles system. All parameters except pressure indicate upflow south of PGM-11, in the PGM-10 area. See also Figure 5.4 for full temperature gradient map.

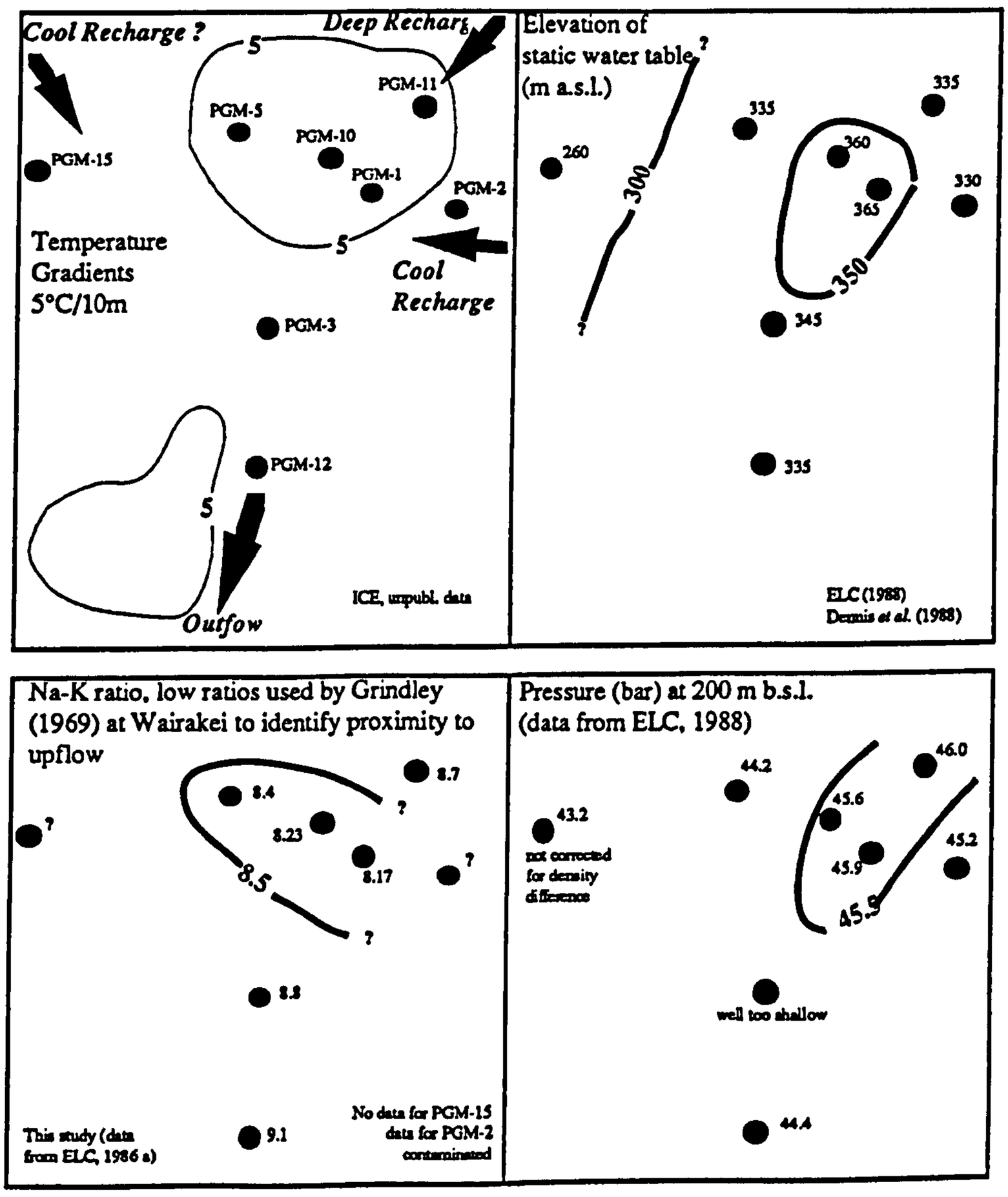

The well log data presented by ELC (1988) suggest that the top of the liquid-dominated reservoir (the static water level) domes up by 30-35 m in the PGM-1 and PGM-10 area compared with *all* the surrounding wells (Figure 5.7), which would be expected above a recharge area. The northern surface heat flow anomaly (Figures 5.4 and 5.7), related to the shallow vapour zone above the boiling zone is centred above PGM-10, not the supposed upflow region and highest liquid-dominated reservoir temperatures north of PGM-11. The vapour zone is best developed at PGM-10 where the 100°C isotherm intersects the surface (Figure 5.5).

Grindley (1969) showed at Wairakei that the Na-K ratios of the reservoir brines rose as minerals were deposited during cooling of the fluid and values were therefore least in the fluids closest to the hotter, upflow area. The ratios at Miravalles (data from ELC, 1986 a) have been plotted in Figure 5.7 and the pattern suggests that the production levels at PGM-1, 5 and 10 may be hydrologically closer to the upflow region than those at PGM-11. The distinction between the ratios is not, however as clear as in the Wairakei case. It is critical to understand where the production levels in the wells are in relation to the maximum measured temperatures before drawing conclusions from chemical data or thermal data as to the location of the recharge zone. The production levels in PGM-1, 5 and 10 coincide with the highest measured temperatures (ELC, 1988), i.e. the wells are tapping the core of the outflow plume (Figure 5.6). PGM-11 on the other hand produces sub-maximum temperature fluid from below the plume core (Figure 5.6), thus explaining the slightly higher Na/K ratios.

The temperature and pressure regime of the reservoir has been interpreted from logs run in static (shut-in) wells. It is well known, however that vertical fluid flow in the wells complicates the picture (e.g. Stefánsson and Steingrímsson, 1980). The most common problem in the slotted liner sections is downflow from cooler reservoirs to deeper reservoirs, resulting in isothermal profiles in deeper well logs. Dennis *et al.* (1988) suggest that the static temperature logs at Miravalles, particularily from the cased parts of the wells (indicated in Figures 5.5 and 5.6) could not be read at face value for this reason.

Temperature and pressure logs from both flowing wells and logs run soon after shut-in to monitor recovery can help resolve this problem.

Deep isothermal zones are present in the slotted liner sections in both PGM-1 and PGM-3, immediately below the productive zones. Fluid downflow may therefore explain the lack of a temperature reversal in PGM-3 that would be expected at this part of the outflow plume (the 240°C isotherm is the maximum downhole temperature) and a reversal of the 240°C isotherm is tentatively shown below PGM-3 in Figures 5.5 and 5.6. The flowing logs from these wells (ELC, 1988) show water entry at the production levels shown in Figure 5.6, at the maximum downhole temperatures, i.e. closest to the centre of the outflow plume. At PGM-5 the temperature increases steadily towards the production zone within the Ignimbrite Unit and the outflow plume signature is not present (downhole flow is impossible here, as only the base of the well liner is slotted, Figure 5.6). All the flowing pressure logs (logs run in producing conditions) show that production is from below the within-well boiling zone, within the liquid-dominated zone. Grigsby *et al.* (1988) found no indication of excess gas or enthalpy in the reservoir fluids and therefore no evidence for natural boiling within the reservoir. It is concluded therefore that most of the reservoir fluid, at production depths at least, is in the liquid phase.

To resolve the apparent paradox of maximum plume temperatures at PGM-11, but an upwelling area at PGM-10 it is necessary to propose a two-stage inflow model as shown in Figure 3.6: Firstly there is deep inflow to the system from the north or north-east of PGM-11, the plume temperature core located within the less permeable Acidic Andesite Unit. There is greater, though cooler fluid flow below this level, however, within the more permeable Volcano-Sedimentary Unit (the production level in PGM-11, Figure 3.6). This deeper, cooler fluid rises up the Las Hornillas fault, from below the PGM-11 levels, giving rise to the plume close to PGM-10. This secondary upflow scenario is compatible with the observation that the 256°C maximum temperature (T_{max}) observed at about 300 m b.s.l. in PGM-11 is nearly 200 m *below* the T_{max} of 246°C in PGM-10. In this model the general reservoir fluid is largely derived from the sub-T_{max} plume fluid with a possible additional component of the high temperature PGM-11 fluid, T_{max} = 256°C. The different amounts of

inflow are controlled by the permeability, which is dominated by the Las Hornillas fault in the PGM-10 area (Figure 5.4). The slight temperature reversal in PGM-10 indicates that this is not the exact upflow region but close to it. The reversals in PGM-2 are more complex and are discussed below in the context of recharge (Section 5.2.3).

5.2.2 The boiling and vapour zones; implications for drawdown

In trying to predict the effect of pressure drawdown the key parameter to define is the extent of the boiling zone at the top of the deep reservoir; i.e. how close the reservoir temperatures are to the boiling curve (illustrated in Figure 5.1). The boiling curve used in this study is for standard fresh water at sea level (from Haas, 1971). The effect of the 0.5 % salinity at Miravalles is negligible as only salinities above about 5% significantly increase the boiling temperature (Haas, 1971). The boiling zone at Miravalles is practically at sea level and significant quantities of excess gas which would shift the boiling curve (Fournier, 1987) are not thought to be present (ELC, 1988 and Grigsby *et al.*, 1988).

It is difficult, however, to use the logs from the cased, uppermost sections of the PGM wells to estimate the temperatures, pressures and phases present at the top of the liquid-dominated reservoir. The casing depths are shown in Figure 5.6. All the PGM pressure logs show atmospheric pressure from the wellhead to a static water-table, below which there is a hydrostatic gradient; the interface is found at between 200 and 400 m depth. For this reason, most of the wells do not produce spontaneously when opened. This cannot represent the true hydrological conditions in the reservoir, because it is known from PH-well data that the groundwater zone is reached at much shallower depths in the borefield (artesian to 50 m).

The problem is illustrated in Figure 5.8 by PGM-5, cased to 1520 m, where the static water table is at 270 m depth, whereas the nearby 270 m well PGM-5R is cased to only 160 m depth. PGM-5R was drilled to investigate the possibility of spent fluid reinjection into the shallow aquifer, but it produces dry steam from 220 m depth. The shut-in temperature profile for PGM-5, however, suggests temperatures of only 140°C at this depth. The PGM-5 temperatures from 270 m to 600 m suggest near steam-saturated conditions w.r.t. within-

well pressures, below which there is a near isothermal zone from 220°C to 240°C towards the production depth at 1520 m.

Figure 5.8 Shallow reservoirs at adjacent wells PGM-5 and 5R. The static water table in PGM-5 at 270 m, at atmospheric pressures, cannot reflect reservoir pressures as this is the location of a superheated steam reservoir in PGM-5 R at 20 bar (data from ELC 1984 a, b and 1988). The temperatures in PGM-5 are thought to be lower than reservoir temperatures, as PGM-5R produces dry steam at 220°C from 220 m depth. A vapour zone can exist at 20 bars pressure if the temperature exceeds 213°C. A pressure of 20 bar corresponds to ~210 m of groundwater at hydrostatic conditions, as shown. The groundwater depth (10 m) is from nearby shallow wells PH-18, 22 and 34 (ICE, unpubl. data).

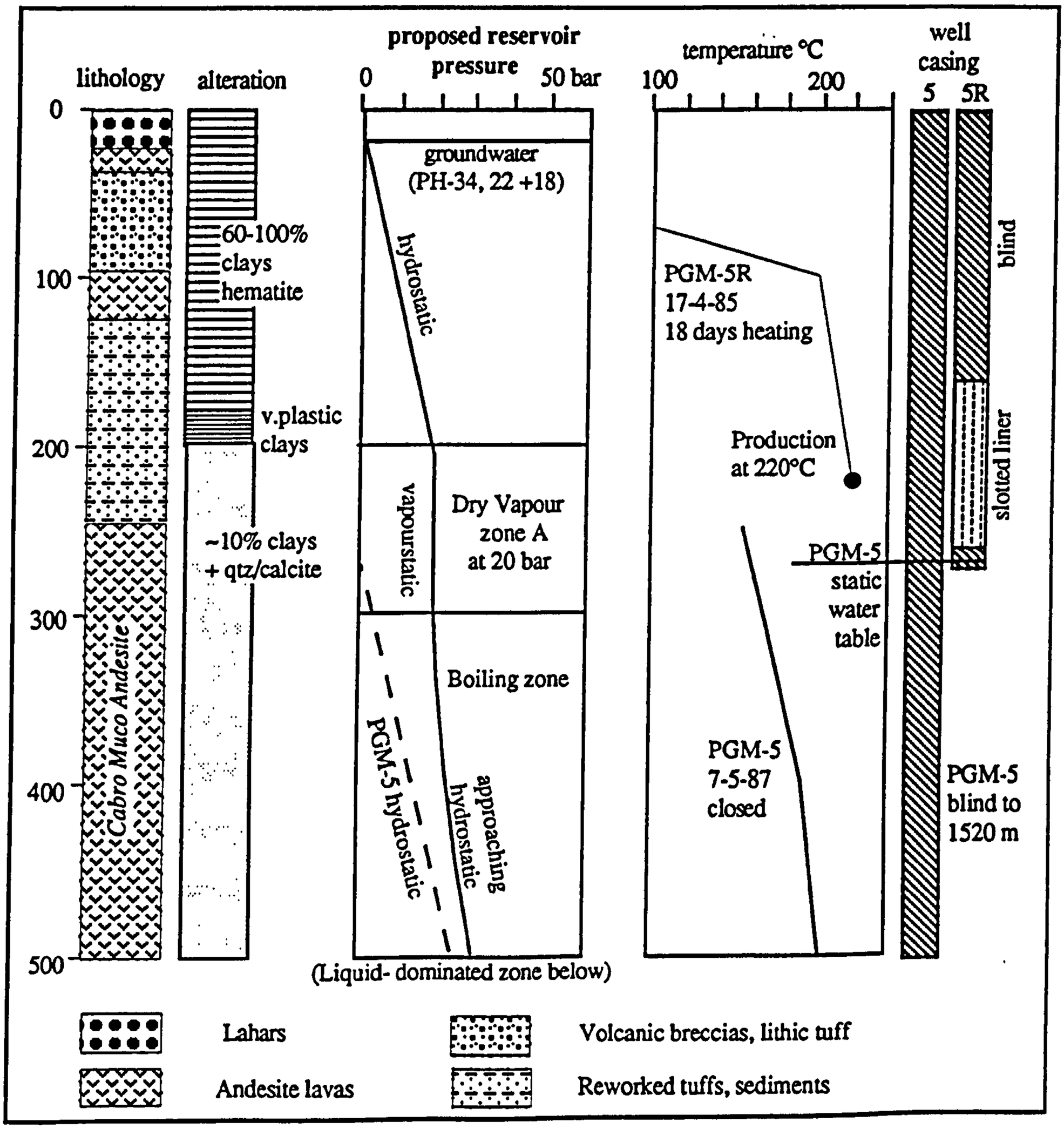

Static temperature and pressure logs for PGM-5R are not available, but ELC (1988) give the shallow vapour zone pressure as 20 Bar, and ELC (1985 b) suggest that temperatures of 220°C must be present at the dry steam production depth of 220 m, to explain the shallower temperature log (shown in Figure 5.8). Temperatures in excess of 213°C are also required

for vapour to exist as a separate state at 20 Bar. To maintain a pressure of 20 Bar at this depth in the reservoir it is either necessary to invoke either a 210 m head of groundwater at hydrostatic conditions (Figure 5.8) or a cap on the steam reservoir. In both PGM-5 and 5R, 60-100% argillic alteration from near the surface to 200 m depth and very plastic clay-hematite from 180-200 m in PGM-5R (ELC, 1985 b) provide a suitable seal above the vapour zone. It is therefore suggested here that a combination of groundwater hydrostatic pressure and argillic alteration are responsible for maintaining the vapour-zone pressures at PGM-5 and that this model is applicable to other areas where the vapour zone is present.

The implication for the logs from the cased sections of the PGM wells is that the PGM-well temperatures are lower than those in the reservoir. The pressure in the deeper slotted liner sections must be equivalent to the reservoir pressures, but reservoir pressures above these levels must depart from hydrostatic to maintain a pressure of 20 Bar in the vapour zone, at the same level as the within-well static water level (at atmospheric pressure). This is possible only if the top of the deep, saline reservoir is liquid-dominated, but at boiling conditions, with small amounts of steam in pores and fractures lowering the overall density, and therefore the pressure gradient (conditions shown in Figure 5.8 from 300 to 500 m depth). Therefore, while there may be no boiling at production depths, it is probable that there is boiling at static water levels within all the wells.

The vapour zone above the reservoir has been suggested by ELC (1986 a and 1988) to be limited to a few tens of metres thickness and restricted to the northern borefield in the area close to the Las Hornillas fault; wells PGM-2, 5, 10 and 11 only. Dennis *et al.* (1988) suggested, however, that a 100 m thick 100°C isothermal zone above the static water level in both PGM-3 and PGM-12 means that the vapour zone also exists in the south. The PGM-12 log of Dennis *et al.* (1988) shows that this vapour zone overlies a slight temperature drop at the top of the sub-boiling curve liquid reservoir (slotted liner log), and is therefore *not* derived from reservoir boiling in this area. The southern vapour zone may be derived from the more extensive vapour zone in the PGM-10 area where the steam is certainly derived from the boiling reservoir. Apart from this point the temperature logs presented by ELC

(1988), measured at various times from 1979 to 1987, are similar to the logs of Dennis *et al.* (1988), measured in late 1986.

The thickness of the perched water table (the groundwater zone in Figures 5.1 and 5.8) is not reported in the well logs (the PGM well casing is blind through the groundwater zone, the vapour zone and the boiling zone). The low-resistivity zone at this depth does not distinguish clays from groundwater but suggests that the groundwater zone could be up to 200 m thick (details in Chapter 3, Figures 3.13, 3.18 and 3.19); its effect cannot therefore be ignored in the estimates of the pressure in the deeper reservoir and vapour zone, where present. The Miravalles groundwater zone is further discussed below (Section 5.4) as natural changes in its thickness are shown to be important by the results of the microgravity studies (Section 5.3).

If the PGM logs reflected the reservoir conditions, it would be possible to subtract the boiling curve from the downhole temperature logs to derive the depth of the groundwater, vapour and the boiling zones and to locate the areas likely to suffer the greatest change in phase for a given pressure drawdown. Given the foregoing discussion, this is not strictly possible, but the extent of near steam saturation conditions in the wells is thought to at least discriminate parts of the reservoir with very different boiling zone thicknesses. The within-well departure of temperatures from boiling (two phase) conditions (ΔT) is shown in the computer-contoured borefield profiles (Figure 5.9, 10°C contours), which are directly comparable to the temperature profiles of Figure 5.6. The zero line (in white) defines the division between boiling conditions above (vapour zone) and saturated conditions below (liquid zone). The division is not sharp in the northern and central parts of the borefield where the temperature profiles are very close to the boiling curve (as reported for the static well logs by Bargar and Fournier, 1988) and ΔT is small over a significant depth below the static water level; the 10°C contours are thus spaced further apart than in the cooler regions, e.g. PGM-15 (Figure 5.9).

Although the ΔT curves may not strictly reflect the reservoir conditions, the broad implications are that a production-induced pressure drop in the borefield will place a greater part of the north-central liquid reservoir in undersaturated conditions, thus creating the

maximum vapour zone expansion in this part of the field and therefore the maximum accompanying gravity change. This result is not surprising, but is only the simplest scenario and the related question of recharge, its depth, asymmetrical distribution, temperature and possible cooling effects on the reservoir boiling curve need to be considered also. Prediction models for reservoir response to exploitation have been investigated by ICE and ELC (ELC, 1988) and are discussed below (Section 5.5).

Figure 5.9 (opposite) West-East and North-South profiles of the departure of the temperature, ΔT, from the boiling curve (derived from borehole data, ELC, 1988, orientation as for temperature profiles, Figure 5.6). Importantly, the data are from cased well static logs, and therefore do not necessarily match the reservoir conditions accurately.

5.2.3 Recharge and the PGM-2 acidity question

The proposed deep, hot inflow north of PGM-11 is not the only fluid entry into the geothermal system. The temperature reversal below sea level in PGM-2 (Figure 5.6) is proposed to result from cooler water entry from the east, over the outflow plume, driven by a natural hydraulic gradient from the highlands in the Bajo Los Chiqueros area (located in Figure 5.3). The composition and source area for the PGM-2 fluids has been the cause of much concern and debate. Initially PGM-2 was only drilled to a depth of 1300 m (Mainieri *et al.*, 1985) and encountered the neutral chloride fluids present in the other wells. At a later stage the well was deepened (PGM-2P) in anticipation of greater temperature and permeability at depth. The fluids recovered at the wellhead, however, both during drilling and after completion were of a very acid nature; pH of 2.8, highly elevated SO_4, Mg, Fe, significantly higher H_2S and K, but lower H_2CO_3 and Ca contents (ELC, 1986 a). As the well casing is blind through the naturally acidic shallow vapour zone, the fluid was believed to be derived from a deep, liquid-dominated acid reservoir. This obviously has serious implications for the production potential of this part of the field and ELC (1986 a and 1988) have therefore considered the PGM-2 site as a reinjection area. Milodowski *et al.*, (in prep.) believed the acidic waters were related to the unusually high levels of quartz vein formation and other extreme alteration in PGM-2P (including Cu, Ag and Au sulphides and tellurides, that have been deposited in other areas where there has been an influx of acidic water into a hydrothermal system). The present acid fluids are not in equilibrium with relict

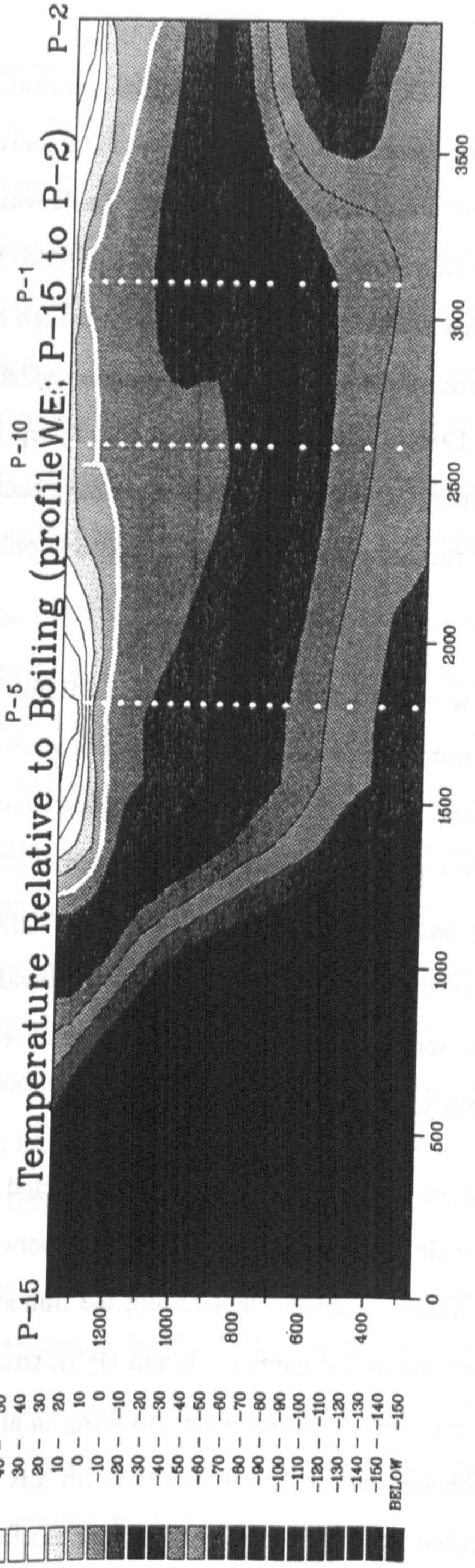
Temperature Relative to Boiling (profileWE; P-15 to P-2)
P-15
P-1
P-5
P-10
P-2
0
500
1000
1500
2000
2500
3000
3500
400
600
800
1000
1200
ABOVE
50
40
30
20
10
0
-10
-20
-30
-40
-50
-60
-70
-80
-90
-100
-110
-120
-130
-140
-150
BELOW

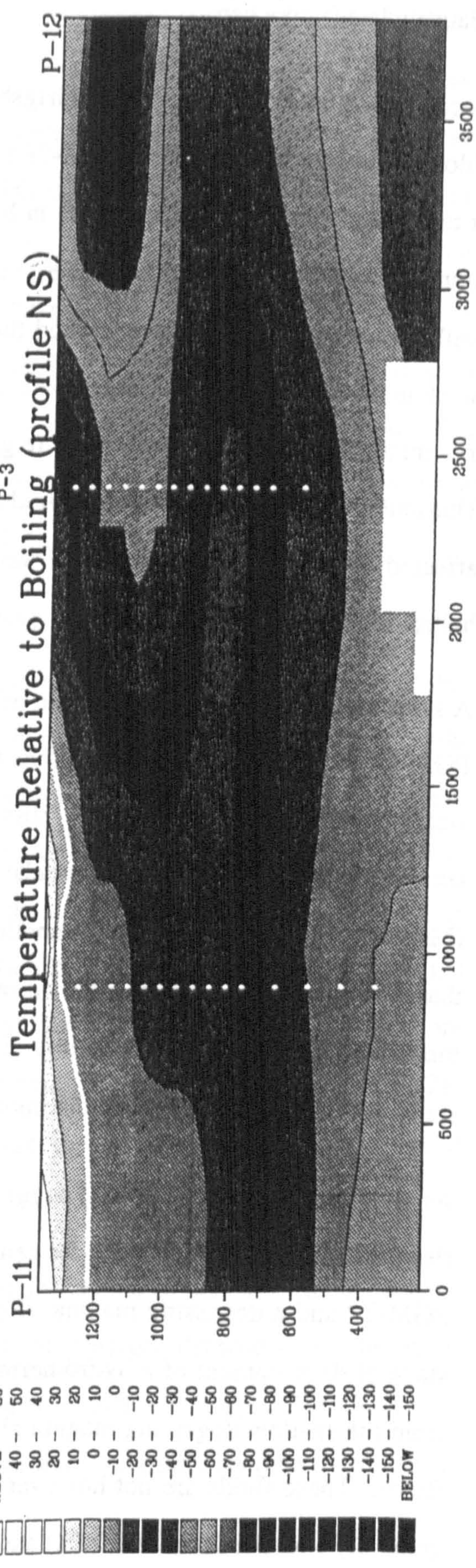
Temperature Relative to Boiling (profile NS)
P-11
P-1
P-3
P-12
0
500
1000
1500
2000
2500
3000
3500
400
600
800
1000
1200
ABOVE
50
40
30
20
10
0
-10
-20
-30
-40
-50
-60
-70
-80
-90
-100
-110
-120
-130
-140
-150
BELOW

mineralisation, however, in PGM-2P such as anhydrite, indicating that acidic fluids are a relatively late feature here.

Recent downhole fluid sampling (Grigsby *et al.*, 1988) suggests that normal, neutral, chloride fluids are present at the PGM-2P production depths indicated in Figure 5.6 (at least at the sample depth of 1825 m, 1087 m b.s.l.), and no evidence for the acidic fluids was found. Following Grigsby *et al.* (1988), the acidic fluids sampled previously at the PGM-2 wellhead were thought to have entered the well from the shallow vapour zone, through a break in the shallow casing. This avoids the need for the more complicated models needed to explain acidic but deep reservoirs (e.g. ELC, 1986 a and Milodowski *et al.*, in prep.). This author believes that the normal fluids sampled by Grigsby *et al.* (1988) may have been affected by the months of downhole freshwater fluid injection at PGM-2, that was only halted two weeks prior to sampling.

A satisfactory model has not yet been proposed to explain the presence of acidic fluids in PGM-2P at depths below 1400 m, fluids that are normally found only in the vapour zone or steam-heated waters (Henley and Ellis, 1983 and Figure 5.5). Previous workers have tentatively proposed alternative models: Drawdown of the surficial waters to these depths (Milodowski *et al.*, in prep. and Rochelle, 1991), but there is no further evidence to suggest that this is possible. Secondly, derivation of SO_4^{2-} from the oxidation of the pyrite found at these depths (ELC, 1986 a), but it is difficult to see how this is achieved without at least some 'starter' acid fluid to cause the initial instability of pyrite.

As an alternative, ELC (1986 a) suggested that the mixed fluids in PGM-2P reflected the rise of magmatic gases through the neutral chloride fluids, suggesting a local link between PGM-2P and a degassing magma. Fournier (1987) suggested that during the immature stage of development of a hydrothermal system the acidic gases (SO_2 and H_2S), straight from the shallow degassing magma chamber, mix with meteoric water resulting in acidic fluids. These fluids are not however in equilibrium with the reservoir rock (in this case generally andesite lavas and tuffs) and the leached Na and K serve to neutralise the fluids, eventually producing neutral chloride waters. These later fluids are the product of several cycles of rock-fluid interaction, the salinity increasing with each cycle (Figure 5.5).

It is possible then that the PGM-2P fluids are indeed a mixture of immature, near-magmatic acid fluids, and the mature, near neutral chloride fluids found in the rest of the field. This is believed to be more reasonable than to invoke downflow of the surficial steam condensate and furthermore, suggests that a degassing magma must be present (or has been very recently present) close to, but to the east of PGM-2. It is not known if the present distribution of fluids in PGM-2P is simply a consequence of the intersection of fractures carrying the acid fluids up from source, or if an extensive acidic reservoir exists at these depths. The latter is potentially more serious for the field development plans as production from nearby wells should draw in this reservoir. The fact that no increase in acidity has been reported from other wells during production or interference tests though, indicates that a natural barrier may presently exist between PGM-2P and the rest of the field.

The 225°C T_{max}, neutral fluid at 100 m b.s.l. in PGM-2 represents the eastern margin of the 246°C PGM-10 outflow plume, but outflow is restrained by the deeper inflow of the cooler, 200°C brines from the east (Figure 5.6). The deep temperature increase to 245°C, below the 200°C temperature reversal in PGM-2P, coincides with the acidic fluid production levels, further suggesting that the acidic fluids are at least partially derived from a degassing heat source, rather than mixing of downflowing but cooler surficial acidic waters. The PGM-2P flowing temperature log (ELC, 1988) shows that the intermediate depth, cooler zone is not tapped during production but both the outflow plume and the deeper 230°C fluid are (production levels shown in Figure 5.6). If a deep acidic reservoir *is* present in PGM-2P, and the fluid is not the result of shallow casing failure, then it may exist beneath the rest of the field but at depths below the boreholes.

How much recharge would come in from the western and central caldera area (most likely to be cooler as in PGM-15, Figure 5.6), as a result of pressure drawdown in the main borefield, is not certain. The present pressure gradients (Figure 5.7) suggest that this area is down-gradient from the northern and eastern recharge areas but might become significant if the pressure drawdown was sufficient.

In summary, the ΔT profiles (Figure 5.9) show that the result of homogeneous pressure drawdown in the borefield would be the expansion of the steam zone in the north-central production area. Total pressure drawdown and phase changes at the top of the liquid-dominated zone will be influenced, however, by both the efficiency of recharge and the response of the different recharge areas to mass withdrawl. Of particular concern is the long-term, post-drawdown efficiency of the barrier that presently prevents the PGM-2P acid fluids mixing with the deep neutral fluids in the other wells.

5.3 Pre-Production Gravity Changes at Miravalles

In order to detect possible gravity changes due to effects other than exploitation, a repeat gravity station network has been monitored since 1987. Low signal to noise ratios have meant that it is difficult to separate real changes from errors, but no significant changes of the magnitude of earlier changes reported by Alvarado and Arguenta (1988) over the PGM-11 area have been identified.

Gravity changes up to 2000 μGal were reported by Alvarado and Arguenta (1988) between four surveys in the area around PGM-11; October 1985 to January to April to May 1986 to March 1987 (changes from October 1985 to May 1986 shown in Figure 5.10). Gravity was measured with a Worden gravimeter, which is somewhat less precise than a LaCoste and Romberg meter, but the apparent changes were still greater than the instrument precision of about 100 μGal. The contoured changes show large variations in both magnitude and direction between closely spaced stations (e.g. between 354 and 355, Figure 5.10) which implies either shallow (anomaly half-width of 300 m) but large density changes within the groundwater or vapour zones, or simply random variation (i.e. the changes are not real).

Simple calculations for an infinite horizontal slab show that a gravity anomaly of 1000 μGal requires the following extreme mass distribution changes: fluctuations of the perched water table require 76 m change assuming 30% porosity and a change from air to water-saturated conditions. A vapour zone saturation change of 0.23 Mg m^{-3} over the whole vapour zone from near the surface to 400 m depth, again assuming a porosity of 30%, would produce a similar gravity change. These height and density changes are minima as the horizontal slab

model calculations produce gravity change maxima, furthermore a porosity of 30 % is also thought to be a maximum value. There is no evidence to suggest that the groundwater table could vary over such short distances by such large amounts, nor is the maximum density of the vapour zone believed to be as high as 0.23 Mg m^{-3}. This suggests that the gravity changes were not genuine and were most likely due to instrumental effects or operator error.

Figure 5.10 Apparent gravity changes observed by ICE (Alvarado and Arguenta, 1988) in the Las Hornillas - PGM-11 area. The anomaly magnitudes are much larger and the wavelengths much shorter than values that are possible for reasonable mass changes in the reservoir, and must be erroneous.

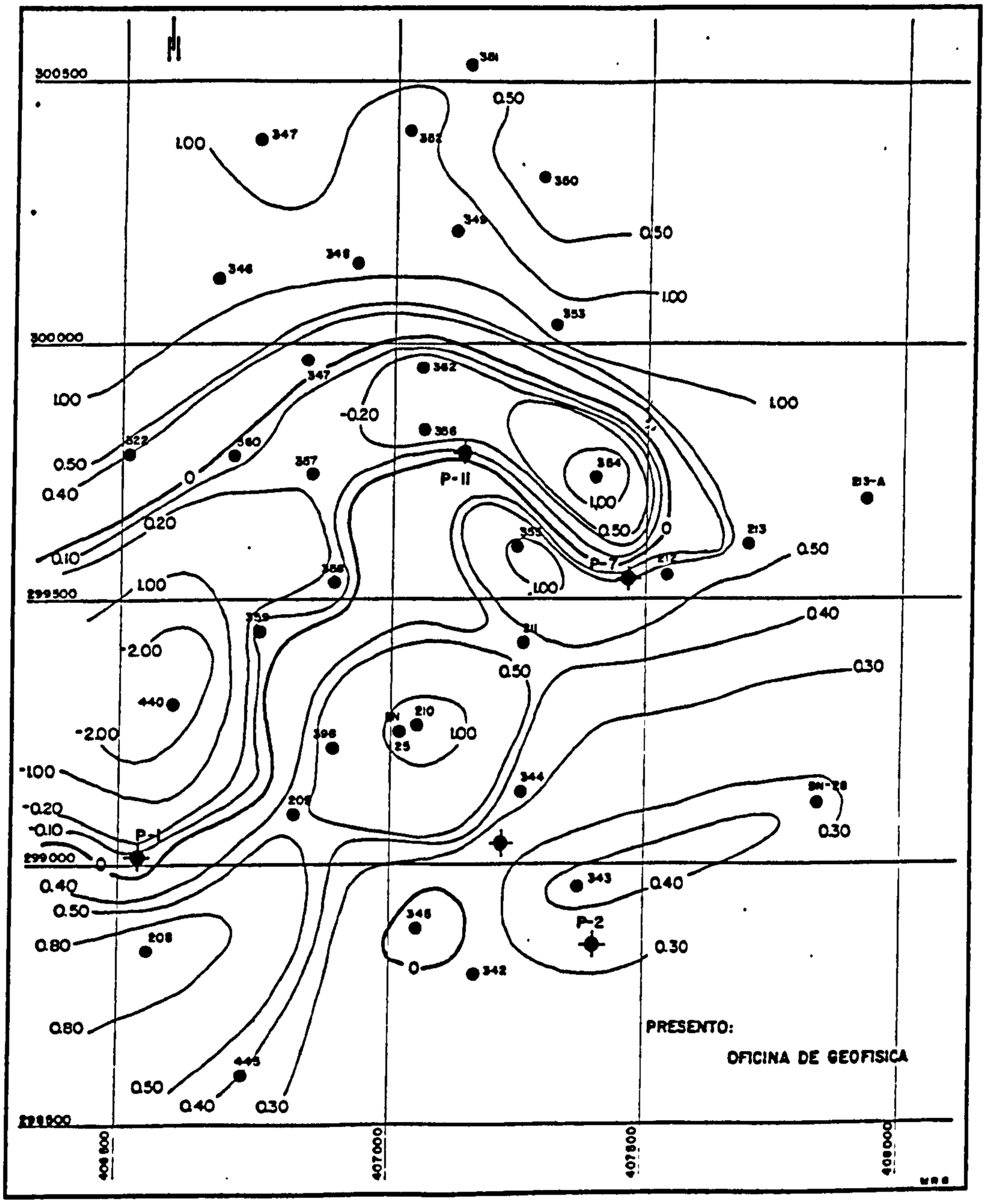

5.3.1 Technique and errors

Gravity data of this study are presented as station values relative to the microgravity base station at the ICE administration site in Guayabo, which is well outside the proposed limits

of the exploitable geothermal field (station location map in Figure 5.3, northern borefield stations in Figure 5.11). Many of the stations are part of the ICE network of Bouguer gravity stations but some are unique to this study. The actual station sites vary from roadside pavements to wellhead foundations to purpose-built concrete benchmarks. Repeat levelling data are available for most but not all the surveys and the limited data do not suggest significant elevation changes during the study period. No elevation corrections have therefore had to be incorporated into the data reduction and analysis. Individual gravity surveys were completed in one or two days, so short-period (weekly and monthly) changes could be assessed.

Stations: In addition to the PGM-11 area a network of stations was set up both within and outside the borefield (Figure 5.3). All the stations in the PGM-11 area (located in Figure 5.11), apart from the wellhead stations, are ICE stations that consist of a small concrete pad that could be relocated in future surveys though more robust stations are recommended for future work (Section 5.5). The borehole stations are located on the level concrete surround of the wellhead foundations, above the steps leading down to the top of the well casing. The base station is located on the first step of 'El Bunker', the ICE directors' accommodation quarters at Guayabo (Figure 5.3), and should be secure for the foreseeable future. This is located close to, but is distinct from the station used as the Bouguer (static) gravity reference point, Gra-91 (located in Figure 5.3); the absolute gravity value at Gra-91 is 0.31 mGal higher than at the ICE base. The extra-borefield stations shown in Figure 5.3 are either benchmarks (BN-), or temporary stations set up during this project close to ICE gravity stations (e.g. station 24 is close to Gra-24).

Elevation changes: Elevation induced gravity changes should follow the Bouguer corrected free-air gradient of about -200 μGal m^{-1} (depending on the choice of reduction density), assuming no density changes below the station. Exploitation induced elevation changes at other fields are very significant (up to 450 mm yr^{-1} subsidence at Wairakei; Allis and Hunt, 1986, shown in Figure 5.1), but inflation and deflation due to resurgence in non-erupting volcanic environments may also be important (e.g. Long Valley; Rundle and Hill, 1988 and Yellowstone; Smith *et al.*, 1989). Repeat levelling surveys in 1984, 1985 and

1986 (Alvarado and Arguenta, 1988) over the floor of the Guayabo caldera and the geothermal area showed no detectable elevation changes (significance level quoted as 7 mm). Repeat levelling conducted during this study in 1987 and 1988 of the stations in the PGM-11 area has also failed to show significant changes between surveys (Table 5.1). Levelling was carried out with a Nikon DTM-1 electronic distance measurement theodolite (Appendix 3B). During a survey the theodolite was placed on a hill, Cerro Los Caballos (500 m south-west of PGM-2), to minimise the errors induced by changing the set-up position. Although most of the stations could be levelled from this position, the hill was some 1500 m from the most northern stations (e.g. 347) and exposed to wind. The successive readings in Table 5.1 fail to show any regular pattern and the apparent changes up to 0.14 m are therefore thought to be related to poor field conditions. Elevation changes due to natural tectonic or magmatic activity in the Miravalles area cannot be entirely ruled out for the period since these surveys, but significant elevation changes have been assumed unlikely in the light of the stability implied by the preceding levelling results.

Table 5.1 The 1987-1988 elevation changes (m) for stations in the northern borefield (locations in Figure 5.11). All stations were tied to 362, except *stations which were levelled relative to Mini-6. Changes are relative to the 1987 value (except*). The changes are not thought to be significant as uncertainty errors are high due to the poor field conditions (see text).

Station	Jan 1987	17-Mar-88	22-Mar-88	24-Mar-88
362	*715.02*	-	-	-
209	703.96	-0.06		-0.07
322	691.00	-0.05		
346	719.73	-0.04		
347	696.74	-0.14		
348	705.53	0.12		
349	737.41	0.08		-0.09
353	719.50	0.04		-0.04
354	738.83		-0.04	
355	726.41	0.15	-0.11	-0.02
502-D	719.44	0.09	-0.07	-0.03
357	710.83	0.06		
359	700.39		0.06	
361	711.43	0.06		
394-B	719.17	0.03	-0.03	-0.07
PGM-11	718.50	0.01	0.03	-0.04
427*		-0.17	0.01	
PGM-1*		-2.50	0.04	
PGM-10*		-16.47	0.03	

Errors: Interpretation of gravity changes depends critically on an understanding of the significance of *individual* changes; that is changes in the relative gravity between the field station and the base station at Guayabo. All gravity readings were corrected for Earth tides

using the tide prediction program of Brouke *et al.* (1972), and an ellipticity correction factor of 1.16. The error in a relative gravity measurement is a combination of the error at the base and the error at the field station and it is therefore not possible to gauge the repeatability of a relative gravity measurement from the repeatability at the base station only. The different errors likely to be incurred during the microgravity surveys of this study broadly follow those assessed by Rymer (1989); external effects (mostly noise), operator errors (instrument levelling, measurement procedure etc.) and instrumental errors (mechanical tares, thermal perturbation and calibration changes). Rymer (1989) suggested that a single reading has a worst case and best case error of 23 and 7 μGal at the 66 % confidence level respectively, but increased noise has sometimes been encountered during the field surveys at Miravalles, resulting in larger total errors. The worst case error on a single difference measurement is therefore 33 μGal and on a *change in value* between two single difference measurements; 47 μGal, both at the 66 % confidence level.

Tares: During a survey day, cross-looping between field stations and repeat readings at the Guayabo base were employed to check for mechanical tares. Tare values up to a few thousand μGal have been detected and can be shown to occur between readings at successive stations. The number of tares seldom exceeds one per day and their effect on calculated differences within one survey day can therefore be removed. The tares are random (Table 5.2, temporal changes in the read value at the base are shown in the bottom row) and distinct from the daily drift that is invoked by some workers to account for what may be better described as tares. It is difficult, however, to distinguish the smaller tares from the errors of poor repeatability during a survey. Observations by Baker (1984) of drift for LaCoste and Romberg tidal gravimeters, that operate on an identical principle to the survey L & R gravimeters, show that real drift is only of the order of 4 μGal per day. Daily drift is not therefore believed to be significant, compared with the much greater effect of mechanical tares, for the G-meter employed during this study, G-105.

Of all the errors discussed by Rymer (1989) the most significant at Miravalles is noise. Field conditions are persistently very windy during the dry season (the measured velocity at La Fortuna is >60 km hr^{-1} average on many days; ELC, 1988), severe enough to prevent

useful measurements in exposed areas. Stations located near trees, fenceposts, telegraph poles or similar structures are most severely affected by the wind as a result of the increased ground noise, but the meter stability itself is also affected by buffeting of the wind. For this reason many of the 1987 and 1988 stations (also used by the ICE 1985 and 1986 surveys, Figures 5.3 and 5.10) were abandoned in the 1989 surveys, which concentrated on a smaller group of protected stations that could be reoccupied in all but the most extreme weather conditions. Repeat readings at the station can resolve some of the noise error but as the noise level largely dictates the accuracy (and therefore the significance) of a reading this means that an absolute, but generally applicable significance level is not possible to determine for a *whole* survey. Noise levels apart, the significance levels of Rymer (1989) have been adopted and the additional individual error values due to noise are discussed in the analyses of the data below.

5.3.2 The 1987 and 1988 microgravity data

A similar set of stations to those occupied by ICE in the PGM-11 area were occupied in March 1987 by members of the Open University using LaCoste and Romberg gravimeters and have been re-occupied in 1988 and 1989 during this study. The PGM-11 area data are presented in Table 5.2 and the station locations and apparent changes are shown in Figure 5.11 a. In addition, repeat readings were made at stations both at other sites in the borefield and outside the borefield (stations listed in Table 5.3 and located in Figure 5.3). The area around the Las Hornillas fumaroles and mudpools was also monitored in 1988 (located in Figure 5.11 b, together with the coincident stations shown in Figure 5.11 a), but many of the stations were destroyed by the migration of the mudpots and creation of new ones before the 1989 season. Variable weather conditions prevented reoccupation of exactly the same number of stations in each survey, hence the gaps in the data. No changes of the magnitude reported by Alvarado and Arguenta (1988) from 1985 to 1986 have been found (Brown *et al.*, 1988, Rymer *et al.*, 1988 and Hallinan *et al.*, 1988 and 1989), but apparent changes have been observed that are above the standard error of 47 μGal.

Variations between the five surveys in 1988 (Tables 5.2 and 5.3) are generally within the error levels and often change sign between data pairs. Changes at station 346 (Table 5.2)

for example, show an increase of 63 μGal between 11 and 18 February but a subsequent decrease of 50 μGal between 18 February and 3 March, suggesting that the 18 February value is inconsistent and false.

Table 5.2 Tide corrected repeat gravity changes from 1987 to 1989 (μGal), shown in Figure 5.11. The 1988 mean value (most readings are from 1988, final 6 columns) is gravity relative to the base at ICE. The repeatability at the base on each survey day in 1988 is shown in the final rows. The tares row is the difference between the readings of observed gravity at the base on successive survey days.

Station	1988 mean	std. dev.	'87-'88	'88-'89	17/1-2/2	2/2-11/2	11/2-18/2	18/2-3/3	3/3-5/4	17/1-5/4
PGM-11	-28901	15	34	37	38	-6	-10			30
11 hut	-28863	30							43	
352	-29063	23	42					32	4	-20
353	-28999	19	-22		-11					
362	-28513	17	6				-26	-14		
502-D	-29465	11			15	-2	-20			-9
322	-25170	10						-7	10	-14
360	-26858	14	29					16	-3	-20
357	-28269	13	16		-1	-33	11	9	2	-12
355	-30212	17	2				-15	26	-25	-39
348	-27157	23	18		-39	13	-37			-37
347	-26148	11	-17		16	-15	-7	-2	-7	-15
346	-31343	21	-4		-5	24	-63	50	-15	-9
361	-28234	20	-44		25	-63	34	6	-3	-1
349	-33644	7	-14				-7	2	8	19
350	-36231	15			-23			26	-6	-22
358	-26136	8								
358a	-25823	9		8		-4	-1	-13	26	
359	-26606	11								
354	-32634	26	16							
354-A	-31555	10					-6	18	-24	
209	-26966	38	-73				65	18	-8	
H1	-25013	13				15	-11	-20		
H2	-29097	11				1	-2	23		
H3	-28477	15		-11		-14	0	-6	-21	-41
H4	-26710	9		22		4	6	10		
H5	-25365	10				-18	2	17		
H6	-26497	23				-16	-3	-21	-18	-58
H7	-28165	15				7	9	20	-33	3
H8	-28139	12				-10	25	-12	-20	-17
H10	-27050	16		10		-18	10	-33	15	-26
H11	-26466	4				0	5	0	-8	-3
H12	-27418	8				7	13	-14		
H13	-29830	11						15		
L1	-31680	19				1	-35	-7	29	-12
L2	-33328	24				60	-30	-1	28	57
L3	-31551	11				-12	-9	-9	13	-17
L4	-31553	13						-23	0	-21
L5	-30574	17				-25	-6	-9		
BN14	-13777		3							
PGM-1	-20149	1		16				2	-1	
PGM-2	-31848	25		3	14			-3	16	-26
PGM-10	-17810	15		-3	6			4	34	27
		av.	0	10	3	-5	-4	3	1	-11
		s.d.	30	15	22	23	24	18	20	25
Base tares					-339	-25	-144	767	930	1189
No. rd'ngs					4	6	2	3	4	5
Std. dev.					5	4	8	16	13	4

Data from stations around 346 fail to support the changes observed there and this is possibly the strongest argument against treating the Gra-346 change as significant. This station is in fact not stable in windy conditions and the apparently steady reading attained in the wind on that day may have been spurious. Possibly significant changes seem to have occurred at the H6 station southwest of the main Las Hornillas area (Figure 3.11 b). Consecutive changes at station H6 are negative, but the data from station H4, only 30 m to the southeast do not show similar changes. Similar arguments may be applied to the other apparently significant data, so that the effective error for the 1987-1988 data for some stations around PGM-11 is higher than 47 μGal.

Figure 5.11 a Repeat gravity data for the 1987-1988 PGM-11 stations, some of which were reoccupied in 1989. The changes vary inconsistently both spatially and temporally due to a low signal to noise ratio. A full discussion in text, data in Table 5.2. The Las Hornillas station locations are shown in Figure 5.11 b.

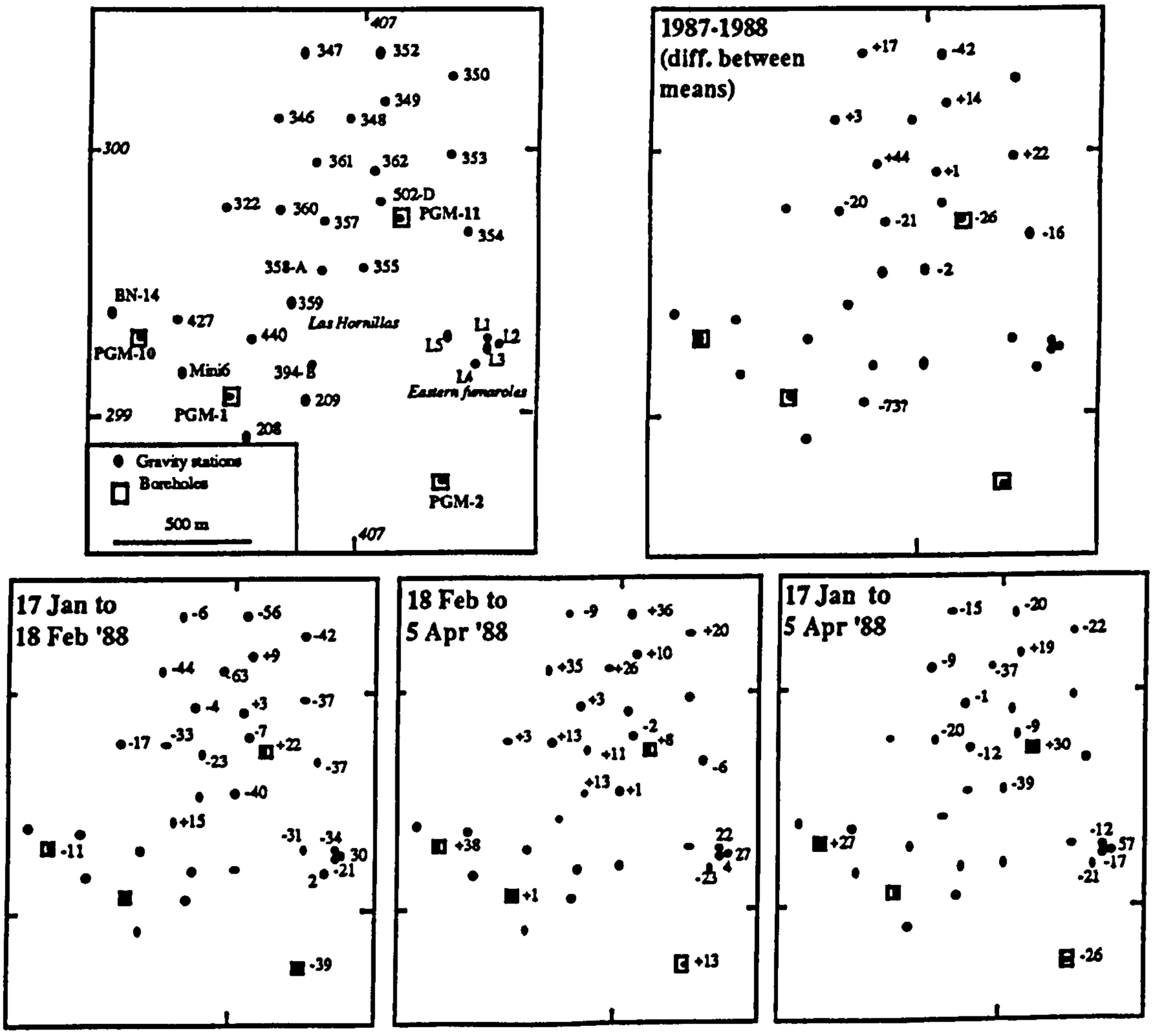

The repeat readings at the base are generally more accurate than those in the field, as the station is sheltered. The low standard deviations of the total number of readings at the base

within each survey day (Table 5.2, final rows) indicates that the repeatability at the base is good (better than the worst case 23 μGal significance level for a single reading). The lower errors in the base station readings, relative to those for the field stations, would not cause major discrepancies in relative base-to-field values, and furthermore cannot be responsible for the variation within the PGM-11 area.

The spatial and temporal inconsistencies of the 1987-1988 changes are difficult to explain in terms of reasonable density changes. The short wavelength form of the apparent changes (especially in the PGM-11 area) requires density changes in the groundwater zone (-13 μGal m^{-1} decrease in water table level assuming 30 % porosity and a density change from 100% saturation to total dryout) or saturation changes in the vapour zone below. During the 1988 survey season there was little rainfall from February to April and as there was therefore no suspected change in the recharge to the groundwater zone, it is unlikely that the fluctuating increases and decreases in the gravity data could be explained in these terms.

Table 5.3 Repeat gravity (μGal) for the general caldera stations (located in Figure 5.3). P stations are at the PGM deep borehole sites. The standard change in a difference error of 47 μGal applies (at the 66 % confidence level).

Station	1988 mean	std. dev.	'87-'88	'88-'89	'87-'89	17/1 -2/2	2/2-11/2	11/2 -3/3	18/2 -3/3	3/3-5/4	2/2-5/4	17/1 -5/4
24	-10974	27	-41	3	-38	-30			39	-22	-24	-54
29	-13087	23	-10	13	3	40			24	-45	-56	-16
BN18	-8622	28	7	5	12				8	-42	-68	
BN16	-8516	16	-15	-10	-25	31			22			
69	-7945	13					-27	28		-14	-13	
BN6	-3197	19	27	12	39	32	-29	40		-36	-25	7
BN10	-7002	17	45	16	60		-14	-25		30	-9	
P 5	-7128	39		-25					-32	94	59	
P 9	-15387	18					-25	-20		21	-24	
219	-8791	7					-15	6		-6	-15	
221	-4914	10		-6				12		-19		
BN11	-8425	39	-57	1	-56	40	6	-46		-52	-92	-52
BN13					37							
177	-18992	22	0				-16	-33		10	-39	
BN12	-8532	16		8			-30	0		-6	-36	
P 3	-6517	8	-51	-3	-53				19	-11		-3
410	-2136	2							4	-2		
183	6691	20		29			-38	-8		15	-31	
P 12	12681	16		13					-27	-8		-26
186	17317	23		5			-41	-12		26	-27	
P 4	28792	14		-10		-3	8	-36		18	-10	-13
149	29806	26		2			0	-50		12	-38	
153	25882	21		-12			-19	-32		27	-24	
156	24609	10		-10			-18	-5		6	-17	
159	24185	5		-20			-1	2		8	9	
Average			-11	1	-2	18	-17	-11	7	0	-25	-22
Std. dev.			35	13	43	29	15	26	25	31	31	23

The overall gravity changes of the difference between the borefield and the base station at Guayabo can be gauged by the average base to borefield station difference (base of Table 5.2), but as these values are small, the apparent changes between the borefield and Guayabo are not thought to be significant.

Figure 5.11 b Microgravity changes in the Las Hornillas fumarole area southwest of PGM-11, some stations located in Figure 5.11 a (values relative to Guayabo, data in Table 5.2). Some successive changes are consistent and possibly significant changes (e.g. H3, H6 and H11), but nearby stations do not always show similar trends, suggesting that the changes are false.

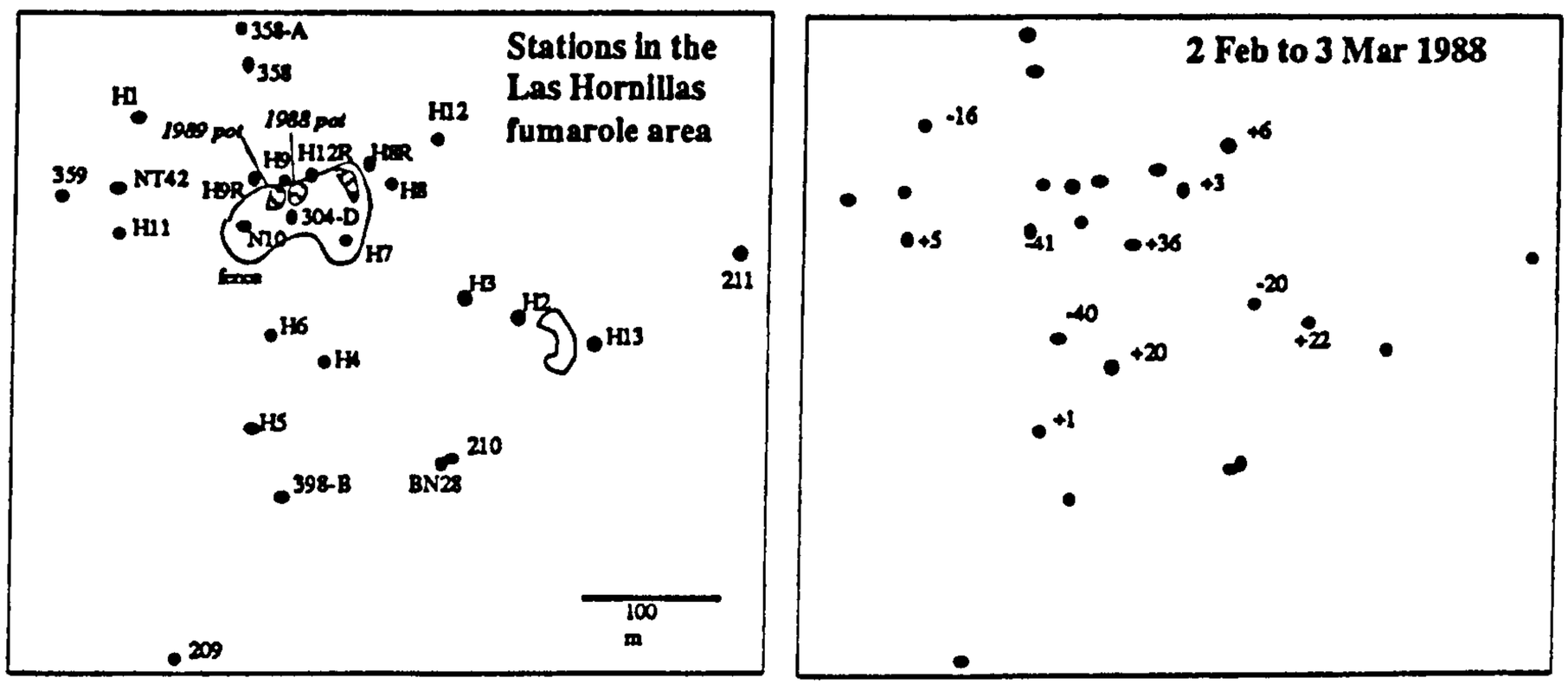

In summary, it is suggested that no significant gravity changes (> 47 μGal standard error for a gravity difference) were observed from 1987 to 1988, or during the 1988 season. There may have been real, minor gravity changes, however, but the low signal to noise ratio (largely due to the wind in the field) has meant that they are not possible to identify. The results of the 1988 well tests (Brown *et al.*, 1988 and Rymer *et al.*, 1989) are discussed below (Section 5.4.1).

5.3.3 The 1989 microgravity data

The unstable 1987-1988 stations were largely abandoned for the 1989 (April to July) monitoring season. During this season the primary objective was to monitor possible mass changes during a reinjection test; the discharge from PGM-11 was injected into PGM-2 via a steam separator (well test data first described by Hallinan *et al.*, 1989, and described below in Section 5.4.2). As a result, temporary stations were set up in the area of PGM-2 and 11 (locations in Figure 5.12) but were networked with the borehole stations occupied in 1987 and 1988 so that the borefield area data sets are comparable. To reduce wind errors from those experienced in previous years (described above) the borehole stations were relocated to below ground level, on the 4th step down into the wellhead pit. The simple change in station position has been corrected for to compare the 1989 data with pre-1989 data by directly measuring the difference between the station positions at each wellhead. As the reinjection test was delayed until July (the end of the season) a comprehensive pre-production data set exists over an extensive period for 1989 (Table 5.4).

The repeatability at the stations is better than for the 1987 and 1988 data set, and the significance levels of any changes are lower. As a result of the higher signal to noise ratio it is suggested that significant non-production related changes can be discerned in the PGM-11 area for the 1989 period. The tare corrected repeatability at the base in 1989, defined here as the standard deviation of the mean of the readings during one survey day (bottom row of Table 5.4), is below 10 μGal on all but two of the days. The repeatability at PGM-11 (the most often measured station in the borefield in 1989) is also below 10 μGal. A change in the relative gravity between the base and PGM-11 greater than 14 μGal is therefore

significant at the 66 % confidence level. It is tentatively proposed that values at other equally stable stations in the field have similar errors if more than one reading has been made during one day. For stations at which only one reading has been made during a survey, the standard error of 33 μGal is used.

Figure 5.12 Map of the 1989 reinjection test gravity stations in the PGM-2 and PGM-11 area.

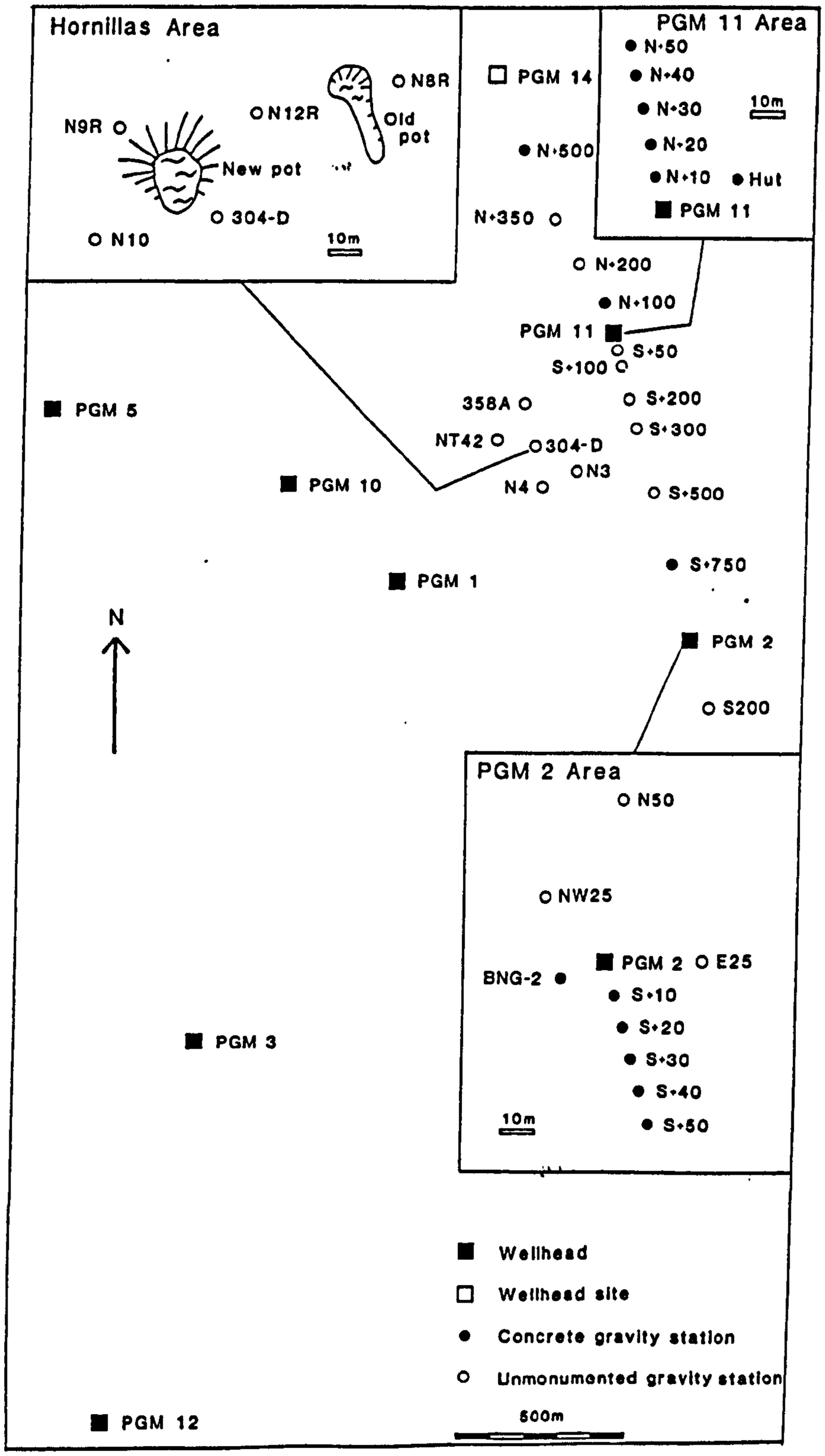

Table 5.4 The 1989 gravity variation data in the PGM-11 and PGM-2 areas.
The number of readings (x), the standard deviation (at PGM-11 and base only) and the change from the previous value (in bold) are shown.

STATION	1988	'88 to	1989			5	6	30	1	2	10	11	16	17	18	23	30	13	5	10	11
(day)	n, sd	'89	mean	n	s.d.	Apr	Apr	Apr	May	May	May	May	May	May	May	May	May	Jun	Jul	Jul	Jul
Base 1			-14262	7	18							(2)-	16 (2)- 0			-7		43 (2)-	-19	(2)- 6 (2)-	
PGM 11, S4			-28664	13	15	(5) 10 4	(4) 5 14	(5) 8 -8	(2) 5 -11	(5) 9 -16	(7) 6 2	(5) 6	-5 (7) 12	open	-5 (2) 13	14	(2) 1 -5	(2) 12 27	(9) 8	(3) 6 -14	(3) 7 4 (2) 10
PGM 11, top	(6) 14	35	-28864						(2)-												[P-2 and 11 open]
N+10			-28881	5	24		(2)-						-34 4	(2)-	-16	20	(2)-	37 (2)-	-10	(2)-	
N+20			-28899	6	15		(2)-				-25		-12 0		3	9	(2)-	25 (2)-	0	(2)-	
N+30			-28949	4	18		(2)-						-33 -5	(3)-		16	(2)-	27 (2)-	-20	(2)-	
N+40			-29006	5	25		(2)-						-43 4		3	-3	(2)-	49 (2)-	-21	(2)-	
N+50			-29065	8	16		(2)-			-32	-2		0 2	(4)-	6	-12	(2)- 27	12 (2)-	-6	(2)- -7	(2)-
N+100			-28471	6	13		-13				11		-9			-10	(2)-	42 (2)-			
N+200			-27979	4	11		-15				-12		17						24	(2)-	
N+350			-27311	4	5		-2				-3		-7						32	(2)-	
N+500			-26620	4	11		-8				-9		-5						23	(2)-	
PGM 14 ,S4			-27530	4	10			(2)-		-20	8		15						-19	(2)-	
PGM 11, Hut	(3) 30	32	-28830	4	16				11		-37		13						36		
S+50 (P.11)			-29252	4	10				8		0		16							6	(2)-
S+100			-29344	3	11				9				16							-3	(2)-
S+200			-29770	3	17				32				-4							12	(2)-
S+300			-29188	2	1								2							8	(2)-
S+500			-30134	3	11				10				-22								
S+750			-30000	4	8					-7	-1		-11						20	(2)-	
PGM 2, S4			-31613	6	6			(3)-	-2	-10 (2)-	-5 (3)-	6 (3)-	0 (3)-						1	(3)-	
PGM 2, top	(6) 24	3	-31845	3	19	(2)-			11 (3)-												
S+10			-31800	2	17			(2)-					-24						31	(2)-	
S+20			-31779	3	7			(2)-			-14		4						5	(2)-	
S+30			-31769	2	15			(2)-					-22						7	(2)-	
S+40			-31801	2	24			(2)-					-34						21	(2)-	
S+50			-31824	4	14			(2)-		-31	12		-9						16	(2)-	
P.2 E25			-31727	4	3				-5		-1		1								
P.2 N50			-32201	4	10				-18		4		17								
P.2 NW25			-31950	4	6				3		-7		15								
BNG-2			-31904	4	9				-6		-15		12								
P.2 S200			-31983	2	6						8										
PGM 1	(5) 1	16	-20133	2	1										1 (2)-						
PGM 3	(4) 8	-3	-6519	2	6												8				
PGM 5	(3) 19	-7	-7153																		
PGM 10	(6) 15	-3	-17813	2	13										18 (2)-						
PGM 12	(5) 16	13	12694	3	18								-34				28				
N3	(4) 8	-20	-28491	2	10														(2)-	-14 (2)-	
N4	(4) 9	21	-26688	2	7															-10	
N8R			-27868	2	1															-1 (2)-	
N9R			-27413	2	17															-28 (2)-	
N10	(5) 16	9	-27040	2	12															17 (2)-	
N12R			-27542	2	7														(2)-	-10	
NT42			-27911	2	14															20 (2)-	
358A	(5) 9	8	-25815	2	0															0	
304-D			-28154	2	8															-11 (2)-	
ICE BASE	1665	-52	1612	mGal		(3) 4 -49	(3) 3 6199	(3) 2 -2	(2) 6 -16	(3) 6 -	(4) 7 -7	(2) 10 -1	(3) 13 -6	(5) 4	-12 (2) 8	-205	(3) 27 -159	(3) 6 -348	(2) 6 -133	(2) 13 -2	(2) 5 1	(3) 9

As discussed earlier, changes of any value become increasingly significant when both temporal and spatial trends can be recognised. The cumulative temporal changes at PGM-11 are shown graphically in Figures 5.13 a and b (filled squares, solid line) together with average changes for the stations close to PGM-11 in the line N+10 to N+100 and the average of all the stations close to PGM-2 from PGM-2 to BNG-2 (all very stable stations, locations in Figure 5.12, data in Table 5.4).

Figure 5.13 a 1989 cumulative temporal gravity variations in the PGM-11, PGM-2 and Base 1 areas (locations in Figure 5.7). PGM-11 and the nearby stations (N+10 to N+100 average) have similar patterns which suggests that the PGM-11 area variations cannot be attributed to random error. The variations at the PGM-2 stations may be different, but the fewer observations and the large uncertainty in April make direct comparison difficult. The late May to July covariation of the borefield with Base 1 suggests that the gravity changes are at the Guayabo base.

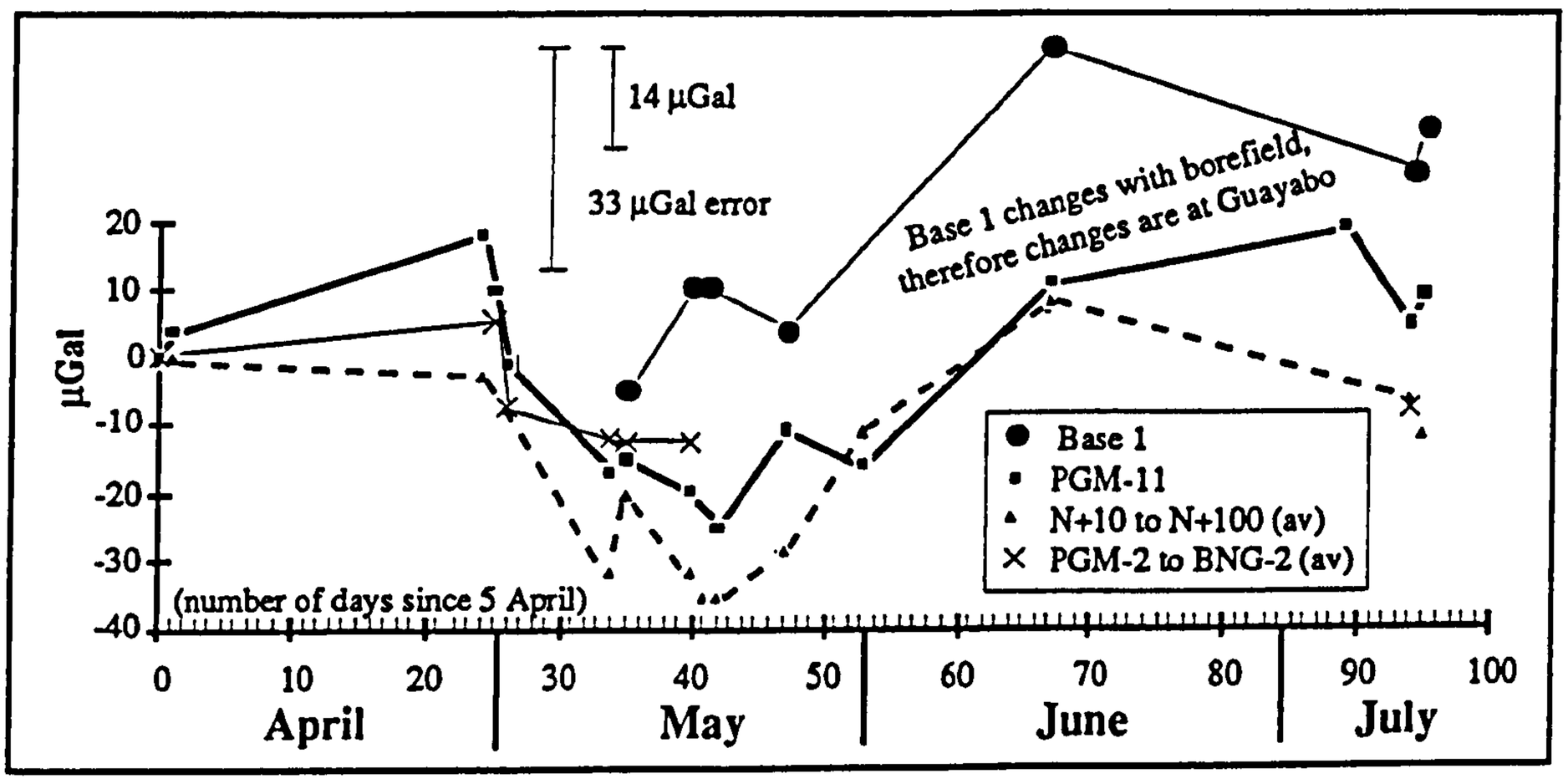

The changes at PGM-11 do not appear as random jumps within the limits of the error bars but there is a significant gravity drop at the beginning of May and a recovery to April values at the beginning of June. In early May it was recognised that the early May changes in the relative value between Guayabo and the borefield were probably significant and to discriminate between mass changes at the Guayabo base and the borefield a second base station, Base 1, was set up outside the caldera (location in Figure 5.3 to the south of Guayabo).

Gravity at the stations N+10 to N+100 varies in accordance with that at PGM-11, but the data for the PGM-2 area are fewer and therefore less convincing, though in general agreement with, the PGM-11 area data. Reliable (i.e. repeatable) data at other stations are scarce (Table 5.4) as the standard errors are larger. That the data from the Base 1 station

change in tandem with the borefield data from late May to July (Figure 5.13 a) is very a useful observation, because it strongly suggests that the gravity changes in this period can largely be attributed to changes at the Guayabo base, not at the borefield. Unfortunately there are no comparable data from the period of gravity decrease in early May.

Figure 5.13 b Individual station variations to the north of PGM-11. The vertical scale is relative, the reference starting point (zero change) for each station is marked by an ellipse. Stations are displayed in spatial order with PGM-11 at the bottom (south). There is less evidence for the May drop from the northern stations (from N+100 to PGM-14) implying the May gravity variation cannot be explained in terms of changes at Guayabo.

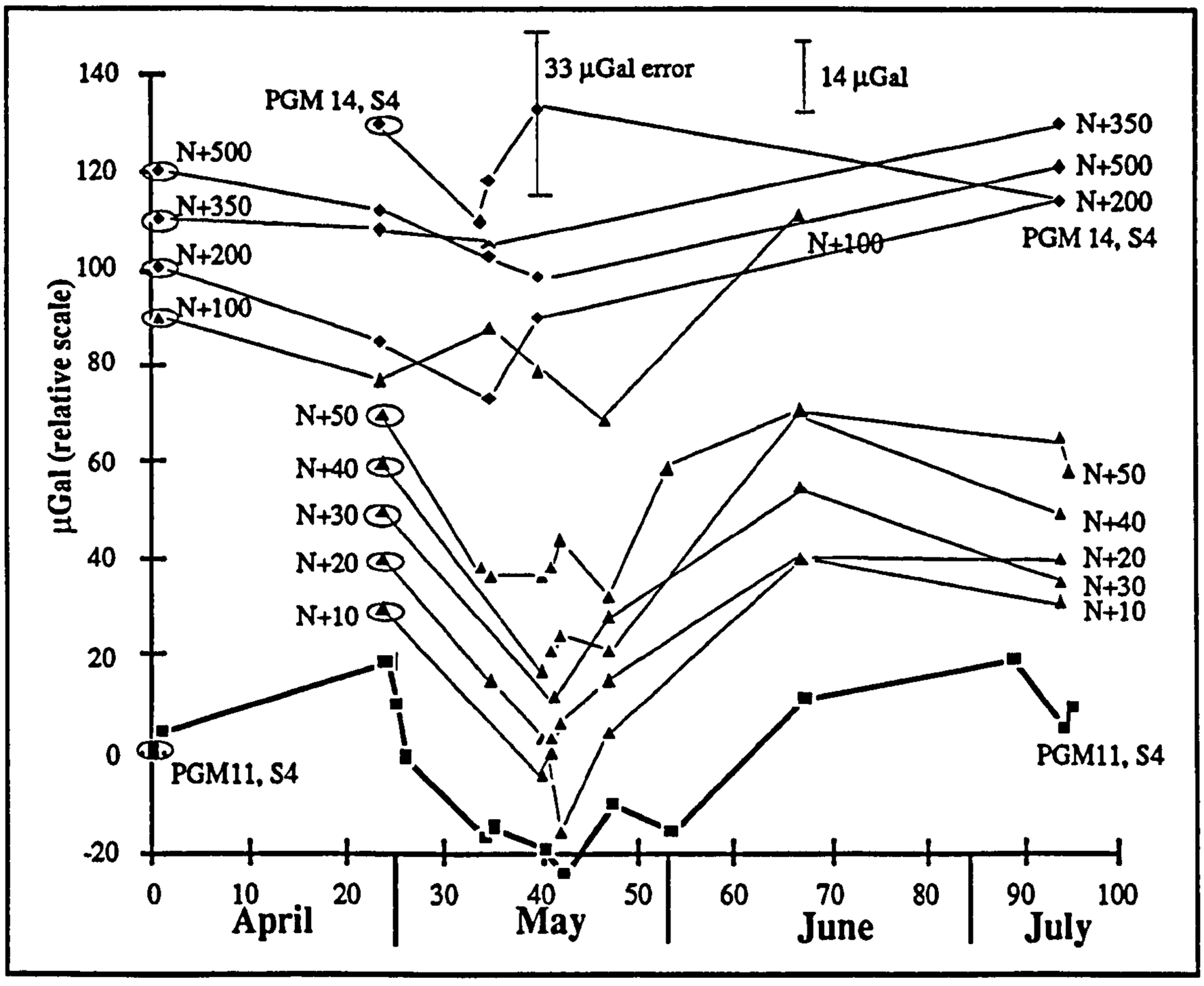

If the actual borefield variations were all similar, it would indeed be reasonable to infer that the real gravity variation was occurring at Guayabo and not necessarily in the borefield. The variations at the stations to the north of PGM-11 do not, however, correlate with those close to PGM-11 (Figure 5.13 b). The PGM-11 gravity drop of 40 µGal at the beginning of May was not observed at stations N+100 to PGM-14 (the most northerly site). Although many of the most northern station data are reliant on single observations, the lack of a sharp decrease at all the stations is believed to be significant. The small gravity decrease at PGM-2 is similar to the northern stations (Figure 5.13 a) and therefore may be distinct from the PGM-11 data.

What then, are the reasons for the gravity changes either in the borefield area or at Guayabo, or the combination of changes at both? The patterns of gravity changes are not related to the days when PGM-11 was producing or PGM-2 was receiving spent brine, so the gravity changes must be related to natural fluctuations in either groundwater levels or reservoir conditions. Elevation changes cannot be ruled out (discussed above) but an elevation increase of 20 cm is required in the PGM-11 area, followed by a similar recovery to explain the observed gravity data and not believed to be realistic. Incorrect tide corrections cannot be responsible as they would have distorted the daily base and field readings equally. The repeatability at Guayabo (Table 5.4) is good during the latter part of the season and cannot be responsible for the apparent changes at Guayabo relative to the rest of the field.

Uneven variations in the groundwater level (that result in a change in thickness) of the perched groundwater table were initially considered the most likely cause for the gravity changes (Hallinan *et al.*, 1989). May 1989 was a period of very little rainfall in both the borefield and Guayabo, followed by increased rainfall in June, but an overall groundwater drop may be expected to be less severe in the low lying Guayabo area, than in the elevated borefield area, or possibly the Base 1 area. Thus the gravity decrease in the borefield in early May could be explained. A 40 μGal gravity decrease requires a 3 m to 10 m drop in the groundwater table for a 30 to 10% porosity respectively (Figure 5.14, left-hand axis). Changes in the saturation level of a 50 m vapour (steam dominated) zone have also been computed for comparison (Figure 5.14 right-hand axis).

Figure 5.14 Rise in groundwater level (or top of liquid-dominated zone) calculated for given increases in gravity and different porosities assuming an infinite slab model and 100% saturation of pore spaces. A change in the saturation level of a 50 m vapour zone gives similar results.

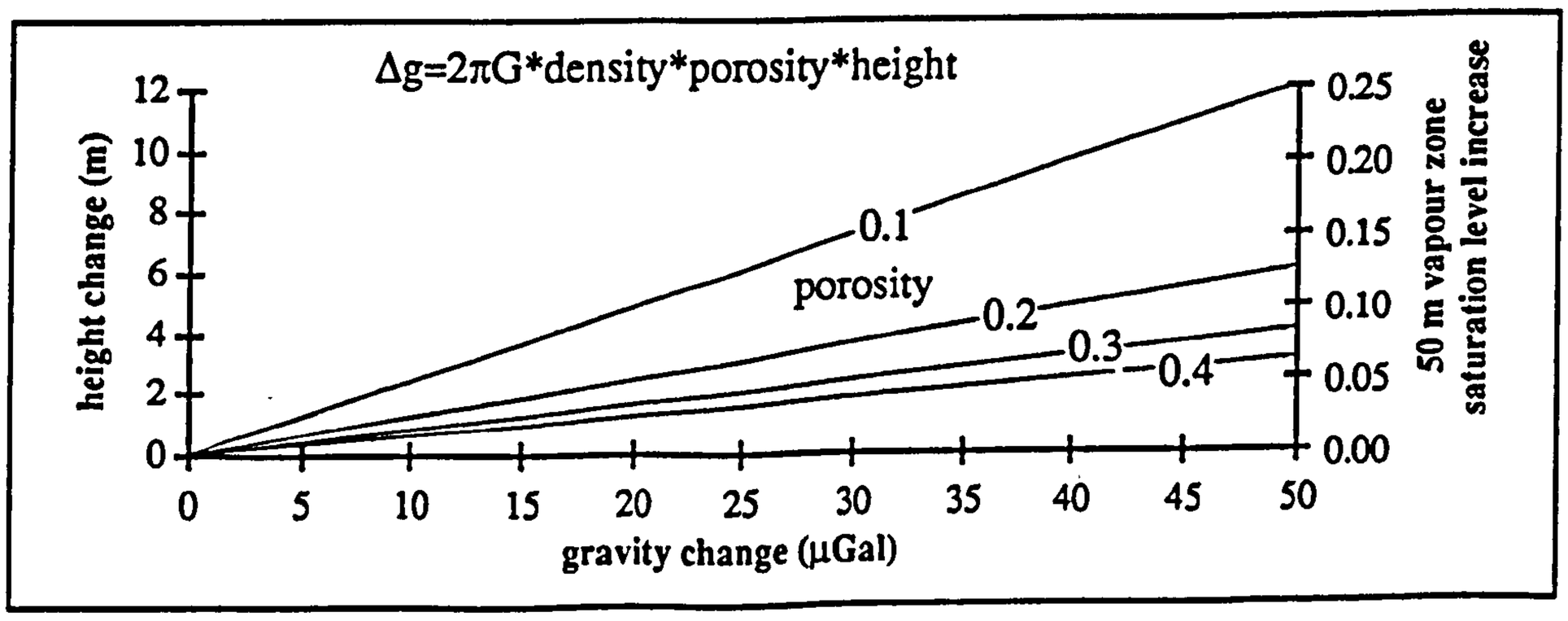

For a greater or lesser thickness of vapour zone the saturation level change decreases or increases respectively in a direct inverse relationship with the thickness. The infinite slab model produces *minimum* groundwater level, saturation level or thickness changes for a given gravity variation; but is a good approximation to variations in the properties of these broadly planar bodies that are close to the surface. The total mass change predicted by a Gaussian integration of the gravity change over the area:

$$M = \frac{1}{2\pi G} \int_{-\infty}^{\infty} \int_{-\infty}^{\infty} \Delta g(x,y) dx dy$$

is difficult to estimate because the areal extent of the detectable changes is poorly constrained. It is however possible to estimate a mass change per unit area, given by:

$$M' = \frac{\Delta g}{2\pi G} \quad (kg\ m^{-2})$$

given Δg in m s^{-2} (10^8 μGal). This gives 954 kg m^{-2} (approximately 1 tonne m^{-2}) for a 40 μGal gravity change, irrespective of the depth of the change, providing of course that the spatial wavelength of the anomaly exceeds the depth to the mass change.

It is not possible to distinguish between the vapour zone saturation level, vapour zone thickness and groundwater level models without independent control, but obviously the former two are only possible in the vapour zone area in the northern and central borefield. Rainfall fluctuations over the shallow recharge area of the flanks of Volcán Miravalles and the borefield may affect the phase balance in the vapour zone and the boiling zone by changing the influx of low temperature fluid. Increased infiltration of cool meteoric water to the vapour zone would increase the saturation level of the existing vapour by favouring condensation, thereby resulting in a gravity increase, and *vice versa*. Natural pulses in the deep reservoir, possibly reflecting changes in the fracture-dominated permeability are known to have occurred at Miravalles; a temperature rise of a few degrees was recorded in PGM-11 in 1986, in the core of the outflow plume (Lionel Vaca, ICE, *pers. comm.*).

In summary it has been shown that non exploitation-related, short period gravity changes *have* occurred in 1989 in the area of PGM-11 and possibly other parts of the borefield and

the caldera including the base station at Guayabo. One of the inferences of these changes is that similar changes may have actually occurred in previous years, but could not be confidently recognised because elevation changes of the order of 20 cm cannot be unequivocally be ruled out and the gravity measurement precision was less. The nature of the gravity changes (a sharp decline followed by a recovery after one month) and lack of any evidence in previous years for elevation changes suggests that elevation changes are an unsatisfactory explanation. Changes in the groundwater level, the saturation level of the vapour zone, or the thickness of the vapour zone (varying the depth to the boiling zone) are the possible sources for natural, short period mass changes.

5.4 Production Test Related Gravity Changes

The 1988 four-day interference test and the preliminary 1989 reinjection tests were monitored for possible gravity changes. Apparently significant gravity decreases during production were observed at the interference test at several producing wells, each monitored by several gravimeters (Brown *et al.*, 1988, Hallinan *et al.*, 1988), but the source of the gravity changes could not be attributed to the comparatively minor production-related mass loss from the reservoir (Rymer *et al.*, 1988). Similar gravity changes were not, however observed during the preliminary reinjection tests in 1989. More recent experimental work, described here, has shown that restricted frequencies of noise and harmonics can cause comparable and greater decreases in gravity observed by at least the LaCoste and Romberg gravimeter, G-105, one of the meters used in the 1988 tests. Elevation changes are ruled out, but production related vibration is tentatively proposed as the most probable cause for the observed gravity changes.

5.4.1 The 1988 interference test

In order to test for possible drawdown interference between wells in different parts of the field, wells PGM-1, 10, 11 and 12 were opened by ICE from 18th to 23rd March 1988, and pressure was monitored in a non-producing well, PGM-5. This provided an opportunity to monitor possible initial production related mass changes at several sites (Table 5.5). Several meters were used simultaneously to enhance confidence in any changes. The meters were

continuously read at locations within 2 m of the wellhead, but at different positions (given in Table 5.5) to enable simultaneous monitoring. The 'hut' stations at PGM-1 and 11 were located at the base step of the maintenance sheds at these sites, 10 m from the wellhead.

Table 5.5 The 1988 PGM-1, 10, 11 and 12 interference tests, wells open from 18-23 March. Values in μGal, are relative to the ICE base, Guayabo and ∂ is the change from the previous value. Notice the apparent decrease in gravity (i.e. *increase* in the negative values) during the producing period (Figure 5.15). Reading positions are 'top' is the normal position on concrete surround, '1st step' is down the steps towards the base of the wellhead and the Hut stations are 10 m from the wellhead.

					.....closed		*wells open*		closed.....							
	18-Feb	∂	3-Mar	∂	17-Mar	∂	*22-Mar*	*23 AM*	∂	23 AM	∂	23 PM	∂	24-Mar	∂	5-Apr
PGM-1																
G-105 (hole)	-20150	2	-20148	12	-20136										-13	-20149
G-105 (Hut)							*-20187*	*-20176*			38	-20144	1	-20143		
PGM-10																
G-105 (top)	-17824	4	-17820			-36	*-17856*	*-17856*	16	-17840	28	-17812	0	-17812	26	-17786
G-513 (top)								*-17882*	50	-17832	42	-17790				
D-61 (5th step)								*-17607*	52	-17555	17	-17538				
								average	39.3		29					
PGM-11																
G-105 (top)	-28903														-2	-28905
G-105 (3rd step)								*-28756*	24	-28732	26	-28706	6	-28700		
G-513 (3rd step)								*-28838*	32	-28806	41	-28765				
G-840 (4th step)								*-28651*	40	-28611	15	-28596				
G-105 (Hut)			-28884	34	-28850	-12	*-28862*								21	-28841
D-61 (Hut)												-28935	49	-28886		
								average	32		27.3		27.5			
PGM-12																
G-105 (top)	12699	-27	12672												-8	12664
G-513 (top)							*12705*		34	12739						
G-840 (top)							*12697*		42	12739	57	12796				
G-105 (5th step)							*12875*		40	12915	-10	12905	59	12964		
D-61 (6th step)												12972	15	12987		
								average	38.7		23.5		37			

Opened wells produced two-phase fluid at a rate of 40 to 80 kg s^{-1} (ICE, 1988, unpubl. data), discharged laterally to a silencer/steam-separator some 15 m from the wellhead. Groundnoise levels were high but one of the surprising results is that it was often possible to take steady, repeatable readings at positions on the concrete surround to the wellhead during full production at all wells except PGM-1 (production data only available from the 'hut' at PGM-1).

It was expected that any mass changes related to phase changes at the boiling levels within the producing wells would be small and therefore gravity measurement errors would have to be kept as low as possible. When a meter is moved between readings the errors are as for single difference values (33 μGal at the 66% confidence level, Rymer, 1989) and therefore the root mean square error for a change in these values at a station is 47 μGal (at the 66% confidence level). In order to improve the significance levels, the meters were kept

stationary during the actual period of well closure and therefore the significance of a value is that of a single reading; 7 μGal (Rymer, 1989) and of a change between successive values; 10 μGal. Base readings taken before and after these periods showed good repeatability and therefore no evidence of tares during the continuous monitoring period.

Strong winds prevented useful measurements during the initial few days of the well test, but it was possible to obtain data on the final two days, when the maximum possible mass changes compared to shut-in conditions would have been expected. Though there are consistently positive changes from the period when the wells were open and the period soon after closure (compare the averaged AM values before and after closure on the 23rd March, Table 5.5), the individual changes are largely not significant at the 66 μGal level. The 23rd March AM data in Table 5.5 are average before-and-after closure data from the continuous data set over this period, shown graphically in Figure 5.15. Continuous, tide-corrected, temporal gravity data are available from PGM-10, 11 and 12 during which time meters were not moved (except where indicated at PGM-10) so that differences greater than 10 μGal should be significant. The results from each meter have had to be shifted on the gravity scale to coincide with the scale of G-105, the gravity scale shown in Figure 5.15, due to small calibration differences between each meter (a discussion of calibration differences is given in Rymer, 1989). The calibration differences are only significant over 10s of *m*Gal and not significant for the gravity variations of the order of 10s of μGal measured at each wellhead, whatever the absolute gravity difference between the wellhead and the base station at Guayabo.

Data from producing wells show that although a reading is apparently steady and significant at the time of measurement, there is considerable variation between successive readings (Figure 5.15). Synchronous data from different meters do not always show agreement, suggesting that each meter has behaved in a non-unique fashion. For example, at PGM-11, G-840 recorded gravity continuously for over two hours before well closure but showed an approximately steady cumulative increase of 200 μGal during this time. Over the final half hour before closure meters G-105 and G-513 recorded much less variation than G-840 and only one value for G-513 was significantly different. At the point of closure, both G-105

and G-513 recorded a repeatable increase of 20 μGal, whereas G-840 recorded a 30 μGal increase, shortly followed by a 25 μgal decrease over the same period. At PGM-10, G-105 and G-513 recorded similar increases of gravity of 40 and 30 μGal at the point of closure, but G-513 continued to record further increases totalling 30 μGal, whereas G-105 showed no post-closure increases.

Figure 5.15 Tide corrected gravity data from the 1988 well closures (23rd March), measured by L&R gravimeters G-105, G-513 and G-840. Scales are shifted to compare with the G-105 scale. Meters were not moved between readings except where indicated at PGM-10. G-105 and G-513 showed similar shifts at well closure but G-840 behaved differently from both.

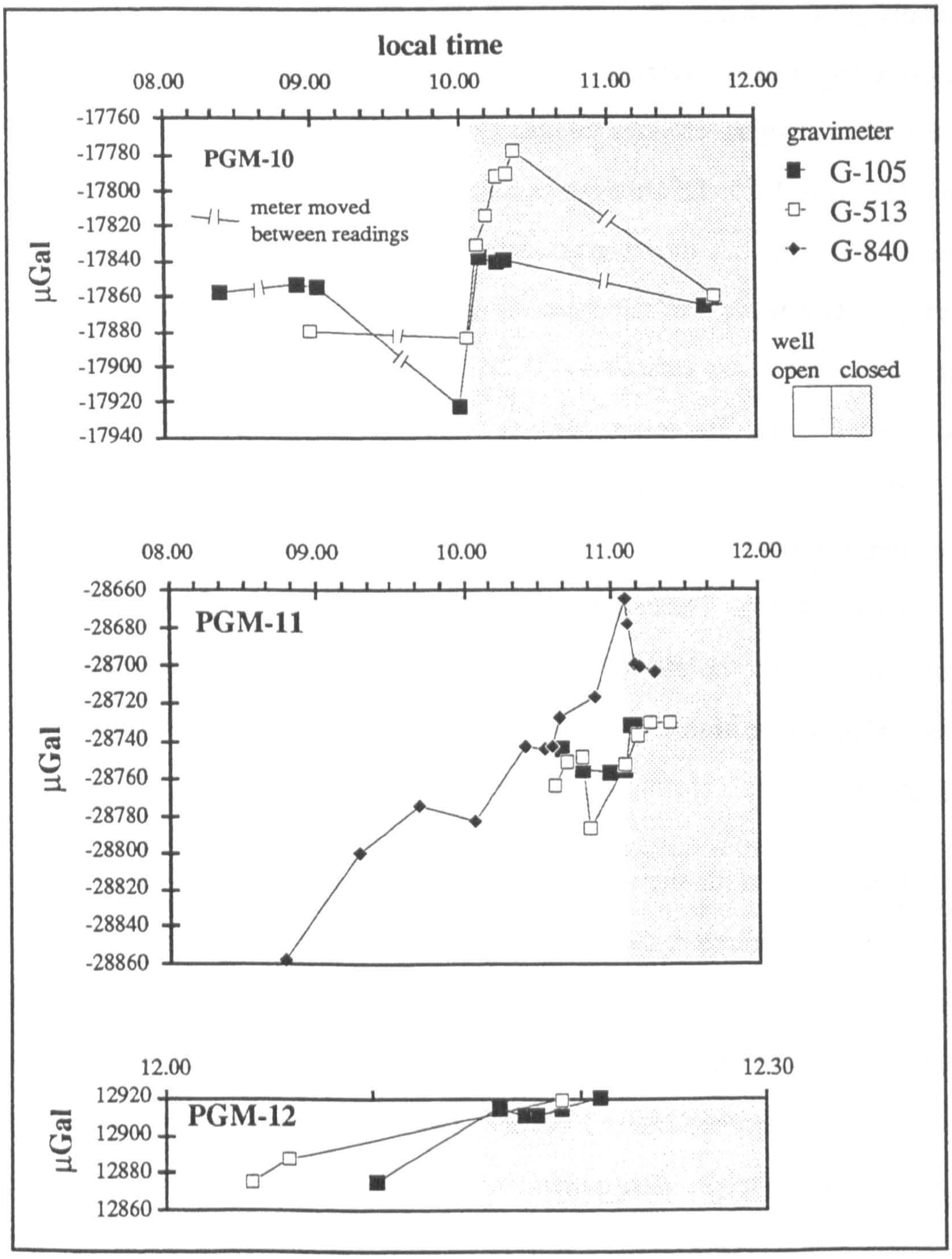

PGM-10 was revisited after monitoring the PGM-11 closure, and G-513 showed a decrease from the post-closure high to a value not significantly different to the post closure G-105 value. At PGM-12 both G-105 and G-513 recorded a similar increase in gravity of 20 μGal at well closure. All wells were closed on the morning of the 23rd March and repeat measurements were made both later the same day (23 PM column in Table 5.5) and on the following days, where it was possible to monitor any possible longer period post-closure changes. Average gravity increases of the order of 20 to 50 μGal were recorded at all wells between morning and afternoon closed measurements. Although these changes are individually significant only if greater than 47 μGal, at the 66% confidence level, it is thought that as similar increases were recorded by several meters (Table 5.5), greater significance may apply.

As the apparent changes from the continuously monitored periods are sometimes contradictory, they are difficult to explain in terms of gravity changes due to mass changes. The meters recorded gravity at positions within 2 m of the wellhead and no differential elevation changes occurred, so why the contradictory data between G-840 and both G-105 and G-513 at PGM-11, and the different post-closure results at PGM-10 from G-105 and G-513? The gravity increase measured at all wells by G-105 and G-513 could be explained by a wellhead elevation drop. One possible cause of elevation changes is if the well casing was coupled to the wellhead foundations and contraction of the casing during post-closure cooling caused subsidence. Elevation was not monitored during well closure, but as the wellheads are not vertically coupled to the foundations and during opening the wellheads actually move by only a few mm in the support collar, post-closure elevation changes are not considered to have occurred. Furthermore, rigorous elevation monitoring of the PGM-11 foundation and surrounding area during well opening and closure in the 1989 tests showed that no elevation changes greater than 1 mm occurred.

It is suggested from later experiments (described below, Section 5.4.3) that the vibration during production affected the gravimeters, so that although no tares were recorded and an apparently stable reading could be taken, the gravity values were nevertheless false and could not be compared with readings taken during the quiet period following well closure.

The vibration may effect each meter differently, thus explaining the apparently contradictory results.

The mass changes required to produce comparable gravity changes to those recorded during the 1988 well tests have been calculated from the assumption that if real they are likely to be related to the slight pressure drawdown that occurs during initial production. Pressure drawdown data are not available for the producing wells in the 1988 test, but some drawdown must have occurred to cause the slight, but significant pressure drop of 0.25 bar measured in PGM-5 (1 km west of PGM-1 and 10) (ICE, 1988, unpubl. data). Pressure logs given in ELC (1988) show that the production levels in PGM-1, 10, 11 and 12 are all within the liquid-dominated zone (hydrostatic gradient) both during normal, static reservoir conditions and during production tests that have been carried out since well completion. Boiling occurs only within the cased section of the well and should not therefore be expected to occur in the reservoir itself at these depths. A pressure drawdown at production depths, however, may cause a pressure drop at the natural boiling zone above - if vertical hydrological communication is sufficiently efficient - causing an expansion of the two-phase zone.

This possible expansion zone has been modelled as an inverted cone, thought to approximate any possible cone or saucer shape of the depression (Figure 5.16). The gravity effect of a density change within this cone has been calculated for a station at a point on the axis of the cone by integrating incremental discs:

$$\Delta g = 2\pi G\rho \left\{ h + cos\alpha[(\alpha^2 cos^2\alpha + h^2 sin^2\alpha)^{1/2} - b cos\alpha + b sin^2\alpha(sinh^{-1}(\frac{2a}{b sin2\alpha} - tan\alpha) - sinh^{-1} cot\alpha)] \right\} \quad ...(1)$$

where G is the gravitational constant

ρ the density change

a the depth to the top of the cone

b the depth to the base of the cone

h the height of the cone (b - a)

α the cone half-angle at the apex

Given that the upper surface of the cone is the pre-production liquid-dominated water level, a can be estimated from the static well logs. The other parameters are more difficult to

estimate but for a given Δg, the cone volume can be constrained within reasonable limits, depending on its height to radius ratio, determined by α. An approximation to equation (1), given that the unknowns are difficult to solve for, is to assume that the mass anomaly of the cone acts as a point source at the centre of gravity of the cone, at a depth of $x = a + h/4$. This results in an underestimate for a cone volume given a certain gravity change, the departure from equation (1) becomes more serious as r increases and x decreases.

$$\Delta g = \frac{GM}{x^2} \quad \text{where the mass of the cone } M = \frac{\pi r^2 h \rho}{3}$$

If x is constrained within reasonable limits it is thus possible to derive r, the upper radius of the cone (Figure 5.16, r is controlled by α in equation (1)):

$$r = x\sqrt{\frac{3\Delta g}{\pi G \rho h}} \quad ...(2)$$

Figure 5.16 The proposed cone model of an expanding steam zone.

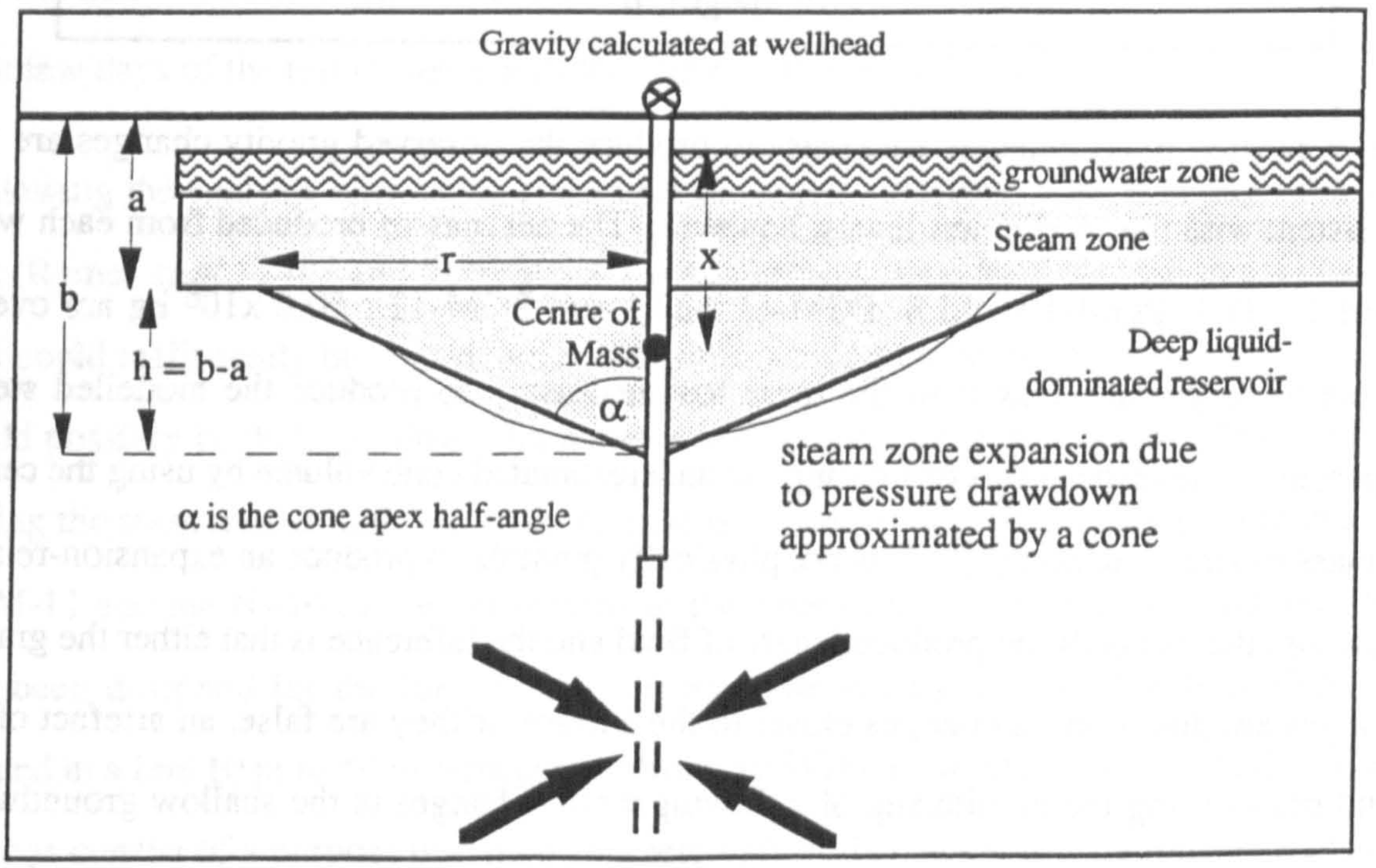

The steam expansion cone dimensions (r *vs.* h) for the observed order of magnitude of gravity changes (50 μGal) are shown in Figure 5.17. The necessary assumptions made are as follows; porosity = 20%, the depth to the boiling zone, a = 300 m (the approximate depth for all wells except PGM-12, 200 m). The dimensions have been calculated for different saturation levels (0.1 to 0.5) of the expansion zone. Because of the assumption in equation (2) that the mass change from liquid to two-phase fluid acts from the centre of mass of the

cone, the mass required to produce the observed gravity anomaly only varies with the depth to the centre of mass, which thus varies with the cone dimensions. The mass does not vary for changes in saturation level (compensated by the change in cone dimensions), but increases with h, the cone height, from 0.7 to 1.0 x10^9 kg.

Figure 5.17 Variation of steam expansion cone dimensions, radius *vs* height (m), illustrated in Figure 5.16, for a given gravity change, 50 μGal, a fixed porosity, 20%, and depth to the boiling zone, 300 m; but for variable steam zone saturation levels, S_o. With the dimensions given here, the lower and upper mass change limits are 0.7 Mt and 1.0 Mt for h = 40 m and 250 m respectively.

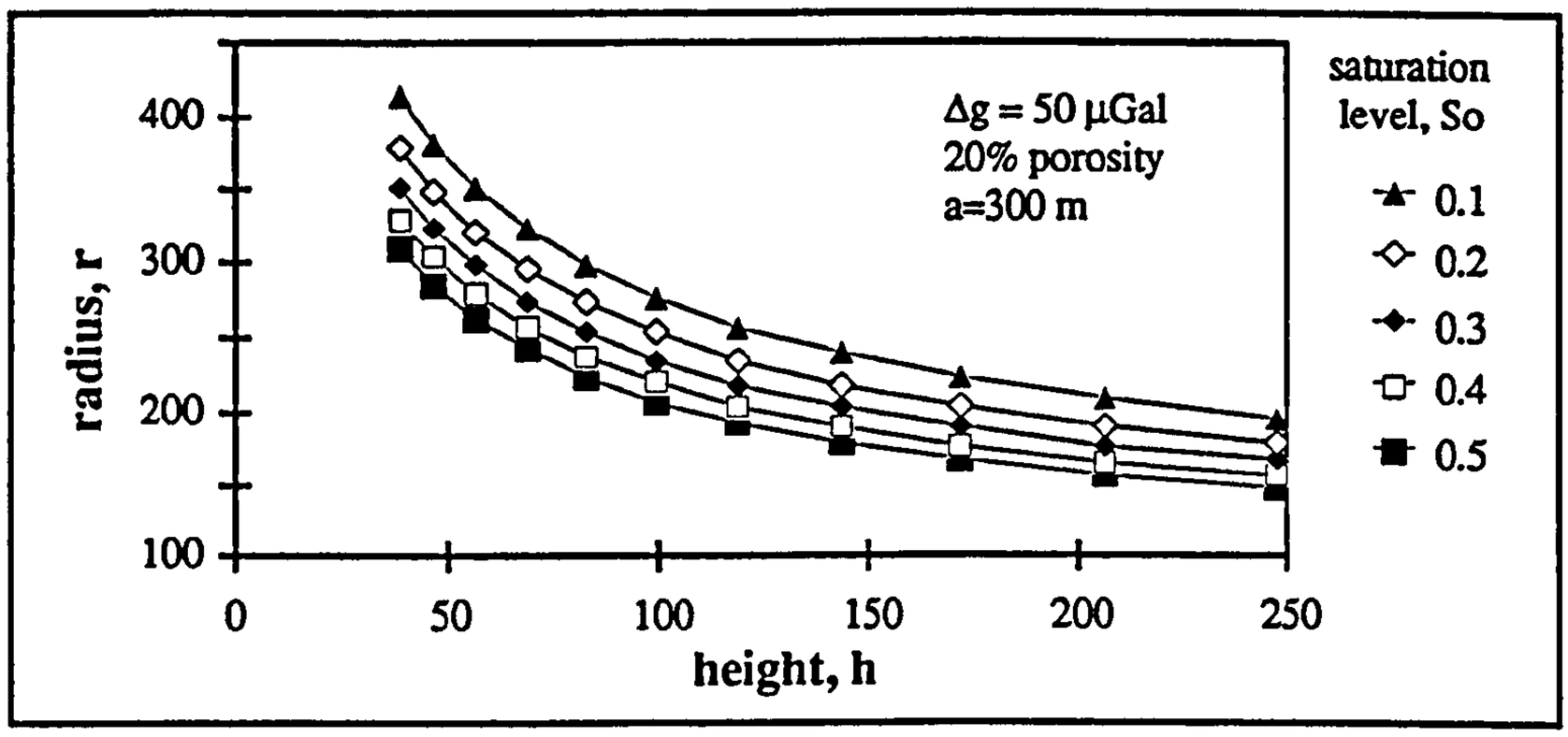

The expansion mass changes necessary to produce the observed gravity changes are not consistent with the production levels, however. The net masses produced from each well; PGM-1 : 27.1, PGM-10 : 15.8, PGM-11 : 33.1 and PGM-12 : 50.6 x10^6 kg are over 2 orders of magnitude *less* than the mass loss necessary to produce the modelled steam expansion cone (especially considering the underestimated cone volume by using the centre of mass model, equation (1)). It is not physically possible to produce an expansion-related mass loss that exceeds the produced mass of fluid and the inference is that either the gravity changes are due to mass changes closer to the surface or they are false, an artefact of the conditions during the monitoring of a flowing well. Changes in the shallow groundwater table thickness would be of the order of 6 m for 20% porosity and 100% dry-out of pores (Figure 5.14) to produce a 50 μGal gravity drop. It is difficult to see how this could be caused in the short time period of the gravity changes by merely halting production in the reservoir some 1000 m below, and is not considered to be a viable explanation. The mass increase possible from condensation of the steam *in* the well, upon well closure, is also not sufficient to generate the gravity changes.

5.4.2 The 1989 reinjection test

ICE engineers planned a six month test in 1989 to examine the feasibility of using PGM-2 as a reinjection well and to test the effectiveness of injecting chemical inhibitors to prevent calcite scaling within a producing well. Fluid produced from well PGM-11 would be passed through a steam separator at an elevation above both wells and the liquid residue piped directly into PGM-2. It was hoped that a rigourous monitoring program at several stations around both wells (located in Figure 5.12) would constrain any small though significant pressure drawdown related mass changes that may have occurred following months of production. The 1989 field season was therefore geared to coincide with the reinjection test, setting up stations a few weeks before the test was due to begin in early 1989. Unavoidable problems arose, however, related to the engineering processes and the inhibitor tests, which resulted in a delay in the full test until July, and then after four days the test had to be cut short. It was unfortunately only possible, therefore, to monitor these first few days of the test (at the end of the 1989 field season, Table 5.4).

Following the analysis of possible causes for the gravity changes of the four day 1988 well test (Rymer *et al.*, 1988 and Section 5.4.1 above) it was considered that any mass changes that could realistically be considered responsible would have to be close to the surface and could possibly be distinguished with a dense station network around the wellhead. Hence during the short term production tests an increased number of repeat readings were made at PGM-11 and the N+10 to N+100 stations at the expense of the more distant stations, that had been designed for the longer period tests. The gravity stations N+10 to N+50 are located in a line 10 m to 50 m respectively from the PGM-11 wellhead (Figure 5.12). These stations consist of a purpose designed concrete base with a 30 cm foundation and a centred metal levelling pin, forming a stable reading platform. Vibrations during production affected the stability of readings from PGM-11 out to N+50, but the noise varied with time and it was possible to make repeatable readings at some time during the tests at each station. Station N+100 is located at the western end of the base of a concrete cattlegrid (buried stations are more stable in the wind), approximately 100 m north of PGM-11. The

cattlegrid was unfortunately flooded during the July test (Table 5.4), preventing measurement at this time, hence it is not included in the test-related data (Figure 5.18).

Figure 5.18 The 1989 well testing values were normalised to N+50, rather than the base station at Guayabo, to look for shallow sourced gravity changes close to PGM-11. The values are differences from the 1989 means (non-producing conditions in Table 5.4). The apparent gravity changes are both random and within the levels of uncertainty and are not therefore thought to be significant.

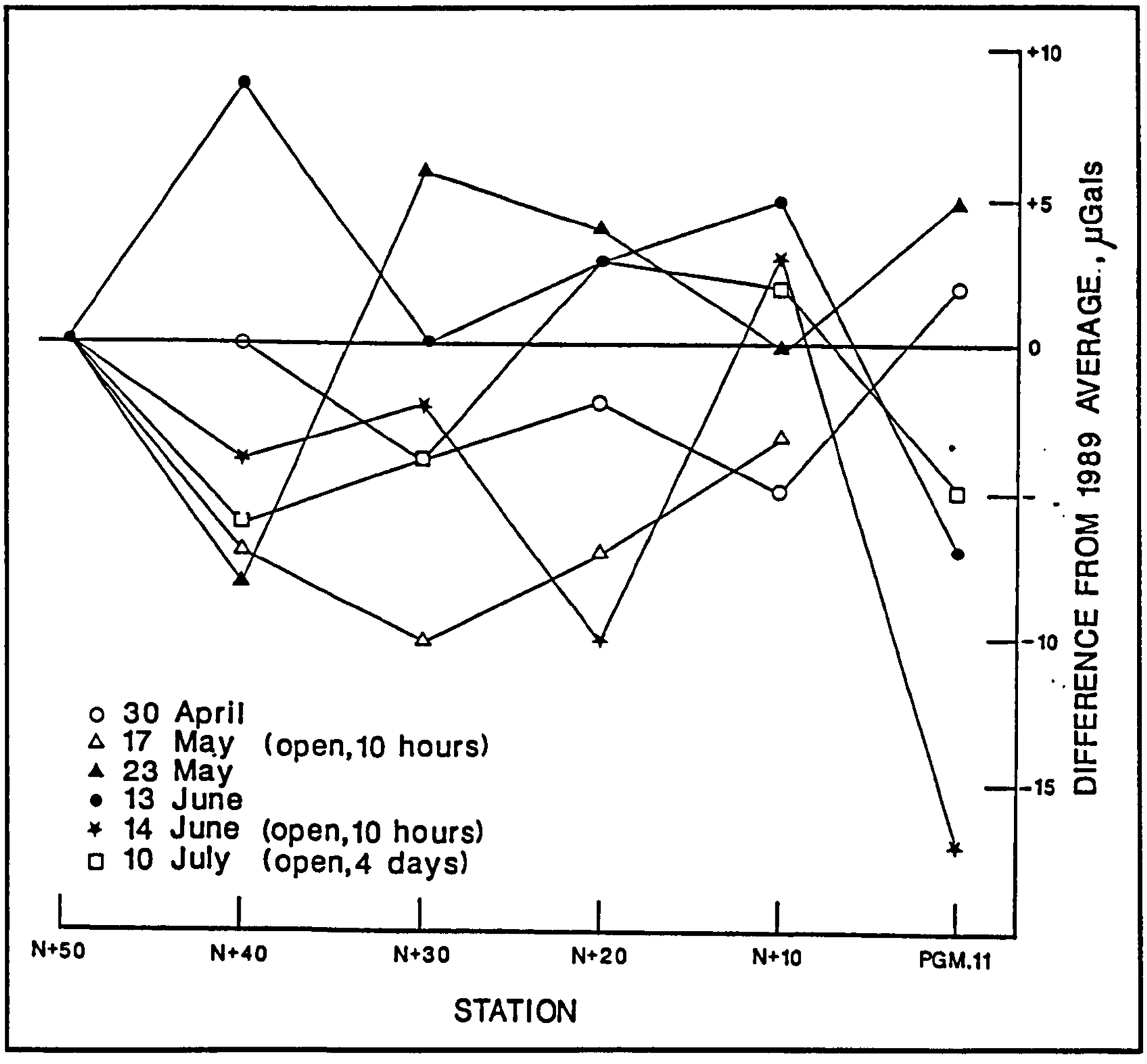

PGM-11 was open for 10 hours on both the 17th May and the 14th June and for four days from the 7th to 10th July. Elevation studies (Table 5.6) of the stations close to PGM-11 show that no significant elevation changes occurred, relative to an emergent corner of the cattlegrid at N+100. This suggests that elevation changes were unlikely during the similar production conditions in 1988. No significant gravity changes were observed during any of the 1989 test periods, either at PGM-11 or any of the surrounding stations (Figure 5.18). To decrease the relatively large errors incurred by comparing differences relative to the distant base at Guayabo (extra transport invariably increases error), the data are presented as changes normalised to readings at Station N+50. At N+50 no significant change relative to

the Guayabo base was observed during either the 17th May or the July 7th to 10th tests (Table 5.4).

Table 5.6 There were no significant (>0.01 m) elevation changes at the stations close to PGM-11 associated with production on May 17th 1989. The reference station was N+100, values in m (station locations in Figure 5.12, gravity results in Figure 5.18).

Station	10-May	17-May
PGM-11	718.000	0.005
N+10	718.522	0.007
N+20	718.577	0.005
N+30	718.678	0.005
N+40	718.777	0.006
N+50	718.906	0.007

The variations shown in Figure 5.18 are apparently random and fall within the error margins. Thus the apparent gravity changes observed at PGM-11 during the 1988 production test were not confirmed in 1989. This supported the earlier suggestion that perhaps the 1988 changes were not related to genuine mass changes during production, and the effects of noise on the performance of a gravimeter were therefore examined further.

5.4.3 The effects of induced vibration on gravimeter G-105

The conclusion from the foregoing discussion must be that there is no reasonable mass change model that satisfactorily explains the 1988 well test gravity data and it is believed that the observed gravity changes were the result of variable meter response to changing conditions. The major difference in conditions at the wellhead sites was the increased noise levels (i.e. vibration) during well production. An experiment has been designed to examine the effects of vibration on the meter behaviour; i.e. whether noise levels alter the physical specifics of any of the meter workings.

Technique: Controlled vibration was induced by passing a single frequency from a signal generator through an amplifier to a 100 W speaker placed face-down, 1 m from the gravimeter, on a secure bench. The gravimeter, G-105, was optically read in the normal way during the experiment, on a baseplate, to replicate the standard field procedure. The bench had a 2 cm plywood top, fastened to an angle iron frame that was secured to the concrete floor of a basement room. The location was effectively free from 'cultural' noise and thus the only uncontrolled disturbance possible would have been from remote earthquakes, the effects of which were not observed during the experiment. The experiment

lasted nearly two hours, during which time the meter was kept unclamped, and the reading light on. The ambient temperature of the room is not thought to have fluctuated and the meter temperature remained constant. In effect, apart from the induced noise, the reading conditions were constant.

The frequency and volume (i.e. amplitude) of the generated square wave were varied in turn. Observed gravity readings, signal frequency and volume are shown as functions of time during the experiment in Figure 5.19. Gravity readings are presented without corrections for the Earth tides, but background gravity and the steady increase totalling 50 μGal is easily discriminated from the sharp vibration-induced displacements. Noise level is given only as a scalar from zero to level 3 (approximately 50 W output). A pilot study (results are not presented because of the higher background noise levels at that site) had suggested that gravity readings were affected at around 40 Hz and thus this frequency was the first to be examined in the later experiment.

Undisturbed (background) gravity could be read to a repeatability of better that 10 μGal. At 37.5 Hz, and volume level 2 a downward displacement of 320 μGal was recorded (10 minutes into the experiment, Figure 5.19). At lower frequencies but the same volume (40 to 65 minutes), the readings were not disturbed. At volume level 1 (at 37.5 Hz) there is a smaller but significant displacement of 20 μGal, but as the volume was incrementally increased from 1 to 1.5 to 2.5 the readings dropped by a further 70 and 580 μGal respectively. At volume levels up to 2.5 the reading needle did not drift from the reading line once the initial adjustment to bring it to the line had been made (a repeatability of better than 10 μGal was still possible). Importantly all the displacements were *downward*. At higher levels, however, the needle vibrated significantly, and became unstable. At level zero after each period of induced displacement, the reading returned to its normal position, indicating that the shift is not due to some irreversible process, such as a normal mechanical tare.

At a constant volume level 2, the frequency was gradually increased through 37.5 Hz to 150 Hz and displacements of 15 and 80 μGal were recorded at 75 Hz and 111 Hz respectively, at or close to the first two harmonic frequencies of 37.5 Hz (75 and 112.5 Hz), but none

near 150 Hz, the third harmonic. At frequencies of 37 and 38 Hz, close to but 0.5 Hz either side of 37.5 Hz there were no significant displacements. When conditions were constant (volume level 2 and at 37.5 Hz) the displaced readings were repeatable, but when conditions were changed and then returned to the previous levels the amount of displacement was usually different.

Figure 5.19 Vibration induced gravity changes for meter G-105 during a continuous 120 minute experiment (time on the horizontal axis). At a square wave frequency of 37.5 Hz, there are negative departures of measured gravity, up to 700 μGal, proportional to the volume. At around the 1st and 2nd harmonics (75 and 111 Hz) there are also displacements up to 60 μGal.

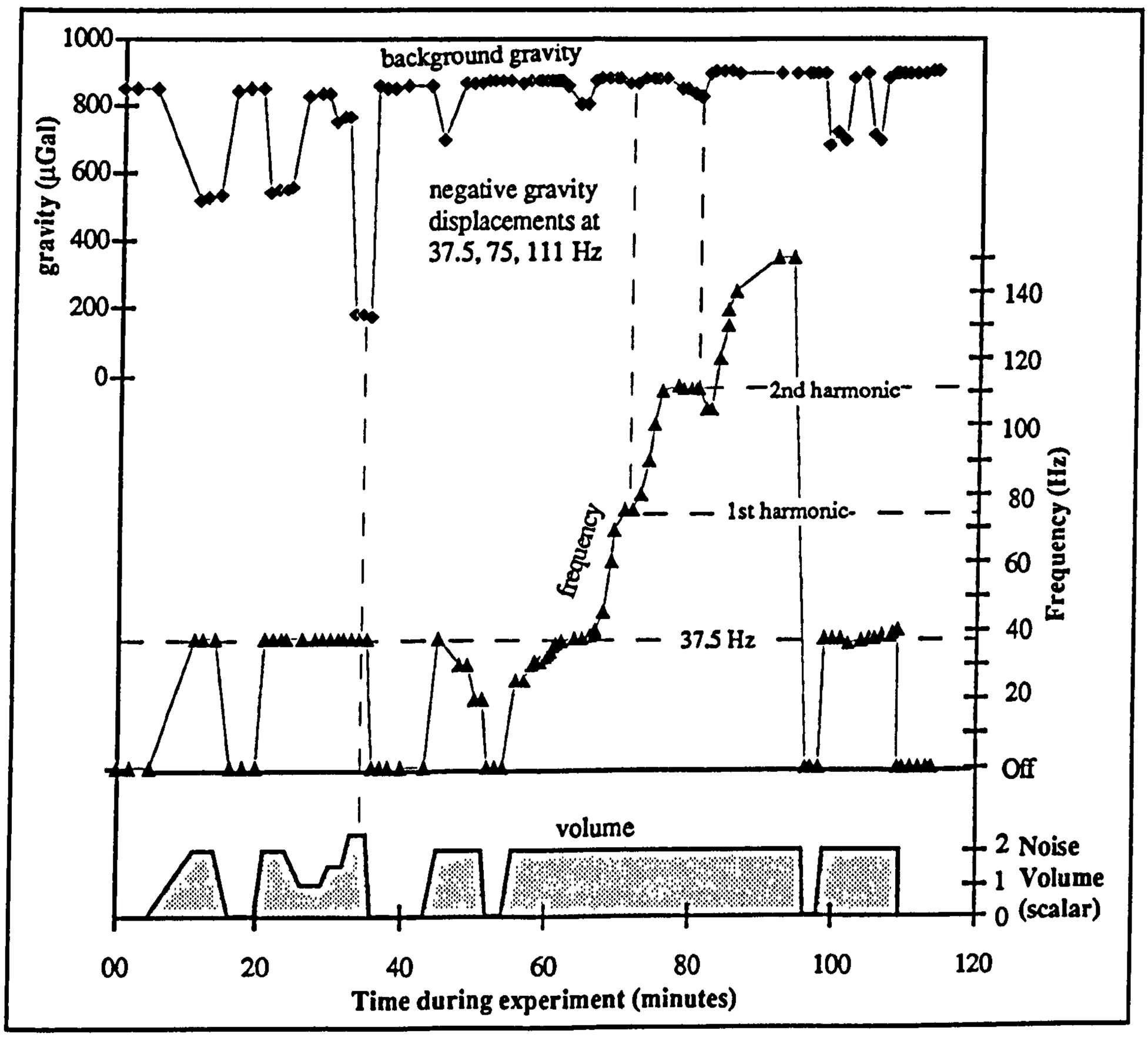

The conclusions of the experiment are that during sufficiently high noise levels at a specific frequency of 37.5 Hz and some of its lower harmonics, the behaviour of meter G-105 is affected such that gravity readings are displaced, always downwards, by up to 700 μGal. Readings are repeatable and apparently normal once the volume and frequency are kept constant at these frequencies. The gravity displacements are always negative and there is a relationship between volume and the amount of shift for a given frequency.

The exact reason for the demonstrated change in meter behaviour has not been rigourously investigated, as the specific dimensions of the component parts of LaCoste and Romberg gravimeters are not generally available. It has been suggested by the manufacturers (Fett, 1990, *pers. comm.*) that the effect of a sinusoidal noise waveform on the air damping mechanisms is a net displacement of one cup relative to the other. This results from unequal frictional forces operating against the forward and reverse acceleration during vibration. An alternative explanation is that the spring (supporting the mass against gravity) length changes by generation of a standing wave along the spring. This effectively lifts the mass, without necessarily involving much actual vibration of the ends of the spring, resulting in the apparent decrease in gravity observed. Furthermore, it is reasonable to assume that a spring would generate standing waves only at a specific frequency of vibration and its harmonics, as observed in the experiment.

Implications for the well test data: LaCoste and Romberg gravimeters are generally believed to be unstable only at low noise frequencies (Rymer, 1989 gave 50 Hz as an approximate limit). During wellhead production there are obviously a variety of vibration frequencies, the component parts of which are liable to change as the production conditions change (namely fluid flow and fluid phase). It is not certain that any of the frequencies that served to reduce the value of gravity read by G-105 in the controlled experiment were present to explain the apparent reduction in gravity observed during production, or how G-105 would behave in a mixed frequency noise that included a 37.5 Hz component. The behaviour of each of the other gravimeters used in the 1988 well test has not yet been examined, but it is reasonable to postulate that each meter may respond similarly to G-105, though possibly at different specific frequencies and with different displacements. The meters behaved differently during well closure and it is suggested here that either the apparent gravity changes were due to different responses of each meter to the vibration (variable spring length etc.), or the meters behaviour varied because they were not positioned equally relative to the vibration source, the producing wellhead. A more general implication is that the stability of the reading needle during a measurement, and repeatability of readings cannot be taken as a guarantee that the reading is not affected by noise.

5.5 Monitoring Future Production

The non-production related and the vibration-induced gravity changes discused above must be catered for in any future microgravity program designed to monitor the evolution of the reservoir. ICE and ELC have modelled the predicted reservoir response to 30 years of exploitation (ELC, 1988), using two end member scenarios; one with natural recharge and one without. From these models it is possible to estimate the possible gravity response to the proposed mass changes both in the production and recharge areas. Based on these estimations a number of recommendations for the future microgravity monitoring are made.

5.5.1 The simulated reservoir models of ELC (1988)

The production strategy outlined by ELC (1988) was that the existing production wells only had a combined potential of 38 MW (excluding PGM-2 and 15) and more production wells needed to be drilled to run the first 55 MW plant, as well as reinjection wells to supplement the capacity of PGM-2 and 15. A further 55 MW plant is projected to come on line four years after the first 55 MW Unit, requiring further drilling. The proven field is judged to be capable of supporting all the necessary production wells (up to 25 wells), and deep reinjection is planned in the western and eastern areas, immediately outside the production area.

The reservoir simulation model used by ELC (1988) allowed the borefield to be treated as a 3-D array of blocks to a depth of 1200 m b.s.l. (Figure 5.20, Section lines WE and NS are as for Figures 5.6 and 5.9). Within each block the porosity, permeability, initial pressure and temperature and the anisotropy of the permeability (horizontal *vs.* vertical) were defined. A number of essential assumptions about the modelling pararmeters had to be made by ELC (1988):

(i) The reservoir begins in a completely liquid state; this may not be quite true given the probable extension of the boiling zone at the top of the reservoir.

(ii) The porosity is everywhere equal to 0.06, a value estimated from other fields rather than from measurements at Miravalles, which suggest higher values (up to 0.21), at least in the Volcano-Sedimentary Unit at PGM-12 (discussed in Chapter 3).

(iii) There is complete heat exchange equilibrium between fluid and rock. This means that the cool recharge fluid derives heat from the reservoir rock very efficiently; and therefore the decline of the fluid temperature is reduced as much of the total heat is stored in the rock, not in the fluid.

(iv) The transmissivity within the different blocks varies according to the lithology; maximum for the Volcano-Sedimentary Unit and minimum for the Acidic Andesite Unit and the Lava-Tuff Unit (of ELC, 1986 a), medium value for the Ignimbrite Unit. In this way it has been possible to reproduce the broad inhomogeneity of the reservoir permeability.

(v) There is total reinjection of the spent brine at the level of the deepest blocks, between 900-1200 m b.s.l..

(vi) A specific steam consumption for each 55 MW Power Unit of 7.5 kg kWh^{-1} at a separation pressure of 6.0 Bar.

Two end-member simulation models were considered by ELC (1988), representing the optimistic and pessimistic outlooks:

Model I There *is* communication across the borders of the model, i.e. recharge is allowed, but only through the lowermost blocks. All the proven and probable production areas are included. In the natural state, the system is sustained by i) 250°C recharge from the northeast (100 kg s^{-1}) and ii) 180°C recharge from the west (30 kg s^{-1}) which together equal the proposed discharge along the outflow plume to the southwest. The flow rates are based on the distribution of pressures measured in the wells, but the western inflow is possibly questionable; an artefact of the density corrections applied to the PGM-15 pressure log (Section 5.3) by ELC (1988). The natural outflow rate is influenced by exploitation, a 30 % reduction for a 30 Bar pressure drop and the western inflow suffers a 50 % reduction for the same pressure drop. The 250°C inflow is unaffected and communication from below the production levels is allowed.

Model II Only the proven production area is considered (the innermost blocks in Figure 5.20), and *no* recharge is permitted; the most pessimistic outlook considered by ELC (1988).

Two different production depths are considered for each of the extraction models above; one shallow at between 100-300 m b.s.l. and one deep at 500-700 m b.s.l. (Figure 5.20). The main considerations for this study are the development of a steam zone at the top of the reservoir (below 200 m a.s.l.), its progressive expansion downwards and the deterioration of temperatures at the margins of the reservoir as a result of injection and recharge of cooler fluid.

Figure 5.20 Total steam zone expansion and deep temperature decline after 30 years production with both Units I and II on line, as predicted by ELC (1988). Drawdown and temperature decline is more serious for the closed system, Model II. The gravity change has been estimated by dividing the drawdown and cooling zones into a number of coaxial, flat, vertical cylinders (bottom figure).

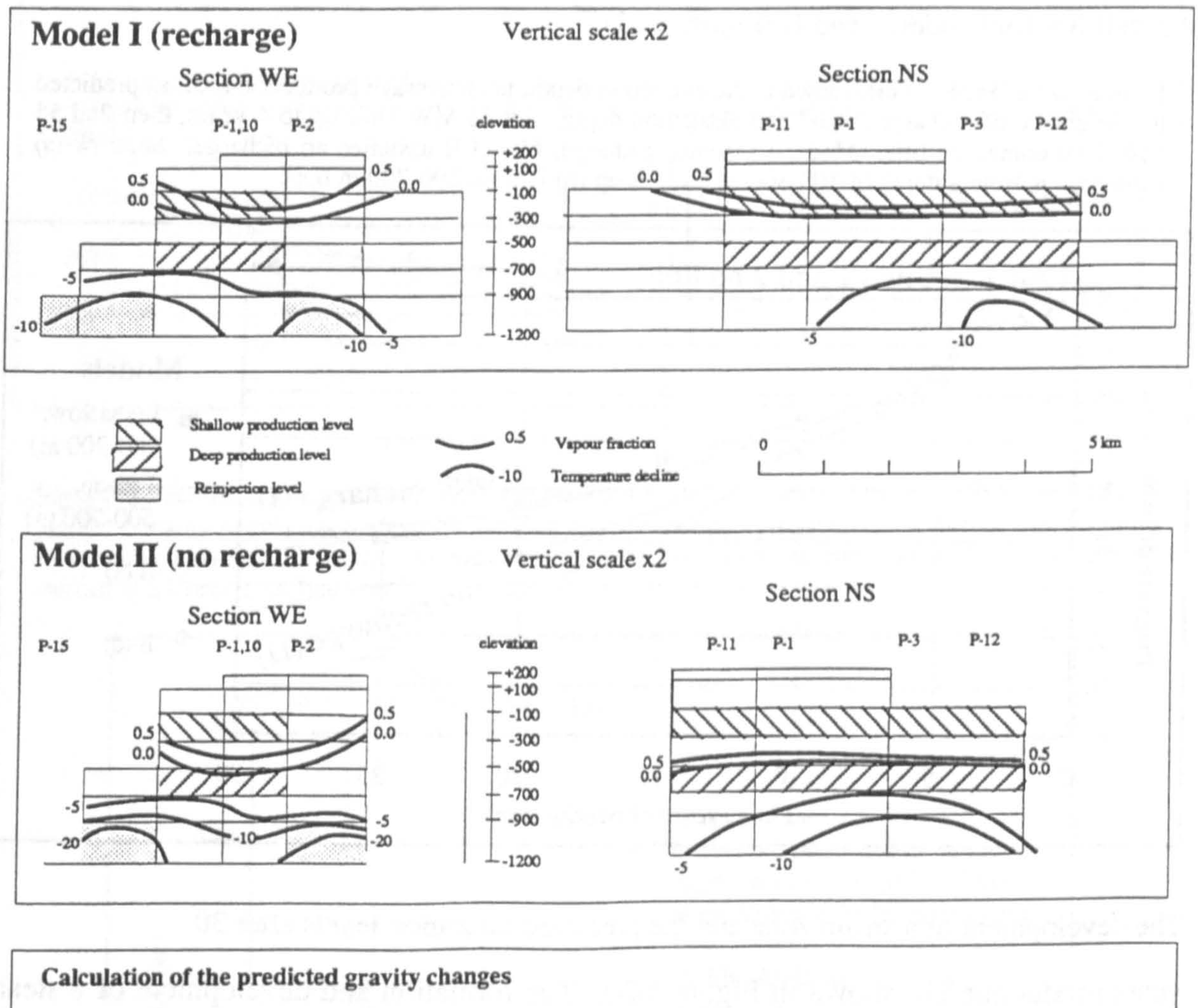

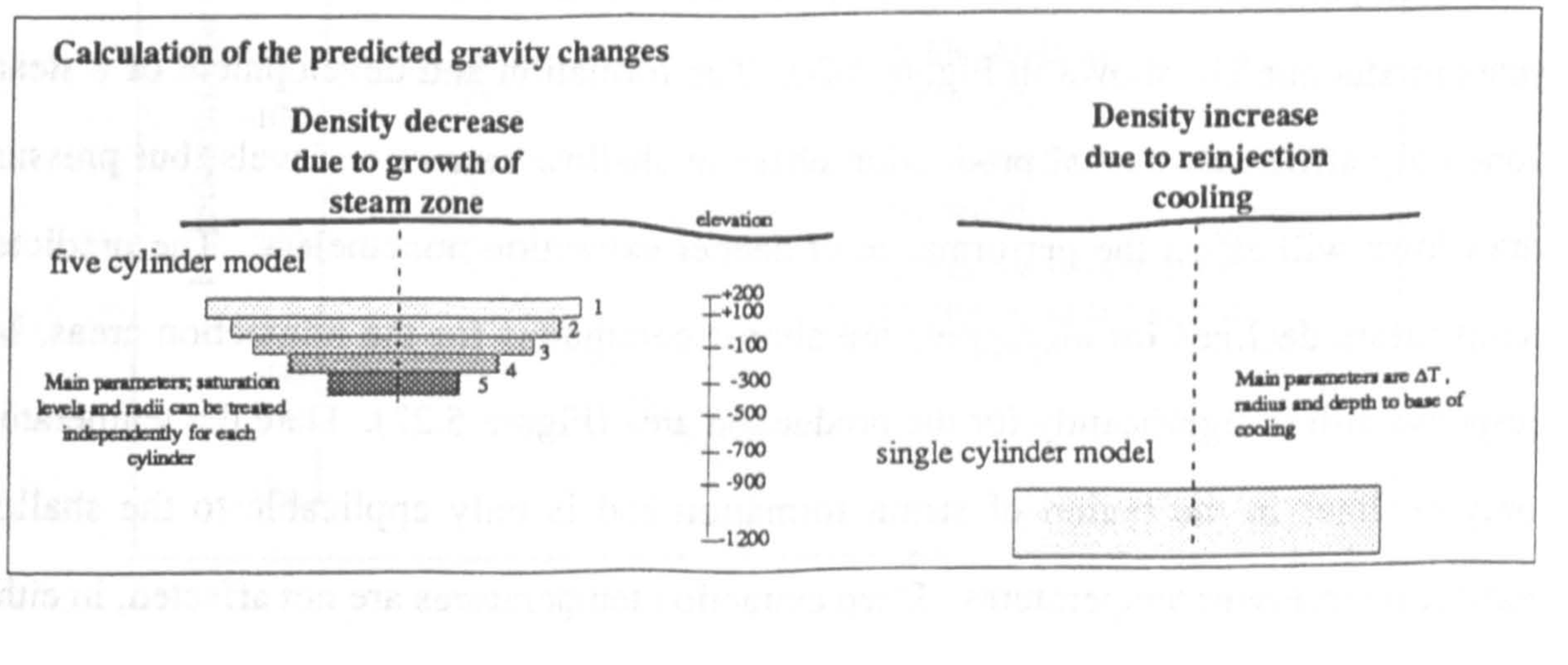

The predicted pressure drawdown in the central part of the borefield (PGM-1 and 10) over 30 years of production and the temperature decline here and in the reinjection areas are shown in Figure 5.21. Due to recharge in Model I the central pressure drawdown after 30 years (25 Bar) is less than for Model II (33 Bar), and noticeably greater for deeper extraction (43 Bar) only in Model II. Initial pressures for shallow and deep extraction are 44 Bar and 77 Bar respectively. The implication for the productive life of the field from Model II is very serious, especially for wells producing from shallow levels. The effect of bringing Unit 2 on line after 4 years is clearly seen, an almost instantaneous pressure drop of 5 to 8 Bar for Models I and II (Figure 5.21).

Figure 5.21 a Pressure drawdown at the extraction depth, in an average production area, as predicted by the choice of recharge model and extraction depth. 1st 55 MW Unit up to 4 years, then 2nd 55 MW Unit comes on line. Model I assumes recharge, Model II assumes no recharge. Shallow (s) extraction is from a depth of 100-300 m b.s.l., deep (d) is from 500-700 m b.s.l..

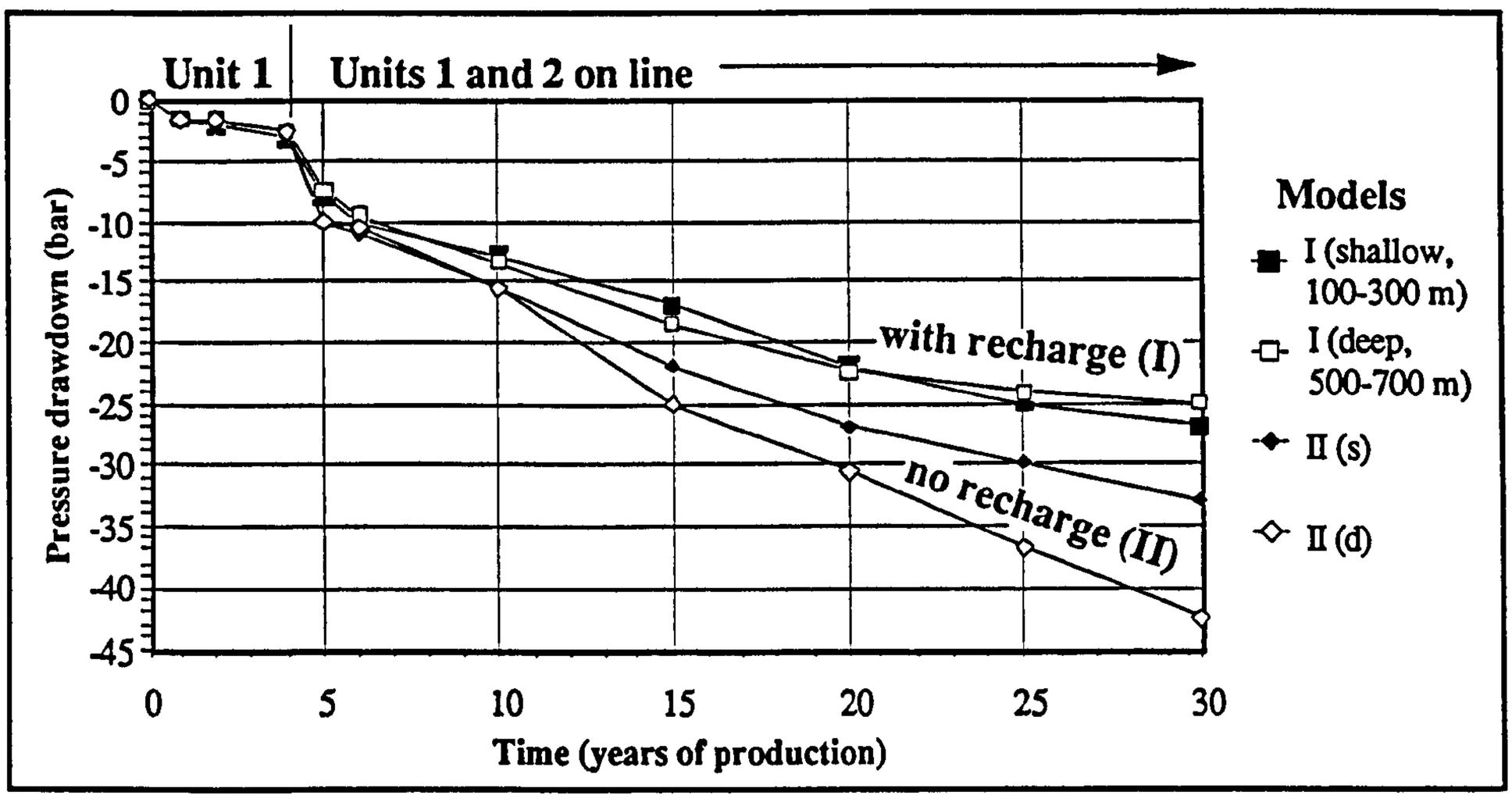

The development of a steam zone and the predicted saturation levels after 30 years production are shown in Figure 5.20. The formation and development of a steam zone only affects the actual production phase at shallow extraction levels, but pressure drawdown will affect the performance of deeper extraction nonetheless. The predicted temperature declines for all models are almost continuous for the reinjection areas, but response differs significantly for the production area (Figure 5.22). Here the temperature only declines in the region of steam formation and is only applicable to the shallow extraction reservoir temperatures. Deep extraction temperatures are not affected, in either

temperatures. Deep extraction temperatures are not affected, in either Model I or II, but reinjection areas suffer temperature declines, the greatest effect being for Model II.

5.21 b, c and d The predicted temperature decline at five year intervals (ELC, 1988). The deep production levels are not affected, but temperature drops in the post-boiling steam zone. The decline in the reinjection areas is at 1050 m b.s.l..
5.21 e The evolution of the steam zone (residual liquid, So) at 200 m b.s.l. for Models I and II.

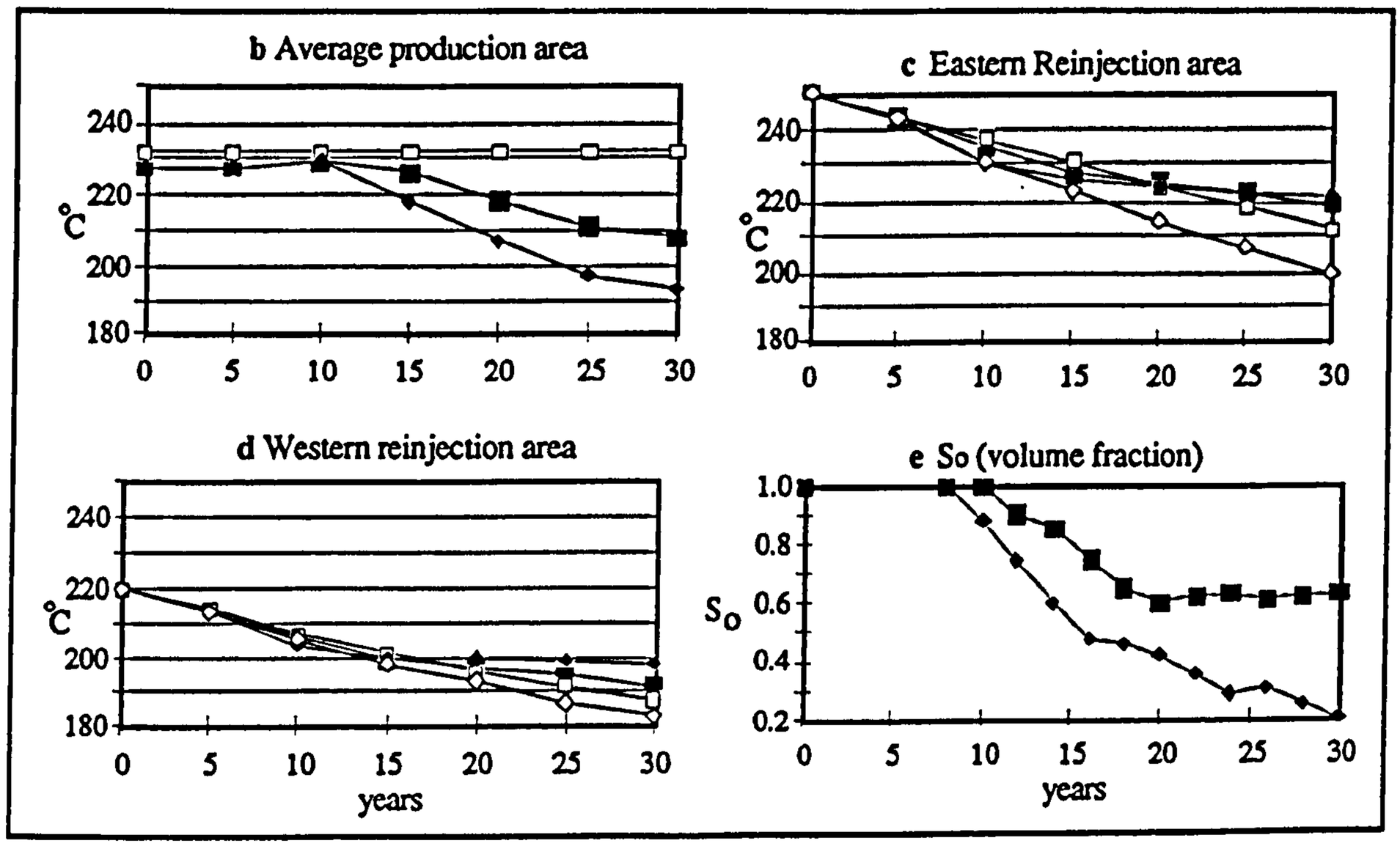

Figure 5.22 The saturation level (So) predicted after 30 years production (from ELC, 1988). The pattern remains largely unchanged by varying the permeability characteristics, except when a linear relationship between the relative permeability of fluid and vapour is used (separation of the phases) instead of a Corey-type function.

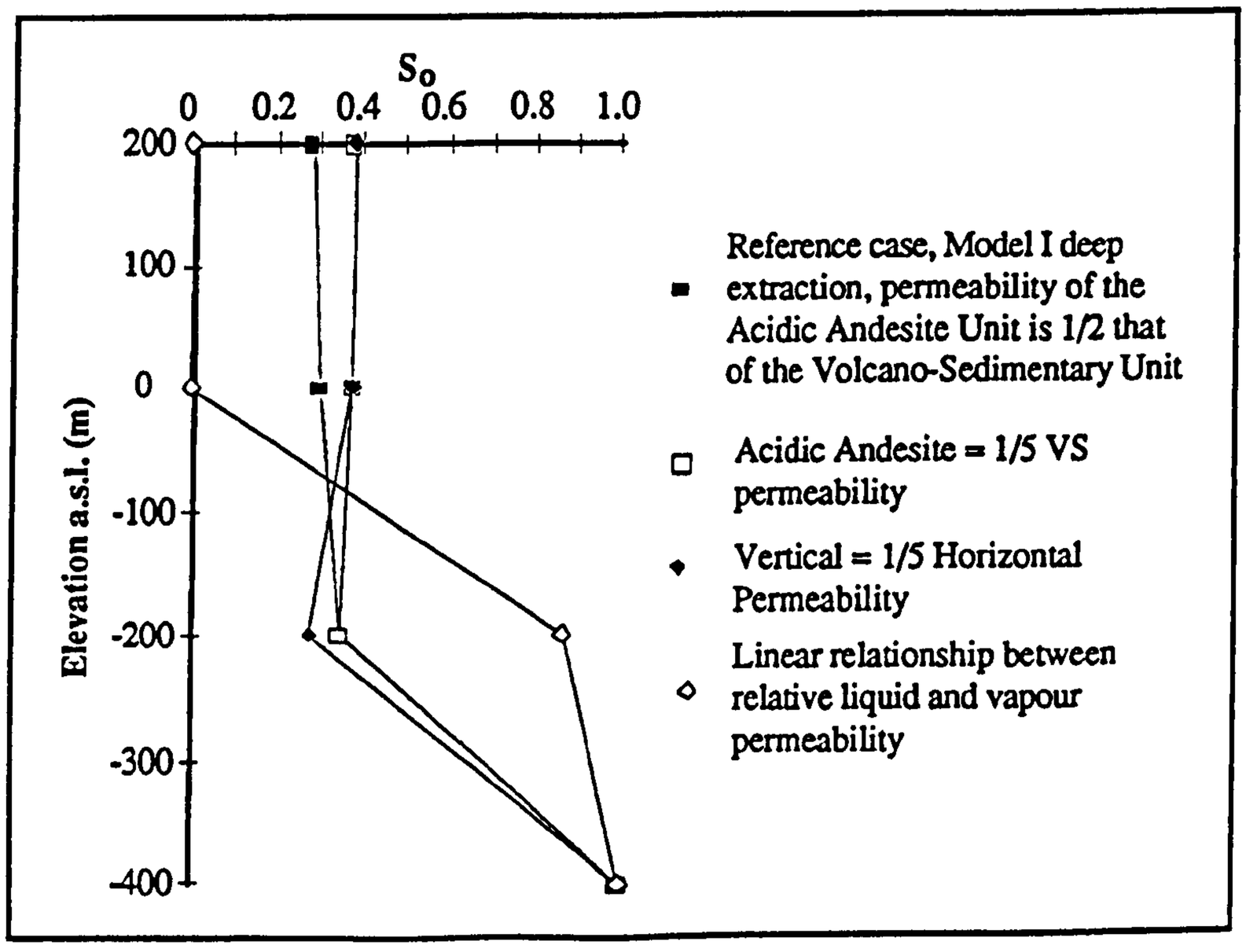

5.5.2 The predicted gravity changes

Given the two extreme reservoir evolution models above of ELC (1988), is it possible to distinguish between them by monitoring gravity? The total predicted gravity changes for 30 years production and changes throughout the lifetime of the field are considered first followed by an analysis of the predicted evolution of gravity with time. The major reservoir-related sources for mass change are the development of the steam zone, its subsequent dryout and deep fluid cooling due to reinjection (Figure 5.20).

To estimate the gravity changes, the steam zone has been approximated by five coaxial, flat, vertical cylinders with an overall saucer shape, and the deep cooling area by a single cylinder (Figure 5.20). The five-cylinder model allows the proposed shape of the steam zone to be matched by varying the radii of each cylinder and the total thickness of the stack. The complicated density contrast (from initial liquid-dominated conditions) is approximated by varying the residual saturation level, porosity and initial temperature of each cylinder as necessary. The results of the five-cylinder model are compared with the results from simpler bodies (infinite slab and single cylinder) (Table 5.7), for both simulation models I and II of ELC (1988). Gravity has been calculated over PGM-10, the centre of the pressure drawdown (Figure 5.20) and for the effect of cooling at both the eastern and western reinjection areas (PGM-2 and PGM-15).

The outer radius of the top cylinder of the steam zone (2500 m) has had to be estimated by projecting the within model limits predicted after 30 years of production by ELC (1988) (Figure 5.20). The locus of the radii of the five cylinders is controlled by a cube root function, to fashion an overall saucer shape. The upper limits of the bodies in both Models I and II is 200 m, the approximate elevation of the boiling zone today and the top of the reservoir defined in the models of ELC (1988). The lower boundary is taken from the depths of drawdown predicted by ELC (1988) (Figure 5.20). The density change within one cylinder is given by, $\partial = \emptyset\rho(S_0\text{-}1)$ Mg m^{-3}, where $\emptyset$ = porosity, ρ = initial fluid density and S_0 = the residual saturation level. The fluid density, ρ, was derived from the water temperature-density data of ESDU (1968).

The least well constrained parameters are S_0 and Ø. A porosity of 0.06 has been adopted to allow comparison with that used by ELC (1988), but it is considered that it may be as much as 0.3 at these shallow levels. This would obviously affect the gravity changes, but would also change the results of the initial simulation (ELC, 1988) of the steam zone dimensions. S_0 is predicted to vary within the steam zone (Figure 5.20), with higher values towards the top of the liquid zone. This variation has been at least partially modelled in the five-cylinder model, by using the average fraction at the depth of each cylinder (Table 5.7). A circular shape for the expansion zone is believed to be a satisfactory estimation, for the purposes of calculating gravity in the centre, of the elongate shape predicted (the north-south stretch can be seen in Figure 5.20).

The gravity changes due to the steam zone expansion are therefore - 423 and -546 μGal for Models I and II respectively (Table 5.7). The absolute values are not thought to be significant to greater than about 100 μGal, however, due to the uncertainty in the porosity and the saturation level. Varying the parameters in each cylinder produces a linear gravity response, but it can be seen that the contribution from the larger, shallower cylinders is dominant (Table 5.7). The sensitivity of the results can be gauged by comparing them with the results obtained by approximating the steam zone shape and composition by more simple bodies. The infinite slab is the simplest approximation, insensitive to the depth and the lateral dimensions of the body and the vertical density variations within. For a slab thickness equal to that used in the five-cylinder model (500 m, Model I and 700 m, Model II), the calculated gravity is almost double that for the five-cylinder model. This means that for a given, observed gravity change, either the vapour zone thickness or the value of $(1-S_0)$ will be underestimated by 50 %, an unsatisfactory approximation. A single cylinder model is depth sensitive, but results in a distortion of the saucer shape to a square outer limit, and does not allow for internal density variation. Using a thickness of 500 m and $S_0 = 0.7$, equal to the average used in the five-cylinder model, a radius of only 1500 m is required to produce a similar gravity change, 1000 m less than that observed in the predicted model.

Table 5.7 Gravity changes (Δg μGal) for different steam zone models; elev (station elevation, m), z1, z2 are relative to sea level, h/5 is cylinder thickness, ρ (Mg m-3) is the original water density calculated from the average cylinder temp T(av), water density = (989.25 - 0.039T - 0.0029T^2)/1000, So is the fraction of residual liquid in the steam zone, 'depth' is depth (m) to T(av) and ∂ is the density change (Mg m-3) in the cooling models. Porosity is assumed to be 6% in all calculations, following ELC (1988).

MODEL I

Gravity (P-10) five cylinder model

	Δg	elev	z1	z2	h/5	radius	ρ	So	depth	T(av)
cylinder		667	200	-300	100	2500				
1	-121.4		200	100		2500	0.865	0.3	517	200
2	-107.7		100	0		2187	0.840	0.3	617	220
3	-91.08		0	-100		1840	0.812	0.3	717	240
4	-71.9		-100	-200		1443	0.805	0.3	817	245
5	-31.02		-200	-300		952	0.805	0.5	917	245
ΔGtotal	-423.1									

Infinite Slab model

model	Δg	z2 - z1	ρ	So	depth	T(av)
a	-708	500	0.805	0.3	717	245
b	-383	270	0.805	0.3	602	245
c	-400	500	0.815	0.61	717	238

Single cylinder model

model	Δg	elev	z1	z2	radius	ρ	So	depth	T(av)
a	-519	667	200	-300	2500	0.812	0.3	717	240
b	-475	667	200	-300	2000	0.812	0.3	717	240
c	-409	667	200	-300	1500	0.812	0.3	717	240
d	-434	667	200	-300	1000	0.812	0.00	717	240

MODEL II

Gravity (P-10) five cylinder model

	Δg	elev	z1	z2	h/5	radius	ρ	So	depth	T(av)
cylinder		667	200	-500	140	2500				
1	-163.5		200	60		2500	0.840	0.3	537	220
2	-141		60	-80		2187	0.812	0.3	677	240
3	-117.9		-80	-220		1840	0.805	0.3	817	245
4	-88.78		-220	-360		1443	0.805	0.3	957	245
5	-34.72		-360	-500		952	0.805	0.5	1097	245
ΔGtotal	-545.9									

Infinite Slab model

model	Δg	z2 - z1	ρ	So	depth	T(av)
a	-992	700	0.805	0.3	817	245
b	-546	550	0.805	0.51	742	245
c	-545	700	0.815	0.62	817	238

Single cylinder model

model	Δg	elev	z1	z2	radius	ρ	So	depth	T(av)
a	-692	667	200	-500	2500	0.812	0.3	817	240
b	-627	667	200	-500	2000	0.812	0.3	817	240
c	-530	667	200	-500	1500	0.812	0.3	817	240
d	-545	667	200	-500	1000	0.812	0.00	817	240

Reinjection Gravity increases (Δg μGal) for single cylinder models of the cooling due to deep reinjection. Cooling from T (0) to T (30) by ΔT after 30 years of reinjection

MODEL I

	Δg	elev	z1	z2	radius	∂	T (0)	ΔT	T(30)
West	4	550	-900	-1200	2500	0.012	200	-10	190
	12	550	-900	-2000	2500	0.012	200	-10	190
	19	550	-900	-3000	2500	0.012	200	-10	190
East	3	750	-1000	-1200	2500	0.014	240	-10	230
	12	750	-1000	-2000	2500	0.014	240	-10	230
	19	750	-1000	-3000	2500	0.014	240	-10	230

MODEL II

	Δg	elev	z1	z2	radius	∂	T (0)	ΔT	T(30)
West	8	550	-900	-1200	2500	0.023	200	-20	180
	24	550	-900	-2000	2500	0.023	200	-20	180
	37	550	-900	-3000	2500	0.023	200	-20	180
East	9	750	-900	-1200	2500	0.028	240	-20	220
	26	750	-900	-2000	2500	0.028	240	-20	220
	41	750	-900	-3000	2500	0.028	240	-20	220

The gravity increase predicted for 30 years of reinjection in the east and west has been calculated for a single cylinder model (bottom of Table 5.7). A radius of 2500 m is considered to be a maximum (given the dimensions predicted, Figure 5.20) but the overall density change and the resultant gravity increases are *not* very large for either Models I or II (4 to 8 μGal for 10 and 20°C cooling), even if the cooling is modelled to 2000 m b.s.l. (12 to 24 μGal), 800 m below the base of the simulation model at 1200 m b.s.l.. These changes are therefore not going to be significant, considering the more dominant decreases due to the proposed lateral and vertical expansion of the steam zone at shallower levels.

Given a standard error of around 33 μGal, it would be possible to distinguish between Models I and II on the basis of the above gravity decreases of 420 to 550 μGal respectively, after 30 years production, but will it be possible to distinguish the models at a more useful earlier stage, when the field is being developed, rather than in its waning stage? The ELC (1988) description of the results of the simulation does not provide a direct evolutionary picture of the steam zone expansion, but does show the temporal change in the steam fraction at the two production depths, 100 and 600 m b.s.l.. No steam develops at the deep level at any stage, but does at 200 m b.s.l., though only after 10 and 8 years of production for Models I and II respectively (Figure 5.22).

Figure 5.23 Predicted temporal gravity decrease due to expansion of a steam zone. The mass change is related to the pressure drawdown predicted by ELC (1988) (Figure 5.21). A significant decrease is not expected before four to five years, after the second 55 MW Unit comes on line. Gravity is not sensitive to differences between the expansion zones expected from Models I and II of ELC (1988) until after 10 years.

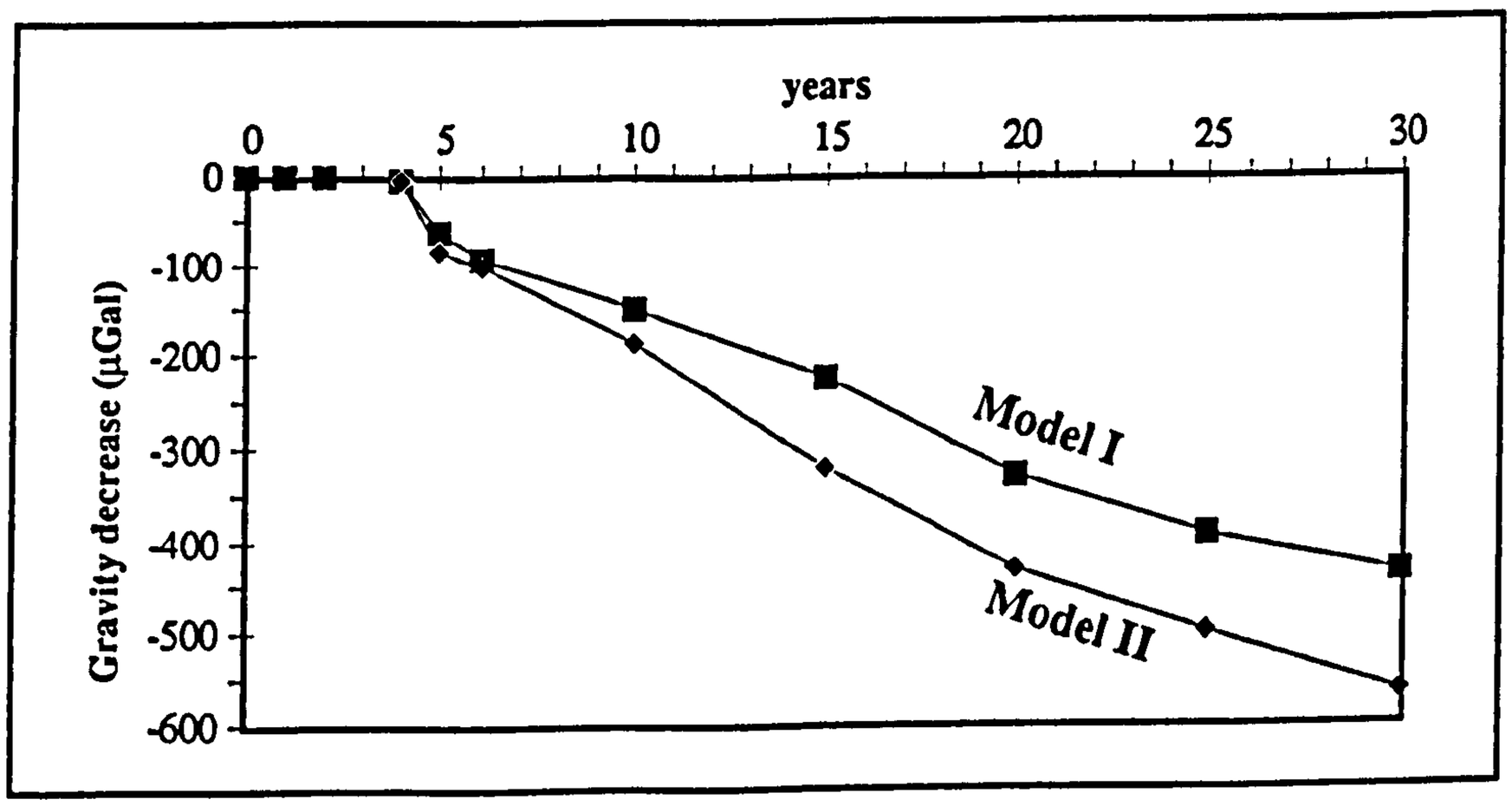

If the pressure drawdown at the shallow extraction level can be related to the predicted expansion of the steam zone, then it is possible to predict the gravity changes at any stage in the life of the field and compare the modelled results with the observed data. It is necessary however, to assume a value for either the saturation level or the thickness of the expanding steam zone, to interpret the vertical distribution of a given change in mass, as Allis and Hunt (1986) suggested for the case at Wairakei. If the steam expansion at Miravalles is limited to the centre of the production field and not over the full breadth of the zone, as predicted after 30 years (Figure 5.20), then it is also necessary to predict the evolution of the radius of the zone. The overall height to radius ratio of the expanding zone has therefore, in this analysis, been assumed to remain constant as have the 30 year values shown in Table 5.7; 1/5 for model I and 7/25 for Model II. The evolving height of the steam zone should be available from the well pressure logs, so that the microgravity results can constrain S_0 independently. The opposing, but lesser gravity increase due to a drop in temperature of the residual liquid in the expanding steam zone must also be calculated. This may have to be done for a number of stacked vertical cylinders to account for the gradual decrease in temperature drop with depth, at least in the liquid dominated zone. A temperature drop is not predicted in the liquid-dominated production zone (Figure 5.21).

The relationship between the pressure drawdown predicted by ELC (1988) and the gravity effect is shown in Figure 5.23. A five-cylinder model is used, as in Figure 5.20, and the relative distribution of S_0 values are assumed to be equivalent to those predicted by ELC (1988) after 30 years for the Model I reference case in Figure 5.22 and Table 5.7. As would be expected, the gravity decrease curves in Figure 5.22 closely follow the pressure drawdown trends. Gravity is not predicted to show much change until the second 55 MW Unit comes on line, where there is a drop of 75 to 90 μGal (Models I and II). Thereafter, gravity decreases almost linearly with time to the values described above after 30 years production. The results are useful as a broad guide to the changes predicted by the reservoir simulation models and, most importantly, can be be used to check for any departures of the true reservoir performance against that predicted.

It is important to remember that there are many potential causes for future gravity changes, some of which are not related to the reservoir evolution, such as seasonal and long-term groundwater changes. It will be necessary to account for as many of these as possible before it is possible to derive reservoir mass changes from the gravity data. Many of these problems are discussed below in the recommendations, but the aim of gravity monitoring is not to derive parameters in the borefield that can be obtained more efficiently from downhole measurements (such as pressure drawdown and production level fluid temperature), but the more intractable information, such as the saturation level in the steam zone and distinguishing cold water influx from hot water recharge at the margins of the field.

5.6 Recommendations For Future Microgravity

The foregoing discussions can be summarised in terms of their implications for the future of precision gravity monitoring during the productive life of the Miravalles Geothermal Field.

The results from the producing fields in New Zealand (summarised by Hunt, 1988), have shown that gravity monitoring is an effective technique for examining i) the expansion of the vapour-dominated zone above the main, liquid-dominated reservoir during the initial exploitation, ii) the development of the steam saturation levels and iii) the relationship between extracted mass and net mass recharge.

An integral part of the program is the repeat levelling of the stations, to correct for subsidence-induced apparent gravity changes. The value of the Free Air gradient cannot be assumed to be constant and should be determined for different survey areas, ideally at every station.

The lesson to be learnt from the Wairakei program (Allis and Hunt, 1986) is the importance of an accurate pre-production data set, both within and beyond the borefield, to monitor the time of greatest gravity change associated with the initial expansion of the steam zone. The suggested spacing and location of stations, shown in Figure 3.24 (from Hallinan *et al.*, 1989), was designed to accommodate the future development of the borefield to the north and south planned by ELC (1988). Also shown in Figure 3.24 are the preferred location of

two base stations, one outside the western caldera wall and the other to the north of the caldera, both away from the presently defined limits of the main reservoir.

Figure 3.24 Proposed layout for the future repeat gravity program at Miravalles. The stations cover an area well beyond the planned borefield, to cover the recharge areas. Two base stations are proposed, one on the western caldera margin, the Mogote Base, T44A, and one to the north of the caldera, the Guayabal Base, both are already accessible from the borefield. Some of the stations of this project were included, (see Figure 5.3 for comparison), others are existing ICE stations, but new stations are required in positions (*) to provide adequate coverage, especially in the recharge area to the northeast of the borefield.

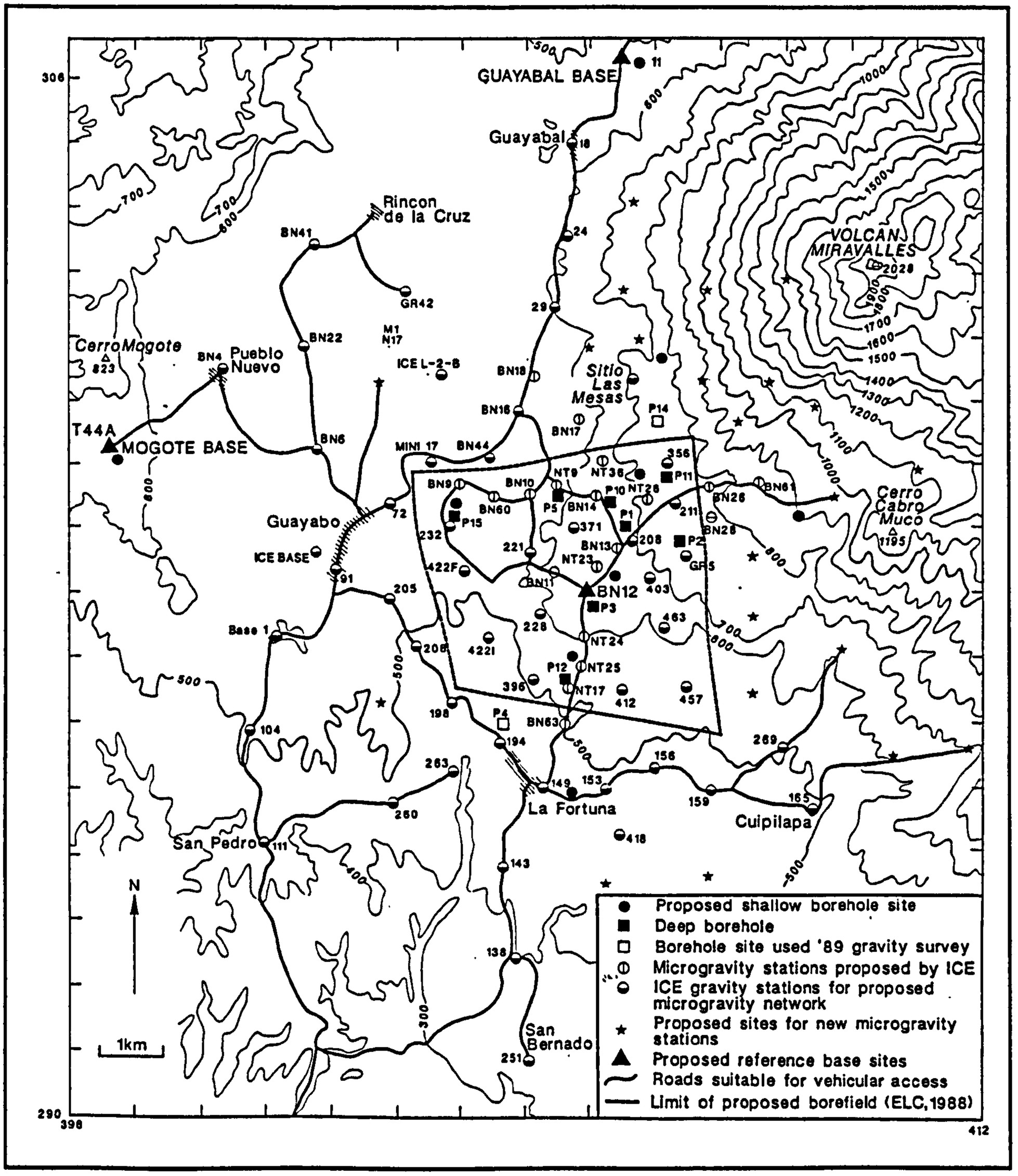

The present depths to and thicknesses of the groundwater zone, the vapour zone and the boiling zone are not constrained by the pressure and temperature logs of the cased sections of the deep wells. It is suggested that the top of the vapour zone is better defined by the

impermeable argillic cap observed in drill cuttings. Both this layer and the deeper geothermal brine reservoir are very good conductors and therefore accurate resistivity profiling could help to identify these depths.

The precision of the gravity data at Miravalles is controlled largely by the repeatability of the readings in the field. Field conditions at Miravalles are hampered by high winds throughout much of the year, especially the dry season, and therefore priority must be given to building stations that are stable in these conditions. As suggested by Hallinan *et al.* (1989), the stations should be placed away from cultural noise sources and trees and be at least partially buried beneath ground level (as shown in Figure 5.25)

Figure 5.25 Cross-section of a suitable design for a repeat gravity station. The station should be at least partially sunk to provide shelter during reading, and should therefore include a drainage system. A non-corrosive levelling pin set in a good foundation is essential, and a cover to prevent damage.

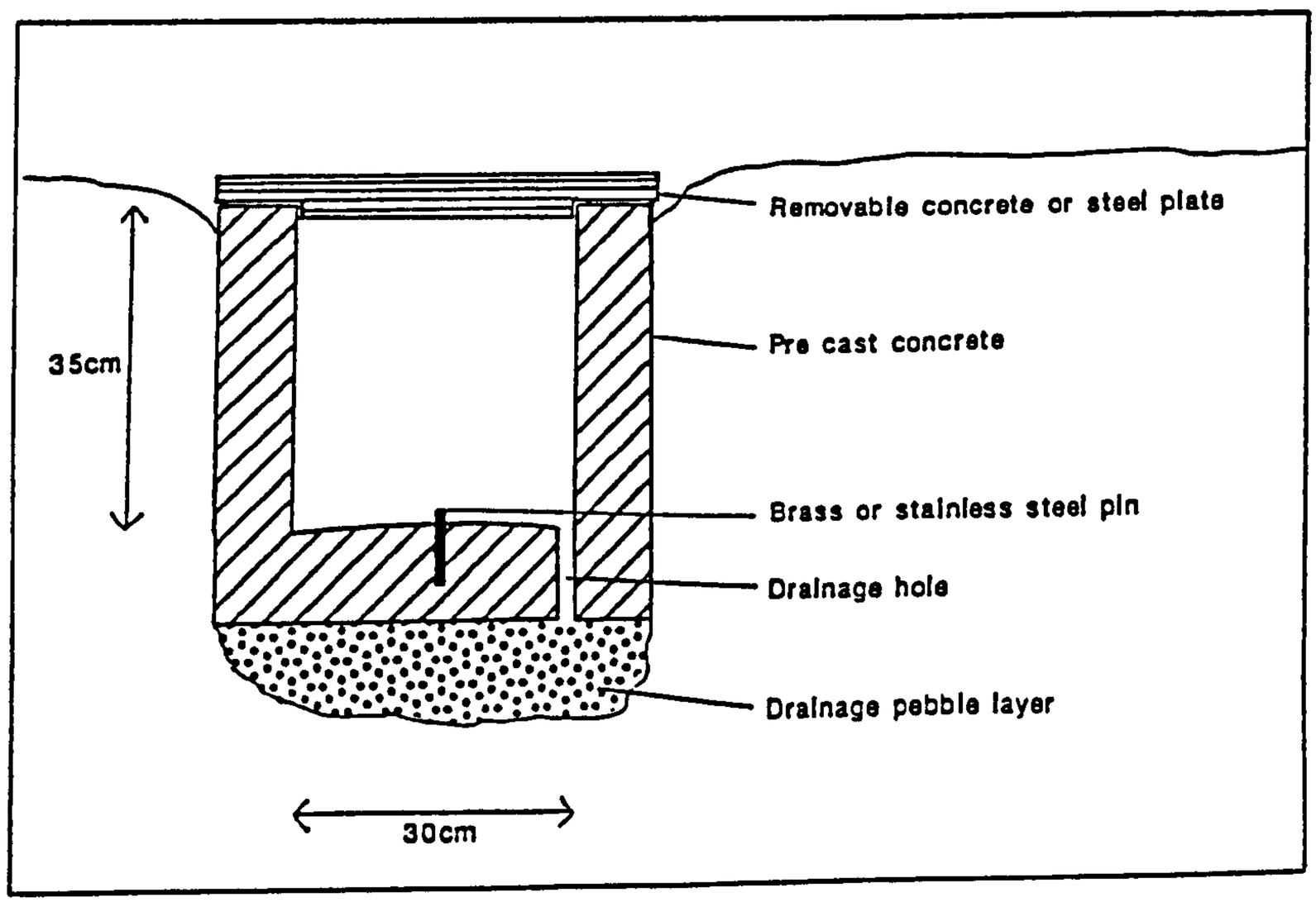

The preliminary investigations at Miravalles have shown that significant gravity changes (up to 40 μGal) occur over short time periods (e.g. the first 10 days of May 1989) that are not thought to be related to the borefield, and certainly not to geothermal production. There is no evidence from the existing repeat levelling data for significant vertical ground movement and the mass changes are most likely to be the result of fluctuations in the groundwater level, brought about by rapid changes in rainfall. The implication is that groundwater levels will have to be monitored in all parts of the survey area, to remove this contribution from the observed gravity (the proposed sites for shallow wells are shown in Figure 2.24).

Vibration at 37.5 Hz, and the first two harmonics of this frequency, causes an apparent downward shift of gravity (up to 750 μGal) measured by the LaCoste and Romberg gravimeter G-105. The shifted readings are repeatable and appear to be stable. The displacement is greatest for 37.5 Hz and increases with vibration amplitude, but the reading eventually becomes unstable as the volume is increased too far. The preferred explanation is that at specific frequencies a standing wave is generated in the restraining spring, decreasing the effective length and therefore causing the observed apparent drop in gravity. It is therefore proposed that the apparent rise in gravity observed by several L&R gravimeters at wellhead stations, during the closure of the four wells at the end of the 1988 production tests, was related to the vibration of the platform during production. It is therefore recommended that the repeat gravity stations should not be placed near vibrating sources (i.e. within 50 m of wellheads, silencers, steam separators, etc. and even pipelines), as although readings may look stable they could equally be false, displaced by the vibration.

The mass changes predicted by the reservoir simulation models of ELC (1988) suggest that gravity changes associated with exploitation will only become significant when the second 55 MW plant comes on line. Gravity must be monitored during the period prior to this however, precisely to test this prediction. As a consequence of exploitation-induced pressure drawdown the natural recharge rates may increase, depending on the transmissivity between the recharge areas and the exploited reservoir. The transmissivity is unlikely to be homogeneous and thus some areas outside the borefield will be drawn on preferentially to others. The ability of the many different recharge areas proposed to date to cope with the demand can therefore be monitored by precision gravity.

In summary, the proposed precision gravity monitoring program should become an integral part of the reservoir modelling at Miravalles.

CHAPTER 6

CONCLUSIONS AND IMPLICATIONS

This final chapter is a synthesis of the conclusions reached during this thesis and a discussion of the implications for future research. The conclusions both contribute to the understanding of the Guayabo caldera and the Miravalles Geothermal Field, on a local level, as well as having a more global significance to caldera research and gravity studies of volcanic regions. The main contributions are:

1) The relationship between Bouguer gravity anomalies and topography in volcanic regions has been thoroughly examined and guidelines for such gravity surveys are proposed.

2) The relative contributions of lithological *vs* hydrothermal control on the density of the strata of the Miravalles reservoir have been defined.

3) A multistage evolutionary model is proposed for the Guayabo caldera that is consistent with both the stratigraphic data and the geophysical models. This has led to:

4) The extrapolation of the drilled reservoir structure along the hydrothermal outflow plume to the southeastern caldera area.

5) The concentric ring fractures identified at Guayabo show that apparently funnel-shaped (or chaotic) calderas may be made up of nested blocks that have subsided relatively coherently, with maximum cumulative subsidence in the centre.

6) A new mass and balance model is proposed to examine the causes for caldera collapse, using gravity data to constrain the intra-caldera mass of the juvenile material.

7) The trans-Guanacaste Arc gravity model shows no regional gradient across the arc but a major crustal discontinuity at the inner margin of the back-arc depression.

8) Field data and experimental results show that LaCoste and Romberg gravimeters record apparent gravity decreases of up to 700 μGal when subjected to steady vibration.

9) The identification of significant gravity changes at Miravalles, related to groundwater levels and not fluid extraction, has important implications for future gravity monitoring.

10) A complete repeat gravity program has been designed to test and complement the existing reservoir simulation models.

6.1 The interpretation of gravity anomalies in volcanic terrain

Volcanic structures are often strongly related to topographic features; for example, compare the depressed nature of calderas to the elevated nature of stratovolcanoes. The limits of the associated deep structure are therefore likely to be broadly coincident with those of the overlying terrain. This leads to a relationship between topography and Bouguer corrected gravity which can mistakenly suggest that a wrong choice of reduction density is the cause, rather than the buried structure. Though the wrong choice of reduction density *will* cause false Bouguer anomalies, the effect can be removed if the reduction density is always used as the reference, or background, density during gravity modelling.

False Bouguer anomalies are also created over elevated regions by not making terrain corrections for zones beyond the immediate survey area. Corrections out to the outer zone of Hammer (1939), 22 km, are insufficient, and would result in a false ~10 mGal anomaly over a volcano like Miravalles, 2000 m above the general terrain. It is recommended that corrections be made out to at least 200 km for studies of regions with similar relief, resulting in missing terrain correction errors of less than ~1 mGal.

6.2 The multi-stage evolutionary history of the Guayabo caldera

The Guayabo caldera is defined as an approximately circular, but segmented, topographic depression, 11 km in diameter along its north-south axis. The western, northern and southern scarps comprise up to 200 m relief of outward-dipping lavas, coarse breccias and tuffs, but the eastern margin is obscured by the post-caldera stratovolcano complex of Volcán Miravalles. Present activity is limited to the surface manifestations of the Miravalles Geothermal Field on the southwestern flanks of Volcán Miravalles.

Four distinct, unwelded to poorly welded tuffs (often separated by a 1-2 m palaeosol) distributed on the Pacific flanks of the Guanacaste Cordillera are believed to have a common source area in the vicinity of the Guayabo caldera. In decreasing order of age these are: the Upper Grey Ignimbrite, the Hornblende Tuff, the La Ese Pumice and the Guayabo Proximal Breccia. The age of, and time span between, the individual tuffs are not well constrained

but have yielded K-Ar ages between 1.6 Ma. (Upper Grey Ignimbrite) and 0.6 Ma. (La Ese Pumice). However, an older and unrelated distinctive tuff, the Biotite Tuff, has yielded three consistent K-Ar glass ages of around 1.42 Ma. with slightly older mineral ages (Table 2.2, Chapter 2). However, of the five dates of the caldera scarp lavas there is only one K-Ar age, 2.3 ± 1.0 Ma., from the oldest lavas of the western caldera wall, that is *older* than those of the Guayabo outflow tuffs. Other lava samples have whole rock K-Ar ages between 0.6 ± 0.2 Ma. (Cerro Mogote) and 0.2 ± 0.1 Ma. (Cerro Espiritu Santo), significantly *younger* than the outflow tuffs. Despite their apparently younger age, (discussed in Chapter 2), field exposures fail to demonstrate that the entire caldera wall lava sequence is actually overlain by the tuffs. Some of the key observations are as follows: i) breccias, tuffs and lavas in the southern caldera scarps can be correlated with parts of the uppermost 500 m of the stratigraphy drilled inside the caldera, close to the southeastern margin, and ii) the youngest extra caldera tuff, the Guayabo Proximal Breccia, is cut by the southern caldera margin.

The apparent contradiction presented by the young ages of the caldera wall lavas compared to the outflow tuffs can therefore be explained if the present depression of the Guayabo caldera is related to subsidence *after* emplacement of the outflow tuffs.

The deeper stratigraphy drilled within the caldera consists of a distinctive basal, partially-welded lithic tuff (the Ignimbrite Unit) overlain by almost 1000 m of intercalated lavas, poorly consolidated lithic tuffs and reworked tuffs in laterally variable proportions (the Volcano-Sedimentary Unit). (This deep stratigraphy is the host rock for the geothermal reservoir). It has not been possible, however to relate any of these VS tuffs to the oldest two outflow tuffs, but it remains possible that the intra-caldera equivalents, if any, may be in the central and western parts of the caldera. The >800 m thick Ignimbrite Unit, at a typical depth of 1500 m, pre-dates the stratigraphy related to the Guayabo caldera but may, in fact, be the intra-caldera deposit of an older, but larger caldera of unknown nature, related to the oldest, most extensive and primitive outflow ignimbrites in Guanacaste, the Bagaces Group. Electrical sounding data show the broad continuity of the Ignimbrite Unit, the resistive basement, and the Volcano-Sedimentary Unit (the overlying conductor

corresponding to the geothermal reservoir host rocks) across at least the southeastern caldera margin, confirming the suggestion that these units predate the Guayabo caldera.

The structure of the Guayabo caldera has been clarified by the gravity data. A 10 mGal negative anomaly is centred within the caldera, 3 km north-west of the geothermal borefield. The maximum rate of change in gravity gradient is 1-2 km inside the topographic margin and defines the steep faulted margins of the low density Pumice Unit. The Pumice Unit was drilled in only one borehole at a depth of 400-550 m and is the intra-caldera equivalent of the La Ese Pumice. The nature of the gravity field reflects the collapse of individual arcuate sectors with the greatest cumulative collapse in the centre. The latest subsidence events post-date most of the intra-caldera stratigraphy, and occurred across faults that are broadly coincident with the present topographic margins. The elongation of the gravity low across the western edge of the southern caldera margin is likely to reflect an initial subsidence of the Guayabo caldera along a preferential north-south axis, into which the Pumice Unit (and possibly the earlier two tuffs) were concentrated. Later subsidence was concentrated within the present caldera margins, cross-cutting the initial north-south trend. Yet further north-south subsidence has occurred in the eastern part of the main caldera to form the Aguas Claras and La Fortuna grabens.

The maximum positive gravity anomaly is located on the eastern caldera margin at Bajo Los Chiqueros, the site of the most voluminous late- and post-caldera stratocone activity, and the anomaly is therefore interpreted as a dense intrusive complex.

These views are the best available reconciliation of the geophysical data and the stratigraphic data studied and revised by this study. In summary most of the stratigraphy within the borefield *pre-dates* the formation of the present expression of the Guayabo caldera. This contrasts strongly with previous models (e.g. ELC, 1986 a) where the entire drilled stratigraphy was thought to be part of the caldera fill. Geochemical studies of the intra- and extra-caldera tuffs would clarify some of the proposed correlations. Isopach maps of the outflow tuffs should be made, together with a size distribution study of the pumice and lithic fractions, to pinpoint the source vents within the caldera area.

6.3 The implications for the Miravalles Geothermal Field

Density determinations of over 500 samples of borehole cuttings have shown that the high temperature hydrothermal alteration assemblages of the liquid-dominated reservoir cause an increase in density, whereas the argillic zones that are characteristic of the vapour and boiling zones cause a density decrease. The former effects of propylitization are more important to the overall density structure, and are partially responsible for the gravity high over the northern high temperature field. The lithological density contrasts described above, however, are found to cause most of the observed gravity anomalies. The gravity high at the PGM-4 site cannot be explained by either the presence of the low permeability Acidic Andesite Unit or hydrothermal propylitization; an intermediate intrusive body below a depth of ~700 m is proposed instead. The model implies that only the deep permeability should be reduced, serving to direct the hydrothermal outflow plume upwards. This is in agreement with both the heat flow anomaly and neutral chloride springs observed at La Fortuna.

The revised model for the Guayabo caldera suggests that the presently defined reservoir host rocks, the pre-caldera Ignimbrite and Volcano-Sedimentary Units, continue beneath the southeastern caldera margin. The most important structural control on the outflow plume in this area is therefore not the caldera margin, but the more recent La Fortuna graben, together with the proposed deep intrusive body. Given the high permeability encountered in the nearby well PGM-12, the reservoir permeability in this southern area should be sufficient for exploitation. The deciding factors will be two adverse effects; the drop in temperature along the outflow plume, and the lower wellhead elevations with respect to the power plant sited further to the north, close to PGM-3.

6.4 The structure of the Guanacaste Arc

The compiled gravity data show that, unsurprisingly, the gravity anomalies are largely related to volcanic structure. The general pattern reflects the density contrast between the sites of stratovolcano formation and those of volcano-tectonic depressions. The Guanacaste Arc basement rocks comprise a dense ophiolitic suite that is commonly exposed along the outer arc, to the south of the Late Cretaceous to Miocene Santa Elena suture, but similar

rocks were only recently identified behind the arc in the southern part of the cross-cutting post-Miocene Nicaraguan Depression. The trans-arc traverse, through the Guayabo caldera and across Volcán Miravalles, shows a major gravity couple behind the arc, associated with the inner margin of the Nicaraguan Depression. The 35 mGal gravity couple is most reasonably modelled in terms of at least 1 km throw across the southern margin with a density contrast of - 0.75 Mg m^{-3} between the footwall and the low density fill of the Depression. The high is not located over the topographic ridge but over the foot of the scarp; an extension of the lava-dominated ridge cannot therefore explain the high density, and the buried footwall is thought to be a near surface outcrop of the basement.

The observed and modelled occurrences of the basement behind the arc are all to the south of the proposed eastward continuation of the Santa Elena suture. The basement to both the Guanacaste Arc and back-arc may have been upthrown to the south of the suture, relative to the southern Nicaraguan basement, as observed on the outer arc. Subsequently, uplift of the inner margin footwall of the cross-cutting Nicaraguan Depression brought the basement closer to the surface. The proposed basement model is preliminary and the present limits of the gravity data over and behind the arc in northern Costa Rica need to be extended towards Nicaragua to further examine the correct location and orientation of the divide between northern Costa Rica and southern Nicaragua.

No regional gravity gradient, associated with the geometry of the subduction zone, is identified across the arc. Furthermore, there is no evidence for the low density silicic plutonics that are characteristic of the Miocene geology of southern Costa Rica and responsible for the regional gravity low there. The abundant evidence for high level silicic activity in Guanacaste, from the Santa Rosa Ignimbrite Plateau, is not therefore matched by evidence for deep seated equivalents. It is suggested, in agreement with previous proposals, that there is a marked contrast between the crustal state of Guanacaste and the rest of Costa Rica, the latter being in a more advanced state of transition towards continental crust.

6.5 The implications for caldera studies

Gravity studies over calderas have traditionally been used to distinguish funnel-shaped from piston-shaped collapse structures, but it has been shown during the analysis of the data over the Guayabo caldera that it is possible to define smaller scales of structural detail that are pertinent to the collapse mechanism debate. The multi-stage collapse of the Guayabo caldera floor across discrete, concentric sets of well spaced ring fractures, with the earliest - and maximum cumulative - subsidence in the centre, has resulted in an apparently funnel-shaped structure. This contradicts some previous suggestions that funnel structures, typical of the Japanese calderas for example, formed by chaotic collapse of the floor, rather than across discrete sets of ring faults. It is suggested that detailed, constrained gravity studies should be conducted at other so-called funnel calderas, especially in Japan where many have been drilled for geothermal resources.

The timing of subsidence is crucial to the understanding of the cause of collapse. Collapse due to evacuation of the sub-caldera magma chamber during eruption of the outflow tuffs predicts a balance between the caldera volume and the DRE volume of the erupted products. Often the greatest uncertainties are the volume of the buried part of the caldera and the mass of erupted material therein. A gravity low, associated with the density contrast between the wallrock and the fill, is commonly observed over silicic calderas. The integrated mass deficiency can therefore be used to constrain both the mass and volume of the caldera fill and a new balance model is proposed, based on this principle. The model is sensitive to density uncertainties only when the wallrock to fill density contrast is $< \sim 0.30$ Mg m^{-3}, which is lower than the values usually observed. Because the intra-caldera lithics are largely derived from the wallrock, the gravity anomaly is proportional to the volume of the juvenile material, regardless of the lithic content. The model therefore accounts for the lithic fraction of the caldera fill, without requiring the actual fraction to be constrained.

The balance model showed that a simple collapse mechanism cannot explain the observed mass and volume distributions at both the Guayabo and Aira calderas. The mass of erupted material at Guayabo is insufficient to explain the caldera volume. Post-tuff subsidence is

proposed, in agreement with the stratigraphic and geophysical evidence for late stage movement on the topographic margin ring faults. This subsidence is thought to be related to magma withdrawl during the late development of the stratocone complex on the eastern caldera margin. At Aira, on the other hand, the erupted volume *exceeds* the volume of collapse that was proposed to have accompanied the eruptions. The Aira case does balance, however, if the volume of the caldera depression is attributed to the caldera, rather than partially to the previously proposed pre-caldera depression. The balance model will be tested at other suitable silicic calderas, including the piston-type, to assess the extent to which caldera volume is truly the result magma extraction.

6.6 Repeat gravity monitoring at Miravalles

Repeat gravity monitoring of exploited geothermal fields is already a well established technique, but the non-exploitation related mass changes are not always sufficiently constrained, resulting in ambiguous interpretations of the reservoir evolution. The Miravalles field is currently in the pre-production development stage, and therefore provided an ideal opportunity to isolate possible mass changes that are unrelated to fluid extraction. Variations of up to 40 μGal have been observed, over a period of a few months, in the relative gravity between the base station at Guayabo and both the geothermal field and other areas. The spatial and temporal patterns suggest that the variations are due to fluctuations in the water table, both in the field and more importantly at the base station. Future monitoring will therefore need to assess even short-term groundwater movements.

During the 1988 borehole production tests, apparent gravity increases of up to ~100 μGal were observed following well closure. The mass changes required to explain the gravity data, however, were at least two orders of magnitude greater than the fluid produced and furthermore, similar gravity changes were not identified during similar tests in 1989. Later experiments showed that one of the LaCoste and Romberg gravimeters used during the well tests, G-105, recorded apparently stable gravity decreases of up to 700 μGal when subjected to controlled vibration. For a given signal amplitude, the greatest decreases were observed at a frequency of 37.5 Hz, and lesser decreases were observed at the 1st and 2nd harmonics. The specific response to harmonics, coupled with the fact that the apparent

displacements were always negative, suggests that the effective gravimeter spring length is shortened by the generation of standing waves. The apparent well test gravity changes can be explained by the vibration caused by the rapid fluid flow in the wellhead. The implications are that an apparently stable gravity reading may be displaced from true gravity if noise levels, at the correct frequency (s), are present. Further experiments are planned to determine the response of G-105 and other L&R gravimeters to both single and multiple frequencies, thus reproducing true noise which is made up of several components.

The Miravalles reservoir simulation models of ELC (1988) have been used to predict the gravity changes that should accompany exploitation. The end member simulation models are polarised into i) an optimistic assumption of deep recharge, sensitive to the permeability and the pressure gradient across the reservoir margins, and ii) a pessimistic outlook where the reservoir is a closed system with no recharge. In both cases, exploitation results in a pressure decline and subsequent expansion of the vapour zone at the expense of the underlying liquid-dominated reservoir. The expansion will be greatest in the PGM-10 area, where fluid conditions are presently closest to the boiling curve, and this site should therefore be accompanied by the maximum gravity decrease. The simulation models suggest that the fluid extraction rates required for the first 55 MW plant will be insufficient to cause a significant gravity changes in the first four years. After four years, however, when the second plant is planned to come on line, pressure drawdown will be a maximum and gravity decreases of up to 80-100 mGal are to be expected within the fifth year, with further decreases of between 15 and 20 μGal yr^{-1} thereafter.

Gravity monitoring can therefore be used to test and complement the reservoir simulation models of ELC (1988), and a program has been recommended. The main reference station should be outside the caldera area, but accessible by road and at a similar elevation to the borefield to reduce gravimeter hysteresis errors; the proposed site is immediately to the west of the caldera. The station network should extend beyond the proposed borefield limits so that the effects of recharge can be examined. Most importantly, both a rigourous levelling program and several shallow wells at the base and in the field to check groundwater fluctuations should be be included.

References

Adamek, S. and Tajima, F. (1987) Seismic rupture associated with subduction of the Cocos ridge. *Tectonics* **6, No. 6** 757-774.

Allis, R.G. and Hunt, T.M. (1986) Analysis of exploitaion-induced gravity changes at Wairakei Geothermal Field. *Geophysics* **51, No. 8** 1647-1660.

Alvarado, G. and Argueta, S. (1988) Primeros resultados de las redes de nivelacion y de los inclinometros secos en el Campo Geotermal de Miravalles. *Report for the Departamento de Geología, Instituto Costarricense de Electricidad, San Jose, Costa Rica.*

Alvarado, G., Chiesa, S., Civelli, G., Locati, U., Mainieri, A., Mora, O. and Pecchio, M. (1990 a) Geovolcanologia del area Chorotega hoja Tierras Morenas, Guanacaste, Costa Rica. *Proceedings of the 1990 Congresso Centroamericano, San Jose, Costa Rica.*

Alvarado, G., Chiesa, S., Civelli, G., Locati, U., Mainieri, A., Mora, O. and Pecchio, M. (1990 b) Evolucion geovolcanologica del complejo caldera de Guayabo-Volcán Miravalles. *Proceedings of the 1990 Congresso Centroamericano, San Jose, Costa Rica.*

Aramaki, S. (1984) Formation of the Aira Caldera, Southern Kyushu, ~22,000 years ago. *J.G.R.* **89, No. B10** 8485-8501.

Atkinson, P.G. and Pederson, J.R. (1988) Using precision gravity data in geothermal reservoir enfineering modelling studies. *Proceedings of the Workshop on Geothermal Reservoir Engineering, January 19-21, Stanford UNiversity, California.*

Baba, K. (1975) Gravimetric survey of geothemal areas in Kurikoma and elsewhere in Japan. *Proc. Geothermal Resources, 2nd U.N. Symp. on Development of Geothermal Resources* 2 865-870.

Bacon, C.R. (1983) Eruptive history of Mount Mazama and Crater Lake Caldera, Cascade Range, U.S.A. *J.V.G.R.* **18** 57-115.

Baker, T.F. (1984) Tidal deformations of the Earth *Sci. Prog., Oxford* **69** 197-233.

Bargar, K. and Fournier, R.O. (1988) Fluid-inclusion evidence for previous higher temperatures in the Miravalles Geothermal Field, Costa Rica. *Geothermics* **17 No. 5/6** 681-693.

Bellon, H. and Touron, J. (1978) Contribution de la géochronométrie K-Ar à l'étude du magmatisme de Costa Rica, Amérique Centrale *Bull. Soc. Géol. France* **7, t. XX, No 6** 955-959.

Bergoeing, J. (1982) Dataciones radiométricas de algunas muestras de Costa Rica. *Inf. Sem. Enero-Julio, Inst. Geogr. Nac., San Jose , Costa Rica* 71-86.

Berrangé, J.P. and Thorpe, R.S. (1988) The geology, geochemistry and emplacement of the Cretaceous-Tertiary ophilolitic Nicoya Complex of the Osa Peninsula, southern Costa Rica. *Tectonophysics* **147** 193-220.

Blackwell, D.D. (1985) A transient model of the geothermal system of the Long Valley caldera, California. *J.G.R.* **90, No. B13** 11229-11241.

Blackwell, D.D., Granados, E.G. and Koenig, J.B. (1977) Heat flow and geothermal gradient exploration of geothermal areas in the Cordillera de Guanacaste of Costa Rica. *Geoth. Res. Counc. Trans.* **1** 17-18.

Blake, S. (1981) Eruptions from zoned magma chambers. *J. geol. Soc. London* **138** 281-287.

Bottinga, Y. and Weill, D.F. (1970) Densities of liquid silicate systems calculated from partial molar volumes of oxide components. *Am. J. Sci.* **269** 169-182.

Bourgois, J., Azema, J., Baumgartner, P.O., Tournon, J., Desmet, A. and Aubouin, J. (1984) The geologic history of the Caribbean-Cocos Plate boundary with special reference to the Nicoya Ophiolite complex (Costa Rica) and D.S.D.P. ressults (Legs 67 and 84 off Guatemala): a synthesis. *Tectonophysics* **108** 1-32.

Bowin, C. (1976) Carribean Gravity Field and plate tectonics. *Geol. Soc Sp. Pap.* **169** 1-79.

Brouke, R.A., Zurn, W.E. and Slichter, L.B. (1972) Lunar tidal acceleration on a rigid Earth. *Geophys. Mongr. Ser. Am. Geophy. Un.* **16** 319-324.

Brown, G.C., Everett, S.P., Rymer, H., McGarvie, D.W. and Foster, I. (1991) New light on caldera evolution-Askja, Iceland. *Geology* **19** 352-355.

Brown, G.C., Hallinan, S.E. and Rymer, H. (1988) Geophysical assistance in geothermal field assessment and monitoring, Miravalles, Costa Rica. *Overseas Development Administration Interim Report No. 1 (contract FnI 8788/541/093), Open University, Milton Keynes, England.*

Brown, G.C., Rymer, H. and Thorpe, R.S. (1987) The evolution of andesite volcano structures: new evidence from gravity studies in Costa Rica. *E.P.S.L.* **82** 323-334.

Carle, S.F. (1988) Three-dimensional gravity modelling of the geologic structure of Long Valley Caldera. *J.G.R.* **93, No. B11** 13237-13250.

Carr, M., Rose, W.I. and Stoiber, R.E. (1984) Central America. *In Thorpe, R.S. (ed.) Andesites: Orogenic andesites and related rocks. Wiley.* 149-166.

Cas, R.A. and Wright, J.V. (1987) Volcanic successions: ancient and modern. *Allen and Unwin.*

Chiesa, S., Corella, M. and Mora, O. (1987) Geologia de la Meseta Ignimbritica de Santa Rosa, Guanacaste, Costa Rica. *Report for the Instituto Costarricense de Electricidad, San Jose, Costa Rica.*

Chiesa, S. (1991) El Flujo de Pomez Biotitica del Rio Liberia (Guanacaste) Costa Rica, America Central. *Revista Geologia de America Central (in press).*

Christiansen, R.L. (1984) Yellowstone magmatic evolution: its bearing on understanding large-volume explosive volcanism. *In: Boyd (ed.), Studies in Geophysics: Explosive Volcanism: Inception, Evolution, and Hazards.* 84-95.

Cole, J.W. (1990) Structural control and origin of volcanism in the Taupo volcanic zone, New Zealand. *Bull. Volcanol.* **52** 445-459.

Cordell, L. (1978) Regional geophysical setting of the Rio Grande rift. *Geol.Soc.Am.Bull.* **89** 1037-1090.

Cordell, L., Long, C.L. and Jones, D.W. (1985) Geophysical expression of the batholith beneath Questa Caldera, New Mexico. *J.G.R.* **90, No. B13** 11263-11269.

Corrales, M.F., Koenig, J.B. and Kuwada, J.T. (1977) Exploration of the Guanacaste, Costa Rica, geothermal system. *Geoth. Res. Counc. Trans.* **1** 57-58.

Dalrymple, G.B. and Lanphere, M.A. (1969) Potassium -Argon dating. Principles, techniques and applications to geochronology. *Freeman, 250 pp..*

deBoer, J. (1979) The outer arc of the Costa Rican orogen (oceanic basement complexes of the Nicoya and Santa Elena Peninsulas). *Tectonophysics* **56** 221-259.

deBoer, J.Z., Defant, M.J., Stewart, R.H., Restrepo, J.F., Clark, L.F. and Ramirez, A.H. (1988) Quaternay calc-alkaline volcanism in western Panama: regional

variation and implication for the plate tectonic framework. *J. South Am. Earth Sci.* **1, No. 3** 275-293.

Deer, W.A., Howie, R.A. and Zussman, J. (1966) An introduction to the rock-forming minerals. *Longman.*

Dengo, G. (1962) Tectonic-igneous sequences in Costa Rica. *In Petrological Studies, A.F. Buddington volume. Geol. Soc. Am.* 133-161.

Dennis, B.R., Lawton, R.G., Kolar, J.D. and Alvarado, A. (1989) Results of investigation at the Miravalles Geothermal Field, Costa Rica. Part 1: Well logging. *Los Alamos National Laboratory, New Mexico.* **Report LA-11510-MS, Part 1.**

Di Filippo, M., Geri, G., Marson, I., Palmieri, F., Rossi, A. and Toro, B. (1983) Microvariazoni dela gravita in Italia con particolare riguarado all'area geotermica di Travale. *Proc. II Meeting GNGTS, Rome.*

DiPippo, R. (1986) Geothermal energy developments in Central America *Geoth. Res. Council Bull.* **15, No. 10** 3-14.

Donaldson, I.G. (1982) Heat and mass circulation in geothermal systems. *Ann Rev. Earth Planet. Sci.* **10** 377-95.

Dondanville, R.F. (1978) Geologic characteristics of the Valles Caldera geothermal system, New Mexico. *Trans. Geoth. Res. Council* **2** 157-160.

Dóndoli, C. (1950) Liberia y sus alredores. *Minesterio de Agricultura e Industrias de Costa Rica, Bol. Téc.* **3** 7pp.

Druitt, T.H., Sparks, R.S.J. (1984) On the formation of calderas during ignimbrite eruptions. *Nature* **310** 679-681.

Duprat, A. (1987) Geophysics in Geothermal Prospecting. *In Economides, M. and Ungemach, P. (eds.) Applied Geothermics. Wiley.*

Duprat, A. and Leandro, G. (1986) Informe geofisico para la factibilidad, Proyecto Geotermico Miravalles. *Unpublished report, ICE, San Jose, Costa Rica..*

Eaton, G.P., Christiansen, R.L., Iyer, H.M., Pitt, A.M., Mabey, D.R., Blank, H.R., Jr., Zietz, I. and Gettings, M.E. (1975) Magma beneath Yellowstone National Park. *Science* **188, No. 4190** 787-796.

Economides, M. and Ungemach, P. (1987) Applied Geothermics. *Wiley.*

Eggers, A.A. (1987) Residual gravity changes and eruption magnitudes. *J.V.G.R.* **33** 201-216.

Eichelberger, J.C., Ballard, S., Carrigan, C.R., Goodliffe, A., Hildreth, W., Iwatsubo, E., Kasamayer, P.W., Keith, T.E.C., Kienle, J., Papike, J.J., Pollard, D.D., Stone, D.B., Wallmann, P.C., Ward, P.L., Wilt, M. and Yount, M.E. (1990) Geophysics at Katmai. *Eos* **71** 733-735.

ELC (1983) Informe geológico y volcanológico. *Electroconsult, Milan* **GMV-D-5828.**

ELC (1988) Informe de factabilidad, Planta Geotérmica Miravalles, 2a. unidad. *Electroconsult, Milan* **GMV-D-7023.**

ELC (1984 a) Pozo PGM-5-Informe de porforación y control geológico. *Electroconsult, Milan* **GMV-D-6056.**

ELC (1984 b) Pozo PGM-5R-Informe de porforación y control geológico. *Electroconsult, Milan* **GMV-D-6202.**

ELC (1984 c) Pozo PGM-10-Informe de porforación y control geológico. *Electroconsult, Milan* **GMV-D-6113.**

ELC (1985 a) Pozo PGM-11-Informe de porforación y control geológico. *Electroconsult, Milan* **GMV-D-6206.**

ELC (1985 b) Estudio geológico y estructural de detalle. *Electroconsult, Milan* **GMV-D-6077.**

ELC (1985 c) Pozo PGM-12-Informe de porforación y control geológico. *Electroconsult, Milan* **GMV-D-6601.**

ELC (1986 a) Informe geológico fínal, Proyecto Geotermico Miravalles. *Electroconsult, Milan* **GMV-D-6436.**

ELC (1986 b) Pozo PGM-15-Informe de porforación y control geológico. *Electroconsult, Milan* **GMV-D-6376.**

Elston, W.E. (1984) Mid-Tertiary ash flow cauldrons, Southwestern New Mexico. *J.G.R.* **89, No. B10** 8733-8750.

ESDU (1968) Thermal conductivity, viscosity, heat capacity, density and Prandtl number of solid, liquid and gasoeus heavy water. *In Physical data, Mechanical Engineering sub-series* **1 No. 68023.**

Finn, C. and Williams, D.L. (1982) Gravity evidence for a shallow intrusion under Medicine Lake volcano, California. *Geology* **10** 503-507.

Fischer, R. (1980) Recent tectonic movements of the Costa Rican Pacific coast. *Tectonophysics* **70** 25-33.

Fournier, R.O. (1987) Conceptual models of brine evolution in magmatic-hydrothermal systems. In Volcanism in Hawaii. *U.S.G.S. Prof. Paper* **1350** 1487-1506.

Fournier, R.O., Sorey, M.L., Mariner, R.H. and Truesdell, A.H. (1979) Chemical and isotopic prediction of aquifer temperatures in the geothermal system at Long Valley, California. *J.V.G.R.* **5** 17-34.

Fridrich, C.J. (1990) 3-D structure of the deeply dissected Grizzly Peak cadlera, Colorado: a bridge between calderas and ring complexes. *Eos, Trans AGU* **71 No. 43** 1676.

Furgerson, R.B. and Afonso, P.S. (1977) Electric investigations in the Guanacaste geothermal area (Costa Rica). *Geoth. Res. Counc. Trans.* **1** 99-102.

Galli-Oliver, C. (1979) Ophiolite and island-arc volcanism in Costa Rica. *Geol. Soc. Am. Bull.* **90** 444-452.

Geosystem (1988) Investigaciones geofisicas en el estudio de factibilidad del Proyecto Geotermico Miravalles, informe final..

Gillot, P-Y, Chiesa, S. and Alvarado, G. (1990) Chronoestratigraphia y evolucion del volcanismo Plio-Pleistocenico del norte de Costa Rica. *Proceedings of the 1990 Congresso Centroamericano, San Jose, Costa Rica.*

Goff, F., Shevenell, L. and Gardner, J.N. (1988) The hydrothermal outflow plume of Valles caldera, New Mexico, and a comparison with other outflow plumes. *J.G.R.* **93, No. B6** 6041-6058.

Grigsby, C.O., Goff, F., Trujillo, P.E.Jr., Counce, D.A., Dennis, B., Kolar, J. and Corrales, R. (1988) Results of investigation at the Miravalles Geothermal Field, Costa Rica. Part 2: Downhole fluid sampling. *Los Alamos National Laboratory, New Mexico.* **Report LA-11510-MS, Part 2.**

Grindley, G.W. (1965) The geology, structure, and exploitation, of the Wairakei geothermal field, Taupo, New Zealand. *Bull. N.Z. Department of Scientific and Industrial Research* **75** 11-127.

Gudmundsson, A. (1987) Lateral magma flow, caldera collapse, and a mechanism of large eruptions in Iceland. *J.V.G.R.* **34** 65-78.

Gudmundsson, A. (1988) Formation of collapse calderas. *Geology* **16** 808-810.

Hallinan, S.E., Brown, G.C. and Rymer, H. (1988) Microgravity monitoring at the Miravalles geothermal field-some preliminary results. *Proc. 10th. N.Z. Geothermal Workshop* 145-149.

Hallinan, S.E., Rymer, H. and Brown, G.C. (1989) Geophysical assistance in geothermal field assessment and monitoring, Miravalles, Costa Rica. *Overseas Development Administration Interim Report No. 3 (contract FnI 8788/541/093), Open University, Milton Keynes, England.*

Hammer, S. (1939) Terrain corrections for gravimeter stations *Geophysics* **4** 184-194.

Hantke, G. (1951) Uebersicht über die vulkanische tätigkeit, 1941-1947 *Bull. Volcanol.* **11** 161-208.

Hass, J.L. (1971) The effect of salinity on the maximum thermal gradient of a hydrothermal system at hydrostatic pressure. *Econ. Geol.* **66** 940-946.

Heiken, G. and McCoy, F. Jr. (1984) Caldera development during the Minoan eruption, Thira, Cyclades, Greece. *J.G.R.* **89, No. B10** 8441-8462.

Henley, R.W. and Ellis, A.J. (1983) Geothermal systems ancient and modern: a geochemical review *Earth-Science Reviews* **19** 1-50.

Hildreth, W. (1990) The Katmai eruption of 1912: was the magma stored beneath Novarupta, Trident, or Mount Katmai? Petrochemical and temporal evidence. *Eos, Trans.* **71 No. 43** 1691.

Hulen, J.B. and Nielson, D.L. (1986) Hydrothermal alteration in the Baca Geothermal System, Redondo Dome, Valles Caldera, New Mexico. *J.G.R.* **91 No. B2** 1867-1886.

Hunt, T.M. (1970) Net mass loss from the Wairakei geothermal field, New Zealand *Geothermics* **Special Issue 2** 487-491.

Hunt, T.M. (1977) Recharge of water in Wairakei geothermal field determined from repeat gravity measurements. *N.Z. J. Geol. and Geophys.* **20, No. 2** 303-317.

Hunt, T.M. (1987) Recharge at Broadlands Geothermal Field 1967-1983 determined from repeat gravity measurments. *Geophysics Division, Dept. of Scientific and Industrial Research, Wellington, N.Z.* **Research Report No. 216,.**

Hunt, T.M. (1988) Exploitation-induced gravity changes in New Zealand geothermal fields. *Bureau Gravimetrique International, Bulletin d'Information* **62** 72-85.

Ishihara, K. (1990) Pressure sources and induced ground deformation associated with explosive eruptions at an andesitic volcano: Sakurajima volcano, Japan. *In Ryan, M.P. (ed.), Magma Transport and Storage.* 335-356.

Iyer, H.M. (1984) Geophysical evidence for the locations, shapes and sizes, and internal structures of magma chambers beneath regions of Quaternary volcanism. *Phil. Trans. R.Soc. Lond.* **A310** 473-510.

Jachens, R.C. and Roberts, C.W. (1985) Temporal areal gravity investigations at Long Valley caldera, California. *J.G.R.* **90, No. B13** 11210-11218.

Kamata, H. (1989) Shishimuta caldera, the buried source of the Yabakei pyroclastic flow in Hohi volcanic zone, Japan. *Bull. Volcanol.* **51** 41-50.

Kane, M.F., Mabey, D.R. and Brace, R. (1976) A gravity and magnetic investigation of the Long Valley Caldera, Mono County, California. *J.G.R.* **81, No. 5** 754-762.

Kearey, P. and Brooks, M. (1984) An Introduction to Geophysical Exploration. *Geoscientific Texts, Blackwell.*

Koenig, J. (1980) Technical feasibility report of geological and geophysical findings. *GeothermEx, Inc., Berkeley, California.*

Kuijpers, E.P. (1980) The geologic history of the Nicoya Ophiolite complex, Costa Rica, and its geotectonic significance. *Tectonophysics* **68** 233-255.

Kuno, H., Oki, Y., Ogino, K. and Hirota, S. (1970) Structure of Hakone caldera as revealed by drilling. *Bull. Volcanal.* **34** 713-725.

Leandro, G., Lopez, A., Lezema, G. and Alvarado, G. (1988) Sintesis del modelo geólogico-geofísico del Campo Geotermico Miravalles *Report for the Departamento de Geología, Instituto Costarricense de Electricidad, San Jose, Costa Rica..*

Lehman, J.A., Smith, R.B. and Schilly, M.M. (1982) Upper crustal structure of the Yellowstone Caldera from seismic delay time analyses and gravity correlations. *J.G.R.* **87, No. B4** 2713-2730.

LeMaitre, R.W. (1989) A classification of igneous rocks and glossary of terms. *Blackwell.*

Lezema, G., Alvarado, A. and Mainieri, A. (1988) Modelo geológico-geofísico de la parte sur del Campo Geotérmico de Miravalles. *Report for the Departamento de Geología, Instituto Costarricense de Electricidad, San Jose, Costa Rica..*

Lipman, P.W. (1984) The roots of ash flow calderas in western North America: windows into the tops of granitic batholiths. *J.G.R.* **89, No. B10** 8801-8841.

Lipman, P.W., Self, S. and Heiken, G. (1984) Introduction to Calderas Special Issue *J.G.R.* **89, No. B10** 8219-8221.

Mahood, G. and Hildreth, W. (1983) Nested calderas and trapdoor uplift at Pantelleria, Strait of Sicily. *Geology* **11** 722-726.

Mainieri, A., Granados, E., Corrales and R., Vaca, L. (1985) Miravalles geothermal field, Costa Rica. Technical report. *Transactions of the Geothermal Resources Council* **9, Part 1** 279-283.

Malfait, B.T. and Dinkelman, M.G. (1972) Circum-Caribbean tectonic and igneous activity and the evolution of the Caribbean Plate. *Geol. Soc. Am. Bull.* **83** 251-272.

Marhino de Carvalho, J. Jr. and Erwes, W. (1977) Reduction tables and diagrams for barometric measurements with Thommen altimeters. *Revue Thommen AG, Thommen Instrument Dept., CH-4437 Waldenberg, Switzerland.*

Matumoto, T., Ohtake, M., Latham, G. and Umana, J. (1977) Crustal structure in southern Central America. *Bull. Seis. Soc. Am.* **67, No. 1** 121-131.

Melson, W.G., Barquero, H., Saenz, R. and Fernandez, E. (1986) Erupciónes explosivas de importancia en volcanes de Costa Rica *Bol Vulcanol. (Costa Rica)* **16** 15-19.

Milodowski, A.E., Savage, D., Bath, A.H., Fortey, N.J., Nancarrow, P.H.A. and Shepherd, T.J. (in prep.) Hydrothermal mineralogy in geothermal assessment: Studies of Miravalles Field, Costa Rica and experimental simulations of hydrothermal alteration. *Report WE/89/63, British Geological Survey, Keyworth..*

Minster, J.B. and Jordan, T.H. (1978) Present-day plate motions. *J.G.R.* **83, No. B11** 5331-5354.

Miyamura, S. (1975) Recent crustal movements in Costa Rica disclosed by relevelling surveys. *Tectonophysics* **29** 191-198.

Molnar, P. and Sykes, L.R. (1969) Tectonics of the Caribbean and Middle America regions from focal mechanisms and seismicity. *Geol. Soc. Am. Bull.* **80** 1639-1684.

Mora, O. (1988) Estudio geologico-petrologico de las piroclasticas en los alredores de Bagaces, Provincia de Guanacaste, Costa Rica *Unpublished tesis de Licenciatura, Universidad Nacional, Heredia, Costa Rica. 61 pp.*

Murase, T. and McBirney, A.R. (1973) Properties of some common igneous rocks and their melts at high temperatures. *Geol. Soc. Am. Bull.* **84** 3563-3562.

Newhall, C.G. and Dzurisin, D. (1988) Historical unrest at large calderas of the world. Volume 2. *U.S.G.S. Bull.* **1855.**

Nettleton, L. (1939) Determination of density for reduction of gravimeter observations. *Geophysics* **4** 176-183.

Nishimura, S., Abe, E., Nishida, J., Yokoyama, T., Dharma, A., Hehanussa, P. and Hehuwat, F. (1984) A gravity and volcanostratigraphic interpretation of the Lake Toba region, North Sumatra, Indonesia. *Tectonophysics* **109** 253-272.

Olsen, K.H., Braile, L.W., Stewart, J.N., Daudt, C.R., Keller, G.R., Ankeny, L.A. and Wolff, J.J. (1986) Jemez Mountains Volcanic Field, New Mexico: time term interpretations of the CARDEX Seismic Experiment and comparison with Bouguer gravity. *J.G.R.* **91, No. B6** 6175-6187.

Omori, F. (1916) The Sakurajima eruptions and earthquakes II and III. *IMP. Earthquake Invest. Comm. Bull.* **8** 2,3.

Peccerillo, A. and Taylor, S.R. (1976) Geochemistry of Eocene calc-alkaline volcanic rocks from the Kastamoun area, northern Turkey. *Contrib. Min. Pet.* **58** 63-81.

Pedley, R. (1990) GRAVMAG-User Manual *Integrated Geophysical Services, BGS, Keyworth, England.*

Peterson, P.S. and Rose W.I. Jr. (1985) Explosive eruptions of the Ayarza caldera, southeastern Guatemala. *J.V.G.R.* **25** 289-307.

Pilcher, H. and Weyl, R. (1975) Magmatism and crustal evolution in Costa Rica (Central America). *Geol. Rundsch.* **64** 457-475.

Poppe, L.J., Paull, C.K., Newhall, C.G., Bradbury, J.P. and Ziagos, J. (1985) A geophysical and geological study of Laguna De Ayarza, a Guatemalan caldera lake. *J.V.G.R.* **25** 125-144.

Potts, P.J., Webb, P.C. and Watson, J.S. (1984) Energy-Dispersive X-Ray Flourescence analysis of silicate rocks for major and trace elements. *X-Ray Spectrometry* **13 No. 1** 2-14.

Rapolla, A., Fedi, M. and Fiume, G. (1989) Crustal structure of the Ischia-Phlegrean geothermal fields, near Naples, Italy, from gravity and aeromagnetic data. *Geophysical Journal* **97** 409-419.

Reeder, J.W. (1987) Formation of geothermal resources at Lithospheric subduction zones. *In Economides, M. and Ungemach, P. (eds.) Applied Geothermics. Wiley.*

Risk, G.F., Groth, M.J., Rayner, H.H., Dawson, G.B., Bibby, H.M., MacDonald, W.J.P. and Hewson, C.A.Y. (1977) The resistivity boundary of the Broadlends geothermal field. *Report 123, Department of Scientific and Industrial Research (Geophysics Division), Wellington, New Zealand.*

Rochelle, C.R. (1991) Rock-fluid interactions in the Miravalles Geothermal Field, Costa Rica; mineralogical and experimental studies. *Unpubl. Ph.D. University of Leeds..*

Rundle, J.B. and Hill, D.P. (1988) The geophysics of a restless caldera-Long Valley, California. *Ann. Rev. Earth Planet. Sci.* **16** 251-271.

Rymer, H. (1985) Gravity studies of sub-surface structure and evolutionof active volcanoes in Costa Rica. *Unpub. Ph.D. Open University, U.K.*

Rymer, H. (1989) A contribution to precision microgravity data analysis using Lacoste and Romberg gravity meters. *Geophys. J.* **97** 311-322.

Rymer, H. and Brown, G.C. (1986) Gravity fields and the interpretation of volcanic structures: geological discrimination and temporal evolution. *J.V.G.R.* **27** 229-254.

Rymer, H., Hallinan, S.E. and Brown, G.C. (1989) Geophysical assistance in geothermal field assessment and monitoring, Miravalles, Costa Rica. *Overseas Development Administration Interim Report No. 2 (contract FnI 8788/541/093), Open University, Milton Keynes, England.*

Sandberg, C.H. (1958) Terrain corrections for an inclined plane in gravity computations. *Geophysics* **23** 701-711.

Scandone, R. (1990) Chaotic collapse of calderas. *J.V.G.R.* **42** 285-302.

Segar, R.L. (1974) Quantative gravity interpretation, Valles caldera area, Sandoval and Rio Arriba Counties, New Mexico. *Union Oil Company, California, Open File Report No. NM/Baca-27.*

Self, S., Rampino, M.R., Newton, M.S. and Wolff, J.A. (1984) Volcanological study of the great Tambora eruption of 1815. *Geology* **12** 659-663.

Self, S and Rampino, M.R. (1981) The 1883 eruption of Krakatau. *Nature* **294** 699-704.

Self, S and Rampino, M.R. (1982) Comments on "A geophysical interpretation of the 1883 Krakatau eruption" by I. Yokoyama. *J.V.G.R.* **13** 379-386.

Seyfied, H., Astorga, A., Amann, H., Calvo, C., Kolb, W., Schmidt, H. and Winsemann, J. (1991) Anatomy of an evolving island arc: tectonic and eustatic control in the south Central American fore-arc area. *Spec. Publs. int. Ass. Sediment.* **12** 1-25.

Sigurdsson, H. and Carey, S. (1989) Plinian and co-ignimbrite tephra fall from the 1815 eruption of Tambora volcano. *Bull. Volcanol.* **51** 243-270.

Simkin, T. and Fiske, R.S. (1983) Krakatau 1883-the volcanic eruption and its effects. *Smithsonian Institution Press, Washington, D.C., 464 pp.*

Smith, R.B. and Braile, L.W. (1984) Crustal structure and evolution of an explosive silicic volcanic system at Yellowstone National Park. *In Boyd (ed.), Studies in Geophysics: Explosive Volcanism: Inception, Evolution, and Hazards.* 96-109.

Smith, R.B., Reilinger, R.E., Meertens, C.M., Hollis, J.R., Holdahl, S.R., Dzurisin, D., Gross, W.K. and Klingele, E.E. (1989) What's moving at Yellowstone? The 1987 crustal deformation survey from GPS, levelling, precision gravity and trilateration. *Eos, Trans. AGU* **70** No. 8 113-119, 123-125.

Smith, R.L. (1979) Ash-flow magmatism. *Geol. Soc. Am. Spec. Paper* **180** 5-27.

Smith, R.L. and Bailey, R.A. (1968) Resurgent Cauldrons. *Geol. Soc. Amer. Memoirs* **116** 613-662.

Smith, R.L., Bailey, R.A. and Ross, C.S. (1961) Structural evolution of the Valles Caldera, New Mexico, and its bearing on the emplacement of ring dykes. *Geological Survey Research 1961: Short papers in the geologic and hydrologic sciences* **Article 340** D145-D149.

Sparks, R.S.J. and Walker, G.P.L. (1977) The significance of vitric-enriched air-fall ashes associated with crystal-enriched ignimbrites. *J.V.G.R.* **2** 329-341.

Sparks, R.S.J., Meyer, P. and Sigurdsson, H. (1980) Density variation amongst mid-ocean ridge basalts: implications for magma mixing and the scarcity of primitive lavas. *E.P.S.L.* **46** 419-430.

Spera, F.J. and Crisp, J.A. (1981) Eruption volume, periodicity, and caldera area: relationships and inferences on development of compositional zonation in silicic magma chambers. *J.V.G.R.* **11** 169-187.

Stefánsson, V. and Steingrímsson, B. (1980) Geothermal logging, an introduction to techniques and interpretation..

Steven, T.A., Rowley, P.D. and Cunningham, C.G. (1984) Calderas of the Marysvale Volcanic Field, west central Utah. *J.G.R.* **89, No. B10** 8751-8764.

Stoiber, R.E. and Carr, M.J. (1973) Quaternary volcanic and tectonic segmentation of Central America *Bull. Volcanol.* **37** 304-325.

Suzuki-Kamata, K. and Kamata, H. (1990) The proximal facies of the Tosu pyroclastic-flow deposit erupted from Aso caldera, Japan. *Bull. Volcanal.* **52** 325-333.

Tsuboi, C. (1983) Gravity. *George Allen and Unwin*..

Uniras (1989) AGL/interpolations: user guide and reference manual, ISG 129. *UNIRAS, Soborg, Denmark*..

Uniras (1990) Unimap2000: user manual, ISG 141. *UNIRAS, Soborg, Denmark*..

VanBemmelen, R.W. (1939) The volcano-tectonic origin of Lake Toba (North Sumatra). *De Inginieur Nederlandsch-Indie* **6** 126-748.

VanNess Burbach, G., Frohlich, C., Pennington, W.D. and Matumoto, T. (1984) Seismicity and tectonics of the subducted Cocos Plate. *J.G.R.* **89, No. B9** 7719-7735.

VanRuymbeke, M. (1989) A calibration system for gravimeters using a sinusoidal acceleration resulting from a vertical peiodic movement. *Bull. Géod.* **63** 223-235.

Varga, R.J. and Smith, B.M. (1984) Evolution of the early Oligocene Bonanza caldera, northeast San Juan Volcanic Field, Colorado. *J.G.R.* **89, No. B10** 8679-8694.

Verbeek, R.D.M. (1885) Krakatau. *Govt. Press, Batavia, 495 pp*..

Walker, G.P.L. (1980) The Taupo Pumice: Product of the most powerful known (ultraplinian) eruption? *J.V.G.R.* **8** 69-94.

Walker, G.P.L. (1984) Downsag calderas, ring faults, caldera sizes, and incremental caldera growth. *J.G.R.* **89, No. B10** 8407-8416.

Walker, G.P.L. (1985) Origin of coarse lithic breccias near ignimbrite source vents. *J.V.G.R.* **25** 157-171.

Walker, G.P.L. (1989) Gravitational (density) controls on volcanism, magma chambaers and intrusions. *Aus. J. Earth Sci.* **36** 149-165.

Weyl, R. (1980) Geology of Central America. *Gebrüder Borntraeger, Berlin. 355 pp..*

White, D.E., Muffler, J.P. and Truesdell, A.H. (1971) Vapor-dominated hydrothermal systems compared with hot-water systems. *Econ. Geol.* **66** 75-97.

Williams, D.L. and Finn C. (1987) Evidence for a shallow pluton beneath the Goat Rocks Wilderness, Washington, from gravity and magnetic data. *J.G.R.* **92, No. B6** 4867-4880.

Williams, D.L. and Finn, C. (1985) Analysis of gravity data in volcanic terrain and gravity anomalies and subvolcanic intrusions in the Cascade Range, U.S.A., and at other selected volcanoes. *Society of Exploration Geophysicists.*

Williams, D.L., Abrams, G., Finn, C., Dzurisin, D., Johnson, D.J. and Denlinger, R. (1987) Evidence from gravity data for an intrusive complex beneath Mount St. Helens. *J.G.R.* **92, No. B10** 10207-10222.

Williams, H. (1941) Calderas and their origin. *Calif. Univ. Publ. Geol. Sci. Bull.* **21** 51-46.

Williams, H. (1942) The geology of Crater Lake National Park, Oregon, with a reconaissance of the Cascade Range southward to Mount Shasta. *Cernegie Innt. Washington Publ.* **540** 162 pp.

Williams, H. and McBirney, A.R. (1979) Volcanology *Freeman, Cooper, San Fransisco, Calif..*

Wilson, C.J.N. and Walker, G.P.L. (1985) The Taupo eruption, New Zealand. I. General aspects. *Phil. Trans. R. Soc. Lond. A.* **314** 199-228.

Wollard, G.P. and Strange, W.E. (1962) Gravity anomalies and the crust of the Earth in the Pacific Basin. In: MacDonald, G.A.; Crust of the Pacific Basin. *Geophys. Monog. Am. Geophys. Union* **6** 60-80.

Wunderman, R.L. and Rose W.I. (1984) Amatitlan, an actively resurging cauldron 10 km south of Guatemala City. *J.G.R.* **89, No. B10** 8525-8539.

Yokoyama, I. (1961) Gravity survey on the Aira Caldera, Kyushu, Japan. *Nature* **191** 966-967.

Yokoyama, I. (1963) Structure of caldera and gravity anomaly. *Bull. Volc.* **26** 67-72.

Yokoyama, I. (1981) A geophysical interpretation of the 1883 Krakatoa eruption. *J.V.G.R.* **9** 359-378.

Yokoyama, I. (1983) Gravimetric studies and drilling results at four calderas in Japan. *In: D. Shimozuru and I. Yokoyama (eds.), Arc Volcanism: Physics and Tectonics.* 29-41.

Yokoyama, I. (1987) A quantative consideration of several calderas for study of their formation. *Geofisica Internacional (Revista de la Union Geofisica Mexicana)* **26 No. 4** 487-498.

Yokoyama, I. (1989) Microgravity and height changes caused by volcanic activity: four Japanese examples. *Bull. Volcanol.* **51** 333-345.

Yokoyama, I. and Ohkawa, S. (1986) The subsurface structure of the Aira caldera and its vicinity in southern Kyushu, Japan. *J.V.G.R.* **30** 253-282.

APPENDIX 2 Major element geochemistry

The geochemical data used in Chapter 2 are given here. The data are from two sources; ELC (1983) and samples analysed for this study. Sample locations in Figure 2.5.

Location	Western and northern caldera wall										Cerro Mogote					
This study				CM1a	CM2	CM4	EC74	EC39	CLM4	EC49		CM6	CM7	CM9	CM10	CM11
ELC (1983)	22	23	24								5v					
SiO2	60.37	63.20	56.60	56.80	57.18	57.77	56.28	57.78	49.73	66.70	51.90	51.59	51.39	52.41	52.30	52.24
TiO2	0.67	0.66	0.70	0.76	0.76	0.75	0.72	0.73	0.87	0.51	0.63	0.73	0.85	0.76	0.77	0.78
AlO2	17.00	16.49	18.46	17.13	16.95	17.04	17.38	17.17	18.22	15.21	20.16	18.73	20.95	18.54	18.62	18.47
Fe2O3	2.03	2.06	2.04	8.34	8.30	7.82	8.95	7.53	10.98	4.93	1.93	9.75	9.19	10.00	9.93	9.77
FeO	4.23	3.49	5.13	0.00	0.00	0.00	0.00	0.00	0.00	0.00	6.11	0.00	0.00	0.00	0.00	0.00
MnO	0.14	0.13	0.15	0.16	0.16	0.15	0.16	0.14	0.19	0.10	0.16	0.16	0.16	0.17	0.18	0.18
MgO	2.94	1.75	3.74	4.47	4.34	3.60	4.00	3.68	5.88	1.39	5.06	5.81	3.49	5.50	5.14	5.09
CaO	6.36	5.30	7.76	7.62	7.63	7.05	8.42	7.40	10.71	3.97	9.25	9.81	10.52	9.91	9.98	10.01
Na2O	3.68	3.97	3.42	3.25	3.36	3.38	3.08	3.62	2.56	3.85	3.09	2.71	3.35	2.69	2.77	3.18
K2O	1.55	1.91	1.06	1.26	1.34	1.57	1.36	1.42	0.39	2.56	0.60	0.59	0.75	0.67	0.68	0.67
P2O5	0.22	0.22	0.22	0.20	0.21	0.21	0.20	0.24	0.17	0.02	0.16	0.16	0.25	0.14	0.14	0.17
Loss	*0.00*	*0.00*	*0.00*	*0.70*	*0.45*	*0.70*	*-0.05*	*0.27*	*0.29*	*0.08*	*0.00*	*0.24*	*0.39*	*0.15*	*0.45*	*0.10*
Total	*99.5*	*99.6*	*99.4*	*100.7*	*100.7*	*100.3*	*100.5*	*100.0*	*100.0*	*100.0*	*99.3*	*100.3*	*101.3*	*101.0*	*101.0*	*100.7*

Location	C. Espiritu Santo					La Giganta - Cabro Muco				Sitio las Mesas				Intra-caldera block			
This study					EC8										IC26	IC22	IC34
ELC (1983)	2	2v	3	4		3v	14	15	16	1	12	11	25	7v			
SiO2	61.92	54.39	67.38	60.51	52.92	59.27	52.08	53.46	52.92	58.57	58.56	57.88	57.30	60.17	56.11	56.63	53.83
TiO2	0.59	0.77	0.44	0.58	0.85	0.70	0.76	0.77	0.76	0.69	0.67	0.73	0.65	0.57	0.75	0.72	0.07
AlO2	16.80	18.06	15.51	16.62	17.93	17.66	20.49	18.98	19.28	17.70	17.80	17.81	18.35	17.43	17.65	17.07	17.35
Fe2O3	1.99	2.10	1.79	1.87	10.12	2.10	1.94	2.07	2.01	2.06	2.05	2.05	1.99	1.98	8.74	8.23	9.74
FeO	3.69	6.17	1.70	3.91	0.00	4.39	6.44	6.21	6.31	4.91	4.69	5.16	4.96	3.98	0.00	0.00	0.00
MnO	0.13	0.16	0.10	0.13	0.18	0.13	0.17	0.17	0.17	0.15	0.15	0.15	0.16	0.14	0.16	0.16	0.18
MgO	2.72	4.55	1.14	3.23	4.57	3.14	4.03	4.20	4.10	3.28	3.31	3.20	3.50	2.96	3.82	3.51	4.91
CaO	6.01	8.59	3.27	6.32	9.20	6.85	8.01	8.84	8.82	6.79	6.84	6.85	7.37	6.47	8.01	7.42	9.27
Na2O	3.48	2.88	3.77	3.35	2.99	3.45	2.61	2.92	2.84	3.42	3.45	3.26	3.37	3.36	3.17	3.44	2.84
K2O	1.87	1.37	2.19	1.70	0.83	1.48	1.29	1.28	1.28	1.58	1.63	1.59	1.48	1.83	1.48	1.55	1.10
P2O5	0.20	0.22	0.14	0.20	0.19	0.20	0.25	0.21	0.21	0.21	0.22	0.23	0.19	0.19	0.21	0.22	0.18
Loss	*0.00*	*0.00*	*0.00*	*0.00*	*0.40*	*0.00*	*0.00*	*0.00*	*0.00*	*0.00*	*0.00*	*0.00*	*0.00*	*0.00*	*0.79*	*0.56*	*-0.23*
Total	*99.6*	*99.3*	*99.8*	*99.6*	*100.2*	*99.5*	*99.3*	*99.3*	*99.3*	*99.0*	*99.5*	*99.4*	*99.5*	*99.6*	*99.9*	*99.5*	*99.9*

Location	V.Palaeo-Miravalles			Volcan Miravalles								Santa Rosa Lavas					
This study																	
ELC (1983)	1v	30	10v	7	8	9	10	13	21	29	C. Hin	5	6	17	18	19	20
SiO2	52.15	57.21	54.54	57.89	60.02	59.02	59.09	58.72	59.26	57.30	57.36	57.25	58.05	58.26	57.94	56.55	58.31
TiO2	0.86	0.71	0.79	0.75	0.66	0.65	0.65	0.67	0.64	0.69	0.71	0.69	0.67	0.67	0.66	0.79	0.68
AlO2	20.57	17.97	18.83	17.84	17.44	17.82	17.72	17.73	17.75	18.03	17.22	18.03	18.00	18.16	18.29	18.07	18.35
Fe2O3	2.24	2.06	2.16	2.09	2.03	2.03	2.01	2.05	2.02	2.01	8.24	2.01	2.03	2.05	2.03	2.13	2.03
FeO	6.16	4.95	5.62	5.19	4.26	4.48	4.53	4.78	4.39	5.02	0.00	5.02	4.80	4.62	4.65	5.28	4.61
MnO	0.19	0.14	0.17	0.15	0.14	0.15	0.15	0.15	0.15	0.16	0.16	0.16	0.15	0.15	0.15	0.18	0.15
MgO	3.13	3.41	3.84	3.05	2.78	2.99	2.96	3.16	2.94	3.60	3.74	3.60	3.34	3.24	3.11	3.26	3.01
CaO	9.03	7.56	8.29	6.79	6.42	6.77	6.73	6.80	6.77	7.08	7.38	7.05	6.99	7.09	7.19	7.72	6.70
Na2O	3.19	3.33	3.15	3.30	3.55	3.55	3.50	3.49	3.54	3.35	3.23	3.35	3.50	3.44	3.48	3.31	3.42
K2O	0.77	1.55	1.40	1.60	1.76	1.66	1.66	1.63	1.61	1.53	1.58	1.53	1.56	1.55	1.55	1.45	1.63
P2O5	0.28	0.20	0.24	0.23	0.21	0.21	0.20	0.22	0.22	0.23	0.24	0.23	0.20	0.20	0.20	0.25	0.20
Loss	*0.00*	*0.00*	*0.00*	*0.00*	*0.00*	*0.00*	*0.00*	*0.00*	*0.00*	*0.00*	*0.00*	*0.00*	*0.00*	*0.00*	*0.00*	*0.00*	*0.00*
Total	*99.3*	*99.5*	*99.4*	*99.4*	*99.5*	*99.5*	*99.5*	*99.5*	*99.5*	*99.5*	*100.4*	*99.5*	*99.5*	*99.5*	*99.5*	*99.4*	*99.5*

Location	C. Caballos		Southern caldera margin				PH-30	PH-33	PH-37	PH-35	Extra-caldera lavas			
This study		IC8				EC75					EC72	EC29	EC44	EC53
ELC (1983)	CLB		26	27	28		31	33	34	12v				
SiO2	59.36	59.35	57.73	55.47	55.66	58.34	59.91	59.30	59.38	59.16	53.75	56.97	59.31	57.86
TiO2	0.68	0.76	0.82	0.78	0.78	0.78	0.72	0.67	0.65	0.69	0.80	0.77	0.81	0.82
AlO2	17.00	16.47	17.37	18.26	17.81	18.24	17.00	16.87	17.05	17.12	19.75	16.49	16.27	18.87
Fe2O3	7.48	7.80	2.13	2.11	2.09	8.63	2.07	1.95	1.96	2.08	8.90	8.32	8.09	7.44
FeO	0.00	0.00	5.48	5.71	5.92	0.00	4.19	4.16	4.10	4.22	0.00	0.00	0.00	0.00
MnO	0.15	0.15	0.17	0.16	0.21	0.16	0.19	0.15	0.13	0.13	0.18	0.22	0.13	0.16
MgO	3.35	2.88	2.64	3.89	3.68	4.87	2.81	2.89	3.71	3.68	3.45	3.49	2.95	3.55
CaO	6.96	6.61	7.15	7.73	7.51	8.27	6.39	6.96	6.52	6.69	9.28	7.42	6.18	8.01
Na2O	3.50	3.41	3.29	3.27	3.41	3.85	3.61	3.52	3.43	3.42	3.35	2.91	3.49	3.82
K2O	1.77	2.32	1.68	1.58	1.69	1.23	1.91	1.59	1.61	1.57	0.72	1.98	1.94	1.54
P2O5	0.22	0.20	0.28	0.25	0.25	0.30	0.26	0.22	0.22	0.22	0.25	0.24	0.25	0.32
Loss	*0.00*	*0.56*	*0.00*	*0.00*	*0.00*	*0.47*	*0.00*	*0.00*	*0.00*	*0.00*	*0.14*	*1.02*	*0.89*	*0.63*
Total	*100.8*	*100.5*	*99.4*	*99.4*	*99.3*	*105.1*	*99.6*	*99.5*	*99.5*	*99.5*	*100.6*	*99.8*	*100.3*	*103.0*

APPENDIX 3A Gravity Data

The process of converting observed gravity data into Bouguer Corrected Gravity (BCG) data is known as data reduction (e.g. Kearey and Brooks, 1984):

$$BCG = g_O + C_F + C_L + C_T - C_B \quad ...(1)$$

where g_O is the observed gravity relative to a reference station, C_F is the free air correction for the station elevation relative to a datum plane, C_L is the latitude correction, C_T is the terrain correction and C_B is the Bouguer correction.

The individual components and errors of the data reduction process are examined, further to the data reduction discussion in Chapter 3 (Section 3.1). The gravity data list given in Table 3A.2, at the end of this Appendix, only includes the gravity data measured during this study. The ICE data that were incorporated into this study (from the Miravalles and Tenorio geothermal projects, ICE, 1988 a and 1989, unpubl. data) are not given here. The method of extending the ICE terrain correction data, however, is explained.

Observed gravity data acquisition

During the 1988 and 1989 field seasons gravity was measured at a total of 405 new points in the area in and around the Guayabo caldera, to complement and extend the existing ICE gravity networks (Figure 3.1, the new data are listed in Table 3D.2), using a LaCoste and Romberg G-model gravimeter (G-105). Observed gravity was tied to the base station, Gra-91 (location in Figure 3.1) at the beginning and end of each survey day, and at midday when possible, to check for instrument drift and mechanical tares (Rymer, 1989). Earth Tide corrections were computed using the program of Brouke (1972). The Earth Tide corrected gravity difference between the field station and Gra-91 is g_O, the raw gravity data given in Table 3A.2.

Errors: The objective of the gravity data was to generate a Bouguer Gravity contour map with a resolution of 0.5 mGal within the caldera area and a 1 mGal contour map over the remaining area (Figures 3.7 and 3.8). The error on a single difference gravity value (i.e. g_O

in this study) using a LaCoste and Romberg gravimeter was estimated by Rymer (1989) to be 0.033 mGal, assuming reasonable field conditions. Given that the combined free air correction and terrain correction errors of this study are generally much larger than 0.033 mGal (between ~0.1 and 4 mGal, see below), the uncertainty in g_O is not significant. Errors due to mechanical tares and noise, however, had to be considered. As a general rule of thumb, tares were considered to be significant when greater than ~0.10 mGal. Tares of this magnitude are easy to identify above the general levels of uncertainty but were not common. Looping techniques (i.e. key field stations were revisited several times during a survey day) were employed in the field to isolate the tares that did occur, and where tares could not be isolated between successive stations, the data from the stations between the repeat stations were discounted. Where survey lines from separate days crossed, the coincident field stations were re-measured. Noise levels were variable, and were mostly wind-related. In exposed areas, strong winds prevented measurement, and in the forested and apparently sheltered areas the ground noise from the motion of the trees was often too high to permit a reading. In general, however, it was always possible to obtain a repeatable reading between successive squalls.

The estimated error for g_O is therefore estimated at less than 0.10 mGal. The error for g_O from the detailed Nettleton profiles (Section 3.3.4), however, is taken to be closer to the single difference error of 0.033 mGal (Rymer, 1989), as at least two measurements were made at each station, and field conditions were stable.

Free air correction

C_F was derived using the standard free air gradient, FAG, of 0.3086 mGal m^{-1}.

$$C_F = 0.3086(z - Z) \text{ mGal} \quad \text{.....(2)}$$

where z and Z are the elevation of the station and datum plane above sea level (in this study the datum plane is at 548.50 m, the elevation of the base station, Gra-91, Section 3.1.2). The errors in C_F are therefore related to i) the station elevation errors and ii) the FAG variation. The elevation data are considered in Appendix 3B, but the maximum error is not thought to be greater than 2 m for the majority of the data levelled by altimeter and less than 5 m for the Miravalles summit data. The FAG is not constant in every part of the world,

and varies even on the scale of a few hundred meters, depending on the local gravity anomalies and horizontal field gradients. The FAG was measured at three locations in the Miravalles borefield for the purposes of correcting the microgravity data for any possible elevation changes during steam production and pressure drawdown in the future (Chapter 5). Precision gravity measurements were read over a 2 m vertical height range (using a tripod) and the FAG was found to vary either side of the 0.3086 gradient by up to 0.1 mGal m^{-1}. Measurements were, however, made difficult by the strong winds and the accuracy of the data does not warrant a detailed discussion of the FAG variation here. In any case, the FAG in the borefield would be expected to vary considerably, as the borefield is on a strong lateral gradient related to the Bajo Los Chiqueros High (Figure 3.7).

In practical terms the C_F data for the BCG map can only be computed using a unique free air gradient value, and the standard 0.3086 mGal m^{-1} was used during this study. FAG measurements from several different areas of the BCG survey area would be necessary to test for a significant, regional departure from the standard FAG.

Latitude Correction:

Gravity varies with latitude due to the non-spherical shape of the earth. The latitude correction, C_L, computes the difference between the value of gravity predicted at the field station from that at the base, Gra-91. The formula used in this study follows that adopted in 1967 by the International Union of Geodesy and Geophysics (the International Gravity Formula, IGF), but revised by Mittermayer (1969; as reported by Kearey and Brooks, 1984):

$$C_L\,(\text{mGal}) = 978031.85[0.005278895(\sin^2 L - \sin^2 l) + 0.000023462(\sin^4 L - \sin^4 l)] \quad ...(3)$$

where l and L are the station and base latitudes respectively. The station latitudes were read from the 1:50,000 topographic maps (of the Instituto Geográphico de Costa Rica), simultaneously with the grid reference coordinates and both are given in the BCG data list (Table 3A.2 at the end of this Appendix). The latitude corrections for this study amount to ~0.3 mGal km^{-1} latitude and, as the station locations are known to better than 0.1 km, errors in C_L are not significant for the purposes of this study.

Terrain corrections:

The error incorporated by not making full terrain corrections is broadly related to the elevation of the station above the general terrain (see discussion in Chapter 3). The method used to calculate the relationship between the terrain correction and this elevation difference is explained here. The terrain corrections were computed following the method of Hammer (1939). Topography data for the Hammer zones E to M were read manually from the 1:50,000 scale topographic maps of Northern Costa Rica using in the normal way; the zone radii in kilometres and number of compartments in each zone are given Table 3A.1. The terrain corrections for zones A to D (i.e. from the station out to 170 m) were computed by treating the terrain as a sloping surface following Sandberg (1958), and dividing the local terrain into quadrants where the local ground surface did not have an even slope (e.g. close to a ridge crest). The normal Hammer zones A-M consider the terrain within 22 km of the station but, as discussed in Chapter 3 (Section 3.1.1), restricting corrections to this zone would have resulted in lost terrain correction errors of up to 10 mGal for the Miravalles summit stations. Zones I to M of the normal Hammer zone overlay (for use on 1:50,000 topographic maps) were used on a 1:500,000 map of Costa Rica which extended the terrain corrections to 221 km. These zones are therefore labelled I' to M' and defined in Table 3A.1.

Table 3A.1 The inner and outer radii (r and R km) and number of compartments (n) for each of the Hammer zones, and the approximate cluster diameter used for each zone beyond zone I. M is the outer zone for the standard Hammer zones, but extra zones I' to M' were defined for this study to avoid 'lost' terrain corrections for the higher stations. Zones A-D were computed from the Sandberg (1958) tables.

Hammer zone	R (km)	r (km)	n	cluster size (km)
(A-D)	(0.17)	(0)	-	-
E	0.39	0.17	8	-
F	0.90	0.39	8	-
G	1.54	0.90	12	-
H	2.64	1.54	12	-
I	4.51	2.64	12	-
J	6.73	4.51	16	1
K	10.0	6.73	16	2
L	14.9	10.0	16	3
M	22.1	14.9	16	3
I'	45	22.1	12	7
J'	67	45	16	7
K'	100	67	16	20
L'	149	100	16	20
M'	221	149	16	20

There was a slight overlap between the outer part of the M zone and the inner part of the I' zone overlay charts, but only the non-overlapping part of I' (i.e from 22.1 km to 45 km) was computed.

The Hammer Zone terrain correction method computes the sum of the gravity attraction of the individual compartments in each zone. Each compartment may be defined as the j^{th} segment of a cylindrical annulus of height h, where the annulus is the i^{th} zone (Figure 3A.1). h is the absolute difference between the station elevation and the average elevation of the terrain in the j^{th} segment. The computation for the j^{th} segment of the i^{th} zone is the difference between the attraction of a cylinder of radius, R, equal to the outer radius of the i^{th} zone and the attraction of a cylinder of radius, r, equal to the inner zone radius (Table 3A.1). The terrain correction for each compartment in this zone, is derived by dividing the computation for one zone by the number of compartments in the i^{th} zone, n_i.

Figure 3A.1 The definition of the j^{th} compartment of the i^{th} zone and the zone parameters referred to in the text.

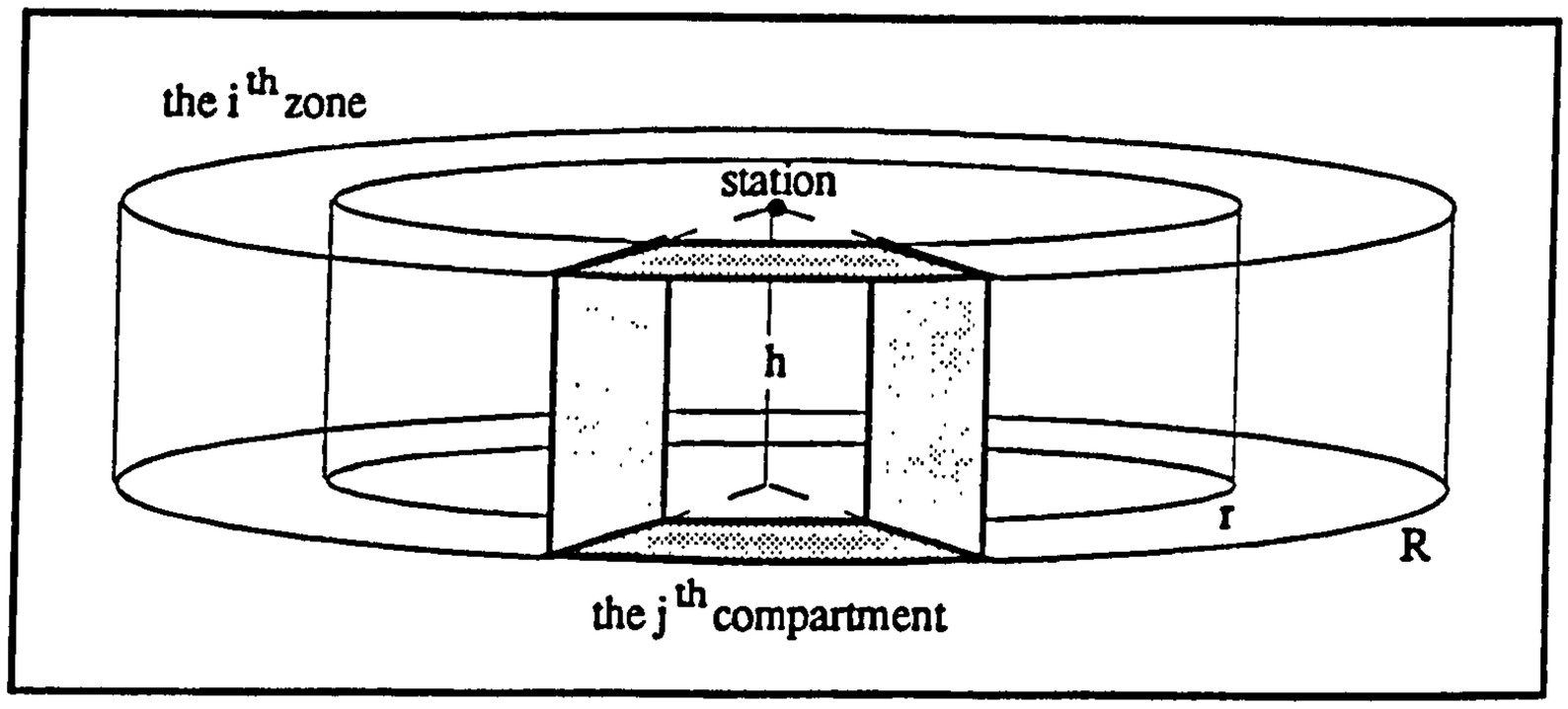

The terrain correction for the j^{th} compartment of the i^{th} zone is:

$$T_{ij} = \frac{2\pi G\rho}{n_i}\{R - r + \sqrt{r^2 + h^2} - \sqrt{R^2 + h^2}\} \times 10^5 \quad \text{mGal.....(3)}$$

where G is the gravitational constant and ρ is the reduction density. A microcomputer spreadsheet was designed to compute sum the contributions from each compartment and each zone, from the elevation data for each compartment and the station elevation, using equation (3). The elevation data for the furthest terrain zones were similar for closely spaced stations and therefore these elevations were defined only once for a given cluster of

stations (concept shown in Figure 3A.2). The cluster size was increased for the more distant zones and the approximate cluster diameters that were considered acceptable for the respective zones are given in Table 3A.1.

Figure 3A.2 The concept of defining an outer zone only once for a cluster of closely spaced stations, rather than for each station. Two station clusters and the relative positions of the corresponding zones are shown. The scale is approximate, and naturally the size of the cluster was increased for the more distant zones (Table 3A.1).

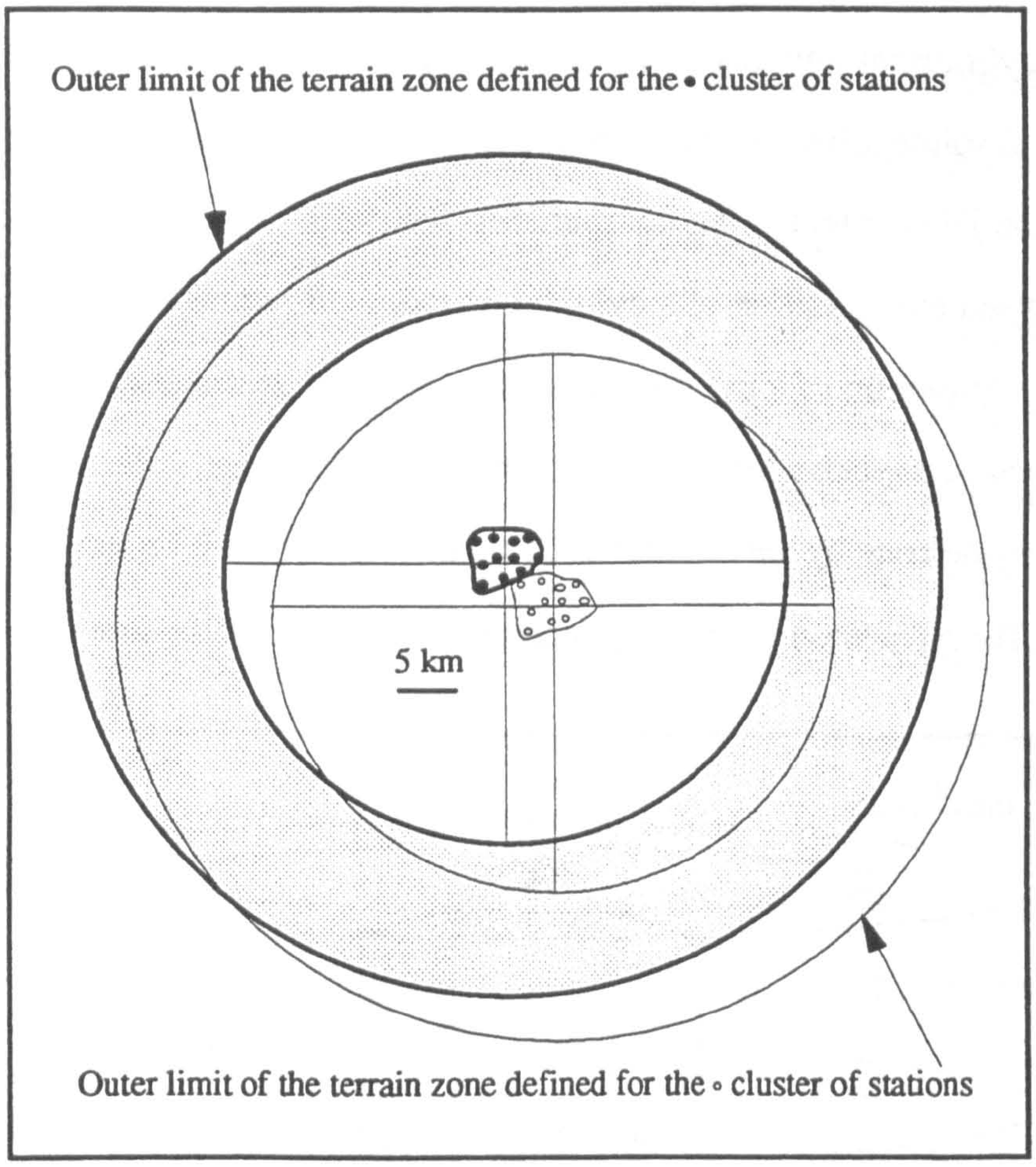

The list of total terrain corrections, C_T, calculated for a reduction density of 2.40 Mg m^{-3}, is given in Table 3A.2. The MGP data (Section 3.2.1) supplied by ICE (1988, unpubl. data) specified terrain correction data out to the M zone. To ensure compatibility with the BCG data of this study, further corrections were made for the area out to 221 km, using the clustering technique described above.

The Tenorio terrain data: The Tenorio terrain correction data provided by ICE (1989, unpubl. data), were specified for the zones out to 2 km only (Section 3.2.2). The Tenorio gravity data were integrated to this study for regional purposes only, and thus it was not considered necessary to compute detailed terrain corrections for each station. The ICE

Tenorio data from the area on the southern slopes of Cerro Espiritu Santo (Figure 3.1) overlaps the southeastern gravity survey area covered during this study. A quantitative relationship between station elevation and terrain correction was estimated for this zone, from the total terrain correction data computed for the stations of this study (Figure 3A.3).

Figure 3A.3 The variation of full terrain correction (C_T) with elevation above sea level (z). The data are from the stations on the southern slopes of Cerro Espiritu Santo of this study.

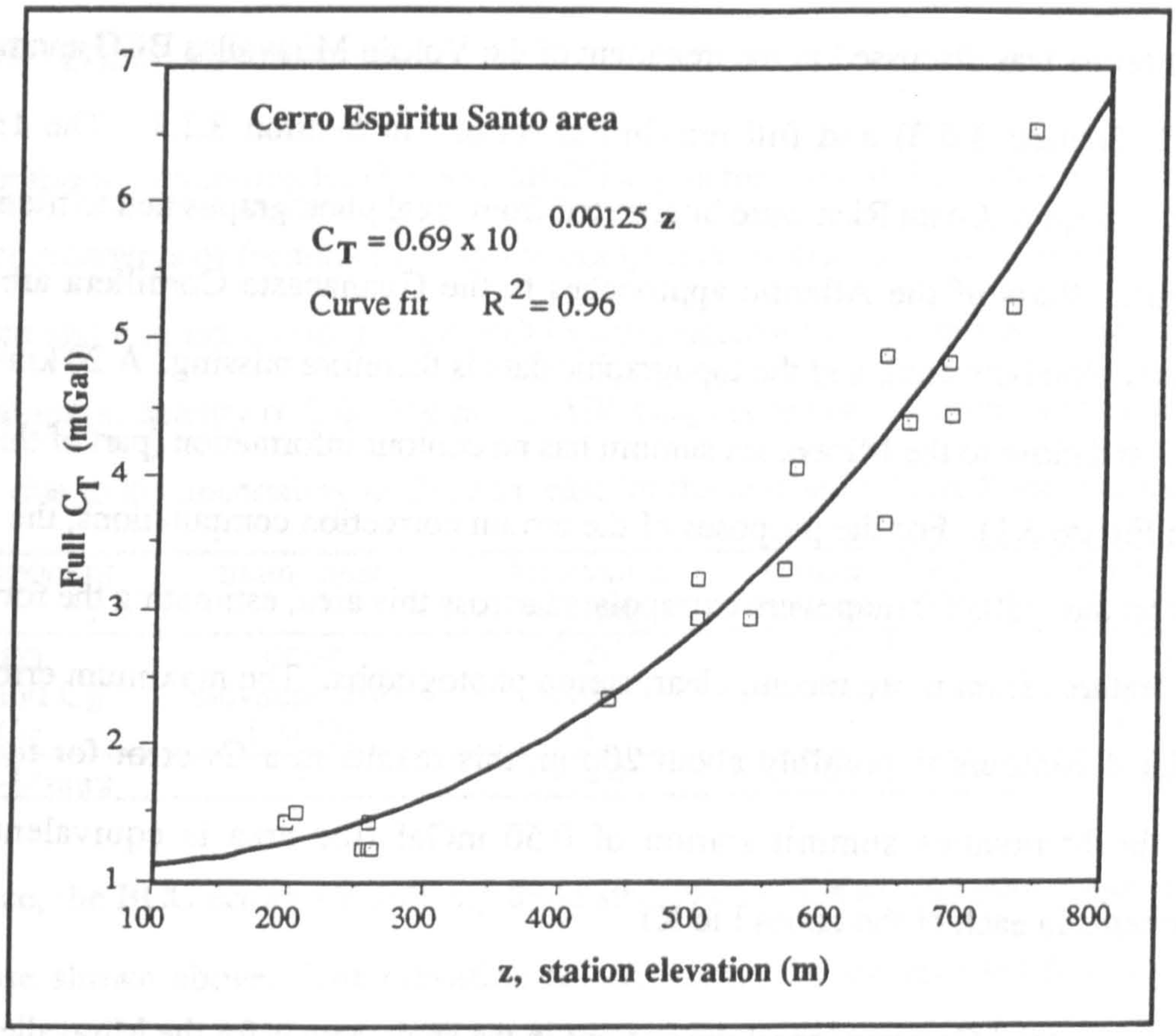

The station elevation range (200-750 m) covers the majority of the ICE stations in the Rio Tenorio Depression and Tierras Morenas area (modelled in Profile WSE, Figure 3.25 a). The exponential curve fitted to the C_T *vs* elevation data closely approximates the observed distribution (correlation coefficient, $R^2 = 0.96$), and the maximum departure of C_T is 0.6 mGal (Figure 3A.3). The full terrain correction for the ICE Tenorio data was computed from this relationship (Figure 3D.3). The variation of the terrain correction out to 2 km as quoted by ICE (1989, unpubl. data) was generally less than 1 mGal as the terrain is relatively regular. In summary, the terrain correction error on the majority of the ICE Tenorio data is believed to be less than 2 mGal.

General terrain correction error: The sources for the largest errors in the computation of terrain corrections are i) for local zones (A-D) where the slope of the ground is steep and/or irregular, ii) the terrain correction error introduced by not making full terrain corrections, iii) the missing topographic contour data in the cloud-covered areas, and iv) the estimated elevation-terrain correction relationship used for the Tenorio data. The question of local zone errors was discussed in the treatment of the Volcán Miravalles BCG anomalies in Chapter 3 (Section 3.6.3) and full terrain corrections in Section 3.1.1. The 1:50,000 topographic maps of Costa Rica were interpreted from areal photographs tied to triangulated spot heights. Parts of the Atlantic approaches to the Guanacaste Cordillera are almost permanently cloud-covered, and the topographic data is therefore missing. A 20 km^2 area to the east of and close to the Miravalles summit has no contour information (part of this area is shown in Figure 3.1). For the purposes of the terrain correction computations, the existing contours on the 1:50,000 map were extrapolated across this area, estimating the form of the missing features from more recent, clear, stereo photographs. The maximum error on the extrapolated contours is possibly about 200 m, this results in a C_T error for the closest station, the Miravalles summit station of 0.50 mGal (the area is equivalent to two compartments in each of the zones I to K).

The maximum total C_T error for all the stations in the study area is for the Miravalles summit data; ~4 mGal (2 mGal local zone A-D slope error, 1 mGal full C_T error and 0.5 mGal missing topographic map error). The C_T error is less for the stations at lower elevations: The caldera floor stations (at ~550 m a.s.l.) generally have a total C_T of less than 2 mGal (e.g. Gra-91; 1.68 mGal) and the error due to missing terrain correction (Figure 3.2) is not thought to exceed 0.2 mGal. As the lost C_T error is equal for both the caldera floor stations and the base station (at the same elevation) the errors cancel out, and therefore the T_C error is not thought to exceed 0.1 mGal.

The Bouguer Correction

The Bouguer correction is computed from the formula for the attraction of an infinite horizontal slab: $C_B = 2\pi G\rho(z - Z) \times 10^5$ mGal.....(5)

The significance of the choice of datum plane and the reduction density, ρ, is discussed in Chapter 3 (Section 3.1.2). The station elevation above the datum, $(z - Z)$, is the major source for error, as for C_T, and the elevation errors are described in Appendix 3B. As C_E and C_B can be considered together in terms of $(z - Z)$; $C_E - C_B = (0.3086 - 2\pi G\rho \times 10^5)(z - Z)$, the contribution to the BCG error from an error in $(z - Z)$ need only be considered once.

Overall BCG errors

The maximum cumulative BCG error, ΔBCG_{max}, is the sum of the errors described above for the components of formula (1). As the component errors vary for different stations, the maximum and minimum errors of the BCG values relative to the base station are considered (for a reduction density of 2.40 Mg m^{-3}). ΔBCG_{max} is greatest for the Miravalles summit stations, due to the uncertainty in C_T, and least for the levelled caldera floor stations.

Component	main cause	Miravalles summit	Caldera floor (levelled)	Caldera floor (altimeter)
g_O	noise	0.20	0.05	0.05
C_E and C_B	elevation error	1.04	0.01	0.4
C_T	lost C_T	4	0.1	0.1
ΔBCG_{max}	**-**	**5.24**	**0.16**	**0.95**

In practice, the BCG errors are unlikely to be strictly cumulative, and may therefore be less than those shown above. The elevation related errors for the levelled ICE stations are minimal, 5 cm (Leandro, *pers comm*). As a general rule of thumb, the BCG data confidence levels are 0.1 mGal for stations in the levelled borefield and caldera area, 0.5 mGal for the part in and around the caldera surveyed by altimeter, 3 mGal for the Miravalles edifice area and, finally, 2 mGal for the Tenorio area.

The Bouguer corrected gravity data of this study

The gravity data that was collected during the 1988 and 1989 field seasons and the corrections for each station (as described above) are given in Table 3A.2 (see following pages).

Table 3A.2 The gravity data measured during this study. The list includes the station reference numbers (No.), names, grid coordinates, elevation above sea level (z), latitude, the Earth Tide corrected observed gravity difference from gravity at Gra-91 (g_O), the absolute gravity values (g_{abs}, as tied to the Gra-91 value, 1st row), the terrain, latitude, free air and Bouguer corrections and finally the Bouguer corrected gravity anomaly relative to Gra-91, BCG.

No.	Station	E'ing km	N'ing km	z m	Lat. degrees	g_o mGal	G_{abs} mGal	C_T mGal	C_L mGal	C_F mGal	C_B mGal	BCG mGal
	Base Gra-91	*402.6*	*298.5*	*548.50*	*10.7105*	*0.00*	*978099.70*	*1.68*	*0.00*	*0.00*	*0.00*	*0.00*
1001	R6k	410.4	303.1	2026.00	10.7464	-337.73	977761.97	53.16	-1.18	455.96	148.61	19.92
1002	R6j	410.2	303.1	1950.00	10.7464	-316.16	977783.54	49.51	-1.18	432.50	140.97	22.03
1003	R6i	409.9	303.1	1921.00	10.7464	-311.22	977788.48	45.57	-1.18	423.55	138.05	17.00
1004	R6camp	409.7	302.8	1759.00	10.7436	-267.00	977832.70	31.86	-1.09	373.56	121.76	13.89
1005	R6h	409.5	302.7	1649.00	10.7427	-239.17	977860.53	28.28	-1.06	339.61	110.69	15.29
1006	R6g	409.3	302.6	1549.00	10.7418	-214.50	977885.20	24.88	-1.03	308.75	100.63	15.79
1007	R6f	408.7	303.1	1317.00	10.7464	-162.75	977936.95	18.34	-1.18	237.16	77.30	12.59
1008	R6e	408.3	303.3	1198.00	10.7482	-137.05	977962.65	16.50	-1.24	200.44	65.33	11.64
1009	R6d	407.9	303.5	1057.00	10.7500	-106.66	977993.04	13.38	-1.30	156.92	51.15	9.52
1010	R6c	407.5	303.6	927.00	10.7509	-77.90	978021.80	9.31	-1.33	116.81	38.07	7.14
1011	R6b	407.2	303.8	804.00	10.7527	-51.25	978048.45	7.74	-1.39	78.85	25.70	6.57
1012	R6a	406.6	304.1	707.00	10.7555	-30.05	978069.65	5.47	-1.48	48.91	15.94	5.23
1013	R5e	408.5	302.7	1284.00	10.7427	-156.88	977942.82	17.80	-1.06	226.98	73.98	11.18
1014	R5d	408.1	302.8	1145.00	10.7436	-126.70	977973.00	16.13	-1.09	184.08	60.00	10.74
1015	R5c	407.5	302.7	966.00	10.7427	-85.85	978013.85	11.53	-1.06	128.84	41.99	9.79
1016	R5b	407.3	302.7	825.00	10.7427	-55.25	978044.45	8.66	-1.06	85.33	27.81	8.19
1017	R5a	406.8	302.0	688.00	10.7364	-26.34	978073.36	5.88	-0.85	43.05	14.03	6.03
1018	R5ar	406.7	301.9	672.00	10.7355	-23.85	978075.85	6.03	-0.82	38.11	12.42	5.37
1019	R3b	407.8	300.9	943.00	10.7264	-78.46	978021.24	9.77	-0.52	121.74	39.68	11.17
1020	R4a	407.6	301.3	876.00	10.7300	-63.99	978035.71	8.18	-0.64	101.07	32.94	9.99
1021	R3a	407.1	300.6	767.00	10.7236	-39.80	978059.90	5.24	-0.43	67.43	21.98	8.78
1022	R2L1	408.8	301.5	1235.00	10.7318	-137.37	977962.33	16.50	-0.70	211.85	69.05	19.55
1023	R3c	408.1	301.3	1027.00	10.7300	-96.28	978003.42	11.16	-0.64	147.67	48.13	12.10
1024	R3d	408.4	301.5	1180.00	10.7318	-128.40	977971.30	15.61	-0.70	194.88	63.52	16.20
1025	R3e	408.6	302.9	1334.00	10.7445	-163.58	977936.12	19.92	-1.12	242.41	79.01	16.94
1026	R3f	409.1	302.3	1476.00	10.7391	-195.63	977904.07	24.07	-0.94	286.23	93.29	18.76
1027	R2a	407.6	300.5	830.00	10.7227	-52.58	978047.12	7.00	-0.40	86.87	28.31	10.90
1028	R2b	408.0	300.7	893.00	10.7245	-64.84	978034.86	7.80	-0.46	106.31	34.65	12.49
1029	R2c	408.2	300.6	982.00	10.7236	-82.24	978017.46	10.68	-0.43	133.78	43.60	16.50
1030	R2d	408.6	300.8	1061.00	10.7255	-97.40	978002.30	10.87	-0.49	158.16	51.55	17.91
1031	R2L2	408.7	301.3	1094.00	10.7291	-104.61	977995.09	12.01	-0.61	168.34	54.87	18.58
1032	R1c	408.9	300.9	1173.00	10.7264	-124.55	977975.15	14.76	-0.52	192.72	62.81	17.92
1033	R1b	408.7	300.7	1049.00	10.7245	-98.44	978001.26	11.97	-0.46	154.45	50.34	15.51
1034	R1a	408.3	300.4	939.00	10.7218	-74.69	978025.01	9.14	-0.37	120.51	39.28	13.64
1035	E650	407.8	299.9	824.00	10.7173	-49.98	978049.72	6.35	-0.22	85.02	27.71	11.78
1036	U87	410.1	299.5	998.00	10.7136	-75.93	978023.77	8.45	-0.10	138.72	45.21	24.24
1037	U86	409.5	299.4	923.00	10.7127	-61.39	978038.31	7.44	-0.07	115.57	37.67	22.20
1038	U85	409.2	299.3	902.00	10.7118	-59.01	978040.69	6.83	-0.04	109.09	35.56	19.64
1039	U88	410.3	299.9	1050.00	10.7173	-86.80	978012.90	9.38	-0.22	154.76	50.44	25.00
1040	U89	411.0	299.8	1122.00	10.7164	-101.37	977998.33	8.80	-0.19	176.98	57.68	24.85
1041	U90	411.0	300.6	1224.00	10.7236	-125.05	977974.65	10.94	-0.43	208.46	67.94	24.30
1042	U91	410.9	301.3	1334.00	10.7300	-153.45	977946.25	16.29	-0.64	242.41	79.01	23.92
1043	U106h	408.4	306.4	642.00	10.7764	-17.03	978082.67	8.00	-2.17	28.85	9.40	6.57
1044	U106	407.1	308.6	446.00	10.7964	27.73	978127.43	3.01	-2.83	-31.63	-10.31	4.91
1045	U106a	407.8	307.2	513.00	10.7836	12.91	978112.61	4.44	-2.41	-10.96	-3.57	5.87
1046	U106b	407.4	308.0	483.00	10.7909	19.59	978119.29	3.53	-2.65	-20.21	-6.59	5.17
1047	U106c	408.2	307.3	552.00	10.7845	5.01	978104.71	4.87	-2.44	1.08	0.35	6.49
1048	U106d	408.6	306.8	585.00	10.7800	-1.01	978098.69	7.10	-2.29	11.26	3.67	9.71
1049	U106e	409.0	307.0	673.00	10.7818	-21.78	978077.92	6.74	-2.35	38.42	12.52	6.82
1050	U106f	409.6	306.5	804.00	10.7773	-50.24	978049.46	8.88	-2.20	78.85	25.70	7.91
1051	U106g	408.8	306.6	645.00	10.7782	-16.33	978083.37	7.89	-2.23	29.78	9.71	7.73
1052	U106i	408.7	306.0	746.00	10.7727	-40.11	978059.59	11.23	-2.05	60.95	19.87	8.47
1053	MNc	409.3	308.2	612.00	10.7927	-10.47	978089.23	4.44	-2.71	19.60	6.39	2.79
1054	MNb	408.9	308.8	533.00	10.7982	7.09	978106.79	3.82	-2.89	-4.78	-1.56	3.12
1055	MNa2	408.3	309.1	498.00	10.8009	13.55	978113.25	3.31	-2.98	-15.58	-5.08	1.69
1056	U106j	408.3	305.7	850.00	10.7700	-61.33	978038.37	9.97	-1.96	93.04	30.33	7.71
1057	U106k	408.5	305.2	970.00	10.7655	-87.84	978011.86	12.38	-1.81	130.07	42.40	8.73
1058	MNa	408.0	309.3	452.00	10.8027	23.94	978123.64	3.31	-3.04	-29.78	-9.71	2.46
1059	MNd	409.5	307.7	653.00	10.7882	-19.10	978080.60	5.40	-2.56	32.25	10.51	3.80
1060	MNe	409.8	307.0	748.00	10.7818	-38.37	978061.33	7.19	-2.35	61.57	20.07	6.29
1061	MNe2	409.9	306.1	900.00	10.7736	-69.92	978029.78	10.69	-2.08	108.47	35.36	10.13

1062	MNf	409.9	305.8	988.00	10.7709	-88.24	978011.46	12.51	-1.99	135.63	44.21	12.03
1063	MNg	410.2	305.5	1175.00	10.7682	-129.14	977970.56	15.39	-1.90	193.34	63.02	12.99
1064	U61e	394.7	301.9	656.00	10.7355	-12.26	978087.44	3.92	-0.82	33.17	10.81	11.52
1065	U61a	395.6	303.3	776.00	10.7482	-39.82	978059.88	3.75	-1.24	70.21	22.88	8.34
1066	U61b	395.8	303.7	835.00	10.7518	-52.45	978047.25	3.99	-1.36	88.41	28.82	8.10
1067	U61c	395.6	304.1	819.00	10.7555	-46.82	978052.88	3.48	-1.48	83.48	27.21	9.77
1068	U61d	395.4	304.6	808.00	10.7600	-43.40	978056.30	3.41	-1.63	80.08	26.10	10.68
1069	U63	394.2	303.7	782.00	10.7518	-36.18	978063.52	3.17	-1.36	72.06	23.49	12.52
1070	U64	395.0	304.5	802.00	10.7591	-40.04	978059.66	3.37	-1.60	78.23	25.50	12.78
1071	U65	395.6	305.2	812.00	10.7655	-44.76	978054.94	3.62	-1.81	81.32	26.50	10.18
1072	U66	396.3	305.5	804.00	10.7682	-44.12	978055.58	3.86	-1.90	78.85	25.70	9.31
1073	U67	397.0	305.7	773.00	10.7700	-39.96	978059.74	3.85	-1.96	69.28	22.58	6.96
1074	U68	397.8	306.0	702.00	10.7727	-27.08	978072.62	3.91	-2.05	47.37	15.44	5.03
1075	U69	398.1	306.4	644.00	10.7764	-15.62	978084.08	3.72	-2.17	29.47	9.61	4.12
1076	U70	398.2	306.8	670.00	10.7800	-20.78	978078.92	5.18	-2.29	37.49	12.22	5.71
1077	U71	398.7	307.4	665.00	10.7855	-21.37	978078.33	6.67	-2.47	35.95	11.72	5.39
1078	U72	400.0	308.5	465.00	10.7955	20.90	978120.60	3.96	-2.80	-25.77	-8.40	3.01
1079	U73	400.3	309.3	447.00	10.8027	24.87	978124.57	3.73	-3.04	-31.32	-10.21	2.76
1080	U114	400.5	310.0	357.00	10.8091	40.38	978140.08	3.92	-3.25	-59.10	-19.26	-0.47
1081	U113	400.9	310.4	347.00	10.8127	47.10	978146.80	3.20	-3.37	-62.18	-20.27	3.33
1082	U112	401.5	310.6	318.00	10.8145	50.65	978150.35	3.55	-3.43	-71.13	-23.18	1.14
1083	RLC17	401.7	309.7	353.00	10.8064	45.32	978145.02	3.16	-3.16	-60.33	-19.66	2.97
1084	U111	402.4	310.2	317.00	10.8109	51.22	978150.92	2.77	-3.31	-71.44	-23.29	0.84
1085	U109	403.9	310.0	325.00	10.8091	52.81	978152.51	2.64	-3.25	-68.97	-22.48	4.03
1086	U110	403.3	310.3	310.00	10.8118	53.89	978153.59	2.53	-3.34	-73.60	-23.99	1.79
1087	U108	404.2	310.2	323.00	10.8109	52.36	978152.06	2.20	-3.31	-69.59	-22.68	2.66
1088	U107	405.3	310.7	326.00	10.8155	51.21	978150.91	1.77	-3.47	-68.66	-22.38	1.55
1089	U104	407.1	310.2	379.00	10.8109	40.02	978139.72	2.15	-3.31	-52.31	-17.05	1.92
1090	U103	406.0	310.8	341.00	10.8164	48.43	978148.13	2.27	-3.50	-64.03	-20.87	2.36
1091	U105	407.1	309.0	397.00	10.8000	36.88	978136.58	2.33	-2.95	-46.75	-15.24	3.07
1092	RLC18	401.4	310.0	338.00	10.8091	48.77	978148.47	3.12	-3.25	-64.96	-21.17	3.17
1093	RLC16	402.1	309.2	386.00	10.8018	38.41	978138.11	3.03	-3.01	-50.15	-16.34	2.95
1094	RLC15	401.7	308.6	472.00	10.7964	21.03	978120.73	3.13	-2.83	-23.61	-7.69	3.73
1095	RLC14	401.4	308.3	500.00	10.7936	16.32	978116.02	3.19	-2.74	-14.97	-4.88	5.00
1096	RLC13	401.3	307.8	541.00	10.7891	7.36	978107.06	3.35	-2.59	-2.31	-0.75	4.88
1097	RLC12	401.3	307.5	625.00	10.7864	-10.08	978089.62	4.17	-2.50	23.61	7.69	5.83
1098	RLC11	401.3	307.3	675.00	10.7845	-21.93	978077.77	4.68	-2.44	39.04	12.72	4.94
1099	RLC10	401.4	307.1	711.00	10.7827	-29.94	978069.76	5.64	-2.38	50.15	16.34	5.44
1100	RLC13r	402.1	307.4	697.00	10.7855	-26.40	978073.30	5.07	-2.47	45.83	14.94	5.41
1101	RLC14r	402.4	307.5	702.00	10.7864	-27.57	978072.13	5.64	-2.50	47.37	15.44	5.82
1102	RLC15r	402.8	307.7	757.00	10.7882	-41.76	978057.94	8.46	-2.56	64.34	20.97	5.83
1103	RLC16r	403.3	307.8	728.00	10.7891	-31.13	978068.57	6.76	-2.59	55.39	18.05	8.70
1104	RLC17r	403.6	307.9	800.00	10.7900	-51.60	978048.10	11.56	-2.62	77.61	25.30	7.97
1105	RLC18r	403.4	307.5	620.00	10.7864	-3.96	978095.74	4.51	-2.50	22.06	7.19	11.24
1106	RLC27	404.8	306.8	580.00	10.7800	1.91	978101.61	3.98	-2.29	9.72	3.17	8.47
1107	RLC28	405.1	306.6	497.00	10.7782	20.12	978119.82	2.96	-2.23	-15.89	-5.18	8.46
1108	RLC29	405.5	306.6	481.00	10.7782	23.20	978122.90	2.97	-2.23	-20.83	-6.79	8.21
1109	RLC19	403.9	307.1	570.00	10.7827	7.59	978107.29	3.07	-2.38	6.63	2.16	11.07
1110	RLC20	404.1	306.7	561.00	10.7791	7.38	978107.08	2.35	-2.26	3.86	1.26	8.39
1111	RLC21	404.1	306.3	556.00	10.7755	4.98	978104.68	2.32	-2.14	2.31	0.75	5.04
1112	RLC22	404.0	305.8	550.00	10.7709	5.62	978105.32	2.16	-1.99	0.46	0.15	4.43
1113	RLC23	404.2	307.0	564.00	10.7818	6.62	978106.32	2.66	-2.35	4.78	1.56	8.47
1114	RLC24	404.4	307.4	588.00	10.7855	0.65	978100.35	3.54	-2.47	12.19	3.97	8.26
1115	RLC25	404.5	307.3	590.00	10.7845	-0.06	978099.64	4.17	-2.44	12.81	4.17	8.62
1116	RLC26	404.7	307.0	604.00	10.7818	-3.74	978095.96	5.64	-2.35	17.13	5.58	9.41
1117	RLC30	405.9	306.8	497.00	10.7800	19.71	978119.41	2.96	-2.29	-15.89	-5.18	7.99
1118	RLC31/G8	406.1	306.9	516.00	10.7800	15.72	978115.42	3.03	-2.29	-10.03	-3.27	8.02
1119	BN41c	401.3	304.7	590.00	10.7609	-0.83	978098.87	2.63	-1.66	12.81	4.17	7.09
1120	BN41a	401.6	303.9	581.00	10.7536	1.23	978100.93	1.83	-1.42	10.03	3.27	6.72
1121	BN41b	401.5	304.3	579.00	10.7573	2.03	978101.73	1.86	-1.54	9.41	3.07	7.02
1122	BN41d	401.0	304.7	627.00	10.7609	-10.87	978088.83	3.47	-1.66	24.23	7.90	5.59
1123	BN41e	400.8	304.8	703.00	10.7618	-30.84	978068.86	3.51	-1.69	47.68	15.54	1.45
1124	BN41f	400.3	304.7	658.00	10.7609	-21.08	978078.62	2.57	-1.66	33.79	11.01	0.93
1125	BN41g	400.0	304.8	709.00	10.7618	-33.94	978065.76	3.15	-1.69	49.53	16.14	-0.77
1126	BN41h	400.6	304.5	740.00	10.7591	-40.66	978059.04	5.42	-1.60	59.10	19.26	1.32
1127	BN41i	400.4	304.2	754.00	10.7564	-45.28	978054.42	6.31	-1.51	63.42	20.67	0.59
1128	BN41j	401.7	304.4	589.00	10.7582	-0.05	978099.65	2.26	-1.57	12.50	4.07	7.38
1129	BN41k	402.1	304.6	574.00	10.7600	3.47	978103.17	2.82	-1.63	7.87	2.56	8.28
1130	BN41l	402.0	305.1	559.00	10.7645	6.38	978106.08	2.19	-1.78	3.24	1.06	7.30

1131	BN41m	402.0	305.6	554.00	10.7691	7.68	978107.38	2.27	-1.93	1.70	0.55	7.48
1132	BN41n	401.8	305.1	661.00	10.7645	-18.18	978081.52	4.66	-1.78	34.72	11.32	6.42
1133	BN23a	401.0	302.8	571.00	10.7436	-2.06	978097.64	1.78	-1.09	6.94	2.26	1.63
1134	BN23b	400.5	303.0	575.00	10.7455	-1.64	978098.06	1.98	-1.15	8.18	2.67	3.02
1135	BN23c	400.0	303.0	575.00	10.7455	-2.68	978097.02	2.03	-1.15	8.18	2.67	2.04
1136	BN23d	399.4	302.9	582.00	10.7445	-5.19	978094.51	2.25	-1.12	10.34	3.37	1.23
1137	BN23e	399.8	303.0	577.00	10.7455	-3.32	978096.38	2.20	-1.15	8.80	2.87	1.98
1138	BN23f	400.7	303.0	576.00	10.7455	-1.40	978098.30	1.98	-1.15	8.49	2.77	3.47
1139	U6	399.0	302.9	595.50	10.7445	-6.23	978093.47	3.36	-1.12	14.50	4.73	4.11
1140	U37	399.6	303.4	593.00	10.7491	-7.21	978092.49	2.33	-1.27	13.73	4.48	1.43
1141	U37a	399.5	303.7	632.00	10.7518	-15.05	978084.65	3.95	-1.36	25.77	8.40	3.23
1142	U37b	399.7	304.1	622.00	10.7555	-12.19	978087.51	2.70	-1.48	22.68	7.39	2.64
1143	U37c	399.7	305.8	595.00	10.7709	-6.90	978092.80	2.94	-1.99	14.35	4.68	2.04
1144	U37d	399.5	306.3	497.00	10.7755	14.72	978114.42	4.76	-2.14	-15.89	-5.18	4.94
1145	U37e	398.8	306.4	601.00	10.7764	-9.28	978090.42	4.49	-2.17	16.20	5.28	2.28
1146	U37f	399.6	306.1	554.00	10.7736	2.49	978102.19	3.71	-2.08	1.70	0.55	3.59
1147	U37g	399.6	305.4	670.00	10.7673	-25.09	978074.61	2.78	-1.87	37.49	12.22	-0.59
1148	U37h	399.7	304.9	704.00	10.7627	-32.66	978067.04	2.78	-1.72	47.99	15.64	-0.93
1149	U21b	398.4	301.7	771.00	10.7336	-44.58	978055.12	4.49	-0.76	68.66	22.38	3.75
1150	U21a	398.3	302.2	732.00	10.7382	-35.15	978064.55	3.15	-0.91	56.63	18.46	3.58
1151	U21	398.2	302.3	701.00	10.7391	-28.35	978071.35	2.52	-0.94	47.06	15.34	3.28
1152	U14	398.4	302.6	637.00	10.7418	-15.48	978084.22	2.73	-1.03	27.31	8.90	2.96
1153	G280a	400.7	301.2	580.00	10.7291	-3.40	978096.30	2.08	-0.61	9.72	3.17	2.95
1154	G280b	401.0	301.2	562.00	10.7291	-1.65	978098.05	2.02	-0.61	4.17	1.36	0.89
1155	G280c	401.5	301.2	560.00	10.7291	-3.76	978095.94	2.02	-0.61	3.55	1.16	-1.63
1156	G280d	402.0	301.2	556.00	10.7291	-4.35	978095.35	2.04	-0.61	2.31	0.75	-3.04
1157	G280e	402.3	301.2	558.00	10.7291	-5.54	978094.16	2.00	-0.61	2.93	0.96	-3.85
1159	G280g	402.8	301.2	567.00	10.7291	-9.10	978090.60	2.14	-0.61	5.71	1.86	-5.40
1160	G280h	403.3	301.2	571.00	10.7291	-10.55	978089.15	2.17	-0.61	6.94	2.26	-5.99
1161	G280i	403.5	301.4	591.00	10.7309	-15.33	978084.37	2.71	-0.67	13.12	4.27	-6.12
1162	G280j	403.9	301.5	569.00	10.7318	-10.83	978088.87	2.17	-0.70	6.33	2.06	-6.77
1163	G280k	404.3	301.5	569.00	10.7318	-10.94	978088.76	2.52	-0.70	6.33	2.06	-6.53
1164	G280l	404.6	301.6	574.00	10.7327	-11.01	978088.69	2.47	-0.73	7.87	2.56	-5.64
1165	G273a	400.1	297.4	550.00	10.6945	1.20	978100.90	1.53	0.53	0.46	0.15	1.90
1166	G273h	401.0	300.2	554.00	10.7109	-2.38	978097.32	1.41	-0.01	1.70	0.55	-1.52
1167	G273b	400.1	297.6	550.00	10.6964	1.41	978101.11	1.51	0.47	0.46	0.15	2.02
1168	G273c	400.3	297.8	545.00	10.6982	0.47	978100.17	1.49	0.41	-1.08	-0.35	-0.04
1169	G273d	400.4	298.2	546.00	10.7018	-0.20	978099.50	1.46	0.29	-0.77	-0.25	-0.64
1170	G273e	400.5	298.7	544.00	10.7064	-0.77	978098.93	1.44	0.14	-1.39	-0.45	-1.81
1171	G273f	400.7	299.2	546.00	10.7109	-0.85	978098.85	1.43	-0.01	-0.77	-0.25	-1.63
1172	G273g	400.9	299.7	553.00	10.7155	-1.97	978097.73	1.42	-0.16	1.39	0.45	-1.46
1173	G273i	400.1	298.0	545.00	10.7000	2.51	978102.21	1.70	0.35	-1.08	-0.35	2.16
1174	G273j	399.8	298.4	545.00	10.7036	4.70	978104.40	1.63	0.23	-1.08	-0.35	4.15
1175	G273l	399.3	299.5	550.00	10.7136	3.49	978103.19	2.27	-0.10	0.46	0.15	4.30
1176	G273m	399.5	300.0	547.00	10.7182	2.08	978101.78	2.27	-0.25	-0.46	-0.15	2.11
1177	G273n	399.5	300.4	579.00	10.7218	-2.63	978097.07	2.58	-0.37	9.41	3.07	4.25
1178	G273p	399.5	300.7	575.00	10.7245	-3.08	978096.62	1.79	-0.46	8.18	2.67	2.09
1179	A3Z	408.8	299.9	877.70	10.7173	-58.67	978041.03	6.96	-0.22	101.59	33.11	14.87
1180	A3Za	408.7	300.4	919.00	10.7218	-68.61	978031.09	8.11	-0.37	114.34	37.27	14.52
1181	A3Zb	409.1	300.8	980.00	10.7255	-82.71	978016.99	12.00	-0.49	133.16	43.40	16.88
1182	A3Zc	409.5	300.9	1075.00	10.7264	-104.79	977994.91	14.55	-0.52	162.48	52.96	17.09
1183	U84	410.0	299.0	1170.00	10.7091	-121.44	977978.26	13.85	0.05	191.79	62.51	20.07
1184	U83	409.7	298.3	886.00	10.7027	-61.04	978038.66	7.89	0.26	104.15	33.95	15.64
1185	U82	409.7	297.6	716.00	10.6964	-25.43	978074.27	6.22	0.47	51.69	16.85	14.43
1186	U81	409.8	297.2	634.00	10.6927	-8.82	978090.88	5.35	0.59	26.39	8.60	13.23
1187	U80	409.9	296.6	584.00	10.6873	1.19	978100.89	4.39	0.77	10.96	3.57	12.05
1188	U79	409.8	295.9	570.00	10.6809	4.19	978103.89	4.06	0.98	6.63	2.16	12.02
1189	U74	409.2	295.8	563.00	10.6800	5.28	978104.98	3.32	1.01	4.47	1.46	10.94
1190	U75	409.5	294.8	499.00	10.6709	19.85	978119.55	3.24	1.31	-15.28	-4.98	12.42
1191	U76	409.6	295.2	539.00	10.6745	11.80	978111.50	2.94	1.19	-2.93	-0.96	12.27
1192	U77	410.7	295.4	635.00	10.6764	-7.58	978092.12	3.66	1.13	26.69	8.70	13.52
1193	U78	411.6	295.6	685.00	10.6782	-17.60	978082.10	4.45	1.07	42.12	13.73	14.63
1194	ESa	411.0	295.3	652.00	10.6755	-10.95	978088.75	4.39	1.16	31.94	10.41	14.45
1195	ESb	411.3	295.0	637.00	10.6727	-9.72	978089.98	4.89	1.25	27.31	8.90	13.15
1196	ESc	411.5	294.7	744.00	10.6700	-36.21	978063.49	6.55	1.34	60.33	19.66	10.66
1197	ESd	411.4	294.2	730.00	10.6655	-33.68	978066.02	5.24	1.48	56.01	18.26	9.12
1198	ESe	411.5	293.8	683.00	10.6618	-26.64	978073.06	4.82	1.60	41.51	13.53	6.08
1199	ESf	411.6	292.5	499.00	10.6500	10.28	978109.98	2.96	1.99	-15.28	-4.98	3.25
1200	ESg	411.6	291.6	436.00	10.6418	21.87	978121.57	2.34	2.26	-34.72	-11.32	1.39

1201	Gr254b	406.3	289.3	258.00	10.6209	64.70	978164.40	1.43	2.94	-89.65	-29.22	6.96
1202	Gr254c	407.2	288.8	253.00	10.6164	63.22	978162.92	1.25	3.09	-91.19	-29.72	4.41
1203	Gr254d	407.9	288.5	258.00	10.6136	63.25	978162.95	1.23	3.18	-89.65	-29.22	5.55
1204	Gr254e	408.7	288.0	261.00	10.6091	62.69	978162.39	1.25	3.33	-88.72	-28.92	5.78
1205	Gr254f	409.1	287.2	206.00	10.6018	74.17	978173.87	1.50	3.57	-105.70	-34.45	6.31
1206	Gr254g	409.8	285.6	199.00	10.5873	73.31	978173.01	1.43	4.04	-107.86	-35.15	4.39
1207	BA1a	401.5	290.1	298.00	10.6282	55.20	978154.90	1.72	2.70	-77.30	-25.20	5.84
1208	BA1	401.3	289.3	282.00	10.6209	60.06	978159.76	1.59	2.94	-82.24	-26.81	7.48
1209	BA2	401.2	288.3	248.00	10.6118	67.23	978166.93	1.32	3.24	-92.73	-30.23	7.60
1210	BA3	400.9	287.4	205.00	10.6036	75.69	978175.39	1.26	3.51	-106.00	-34.55	7.33
1211	BA4	400.5	286.8	162.00	10.5982	83.66	978183.36	1.19	3.68	-119.27	-38.88	6.46
1212	BA5	400.3	286.0	149.00	10.5909	84.64	978184.34	1.91	3.92	-123.29	-40.18	5.69
1213	BA6	400.2	285.2	182.00	10.5836	75.65	978175.35	1.17	4.16	-113.10	-36.86	3.06
1214	BA7	399.9	284.3	168.00	10.5755	76.60	978176.30	1.09	4.42	-117.42	-38.27	1.28
1215	BA8	399.3	283.4	154.00	10.5673	77.86	978177.56	1.02	4.69	-121.74	-39.68	-0.17
1216	BA9	399.1	282.5	134.00	10.5591	81.26	978180.96	1.02	4.95	-127.91	-41.69	-0.67
1217	BA10	398.7	281.6	110.00	10.5509	86.29	978185.99	1.08	5.22	-135.32	-44.11	-0.31
1218	BA11	398.2	280.7	110.00	10.5427	85.37	978185.07	1.08	5.49	-135.32	-44.11	-0.96
1219	BA12	398.8	280.0	97.00	10.5364	88.71	978188.41	1.13	5.69	-139.33	-45.41	-0.07
1220	BM73	398.9	278.1	73.00	10.5191	94.38	978194.08	1.17	6.25	-146.74	-47.83	1.21
1221	BA14	397.4	279.3	82.00	10.5300	92.05	978191.75	1.07	5.90	-143.96	-46.92	0.30
1222	BA15	394.5	279.9	96.00	10.5355	89.17	978188.87	1.04	5.72	-139.64	-45.51	0.12
1223	BA16/BM90	393.2	280.2	90.00	10.5382	87.41	978187.11	1.30	5.63	-141.49	-46.12	-2.72
1224	BA17	391.3	280.2	127.00	10.5382	82.10	978181.80	1.12	5.63	-130.07	-42.40	-0.51
1225	BA18	389.3	280.3	102.00	10.5391	90.12	978189.82	1.03	5.60	-137.79	-44.91	2.19
1226	BA19	389.7	281.2	113.00	10.5473	86.92	978186.62	1.08	5.34	-134.40	-43.80	1.06
1227	BA20	390.9	283.1	134.00	10.5645	80.70	978180.40	1.00	4.78	-127.91	-41.69	-1.43
1228	BA21	390.2	284.0	122.00	10.5727	79.76	978179.46	0.92	4.51	-131.62	-42.90	-5.21
1229	BA22	391.0	284.4	107.00	10.5764	84.52	978184.22	0.99	4.39	-136.25	-44.41	-3.62
1230	BA23	391.3	285.6	128.00	10.5873	80.40	978180.10	1.03	4.04	-129.77	-42.30	-3.68
1231	P14	391.5	286.1	103.00	10.5918	84.60	978184.30	1.43	3.89	-137.48	-44.81	-4.43
1232	P13	391.4	287.3	137.00	10.6027	76.12	978175.82	1.04	3.54	-126.99	-41.39	-6.59
1233	P12	391.2	288.0	157.00	10.6105	71.59	978171.29	1.43	3.28	-120.82	-39.38	-6.81
1234	P11	391.8	290.0	193.00	10.6273	64.69	978164.39	1.80	2.73	-109.71	-35.76	-6.41
1235	P10	392.5	291.5	285.00	10.6409	45.93	978145.63	1.43	2.29	-81.32	-26.50	-6.84
1236	P9	393.6	292.1	311.00	10.6464	41.36	978141.06	1.40	2.11	-73.29	-23.89	-6.22
1237	P8	393.9	292.7	342.00	10.6518	39.21	978138.91	1.32	1.93	-63.73	-20.77	-2.18
1238	P7	394.3	293.7	395.00	10.6609	27.31	978127.01	1.65	1.63	-47.37	-15.44	-3.01
1239	P6	394.9	294.1	381.00	10.6645	32.78	978132.48	1.37	1.52	-51.69	-16.85	-0.85
1240	P5	395.3	295.2	378.00	10.6745	35.16	978134.86	1.74	1.19	-52.62	-17.15	0.94
1241	P4	395.7	295.7	434.00	10.6791	22.77	978122.47	1.55	1.04	-35.33	-11.52	-0.14
1242	P3	395.9	296.3	481.00	10.6845	14.60	978114.30	2.03	0.86	-20.83	-6.79	1.77
1243	P2	395.3	296.9	475.00	10.6900	20.46	978120.16	1.90	0.68	-22.68	-7.39	6.07
1244	P1	396.0	296.6	485.00	10.6873	20.28	978119.98	1.61	0.77	-19.60	-6.39	7.77
1245	U115	400.2	295.4	436.00	10.6764	21.49	978121.19	2.28	1.13	-34.72	-11.32	-0.19
1246	U116	399.8	295.5	416.00	10.6773	28.27	978127.97	1.75	1.10	-40.89	-13.33	1.87
1247	U117	399.2	294.7	357.00	10.6700	38.02	978137.72	2.04	1.34	-59.10	-19.26	-0.12
1248	U118	398.8	294.5	427.00	10.6682	22.90	978122.60	1.58	1.39	-37.49	-12.22	-1.08
1249	U119	398.3	293.9	372.00	10.6627	36.09	978135.79	1.47	1.57	-54.47	-17.75	0.74
1250	U120	397.7	294.4	368.00	10.6673	37.42	978137.12	1.69	1.42	-55.70	-18.16	1.31
1251	U121	397.8	295.1	394.00	10.6736	32.89	978132.59	1.88	1.22	-47.68	-15.54	2.17
1252	U122	397.9	295.7	427.00	10.6791	26.24	978125.94	1.61	1.04	-37.49	-12.22	1.93
1253	U123	397.7	296.1	449.00	10.6827	24.47	978124.17	1.51	0.92	-30.71	-10.01	4.53
1254	U124	397.6	296.6	487.00	10.6873	19.16	978118.86	1.86	0.77	-18.98	-6.19	7.32
1255	U32	398.5	297.2	508.00	10.6927	14.58	978114.28	1.84	0.59	-12.50	-4.07	6.90
1256	U30	398.0	297.4	493.00	10.6945	18.21	978117.91	1.87	0.53	-17.13	-5.58	7.38
1257	U34	399.1	297.5	567.00	10.6955	1.00	978100.70	1.78	0.50	5.71	1.86	5.45
1258	U35	399.6	297.7	582.00	10.6973	-3.56	978096.14	1.93	0.44	10.34	3.37	4.10
1259	U98	397.6	298.6	538.00	10.7055	8.29	978107.99	1.82	0.17	-3.24	-1.06	6.42
1260	U99	397.0	298.3	509.00	10.7027	16.86	978116.56	1.83	0.26	-12.19	-3.97	9.06
1261	U100	396.7	299.0	561.00	10.7091	4.87	978104.57	1.88	0.05	3.86	1.26	7.72
1262	U101	397.2	299.9	630.00	10.7173	-9.15	978090.55	2.28	-0.22	25.15	8.20	8.18
1263	N1	407.4	310.7	373.00	10.8155	41.29	978140.99	2.61	-3.47	-54.16	-17.65	2.25
1264	N2	408.2	310.8	379.00	10.8164	41.43	978141.13	2.55	-3.50	-52.31	-17.05	3.55
1265	N3	408.4	311.5	374.00	10.8227	42.63	978142.33	2.76	-3.71	-53.85	-17.55	3.71
1266	N4	408.2	312.0	363.00	10.8273	46.47	978146.17	2.96	-3.86	-57.25	-18.66	5.30
1267	N5	408.2	312.4	409.00	10.8309	38.15	978137.85	2.93	-3.98	-43.05	-14.03	6.40
1268	N6	408.1	312.9	471.00	10.8355	25.47	978125.17	3.02	-4.13	-23.92	-7.80	6.56
1269	N7	408.1	313.5	485.00	10.8409	25.76	978125.46	2.98	-4.31	-19.60	-6.39	9.54

1270	N8	408.4	313.8	441.00	10.8436	34.70	978134.40	4.17	-4.40	-33.17	-10.81	10.43
1271	N9	409.1	314.4	327.00	10.8491	60.74	978160.44	3.31	-4.58	-68.35	-22.28	11.71
1272	N10	409.4	315.7	225.00	10.8609	85.59	978185.29	2.90	-4.98	-99.83	-32.54	14.54
1273	N11	409.8	316.7	104.00	10.8700	115.56	978215.26	2.04	-5.28	-137.17	-44.71	18.18
1274	N12	409.3	317.8	75.00	10.8800	108.86	978208.56	1.52	-5.62	-146.12	-47.63	4.59
1275	N13	409.0	318.8	62.00	10.8891	101.16	978200.86	1.21	-5.92	-150.13	-48.93	-6.43
1276	N14	408.8	319.9	56.00	10.8991	99.49	978199.19	1.20	-6.25	-151.99	-49.54	-9.70
1277	N15	408.9	320.8	53.00	10.9073	97.71	978197.41	1.09	-6.53	-152.91	-49.84	-12.48
1278	N16	409.7	321.7	52.00	10.9155	98.79	978198.49	0.78	-6.80	-153.22	-49.94	-12.20
1279	N17	410.3	322.4	58.00	10.9218	98.89	978198.59	0.79	-7.01	-151.37	-49.34	-11.05
1280	N18	410.8	322.8	56.00	10.9255	102.87	978202.57	0.78	-7.14	-151.99	-49.54	-7.61
1281	N19(BM48)	411.9	323.9	48.00	10.9355	107.40	978207.10	0.78	-7.47	-154.45	-50.34	-5.08
1282	N20	414.0	330.8	41.00	10.9982	119.54	978219.24	0.58	-9.58	-156.61	-51.05	3.29
1283	N21	413.5	328.0	45.00	10.9727	117.55	978217.25	0.56	-8.72	-155.38	-50.64	2.97
1284	N22(BM46)	412.0	325.7	46.00	10.9518	114.95	978214.65	0.79	-8.02	-155.07	-50.54	1.51
1285	G57a	404.6	305.6	555.00	10.7691	6.09	978105.79	2.39	-1.93	2.01	0.65	6.23
1286	G57b	405.0	305.6	558.00	10.7691	6.42	978106.12	2.35	-1.93	2.93	0.96	7.13
1287	G57c	405.4	305.6	562.00	10.7691	4.81	978104.51	2.86	-1.93	4.17	1.36	6.87
1288	G57d	405.8	305.7	551.00	10.7700	6.40	978106.10	2.86	-1.96	0.77	0.25	6.14
1289	G57e	406.2	305.8	560.00	10.7709	3.74	978103.44	2.87	-1.99	3.55	1.16	5.33
1290	RLC1	402.8	305.3	558.50	10.7664	6.81	978106.51	1.76	-1.84	3.09	1.01	7.13
1291	RLC2	402.7	305.7	555.00	10.7700	6.88	978106.58	1.77	-1.96	2.01	0.65	6.36
1292	RLC3	402.3	306.0	560.70	10.7727	6.87	978106.57	2.04	-2.05	3.76	1.23	7.72
1293	RLC4	401.9	306.3	566.10	10.7755	6.55	978106.25	2.67	-2.14	5.43	1.77	9.06
1294	RLC5	401.7	306.4	576.00	10.7764	4.42	978104.12	2.92	-2.17	8.49	2.77	9.21
1295	RLC6	401.6	306.5	628.50	10.7773	-7.16	978092.54	3.59	-2.20	24.69	8.05	9.19
1296	RLC7	401.4	306.6	650.00	10.7782	-13.34	978086.36	3.42	-2.23	31.32	10.21	7.28
1297	RLC8	401.3	306.7	683.20	10.7791	-19.41	978080.29	4.54	-2.26	41.57	13.55	9.21
1298	RLC9	401.3	306.9	714.20	10.7809	-28.42	978071.28	5.18	-2.32	51.14	16.67	7.23
1299	U1	399.2	301.5	582.60	10.7318	-1.43	978098.27	2.74	-0.70	10.52	3.43	6.03
1300	U2	399.1	301.8	583.50	10.7345	-1.43	978098.27	2.73	-0.79	10.80	3.52	6.11
1301	U4	399.1	302.2	585.80	10.7382	-2.03	978097.67	2.69	-0.91	11.51	3.75	5.83
1302	U6	399.1	302.9	595.50	10.7445	-6.23	978093.47	3.03	-1.12	14.50	4.73	3.78
1303	U7	399.0	303.0	598.70	10.7455	-6.82	978092.88	2.83	-1.15	15.49	5.05	3.62
1304	U8	399.0	303.0	607.30	10.7455	-8.80	978090.90	2.77	-1.15	18.15	5.91	3.38
1305	U10	398.8	303.1	616.10	10.7459	-10.82	978088.88	2.83	-1.16	20.86	6.80	3.23
1306	U11	398.8	303.0	621.50	10.7455	-11.00	978088.70	2.96	-1.15	22.53	7.34	4.32
1307	U13	398.7	303.0	633.00	10.7450	-14.31	978085.39	2.81	-1.13	26.08	8.50	3.26
1308	U13a	398.7	302.9	669.60	10.7441	-23.00	978076.70	2.75	-1.10	37.37	12.18	2.16
1309	U14	398.6	303.0	637.00	10.7450	-15.48	978084.22	2.51	-1.13	27.31	8.90	2.62
1310	U16	398.4	302.9	666.40	10.7445	-22.13	978077.57	2.78	-1.12	36.38	11.86	2.38
1311	U18	398.5	302.7	665.20	10.7427	-21.68	978078.02	2.52	-1.06	36.01	11.74	2.38
1312	U19	398.4	302.6	674.70	10.7418	-23.12	978076.58	2.46	-1.03	38.95	12.69	2.89
1313	U20	398.4	302.8	681.00	10.7432	-24.72	978074.98	2.85	-1.07	40.89	13.33	2.94
1314	U22?	397.9	302.5	728.10	10.7405	-34.37	978065.33	2.72	-0.98	55.42	18.06	3.04
1315	U25?	397.0	302.4	717.70	10.7400	-30.58	978069.12	3.02	-0.97	52.22	17.02	4.99
1316	U27?	397.1	302.2	688.80	10.7377	-22.99	978076.71	2.28	-0.89	43.30	14.11	5.91
1317	T44A	398.5	300.3	661.00	10.7209	-19.13	978080.57	2.13	-0.34	34.72	11.32	4.39
1318	T44Aa	398.5	300.5	667.00	10.7227	-20.16	978079.54	2.19	-0.40	36.57	11.92	4.61
1319	T44Ab	398.6	300.8	688.00	10.7255	-24.18	978075.52	2.57	-0.49	43.05	14.03	5.24
1320	T44Ac	398.6	301.1	712.00	10.7282	-28.94	978070.76	3.13	-0.58	50.46	16.45	5.94
1321	T44Ad	398.7	301.4	750.00	10.7309	-38.19	978061.51	4.61	-0.67	62.18	20.27	5.99
1322	T44Ae	398.5	300.0	667.00	10.7182	-19.13	978080.57	2.54	-0.25	36.57	11.92	6.13
1323	T44Af	398.4	299.7	671.00	10.7155	-19.34	978080.36	2.93	-0.16	37.80	12.32	7.24
1324	T44Ag	398.1	299.6	630.00	10.7145	-9.69	978090.01	2.52	-0.13	25.15	8.20	7.97
1325	T44Ah	398.0	299.3	603.00	10.7118	-4.16	978095.54	2.03	-0.04	16.82	5.48	7.49
1326	T44Ai	397.8	299.1	570.00	10.7100	4.19	978103.89	2.01	0.02	6.63	2.16	9.01
1327	T44Aj	397.3	298.6	582.00	10.7055	0.68	978100.38	2.33	0.17	10.34	3.37	8.47
1328	TR39	399.4	300.4	672.00	10.7214	-21.69	978078.01	4.34	-0.35	38.11	12.42	6.31
1329	MB1	400.0	301.3	578.40	10.7295	-2.92	978096.78	1.80	-0.62	9.23	3.01	2.80
1330	MB2	399.9	301.2	578.90	10.7291	-3.00	978096.70	1.80	-0.61	9.38	3.06	2.84
1331	MB3	399.9	301.2	578.90	10.7286	-3.10	978096.60	1.80	-0.59	9.38	3.06	2.75
1332	MB4	399.8	301.1	579.30	10.7282	-3.22	978096.48	1.80	-0.58	9.50	3.10	2.73
1333	MB5	399.7	301.1	579.80	10.7277	-3.10	978096.60	1.80	-0.56	9.66	3.15	2.97
1334	MB6	399.6	301.0	580.20	10.7273	-3.11	978096.59	1.81	-0.55	9.78	3.19	3.06
1335	MB7	399.5	301.0	581.30	10.7268	-2.89	978096.81	1.82	-0.53	10.12	3.30	3.54
1336	MB8	399.4	300.9	581.80	10.7264	-2.97	978096.73	2.03	-0.52	10.28	3.35	3.79
1337	MB9	399.3	300.8	582.70	10.7255	-2.11	978097.59	2.24	-0.49	10.55	3.44	5.08
1338	MB10	399.3	300.8	584.90	10.7250	-2.14	978097.56	2.31	-0.47	11.23	3.66	5.59

1339	MB10a	399.2	300.8	586.10	10.7245	-2.40	978097.30	2.33	-0.46	11.60	3.78	5.61
1340	MB11	399.2	300.7	593.90	10.7245	-4.34	978095.36	2.36	-0.46	14.01	4.57	5.33
1341	MB12	399.2	300.7	604.90	10.7245	-7.30	978092.40	2.33	-0.46	17.41	5.67	4.62
1342	MB13	399.1	300.6	617.10	10.7236	-10.59	978089.11	2.37	-0.43	21.17	6.90	3.94
1343	MB14	399.0	300.6	634.50	10.7232	-14.45	978085.25	2.30	-0.41	26.54	8.65	3.65
1344	MB15	399.0	300.6	651.00	10.7232	-17.79	978081.91	2.30	-0.41	31.63	10.31	3.74
1345	MB16	398.9	300.6	656.50	10.7228	-19.35	978080.35	2.37	-0.40	33.33	10.86	3.41
1346	MB17	398.8	300.6	660.20	10.7224	-20.26	978079.44	2.27	-0.39	34.47	11.24	3.18
1347	MB18	398.7	300.4	661.00	10.7218	-20.13	978079.57	2.28	-0.37	34.72	11.32	3.51
1348	MB19	398.7	300.4	660.10	10.7218	-19.70	978080.00	2.27	-0.37	34.44	11.23	3.73
1349	MB20	398.6	300.4	659.10	10.7218	-19.20	978080.50	2.21	-0.37	34.13	11.12	3.97
1350	MB21	398.5	300.4	653.80	10.7218	-17.91	978081.79	2.15	-0.37	32.50	10.59	4.10
1351	U45	398.4	300.1	651.90	10.7191	-17.30	978082.40	2.13	-0.28	31.91	10.40	4.38
1352	U46b	398.1	300.4	657.70	10.7218	-18.58	978081.12	2.29	-0.37	33.70	10.98	4.38
1353	U53r?	392.9	300.3	562.00	10.7209	8.68	978108.38	2.78	-0.34	4.17	1.36	12.25
1354	U55?	391.9	300.8	638.00	10.7259	-9.30	978090.40	3.12	-0.50	27.62	9.00	10.26
1355	273k	399.5	298.8	548.00	10.7073	5.64	978105.34	1.90	0.11	-0.15	-0.05	5.86
1356	U46	398.0	300.7	661.00	10.7287	-18.86	978080.84	2.24	-0.59	34.72	11.32	4.51
1357	U47	397.4	300.8	655.50	10.7300	-16.08	978083.62	2.14	-0.64	33.02	10.76	6.00
1358	U59	396.9	301.0	608.50	10.7324	-3.86	978095.84	2.26	-0.72	18.52	6.04	8.48
1359	U48	396.3	301.3	613.00	10.7342	-4.06	978095.64	2.28	-0.78	19.90	6.49	9.18
1360	ICE-GG	395.9	301.6	660.00	10.7370	-14.73	978084.97	2.46	-0.87	34.41	11.22	8.38
1361	U58	395.5	301.8	665.00	10.7388	-14.76	978084.94	2.30	-0.93	35.95	11.72	9.17
1362	U61	395.3	302.6	713.00	10.7467	-25.28	978074.42	2.89	-1.19	50.76	16.55	8.96
1363	U49	395.3	301.3	643.00	10.7347	-9.37	978090.33	2.26	-0.79	29.16	9.51	10.07
1364	U50	394.4	301.1	570.00	10.7324	8.11	978107.81	2.18	-0.72	6.63	2.16	12.37
1365	U51	394.2	301.3	612.00	10.7351	-0.23	978099.47	2.29	-0.81	19.60	6.39	12.79
1366	U52	393.8	301.4	575.00	10.7356	7.16	978106.86	2.29	-0.82	8.18	2.67	12.46
1367	U53	393.3	301.3	565.00	10.7324	7.85	978107.55	2.78	-0.72	5.09	1.66	11.67
1368	U54	392.6	301.3	542.00	10.7342	12.77	978112.47	3.53	-0.78	-2.01	-0.65	12.49
1369	U62	392.5	302.5	670.00	10.7449	-14.22	978085.48	2.94	-1.13	37.49	12.22	11.19
1370	BM738	392.7	303.4	738.00	10.7532	-27.79	978071.91	3.01	-1.40	58.48	19.06	11.56
1371	GRA284	400.1	301.4	577.45	10.7305	-2.84	978096.86	1.79	-0.65	8.93	2.91	2.64
1372	E+80	400.0	301.3	578.47	10.7305	-2.91	978096.79	1.85	-0.65	9.25	3.01	2.84
1373	E+70	399.9	301.3	578.43	10.7305	-2.70	978097.00	1.87	-0.65	9.24	3.01	3.06
1374	E+60	399.8	301.3	579.06	10.7305	-2.70	978097.00	1.87	-0.65	9.43	3.07	3.20
1375	E+50	399.7	301.3	579.59	10.7305	-2.33	978097.37	1.91	-0.65	9.59	3.13	3.71
1376	E+40	399.6	301.3	579.96	10.7305	-1.96	978097.74	1.97	-0.65	9.71	3.16	4.22
1377	E+20	399.4	301.3	580.34	10.7305	-1.28	978098.42	2.23	-0.65	9.83	3.20	5.24
1378	E+15	399.4	301.3	580.62	10.7305	-1.20	978098.50	2.30	-0.65	9.91	3.23	5.45
1379	E+10	399.3	301.3	580.89	10.7305	-1.23	978098.47	2.38	-0.65	10.00	3.26	5.55
1380	E+5	399.3	301.3	581.50	10.7305	-1.31	978098.39	2.45	-0.65	10.18	3.32	5.67
1381	0,0	399.2	301.3	583.26	10.7305	-1.72	978097.98	2.51	-0.65	10.73	3.50	5.68
1382	W+5	399.2	301.3	586.07	10.7305	-2.38	978097.32	2.83	-0.65	11.59	3.78	5.93
1383	W+15	399.1	301.3	599.73	10.7305	-5.42	978094.28	3.72	-0.65	15.81	5.15	6.62
1384	W+20	399.1	301.3	611.74	10.7305	-8.40	978091.30	3.78	-0.65	19.52	6.36	6.20
1385	W+25	399.0	301.3	645.14	10.7305	-15.54	978084.16	4.00	-0.65	29.82	9.72	6.22
1386	W+30	399.0	301.3	673.36	10.7305	-21.80	978077.90	4.01	-0.65	38.53	12.56	5.85
1387	W+35	398.9	301.3	697.82	10.7305	-27.25	978072.45	4.08	-0.65	46.08	15.02	5.56
1388	W+40	398.9	301.3	717.01	10.7305	-31.64	978068.06	4.30	-0.65	52.00	16.95	5.37
1389	W+45	398.8	301.3	733.44	10.7305	-35.44	978064.26	4.28	-0.65	57.07	18.60	4.98
1390	W+50	398.8	301.3	745.66	10.7305	-38.20	978061.50	4.28	-0.65	60.84	19.83	4.76
1391	W+55	398.7	301.3	752.26	10.7305	-39.59	978060.11	4.22	-0.65	62.88	20.49	4.69
1392	W+60	398.7	301.3	757.71	10.7305	-40.87	978058.83	4.32	-0.65	64.56	21.04	4.64
1393	NW3	398.6	301.6	818.73	10.7305	-57.55	978042.15	9.23	-0.65	83.39	27.18	5.56
1394	W+65	398.6	301.3	759.77	10.7305	-41.41	978058.29	4.37	-0.65	65.20	21.25	4.57
1395	W+70	398.6	301.3	757.14	10.7305	-40.76	978058.94	4.27	-0.65	64.39	20.99	4.58
1396	W+80	398.5	301.3	740.07	10.7305	-36.27	978063.43	3.59	-0.65	59.12	19.27	4.83
1397	W+90	398.4	301.3	725.35	10.7305	-32.11	978067.59	2.93	-0.65	54.58	17.79	5.27
1398	W+100	398.3	301.3	714.67	10.7305	-29.42	978070.28	2.69	-0.65	51.28	16.71	5.50
1399	W+110	398.2	301.3	704.37	10.7305	-27.13	978072.57	2.38	-0.65	48.10	15.68	5.34
1400	W+120	398.1	301.3	701.05	10.7305	-26.83	978072.87	2.41	-0.65	47.08	15.34	4.98
1401	W+130	398.0	301.3	704.28	10.7305	-27.64	978072.06	2.50	-0.65	48.07	15.67	4.93
1402	W+140	397.9	301.3	701.31	10.7305	-27.22	978072.48	2.66	-0.65	47.16	15.37	4.90
1403	W+150	397.8	301.3	692.16	10.7305	-24.94	978074.76	2.46	-0.65	44.33	14.45	5.07
1404	W+170	397.6	301.3	689.44	10.7305	-24.17	978075.53	2.44	-0.65	43.49	14.18	5.25
1405	W+180	397.5	301.3	697.47	10.7305	-25.75	978073.95	2.59	-0.65	45.97	14.98	5.50

APPENDIX 3B The elevation data

The precision of the gravity station elevation data is critical to the estimation of the overall BCG anomaly errors (Appendix 3A). Ideally, all gravity stations should be levelled by theodolite to produce elevation errors of less than ~0.20 m, and therefore BCG uncertainties less than 0.05 mGal. (The ICE gravity stations incorporated into this study were all levelled by theodolite to a precision of ~0.05 m, Leandro, *pers. comm.*). In practice, however, levelling surveys are both time and labour intensive and were not used for most of the areas surveyed during this study, except the key traverses across the caldera floor and margins (Figure 3.1). Instead, the majority of the station elevations were determined by running barometric altimeter surveys. These were conducted simultaneously with the gravity surveys, rather than as individual processes, allowing time to repeat both.

The precision levels for barometric altimetry are only as good as the control on the climatic variables that need to be corrected for to derive an absolute elevation difference from the barometric difference. The altimeter data reduction technique is described here, followed by an account of the relatively straightforward use of theodolite levelling in this study.

Altimeter data:

A set of four Thommen Altimeters were used during this study; the data reduction technique and conversion tables used were specified by Marinho de Carvalho *et al.* (1977). Altimeters operate on the principle that atmospheric pressure decreases with elevation and the many factors that effect this relationship can be divided into i) absolute parameters that are applicable to ideal stable atmospheric conditions and ii) parameters related to variable climatic conditions. The former relate to the density of the local air column between stations; temperature, humidity and the average elevation above sea level. The latter are concerned with local climate fluctuations (e.g. the passage of weather fronts and the pressure variations associated with wind velocity changes) overprinted on the general diurnal pressure variations that are related to the daily temperature changes in the entire atmosphere.

Field technique

The field procedure operated on the principle that a daily pressure variation curve could be used to subtract the change in pressure during the time period between altimeter readings at successive stations. One pair of altimeters were read at the base camp in Guayabo (close to Gra-91, Figure 3.1) at half hour to one hour intervals by ICE personnel (Figure 3B.1) and one pair of altimeters was used during the field survey. It was assumed that, in general, the climatic variation experienced by the base pair reflected the field conditions. It was not, however, strictly possible to extrapolate this assumption for the surveys of the extreme areas, such as the exposed and often clouded Miravalles summit area.

Figure 3B.1 The recorded inverse of the daytime barometric variation over a period of 16 days at Guayabo. A similar pattern is followed each day, but the differences between the daily extremes is more variable.

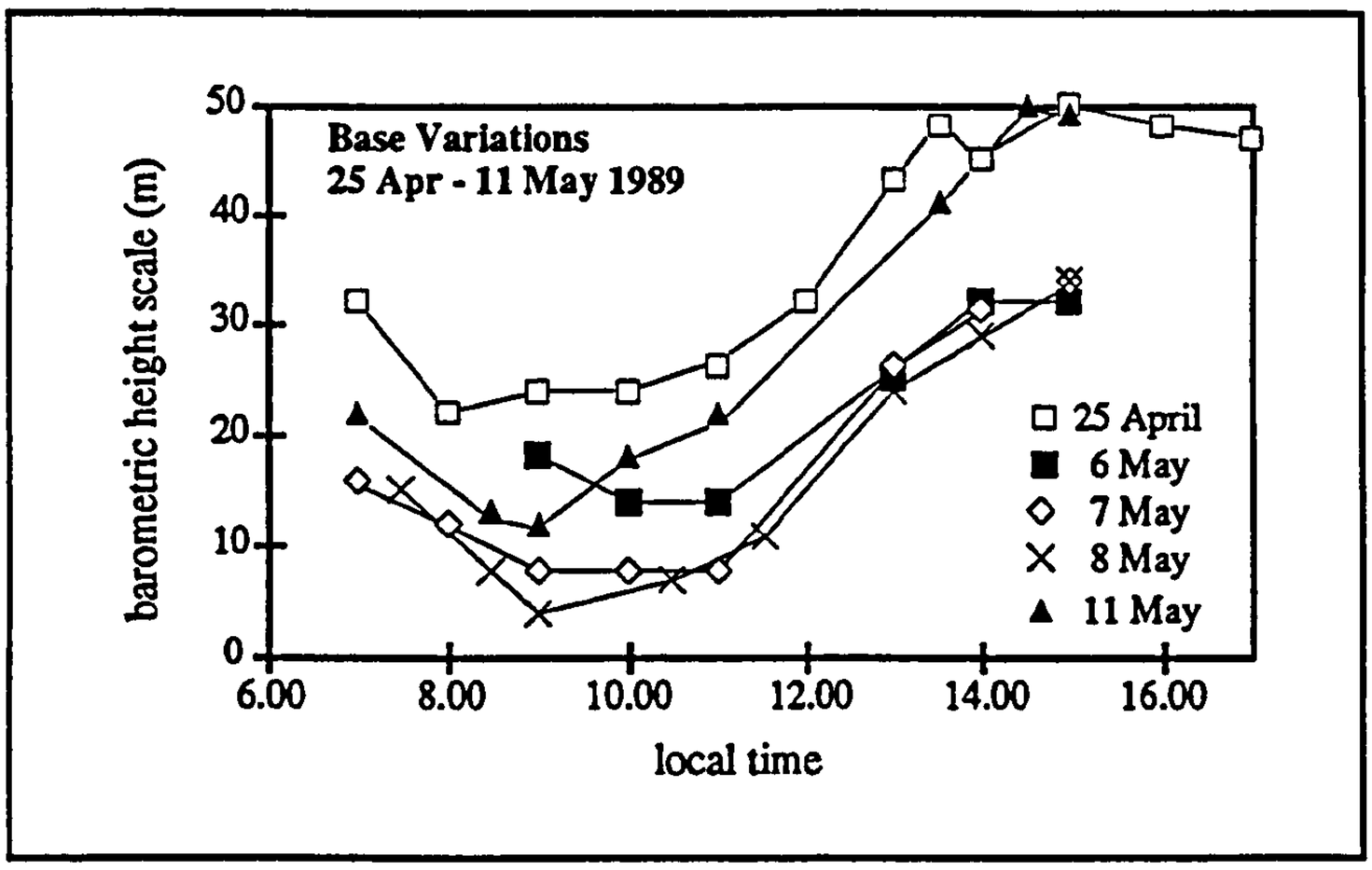

The daily pressure variation followed a similar pattern each day (the barometric height at the base, shown in Figure 3D.1, varies as the inverse of pressure); the apparent barometric height dipped in the early morning, levelling off during the morning, rising through midday, and levelling off again in mid afternoon. There is a suggestion from the few late afternoon base readings that the barometric height falls off again in the late afternoon, which is reasonable given the morning reading is always less than in the afternoon. This reflects the density variation of the local air column due to temperature changes. (The actual curves used to subtract the base variation were smoothed between readings).

All four altimeters were read together at the beginning and end of each survey day to check for drift; drift was not common, and was always restricted to the field pair. In practice the drift was found to be analogous to the mechanical tares experienced by gravimeters (Appendix 3A) and the data from the errant altimeter could be isolated between successive stations. At each station the raw barometric height, both the wet and dry temperatures and the time were recorded.

A looping procedure was adopted to check i) that the general pressure variation was similar to that at the base, ii) to isolate the particular meter when an inter-meter tare was noticed and iii) to network the altimeter results between surveys. Stations were read once on the outward leg of a survey and readings were repeated at several stations during the return leg. At every available opportunity, the surveys were tied to either benchmarks of the national grid (located in Figure 3.1) or levelled gravity stations. Usually it was possible to tie both ends of the survey line to a levelled reference station. The surveys on the flanks of Volcán Miravalles, however, could only be tied to control points at the foot of the volcano. The station R6k is located at the broad crest of the summit (Figure 3.29 a) for which a spot height of 2028 m was determined from stereo air photos by the Instituto Geográphico de Costa Rica. The corrected barometric height of 2026 m for R6k was thus within 2 m of this value.

Altimeter Data Reduction

Where possible, the repeat readings in the field were used to construct a skeleton variation curve and the missing parts of the curve were 'calibrated' from the base station curve. In this way it was possible to derive an apparent barometric height variation curve that represented the field conditions. The apparent barometric height change that occurred in the specified time interval between successive stations was subtracted from the observed barometric height difference to give $\Delta h''$. The final, *corrected* barometric height difference, Δh, between two stations is derived from $\Delta h''$ from the corrections specified by Marinho de Carvalho *et al.* (1977). The given parameters are:

$\Delta h''$ barometric height difference

H_m average altitude

t_d average dry bulb temperature

t_w average wet bulb temperature

l_m average latitude

The process is divided into two stages, the first temperature correction gives the preliminary corrected height difference:

$$\Delta h' = \Delta h'' \left\{\frac{t_d - (15 - 6.5\text{x}10^{-3} H_m)}{273}\right\}$$ .....$\Delta h'$ is used for the final corrections.

$\Delta h = \Delta h' + C_{u1} + C_{u2} + C_g$ .....where C_{u1} and C_{u2} are the first and second humidity corrections and C_g is the gravity correction, based on the average latitude, l_m.

C_{u1} is a function of both the humid temperature and the pressure and was derived by hand from the tables specified by Marinho de Carvalho *et al.* (1977),

$C_{u2} = - 6.62\text{x}10^{-4} \Delta h' \Delta t_w$ .....where $\Delta t_w = t_d - t_w$, and finally,

$C_g = \Delta h' \{0.00264 \cos 2l_m + \frac{H_m}{3189000}\}$.

All the corrections, except C_{u1}, were computed using a microcomputer spreadsheet, designed during this study. The most important corrections were the 1st temperature and the 1st humidity corrections. Δh was calculated between successive stations (the so-called jump method), starting with the difference from the reference point, both on the the outward and the return legs of the survey. The successive differences were simply integrated to derive the elevation of all the stations. The results of the outward and return legs were compared to check for consistency and then averaged to produce the final station elevations (given in Table 3A.2). An integration process was preferred to calculations of the height differences between individual stations and the reference station as the latter would have introduced greater averaging errors, given that climatic conditions often changed rapidly in the field.

Errors

Uncertainties were mostly climate-related (i.e. associated with the applicability of the pressure variation curves) and not usually associated with operator errors, such as misreading. The reading precision for Thommen altimeters is 0.5 m and for the thermometers, 0.5°C. The changes in climate between successive stations, however,

introduced averaging errors into the temperature and humidity corrections as t_d, t_w and Δt were no longer representative of the air column between the two stations.

An example of the repeatability of results is shown in Table 3B.1. The RLC 1-20 stations (tied to Gra-50, an ICE gravity station in Rincon de la Cruz) refer to the Cerros La Montañosa Nettleton traverse (location in Figure 3.1 and cross section in Figure 3.11). The stations were levelled by ICE personnel in the 1989 field season, following two altimeter surveys by this author over the first part of the traverse. The data in Table 3B.1 only represent the first half of the profile and station RLC-10 is not a reference point; elevations for the second half, though levelled by theodolite, were measured only once by altimeter, and therefore are not shown here. The average altimeter data are consistently ~3-4 m lower than the levelled data, suggesting the discrepancy may not be random, but the culpable source of error could not be isolated.

Table 3B.1 The results of two 1989 altimeter surveys in April (to the nearest metre) compared to the levelled data.

RLC stations	14th April altimeter	20th April altimeter	Altimeter average	Levelled (ICE)	Difference
1	557	554	555	558.5	+3.5
2	554	551	552	555.0	+3
3	558	556	557	560.7	+2
4	560, 563	560, 562, 564	562	566.1	+4
5	573	571	572	576.1	+4
6	624	625	624	628.5	+4
7	647,646	647	647	650.0	+3
8	677	681	679	683.2	+4
9	709	713	711	714.2	+3
10	711, 711	713, 713	712	715.4	+3

The repeatability of the altimeter results, as shown in Table 3D.1, was better than 5 m, and this has been used as a general health warning to the elevations derived from one altimeter survey. Repeatability was improved to ~2 m for surveys where the time periods between successive readings were shorter, over relatively even terrain during settled climatic conditions, as, for example, for the few altimeter surveys of the caldera floor area (points located in Figure 3.1).

Theodolite measurements

Precise levelling was required for the microgravity studies (Chapter 5), the surveys over the western caldera wall (including the Nettleton profiles) and their extensions over the caldera floor (Chapter 3, located in Figure 3.1). A Nikon DTM-1 electronic distance measurement (EDM) theodolite was used for this purpose. The general field technique was to position the theodolite such that a maximum number of stations could be tied to the reference station in the minimum number of steps. Internal corrections were made for temperature and pressure, and the general uncertainty in vertical differences, gauged from experience rather than the manufacturer's specifications, is less than 5 cm over horizontal distances of less than 1 km, the maximum distance between stations levelled during this study. Errors were compounded each time the theodolite was moved during a survey, but as the number of jumps in any one survey varied from 1 to 10 (short sight lines in vegetated areas), the uncertainty is between ~5-30 cm, which results in a Bouguer corrected gravity (BCG) errors of ~0.01-0.06 mGal (Appendix 3A). The precision is therefore more than sufficient for the Bouguer gravity station elevations.

The horizontal sight lengths during the microgravity surveys were usually less than 1 km, and triangulation of stations showed a repeatability of better than 5 cm, which converts to a BCG gravity uncertainty of 10 μGal, more precise than the repeatability of the gravity data (Chapter 5).

APPENDIX 3C Densities

The results of the density measurements of the surface exposure and borehole cuttings samples are given here. The measurement technique is described in Chapter 3 (Section 3.3).

i) Surface sample densities

The samples have been grouped into stratigraphic order in the same order as Table 3.1. The listings overleaf include the sample number, grid coordinates (comparable with the Figures in the main text), geographic location, lithology, grain (ρ_r), wet (ρ_w) and dry (ρ_d) densities and the porosity, ($\varnothing$).

Densities of surface samples, exposed outcrop unless stated as a block

Sample	E'ing	N'ing	Location	Lithology	ρ_r	ρ_w	ρ_d	ϕ
			Caldera Wall Lavas					
EC8	410.1	294.5	Cerro Espiritu Santo	Ol Andesite	2.78	2.75	2.74	1
CLM1	402.8	307.7	Cerros La Montañosa	Ol Andesite block	2.65	2.55	2.49	6
CLM2	402.1	307.4	Cerros La Montañosa	Andesite block	2.78	2.77	2.77	0
CLM4	402.2	309.2	Cerros La Montañosa	Basalt block	2.88	2.88	2.88	0
EC74	405.3	305.6	Cerros La Montañosa	Andesite	2.81	2.76	2.73	3
EC37	404.9	306.8	Cerros La Montañosa	Andesite block	2.48	2.41	2.35	6
EC38	404.9	306.8	Cerros La Montañosa	Andesite block	2.68	2.65	2.64	1
EC14	399.0	300.6	West Caldera wall	Andesite	2.67	2.65	2.64	1
EC39	399.5	303.7	West Caldera wall	Andesite	2.74	2.73	2.72	1
EC45	399.6	298.3	West Caldera wall	Andesite	2.74	2.71	2.70	1
EC46	399.3	300.0	West Caldera wall	Ol Andesite	2.76	2.75	2.74	1
EC48	399.4	300.2	West Caldera wall	Andesite	2.75	2.74	2.73	1
EC57	399.3	300.4	West Caldera wall	Ol Andesite	2.74	2.72	2.70	2
EC75	400.1	297.7	Laguna Mogote south scarp	Ol Andesite	2.76	2.73	2.72	1
CM1b	399.2	300.9	Cerro Mogote base	Ol Andesite	2.72	2.69	2.66	3
CM2	399.1	301.0	Cerro Mogote base	Ol Andesite	2.77	2.75	2.73	2
CM4	399.0	301.2	Cerro Mogote base	Ol Andesite	2.66	2.62	2.59	3
CMQ6	398.9	303.2	Cerro Mogote base	Ol Andesite	2.64	2.61	2.59	2
EC4	398.9	303.2	Cerro Mogote quarry	Ol Andesite	2.70	2.67	2.65	2
SH1b	399.2	399.5	Laguna Mogote west scarp	Ol Andesite	2.78	2.78	2.77	0
SH7b	398.9	303.2	Cerro Mogote quarry	Andesite/Dacite ?	2.45	2.34	2.26	8
SH8	398.9	303.2	Cerro Mogote quarry	Andesite/Dacite ?	2.30	2.14	2.02	12
EC49	400.5	304.1	Hill 777	Dacite	2.57	2.51	2.47	4
EC50	400.5	304.0	Hill 777	Dacite	2.54	2.50	2.47	3
				Andesites Average	2.72	2.70	2.68	1.9
				Std dev	0.08	0.10	0.11	1.7
CM6	398.9	301.2	Cerro Mogote flank tuff (6?)	Basalt block	2.82	2.76	2.73	3
CM7	398.8	301.2	Cerro Mogote flank tuff (6?)	Basalt block	2.78	2.76	2.75	1
CM9	398.7	301.3	Cerro Mogote flank	Mogote Basalt	2.84	2.81	2.80	1
CM10	398.5	301.6	Cerro Mogote summit	Mogote Basalt	2.83	2.80	2.79	1
CM11	398.5	301.6	Cerro Mogote summit	Mogote Basalt	2.85	2.84	2.84	0
SH16	398.5	301.6	Cerro Mogote summit	Mogote Basalt	2.61	2.48	2.41	8
				Unvesic. Average	2.82	2.79	2.78	1.2
				Std dev	0.03	0.03	0.04	1.1
			Extra-Caldera Lavas					
EC25	408.4	313.8	Fila La Armenia, N8 quarry	Grey Andesite	2.50	2.45	2.44	1
EC26	408.4	313.8	Fila La Armenia, N8 quarry	Vesic. Andesite	2.40	-	-	-
EC29	408.0	312.9	Fila La Armenia, N5	Andesite	2.74	2.73	2.73	0
EC30	408.9	314.0	Fila La Armenia, N8-N9	Andesite	2.52	2.49	2.47	2
EC72	411.4	310.2	Fila La Arm. (Finca Arm.)	Andesite	2.78	2.77	2.77	0
EC44	396.3	296.3	Q. Gloria (sub-Biotite Tuff)	Andesite	2.70	2.68	2.67	1
EC52	410.1	284.9	Q. Santa Fe (sub-Biotite Tuff)	Andesite	2.63	2.62	2.61	1
U47	397.3	300.9	San Jorge-Guayabo road	Andesite Block	2.62	2.57	2.53	4
EC53	395.8	301.8	San Jorge-Guayabo road	Andesite Block	2.71	2.69	2.68	1
EC55	394.8	301.9	San Jorge-Finca Estrella road	Andesite Block	2.69	2.68	2.67	1
U62	402.6	302.5	Rincon road quarry	Andesite (post-Bi. Tuff)	2.71	2.71	2.71	0
EC56	397.0	298.3	Rio C. Gordo (sub-Bi.Tuff)	Andesite	2.63	2.62	2.61	1
				Average	2.64	2.64	2.63	1.1
				Std dev	0.11	0.10	0.11	1.1
			Extra-Caldera Tuffs					
EC13c	393.9	301.4	West San Jorge quarry	(Guayabo?) Tuff Matrix	2.26	2.06	2.00	6
EC1	395.6	295.5	Limonal, P4	Upper Grey Ignimbrite	2.30	2.04	1.90	14
EC27	411.3	322.4	San Jose de Upala, N18-N19	Upper Grey Ignimbrite	1.94	-	-	-
EC31	391.3	285.6	BA 23, north west of Bagaces	Upper Grey Ignimbrite	1.87	-	-	-
EC2	393.8	292.5	Cuesta Magnitos, P8-P9	Biotite Tuff	2.39	1.95	1.67	28
EC3 (1a)	392.1	290.3	Cuesta Magnitos, P10-P11	Biotite Tuff	2.19	1.79	1.46	33
EC3 (1b)					2.17	1.77	1.43	34
EC3 (2a)					1.81	1.55	1.29	26
EC3 (2b)					1.84	-	-	
EC32	399.0	282.3	Salitral, BA9	Biotite Tuff	1.96	-	-	-
EC33	400.0	286.5	Salitral, BA4	Biotite Tuff	1.80	-	-	-
EC15	392.6	301.3	San Jorge	Biotite Tuff	2.09	-	-	-
				Intra-sample Average	2.10	1.96	1.76	20.3
				Std dev	0.22	0.13	0.25	12.4

Surface samples continued

Sample	E'ing	N'ing	Location	Lithology	ρ_b	ρ_w	ρ_d	ϕ
			Tuff Lithics					
EC70a	409.1	300.7	Santa Rosa Pumice	2 Px Andesite	2.76	2.76	2.76	0
EC70b	409.1	300.7	Santa Rosa Pumice	2 Px Andesite	2.73	2.73	2.73	0
EC70c	409.1	300.7	Santa Rosa Pumice	2 Px Andesite	2.22	2.14	2.07	7
SH17	401.7	297.3	La Ese-Guayabo road cut	2 Px, Ol Andesite	2.75	-	-	-
SH20	401.1	297.0	La Ese-Guayabo road cut	2 Px, Ol Andesite	2.67	-	-	-
EC13b	393.9	301.4	West San Jorge quarry	Dacite	2.44	2.30	2.21	9
EC13d	393.9	301.4	West San Jorge quarry	2 Px Andesite	2.73	2.72	2.72	0
EC41a	400.5	397.4	S. Ex-Caldera Margin (6)	U. Tuff Lithics (andesite)	2.46	2.38	2.33	5
EC41b	400.5	397.4	S. Ex-Caldera Margin (6)	U. Tuff Lithics (andesite)	2.37	2.29	2.24	5
EC41c	400.5	397.4	S. Ex-Caldera Margin (6)	U. Tuff Lithics (andesite)	2.42	2.37	2.33	4
				Average	2.55	2.46	2.42	3.75
				Std dev	0.19	0.24	0.27	3.45
EC13a	393.9	301.4	West San Jorge quarry	Bi. Microgranite	2.41	2.33	2.28	5
SH29a	400.6	295.7	La Ese quarry (6)	Microgranite	2.60	2.53	2.48	5
SH29b	400.6	295.7	La Ese quarry (6)	Microgranite	2.60	2.54	2.50	4
SH29c	400.6	295.7	La Ese quarry (6)	Microgranite	2.62	2.52	2.46	6
SH29d	400.6	295.7	La Ese quarry (6)	Microgranite	2.63	2.54	2.48	6
				Average	2.57	2.49	2.44	5.0
				Std dev	0.09	0.09	0.09	0.9
EC13c	393.9	301.4	West San Jorge quarry	Welded Tuff	2.40	2.29	2.22	7
EC58a	400.6	295.7	La Ese quarry (6)	Welded Tuff	2.48	2.41	2.36	5
EC58b	400.6	295.7	La Ese quarry (6)	Welded Tuff	2.43	2.39	2.36	3
EC58c	400.6	295.7	La Ese quarry (6)	Welded Tuff	2.50	2.35	2.24	11
EC58d	400.6	295.7	La Ese quarry (6)	Welded Tuff	2.53	2.39	2.30	9
SH22	401.7	297.3	La Ese-Guayabo road cut (6)	Welded Tuff/Rhyolite	2.55	-	-	-
SH23	401.7	297.3	La Ese-Guayabo road cut (6)	Basic Welded Tuff	2.50	-	-	-
SH24	401.1	297.0	La Ese-Guayabo road cut (6)	Basic Welded Tuff	2.46	-	-	-
SH25	401.1	297.0	La Ese-Guayabo road cut (6)	Basic Welded Tuff	2.48	-	-	-
SH27	401.0	296.3	La Ese-Guayabo road cut (6)	Basic Welded Tuff	2.50	-	-	-
SH28	401.0	296.3	La Ese-Guayabo road cut (6)	Basic Welded Tuff	2.44	-	-	-
				Average	2.48	2.37	2.30	7.1
				Std dev	0.04	0.05	0.07	3.2
			V. Miravalles Lavas					
EC21	408.7	306.5	North-west flank	Andesite	2.64	2.59	2.55	4
EC23	408.4	305.7	North-west flank	Andesite	2.57	2.51	2.47	4
EC24	408.7	305.2	North-west flank	Ol Andesite	2.50	2.44	2.40	4
SH10	408.8	302.2	West flank, Cerro Hinchada	2 Px Andesite	2.70	2.65	2.62	3
SH11b	408.8	302.2	West flank, Cerro Hinchada	2 Px Andesite	2.58	2.52	2.48	4
R3e1	408.7	301.9	West flank	Ol Andesite	2.61	2.57	2.55	2
R3e2	408.7	301.9	West flank	Andesite	2.43	2.20	2.03	17
R3e3	408.7	301.9	West flank	Andesite	2.64	2.55	2.50	5
R5c	407.6	302.7	West flank	Andesite	2.54	2.39	2.29	10
R5ef	408.8	303.0	West flank	Andesite	2.63	2.37	2.20	17
R6a	406.4	304.2	West flank	Ol Andesite	2.68	2.53	2.44	9
R6e1	408.6	303.1	West flank	Andesite	2.66	2.55	2.49	6
R6e2	408.6	303.1	West flank	Andesite	2.53	2.45	2.41	4
				Average	2.59	2.49	2.42	6.8
				Std dev	0.08	0.12	0.16	5.0
			Santa Rosa Lavas					
IC11	407.2	298.4	S-east of C. Los Caballos	2 Px Andesite	2.72	2.67	2.64	3
IC12	407.2	298.4	S-east of C. Los Caballos	Andesite	2.60	2.48	2.41	7
IC17	407.6	298.8	N-east of C. Los Caballos	Andesite	2.66	2.63	2.61	2
EC61	411.0	300.6	Bajo Los Chiqueros	Andesite block	2.63	2.54	2.48	6
EC62	411.0	299.8	Bajo Los Chiqueros	Andesite	2.65	2.61	2.60	1
EC63	410.2	300.0	Bajo Los Chiqueros	Andesite	2.58	2.53	2.50	3
EC67a	409.3	299.4	Santa Rosa- Bajo Los Chiq.	Andesite	2.39	2.35	2.32	3
EC67b	409.3	299.4	Santa Rosa- Bajo Los Chiq.	Andesite	2.40	2.29	2.22	7
EC67c	409.3	299.4	Santa Rosa- Bajo Los Chiq.	Andesite	2.37	2.26	2.18	8
				Average	2.56	2.48	2.44	4.4
				Std dev	0.13	0.15	0.17	2.6

ii) Borehole cuttings densities

The results of the density analyses of cuttings samples from the geothermal wells of the Miravalles Geothermal Project, conducted during the 1989 field season, are presented here. The grain density, ρ_r, was measured using the technique described in Chapter 3. The sample depth (m) and ρ_r data tables are listed in the numerical order of the wells PGM-1 to PGM-15. LC=Late Cabro Muco Volcanic Unit, CM=Cabro Muco Andesite Unit, PUM=Pumice Unit, VS= Volcano-Sedimentary Unit, (LT=Lava-Tuff Unit of ELC, 1986 a), AA=Acidic Andesite Unit, IG=Ignimbrite Unit. Stratigraphic unit average densities shown in italics.

(m)	ρ_r	(m)	ρ_r	(m)	ρ_r
1	LC		CM		VS
14	2.47	315	2.32	501	2.62
20	2.52	333	2.44	528	2.51
39	2.32	351	2.45	537	2.47
46	2.51	370	2.50	567	2.61
57	2.31	388	2.61	592	2.43
74	2.50	406	2.61	610	2.51
92	2.38	423	2.67	629	2.44
109	2.21	446	2.70	647	2.41
127	2.27	464	2.67	665	2.44
147	2.44	484	2.64	705	2.52
158	2.17		*2.56*	722	2.39
171	2.14			742	2.52
187	2.16			762	2.60
203	2.18			782	2.55
214	2.10			802	2.55
232	2.19			823	2.53
249	2.10			837	2.65
265	2.10			861	2.49
285	2.23			876	2.60
302	2.32			890	2.67
	2.28			909	2.69
				920	2.70
				938	2.65
				962	2.56
				977	2.54
					2.55

(m)	ρ_r	(m)	ρ_r	(m)	ρ_r
2	LC		CM		AA
4	2.01	345	2.65	537	2.56
15	2.35	366	2.60	552	2.57
27	2.58	381	2.41	564	2.56
46	2.56	402	2.70	582	2.59
64	2.66		*2.59*	607	2.59
82	2.69			622	2.53
101	2.63			640	2.55
119	2.59	VS		659	2.57
139	2.39	421	2.71	677	2.52
149	2.56	436	2.56	695	2.58
171	2.39	454	2.67	710	2.56
189	2.51	476	2.69	729	2.52
207	2.39	494	2.58	768	2.60
226	2.16	512	2.55	787	2.58
241	2.41		*2.63*	805	2.50
262	2.21			826	2.57
277	2.57			845	2.60
290	2.59				*2.56*
302	2.33				
323	2.48				
	2.45				

(m)	ρ_r	(m)	ρ_r	(m)	ρ_r
3	LC		CM		VS
9	2.63	244	2.54	625	2.46
21	2.56	262	2.59	643	2.53
34	2.21	280	2.47	655	2.46
46	2.21	314	2.33	665	2.51
55	2.30	335	2.30		*2.49*
73	2.23	354	2.25		
91	2.10	375	2.31		
113	2.38	393	2.65		
134	2.40	412	2.68		
168	2.52	430	2.61		
195	2.52	445	2.65		
210	2.13	463	2.67		
229	2.18	482	2.60		
	2.34	500	2.64		
		518	2.66		
		543	2.63		
		561	2.62		
		579	2.42		
		595	2.40		
		610	2.49		
			2.53		

(m)	ρ_r	(m)	ρ_r	(m)	ρ_r	(m)	ρ_r	(m)	ρ_r	(m)	ρ_r
5	LC		CM		AA		VS		LT		IG
8	2.38	259	2.55	530	2.62	872	2.58	1021	2.50	1381	2.58
17	2.24	280	2.27	552	2.61	893	2.56	1043	2.52	1402	2.58
27	2.37	296	2.54	573	2.60	915	2.68	1064	2.57	1424	2.57
40	2.29	317	2.54	595	2.58	936	2.41	1085	2.58	1445	2.56
55	1.97	338	2.45	616	2.58	957	2.51	1107	2.53	1466	2.59
67	2.24	360	2.57	659	2.60	979	2.47	1128	2.46	1488	2.62
76	2.14	381	2.58	680	2.53	1000	2.46	1162	2.53	1509	2.63
88	2.13	402	2.60	701	2.60		*2.52*	1171	2.57	1524	2.62
101	2.29	424	2.61	723	2.56			1192	2.49	1576	2.63
113	2.23	445	2.61	744	2.57			1213	2.63	1601	2.58
134	2.44	466	2.60	765	2.57			1232	2.61	1622	2.58
155	2.15	488	2.61	787	2.61			1256	2.47	1643	2.63
177	1.97	509	2.60	808	2.63			1277	2.66	1665	2.65
198	2.06		*2.55*	829	2.57			1299	2.68	1689	2.62
216	2.18			851	2.56			1317	2.50	1707	2.58
238	2.43				*2.59*			1338	2.57		*2.60*
	2.22							1360	2.60		
									2.56		

(m)	ρ_r	(m)	ρ_r
5R	LC		CM
6	2.37	249	2.42
18	2.51	264	2.33
30	2.43		*2.38*
42	2.27		
54	2.00		
66	2.16		
78	2.38		
90	2.21		
102	2.31		
123	2.16		
144	2.33		
165	2.09		
186	1.97		
207	2.30		
228	2.43		
	2.26		

Appendix 3C (continued)

(m)	ρ_r	(m)	ρ_r	(m)	ρ_r	(m)	ρ_r	(m)	ρ_r	(m)	ρ_r	(m)	ρ_r	(m)	ρ_r
10	LC		AA	**11**	LC		CM	**12**	LC	**15**	LC		VS		VS
6	2.60	579	2.55	3	2.43	323	2.67	5	2.15	6	2.43	573	2.42	1110	2.57
24	2.52	598	2.50	9	2.44	341	2.57	21	2.52	18	2.27	597	2.21	1131	2.51
43	2.66	619	2.62	15	2.44	351	2.59	39	2.42	27	2.25	618	2.16	1152	2.54
61	2.70	637	2.62	21	2.49	360	2.62	60	2.31	42	2.40	639	2.40	1176	2.26
79	2.37	659	2.56	27	2.64	378	2.66	78	2.39	54	2.44	660	2.44	1200	2.46
104	2.43	677	2.58	34	2.48	396	2.61	99	2.23	66	2.28	681	2.56	1221	2.47
116	2.37	698	2.62	40	2.37	415	2.59	114	2.60	78	2.55	702	2.46	1242	2.57
152	2.19	720	2.63	46	2.53	433	2.62	135	2.56	90	2.66	723	2.59	1263	2.34
171	2.17	738	2.50	52	2.35	451	2.61	174	2.45	102	2.55	744	2.51	1284	2.41
189	2.11	753	2.45	58	2.23	470	2.61		*2.40*	123	2.49	765	2.50	1305	2.58
207	2.29	771	2.51	64	2.33	488	2.67		CM	138	2.24	786	2.51	1326	2.53
226	1.99	796	2.55	70	2.27	506	2.59	195	2.66	144	2.67	810	2.56	1347	2.66
244	2.39	820	2.61	88	2.10	524	2.60	216	2.67	165	2.61	834	2.46	1368	2.57
262	2.27	838	2.50	95	2.09		*2.62*	237	2.67	186	2.54	846	2.36	1389	2.59
280	2.38	857	2.66	101	2.13		AA	261	2.67	207	2.42	855	2.41		*2.50*
302	2.36	875	2.56	107	2.31	543	2.58	279	2.26	231	2.47	876	2.40		IG
317	2.36	893	2.66	113	2.30	561	2.43	303	2.44	252	2.12	897	2.42	1410	2.60
	2.36	912	2.64	119	2.30	579	2.43	330	2.10	273	2.37	918	2.49	1431	2.63
	CM	927	2.57	125	2.41	601	2.48	345	1.98	285	1.98	939	2.47	1452	2.62
335	2.60	945	2.63	131	2.36	616	2.40	366	2.58	306	2.16	960	2.43	1476	2.52
354	2.59	960	2.61	137	2.53	634	2.51	387	2.63	324	2.15	981	2.34	1503	2.50
372	2.43	982	2.70	143	2.57	652	2.59	396	2.65	345	2.27	1005	2.45	1527	2.49
390	2.57	1000	2.63	149	2.59	677	2.42	411	2.63		*2.38*	1026	2.35	1551	2.58
409	2.60	1021	2.58	155	2.59	692	2.41		*2.50*		PUM	1047	2.38	1575	2.53
427	2.61		*2.59*	174	2.14	704	2.58		VC	366	1.92	1068	2.46	1602	2.59
445	2.61		VS	180	2.12	723	2.40	430	2.21	384	1.96	1089	2.42	1653	2.54
463	2.64	1043	2.57	192	2.16	741	2.62	441	2.35	405	1.46	*0.10*	*2.43*	1704	2.56
473	2.60	1061	2.60	198	2.46	759	2.62	462	2.42	426	0.96			1755	2.59
540	2.59	1076	2.58	204	2.13	780	2.65	483	2.43	444	1.41			1806	2.59
	2.58	1098	2.62	210	2.34	801	2.68	504	2.41	468	1.29			1854	2.57
		1116	2.47	216	2.60	822	2.71	522	2.31	489	1.64			1908	2.60
		1134	2.47	223	2.56	843	2.58	546	2.44	510	1.97			1959	2.58
			2.55	229	2.49	882	2.71	560	2.35	531	2.18			2010	2.56
			LT	232	2.45	924	2.52	564	2.41	552	2.42			2022	2.60
		1152	2.58	235	2.28	939	2.69	576	2.46		*1.72*			*0.04*	*2.57*
		1171	2.60	241	2.30	1014	2.67	708	2.38						
		1189	2.62	247	2.29		*2.56*	771	2.46						
		1207	2.58	253	2.29			*0.07*	*2.39*						
		1226	2.45	259	2.56										
		1241	2.61	265	2.65										
		1262	2.57	271	2.67										
		1256	2.58	277	2.67										
			2.57	284	2.58										
				302	2.52										
				0.17	*2.40*										

Figure 2.9 a The revised east-west stratigraphy from detailed borehole drilling reports (details in Section 2.3). Emphasis is on correlation of lithological units, not stratigraphic units, therefore in the interests of clarity, only key units shown . (See Figures 2.2 a and 2.5 for location). The Pumice Unit (PUM) is proposed to be younger than the CMA, the exact nature of the contact is modelled in Chapter 3 (Profile AA). The lava-tuff VS at PGM-15 is thought to have been part of a western andesite stratovolcano, (Volcán Guayabo) whereas the AA source was to the east. The top of the Ignimbrite Unit is at almost the same elevation in all wells, except perhaps PGM-1 where the presence of the IG is inferred from low drilling velocities, suggesting no major vertical displacement between wells, other than on the proposed faults bordering the anomalous stratigraphy at PGM-1.

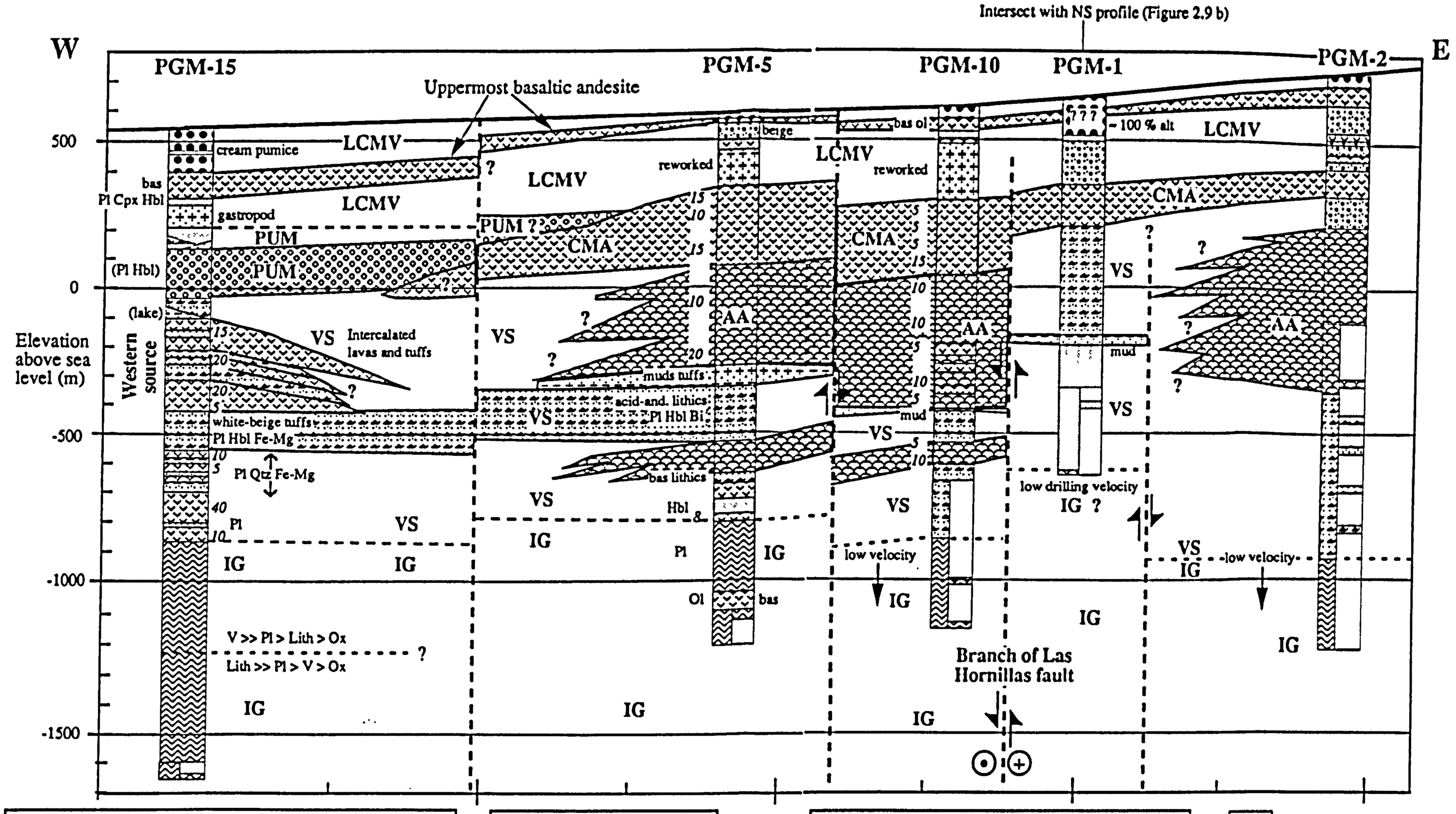

Lithologies

Lahars	Volcanic breccia
Andesite lavas	Lithic tuffs
bas Basaltic andesite lavas	Sediments
Acidic andesite lavas	Reworked tuffs
Crystal-vitric Tuffs	Pumice
	Welded tuffs

10	Porphyritic index
Pl	Plagioclase
Hbl	Hornblende
Bi	Biotite
Fe-Mg	Mafic minerals
Qtz	Quartz
Ol	Olivine
Ox	Oxides
(hbl)	Traces only
Lith	Lithic Fragments
V	Vitrics-glass

Stratigraphic Units

LCMV	Late Cabro Muco Volcanic Unit
PUM	Pumice Unit
CMA	Cabro Muco Andesite Unit
AA	Acidic Andesite Unit
VS	Volcano-Sedimentary Unit
IG	Ignimbrite Unit

1 cm = 150 m
No vertical exaggeration

Full recovery of cuttings
No recovery, interpolated
Cored section
Inferred fault
Inferred contact

Figure 2.9 b The revised north-south stratigraphy (See Figure 2.9 a for key, see Figures 2.2 a and 2.5 for location). Intersection of east-west section at PGM-1. The upper CMA lavas at PGM-3 may be distinct from the lower CMA lavas (as separated by the breccia at PGM-12). The breccia at PGM-12 could therefore correlate with the LCMV (See Section 2.3 for discussion). For continuity of shallow stratigraphy south of PGM-12 see Figure 2.10 a.

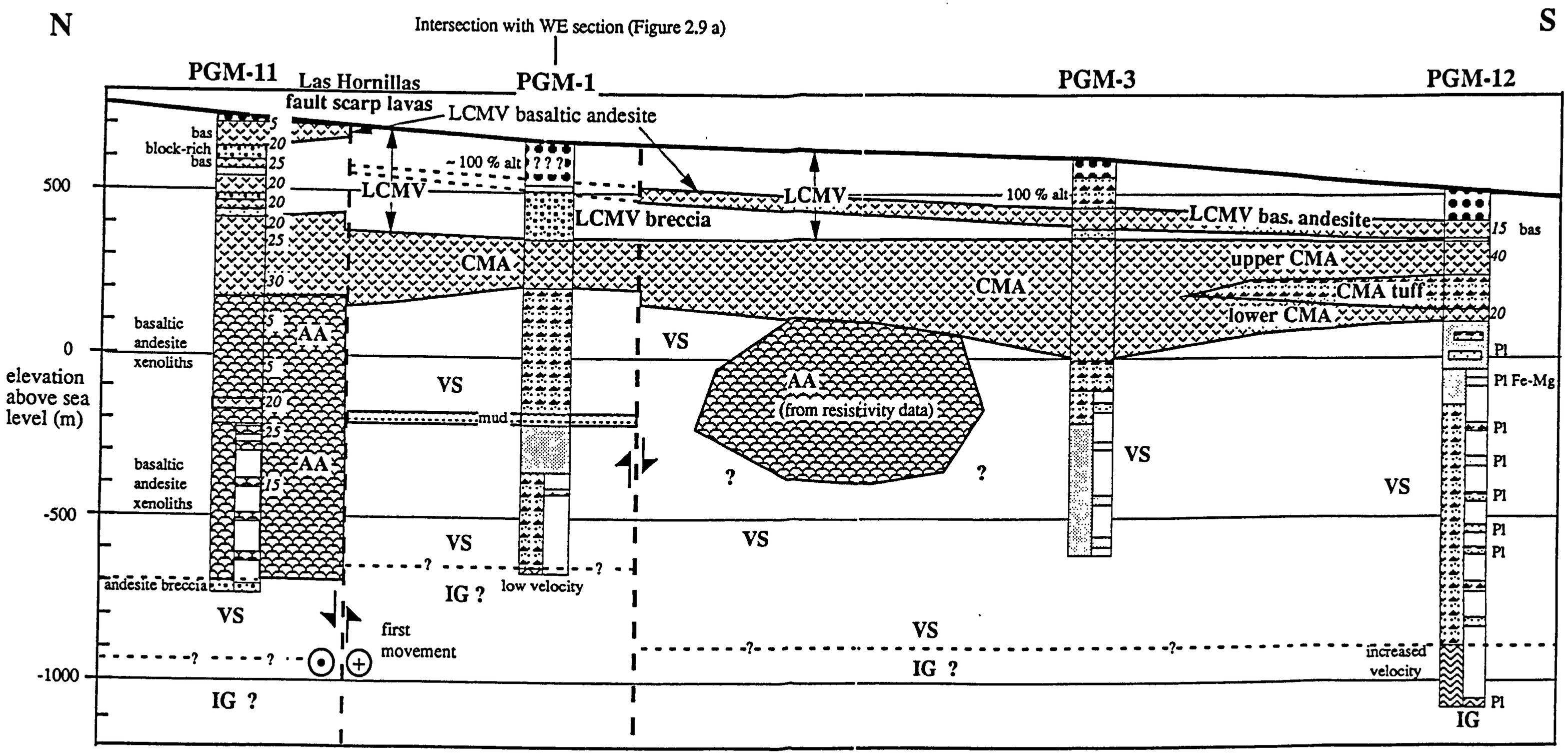

Figure 2.10 a Shallow stratigraphy from Temperature Gradient (PH-) Boreholes, Deep (PGM-) Boreholes and surface samples. Faults are shown in Figures 2.5 and 2.10 b. Some of the thin LCMV andesites drilled may be large blocks in debris flows rather than *in situ* lavas. Discussion of correlations in Chapter 2.

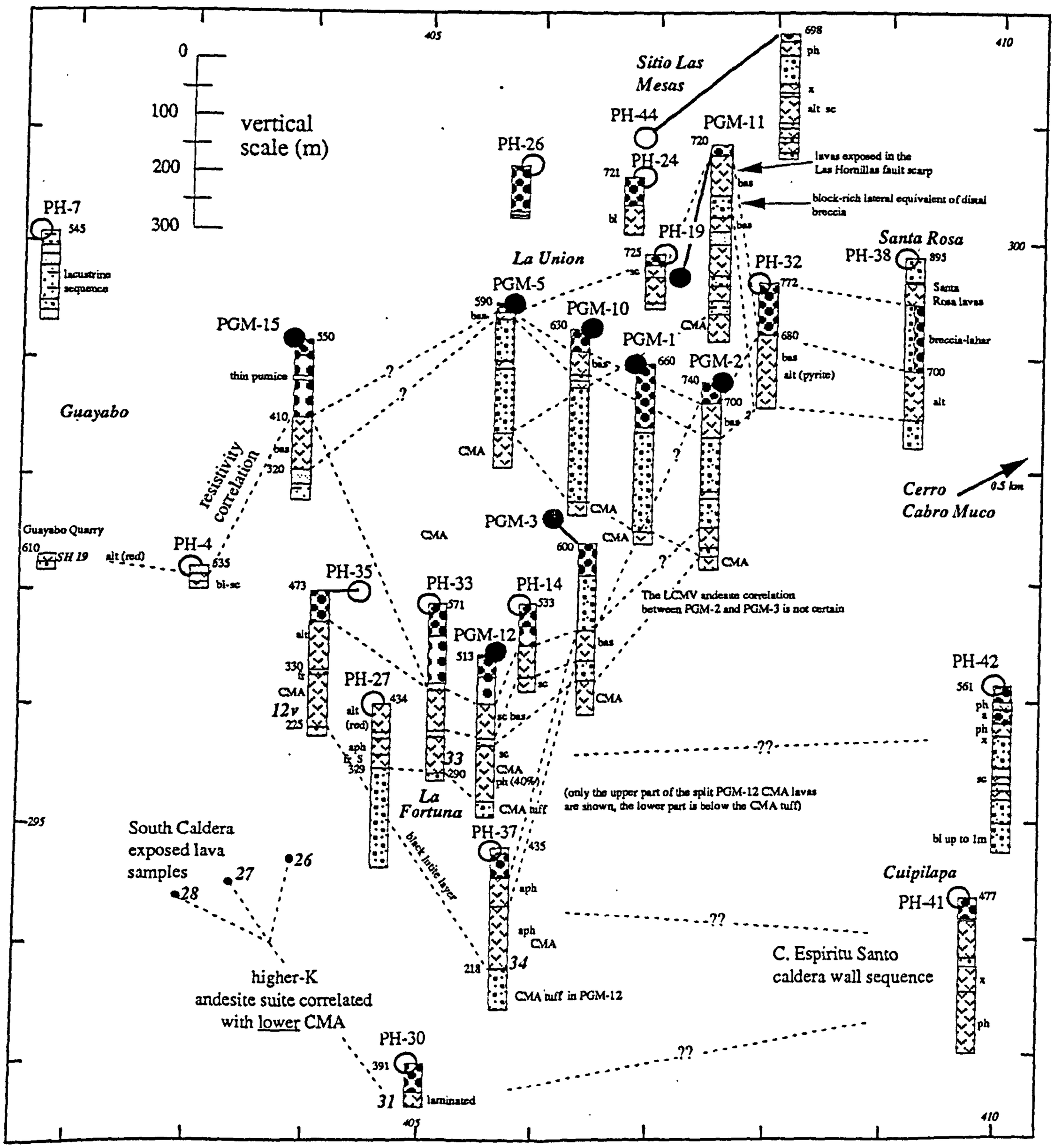

Lahars
Volcanic Breccia - Tuff
Andesite Lavas
Lithic Tuffs
Sediments (lacustrine-alluvial)
Crystal-Vitric Tuffs
PH- temperature gradient boreholes
PGM- deep geothermal wells

CMA	Cabro Muco Andesite Unit
aph	Aphanitic
ph (40)	Porphyritic (index)
bas	Basaltic andesite (petrographically defined)
sc	Scoriaceous
bl	Blocky (a-a lava)
alt	Alteration
S	Sulphur
fr	Fractured

Correlation
610 Elevation a.s.l.
35 Lava Sample

GEOLOGICAL MAP

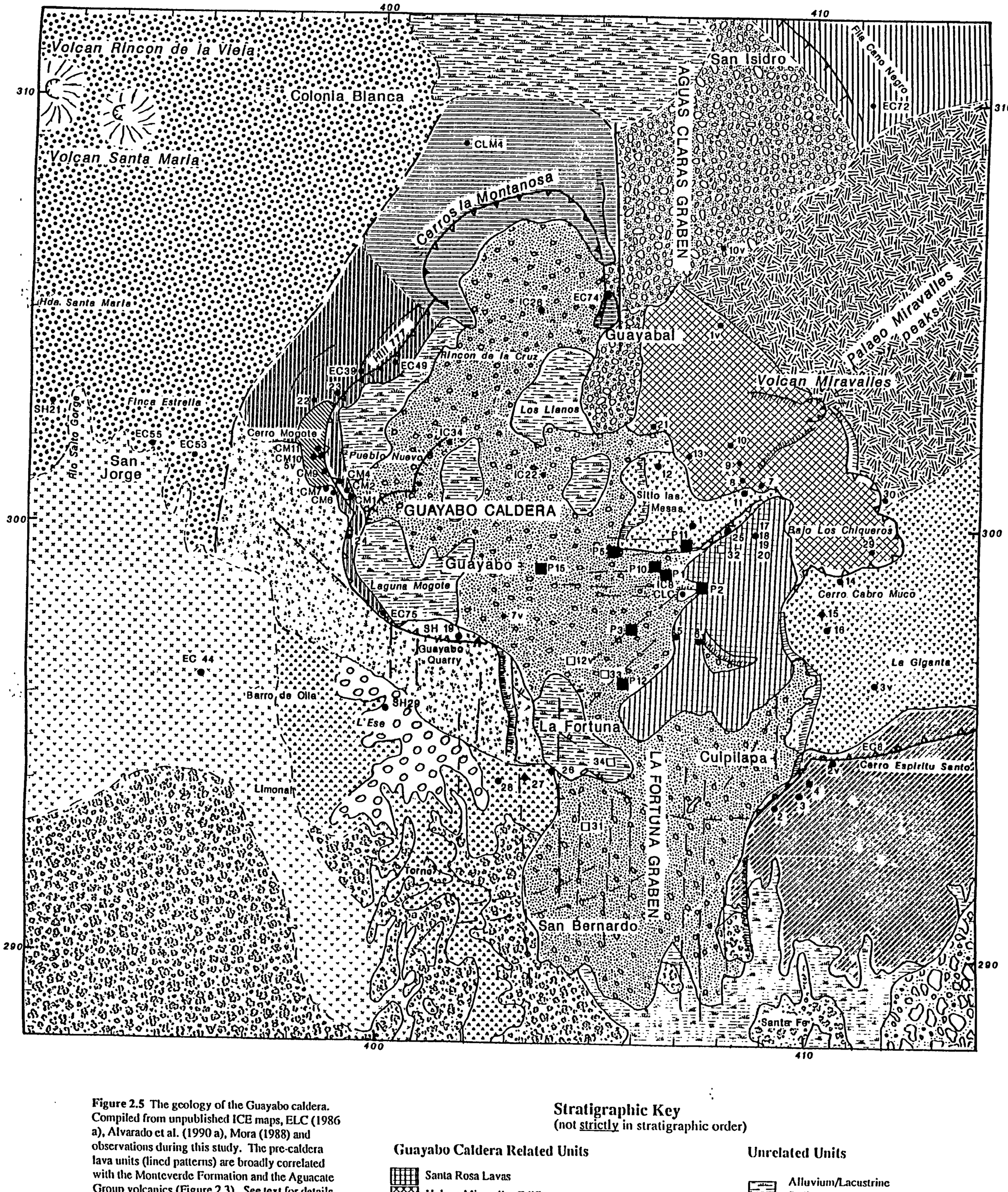

Figure 2.5 The geology of the Guayabo caldera. Compiled from unpublished ICE maps, ELC (1986 a), Alvarado et al. (1990 a), Mora (1988) and observations during this study. The pre-caldera lava units (lined patterns) are broadly correlated with the Monteverde Formation and the Aguacate Group volcanics (Figure 2.3). See text for details.

■P15 Deep, PGM- borehole
Approximate stratigraphic boundary
Major collapse structure
morphotectonic scarp
ELC (1986 a) southern caldera margin lineament
" with inferred downthrow
●12 lava sample
□31 PH-well lava sample

Stratigraphic Key
(not strictly in stratigraphic order)

Guayabo Caldera Related Units

- Santa Rosa Lavas
- Volcan Miravalles Edifice
- Debris Flow-Lahar (Guayabo-La Fortuna)
- Debris Flow-Lahar (Aguas Claras)
- Palaeo-Miravalles Stratocone Complex Edifice
- Cabro Muco-La Giganta Stratocone Edifice

Unrelated Units

- Alluvium/Lacustrine Sediments
- Volcan Tenorio Lahar
- Undifferentiated Rincon de la Vieja Complex

Tuffs

- Guayabo Proximal Breccia (and undifferentiated late tuffs)
- La Ese Pumice
- Hornblende Tuff
- Upper Grey Ignimbrite
- ◄ — — — — — — — — — stratigraphically older
- Biotite Tuff

Guayabo caldera wall and older lavas

- Mogote Basalts
- Espiritu Santo Unit
- West Caldera Wall Unit
- Cerros la Montanosa Unit
- Fila La Armenia Unit